Nanomaterials for the Life Sciences

Edited by Challa Kumar

WILEY-VCH

Nanostructured Oxides

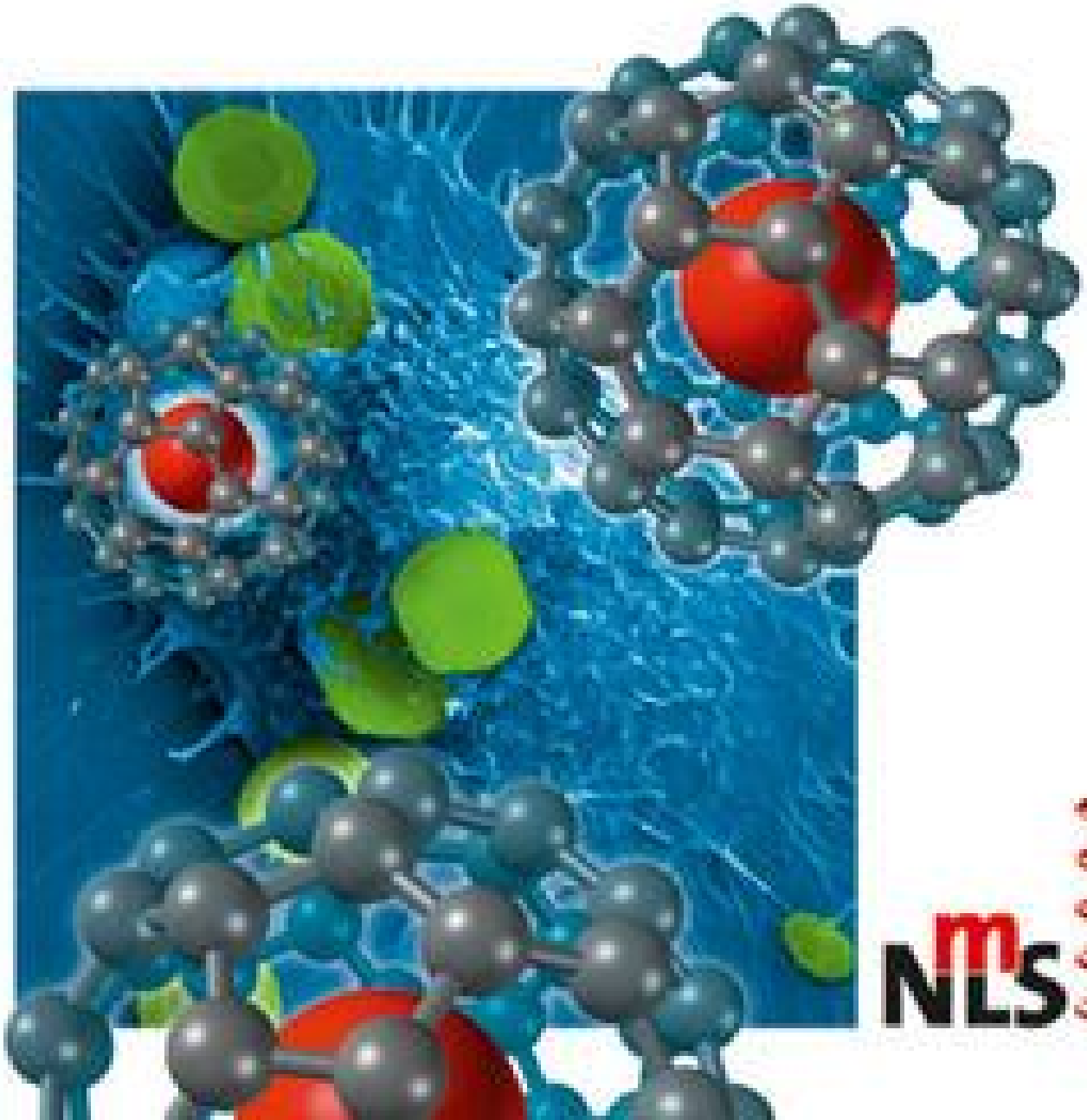

NLS

Contents

Nanomaterials for the Life Sciences Vol. 2: Nanostructured Oxides. Edited by Challa S. S. R. Kumar

ISBN: 978-3-527-32152-0

1
The Biomimetic Synthesis of Metal Oxide Nanomaterials

Leila F. Deravi, Joshua D. Swartz and David W. Wright

1.1
Introduction

Traditionally, synthetic approaches for the production of functional metal oxide materials have involved high-temperature reaction environments with energy-intensive techniques such as laser ablation, ion implantation, chemical vapor deposition (CVD), photolithography or thermal decomposition [1]. The incorporation of these techniques has provided a rapid prototyping technique, essential for the commercial development of current minimum feature-sized semiconducting integrated circuits. However, the production of these devices has been achieved at a high price, with the primary challenges currently faced by high-throughput fabrication laboratories including the high cost of laborers and instruments, high-temperature reaction conditions, and a surplus in generated waste [1]. In fact, the cost of fabrication facilities are estimated to reach an outstanding US$100 billion per facility by the year 2020, as the demand for smaller, lighter and faster materials continues to grow [1]. But, more importantly, manufacturers are progressing in this manner at the expense of the environment, as they accumulate hazardous chemical wastes [2]. For decades, research teams in the semiconductor industry have been seeking alternative methods to passivate not only the rate of waste production but also the cost of spending.

The most accessible resource for the synthesis of functional materials under ambient conditions is found in biology. From highly ordered nanostructures to genetically controlled reactive surfaces, systems in biology perpetually demonstrate their ability to find effective solutions to multifaceted, real-world problems using a rigorous process of natural selection [3–7]. The versatility of biology's incredible portfolio encourages researchers to develop modified syntheses derived from Nature. Hence, their findings have been successfully organized into the field of biomimetics, or bioinspired research, which encompasses alternative approaches towards developing nanomaterials with technological applications [8]. Based primarily on the designs, mechanisms and processes found in Nature, biomimetics

Nanomaterials for the Life Sciences Vol. 2: Nanostructured Oxides. Edited by Challa S. S. R. Kumar

ISBN: 978-3-527-32152-0

encompasses the field of structural biology while interfacing engineering, materials science, physics and chemistry [4, 8].

Biomimetics infers the manipulating and mimicking of natural architectures and processes of biologically produced minerals (biominerals) to direct the synthesis of non-natural materials. For instance, the architecture of one of the most abundant biological species on the planet – the virus – has recently been manipulated to serve as containers for the synthesis of a variety of functional molecular cargoes [9, 10]. In particular, the positively charged interior of the cowpea chlorotic mottle virus (CCMV) has been used as a container for the nucleation of spatially confined metal oxide nanomaterials [10]. On a larger and more complex scale, versatile strategies for substrate modification have been developed directly, through inspiration from the surface-mediated mineralization of biological organisms [3]. The eggshell matrix proteins from the Chinese soft-shelled turtle (composed primarily of aragonite, $CaCO_3$) were isolated, and revealed properties that are necessary for embryonic survival [3]. It was suggested that the matrix proteins contained pelovaterin peptides as their major unit that self-assembled into micelles, altering the interfacial energy of the eggshell [11]. Applications of such controlled mineralization could be applied to the successful construction of functional two-dimensional (2-D) reactive surfaces, with reduced nonspecific adsorption [12–15].

Bioinspired research is based on identifying and emulating the principles of biomineralization in natural systems, instead of copying them directly. In fact, most strategies incorporated by natural systems are not directly applicable to engineered materials, so the need for alternative synthetic routes are required for the incorporation of non-natural elements, such as barium, nickel, copper or aluminum, with functional nanoscale properties [1, 8]. From a materials perspective, highly intact biological structures such as diatoms, bacteria, proteins or butterfly wings provide an excellent source of inspiration for their synthesis. In this chapter we have included the details of a wide variety of mediated nanomaterial syntheses, their response to variable parameters, and their ability to retain a functionalized, controlled stability over time.

1.2 Metal Oxides in Nature

To date, as many as 60 biominerals have been identified as being necessary for the correct function of organisms, and more than 60% of these are reported to be coordinated to either hydroxyl moieties or water molecules, enabling the rapid release of ions in solution [7]. Metal oxides, in particular, provide a fundamental stepping-stone for the development of functional nanomaterials. In an oxidative environment, such as the atmosphere of the Earth, oxides are the lowest free energy states for most metals in the Periodic Table and demonstrate applications ranging from semiconductors to insulators [16]. As insulators, SiO_2 and Al_2O_3 are the two most commonly used supports for catalysis, as they are nonreducible

oxides [16]. Semiconductors, such as ZnO and SnO_2, have high electrical resistivities that provide alternative templates for gas sensors [16].

Surprisingly, the properties associated with metal oxides in technology are not so far removed from what is observed in natural systems. Through precisely tuned processes, Nature is able to synthesize a variety of metal oxide nanomaterials under ambient conditions; the magnetic navigation device found in magnetotactic bacteria (MTB) is one such example [17]. Here, magnetite (Fe_3O_4) nanocrystals are aligned with the Earth's geomagnetic field and contained within specific organelles known as magnetosomes [17]. Fresh water salmon, for example, utilizes these magnetic nanoparticles in the nasal cavities of their forehead as a biomagnetic compass during migration [18].

1.2.1 Components of Biomineralization

Nature dictates the basic structure and function of metal oxides in biology by a set of genetically controlled rules. In order to utilize these principles as inspiration for a variety of non-natural biomaterial syntheses, we must first understand their purpose. For example, organic ligands in the form of an amino acid side chain, lipids or carbohydrates – all of which are found in biological systems – direct the assembly of highly structured metal oxide nanomaterials [19]. Free metal ions act as Lewis acids in the hydrolysis of a precursor before it completely binds to the donor ligand (Lewis base) [20]. In addition, most of these metals in Nature follow similar trends, as laid out by the hard–soft acid–base (HSAB) theory [20]. The charge associated with the Lewis acid metal facilitates an energetically favorable nucleophilic attack on the carbonyl of the ligand. Because of the effective charge of the metal–ligand coordination, there are two alternative ways that this attack can occur. 'Soft metals' (Pt^{2+}, Au^{2+}, Cu^{2+}, Cd^{2+}) that are large and polarizable with low oxidation states bind with 'soft ligands' (carbonyls, CN^-, RS^-) in order to balance their charge [20]. However, 'hard metals' (first row transition metals) are smaller and less polarizable, and are balanced by accepting lone pair electrons associated with 'hard ligands', such as H_2O, amines, phosphates or alcohols [20]. The ligand donor type can affect the redox potential of the coordinated metal, its stereochemistry, and its subsequent reactivity within a biological system.

With that in mind, there are several examples in Nature where ligands are used to create metal oxide structures. In order to identify the components that adhere specifically to metal surfaces, various research groups have developed methods for screening libraries of up to 10^7 protein or peptide sequences that are responsible for inducing specific metal oxide mineralization [21, 22]. Once the sequence is selected, optimal peptide- or non-peptide-based mimics can be synthesized and subsequently applied to a wide range of nanomaterial syntheses. Among the techniques developed to isolate specific metal-bound peptides or proteins, phage display (PD) and cell surface display (CSD) are the most widely used [19, 21]. Combinatorial PD is used to specify the selectivity of the peptide–substrate interaction. In this method, a phage is created on an ensemble of bacterial particles, each

displaying different combinations of amino acids that are fused to the surface protein of the metal particle [23]. Peptides bound specifically to the crystal surface are then eluted from the surface, amplified using the polymerase chain reaction (PCR), and re-reacted up to five separate times [19]. After the fourth and fifth cycles, the resultant phage is sequenced, and the peptide responsible for binding to the surface of the crystal is identified [19].

An alternative approach to identifying surface ligands is that of CSD. Here, the process involves an analytical approach for the quantification of binding constants and dissociation rates *in situ* of up to 10^4 protein molecules per cell [24]. CSD permits the isolation of proteins that display ligand-binding, catalytic or electrochemical properties. Protein libraries on a specific cell surface can be labeled with a soluble ligand and quantitatively screened for reactivity by using flow cytometry [24]. Although, the identification of biomolecules specific for a metal is crucial in developing a particular biomimetic synthesis, it must be understood that peptides and proteins, alone, are not responsible for metal oxide formation in biology. In fact, the properties of these biomolecules *in situ* are a direct result of their reaction environment [25].

1.2.2 Biomineralization Optimization

From the supramolecular to the cellular level, assemblies of lipids, glycoproteins or nucleotides in Nature are necessary determinants, defining specific reaction sites along organelles, membranes or cell walls [20]. Understanding the basic theory, process and components behind the biomineralization of metal oxides is the first step in developing functional biomimetic materials. As noted before, the strategies and precursors incorporated by natural systems cannot be directly applied to engineered materials. For this reason, alternative routes are necessary to build and optimize the properties specific to metal oxide nanomaterials. The specific reaction conditions (length of reaction time, pH) are often tailored, depending on the desired structure and reactivity of the material; however, a typical approach to biomimetic synthesis often requires a developed precursor, in the form of a metal salt, suspended or dissolved in an aqueous medium, and coordinated to a structure-directing agent. Both, natural (peptides, starches, proteins) and synthetic (dendrimers, block copolymers) polymers can be used as structure-directing agents for inducing the biomineralization of metal oxides [6]. They assemble in an ionic solution to direct the size, shape and mean distribution of the resultant product. Recent investigations have even incorporated surface-modified macromolecular templates in the form of a polystyrene latex bead, to direct the control and morphology of metal oxides (Figure 1.1).

Previously, diblock copolymers of ethylene oxide (EO), methacrylic (MAA) and double hydrophilic graft copolymers (PMAA or poly(vinyl sulfonate) backbones) were used separately without the latex beads to synthesize ZnO nanoparticles. It was demonstrated that the electrostatic charge associated with copolymers of vinyl-sulfonate exhibit a more active range of control over the resultant structure than

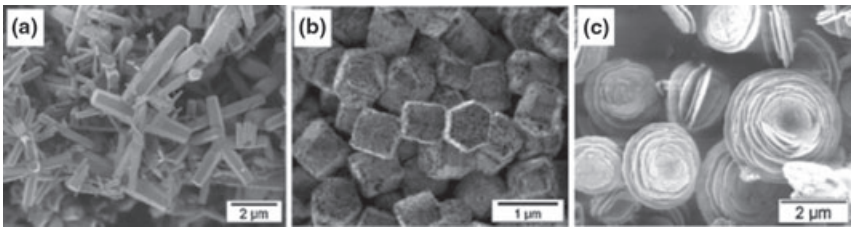

Figure 1.1 Zinc oxide materials synthesized (a) in the absence of latex beads, (b) in the presence latex beads functionalized with 9 g l^{-1} of poly(styrene-acrylic acid), and (c) latex beads (removed by calcinations at 600 °C) functionalized with 3 g l^{-1} poly(styrene-maleic acid). Latex beads can be easily synthesized using mini-emulsion polymerization, and their functional surfaces tuned for specific ZnO properties. Reproduced with permission from Ref. [6]; © 2007, Wiley-VCH Verlag GmbH & Co. KGaA.

others did at the same fraction [6]. The activity of vinyl-sulfonate was optimized by anchoring it onto a hierarchal, supramolecular network of latex beads, thus demonstrating an alternative approach to controlling the synthesis of ZnO. As shown in Figure 1.1, ZnO was precipitated in the presence of the beads, yielding hybrid polymer–inorganic materials with various morphologies [6].

Control over the shape of a nanoparticle can affect not only the particle in isolation but also its interaction with other particles. However, the impact on the specific size of the material can determine the magnetic, electronic and chemical properties of nanoparticles [26, 27]. Such size-dependency has been observed in γ-Fe_2O_3 nanoparticles, with 55 nm particles exhibiting ferromagnetic behavior while their 12 nm counterparts produced superparamagnetic behavior, but with no hysteresis [18]. The chemical reactivity of the smaller nanoparticle will be enhanced due to its larger surface area per unit mass. Moreover, the decreased particle size will also decrease the overall magnetic anisotropy of the particle, thus inducing the change to superparamagnetic [28]. Novel methods of creating metal oxide nanoparticles of a defined size are necessary for achieving not only desired magnetic properties, but also electronic and chemical properties.

1.3
Biomimetic Synthesis of Metal Oxide Nanomaterials

In its most basic form, a material synthesized on the nanoscale infers a smaller, more reactive particle. In order to exercise control over the design and presentation of a particle in this size regime, several research groups have developed alternative approaches to synthesizing nanostructured materials under ambient conditions [29]. The well-defined, structural organization witnessed in biologically derived minerals such as these has inspired low-temperature syntheses that are favorable because they minimize the onset of particle degradation, which is often a factor in high-temperature reaction processes [30]. Generally, a biomineral can be induced, controlled or mediated by its reaction environment [3]. Induced syntheses

are most common in single-celled organisms, such as fungi or bacteria, and typically occur within a charged, open environment. The mineralized product remains dynamic and typically does not have a specific function within the system [7, 18, 20].

Biologically controlled, or constrained, reactions yield minerals with a minimal size distribution that are localized to a confined area, defined by a cell wall, lipid bilayer or vesicle [7]. This mineralized product has functional properties that are dependent on its origin of synthesis (extra-, inter- or intracellularly) [3, 20]. On the other hand, biologically mediated mineralization is often genetically controlled by the organism within unconstrained, open environments, while incorporating peptides, proteins, nucleic acids or polymers as templates during synthesis [3]. For instance, the proteins in diatoms, radiolarian and sponges produce SiO_2 that serves as their exoskeleton in the ocean, while biopolymers associated with echinoderms and nacreous layers mediate the production of single calcite crystals that serve as their protective coating [29, 31]. The valuable properties associated with constrained or unconstrained metal oxide synthesis in specific biological systems has inspired the development of functionalized nanomaterials, and these will be discussed here.

1.4 Constrained Biomineralization

Synthetic control over the physical and chemical properties of a nanoparticle can be tuned according to its biological micro- or nano-environment. Some of the most notable platforms that are currently being used for the controlled synthesis of metal oxides include the apoprotein ferritin, viral capsids or bacterial cages; however, recently adapted biotemplates, such as self-assemble peptide nanorings or porous butterfly wings, have been used as unique platforms and have yielded interesting structures. These molecular architectures offer constrained environments that yield a small distribution of nanoparticle size under ambient conditions, and will be discussed as viable alternatives for the synthesis of functional nanomaterials.

1.4.1 Bacterial Synthesis of Metal Oxide Nanomaterials

At least one-third of the elements in the Periodic Table have experienced changes in valence states induced by microbial activity. While some metals (iron, calcium, potassium) serve as an essential source for nutrients in bacterial systems, others are introduced as contaminants (lead, nickel, cobalt, cadmium) [2]. This cohabitation with such heavy-metal pollutants has forced organisms among marine bacteria to develop a high metal tolerance, which in turn makes them an interesting source for templating the constrained synthesis of metal/metal oxide nanoparticles.

Magnetic metal oxides nanoparticles have aroused particular interest because their properties can be tuned according to their size and shape. Exchange coupling at the interface of ferri/ferromagnetic and antiferromagnetic phases, as seen in nanoscale materials, can be applied as high-density magnetic storage devices or components for enhanced sensor development. Current wet-chemistry approaches, demonstrating control over the magnetic exchange bias of a nanoparticle, require expensive organometallic precursors and high-temperature reaction conditions. On the other hand, biologically produced microbes reduce metal ions in aqueous media to form stable suspensions of nanoparticles coated with biomolecules (proteins, peptides). This coating not only activates the modified properties of the nanoparticle, but also prevents particle agglomeration, thus stimulating the growth of discrete nanoparticles within a solution.

1.4.2
Synthesis of Protein-Functionalized Ferromagnetic Co_3O_4 Nanocrystals

A marine bacterium culture (obtained from the Arabian seacoast) has been used as the host system for the constrained synthesis of cobalt oxide (Co_3O_4) [2]. In this synthesis, the precursor, cobalt acetate (Co^{2+}) was incubated with the bacterium in an aqueous solution, and the as-synthesized particles displayed average diameters of 6 nm. After mild calcination (200 °C for 2 h), the particles grew larger (50 nm), inferring that its protein-passivating layer had degraded, causing particle aggregation. Of the 15 strains isolated from the bacterium culture, only one gave a visible indication of the formation of nanoparticles. Phylogenetic sequencing revealed that this oligonucleotide strand could potentially be the source of hydrolysis and reduction of the precursor salt [2].

At room temperature, bulk Co_3O_4 has been synthesized with a cubic spinel, antiferromagnetic phase. On the nanoscale, however, Co_3O_4 adapts an overall ferromagnetic type behavior because the uncompensated spins at the nanoparticle surface becomes a large fraction of the total number of spins. The as-synthesized nanoparticles were characterized using X-ray diffraction (XRD) and identified as crystalline. After heating above 930 °C (a reducing environment), the composite material was transformed into the CoO phase, which suggested that, at room temperature, Co_3O_4 is the thermodynamically preferable state [2]. Despite there being a dominant presence of Co^{3+} ions, X-ray photoelectron spectroscopy (XPS) identified trace amounts of Co^{2+} within the Co_3O_4 composite. Among the 24 Co-ions in the Co_3O_4 unit cell, it was predicted that eight Co^{2+} ions were located in the tetrahedral sites and 16 Co^{3+} ions in the octahedral sites. This mixed-valence state within the unit cell was understood to be the cause of the nanoparticle's overall magnetic moment (Figure 1.2).

The mechanism behind the oxidation of the cobalt precursor and subsequent Co_3O_4 precipitation within the bacterium host (Co^{2+} to Co^{3+}) was examined. A nonspecific intake of toxic Co ions within the host forced a spontaneous reaction that was balanced by the homeostasis of the system through developed resistance mechanisms. Through the basics of biology, it was predicted that Co^{2+} enters and

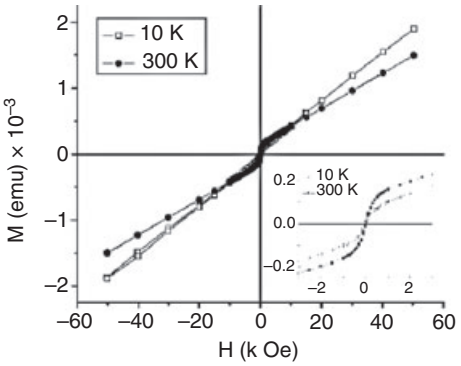

Figure 1.2 Magnetization versus magnetic field measurements of Co_3O_4 shows a nonlinear reversible behavior once calcined at 10 and 300 K. The plot did not show saturation until the highest applied field (50 kOe), which is a result of nonzero net moment and ferromagnetic-type behavior of nanoparticles with Co^{3+} at octahedral sites. The inset shows an exaggerated view of the region of hysteresis. Reprinted with permission from Ref. [2]; © 2006, American Chemical Society.

exits the cell through an efflux pump, during which process Co^{2+} was either filtered through a cation diffusion facilitator (CDF) or was exported by resistance nodulation cell division (RND) proteins. Either way, the bacterial capsule was understood to bind and concentrate the metal ions along its walls, forming a cooperative, self-organized colony to resist induced external stress. This possible interbacterial communication involved in oxidizing precursor ions has exposed valuable properties associated with constrained synthesis, and can be used to control the synthesis of a number of additional metal oxides.

1.4.3
Room-Temperature Synthesis of Barium Titanate

As a source for nonvolatile memory, microelectromechanical device, or thin-film capacitor, barium titanate (BT) is an important electroceramic material with ferroelectric properties [32]. Most reported room-temperature syntheses have produced a cubic, paraelectric-phased BT; however, sub-10 nm, tetragonal and ferroelectric phases are desirable for successful implementation within miniaturized devices. For this reason, a purely biological approach was used to synthesize BT nanoparticles with constrained sizes using the plant pathogenic fungus *Fusarium oxysporum* as the host system. Aqueous solutions of barium acetate ($(CH_3COO)_2Ba$) and potassium hexafluorotitanate (K_2TiF_6) were reacted with *F. oxysporum* [32]. The fungal proteins were responsible for the hydrolysis and confinement of these precursor materials, inducing BT nanoparticles. The free Ba^{2+} and acetate ions released from barium acetate were understood to coordinate to the free TiF_6^{2-} ions, using the extracellular proteins in the fungus. In order to approximate the percentage of biomaterial attached to the particle, the sample was

heated to 400 °C, after which thermogravimetric analysis (TGA) determined that there was up to 50% weight loss from the starting material. Both, transmission electron microscopy (TEM) and XPS were used to identify the BT nanoparticles (which had a size distribution of 4 ± 1 nm), while selected-area electron diffraction (SAED) was used to confirm that the particles were in the tetragonal phase.

Both, differential scanning calorimetry (DSC) and superparamagnetism (SPM) were used to probe the ferroelectricity of the as-synthesized nanoparticles and at various degrees of calcination. When SPM was used to investigate the polarizability of the nanoparticles in the ferroelectric phase, the peak broadening in the maxima of the temperature-dependent dielectric response and the DSC maximum at ferroelectric transition suggested that the as-synthesized particles behaved as a 'ferroelectric relaxer' material. Results indicated that BT nanoparticles were successfully written and read on a substrate in response to an applied external electric field. This confirmed that reactivity, coupled with the biologically constrained synthesis of sub-10 nm BT particles, is thought to revolutionize microelectronics industries. Hence, this method represents a nonvolatile and economically feasible alternative to current solid-state techniques for the production of highly controlled functional nanomaterials.

1.4.4 Biomimetic Synthesis of Magnetite

Iron oxides are technologically relevant metal oxides because, like cobalt oxide, they possess multivalent oxidation states that can be tuned specifically for an application, such as a catalytic template in sensor development or a substrate for drug delivery. Magnetite (Fe_3O_4), which is naturally found in the magnetosomes of MTB or other iron-reducing bacteria, is a well recognized example of controlled biomineralization [17, 18]. Once crystallized intracellularly, magnetite nanoparticles align with the Earth's magnetic field to serve as a navigational compass for a number of aquatic animals [18]. Salmon, for example, utilize the magnetite located in their head for magnetic navigation that can last up to three years over tens of thousands of kilometers [18].

The morphology of magnetite varies according to the different bacterial strains associated with the lipid membrane of the magnetosome (Figure 1.3), as the membrane defines the biochemical composition of the subsequent metal oxide. A number of successful biomimetic approaches aimed at modifying the biological synthesis of magnetite have been developed, incorporating constrained biological environments. These mimics can be tuned by either chemical or genetic modification to yield interesting properties that are technological significant.

1.4.4.1 Biomimetic Synthesis of Iron Oxide

The magnetic properties of iron oxides, specifically magnetite, are of particular interest to materials scientists because they are associated with potential applications, ranging from magnetic storage devices to magnetic resonance imaging (MRI) contrast agents [17]. Unfortunately, the biosynthesis of magnetite can often

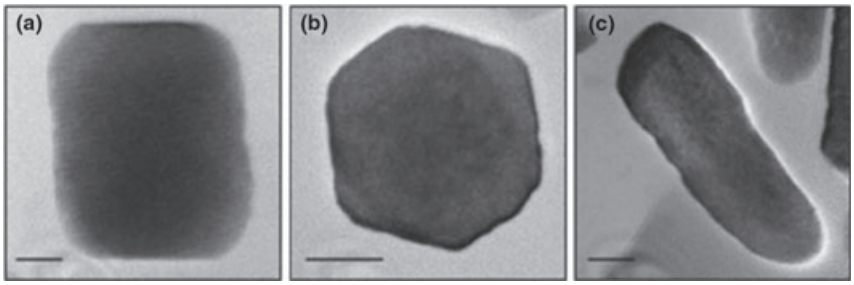

Figure 1.3 Transmission electron microscopy images (scale bar = 20 nm) of magnetosomes from various bacterial strains. (a) Pseudo-hexagonal prism; (b) Cubo-octahedral crystal; (c) Tooth-shaped. Reproduced with permission from Ref. [17];

be slow (one week) under unfavorable anaerobic conditions; however, varying the reaction conditions (such as length of reaction time, pH) or starting materials has revealed several interesting properties associated with the nanoparticles. The chemical synthesis of various phases of iron oxide using alfalfa bioreduction (*Medicago sativa*) was completed and examined under low-magnification microscopy and elemental analysis (30 micrographs per sample) [33].

Varying the reaction conditions has produced different species of iron oxides while maintaining nanometer control (>10 nm) over the distribution of nanoparticles. The smallest nanoparticles were synthesized at pH 10 (3.6 ± 1.6 nm), and this led to a generation of magnetite clusters which coexisted with wuestite-like clusters. A preference for magnetite formation was exhibited at pH values of 7 and 10. A multimodal distribution of average sizes of nanoparticles was evidenced at pH 3 (6.2 ± 3.4 nm), whereas at pH 5 the mean particle size was increased to 7.2 ± 2.5 nm. At pH 7 and 10, the particle sizes were 4.1 ± 1.9 and 3.5 ± 1.6 nm, respectively (Figure 1.4). The chemical potential required to reduce the metal oxide system has been affected by the variation in pH, as indicated by the distribution in the size and phase of iron oxide composites.

Both, high-resolution TEM images and fast Fourier transformed (FFT) spectra were used to determine the structure of the resultant iron oxide. At pH 3, both rounded and irregular-shaped nanoparticles had planar spacings corresponding to the wuestite-like iron oxide ($Fe_{0.902}O$ cubic phase) at different zone axes. At pH 5, the nanoparticles had a slightly different morphology that showed two domains in one particle; the larger domain was subsequently analyzed and shown to have characteristic angles matching magnetite-like iron oxide (Fe_3O_4). A second particle studied had a more homogeneous structure, which corresponded to a wuestite-like particle. At pH 7 there was evidence of both wuestite and magnetite clusters that were similarly oriented within the same region. However, at pH 10 several particles within the same region were noted to have cubic-like arrays with a hexagonal

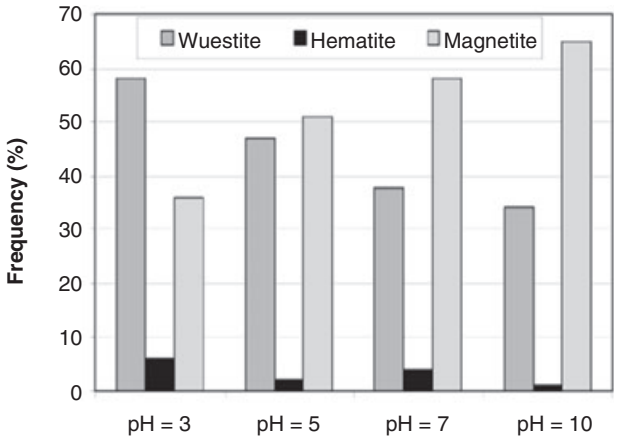

Figure 1.4 Distribution of structures for variable pH samples. Reprinted with permission from Ref. [33]; © 2007, American Chemical Society.

$$FeCl_3 + H_2O \rightarrow [Fe(H_2O)_n]^{3+} + H_2O$$

$$R + [Fe(H_2O)_n]^{3+} + H_2O \rightarrow [Fe(H_2O)_n]^{2+} + H^+ + R\text{–}OH$$

$$[Fe(H_2O)_n]^{2+} + 2R^- + H^+ + OH^- \xrightarrow{pH} Fe^{2+}O^{2-} + Fe^{2+}Fe^{3+}O^{2-} + R\text{–}H + R\text{–}OH^-$$

Scheme 1.1 Reprinted with permission from Ref. [33]; © 2007 American Chemical Society.

profile and a hexagonal internal contrast that matched the wuestite and magnetite structures.

The cations within the magnetite unit cell (fcc close-packed lattice of oxygen anions) were responsible for the induction of zig-zag or square shapes. In each unit cell, the lattice array was either octahedral (eight Fe^{2+} in each cation site) or a homogeneously distributed among tetragonal and octahedral (16 Fe^{3+}) packed sites. Hematite models have a signature hexagonal distribution with rectangular arrays, associated with Fe^{3+} cation packing, and are predominately seen in syntheses conducted at pH 3 (6% compared to negligible amounts found in the four other syntheses).

Powder-milled alfalfa (garlic acid, denoted as 'R' in the reactions in Scheme 1.1) was used to reduce the iron in the Fe component in this synthesis. The variation in crystal morphologies was generated according to the amount of Fe^{2+} available for reaction in the final step, while the pH-dependent morphology of the metal nanoparticles exposed the preferential reduction of iron into Fe^{2+} during the biosynthesis process.

1.4.5 Metal Oxide Synthesis within a Protein Cage – Ferritin

The defined architecture of the metalloprotein ferritin, a natural complex of iron oxide, is found in almost all domains of life and has been used as a constrained reaction vessel for the synthesis of a number of non-natural metal oxides [28, 34]. The protein ferritin consists of 24 subunits that self-assemble into a cage, consisting of a threefold hydrophilic channel coordinated to a fourfold hydrophobic channel [20, 28]. In biology, Fe(II) is introduced into the core of the apoprotein through its hydrophilic channels; where the ferrous ion is catalytically oxidized to a less-soluble ferric ion, Fe(III) [20]. The ferric ion then undergoes a series of hydrolytic polymerizations to form the insoluble ferric oxyhydroxide mineral (ferrihydrite), which is physically constrained by the size of the protein cage (12 nm outer diameter, 8 nm inner diameter) [35]. The enzyme ferrous oxidase is coordinated within the protein cage, the interior and exterior of which is electrostatically dissimilar, to produce spatially defined minerals.

1.4.5.1 Mineralization of Non-Natural Metal Oxides Using Ferritin

The photoinduced mineralization of iron, titanium and europium oxyhydroxide nanoparticles has been successfully achieved using the protein cage, ferritin [35]. This photochemical reduction closely resembles the Fe(III) to Fe(II) reduction of marine siderophores with a citrate background [35]. In this synthesis, a known concentration of metal ion was loaded into a 12 m*M* solution of citrate and ferritin, and illuminated with a xenon arc lamp (320–750 nm) for over 2 h. The citrate solution induced an electrostatic environment that was essential for discrete nanoparticle synthesis in the reaction, without which the bulk precipitation was illuminated. After a 2 h reaction time, the high oxidation state metal ions were photoreduced, whereas in the presence of air the lower state underwent reoxidation to the final, oxyhydroxide state. All products were characterized using dynamic light scattering (DLS) and found to have similar sizes (12 ± 1 nm). Samples stained with uranyl acetate were analyzed with TEM, while the intact protein cage was visible, forming an outer diameter around the metal oxide cores of 5.7 ± 1 nm.

1.4.5.2 Mixed Mineralization Using Ferritin

Oxidation of the iron core in ferritin was used and applied to the mixed mineralization reactions of cobalt and iron. It is understood that, if synthesized correctly, this composite material would have tailored magnetic properties, inducing the exchange coupling of ferro/anti-ferromagnetic properties; wherein, the exchange bias is self-manifested and defined by a unidirectional hysteresis loop. Control over the magnetic behavior of a nanoparticle could, potentially, lead to additional magnetic anisotropy effects for use as magnetic storage and recording devices. Klem and coworkers have demonstrated the constrained synthesis of $Co_xFe_{3-x}O_4$ with an exchange bias by means of an enhanced magnetic response [28].

For this synthesis, a deaerated solution of iron $[(NH_4)_2Fe(SO_4)\cdot 6H_2O]$, cobalt $[Co(NO_3)_2\cdot 6H_2O]$ and H_2O_2 was added to apoferritin in NaCl (pH 8.5, 65 °C, under

nitrogen), and the reaction allowed to continue until a homogeneous, dark brown solution was formed. Light-scattering measurements showed no increase in the average diameter of ferritin after metal encapsulation. TEM images showed the core sizes to be consistent with the inner diameter of the ferritin (6.8–7.4 nm diameter), while SAED indicated that with 33% Co doping, the *d*-spacings were consistent with the spinel phase of Co_3O_4 and the inverse spinel magnetite phase of Fe_3O_4. When using a rapid (5 min) synthetic method, Co is likely incorporated into the rapidly forming Fe_3O_4 lattice, which has enhanced the blocking temperature, inducing a loss in exchange bias. Under slow synthesis conditions (30 min), however, it was suggested that Fe_3O_4 formation would precede the nucleation and growth of Co_3O_4 on the basis of standard reduction potentials (Fe^{3+} and Co^{3+} are 0.771 and 1.808, respectively). The magnetic properties of the complex nanoparticle can be tuned according to its applications, depending on the mode of synthesis.

1.4.6
Viral Templates for Metal Oxide Synthesis

Conceptually, viruses and the metalloprotein ferritin are similar in that they are both assembled protein cages that serve as a host system for mineralized guest materials [9, 10]. The function of ferritin is to store and transport iron oxyhydroxide, while that of virus capsids is to store and transport organic polymers or nucleic acids [9, 20, 36]. Viruses are composed of repeating subunits which assemble into highly symmetric architectures that provide templates for nanoengineering biominerals. As molecular containers, viruses have three important interfaces: (i) the exterior; (ii) the interior; and (iii) the interfacial region of the protein subunits (Figure 1.5) [9]. Because the exterior surface of the viral capsid

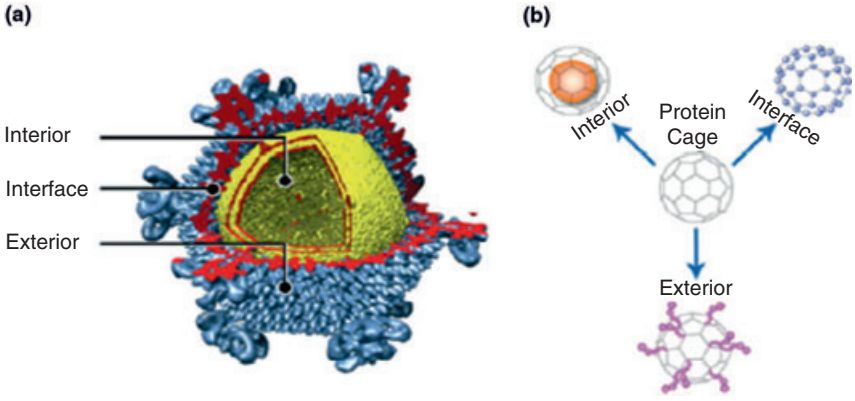

Figure 1.5 (a) Cryoelectron microscopy reconstruction of icosahedral symmetry of *Sulfolobus* turreted virus; (b) Three interfaces within a protein cage available for modification. Reproduced with permission from Ref. [36]; © 2007, Wiley-VCH Verlag GmbH & Co. KGaA.

is highly symmetric, every functional group is spatially defined over the entire cage; thus, the reactive sites can be genetically engineered for multivalent ligand presentation [36].

The capsid interior has been used to direct nanoparticle synthesis; for instance, the basic, positively charged interior of the cowpea chlorotic mottle virus (CCMV) has been utilized for the mineralization of a range of polyoxometalate species [9, 10]. In this synthesis, empty virions were incubated with precursor ions $(WO_4^{2-}, VO_3^-, MoO_4^{2-})$ at neutral pH, whereupon the virus exits in its open, or swollen, state will provide a pathway for ions to flow into and out of the cavity [10]. At pH 5.0, the capsid pores close to induce oligomerization, yielding large polyoxometalate crystals. The mineralized particles are then isolated and purified by centrifugation on sucrose gradients, and their subsequent size distribution is documented using TEM.

The interface between the capsid interior and exterior is defined by a series of noncovalently bound peptides. Within the icosahedral formation of the CCMV are 60 pores, each 2 nm in diameter, that open and close to allow ions and molecules to enter the interior, thus serving as a method of communication between interior and exterior. Because the virus capsid is a metastable, dynamic structure, the manipulation of its composition could introduce major structural changes from its original icosohedral formation to a sheet-like or tubular morphology. However, modifying the virus exterior with small molecules or biological ligands could have potential applications ranging from surface display or cell targeting to drug delivery [9]. Controlling the ligands associated with the virus can also be used to identify specific peptide or protein communications, similar to the commonly practiced phage display methods [9]. Identifying such active peptides would not only enable additional, specific templates for biomineralization but also provide a unique view into the architecture of specific viral capsids.

1.4.7
Hydrolysis of Metal Oxides Using Peptide Nanorings as Templates

The synthesis of biominerals within the confined volumes of vesicles, microemulsions or reverse micelles elucidates a defined location for contained reactivity. Among these three systems, the constrained, ionic environment within vesicles is the most preferable microenvironment because it is not a dynamic system [37]. The biosynthesis of single-crystalline calcite within sea urchin larvae, for example, occurs inside a curved compartment with a constrained volume where the reaction is regulated by catalytically active biomolecules [37]. The high surface tensions in such confined cavities are suspected to have a considerable impact on the ensuing phase of the nanoparticle. Various research groups have used these micro- or nano-environments to provide inspiration for the confined synthesis of non-natural metal oxides by incorporating similar concepts. In the following examples, self-assembled reaction environments (peptide nanorings) were initiated by peptide monomers and metal precursor ions to yield uniform and specific phases of metal oxide nanomaterials [38, 39].

1.4.7.1 Enzymatic Peptide Nanoassembly of Crystalline Ga_2O_3

As a wide band-gap material that provides light emission over a broad range, β-Ga_2O_3 is currently being studied to exploit its potential applied, optoelectronic properties [38]. Assembled peptides were used as nanoreactors to grow the kinetically unfavored β-Ga_2O_3, which in turn provided a porous template for an efficient dehydration and water-exclusion pathway, as well as a high surface tension control that was built into the peptide cavities during the crystal growth process. This reaction was completed in a two-step process where enzymatic peptides were first assembled to template crystal growth, after which ordered single crystals were aligned through an aggregation-driven fusion. The nucleated particles were then capped by assembled peptides in solution. When the composite solution was sintered at 900 °C, the peptide templates were removed and the particles transformed into an aggregated GaN phase.

Bola-amphiphile peptide monomers and (bis (*N*-α-amidoglycylglycine)-1,7-heptanecarboxylate) were used to cap and catalyze the growth of β-Ga_2O_3 nanoparticles. Such particle capping was essential in this synthesis because, in its absence, GaOOH would be synthesized (Figure 1.6). The bola-amphiphile peptide monomers were reacted with the precursor, gallium(III) chloride, for one month at pH 10, after which time both TEM and SAED were used to show that the particles displayed 50 nm diameters, and were arranged in a monoclinic crystal structure. In addition, high-resolution TEM images showed layers of the peptide surrounding the core nanoparticle.

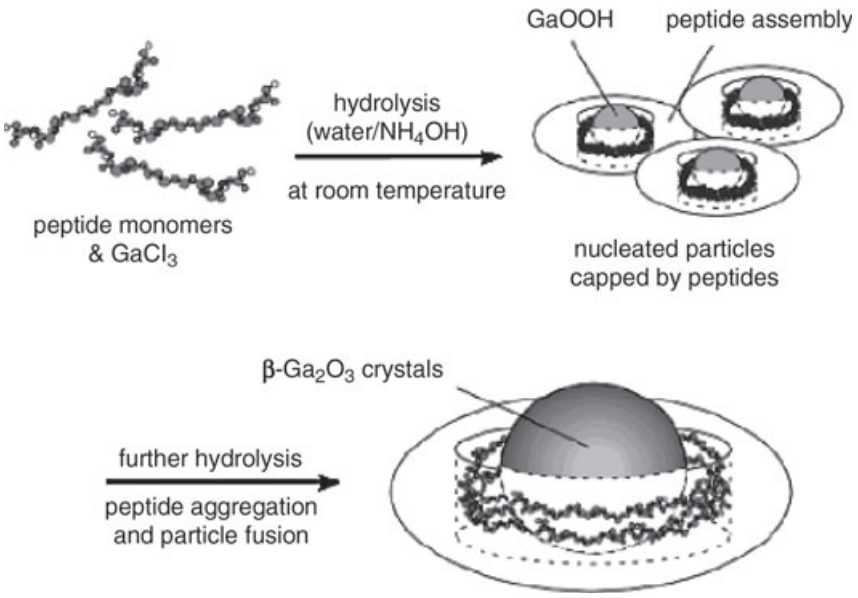

Figure 1.6 Illustration of catalytically grown β-Ga_2O_3 nanoparticles. Reprinted with permission from Ref. [38]; © 2007 American Chemical Society.

It is understood that, although the base solution hydrolyzes gallium precursors to form GaOOH, it is not strong enough to carry out the reaction, and for this reason the peptides are considered to have a catalytic function. Photoluminescence evidence confirmed the emission of the nanoparticles (389 nm), which was in agreement with previously reported values for β-Ga_2O_3. Fourier transform–infrared (FTIR) spectra subsequently indicated that the gallium hydrolysis was completed adjacent to the carboxyl and amine moieties within the assembled peptide, through a bridged metal–bridged metal complex (COO—Ga-NH^{2+}). In order to investigate the importance of the nucleophilicity of this carboxyl moiety, the pH of the composite solution was adjusted to 7, and after a four-week incubation with the gallium precursor, only GaOOH crystals were observed. At neutral pH the protonated carboxyl group was shown to be weakly bound to the amine group, thus affecting the degree of gallium hydrolysis.

In addition, the importance of the bola-amphiphile template was tested. As a control, Nuraje and coworkers used the silicatein peptides that are associated with templating the hydrolysis and condensation of SiO_2 in sponge spicules. In this study, the nucleophilic hydroxyl of the serine and the primary amine from the histidine and lysine of silicatein catalyzed the hydrolysis of GaOOH and γ-Ga_2O_3 over a wide size range. Although such a wide distribution in size would limit this synthetic technique for use in industry, the control of nanoscale sizing using a specific hydrolyzing template (as for the synthesis of β-Ga_2O_3 nanoparticles) could introduce valuable properties that depend strictly on the mode of synthesis.

1.4.7.2 Synthesis of Ferroelectric BT Nanoparticles Using Peptide Nanorings

As mentioned previously, the ferroelectric and optoelectronic properties of ternary oxides such as BT can be applied to the next generation of miniaturized capacitors or random access memories [39]. In the past, BT has been synthesized at room temperature in the cubic phase, and does not exhibit ferroelectric behavior. However, Nuraje and coworkers recently reported a one-pot synthesis of ferroelectric BT in the tetragonal phase, as confirmed by electron diffraction [39]. The precursor $BaTi(O_2CC_7H_{15})[OCH(CH_3)_2]_5$ was hydrolyzed by peptide templates [bola-amphiphile peptide and (bis (*N*-α-amidoglycylglycine)-1,7-heptanecarboxylate] to produce BT nanoparticles at room temperature. When the peptide template and Ba-precursor were added together, and incubated for between one and four days in the dark, the peptide monomers were seen to self-assemble into nanorings. Atomic force microscopy (AFM) was then used to show that the BT had been synthesized exclusively within the nanoring cavity, with the average diameter (49 ± 11 nm) of the nanorings indicating a monodisperse size distribution. Raman spectroscopy confirmed the formation of BT through a Ti–carboxylate ligation and a Ti–O–Ti stretch [39]. In order to validate this coordination, the composite solution of peptide shells was irradiated with UV light (355 nm) for 10 h, after which the peptide shells were displaced, inferring that the onset of irradiation had rendered the Ti–carboxylate linkage ineffective. Subsequently, AFM was used to identify the average diameter of the metal oxide nanoparticles alone, as 12 ± 1 nm, after UV irradiation. Interestingly, as the pH of the peptide/precursor solution

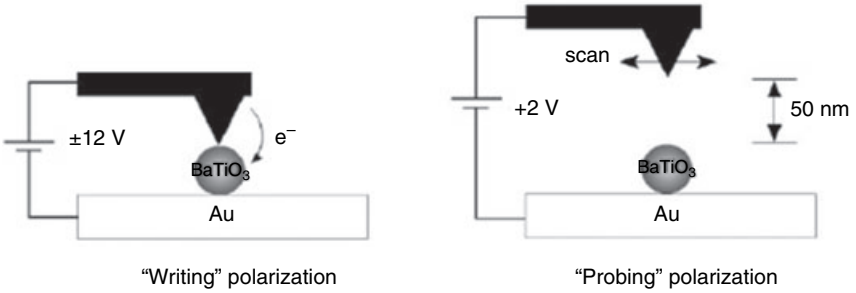

Figure 1.7 Schematic of electrostatic force microscopy (EFM). The electric potential applied to the $BaTiO_3$ nanoparticles using a conductive AFM tip has been varied to test its nanometer-scale ferroelectric property. In these experiments, a +12 V_{write} potential was initially applied to the nanoparticles, and the subsequent EFM image was scanned under an applied V_{probe} potential of +2 V. Reproduced with permission from Ref. [39]; © 2006, Wiley-VCH Verlag GmbH & Co. KGaA.

changed from 4.5 to 10, the average diameter of the system fell from 49 to 23 nm, and this in turn affected the size of the resultant crystals (from 12 to 6 nm).

In order to monitor the nanoscale ferroelectric properties of BT, electrostatic force microscopy (EFM) was used to manipulate the polarization of the ferroelectric field (Figure 1.7). First, a voltage was applied to the cantilever tip (V_{write}), which gently touches the nanoparticle surface. Once the polarization has been written, the resultant polarization was probed with a lower voltage (V_{probe}) by measuring the shift in resonance of the AFM tip, using EFM. A positive applied V_{write} (+12 V) on a 12 nm particle produced a brighter contrast image than did V_{probe} of +2 V. When +12 V had been written onto the same particle, the V_{probe} was applied, and induced a darker contrast image.

1.4.8
Synthesis of ZnO from Templated Butterfly Wings

The wonderful array of colors associated with different species of butterflies often attracts the eye for aesthetic purposes only. Although used for sexual signaling or defense mechanisms (camouflage), the color of the butterfly wings is actually necessary for its survival. Designed for aerodynamics and protection, the microstructure of butterfly wing scales (which are the cuticular products of a cell) are composed of a lightweight, porous material with alternate layers of chitin and air [40]. Although the precise chemical composition of the scales is not known, chitin and the proteins resilin and scleretin have been identified within the insect cuticle. The scales are composed of long, parallel ridges that are connected by cross-ribs (1280 nm long, 380 nm wide) [41] that do not contribute to the color of the butterfly but rather offer defined regions that can be manipulated for further functionalization.

Zhang and coworkers utilized the wing's porous architecture and the terminal hydroxyl and amino moieties of surface proteins to direct the constrained synthesis

of tubular ZnO nanowires [40, 42]. Tubular materials of high porosity are understood to have properties suitable for catalysis or device storage [40]. For this process, a zinc nitrate ($Zn(NO_3)_2$) solution in ethanol was coated onto the surface of the wing after a 12 h incubation at room temperature [40], and the functionalized wing was then washed extensively with deionized water to ensure that the Zn^{2+} ions had been effectively adsorbed within the surface hydroxyl and amino groups of chitin. The wing was then placed in an oven at 500 °C for 2 h, during which time the flat scales of the wings were broken apart along their stress ridges and the chitin substrate was burned. As a consequence, the calcified product yielded ZnO microtubes within the ceramic wings.

Subsequent X-ray diffraction (XRD) studies confirmed that the resultant composites had a zincite hexagonal structure, while field emission scanning electron microscopy (FESEM) was used to determine the dimensions of the microtubes produced (3.0 μm diameter). When the shrink ratios were calculated, the distance between the ridges and the length of the tubes was calculated to have shrunk approximately 45.7% and 41.6%, respectively, from the original template, which inferred that the microtubes had grown directly from the wing scales. Cathode luminescence from the free exciton at 3.24 eV documented two emission bands ($\lambda = 381$ and 572 nm) of the as-synthesized ZnO. Although not confirmed, it is believed that the origin of the emission is a result of center defects of oxygen, indicating that the tubes sustain a low oxygen content, which is consistent with previous ZnO syntheses using block copolymers or solid-state conditions [40].

1.4.9 Ionic Liquid-Assisted Co_3O_4 Synthesis

As a magnetic p-type semiconductor that can be used in catalysis, sensor optimization or energy storage, Co_3O_4 has previously been synthesized using thermal decomposition, CVD or chemical spray pyrolysis of an oxidized Co product. Unfortunately, these reaction conditions are not only unfavorable for the synthesis of Co_3O_4 nanocrystals because their high-temperature reaction conditions, but they also induce a low product yield. In an attempt to overcome this setback, Zou and coworkers have used a relatively new technique incorporating room-temperature ionic liquids (RTILs) to direct the synthesis of the Co_3O_4 nanocrystals [43]. RTILs have recently attracted attention as stable, highly reactive solvents, with good electrical conductivity, high ionic mobility and good chemical and thermal stabilities [44].

In this synthesis, an ionic liquid, 1-*n*-butyl-3-methylimidazolium hydroxide ([BMIM]OH) was dissolved in $Co(NO_3)_3 \cdot 6H_2O$ at room temperature (Scheme 1.2) and, over a 30 min period, both NaOH and H_2O_2 were added separately to the solution. After a 6 h period of stirring, a black-brown precipitate was collected, purified and dried in the oven at 80 °C for 10 h. The ionic liquid was collected and reused. The crystal structure of the resultant Co_3O_4 nanocrystals was determined using XRD analysis, and its composition confirmed by IR spectrometry. The diffraction peaks indicated a cubic spinel system with lattice parameters similar to

$$Co^{2+} + 2OH^- \rightarrow Co(OH)_2$$

$$3Co(OH)_2 + H_2O_2 \xrightarrow[\text{r.1, stirring}]{\text{[BMIM]OH}} Co_3O_4 + 4H_2O$$

Scheme 1.2 Ionic reaction of cobalt precursor in the presence of NaOH and H_2O_2. Reprinted from Ref. [43] with permission from Elsevier.

that reported previously, while scanning electron microscopy (SEM) imaging showed the nanocrystal sizes to range from 10 to 50 nm, with a spherical appearance. These polar, ionic solvents offer a highly reactive environment because of the low interfacial tension, which induces catalysis and subsequent nucleation of the nanocrystals. When the Co-precursor has been added, the reactants disperse into the solvent to form many thousands of reactor sites that can be reused over and over again, thus providing a low-cost method for the rapid production of Co_3O_4.

1.4.10 Conclusions

While the use of metal oxide nanoparticles is dependent on their synthesis and subsequent magnetic or ceramic properties, size homogeneity is also necessary because the nanoparticles' properties are related directly to their size. Natural templates, such as butterfly scales, peptide nanorings and bacterial or protein cages, can be tuned to induce narrow size distributions that have yet to be seen within an industrial setting. These chemically engineered systems have been proven to serve as viable nanoscale templates for the constrained biomimetic synthesis of higher-ordered metal oxide nanoparticles with unique properties specific to their synthesis.

1.5 Mediated Mineralization

The structure of certain biogenic organisms is understood to be mediated by the cooperative reactivity of self-assembled macromolecules within aqueous solutions. Such hierarchical, supramolecular assemblies have revealed interesting morphological properties that can be applied directly to materials development. Diatoms and echinoderms are two independent examples of organisms that exhibit genetically controlled metal oxide structures with technologically relevant properties [31, 45]. Although progress has been made in identifying their structure-directing precursors, their complex biomineral shapes have yet to be fully recapitulated, and progress in this area is described in the following sections. By isolating the biomolecules responsible for cell wall mineralization and documenting their

reactivity, it has become possible to incorporate the specific, reactive moieties of peptide- and nonpeptide-based analogues for the biomimetic synthesis of novel nanomaterials.

1.5.1 The Three-Tier Architecture of Nacreous Layers

Mother-of-pearl (nacreous layer) possesses interesting morphological properties that are dependent on its aragonite–biopolymer coordination. Evidence has suggested that these biopolymers are incorporated into the composite framework of the mineral and are responsible for inducing different morphological properties of the organism [29]. Electron microscopy has been used to characterize these hybrid composites, and has shown that the macroscopic periodic orientation of the nacreous layer is assembled through a three-tier process of repetitive growth, inhibition, and regrowth [29]. The layered aragonite composites (tier 1) have been predicted to be perfectly aligned through a series of mineral bridges (tier 2) (1–5 μm wide and 200–700 nm thick). These bridges are assembled by nanobuilding blocks (tier 3) that have aggregated into hexagonal plates (Figure 1.8) [29].

Non-natural mimics of the assembled nacreous layer have been synthesized, displaying similar nanoscale architectures under ambient conditions. In these studies, the biomimetic crystallization of host organic molecules, generated

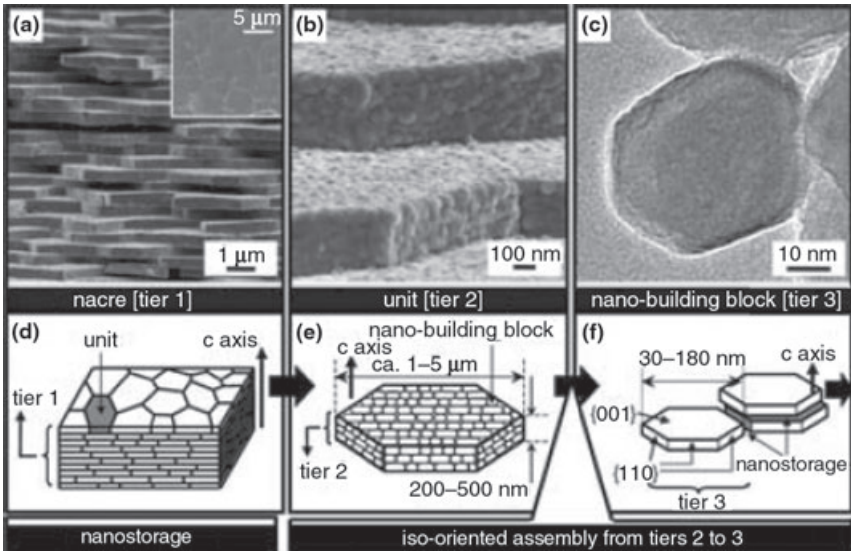

Figure 1.8 The three identified tiers of the nacreous layer. (a,b) FESEM images and (c) FETEM image; (d–f) Schematic representations of tiers 1, 2 and 3, respectively. Reproduced with permission from Ref. [29]; © 2005, Wiley-VCH Verlag GmbH & Co. KGaA.

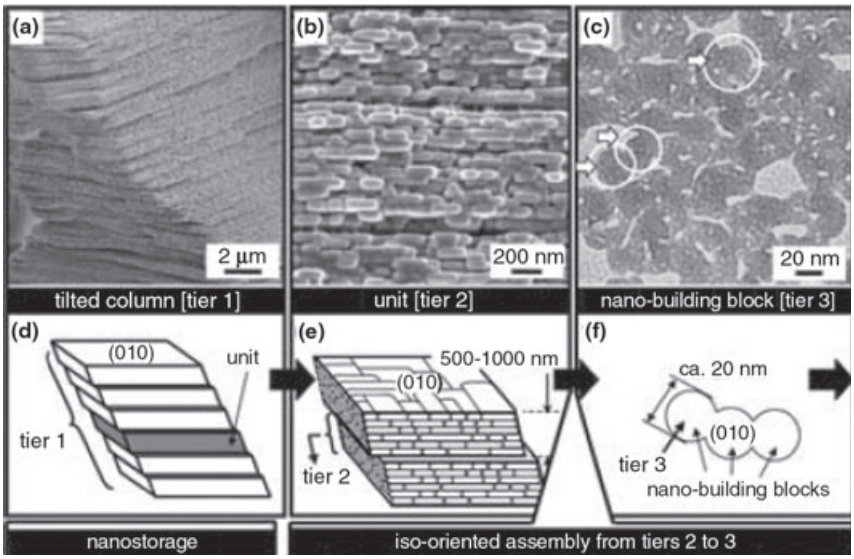

Figure 1.9 The three identified tiers of the K_2SO_4–PAA biomimetic assembly. (a,b) FESEM images; (c) FETEM image; (d–f) Schematic representations of tiers 1, 2 and 3, respectively. Reproduced with permission from Ref. [29]; © 2005, Wiley-VCH Verlag GmbH & Co. KGaA.

through a potassium sulfate (K_2SO_4) and poly(acrylic acid) (PAA) composite reaction, were shown spontaneously to form three-tier assemblies. Electron microscopy revealed that tier 1 consisted of an assembly of plates composed of square units (tier 2), approximately 0.5–1.0 µm thick. However, when magnified at a higher resolution these squares were shown to originate at nanoscale defect sites that were bridged by 20 nm building blocks (tier 3) (Figure 1.9). The physical properties associated with these packed, nanoscale building blocks were probed using photoluminescence, whereby hydrophobic and hydrophilic organic dyes were encapsulated within the defect sites of the three-tier matrices. After time, an examination of the photoluminescence showed that the stored dyes were still actively fluorescing, potentially providing an interesting source for molecular storage.

1.5.2 Echinoderms

The three-tier assembly documented for mother-of-pearl can be extended to the nanoscale architectures of other mineralized organisms. The sponge skeletal organization of echinoderms, for example, is composed of calcitic nanobricks of one, single Mg-bearing calcite crystal. Three species of echinoderms and one shell of a sea urchin were analyzed using FESEM, field emission TEM (FETEM), SAED

and XRD [31]. Although the organic composite membrane of the shells could be extracted using an aqueous solution of sodium hypochlorite (5% NaClO), the biopolymer remained associated specifically to the remaining rhombohedral calcite crystals. The nanobricks (submicron domains) of occluded biological macromolecules exposed on the cell surface of echinoderms were shown to be interconnected through a series of defined bridges at their nanoscale defect sites, similar to those found on nacreous layers [31].

The crystalline, calcitic domains of echinoderms were studied on a molecular level and shown to be electrostatically driven by assemblies of biomolecules with carboxy moieties. In fact, Addadi and coworkers have identified biological molecules associated with the sea urchin spine as water-soluble proteins, rich in aspartic and glutamic acid [46]. These amino acids were proposed to occupy the boundary sites between the crystalline domains of the nanobricks, inducing a necessary electrostatic environment for further reactivity. Similar to nacreous layers, the nanobrick growth of echinoderms is initiated along the defect sites of the biopolymer/nanobrick interface, thus exposing potential molecular storage units (Figure 1.10). The reported literature on the biopolymer-mediated synthesis of tightly packed nanobrick layers within species of echinoderms can be applied to the bioinspired synthesis of non-natural metal oxides.

1.5.2.1 Biomimetic Synthesis of Metal Oxides Using Echinoderms as Inspiration

By utilizing the fundamental Lewis acid and base interaction, defined organic molecules were used in conjunction with appropriate precursors under variable conditions to rapidly precipitate nanoparticles with constrained sizes. Specifically, mosaic assemblies of nanowires of ZnO and nanocrystals of Mn_3O_4 and $Co(OH)_2$ were synthesized using different polymeric backbones [30, 47]. The mosaic assemblies within these metal oxides are initiated from the nanocrystals themselves and, as seen in echinoderms and nacreous layers, these materials were grown, inhibited and regrown at the defect sites of bridged nanocrystals. In these reactions, the incorporated polymeric backbone generated an electric dipole moment that induced an internal self-assembly of the primary crystals *in vitro;* these assemblies were then reorganized into a highly specific metal oxide crystal structure with functional properties.

1.5.2.1.1 Nanoscale Building Blocks for ZnO Nanowires

Interesting properties associated with one-dimensional (1-D) zinc oxides can be employed in both electronic and optoelectronic applications [30]. Previously synthesized using vapor-phase thermal evaporation, wurtzite-type ZnO has potential applications which range from gas sensors to varistors, because of its wide-bandgap semiconducting properties. The 1-D lateral growth of ZnO is especially significant because it can be used as an ultrasensitive biochemical detector or field-effect transistor. For this reason, a low-temperature synthesis was developed to optimize the production of ZnO for such applications. The resultant synthesis produced 1-D mosaic structures reminiscent of the molecular architecture of echinoderms [30].

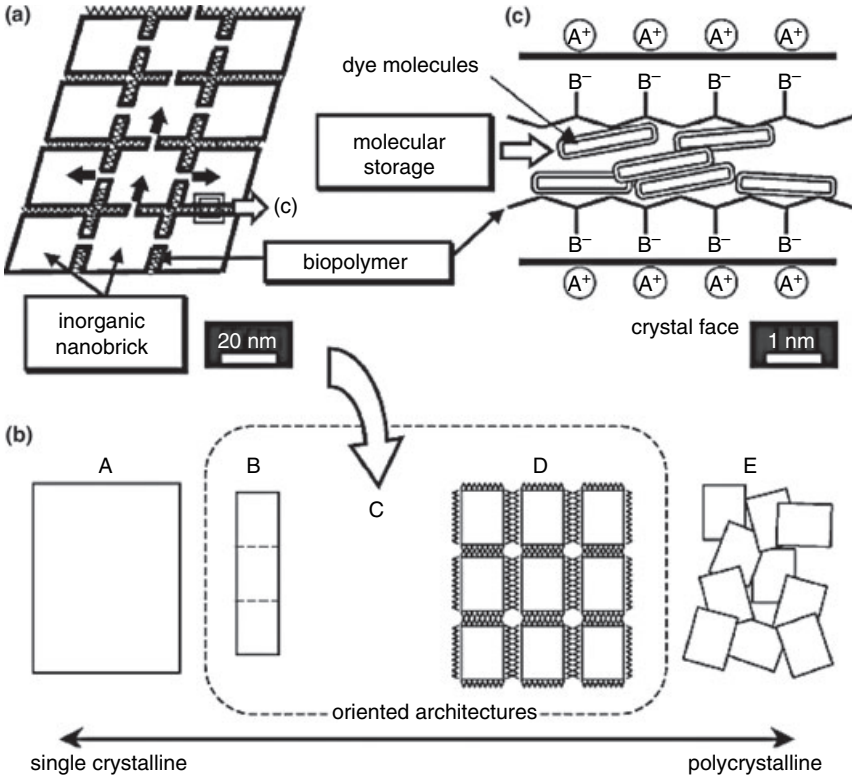

Figure 1.10 Schematic of nanoengineered nanobricks of nacreous layer and echinoderms. (a) Nanobricks oriented involving nanobridges; (b) Schematic of oriented architectures from single crystalline (A) to oriented attachment (B–D); (c) Interaction between the nanobricks and biopolymers producing the emergence of molecular storage and (E) polycrystalline arrangement. Reproduced with permission from Ref. [31]; © 2006, Wiley-VCH Verlag GmbH & Co. KGaA.

Yahiro and coworkers prepared this synthesis using an aqueous solution of zinc heptahydrate ($ZnSO_4 \cdot 7H_2O$) and ammonium chloride (NH_4Cl) at fixed molar ratios. The pH was adjusted to 9.5, and again to 11, using NaOH. Pyranine (8-hydroxy-1,3,6-pyrenetrisulfonate) was added in various molar ratios (Figure 1.11), after which the solution was aliquoted onto glass slides for ZnO film nucleation and growth and incubated for 24 h at 60 °C. The resultant slides were characterized using electron microscopy.

The anionic pyranine molecule was expected to direct the lateral growth of ZnO nanowires on a two-dimensional (2-D) surface [30]. Control studies with an absence of pyranine induced nanorods of wurtzite ZnO that grew vertically along the c-axis, as characterized by XRD analysis. At low molar ratios of pyranine, c-axis-oriented nanorods were also formed, but in hexagonal patterns; in contrast, at high molar ratios of pyranine the oriented growth became laterally elongated, extending in a desirable direction across the substrate. An electron energy-loss spectroscopic

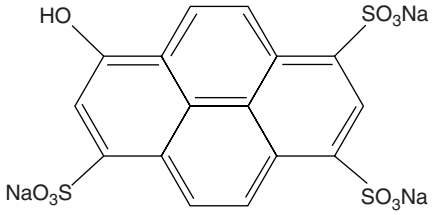

Figure 1.11 Structure of pyranine. Reproduced with permission from Ref. [30]; © 2006, Wiley-VCH Verlag GmbH & Co. KGaA.

(EELS) analysis suggested that the pyranine had become wrapped around the developing nanowires during the synthesis, while both energy-filtered (EF) TEM and high-frequency (HF) TEM analyses indicated that, during the aqueous synthesis, the pyranine molecules had been incorporated into the growing ZnO matrix by adsorbing to the faces of the hexagonal ZnO lattice points, thus inhibiting crystal growth perpendicular to the c-axis.

A closer examination of the composition, using high-angle annular dark-field scanning transmission electron microscopy (HAADF-STEM), showed that the nanowires were actually composed of nanograins (5.8 nm grain size, based on XRD peaks). The interior granular structures were understood to be composed of bridged nanocrystals that were oriented by the pyranine molecules, which inferred that the pyranine precursor was essential for the mediated synthesis of ZnO nanowires. Because there was no evidence of branching wires during the growth process, the 1-D morphology could be attributed to an anisotropic growth of a weak seed particle that bridged adjacent particles together. Hence, pyranine not only induced an electrostatic environment that enabled the assembly of structured ZnO nanograins, but also oriented ZnO growth, producing an ordered arrangement of nanowires on the 1-D scale.

1.5.2.1.2 **Manganese Oxide and Cobalt Hydroxide** Manganese and cobalt materials are technologically important as electrochemical, magnetic and catalytic metal oxides. Oaki and coworkers have developed a biomimetic synthesis, incorporating PAA to template manganese oxide and poly(ethyleneimine) (PEI) to template cobalt hydroxide nanoflakes with interior mosaic structures [47]. Previously, manganese oxide nanocrystals have been synthesized using a solid-state reacted precursor [48], while other syntheses have produced plate and sheet-like morphologies of manganese oxide with submicron feature sizes. As an alternative approach, a 1-D polymer template was used to demonstrate a controlled, room-temperature synthesis of both manganese oxide and cobalt hydroxide. By utilizing these templates, the resultant nanoparticles were built from the bottom up and exhibited an internal hierarchical assembly of mosaic nanocrystals, similar to structures seen in echinoderms.

A mixture of manganese chloride tetrahydrate ($MnCl_2 \cdot 4H_2O$) and PAA immediately formed a clear orange liquid that became turbid after several hours of

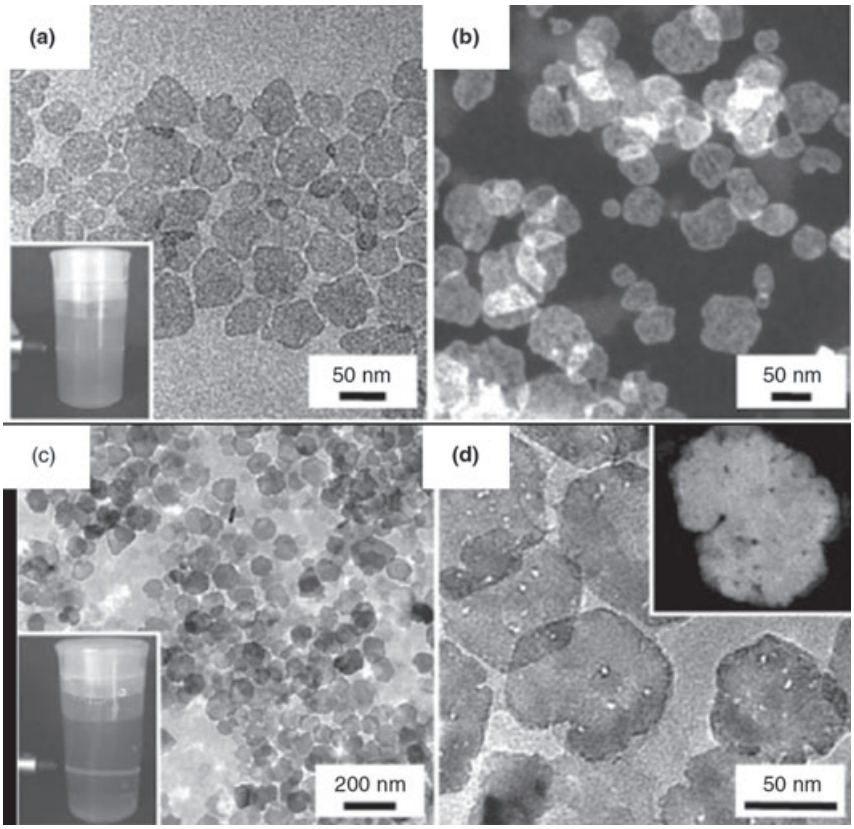

Figure 1.12 Overview of manganese oxide and cobalt hydroxide nanoflakes. (a,b) Manganese oxide with (a) FETEM image and Tyndall light scattering inset and (b) HAADF-STEM image of magnified flakes; (c,d) Cobalt hydroxide nanoflakes with (c) FETEM image and dispersed inset and (d) HAADF-STEM of mosaic structure. Reproduced from Ref. [47], by permission of the Royal Society of Chemistry.

mixing. Both, FETEM and HAADF-STEM showed that the particles in solution were actually hexagonal nanoflakes on the order of 50 nm and composed of 2–3 nm nanograins (mosaic structure) with an approximate 10 nm thickness (Figure 1.12a,b). The presence of manganese oxide was confirmed by energy-dispersive X-ray (EDX) analysis, while HRTEM and FFT suggested a birnessite crystal lattice composed of edge-shared MnO_6 octahedrons. A dispersed liquid film of Mn_3O_4 was drop-cast onto a silicon wafer, and an FT-IR spectrum collected. The results indicated that the mosaic interior of the birnessite-type manganese oxide contained a PAA-controlled crystal structure in the presence of sodium ions.

A similar synthesis incorporating cobalt chloride hexahydrate ($CoCl_2 \cdot 6H_2O$) and PEI produced a reddish-yellow composite solution that was shown to be composed of hexagonal nanoflakes that were less than 100 nm in size. Both, FETEM and

FESEM were used to identify the rough features of the nanoflakes, which were shown to be approximately 10 nm thick and composed of 5 nm crystals (Figure 1.12c,d).

An EDX analysis confirmed the composition of $Co(OH)_2$–PEI containing traces of sodium ions and water molecules in between the monolayers of a brucite-type crystal lattice. Finally, SAED, HRTEM, FFT, XRD and FT-IR were each used to confirm that the material was composed of octahedral coordinated cobalt nanoflakes with intercalated sodium ions in a brucite-type structure.

The results from both syntheses have indicated that tailoring the polymer template for a specific metal precursor could yield functional nanomaterials with highly controlled properties. The nanoflakes of manganese oxide and cobalt hydroxide were synthesized with mosaic interiors that were ascribed to a stepwise crystal growth. Similar to the formation shown in Figure 1.11, this growth can be understood as a series of inhibitions and regrowths at the defect sites, as demonstrated previously for the echinoderms.

1.5.3 Diatoms

In Nature, diatoms represent one of the largest groups, and perhaps one of the most studied single-celled eukaryotic microalgae found in almost every seawater and freshwater habitat. These microorganisms have silica-based cell walls, which range in size from ~50 to 500 nm (Figure 1.13) [49]. Although diatom silica is X-ray amorphous, it still exhibits highly regular and rather exquisite patterns of pores, ridges or tubular structures that are formed under genetically controlled processes. Studies using electron microscopy have revealed that the valves and girdle bands associated with silica formation are formed inside the cell, within highly specialized membrane-bound compartments called silica deposition vesicles (SDVs) [50]. When morphogenesis has been completed, these silica species are deposited on the cell surface using SDV exocytosis.

Currently, microelectronics relies on bulk silica as an important dielectric material that is often used as an insulating template for further reactivity. On the nanoscale, silica can be synthesized by polymerizing silicic acid in an aqueous system, or through hydrolysis and condensation of silicon alkoxides in the Stöber synthesis [51]. The mechanism of these two methods is unique. The first method is dominated by monomers and tetra-functionalized species, such that the resultant silicate sols are uniform, which means that they are fully hydrolyzed and grow by monomer addition. In contrast, for the second method, di- and trifunctionalized species are dominant for alkoxides. Regardless of the synthesis used, these particles induce a fractal interior with minimal morphological control due to their common template, ammonium hydroxide [51].

In Nature, specific silicon transport proteins (SITs) produced by diatoms are responsible for the uptake and delivery of orthosilicic acid ($Si(OH)_4$, $pK_a = 9.8$) to the diatom. Within the cell, orthosilicic acid is then concentrated up to 1000-fold, resulting in the condensation of amorphous, hydrated silica [45]. Strikingly, the

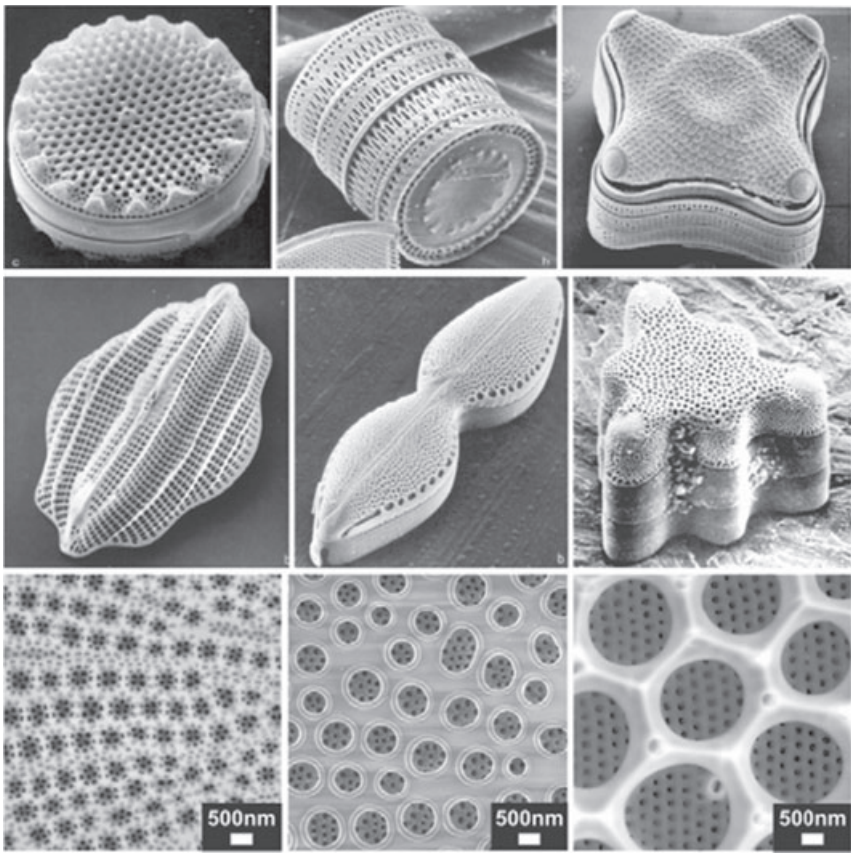

Figure 1.13 Scanning electron microscopy images of the cell walls of a variety of diatom species. Reprinted from Ref. [45], with permission from Elsevier.

polycondensation of silica occurs in neutral to slightly acidic pH conditions, under ambient temperatures and pressures. Although these conditions are considered mild, diatoms still have control over the product morphology. It is understood that the patterns created by diatoms are species-specific, and consequently their directed growth process must be regulated in a genomic manner [51].

Recently, significant effort has been devoted to determining the specific templates used by different species of diatoms in silica formation. Although, diatom cell walls consist primarily of silica doped (~97%) with trace amounts of aluminum and iron, they also contain a wide variety of incorporated organic molecules and proteins [52]. In fact, solid-state nuclear magnetic resonance (NMR) spectroscopy has revealed that some these molecules and coat proteins are encapsulated within the silica matrix [53, 54]. Two main templates for silica growth were identified after dissolution of the silica cell wall with hydrogen fluoride (HF) or ammonium fluoride. In the following sections, we will show how these templates have been

optimized and utilized for further reactivity, thereby revealing interesting properties that are directly applicable to the synthesis of novel nanomaterials.

1.5.3.1 Biological Synthesis of Silica Nanoparticles

Extracted and purified from up to three species of diatoms (*Cylindrotheca fusiformis, Thalassiosira pseudonana* and *Eucampia zodiacus*), silaffins are polypeptides (4–17 kDa) with a variety of post-translational modifications, including proplylamino-functionalized lysine side chains (Figure 1.14) [49]. Currently, four silaffin genes have been identified (one from *C. fusiformis* [*sil1*] and three from *T. pseudonana* [*tpSil1, tpSil2* and *tpSil3*]), which encode for eight known polypeptides. Of these four genes, only *tpSil1* and *tpSil2* have shown sequence similarities, likely from gene duplication; however, the overall lack of sequence similarity strongly suggests that the post-translational modifications of silaffins are critical to their function. These post-translational modifications include the monohydroxylation of lysine and proline, dihydroxylation of proline, *o*-phosphorylation of serine, threonine, hydroxyproline and hydroxylysine, glycosylation, sulfation of carbohydrate moieties, and the alkylation of ε-amino groups of lysine [52, 55]. These modifications are charged and stabilized through electrostatic interactions between the phosphate groups on one silaffin to the charged amines of another, inducing a self-assembled template available for further reactivity.

The different structures associated with different species of diatoms are directly related to the silaffin being studied. For instance, spheres (silaffin-1/2L mixture from *T. pseudonana* [56]), dense plates (silaffin-3 from *T. pseudonana* [56]) or porous sheets (silaffin-1/2H mixture from *T. pseudonana* [56] or natSil-2 from *C. fusiformis* [57]) are all a function of a precursor template. While silaffins are responsible for controlling which shapes are formed in the SDV, positively charged long-chain polyamines (LCPAs) are an integral part of silica condensation [45]. Those silaffins that are negatively charged must be stabilized by the LCPAs, or the

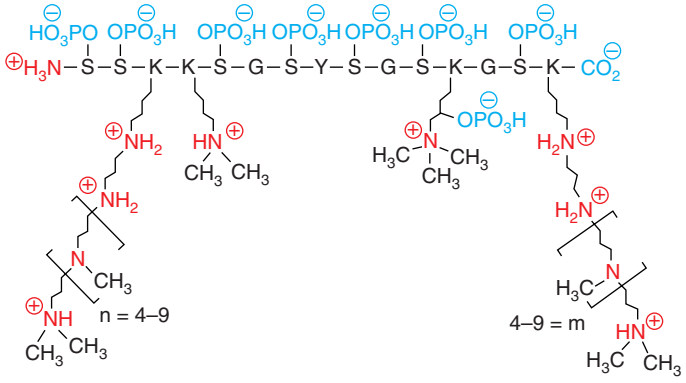

Figure 1.14 Chemical structure of silaffin-1 A_1 from *C. fusiformis*. Reproduced with permission from Ref. [55]; © 2006, Wiley-VCH Verlag GmbH & Co. KGaA.

recently discovered silacidins [58] (in *T. pseudonana*), to complete silica condensation.

The LCPAs are nonprotein components (>3.5 kDa) that have been found encapsulated in the silica matrix of the diatom, and isolated through a series of HF extractions [59]. Unlike silaffins, which have a peptide backbone, these polyamines consist of linear chains of C–N-linked PEI units that are bonded to a putrescine or putrescine derivative backbone. The chemical composition of these LCPAs is unique for each diatom species, with variable repetitions and degrees of methylation.

Similar to the reactivity of silaffins, silica production in the presence of LCPA and silicic acid requires an addition of counteranion in the form of phosphate, sulfate or citrate ions. This electrostatic matrix is projected to induce the formation of silica by the microscopic aggregation of LCPAs and subsequent phase separation into a LCPA–anion-rich microdroplet [50]. In his 2002 theory of cell wall morphogenesis, Manfred Sumper suggested that the formation of secondary patterns, as seen on the diatom cell wall, is related to the wall-to-wall distance of the areolae, hexagonally packed polyamine monolayers and the polyanion concentration, on the surface of the SDV [14]. For example, a size-control experiment using LCPAs from *Stephanopyxis turris* has shown that the size of nanoparticles was dependent not only on the phosphate concentration but also on whether orthophosphate or a more highly charged pyrophosphate was used [60].

The biological mechanism of diatom silica formation has been demonstrated as a valuable source for bioinspired templates for non-natural metal oxide synthesis at ambient temperatures and near-neutral pH. Moreover, silica nanostructures can be tuned according to a specific template, providing functional properties that can be directly applied in the design of nanomaterials. These syntheses have integrated moieties that are tuned for a specific function, such as the encapsulation of functional enzymes [61, 62] and controlled construction of nanomaterials through nanoscale building blocks [63–65]. Thus, we will focus here on how these synthetic strategies control and optimize silica formation, and how such materials can (potentially) be used in a variety of applications.

1.5.3.2 **Biomimetic Synthesis of Silica Nanoparticles**

Mimicking the nanopatterns of the diatom cell wall remains a major challenge for materials scientists because the natural reaction mechanism is still unknown, with many essential components for silica precipitation yet to be discovered. However, it is well known that the terminal amine templates interact with monosilicic acid to induce the specific morphology of the resultant silica. A variety of different silica precursors have been used with a number of templates, including tetramethyl orthosilicate (TMOS) [62, 66–73], tetraethyl orthosilicate (TEOS) [63, 74, 75], tetrakis(2-hydroxyethyl) orthosilicate (THEOS) [74], sodium silicate [65], a silicon–catecholate complex [64, 76] and dipotassium tris(1,2-benzenediolato-*O,O′*) silicate [77]. In addition, a variety of bioinspired templates have been used, including synthetic and natural polypeptides [63, 66, 75], polyamines [68, 73, 76], and even modified organic materials, including cellulose [74] and chitosan [78].

Recently, synthetic or natural polypeptides have been created or modified to serve as silica condensation templates. Examples of these include the poly(amino acids) [79], the diatom-derived R5-peptide [66], chimeric polypeptides [64, 67], block copolypeptides [71, 72, 75, 80], lanreotide [63] and even the naturally occurring protamine [65]. These polypeptides have been used to produce a variety of silica shapes and sizes, which can be tuned to perform a variety of applications, including transport and the separation of encapsulated materials [62], or potentially for drug delivery [73].

1.5.3.2.1 **Block Copolypeptides** Block copolypeptides, which have been used as templates for controlled silica formation [71, 72, 75, 80], consist of covalently linked domains (domains) of hydrophilic and hydrophobic polypeptides. Due to their unique polarities, these block segments induce an amphiphilic character, resulting in self-assembled vesicles in aqueous solution [75]. For example, a copolypeptide consisting of polymers of linked lysine and glycine residues (Lys-*b*-Gly), was used as a silica template in the presence of orthosilicic acid and phosphate buffer at pH 7.2 [72]. Different methods of silica precipitation were tested by changing the amount of silica precursor or the amount of phosphate present during precipitation. In Method I, 6 mmol of silica precursor was used, while in Methods II and III 30 mmol was used. In addition, Method III included 7.5 mmol more phosphate buffer than the other two methods (0.1 *M*). An increase in phosphate buffer (Method III) resulted in a spherical morphology (40–120 nm diameter), while the other two methods produced mostly platelets for the Lys-*b*-Gly block copolypeptides (Table 1.1).

The formation of platelets or spheres with the Lys-*b*-Gly copolypeptide suggested that there was a morphological dependence on the phosphate concentration and solubility of the hydrophobic block. As the relative hydrophobicity was increased though the addition of Gly residues, substitution of the Gly block with the more hydrophobic Ala block, or the loss of Lys residues, the solubility of the copolypeptide was decreased, making it more susceptible to phase separation. The hydrophobic block was more energetically stable when it was associated, rather than by

Table 1.1 Silica morphology for each copolypeptide at different synthesis conditions.

***Co*-polypeptide**	**Morphology (Methods I, II)**	**Morphology (Method III)**
Lys_{200}-*b*-Gly_{50}	Platelets	Spheres
Lys_{340}-*b*-Gly_{85}	Platelets	Spheres
Lys_{110}-*b*-Gly_{55}	Spheres and platelets	Spheres
Lys_{320}-*b*-Gly_{160}	Platelets	Spheres
Lys_{400}-*b*-Ala_{100}	Spheres	Spheres
Lys_{390}-*b*-Ala_{65}	Spheres	Spheres
Lys_{450}	Platelets	Platelets

being free in solution, so aggregation of this region was induced and the condensation of spherical silica was promoted, rather than platelets. In addition, an increase in phosphate ions (Method III) had a similar effect by electrostatically interacting with the hydrophilic lysine block and promoting silica sphere production. Thus, by optimizing the hydrophobicity of the template and the phosphate concentration, specific morphologies could be obtained. In addition, the platelets from Method II were smaller than those from Method I, as a result of the higher concentration of silica precursor and subsequent increase in the rate of nucleation (Figure 1.15).

Cyclic lanreotide is a dicationic octapeptide that self-assembles into nanotubes in water with a monodispersed diameter of 24.4 nm and a wall thickness of 1.8 nm [63]. This polypeptide has two exposed protonatable amine groups that can be used as catalytic sites for silica condensation (Figure 1.16).

By exposing the nanotubes to a TEOS-derived $Si(OR)_3O^-$ precursor, silica was deposited and bundles of silica nanofibers were formed with a total length up to 7 μm, and each nanotube extending up to 3 μm. A TEM analysis determined that the dried fibers consisted of bundles of aligned nanotubes with homogeneous inner and outer diameters of 14–16 nm and 28–30 nm, respectively. In addition, the two concentric tubes were both 1.4 nm thick, and separated by 2 nm, which is the approximate width of the lanreotide molecule. The proposed dynamic templating mechanism suggested that the cationic lanreotide nanotube surface catalyzed the silica condensation by electrostatic forces, and the consequent anionic silica deposits promoted additional lanreotide assembly through synergetic neutralization of the entire system (Figure 1.17).

Not only does this templating mechanism provide insight into the potential fundamental mechanisms used in biological systems, but it also allows for the production of superstructures that greatly exceed the size of the original template [81]. Consequently, a variety of new silica structures can be synthesized that maintain nanoscale properties even in the microscale or larger.

1.5.3.2.2 **R5 Peptide** The R5 peptide (H_2N-SSKKSGSYSGSKGSKRRIL-CO_2H) is an unmodified biomimetic analogue of the silaffin precursor peptide (sil1p) in *C. fusiformis* that exhibits silica condensation activity at neutral pH in a buffered phosphate–citrate solution [13]. Several enzymes have been encapsulated within the silica matrix with the R5-peptide as the silica template, including catalase, horseradish peroxidase and butyrylcholinesterase [61, 66]. The silica matrix provides an inert cage around the enzyme, which not only protects it from the surrounding environment and increases its shelf life, but also provides the basis for biosensors and catalysts. In fact, it is not only enzymes that have been encapsulated – CoPt and CdSe and ZnS nanoparticles have also been successfully encapsulated into the silica matrix [61]. These magnetic nanoparticles may serve a wide variety of applications, including catalysis, biological labeling and detection and electronics [69]. In addition, the encapsulated magnetic particles have potential use in enzyme encapsulation, as they might provide a physical means for separating the enzyme from the reaction mixture.

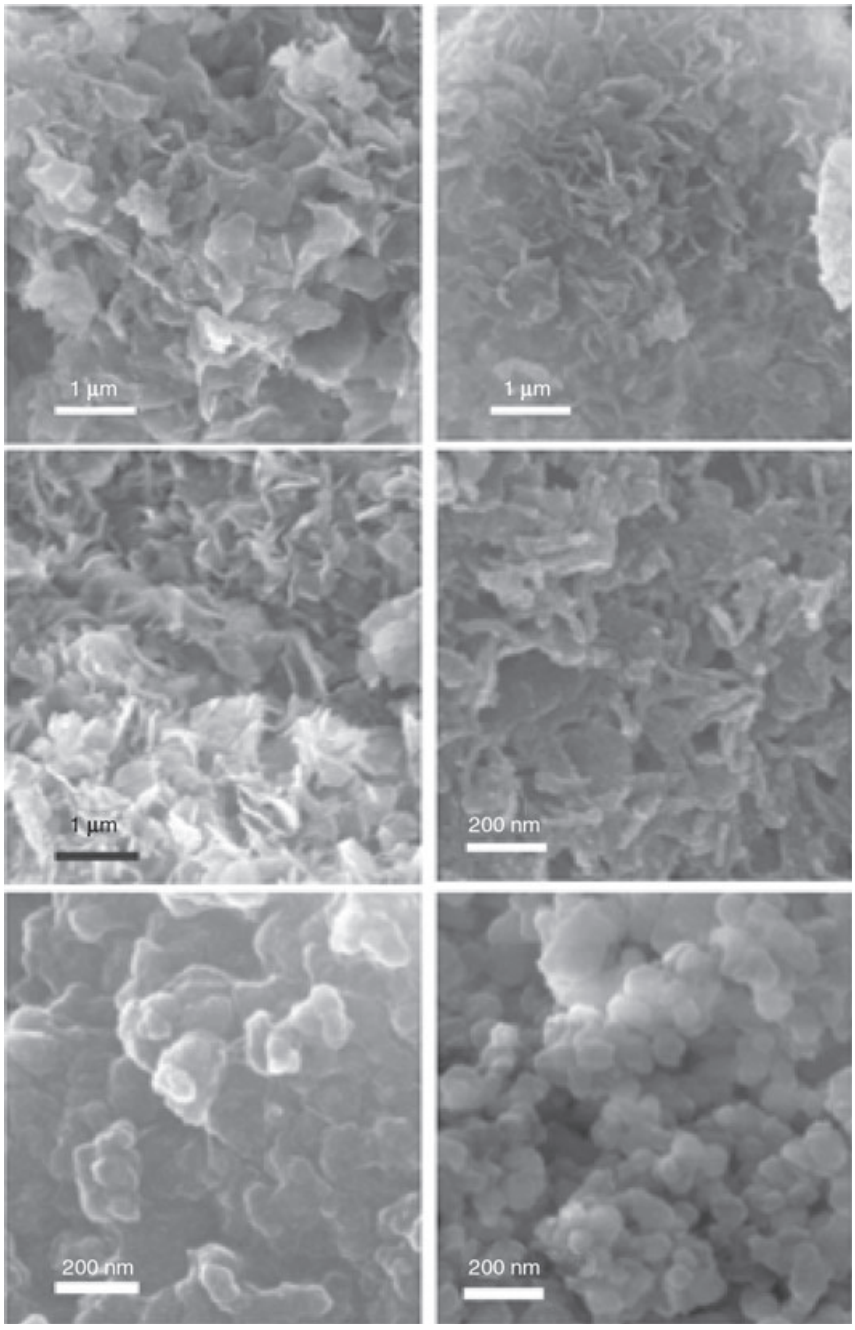

Figure 1.15 Field-emission scanning electron microscopy images of silica nanoparticles synthesized using (left) Lys_{340}-*b*-Gly_{85} and (right) Lys_{320}-*b*-Gly_{160} using (top to bottom) Methods I, II and III respectively. Reproduced with permission from Ref. [72]; © 2007, Wiley-VCH Verlag GmbH & Co. KGaA.

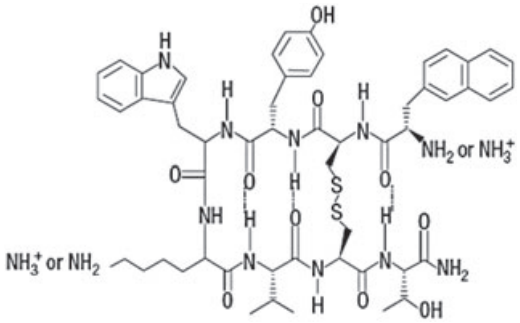

Figure 1.16 Structure of lanreotide showing the two charged amine sites responsible for silica condensation. Reprinted from Ref. [63] by permission from Macmillan Publishers Ltd.

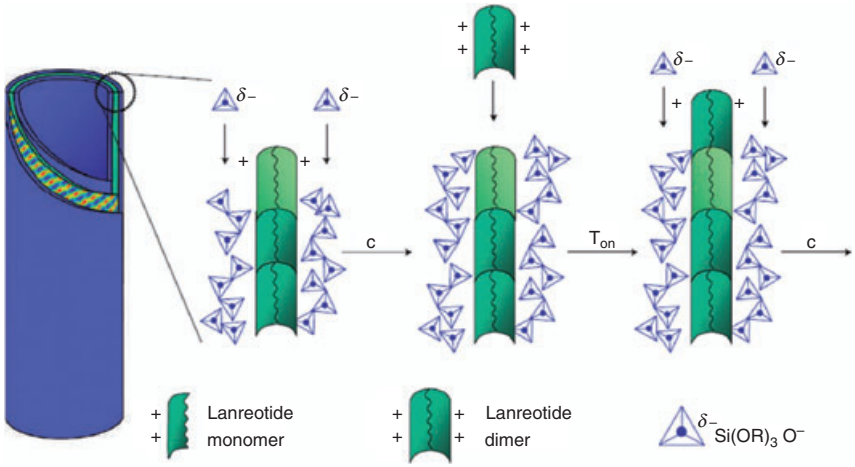

Figure 1.17 Dynamic templating model for the mechanism of silica condensation into nanofibers. The cationic lanreotide nanotube surface utilizes electrostatic attraction to catalyze silica condensation (step C) and the anionic silica deposit promotes additional lanreotide assembly (step T_{on}) through neutralization of the system. Reprinted from Ref. [63] by permission from Macmillan Publishers Ltd.

Chimeric (fusion) proteins that incorporate the R5 peptide have been synthesized to control and precipitate silica nanoparticles. Po Foo and coworkers have utilized a two-component chimeric protein consisting of the R5 polypeptide (from *C. fusiformis*) and the self-assembling domain based on the consensus repeat in the major ampullate spidroin protein 1 (MaSp1) of *Nephila clavipes* spider dragline silk [64]. MaSp1 forms highly stable β-sheet secondary structures that can be spun into intricate fibers which, when fused with the silica-templating R5-peptide, allow for the formation of film-like and fibrous silica structures (Figure 1.18).

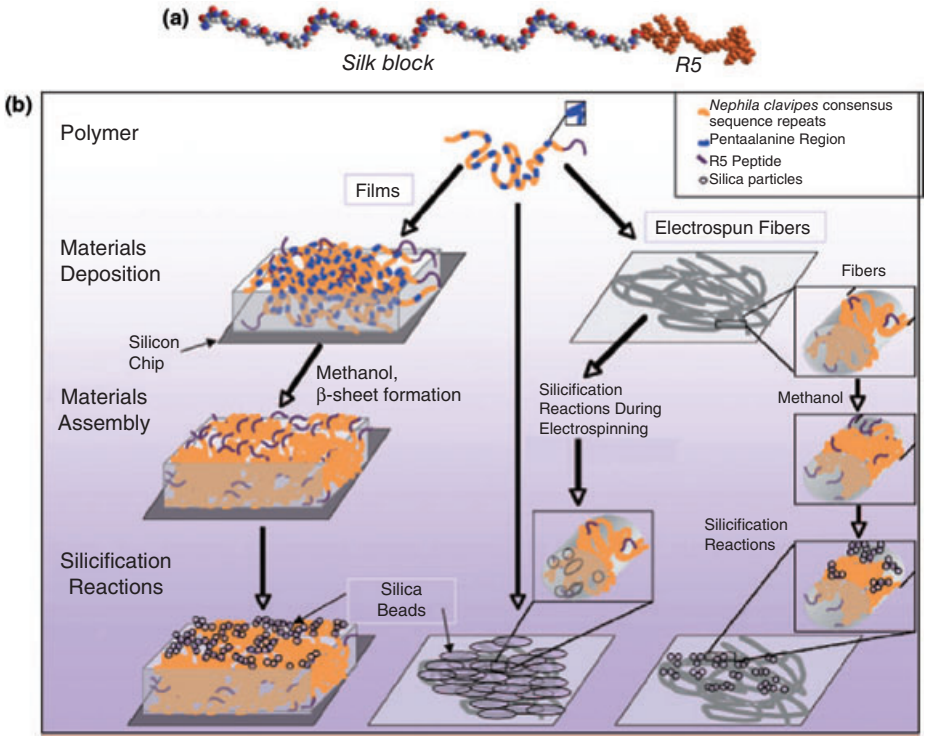

Figure 1.18 Schematic representation of the fusion protein and its use in controlled silica nanomaterial formation. (a) Schematic of the chimeric polypeptide consisting of the R5 and silk polypeptides; (b) Model of R5-silk polypeptide processing into films and fibers and subsequent silication reactions. Reproduced from Ref. [64]; © 2006 National Academy of Sciences, USA.

Two different silk motifs were investigated, one with and one without a cell-binding motif. When silica precipitation was conducted under ambient temperatures and near-neutral pH with ratios of Si : N = 22 : 1 in solution, silica nanospheres with >1 μm diameter were synthesized for both fusion proteins. Thermal analysis determined that ~90% of the material was the templating protein and 10% was silica. Nitrogen absorption analysis showed pore radii <10 Å and low surface areas (~10 $m^2 g^{-1}$), which are smaller than the R5-peptide-templated silica nanospheres (pore radii 35 Å, surface area 600 $m^2 g^{-1}$). Although silica precipitation was successfully conducted with the free R5-silk peptide in solution, the silk moiety provides a means for size and shape control for the growing silica nanocomposite. When these chimeric proteins were spun into fibers via electrospinning, silica nanospheres were formed with much smaller diameters (200–400 nm). In addition, when the chimera CRGD15mer + R5 was electrospun concurrently with the silica condensation reaction, silica was deposited in and on the fibers, resulting in elliptically shaped silica particles that were fused to the fibers. As a result, processing

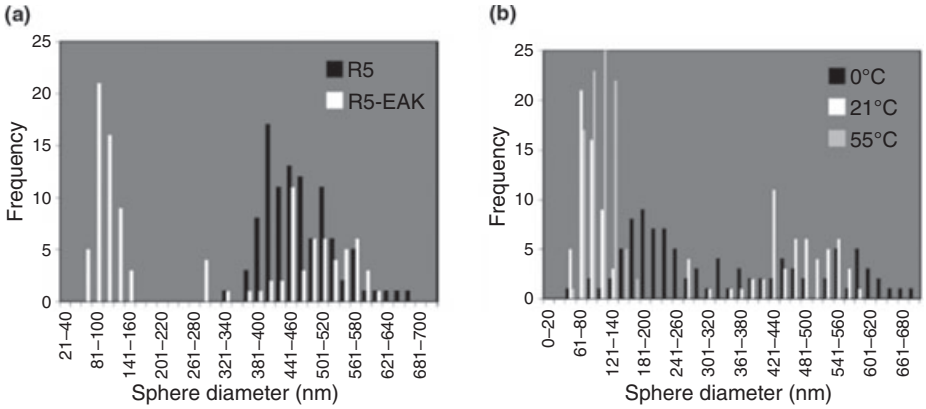

Figure 1.19 (a) Sphere diameter distribution for silica particles precipitated using R5 peptide (black) and R5-EAK_1 (white); (b) Sphere size distribution for silica particles formed with R5-EAK_1 at different temperatures. Reprinted with permission from Ref. [67]; © 2008, American Chemical Society.

modifications can be tailored to structural templates, inducing silica nanoparticles of specific sizes and morphologies. Most importantly, as this reaction is conducted under mild conditions, these fibers have a variety of potential applications in specialty materials, including those used in the biomedical field [64].

Another chimeric polypeptide consisting of the R5-peptide and a self-assembling hydrophobic–phobic (HP) protein monomer capable of self-assembly was also used to direct silica precipitation *in vitro* at neutral pH and ambient temperatures [67]. The HP monomer consisted of an n-AEAEAKAKAEAEAKAK-c sequence, called EAK_1. These monomers self-assemble into stable β-sheet supramolecular structures due to their binary patterns, and this leads to hydrophobic and hydrophilic faces, where favorable side-chain interactions result in aggregation through hydrophobic and electrostatic interactions, respectively. Thus, an EAK_1–R5 chimeric polypeptide assembles into fibrous aggregated hydrogels and precipitates silica nanospheres with sizes that are dependent on the reaction temperature (Figure 1.19).

The size distribution of the control R5 template for silica formation produced a distribution of nanoparticles in the diameter range of 402 to 530 nm, as opposed to the R5-EAK templates, which showed a bimodal range of diameters from 63 to 103 nm and from 385 to 541 nm, respectively. However, at higher temperatures, the R5-EAK_1 peptide promoted rapid nucleation, resulting in a loss of bimodal character and subsequently the production of smaller silica nanoparticles (64–116 nm diameter). Not only does the change in diameter size with different temperatures allow for the production of size-specific tailored silica nanocomposites, but the loss of bimodal character at a higher temperature also allows for an even tighter control of the silica structure under these conditions. By adjusting this morphology under mild reaction conditions, biologically active matrices can be

synthesized and perhaps used in solid-state enzymatic catalysis, physiologically active biomatrix implants and, potentially, also biosensors [67].

1.5.3.2.3 **Poly-L-Lysine** Poly-L-lysine (PLL) has been implicated in silica formation because of its ability to adopt an α-helix, β-sheet or random coil conformation. PLL is an excellent silica template due to its ability to create different silica morphologies by simply changing the reaction conditions to afford a specific secondary structure. Hawkins and coworkers have shown that silica pore sizes could be modified by changing the secondary structure of the polyamine [82]. For example, silica composites that are formed by α-helix PLL under basic conditions (pH 11.2) produced 1.5 nm pore sizes, whereas silica formed using PLL β-sheets (heated to ~52 °C) resulted in larger pore sizes (~1.5–8 nm). In both cases, silica formation was dependent on the PLL concentration and reaction conditions.

More recently, Tomczak and coworkers have shown that hexagonal silica platelets could be synthesized using PLL as a precursor [83], with the morphology of silica species being tailored according to the molecular weight of the PLL used. Higher molecular-weight PLLs (>100 lysines) produced hexagonal silica platelets, while lower molecular-weight PLLs afforded silica nanospheres. Although PLL is a random coil at near-neutral pH (7.5), electrostatic interactions between the larger PLL templates and the silica promotes an α-helical structure formation during condensation, resulting in hexagonal plates (Figure 1.20).

Gautier and coworkers have also utilized PLL by incorporating the template into the pores of polycarbonate membranes to further control the silica size and morphology [84]. Silica formation within confined spaces is important for a variety of materials applications. For example, silica-encapsulated enzymes integrated into a micro- or nano-filter could be used in catalysis, where the substrate would pass through the membrane, interact with the enzyme, and pass through the filter as the product.

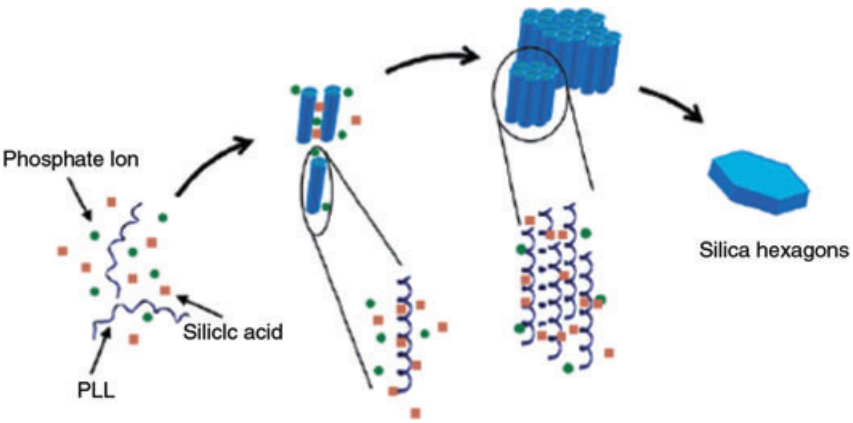

Figure 1.20 Proposed model of PLL-induced condensation of silica platelets. Reprinted with permission from Ref. [83]; © 2005, American Chemical Society.

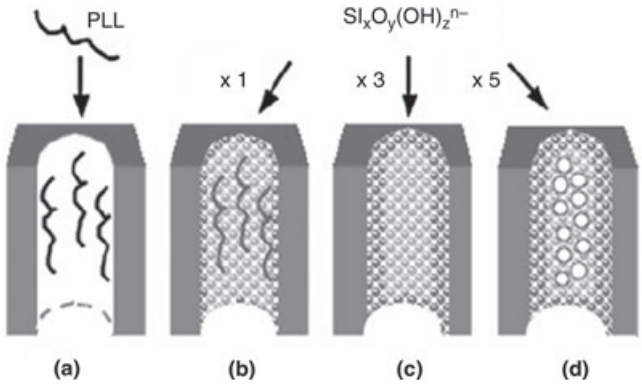

Figure 1.21 Schematic of silica tube formation. (a) PLL is first integrated onto the surface of the pore; (b) Addition of silicates initially results in the formation of a silica shell; (c) Multiple additions of silicates thicken the silica shell; (d) Further addition of silicates results in core particle growth. Reprinted from Ref. [84] with permission from Elsevier.

Rod-like silica tubes were synthesized when PLL was integrated into polycarbonate membrane pores (sizes ranging from 1200, 400 and 200 nm) (Figure 1.21). Multiple successive impregnations (fivefold) of the pores with sodium silicate resulted in the formation of a silica-filled pore, while the thickness of the silica wall decreased as its pore size decreased. In addition, TEM analysis determined that the primary particle diameter was independent of the pore size (~9 nm). However, this primary pore diameter was smaller than for silica formed on the surface (~11 nm), which is most likely the result of PLL localization in the pore rather than of silicate–PLL interactions.

1.5.3.2.4 **Polyamines** Nonpeptide biomimetic analogues to silica-precipitating peptides are drawn from the isolated LCPAs found on the cell walls of diatoms. Some of these polyamines include poly(allylamine) [79], (PEI) [73], *N*-methylpropylamine (PA) [76] and amine-terminated dendrimers [62, 68–70]. Each of these classes of compound represents a different structural aspect to silica templating, including the number of amines, the number of spacer atoms between the amines, its relative degree of methylation, and the presence and number of branching elements. All of these factors affect the resultant physical properties and subsequent reactivity of the silica nanoparticle produced.

Poly(ethyleneimine) Poly(ethyleneimine) is a branched polyamine ($M_w = 1800$) consisting of a 1 : 2 : 1 ratio of primary, secondary and tertiary amines that makes it structurally similar to polyamines isolated from *S. turnis* and *C. fusiformis* [85]. These PEIs were integrated as spherical reverse micelles (RMs) made from bis(2-ethylhexyl) sulfosuccinate sodium salt (AOT) in iso-octane, providing a constrained environment for silica precipitation. These RMs exchanged their contents

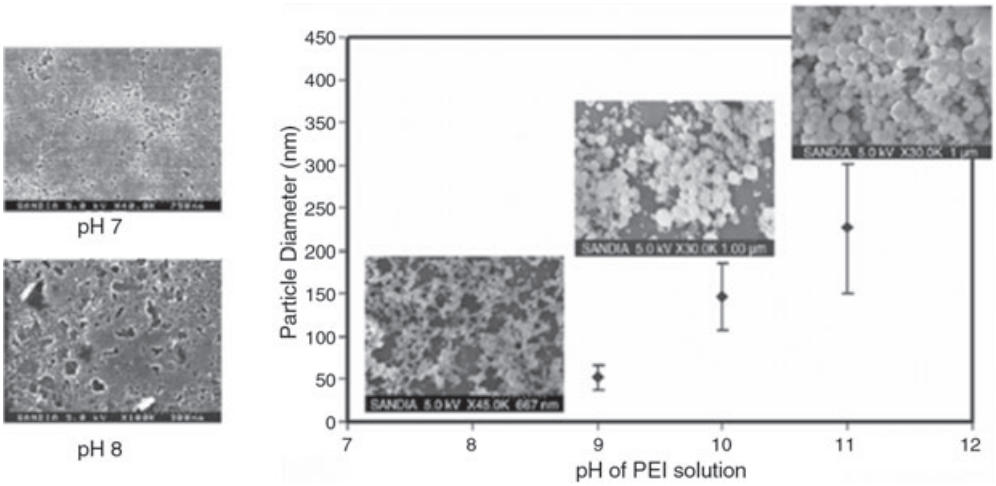

Figure 1.22 Diameter and dispersity of silica particles formed in aqueous PEI solutions at 0.05 *M* primary-amine concentration and 1 *M* silicic acid in a 4:1 volume ratio at pH 9, 10 and 11. SEM images of the nanoparticles are provided as inserts, and the silica formed in pH 7 and pH 8 is shown on the left. Reproduced with permission from Ref. [73]; © Wiley-VCH Verlag GmbH & Co. KGaA.

quickly through fusion and redispersion processes (106–108 $m^{-1} s^{-1}$). Consequently, PEIs reacted with silicic acid from a tetramethylorthosilicate (TMOS) precursor produced silica nanoparticles with a size and structure control that was dependent on the size of the RM [73]. Before testing silica precipitation in the RM, condensation of silica was investigated at a variety of pH values (6.3–11.2) in water. An instantaneous precipitation occurred at basic pH (9–11), a slow deposition of amorphous silica matrix at near-neutral pH, and no precipitation occurred for acidic pH (Figure 1.22).

Consequently, it was expected that PEI would provoke a similar pH dependence when reacted with the RM. However, when PEI and silicic acid were incorporated into the RMs prepared in iso-octane, the initial pH of the amine solution was negligible in terms of controlled silica growth. The pH of the AOT was confirmed with 8-hydroxypyrene-1,3,6-trisulfonic acid (HPTS); it was determined that the local pH remained consistent (≥9), independent of the pH of the inserted PEI. In addition, changes in the size of the water pool (w_o = 5–40, where $w_o = [H_2O]/[AOT]$) led to the production of a variety of particle sizes. The smallest RMs (w_o = 5) fashioned very small amounts of silica due to the tight interactions between the water molecules, the anionic sulfonate groups of the AOT, and cationic sodium ions. However, larger RMs (w_o = 10) resulted in hollow silica shells with diameters on the order of 1 μm. In this case, the RM remained stable during the reaction, and the silica units only interacted by micellar exchange. For the largest RM sizes (w_o ≥ 20), destabilization of the RM occurred due to the addition of additional water

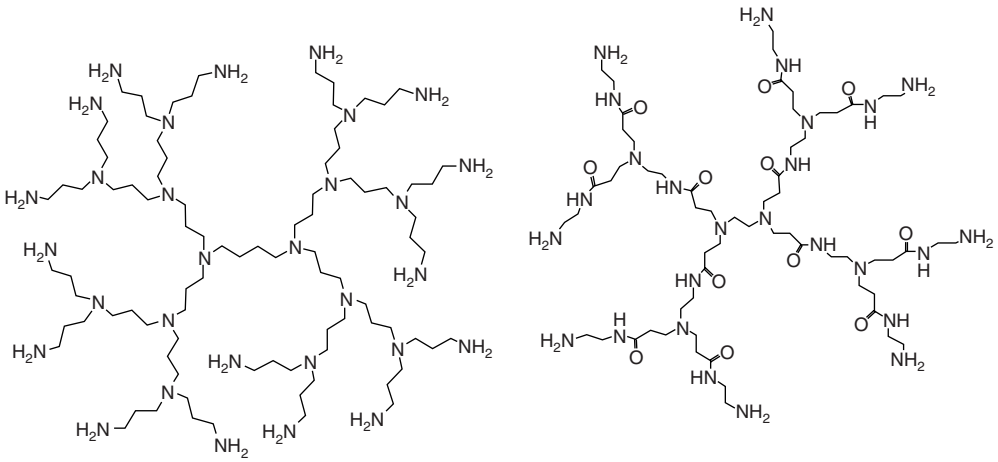

Figure 1.23 Chemical structure of the G-3 PPI dendrimer (left) and G-1 PAMAM dendrimer (right). Reprinted with permission from Ref. [68]; © 2004, American Chemical Society.

molecules in the RM from the condensation of silanol groups, thus increasing the w_0 during the reaction.

Therefore, RMs with an initial $w_0 = 20$ became unstable as soon as the reaction was initiated, and this resulted in tri-modal nanosphere diameter distributions (56 ± 6, 172 ± 31 and >200 nm, respectively). This suggested multiple destabilization pathways of the RMs during the condensation, resulting in different silica sizes. Moreover, the morphology of the silica was determined by the size of the RM, as well as its stability during the condensation reaction. By understanding the mechanism of this reaction, the sizes and shapes of silica could be tuned to serve a variety of functions, including an inert matrix for catalysis, drug delivery and transport [37].

1.5.3.2.5 **Dendrimers** Amine-terminated dendrimers are unique, unimolecular polymer templates with defined reactivity as a function generation size (the number of branching elements). Dendrimers have been utilized as a template, capable of localizing a high concentration of biomimetic moieties, including silica [68]. Not only have dendrimers been used as stabilizing templates for sol–gel composites [68], but amine terminated polypropylenimine (PPI) and polyamidoamine (PAMAM) dendrimers have also been used as nonpeptide mimics to the unmodified R5 peptide for the controlled formation of silica nanospheres (Figure 1.23) [62, 68–70].

Positively charged dendrimers only produce silica nanospheres in the presence of an anion, such as phosphate, sulfate or acetate, at pH 7.5. The size of silica produced is dependent on the generation size of the dendrimer, where larger generations produce larger silica nanospheres. Comparisons between the PPI and PAMAM dendrimers have revealed that the PPI dendrimer has a reduced specific

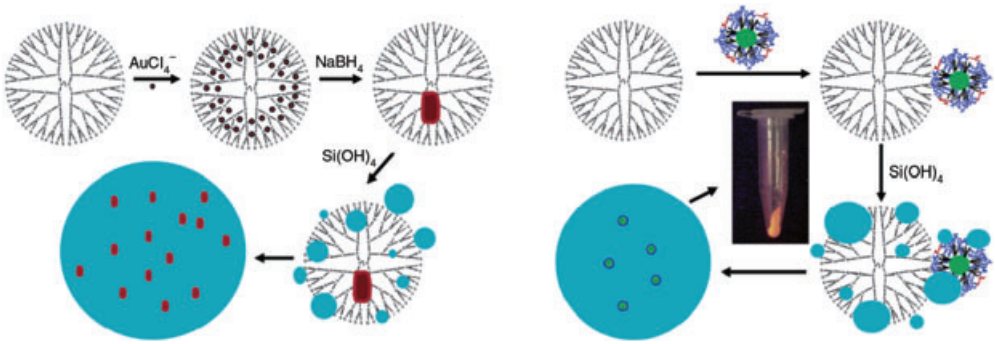

Figure 1.24 Schematic silica encapsulation of Au^0 nanoparticles (left) and CdSe/ZnS core shell AMP quantum dots. Reprinted with permission from Ref. [69]; © 2004, American Chemical Society.

activity because it precipitates silica much faster than does the PAMAM dendrimer of similar generation size [68]. For this reason, detail of the remaining syntheses will be limited only to the PAMAM dendrimer.

Incorporating known concentrations of dendrimers into the silica matrix has enabled specific morphological control over the nanoparticles under mild conditions. This control could be modified and applied directly to the encapsulation of functional components that are necessary for catalysis, biological labeling and detection, and electronic devices [62, 69]. Generation 4 (G4) PAMAM dendrimers have been used to catalyze the encapsulation of gold nanoparticles and CdSe and ZnS core shell AMPQuantum Dots [69]. In this reaction, cationic gold (Au^{3+}) is coordinated to the amine groups of the G4 PAMAM dendrimer, where it is reduced to Au^0 by $NaBH_4$. After lyophilization, energy dispersive X-ray spectrometry (EDS) analysis determined that the gold was either surface-passivated or incorporated with within the dendrimer matrix (Figure 1.24).

Although many of the surface dendrimer amines are occluded by the gold or quantum dot nanoparticles, silica condensation still occurs. In fact, the CdSe/ZnS core shell quantum dots with negatively charged surface carboxylates were encapsulated with 99% efficiency, which suggests that the electrostatic attraction between the quantum dots and the templates was sufficient for encapsulation of these materials [69].

Enzymes have also been incorporated into the PAMAM dendrimer to produce silica nanoparticles. At physiological pH, the interaction between an enzyme and the cationic surface of the PAMAM dendrimer plays an important role in forming supramolecular complexes. As a result, the cationic dendrimer (pK_a ~9.5) interacts with low-p*I* enzymes. For example, glucose oxidase (GO, p*I* ~4.2) was encapsulated in water with a quantitative yield. As phosphate ions compete with the enzyme, GO was poorly encapsulated as phosphate buffer concentrations increased because the phosphate ions significantly reduced the electrostatic interactions between the enzyme and dendrimer (Figure 1.25).

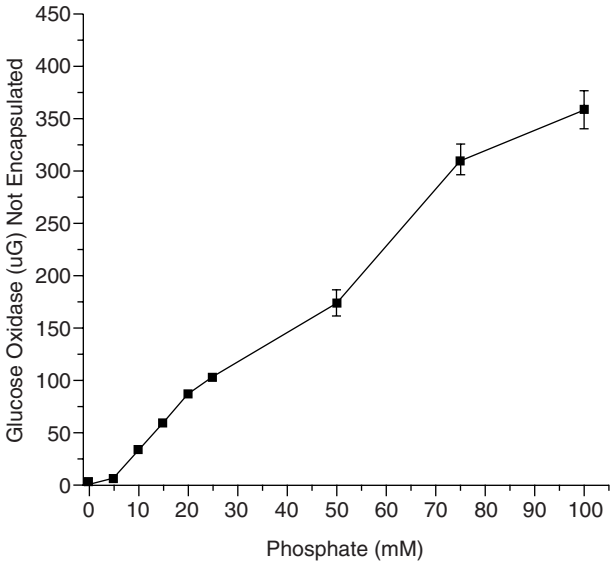

Figure 1.25 Effect of increasing the phosphate buffer concentration on GO encapsulation. Note: initial reactions contained 400 μg of GO. Reproduced with permission from Ref. [62]; © Wiley-VCH Verlag GmbH & Co. KGaA.

A 50% loss in enzymatic activity under optimal conditions was most likely due to unfavorable orientations in the silica framework, or to alterations in steady-state conditions due to a local increase in enzyme concentration in the silica. Long-term storage effects were examined and enzymatic activity was consistent after 30 days of storage at room temperature in buffered solutions. The silica framework provides not only a structural matrix around the enzyme, which physically blocks much of the natural degradation of the enzyme, but also a physical barrier against invading species such as bacteria [62].

1.5.3.2.6 **Effects of Variations of Unbranched Polyamines** Unbranched polyamines were modified to direct control over the size and morphology of silica composites. In order to assess the role of polyamine structure in controlling the morphology of silica nanoparticles, Belton and coworkers have utilized modified polyamines with different degrees of polymerization, different levels of amine methylation, and different lengths of amine chain spacers (Figure 1.26) [77]. The degree of polymerization was evaluated by comparing two naturally occurring polyamines, spermidine and spermine, to the other synthetic polyamines. Amine methylation was investigated through a set of *N,N′*-(bis-3-aminopropyl)-1-3-diaminopropanes with levels of methylation from 0 to 4. For each experiment, dipotassium tris(1,2-benzenediolato-*O,O′*)silicate served as the silica precursor.

Hollow silica nanoparticles are of particular interest due to their potential applications in adsorptive filters, ultrasound imaging, photonic band gap materials and

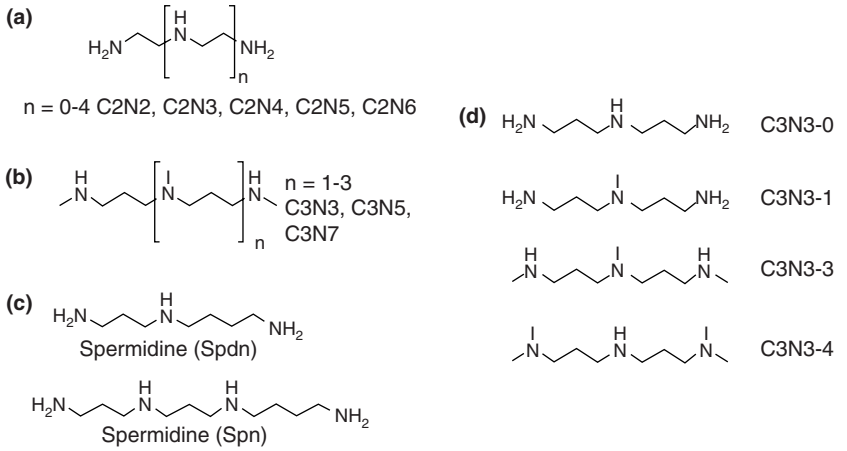

Figure 1.26 Polyamines used in this study. (a) Ethyleneamines; (b) Propylamines; (c) Natural amines spermine and spermidine; (d) C3N3 with varying degrees of methylation. Reproduced with permission from Ref. [77]; © 2008, National Academy of Sciences, USA.

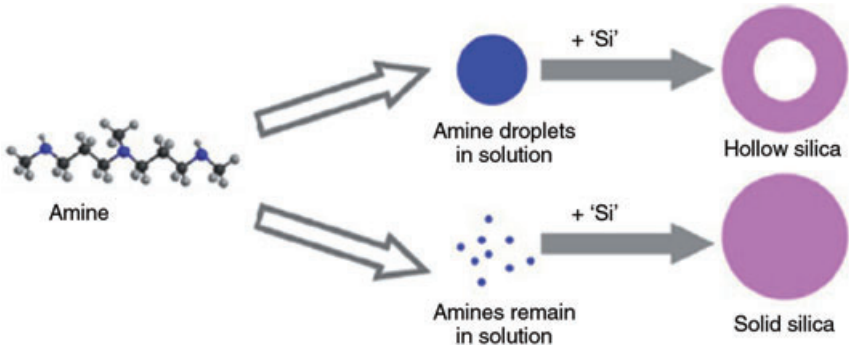

Figure 1.27 Schematic representation of the microemulsion formation leading to hollow silica structures. Reproduced with permission from Ref. [77]; © 2008, National Academy of Sciences, USA.

catalysis [39]. For all of investigated samples, there were mixtures of solid and hollow particles associated with the number of amines per molecule, the amine–amine separation and the size of the polyamine. The larger propylamines, which are the most hydrophobic and most readily form microemulsions, were the most efficient in generating hollow silica nanoparticles.

Two critical factors were identified for controlling the nature of the resultant silica composite in this reaction. First, the template's ability to produce microemulsions determined whether solid or hollow silica was formed (Figure 1.27) [77]. Second, the reaction kinetics of the composite was shown to increase according to the degree of charge associated with the microemulsions. A positively

charged microemulsion introduced a water-free microenvironment, where water removal promoted the condensation of controllable silica.

The kinetics of each silica condensation reaction were quantified using the molybdenum blue method, which is sensitive to monomeric and dimeric silicic acid. Within the initial condensation time, there was a third-order linear relationship between $[Si(OH)_4]^{2-}$ and time. As a result, it was concluded that polyamines with a threefold increase in their third-order rate constant were kinetically active. C2N2-4 and the naturally occurring polyamines spermidine and spermine observed no rate enhancement. All of the propylamines and longer-chain ethyleneamines significantly influenced condensation rates, with C3N7 having a 14-fold increase in catalytic activity.

Increasing the methylation levels in the C3N3 species also increased the third-order rate constant. For all of the kinetically active species, the silica nanoparticles produced were nonporous, which is most likely due to rapid nucleation. Thus, by modifying the composition of the polyamine, the ability to produce microemulsions which lead to hollow silica and the porosity of the silica can be tailored, leading to the production of a variety of potential nanomaterials [77].

1.5.3.3 **Other Biomimetic Templates**

Other natural biomimetic templates that utilize amines as the catalytic sites for silica precipitation have also been reported [74, 78]. Cellulose was recently used as a rigid backbone for silica nanotube formation by introducing oligopropylamido side chains derived from dipropylenetriamine (DPTA) to the C-6 position of almost all of the anhydroglucose units (AGUs) (Figure 1.28) [74].

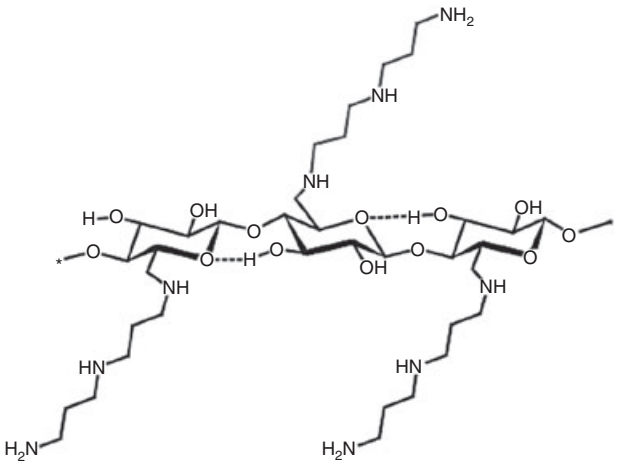

Figure 1.28 Structure of dipropylenetriamine (DPTA) cellulose tosylate. Note that some tosylate residues are present at the C-2 and C-6 positions during the synthesis, as indicated by ^{13}N NMR spectroscopy. Reproduced with permission from Ref. [74]; © 2007, Wiley-VCH Verlag GmbH & Co. KGaA.

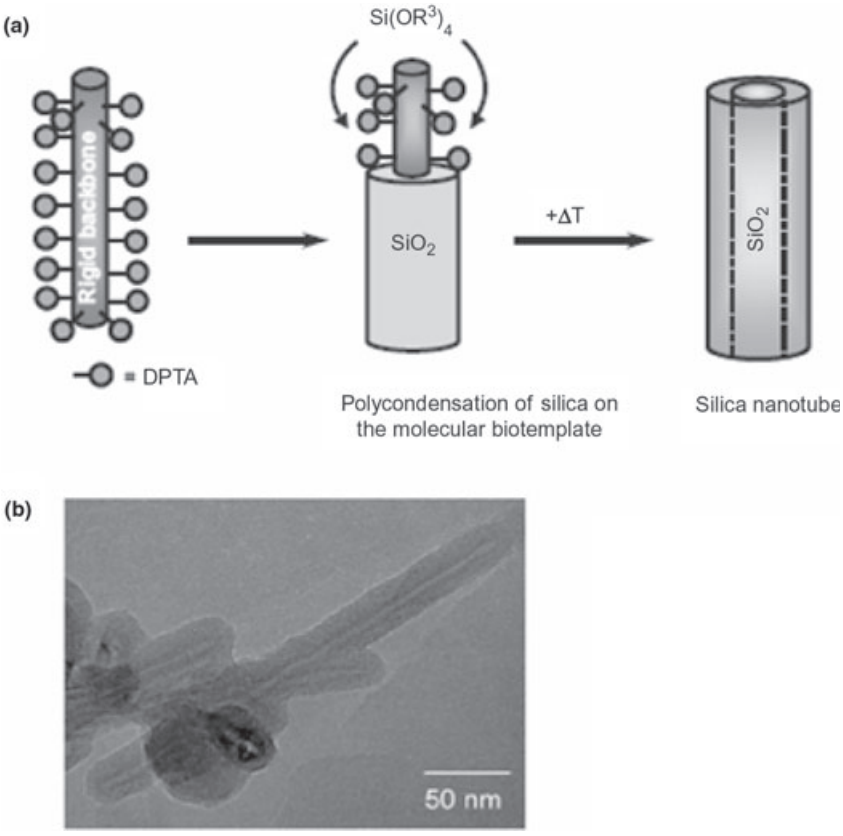

Figure 1.29 (a) Schematic representation of the formation of silica nanotubes from a functionalized biopolymer; (b) TEM images of silica nanotubes formed using the DPTA cellulose tosylate template. Reproduced with permission from Ref. [74]; © 2007, Wiley-VCH Verlag GmbH & Co. KGaA.

These silica nanotubes are technologically significant because they could be used as a nonconductive substitute for carbon nanotubes and as templates for further reactivity. The rigidity of the cellulose backbone exposes its surface amines in water, inducing a hydrogen-bonded amine–silica network (Figure 1.29).

The resultant nanotubes exhibited diameters of 10–30 nm, inner core diameters of ~3 nm, and lengths of up to 500 nm. The proposed mechanism of condensation shows that the silica monomers interact with two amino groups on the DPTA through hydrogen bonding. This localization of silica precursor along the catalytic amine sites of cellulose then induces a lateral growth of nanotubes. Following the initial silica growth, the condensation is repeated (albeit in a disordered fashion), and this results in a tubular coating of amorphous silica [74].

1.5.3.4 Non-natural Metal Oxide Synthesis Using Biomimetic Peptides

Although fewer reports have been made than for the biomimetic synthesis of silica, other metal oxides have also been created under ambient conditions using synthetic and natural templates. For example, germania (GeO_2) was synthesized under ambient conditions and neutral pH with poly (allylamine hydrochloride) (PAH) as the condensation template [86]. The physical and chemical properties of germania are of interest because of its potential application for enhancing optical fibers and other optoelectronic applications [87]. The reaction of PAH and a germanium precursor induced germania nanospheres when the reaction mixture was simply combined, but highly anisotropic rod-like morphologies were observed when the reaction mixture was stirred. This change in morphology was most likely caused by perturbation of the orientation of the self-assembled PAH molecules and solution, which was then followed by nucleation and growth of the germania nanoparticles [86]. These changes in morphology suggest that different types of nanostructures could be formed simply by agitating the reaction mixture at different frequencies.

Titania (TiO_2) has been synthesized incorporating a variety of peptides, including R5 peptide, PLL, spermidine and spermine [88, 89]. Although it is not as naturally abundant as silica, TiO_2 has been identified in the comb of the hornet *Vespa orientalis*, the test (skeleton) of the foraminiferan *Bathysiphon argenteus*, and also in leukocytes and osteosarcomas in humans [89]. Recently, Sewell and coworkers have utilized a PLL and R5 peptide template to catalyze the precipitation of titania nanoparticles (sizes of 80–200 nm and 30–60 nm, respectively) under ambient conditions [88]. Interestingly, the presence of phosphate ions in the R5 peptide reaction had no effect on titania precipitation, unlike that observed for silica. The same was true for the PLL-synthesized titania nanoparticles; in contrast to observations with silica, the length of the PLL chain did not affect the resultant shape of titania nanoparticles. The fact that the latter were all spherical suggested that the titania plays a larger role in its own developing structure than does PLL during condensation [88].

Cole and coworkers have also synthesized titania nanoparticles by incorporating spermidine and spermine as the condensation templates [89]. A SEM analysis of the resultant nanoparticles revealed that the structures were composed of irregular polyhedra, ranging from 100 to 800 nm in diameter for spermidine and from 50 to 300 nm for spermine. A powder analysis showed that both the spermidine- and spermine-templated titania nanoparticles were X-ray amorphous at room temperature. Crystallization was induced at higher temperatures (800 °C). For the spermidine titania, crystalline patterns were evident at 600 °C and 800 °C (Figure 1.30), which corresponded to an anatase phase with trace amounts of rutile.

An interesting pH and temperature dependence of titania formation was also identified. At higher temperatures, the titania nanoparticles for spermidine-templated titania became smaller in diameter, which was predicted to be caused by a faster nucleation rate. Interestingly, there was no notable temperature dependence for the significantly faster spermine-templated titania precipitation over the range of 5–80 °C; at this temperature, the reaction was kinetically faster, negating any temperature effects. A similar trend was observed for pH dependence, where

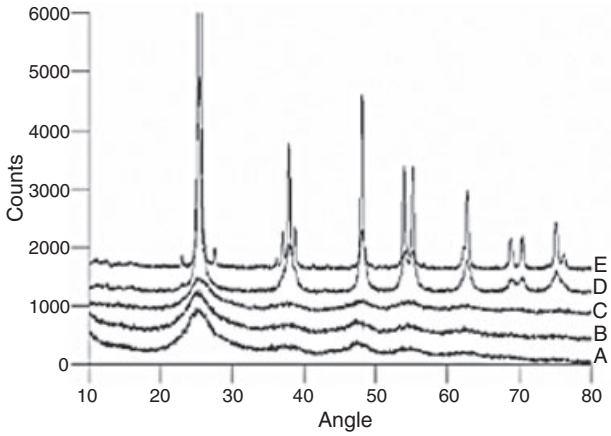

Figure 1.30 X-ray diffraction data from titania precipitated with spermidine and annealed to (A) room temperature, (B) 200 °C, (C) 400 °C, (D) 600 °C and (E) 800 °C. Reprinted with permission from Ref. [89]; © 2007, American Chemical Society.

spermine precipitated titania independent of the pH (2.9–12.6). Spermidine-templated precipitation, however, occurred only between pH 5.3–12.6, where polyhedrals were documented in the pH range of 8–9.

1.5.4
Conclusions

Today, as increasing amounts of information are produced relating to the biological mechanisms that drive the silica formation of diatoms, evolved biomimics are being created that will continue to reveal applications beyond catalysis, biosensing and drug delivery. Among all of the templates described here, however, one point is clear – that templates have a major influence on the size and morphology of the silica nanoparticle. For example, the recent discovery of silacidins (polyanions required for silica formation *in vivo*) suggests that the anion might have an effect on the size and morphology of the silica nanoparticles produced. Clearly, a more complete understanding of how factors such as template structure and reaction conditions (i.e. pH, temperature, anion concentration) affect the sizes and shapes of silica nanoparticles will have a profound influence on the investigations of future materials scientists in this area.

1.6
Future Perspectives: Processing Metal Oxide Nanomaterials

Lessons learned from the biomimetic, *in vitro* syntheses of metal oxides have resulted in efficient, low-temperature approaches towards the development of

nanoengineered materials. In fact, these approaches are already being harnessed in the next generation of biomimetic materials, namely 2-D patterned metal oxides. For example, a number of different deposition techniques for biomimetic patterning have been incorporated to mimic the microstructure of the diatom cell wall. Specifically, techniques which include solenoid jet printing, lithographic patterning and direct ink writing (DIW) have been used to deposit a variety of silica-precipitating precursors [90–92]. Coffman and coworkers have used both solenoid jet printing and photolithography to pattern PLL and (3-aminopropyl)-trimethoxysilane, respectively. Although these methods have provided a unique approach towards developing a controllable template for silica precipitation, they have been limited either by large, non-uniform spots (solenoid jet printing), or by smaller, unresolved spots (lithography) [90].

Rapid prototyping techniques using computer-aided deposition have been developed to eradicate these setbacks. For instance, Xu and coworkers have integrated DIW to directly deposit ($40\,\mu m\,s^{-1}$) polyamine-rich inks [91]. In these experiments, polyelectrolyte inks were loaded into a syringe and robo-casted onto a substrate using a computer-animated design. The patterned surfaces were then hydrolyzed with silicic acid to condense the micropatterned silica. When auger electron microscopy was used to map the distribution of silica along the patterns, both silicon and oxygen were seen to be distributed uniformly about the pattern [91].

Using a different approach, Kisailus and coworkers integrated soft-lithography stamping to micropattern γ-Ga_2O_3 using a selection of catalytic enzymes associated with silicatein peptides [92]. Here, thiolyated ligands composed of nucleophilic hydroxyl and hydrogen-bonded amine moieties derived from silicatein were assembled onto poly(dimethylsiloxane) (PDMS) stamps which were then applied to gold substrates and reacted with precursor solution. The strong binding affinity between the –SH group and gold substrates induced the formation of hydroxyl self-assembled monolayers (SAMs) available for further reactivity [92]. In fact, once immersed in a precursor solution of gallium nitrate, these hydroxyl groups served as a site for the condensation of γ-Ga_2O_3. The surface energy of the ordered monolayers provided a defined area for hydrolysis of gallium nitrate and subsequent ripening, dissolution and precipitation of γ-Ga_2O_3. This control could be used for the surface-catalyzed systems at low temperatures for novel electronic or optical applications.

Additional rapid prototyping techniques today are beginning to attract interest in biomaterials deposition. One such technique – piezoelectric inkjet printing – is a noncontact method that employs a user-controlled waveform to deposit known amounts of material onto a variety of substrates [93]. With the advent of such readily available deposition techniques, even more metal oxides could be printed on the 2-D scale [88, 93]. The constrained and unconstrained syntheses of metal oxides reported to date can now be incorporated with these newer technologies to bridge the *in vitro* and macromolecular worlds of biology and materials science, together expanding new frontiers in nanomaterial design.

References

1 Wolf, S. (2004) *Microchip Manufacturing*, Lattice Press, Sunset Beach.

2 Kumar, U., Shete, A., Harle, A.S., Kasyutich, O., Schwarzacher, W., Pundle, A. and Poddar, P. (2008) Extracellular bacterial synthesis of protein functionalized ferromagnetic Co3O4 nanocrystals and imaging of self-organization of bacterial cells under stress after exposure to metal ions. *Chemistry of Materials*, **20**, 1484–91.

3 Weiner, S. and Dove, P.M. (2003) *An Overview of Biomineralization Processes and the Problem of the Vital Effect*, Vol. 54, The Mineralogical Society of America, Washington, DC.

4 Bar-Cohen, Y. (2006) Biomimetics – using nature to inspire human innovation. *Bioinspired Biomimcry*, **1**, 1–12.

5 Carney, C.K., Harry, S.R. and Sewell, S.L. (2007) Detoxification biominerals. *Topics in Current Chemistry*, **270**, 155–85.

6 Gorna, K., Munoz-Espi, R., Grohn, F. and Wegner, G. (2007) Bioinspired mineralization of inorganics from aqueous media controlled by synthetic polymers. *Macromolecular Biosciences*, **7**, 163–73.

7 Perry, C.C. (1998) *Biomaterials*, John Wiley & Sons, Inc., New York.

8 Fratzl, P. (2007) Biomimetic materials research: what can we really learn from nature's structural materials? *Journal of the Royal Society Interface*, **4**, 637–42.

9 Douglas, T. and Young, M. (2006) Viruses: making friends with old foes. *Science*, **312**, 873–5.

10 Douglas, T. and Young, M. (1999) Virus particles as templates for materials synthesis. *Advanced Materials*, **11**, 679–81.

11 Lakshminarayanan, R., Vivekanandan, S., Samy, R.P., Banerjee, Y., Chi-Jin, E.O., Teo, K.W., Jois, S.D.S., Kini, M. and Valiyaveettil, S. (2008) Structure, self-assembly, and dual role of a b-defensin-like peptide from the Chinese soft-shell turtle eggshell matrix. *Journal of the American Chemical Society*, **130**, 4660–8.

12 Lee, H., Dellatore, S.M., Miller, W.M. and Messersmith, P.B. (2007) Mussel-inspired surface chemistry for multifunctional coatings. *Science*, **318**, 426–30.

13 Kroger, N., Deutzmann, R. and Sumper, M. (1999) Polycationic peptides from diatom biosilica that direct silica nanosphere formation. *Science*, **286**, 1129–32.

14 Sumper, M. (2002) A phase separation for the nanopatterning of diatom biosilica. *Science*, **295**, 2430–3.

15 Zurcher, S., Wackerlin, D., Bethuel, Y., Malisova, B., Textor, M., Tosatti, S. and Gademann, K. (2006) Biomimetic surface modifications based on the cyanobacterial iron chelator anachelin. *Journal of the American Chemical Society*, **128**, 1064–5.

16 Henrich, V.E. and Cox, P.A. (1994) *The Surface Science of Metal Oxides*, Cambridge University Press, Boston.

17 Lang, C., Schuler, D. and Faivre, D. (2007) Synthesis of manetite nanoparticles for bio- and nanotechnology: genetic engineering and biomimetics of bacterial magnetosomes. *Macromolecular Biosciences*, **7**, 144–51.

18 Jun, Y.-W., Seo, J.-W. and Cheon, J. (2008) Nanoscaling laws of magnetic nanoparticles and their applicabilities in biomedical sciences. *Accounts of Chemical Research*, **41**, 170–89.

19 Whaley, S.R., English, D.S., Hu, E.L., Barbara, P.F. and Belcher, A.M. (2000) Selection of peptides with semiconductor binding specificity for directed nanocrystal assembly. *Nature*, **405**, 665–8.

20 Lippard, S.J. and Berg, J.M. (1994) *Principles of Bioinorganic Chemistry*, University Science Books, Mill Valley.

21 Nakanishi, H. and Kahn, M. (1998) *Peptide Mimetics*, Oxford University Press, New York.

22 Brown, S. (1997) Metal-recognition by repeating polypeptides. *Nature Biotechnology*, **15**, 269–72.

23 Chen, W. and Georgiou, G. (2002) Cell-surface display of heterologous proteins: from high-throughput screening to environmental applications. *Biotechnology and Bioengineering*, **79**, 496–503.

24 Wittrup, K.D. (2001) Protein engineering by cell-surface display. *Current Opinion in Biotechnology*, **12**, 395–9.

25 Tomczak, M.M., Slocik, J.M., Stone, M.O. and Naik, R.R. (2007) Bio-inspired approaches to inorganic material synthesis. *Biochemical Society Transactions*, **35**, 512–15.

26 Poole, C.P. and Owens, F.J. (2003) *Introduction to Nanotechnology*, John Wiley & Sons, Inc., Hoboken.

27 Liu, W.-T. (2006) Nanoparticles and their biological applications. *Journal of Bioscience and Bioengineering*, **102**, 1–7.

28 Klem, M.T., Resnick, D.A., Gilmore, K., Young, M., Idzerda, Y.U. and Douglas, T. (2007) Synthetic control over magnetic moment and exchange bias in all-oxide materials encapsulated within a spherical protein cage. *Journal of the American Chemical Society*, **129**, 197–201.

29 Oaki, Y. and Imai, H. (2005) The hierarchical architecture of nacre and its mimetic material. *Angewandte Chemie*, **117**, 6729–33.

30 Yahiro, J., Oaki, Y. and Imai, H. (2006) Biomimetic synthesis of wurtzite ZnO nanowires possessing a mosaic structure. *Small*, **2**, 1183–7.

31 Oaki, Y. and Imai, H. (2006) Nanoengineering in echinoderms: the emergence of morphology from nanobricks. *Small*, **2**, 66–70.

32 Bansal, V., Poddar, P., Ahmad, A. and Sastry, M. (2006) Room-temperature biosynthesis of ferroelectric barium titanate nanoparticles. *Journal of the American Chemical Society*, **128**, 11958–63.

33 Herrera-Becerra, R., Zorrilla, C. and Ascencio, J.A. (2007) Production of iron oxide nanoparticles by a biosynthesis method: an environmentally friendly route. *Journal of Physical Chemistry C*, **111**, 16147–53.

34 Theil, E.C., Sayers, D.E. and Brown, M. A. (1970) Similarity of the structure of ferritin and iron dextran (imferon) determined by extended X-ray absorption fine structure analysis. *Journal of Biological Chemistry*, **17**, 8132–4.

35 Klem, M.T., Mosolf, J., Young, M. and Douglas, T. (2008) Photochemical mineralization of europium, titanium, and iron oxyhydroxide nanoparticles in the ferritin protein cage. *Inorganic Chemistry*, **47**, 2237–9.

36 Uchida, M., Klem, M.T., Allen, M., Suci, P., Flenniken, M., Gillitzer, E., Varpness, Z., Liepold, L.O., Young, M. and Douglas, T. (2007) Biological containers: protein cages as multifunctional nanoplatforms. *Advanced Materials*, **19**, 1025–42.

37 Loste, E., Park, R.J., Warren, J. and Meldrum, F.C. (2004) Precipitation of calcium carbonate in confinement. *Advanced Functional Materials*, **14**, 1211–20.

38 Lee, S.-Y., Gao, X. and Matsui, H. (2007) Biomimetic and aggregation-driven crystallization route for room-temperature material synthesis: growth of beta-Ga_2O_3 nanoparticles on peptide assemblies as nanoreactors. *Journal of the American Chemical Society*, **129**, 2954–8.

39 Nuraje, N., Su, K., Haboosheh, A., Samson, J., Manning, E.P., Yang, N.-I. and Matsui, H. (2006) Room temperature synthesis of ferroelectric barium titanate nanoparticles using peptide nanorings as templates. *Advanced Materials*, **18**, 807–11.

40 Zhang, W., Zhang, D., Fan, T., Ding, J., Guo, Q. and Ogawa, H. (2006) Fabrication of ZnO microtubes with adjustable nanopores on the walls by the templating of butterfly wing scales. *Nanotechnology*, **17**, 840–4.

41 Biro, L.P., Balint, Z., Kertesz, K., Vertesy, Z., Mark, G.I., Tapaszto, L., Vigneron, J.-P., Lousse, V. and Biro, L.P. (2007) Photonoic crystal structures of biologic origin: butterfly wing scales. *Materials Research Society Symposium Procedures*, **1014**, AA07-08-16.

42 Zhang, W., Zhang, D., Fan, T., Ding, J., Gu, J., Guo, Q. and Ogawa, H. (2006) Biomimetic zinc oxide replica with structural color using butterfly (*Ideopsis similis*) wings as templates. *Bioinspired Biomimcry*, **1**, 89–95.

43 Zou, D., Xu, C., Luo, H., Wang, L. and Ying, T. (2008) Synthesis of Co_3O_4 nanoparticles via an ionic liquid-assisted methodology at room temperature. *Materials Letters*, **62**, 1976–8.

44 Wilkes, J.S. and Zaworotko, M.J. (1992) *Chemical Communications*, **13**, 965–7.

45 Kröger, N. (2007) Prescribing diatom morphology: toward genetic engineering of biological nanomaterials. *Current Opinion in Chemical Biology*, **11**, 662–9.

46 Aizenberg, J., Hanson, J., Koetzle, T.F., Weiner, S. and Addadi, L. (1997) *Journal of the American Chemical Society*, **119**, 881–6.

47 Oaki, Y. and Imai, H. (2007) Biomimetic morphological design for manganese oxide and cobalt hydroxide nanoflakes with a mosaic interior. *Journal of Materials Chemistry*, **17**, 316–21.

48 Vazquez-Olmos, A., Redon, R., Rodriguez-Gattorno, G., Mata-Zamora, M.E., Morales-Leal, F., Fernandez-Osrio, A.L. and Saniger, J.M. (2005) *Journal of Colloid and Interface Science*, **291**, 175.

49 Gröger, C., Lutz, K. and Brunner, E. (2008) Biomolecular self-assembly and its relevance in silica biomineralization. *Cell Biochemistry and Biophysics*, **50**, 23–39.

50 Sumper, M. (2002) A phase separation model for the nanopatterning of diatom biosilica. *Science*, **295**, 2430–3.

51 Halas, N.J. (2008) Nanoscience under glass: the versatile chemistry of silica nanostructures. *ACS Nano*, **2**, 179–83.

52 Noll, F., Sumper, M. and Hampp, N. (2002) Nanostructure of diatom silica surfaces and of biomimetic analogues. *Nano Letters*, **2**, 91–5.

53 Brunner, E. and Lutz, K. (eds) (2007) *Handbook of Biomineralization: Biomimetic and Bioinspired Chemistry*, Vol. 2, Wiley-VCH Verlag GmbH, Weinheim.

54 Christiansen, S.C., Hedin, N., Epping, J.D., Janicke, M.T., del Amo, Y., Demarest, M., Brzezinski, M. and Chmelka, B.F. (2006) Sensitivity considerations in polarization transfer and filtering using dipole-dipole couplings: implications for biomineral systems. *Solid State Nuclear Magnetic Resonance*, **29**, 170–82.

55 Sumper, M. and Brunner, E. (2006) Learning from diatoms: nature's tools for the production of nanostructured silica. *Advanced Functional Materials*, **16**, 17–26.

56 Poulsen, N. and Kroger, N. (2004) Silica morphogenesis by alternative processing of silaffins in the diatom *Thalassiosira pseudonana*. *Journal of Biological Chemistry*, **279**, 42993–9.

57 Poulsen, N., Sumper, M. and Kroger, N. (2003) Biosilica formation in diatoms: characterization of native silaffin-2 and its role in silica morphogenesis. *Proceedings of the National Academy of Sciences of the United States of America*, **100**, 12075–80.

58 Wenzl, S., Hett, R., Richthammer, P. and Sumper M. (2008) Silacidins: highly acidic phosphopeptides from diatom shells assist in silica precipitation in vitro. *Angewandte Chemie International Edition*, **47**, 1729–32.

59 Kroger, N., Deutzmann, R., Bergsdorf, C. and Sumper, M. (2000) Species-specific polyamines from diatoms control silica morphology. *Proceedings of the National Academy of Sciences of the United States of America*, **97**, 14133–8.

60 Sumper, M. and Kroger, N. (2004) Silica formation in diatoms: the function of long-chain polyamines and silaffins. *Journal of Materials Chemistry*, **14**, 2059–65.

61 Naik, R.R., Tomczak, M.M., Luckarift, H.R., Spain, J.C. and Stone, M.O. (2004) Entrapment of enzymes and nanoparticles using biomimetically synthesized silica. *Chemical Communications*, 1684–5.

62 Miller, S.A., Hong, E.D. and Wright, D. (2006) Rapid and efficient enzyme encapsulation in a dendrimer silica nanocomposite. *Macromolecular Bioscience*, **6**, 839–45.

63 Pouget, E., Dujardin, E., Cavalier, A., Moreac, A., Valery, C., Marchi-Artzner, V., Weiss, T., Renault, A., Paternostre, M. and Artzner, F. (2007) Hierarchical architectures by synergy between dynamical template self-assembly and biomineralization. *Nature Materials*, **6**, 434–9.

64 Wong Po Foo, C., Patwardhan, S.V., Belton, D.J., Kitchel, B., Anastasiades, D., Huang, J., Naik, R.R., Perry, C.C. and Kaplan, D.L. (2006) Novel nanocomposites from spider silk-silica fusion (chimeric) proteins. *Proceedings of the National Academy of Sciences of the United States of America*, **103**, 9428–33.

65 Zhang, Y., Wu, H., Li, J., Li, L., Jiang, Y., Jiang, Y. and Jiang, Z. (2008) Protamine-templated biomimetic hybrid capsules: efficient and stable carrier for enzyme encapsulation. *Chemistry of Materials*, **20**, 1041–8.

66 Luckarift, H.R., Spain, J.C., Naik, R.R. and Stone, M.O. (2004) Enzyme immobilization in a biomimetic silica support. *Nature Biotechnology*, **22**, 211–13.

67 Marner, W.D., Shaikh, A.S., Muller, S.J. and Keasling, J.D. (2008) Morphology of artificial silica matrices formed via autosilification of a silaffin/protein polymer chimera. *Biomacromolecules*, **9**, 1–5.

68 Knecht, M.R. and Wright, D.W. (2004) Amine-terminated dendrimers as biomimetic templates for silica nanosphere formation. *Langmuir*, **20**, 4728–32.

69 Knecht, M.R. and Wright, D.W. (2004) Dendrimer-mediated formation of multicomponent nanospheres. *Chemistry of Materials*, **16**, 4890–5.

70 Knecht, M.R., Sewell, S.L. and Wright, D.W. (2005) Size control of dendrimer-templated silica. *Langmuir*, **21**, 2058–61.

71 Jan, J.S., Lee, S., Carr, C.S. and Shantz, D.F. (2005) Biomimetic synthesis of inorganic nanospheres. *Chemistry of Materials*, **17**, 4310–17.

72 Jan, J.-S. and Shantz, D.F. (2007) Biomimetic silica formation: effect of block copolypeptide chemistry and solution conditions on silica nanostructure. *Advanced Materials*, **19**, 2951–6.

73 Bauer, C.A., Robinson, D.B. and Simmons, B.A. (2007) Silica particle formation in confined environments via bioinspired polyamine catalysis at near-neutral pH. *Small*, **3**, 58–62.

74 Zollfrank, C., Scheel, H. and Greil, P. (2007) Regioselectively ordered silica nanotubes by molecular templating. *Advanced Materials*, **19**, 984–7.

75 Cha, J.N., Stucky, G.D., Morse, D.E. and Deming, T.J. (2000) Biomimetic synthesis of ordered silica structures mediated by block copolypeptides. *Nature*, **403**, 289–92.

76 Annenkov, V.V., Patwardhan, S.V., Belton, D., Danilovtseva, E.N. and Perry, C.C. (2006) A new stepwise synthesis of a family of propylamines derived from diatom silaffins and their activity in silicification. *Chemical Communications*, 1521–3.

77 Belton, D.J., Patwardhan, S.V., Annenkov, V.V., Danilovtseva, E.N. and Perry, C.C. (2008) From biosilicification to tailored materials: optimizing hydrophobic domains and resistance to protonation of polyamines. *Proceedings of the National Academy of Sciences of the United States of America*, **105**, 5963–8.

78 Chang, J.S., Kong, Z.L., Hwang, D.F. and Chang, K.L.B. (2006) Chitosan-catalyzed aggregation during the biomimetic synthesis of silica nanoparticles. *Chemistry of Materials*, **18**, 702–7.

79 Lutz, K., Groger, C., Sumper, M. and Brunner, E. (2005) Biomimetic silica formation: analysis of the phosphate-induced self-assembly of polyamines. *Physical Chemistry Chemical Physics*, **7**, 2812–15.

80 Wong, M.S., Cha, J.N., Choi, K.S., Deming, T.J. and Stucky, G.D. (2002) Assembly of nanoparticles into hollow spheres using block copolypeptides. *Nano Letters*, **2**, 583–7.

81 Brunner, E. (2007) Biomimetic synthesis: double-walled silica nanotubes. *Nature Materials*, **6**, 398–9.

82 Hawkins, K.M., Wang, S.S.S., Ford, D.M. and Shantz, D.F. (2004) Poly-L-lysine templated silicas: using polypeptide secondary structure to control oxide pore architectures. *Journal of the American Chemical Society*, **126**, 9112–19.

83 Tomczak, M.M., Glawe, D.D., Drummy, L.F., Lawrence, C.G., Stone, M.O., Perry, C.C., Pochan, D.J., Deming, T.J. and Naik, R.R. (2005) Polypeptide-templated synthesis of hexagonal silica platelets. *Journal of the American Chemical Society*, **127**, 12577–82.

84 Gautier, C., Lopez, P.J., Livage, J. and Coradin, T. (2007) Influence of poly-l-lysine on the biomimetic growth of silica tubes in confined media.

Journal of Colloid and Interface Science, **309**, 44–8.

85 Sumper, M. Lorenz, S. and Brunner, E. (2003) Biomimetic control of size in the polyamine-directed formation of silica nanospheres. *Angewandte Chemie International Edition*, **42**, 5192–5.

86 Patwardhan, S.V. and Clarson, S.J. (2005) Bioinspired mineralisation: macromolecule mediated synthesis of amorphous germania structures. *Polymer*, **46**, 4474–9.

87 Margaryan, A.A. and Liu, W. (1993) Prospects of using germanium-dioxide-based glasses for optics. *Optical Engineering*, **32**, 1995–6.

88 Sumerel, J., Lewis, J., Doraiswamy, A., Deravi, L.F., Sewell, S.L., Gerdon, A.E., Wright, D.W. and Narayan, R.J. (2006) Piezoelectric ink jet processing of materials for medical and biological applications. *Biotechnology Journal*, **1**, 976–87.

89 Cole, K.E. and Valentine, A.M. (2007) Spermidine and spermine catalyze the formation of nanostructured titanium oxide. *Biomacromolecules*, **8**, 1641–7.

90 Coffman, E.A., Melechko, A.V., Allison, D.P., Simpson, M.L. and Doktycz, M.J. (2004) Surface patterning of silica nanostructures using bio-inspired templates and directed synthesis. *Langmuir*, **20**, 8431–6.

91 Xu, M., Gratson, G.M., Duoss, E.B., Shepherd, R.F. and Lewis, J.A. (2006) Biomimetic silicification of 3D polyamine-rich scaffolds assembled by direct ink writing. *Soft Matter*, **2**, 205.

92 Kisailus, D., Truong, Q., Amemiya, Y., Weaver, J.C. and Morse, D.E. (2006) Self-assembled bifunctional surface mimics an enzymatic and templating protein for synthesis of a metal oxide semiconductor. *Proceedings of the National Academy of Sciences of the United States of America*, **103**, 5652–7.

93 Deravi, L.F., Sumerel, J.L., Gerdon, A.E., Cliffel, D.E. and Wright, D.W. (2007) Output analysis of materials inkjet printer. *Applied Physics Letters*, **91**, 113114–16.

Abstract

Depending on their coordination *in vivo*, metal clusters operate as oxygen or electron transporters, structural determinants, or as signals for cellular communication. The basic chemistry behind these genetically controlled nanomaterials can be identified, once the coordinated metals have been isolated from their natural environment, and applied towards the synthesis of a wide range of materials. A bioinspired, or biomimetic, approach to materials synthesis would reduce the generation of excess waste from the high-temperature reaction environments currently used, and enable further functionalization with specific control of nanoparticle morphology. In this chapter, we will focus exclusively on metal oxide clusters and crystals, presenting an overview of current techniques used for the biomimetic syntheses of nanomaterials.

Keywords

biomineralization, biomimetics, synthesis, metal oxide, nanomaterials, materials synthesis

2
Synthesis of Symmetric and Asymmetric Nanosilica for Materials, Optical and Medical Applications

Yongquan Qu, Jennifer Lien and Ting Guo

2.1
Introduction

Silica (SiO_2), which is one of the most abundant compounds on Earth, is composed of the two most abundant elements – oxygen and silicon. Although the potential application of silica could be enormous, aside from windows, glass, optical fibers and quartz watches (a form of crystalline silica), it has found only a limited use. One might question whether this lack of utility of such a widely available material is due to lack of understanding of the material itself, to a lack of more advanced research on this popular material, or both. In this chapter we will examine this situation from a specific angle, namely the symmetry of silica nanomaterials, the aim being to analyze those results which have been reported in order to help answer the question posed above.

Among all forms of silica, silica nanomaterials or nanosilica have become more popular in recent years. The obvious benefits of nanosilica are its biological compatibility, synthetic and geometric versatility, and low cost. The OH groups on the surface of SiO_2 can be easily modified to chemically link the surface of nanosilica to other organic and inorganic compounds. In addition, because bulk silica or glass is optically transparent (both ultraviolet and visible), its nanoscale counterparts may also be used as light transmitters or platforms while having their surfaces decorated with a variety of chemical entities. These properties make nanosilica a good candidate for sensors and, more specifically, for optical signal transducers. For any nanomaterials which include nanosilica, their transparency changes as a function of their size; consequently, other size-related effects (such as quantum confinement effects) in combination with this transparency dependency means that nanosilica should be an interesting candidate as a critical component in sensors.

The newly developed nanosilica discussed here can adopt many forms, including nanocoils, helices, nanoparticles and nanotubes, that differ widely from the other more traditional silica materials that have long been recognized. For example,

Nanomaterials for the Life Sciences Vol. 2: Nanostructured Oxides. Edited by Challa S. S. R. Kumar

ISBN: 978-3-527-32152-0

a silica sol–gel has nanoscale features such as pore size, and represents a specialized form of silica that has been widely used to date. Consequently, the discussions here are limited to those new nanomaterials that have true nanometer-sized outer dimensions and have been developed within the past decade. All of these should exist as isolated nanomaterials, without the formation of extensive networks.

The geometry of the true nanosilica forms can be defined using two general parameters, namely shape and size. Among the range of nanosilica forms (see Figure 2.1), all have at least one dimension that is on the order of nanometers (1–1000 nm). While it is possible to categorize all of these nanosilica according to their exact shapes, to do so would be tedious and less conducive to explaining the significance of structure and its link to functionality. Consequently, it is suggested that these nanomaterials be divided into two general categories, namely symmetric and asymmetric. Among the examples shown in Figure 2.1, the top panel shows six symmetric nanosilica materials, and the lower panel six asymmetric materials.

The benefit of this division can be illustrated from several perspectives. From a synthetic point of view, the division is significant as synthesis normally results in the production of symmetric materials. Hence, the synthesis of asymmetric nanosilica and molecular species are quite unique by themselves. The division can thus be viewed as a helpful hint to understanding the synthesis of helical materials and other asymmetric nanomaterials. The origin of the production of asymmetric nanosilica is believed to be the nature of the different catalysts or templates involved, while the exact growth mechanism depends on the structure of these catalysts or templates. To date, asymmetric nanosilica has not been prepared without these two assisting species.

This division can also be viewed favorably from the perspective of functionality. Asymmetric materials possess certain unique properties, with the symmetry making interactions with other materials more selective and specific. An example is DNA, which is helical; helicity is a special type of asymmetry where the pitch and diameter of the helix determine how the materials interact with their counterparts. Asymmetric catalysis follows the same principle. Furthermore, the interaction between helical nanomaterials and other materials can be tuned by using the surfactants on the helices, and manipulating this factor of symmetry will provide another 'handle' to control the function of the materials.

From the mechanical application point of view, asymmetric nanomaterials such as silica nanocoils should have a much greater compressibility and expansibility than symmetric nanowires or nanorods. This unique property may be employed to create unique applications. For example, the magnetically controlled opening and closing of pitches in the helical coils may be used as a drug delivery vehicle, although until now this property has not been utilized, most likely due to the lack of manipulation of these asymmetric nanomaterials.

The significance of the symmetry of nanosilica can also play a role in optical applications. For example, nanocoils may have intriguing optical properties due to their lack of symmetry although, again, such applications have not yet been developed due to a lack of precise control of the nanocoils or helices.

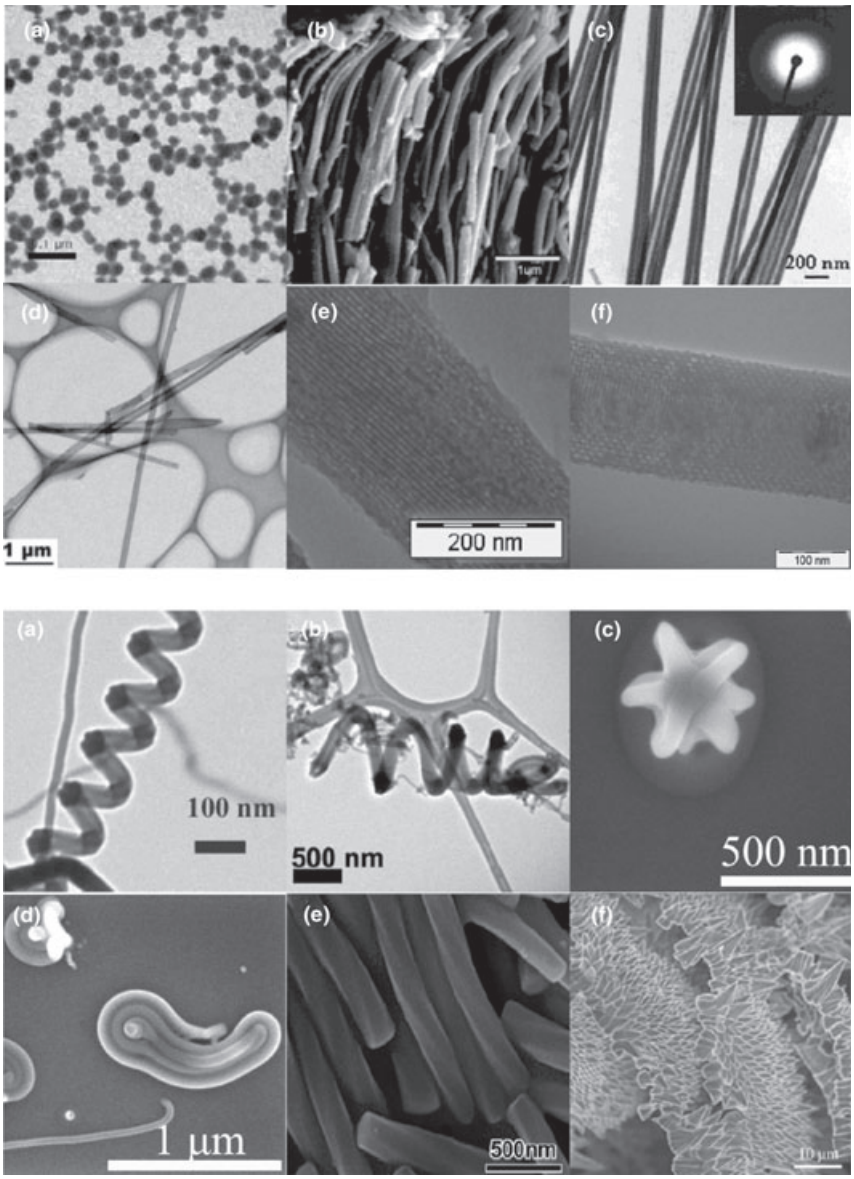

Figure 2.1 The shapes of nanosilica. The top panel shows symmetric nanomaterials: (a) nanoparticles [1]; (b) nanorods [2]; (c) nanowires and nanofibers (straight) [3]; (d) nanotubes [4]; and (e,f) mesoporous nanomaterials [radially (f) and parallel (e) channels] [5]. The lower panel shows asymmetric nanomaterials: (a) coiled nanowires; (b) coiled nanotubes [6]; (c) nanostar; (d) nanoropes; (e) 'nano French-fries' [7]; and (f) nanoflowers [8].

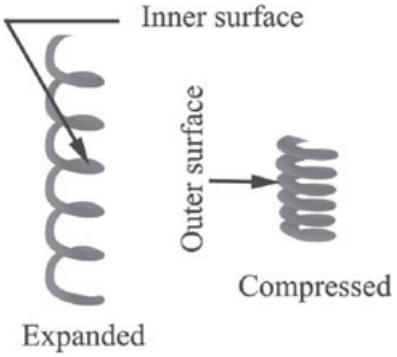

Figure 2.2 A silica nanocoil in two states – expanded and compressed. The inner or protected surface and the outer or exposed surface are shown.

From a pure geometric point of view, asymmetric nanomaterials are of interest because they create unique topological shapes that normal symmetric materials do not possess. Controlling the pitch and diameter of the helical coils provides yet another 'handle' by which the surface area can be tuned, in turn to maximize the protected or noncontact area and to incorporate other nanomaterials into the asymmetric nanomaterial. This arrangement may be explained more easily using Figure 2.2, which shows a nanocoil and its geometrically significant regions, including the inside or more-protected area that is shielded from the attack of other nanomaterials around the nanocoil, the space between the pitches, the diameter, length and the outer area. Other nanomaterials such as nanoparticles can be integrated into the asymmetric nanomaterials to increase functionality, and thus applicability (these are not shown in Figure 2.2). Therefore, asymmetric nanomaterials will possess not only unique properties but also the common properties of symmetric nanosilica.

A typical asymmetric nanosilica, a chiral/helical nanowire, is shown in Figure 2.3 (the cobalt catalyst that assists the growth of this coil is not shown here). The cross-section of the nanowire is not cylindrical but more marquise-like, which makes this nanomaterial even more asymmetric. In most cases, the occurrence of left-handed and right-handed nanocoils, counting from the origin of nanoparticle catalyst-attaching end, is approximately the same. It is worth pointing out that chirality is a more general and widely applicable definition than helicity, which refers to materials with many repeating units along a direction. Chiral materials, on the other hand, can have just one unit, although both chiral and helical materials are asymmetric. Hence, asymmetry is not necessarily the synonymous with chirality; rather, chirality is simply one form of asymmetry. Other asymmetric nanomaterials include nanostars, nanorods and 'nano French-fries' (see Figure 2.1).

Within this chapter we will survey the relevant literature by summarizing the results according to the synthesis (Section 2.2), characterization (Section 2.3) and

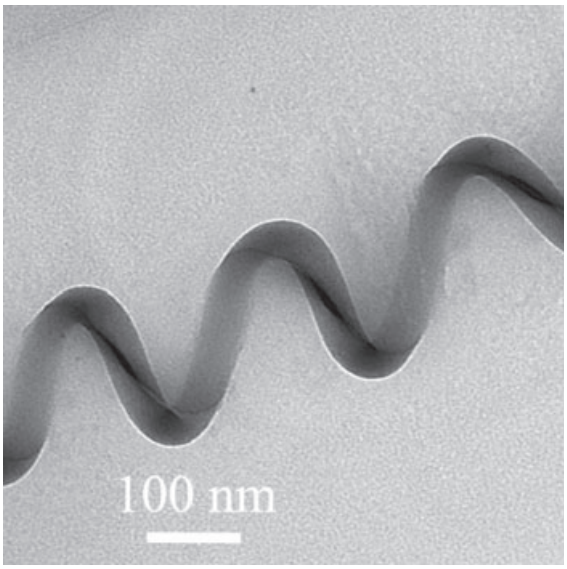

Figure 2.3 Illustration of an asymmetric silica nanocoil catalyzed with a cubic cobalt oxide nanoparticle. Note the edges of a marquise-like cross-section.

applications (Section 2.4) of these nanosilicas. Because most applications have a synthesis section, but not vice versa, the description of synthetic efforts listed under applications may be duplicate in the synthesis section. In addition, the methods available to date for characterizing these nanosilicas will be reviewed, and comments made on those methods that might be critical in improving our understanding of such nanomaterials and their applications. Finally, the applications of both symmetric and asymmetric nanosilica will be reviewed.

2.2
Synthesis of Nanosilica

As nanosilica include both symmetric and asymmetric types, many methods exist by which these nanomaterials can be prepared. Those methods used to synthesize nanosilica, whether symmetric or asymmetric, are listed in Table 2.1 (methods used to functionalize the nanomaterials after creation of the nanosilica have been excluded).

2.2.1
Symmetric Nanosilica

The most common means of preparing symmetric nanosilica (e.g. nanobeads) is via the Stöber reaction, by the hydrolysis and condensation of tetraethylorthosilicate

Table 2.1 Synthesis of nanosilica. The data relate to the types of material synthesized, symmetry of the material, whether it is made via catalytic processes, a brief description of the method, and the appropriate reference.

Material	Symmetry	Catalytic	Methods	Reference
Silica nanospheres 200–1500 nm in diameter	Symmetric	No	Hydrolysis of TEOS in basic solution of NaOH and NH_3(aq.) (Stöber method)	[9]
Silica nanowires 15–40 nm in diameter	Symmetric	Yes (silica)	1050 °C in presence of methane and hydrogen gas.	[10]
Silica nanowires of consistent diameter, 50 nm	Symmetric	Yes (Ga)	Side reactions with gallium on silicon substrate, ammonium, and In_2O_3 as a catalyst. GaN nanowires and spheres are also formed in the reaction.	[11]
Nanocables or tubes, 10 nm-thick shell, hollow inside, and with full diameter anywhere between 50 and 150 nm	Symmetric	Yes (Au)	Simultaneously evaporating ZnSe and SiO. Au on Si wafers is used, and absorbs SiO vapors carried by H_2 gas. Silica nanotubes have ZnSe core and silica coating.	[12]
Silica nanotubes with radial mesopores of average diameter of 94, 62, 27, 33 and 45 nm	Symmetric	No	Made by changing parameters in the gel. Inner wall stayed at a constant thickness of 4 nm. This synthesis uses chiral anionic surfactants with silica and aminosilane, a costructure-directing agent.	[13]
Silica-coated multiwalled carbon nanotubes	Symmetric/Asymmetric	No	Chemical oxidation using a phase-transfer catalyst.	[14]
Silica nanocomposites	N/A	No	Polymerization from a monomer yields polydiacetylene/silica nanocomposites. Crystals precipitate in solution and then exposure to UV, X-ray or gamma-ray light initiates a coupling to form a single polymer chain that is malleable and soluble.	[15]

Table 2.1 *Continued*

Material	Symmetry	Catalytic	Methods	Reference
Nanoquartz	Symmetric	No	Amorphous silica dissolved in NaOH can be reformed as quartz under controlled conditions. Care should be taken to maintain a pH just over neutral because yields are affected by changes in pH.	[16]
Magnetic hollow silica nanospheres	Symmetric	No	First, $Fe_3O_4/CaCO_3$ nanoparticles are made through rotating packed-bed method with reaction occurring in two 'phases'. A sol–gel technique is then employed to make magnetic hollow silica nanospheres. Finally, templates are used to make the material porous.	[17]
S-FITC-MSN between 80–150 nm and T-FITC-MSN also between 80–150 nm with lengths between to 400–1000 nm	Symmetric	No	MSN material prepared by mixing fluorescein isothiocyanate with 3-aminopropyltrimethoxysilane with anhydrous DMF as solvent. *N*-cetyltrimethylammonium bromide is then dissolved in water and made basic. TEOS is added to CTAB solution and mixed with the other prepared solution to give S-FITC-MSN.	[18]
Silica nanobeads, roughly 20 nm	Symmetric	No	Aq. solution of TMOS and $Ru(bpy)_3$ added to nanoemulsion of cyclohexane, Triton X-100, and *n*-hexanol. Consistent shaking to promote diffusion of TMOS into aq. droplets. TMOS followed by APTS and THPMP. Capped with CTMS.	[19]
Helical silica nanofibers, 100–300 nm	Symmetric/Asymmetric	No	Achiral cationic surfactant under acidic conditions	[20]

Table 2.1 *Continued*

Material	Symmetry	Catalytic	Methods	Reference
Silica nanocoils/springs	Asymmetric	Yes (Au)	Liquid–vapor–solid growth mechanism. Milder temperatures needed to produce two types of nanowire: single and multiple intertwined	[20]
Silica nanoparticles, length of 50 nm and diameter of 20 nm	Asymmetric	Yes (Co)	High temperatures between 1035–1075 °C. Catalysis with isotropic or spherical Co nanoparticles as well as anisotropic or cubic are used	[21]
Amorphous helical silica nanosprings, 80–140 nm in diameter, up to 8 microns in length	Asymmetric	Yes (Fe)	Chemical vapor deposition technique	[22]
Helical silica nanostructures	Asymmetric	No	Sol–gel polymerization using chiral cationic gelator to induce formation of helical bundles (many silica nanotubes). Acidic conditions needed for helicity. Straight nanotubes obtained under basic conditions.	[23]
Silica nanofibers or bundles	Asymmetric	No	Binary sol–gel method	[24]
Helical silica nanostructures	Asymmetric	No	Surfactants used as templates	[25]
Helical nanomaterials	Asymmetric	No	Cosurfactants used to modify synthesis of regular mesoporous silica nanomaterials	[26]
Hierarchical silica nanotubes with radially oriented mesoporous channels perpendicular to central axis of tube	Asymmetric	No	Costructure-directing agent used along with silica precursor. Chiral surfactant necessary. Modifying synthesis gel composition changes average inner diameter; diameter of wall remains constant at 4 nm.	[13]

NA = Not available.

(TEOS) in methanol or ethanol with base catalysts, as discussed recently by Halas [27]. Other common methods of preparing symmetric silica nanowires include the condensation of silicon sources in the gas phase on nanoparticle catalysts [21, 27, 28]. The size of the silica beads can be controlled by changing the silicates, base catalyst, and the amount of water in the system [1]. For example, the metal catalysts in the case of a nanowire can be used to control the diameter of long, straight silica nanowires with a circular cross-section. Moreover, both catalytic and noncatalytic methods can be used to synthesize these symmetric nanosilica.

2.2.1.1 Catalytic Methods

When a catalyst is used in the preparation, three basic growth mechanisms are usually possible:

- A vapor–liquid–solid (VLS) growth model.
- A vapor–solid–solid (VSS) model.
- An all-solid model (SSS) or a solid–liquid–solid (SLS) model.

The three phases refer to the feedstocks, the catalysts, and the form of the nanomaterials produced, respectively. As nanosilica are usually in a solid form at the growth temperatures, the final phase is almost always solid, while the catalysts may be either solid or liquid (see Figure 2.4). Solid-form catalysts may represent the key for producing asymmetric nanosilica such as nanocoils, where the phase of the feedstocks may be gas, liquid or solid. The three mechanisms are depicted diagrammatically in Figure 2.4; any variations to these methods usually focus on changes to the phase of the feedstock and the catalysts.

Many nanosilica are prepared catalytically, most likely due to the increased mobility of SiO_2 in these catalysts at these relatively high reaction temperatures. For example, various forms of symmetric silica nanostructures such as capsules, rods, tubes and thorns can be synthesized via catalytic methods. In one example, cobalt nanoparticles were used by Carter *et al.* as catalysts to synthesize straight silica nanowires [21]. Here, cobalt nanoparticles were deposited on silicon wafers, which were then placed in a high-temperature furnace for nanowire production. After growth, amorphous silica nanowires of 5 to 50 nm diameter and with lengths of microns to millimeters were produced. The Co nanoparticles could be clearly seen at the tips of many nanowires, the cross-sections of which were round, with lengths persisting in the region of many microns, rendering the wires both straight and symmetric.

In another investigation, Zhang *et al.* synthesized nanosilica by reacting polyvinylpyrrolidone (PVP) with water and Au. First, a concentrated gold nanoparticle suspension was diluted with ethanol, after which the solution was mixed with PVP in *n*-pentanol and stirred for 20 min before the addition of aqueous ammonia [29]. The reaction led to the formation of PVP–water-malleable structures which acted as a surface where the hydrolysis of TEOS could take place. This gave rise to pure silica nanostructures that were symmetric along an axis, but bent in different ways under various experimental parameters including the amount of PVP, the quantity

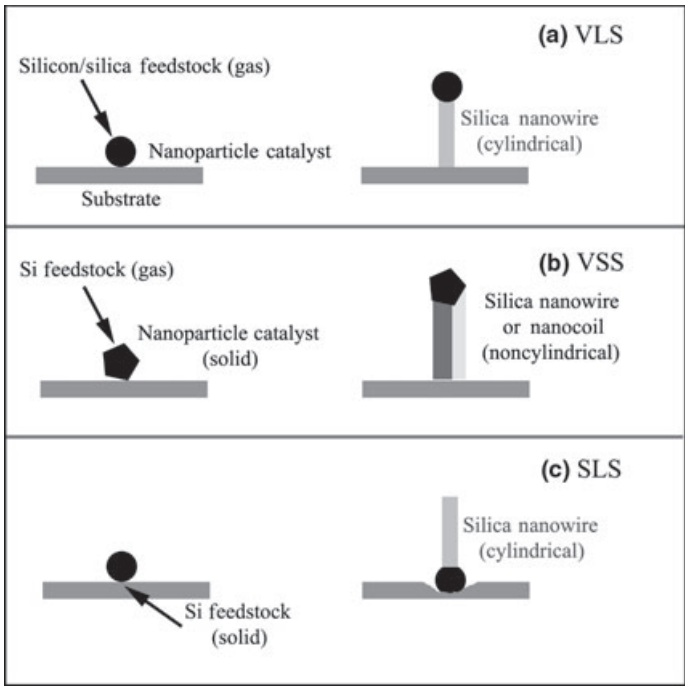

Figure 2.4 Three typical growth models for the catalytic synthesis of nanosilica. (a) VLS = vapor–liquid–solid; (b) VSS = vapor–solid–solid; (c) SLS = solid–liquid–solid. Solid–solid–solid (SSS) is similar to SLS).

of ethanol used to dilute the Au nanoparticle suspension, and the volume of ammonia solution used.

Another synthesis by Wang *et al.* involved the use of pre-made nanoparticle catalysts. Here, silica nanowire arrays were synthesized as a side product of the reaction with gallium and ammonium in the presence of the catalyst, In_2O_3 [11]. The synthesis involved placing liquefied Ga over a Si substrate, dissolving In_2O_3 powder in ethanol, followed by addition of the mixture on top of the Ga–Si substrate. The system was then heated to 400 °C for 2 h under a continuous flow of argon, after which the temperature was slowly increased to 900 °C for 20 min with a continuous flow of NH_3 (gas) and argon. The products were deposited on the substrate surface and, upon reaction completion, GaN nanowires and spheres and silica nanowire arrays were all found on the Si substrate. This synthesis represents an example of the VLS growth model shown in Figure 2.4.

Another method of preparing silica nanotubes, again via the VLS pathway, was through a simultaneous evaporation of ZnSe and SiO [12]. For this, the SiO powder was placed in a quartz tube with the ZnSe powder on top by some distance, and with a gold-coated silicon wafer located below, again by some further distance. In this way, a pressure of 10 Torr was created by heating, after which argon mixed

with 8% H_2 gas was added, followed by a steady increase in temperature. The ZnSe powder began to react with the hydrogen gas to form Zn and H_2Se. Under these reaction conditions the SiO powder became vaporized, and the vapors were carried down to the gold by the carrier gas. Eventually, the vapors were absorbed by the Au on the silicon wafers at a temperature between 800 and 900 °C. After a sufficiently long reaction time, and if the concentrations of Zn, H_2Se and SiO vapors were sufficiently high, the Zn and H_2Se would react to form ZnSe and hydrogen gas. At higher temperatures, the SiO was seen to decompose to produce silica and silicon, whereas at lower temperatures (800 °C) cables were observed with a ZnSe core and a silica outer coating.

Occasionally, the catalyst may even be the silica itself. For example, silica nanowires can be produced using silica nanoparticles as catalysts at very high temperatures in the presence of methane and hydrogen gas, as described by Lee *et al.* [10]. In this reaction the silica nanowires are synthesized from graphite-like layers that form around the base silica nanoparticles, which suggests that the silica nanowires grow either through the vapor (stock)–solid (catalysts) phases, or through the VSS model shown in Figure 2.4.

2.2.1.2 **Noncatalytic Growth**

Several methods are available to prepare nanosilica without the use of catalysts, and one of the most frequently used is shown schematically in Figure 2.5. As an example, Yu *et al.* used chiral anionic surfactants and a silica precursor in the

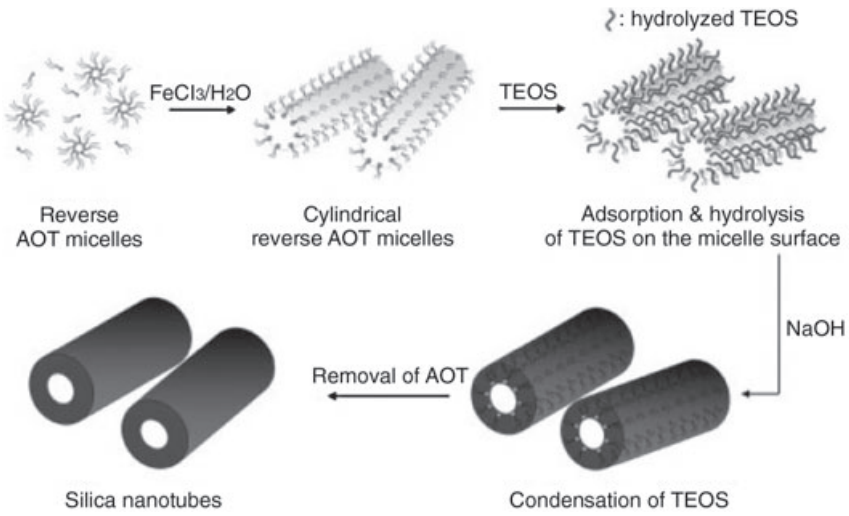

Figure 2.5 A typical method for the synthesis of nanosilica, without using catalysts or catalysts in the traditional sense. In this case, TEOS is condensed to form nanotubes on the surface of cylindrical micelles. After removal of the micelles and treatment of the TEOS nanotubes, silica nanotubes are formed. (Adopted from Ref. [30].)

presence of a costructure-directing agent such as aminosilane to synthesize silica nanotubes with many radial mesoporous channels traveling perpendicular to the axis along the tube [13]. Although the mechanisms were unclear, the chiral surfactant was seen to play an important role in the success of this synthesis, which does not function with achiral or racemic surfactants. The carboxylic surfactants used were partially neutralized, and formed lipid bilayers when reacted with inorganic acids. The lipid bilayer template exhibited helicity, and this mold – along with the aminosilane and silica precursor – helped to form the radial mesopores in the final structure. In this process, the width of the porous nanotubes could be varied, by changing either the neutralization of the surfactants or the hydrochloric acid-to-surfactant ratio.

Another noncatalytic procedure involved modifying the surface of multiwalled carbon nanotubes (MWNTs) to create silica nanotubes [14]. For this, the critical point is to find a way for the MWNTs to adhere well to silica, and by modifying the MWNT surface using phase-transfer catalysts (PTCs), it was possible to synthesize evenly coated MWNTs. Acids (nitric, sulfuric, etc.) are often used as oxidizing agents on carbon nanotubes; however, as these may cause damage to the nanotubes the use of a PTC to achieve chemical oxidation represents a good alternative. Kim *et al*. carried out an oxidation using a PTC to increase efficiency and selectivity while reducing damage to the MWNTs. The latter were modified with OH groups by using tetrapropyl ammonium bromide (TPABr) as the PTC with $KMnO_4$, and the product then modified with SiH_4. This helped to maximize the amount of silica that could be accommodated by the MWNTs. Silane-modified MWNTs were shown to undergo a reaction with TEOS which occurred very preferentially, mainly because the now-basic MWNTs showed an affinity towards the acidic silicate compound. As the reaction proceeded favorably, this overall method would allow the effective formation of silica nanotubes of desired thickness.

Lu *et al*. prepared polydiacetylene (PDA) in a single crystal form via a solid-state polymerization. From the monomer, single crystals were formed by a slow precipitation in solution [15], after which exposure to UV, X-ray or gamma-ray sources initiated a reaction that coupled the conjugated diacetylenic linkages to form a single polymer chain. The final polymers proved to be both malleable and soluble. In this synthesis, the silica nanocomposites became a part of the PDA system and were present in the final nanocomposites, which exhibited transparency and had an adequate mechanical strength. The formation of micelles is important in order to locate the silica surfactant micelles in the correct order, and for this the diacetylene surfactants must have their hydrophilic ends facing the water or nanocomposites. Increasing hydrophilicity favors more orderly structures, and in this way the silica nanocomposites create a much greater functionality than the polymer would have alone.

As noted above, straight silica nanowires are usually prepared using metallic catalysis and, in the absence of these catalysts, straight amorphous silica nanowires are less commonly produced. Wei Q. *et al*. prepared straight silica nanowires without catalytic assistance somewhat accidentally, because their original aim was to produce ZnO nanomaterials using zinc carbonate hydroxide and graphite at

high temperatures [31]. Yet, rather than ZnO nanostructures, straight silica nanowires were obtained. As the silicon wafer was the only source of silicon able to facilitate the observed reaction, the authors suggested that, to account for the unexpected formation of straight silica nanowires, the high temperature had caused the ZnO to decompose. This would then react with graphite, creating excess carbon dioxide and water vapor that would readily oxidize the Si wafer to produce silica materials that would then stack up to produce the silica nanowires.

Bertone *et al.* prepared synthetic silica or amorphous silica by using particles bonded together by hydrogen bonds to form linked aggregates with a high surface area and good solubility [16]. These particles could be dissolved in NaOH and reformed as quartz. After reacting in base for about 2 h, a white powder appeared in solution, but this could be recovered by a separation based on the different rates of diffusion through a semipermeable membrane (a mesoporous material or powder). Here, it is important to maintain a weak basic solution throughout the reaction to avoid reduced yields; typically, a too-basic solution would reduce the quartz formed, whereas a too-acid solution would yield impure products (e.g. quartz mixed perhaps with the original amorphous silica). After separation, the quartz would precipitate out within 5 h at 0.1 *M* NaOH and 250 °C. Both, X-ray diffraction (XRD) analysis and transmission electron microscopy (TEM) confirmed that the material synthesized was α-quartz.

Both spherical fluorescein isothiocyanate-doped mesoporous silica nanomaterials (S-FITC-MSN) and tubular fluorescein isothiocyanate-doped mesoporous silica nanomaterials (T-FITC-MSN) are synthesized to assess the rate of endocytosis based on several factors, as described by Trewyn *et al.* [18]. For general synthetic methods, the mesoporous silica nanomaterials can be prepared by mixing fluorescein isothiocyanate (FTIC) with 3-aminopropyltrimethoxysilane with anhydrous dimethylformamide (DMF) as solvent. *N*-cetyltrimethylammonium bromide (CTAB) is then dissolved in water and made basic with NaOH, followed by a temperature increase. TEOS is added dropwise to the CTAB solution, after which the other prepared solution is mixed in to produce S-FITC-MSN as an orange powder. The synthesis for tubular structure is very similar; the only differences being the concentrations of TEOS, CTAB and NaOH. The size for spherical FITC-MSN ranges from 80 to 150 nm; a similar range was seen for tubular FITC-MSN, but with the tube stretching out for up to 100 to 400 nm. The aggregation of MSNs is typically investigated by use of the zeta potential, for which the tubular FITC-MSN has a lower value. It should be noted that the zeta potential is an indication of how much repulsion exists between like particles in dispersion. A lower zeta potential means less stability, and thus more ability to aggregate – which is another reason why the tubular structure is less efficient than the spherical.

Magnetic nanoparticles that have superparamagnetic properties are useful for controlled drug delivery, bioseparation, image enhancement in magnetic resonance imaging (MRI), and thermal therapy for treating cancer. However, a major problem that occurs with their use in pure form is that they degrade rapidly and form aggregates in nature. Nonetheless, in order to utilize these properties while

avoiding the problems, it is possible to completely coat the outside of the magnetic nanoparticles with silica. In the synthesis by Zhou *et al.*, $Fe_3O_4/CaCO_3$ nanoparticles were first prepared using a rotating packed bed (RPB) method, with a physical flow through the two phases [32]. Here, the two phases flow against each other; the gas phase flows radially inward while the liquid phase flows radially outward. In one phase of the continuously rotating reaction, the Fe_3O_4 is hydrolyzed, while in the other phase the carbon dioxide and $Ca(OH)_2$ react. A sol–gel technique can then be used to generate the magnetic hollow silica nanospheres. As porous structures are more functional, the nanospheres were made to be porous by using templates of hexadecyltrimethylammonium bromide and octane.

Hollow silica nanoparticles can be synthesized under moderate conditions using luminescent CdSe/ZnS nanoparticles, as described by Darbandi *et al.* [9]. The synthesis is conducted at room temperature within reverse micelles and by way of a modified water-in-oil microemulsion system, where silica is formed from the hydrolysis of TEOS. Here, the silica acts as a host for the CdSe/ZnS nanoparticles while the latter is simultaneously dissolved. The extent of this dissolution is determined by the amount of ammonia aqueous solution used and the reaction time. In a typical synthesis, cyclohexane is added to polyethylene glycol nonylphenyl ether (the surfactant), pre-prepared luminescent CdSe/ZnS nanoparticles in chloroform, and TEOS, and the mixture then stirred vigorously to form the microemulsion. After 30 min, aqueous ammonia is added to initiate the encapsulation, and the reaction is then left overnight at room temperature before the nanoparticles are precipitated. By increasing the amount of ammonia used, the core particles become increasingly dissolved to the point where hollow spheres can be obtained (250 µl ammonia solution). Similarly, an increase in the duration of the reaction will yield nanoparticles with increasingly dissolved cores.

2.2.2 Asymmetric Silica Nanomaterials

The preparation of asymmetric nanosilica differs slightly from that of their symmetric counterparts, the main difference being an involvement of templates or anisotropic catalysts [28]. The addition of these materials initiates an asymmetric growth of nanomaterials, thus producing helical nanomaterials. In the template nanosilica, a further treatment of as-made silica-like nanomaterials is required to convert them into real silica nanomaterials. However, in the catalytic growth of helical nanomaterials such as nanocoils, no post-synthesis treatment is required.

2.2.2.1 Catalytic Growth

Catalysts are used to synthesize silica nanocoils or nanosprings. For example, Wang and coworkers used gold nanoparticles as catalysts to produce silica nanosprings [20]. Here, mats of nanosprings were grown via the VLS mechanism using a gold catalyst, where the deposition temperature was at as low as 350 °C. The yield was very high (close to 100%), the results repeatable, and two types of nanospring were observed: the first type was formed from a single nanowire, whereas the

second consisted of multiple intertwined nanowires. A patterned deposition of nanosprings could be achieved using this technology.

Cobalt nanoparticles have been used to produce silica nanocoils by Qu *et al.* [28], who employed a much higher reaction temperature (ca. 1000 °C). Although silicon wafer was the only source of silicon, the growth model could be either VSS or SSS. Moreover, the nanocoils had a much shorter persistence in length and diameter, of the order of 50 nm and 20 nm, respectively, than the straight silica nanowires mentioned above. Both, isotropic or spherical cobalt nanoparticles and anisotropic nanoparticles or cubic Co_3O_4 nanoparticles were employed as catalysts [33] and, within a narrow temperature window between 1035 and 1075 °C coiled silica nanowires could be prepared. With small spherical cobalt nanoparticles, the authors created alternating coiled–straight nanowires simply by raising and lowering the reaction temperature, allegedly by controlling the isotropy of the nanoparticle catalysts. The persistence in length was much shorter than that of straight wires, and the cross-sections ranged from round to irregular (see Figure 2.3), with a marquise-like shape. The authors attributed the growth of these irregular cross-sectioned silica nanowires to the use of anisotropic cobalt catalysts.

Zhang *et al.* synthesized amorphous helical SiO_2 nanosprings (80–140 nm diameter, up to 8 μm length) by using a chemical vapor deposition (CVD) technique [22] and Fe nanoparticles as catalyst. In this reaction, an alternating growth of helical nanosprings was also observed in the middle of a straight nanowire, which the authors suggested was caused by a perturbation during growth of the straight nanowire. Such perturbation could be derived from the addition of trace amounts of carbon into the Fe nanoparticles, thus rendering them anisotropic and creating a VSS growth environment.

2.2.2.2 **Noncatalytic Growth**

The condensation of silica can also be controlled with surfactants or, in other words, a template effect, as demonstrated by many groups. This is because the hydrophobic force created by high-density surfactants on the surface of silica nanofibers or nanotubes is sufficient to twist the nanomaterials to become helical or asymmetric.

Helical silica were first synthesized, using a template effect, by Ono *et al.* [34]. The template used was a cholesterol-based organogel system, while the cationic charge was shown to be sparsely distributed among the organogel fibers and to play an essential role. During the past few years, more research groups have employed this approach. For example, Yang *et al.* used a noncatalytic method to synthesize silica helical nanostructures with probably the longest persistence length [35]. For this, they used a gelator to induce the formation of helical bundles, which comprise multiple-strand gel fibers. The helical nanobundles were prepared via sol–gel polymerization using a chiral cationic gelator, with the extent of helicity depending on the synthetic environment. For example, in acidic conditions the bundles were helical, while under basic conditions they were straight. This clearly showed that the formation of helical bundles depended on the interactions between individual silica nanotubes. The same authors also synthesized other helical

nanostructures, which they referred to as nanofibers [23]. In a separate study, Li *et al.* identified similar nanosilica under similar acidic conditions using TEOS and CTAB [36]. Again, the helicity was believed to derive from the hydrogen bonding between the surfactants as they stacked together. In a similarly procedure, and using cationic gelators, Yang *et al.* also prepared silica nanosprings [37].

This surfactant-controlled synthesis of helical silica nanofibers or nanobundles has also been reported by Jung *et al.* [24], who used a binary sol–gel process to produce a helical form of silica nanofibers. The formation was explained as 'hydrogen bonding-controlled'. Later, Sugiyasu *et al.* used the same method to produce a double helix system [38], while Seddon *et al.* used the surfactants as a template to control the growth of helical silica nanostructures [25]. Zhang *et al.* employed bona fide cosurfactants to alter the synthesis of regular mesoporous silica nanomaterials into making helical nanomaterials [26], although the helicity was not greatly apparent.

Previously, helical silica nanotubes were prepared by Yu *et al.* by using the surfactant template method [13]. Here, hierarchical silica nanotubes with radially oriented mesoporous channels perpendicular to the central axis of the tube were synthesized using a self-assembled chiral anionic surfactant, a costructure-directing agent (CSDA), and a silica precursor. By manipulating the synthesis gel composition, silica nanotubes with varying dimensions were prepared, with average inner diameters of 94, 62 and 62 nm corresponding to wall thicknesses of 27, 33 and 45 nm, respectively. For all three nanotubes, the diameter of the wall mesopores was kept constant at 4 nm. These materials with such a unique structure may be produced only with chiral surfactant, and the existence of helicity in the lipid bilayer template was confirmed using circular dichroism spectroscopy. The mesopores which penetrated from outside to inside of the silica nanotubes were thought to originate from the initial formation of self-assembled lipid tubes with helical bilayers, which in turn reassembled to form mesopores in the wall of the nanotubes upon the addition of a CSDA and a silica source. These studies were based on some earlier investigations conducted by Wu *et al.* [7].

2.3 Characterization

The characterization of nanosilica incorporates many conventional microscopic and analytical methods. The details of such methods, the parameters that can be determined with them, and the associated references are summarized in Table 2.2. The main parameters to be identified are the morphology, surface characterization and measurement of optical properties of either the silica core or the surfactants. Although, in order to produce specific nanosilica, a good knowledge of these methods and other novel techniques is clearly required, they will not be described in great detail at this point.

The first type of measurement is morphologically oriented, and for this electron microscopy offers both dimensional and elemental analysis of the nanomaterials.

Table 2.2 Analytical methods used for characterizing nanosilica.

Method	Description	Properties	Reference
TEM/EDX/EELS	TEM and X-ray analysis or spectroscopy are used to analyze structure and composition. EELS is used for additional characterization.	Morphology, composition	[9]
SEM/FESEM	SEM is similarly used with energy-dispersive analysis (EDS) to characterize and analyze structure. FESEM used to determine size and morphology.	Morphology, composition	[12]
HRTEM	HRTEM also used with EDS	Morphology, composition	[39]
CD	Characterization of surfactants (or other structures with handedness) can be made using circular dichroism (CD).	Helicity	[13]
EDAX	Energy-dispersive analysis by X-ray spectrum	Composition	[13]
XRD	XRD is used to characterize the structure of materials as well as to compare newly synthesized materials to a reference starting material for instance.	Structure	[40]
Raman spectroscopy	Provides information about molecular structure and orientation based on the different vibrational relaxations observed by unique structures.	Vibrations between chemical bonds	[41]
Fluorescence	Analyzes fluorescence	Emission, band gap	[42]
NMR	Nuclear magnetic resonance.	Composition, surface composition	[28]
SQUID	Superconducting quantum interference magnetometry	Magnetism	[17]
Photoluminescence spectroscopy	Provides intensity of light emission	Shows peaks of excitation	[39]
Rutherford backscattering spectroscopy (RBS)	High-energy ion scattering	Structure and composition	[41]

Table 2.2 *Continued*

Method	Description	Properties	Reference
SAXS	Small-angle X-ray scattering. Nonuniform structures at the nano size level will scatter X-ray light at various low angles to provide information about structure and characteristics.	Shape, size (even pore size), surface to volume ratio	[43]
SFM/AFM	Scanning force microscopy/atomic force microscopy	Structure and composition	[43]
STEM	Scanning transmission electron microscope (dark-field method)	Structure and composition	[43]

A relatively new method, which is based on high-resolution transmission electron microscopy (HR-TEM), may prove to be critical in our understanding of these new materials [9]. With HR-TEM, it is possible to use elemental analysis to create elemental specific high-resolution morphological images, the main benefit being that it is possible to isolate the morphology of each element and thus achieve a much better understanding of the nanomaterial structure.

The second type of measurement deals with the composition and surface characterization. Here, nuclear magnetic resonance (NMR) typically can be used to selectively determine the surfactants [44]. Alternatively, electron energy loss spectroscopy (EELS) can be used to obtain composition information, including the surface composition.

A third type of measurement is aimed at characterizing the optical properties of the nanomaterials, and for this both conventional optical microscopy and transmission UV-visible spectroscopy are applicable. Another method – circular dichroism – can be used to study the helicity of silica nanomaterials, while Raman spectroscopy has also been used for their characterization.

2.4 Applications of Symmetric and Asymmetric Nanosilica

The thrust behind the advancement of any field depends on the application potential or real benefits, much more so than the materials themselves, and the same rule applies to nanosilica – whether symmetric or asymmetric. In the following sections we will survey the applications of both symmetric and asymmetric nanosilica. It will become clear that asymmetric nanosilica, at present, have far fewer applications than their symmetric counterparts, although several excellent obvious

potential uses have been identified. It is hoped that, by comparing these two types of material, research groups will be more likely to expand the applications of asymmetric nanomaterials into the traditional territories presently occupied by symmetric nanosilica, especially as the asymmetric nanomaterials possess certain unique properties that symmetric nanomaterials do not.

Several excellent reviews, each with a different emphasis, have been published in recent years. An example is the review of Halas, who discusses in particular the chemistry of silica nanostructures [27]. However, the present discussion will center on a comparison between symmetric and asymmetric nanosilica.

2.4.1 Symmetric Nanosilica

Nanosilica possess many properties that make them suitable for medical and biological applications, the details of which are summarized for both symmetric and asymmetric silica nanomaterials in Table 2.3. It is clear from these data that the applications of asymmetric nanosilica still require much effort, with the 'road block' perhaps being caused by a lack of manipulation of the asymmetric silica nanostructures such as silica nanocoils. Yet, when the synthesis and manipulation are fully under control, it is believed that the applications will be developed very quickly. In the following sections we summarize and compare the applications of these nanomaterials, with the hope that those interested in using asymmetric nanosilica will gain the necessary insight and background knowledge to develop and improve these applications. In the following section, we review those applications based on the properties of nanosilica.

2.4.1.1 Silica Nanomaterials as Drug Delivery Vehicles

Nanosilica can be used to deliver drugs, such as new genes, proteins, small-molecule drugs or other nanoscale materials. In particular, the versatility of either the silica surface or the pores could be utilized as an effective delivery vehicle.

In one example, Trewyn *et al.* showed how silica nanoparticles could penetrate membranes [18] by using spherical and tube-shaped MCM-41 fluorescein-labeled mesoporous silica nanomaterials (MSNs). Both materials have hexagonally arranged mesopores with a high surface area (>950 $m^2 g^{-1}$) and a narrow distribution of pore diameters, while an overall size of the order of a few hundred nanometers. In these studies, flow cytometry and fluorescence confocal microscopy were used to characterize the cellular uptake efficiency and kinetics of both MSNs, measured in a cancer cell line (Chinese hamster ovary; CHO) and a noncancerous cell line (fibroblasts). The correlation was investigated between the particle morphology and aggregation of MSNs and the effectiveness of cellular uptake. In another report, Radu *et al.* discussed the use of MSNs in performing gene transfection, when second-generation PAMAMs covalently linked to the surface of the MSNs were used to deliver the gene into cells [48]. Lai *et al.* also used the same MSNs to deliver neurotransmitters encapsulated within the pores of MSNs [49].

Table 2.3 Applications of symmetric and asymmetric nanosilica.

Material	Properties	Applications	Reference
Silica nanofibers	Structural flexibility	Nanomechanical, electronmagnetic devices, resonators, composite materials	[20]
Mesoporous silica nanospheres	Symmetry, thousands of loadable parallel channels running from one end to other, large surface area-to-volume ratio	Diagnosis, therapeutics, carriers (drugs and more), gas/metal ion absorbance	[40]
$CdSe/ZnS/SiO_2$	Luminescence (core)	Optical nanoscale applications.	[12]
Silica nanowires	Luminescence (blue)	Nanoscale optical-based electronics. In particular, amorphous silica nanowires have been shown to emit blue light that could serve well in integrated optical nanodevices. Also have applications in photonics and biosensing.	[39]
Carbon nanotubes coated with silica	General in catalysis, magnetic and optical	Applications in light-related studies, magnetism and catalysis.	[14]
Silica nanocomposites (polydiacetylene/silica)	Optical transparency and mechanical strength	Biomolecular sensors and light-emitting electronics.	[15]
Nanoquartz	Piezoelectric	Material engineering, motors and actuators.	[16]
Magnetic hollow silica nanospheres	Superparamagnetic	Controlled drug delivery, bioseparation, enhancing image in MRI, thermal therapy (form of cancer treatment)	[17]
Spherical fluorescein isothiocyanate-doped MSNs (S-FITC-MSN) and tubular fluorescein isothiocyanate-doped MSNs (T-FITC-MSN)	Fluoresces, large surface area, tunable pore size	Biological marker, imaging, controlled drug delivery/release	[18]

Table 2.3 *Continued*

Material	Properties	Applications	Reference
Silica nanobeads	Doping capacity (with fluorescent materials), large surface-area-to volume ratio	Drug delivery, biosensing, and fluorescent labeling of biomolecules to aid in biological studies. Also have optical, magnetic and catalytic applications.	[45], [19]
Silica nanotubes	Hydrophilic inner and outer walls, highly functional surface	Nanoscale sensors and electric devices, optical, magnetic, catalytic applications as well as bioseparation	[13]
Hollow silica nanocapsules	Insulation	Catalysis, bioseparation, controlled drug release and delivery, man-made cells, materials modified to have better insulating properties, or lower dielectric constant.	[46]
Silica nanorods	Combined functionalities, rigid structure, large pore volume, biocompatibility, surface functionality	Biomarker, drug delivery (carrier), can be made to fluoresce, MRI, contrast agents	[47]
Silica nanosprings	Luminescence, type of nanowire	Nanoscale electronics and optics, nanomechanical, and composite materials	[22]

Elsewhere, various other hollow mesoporous nanosilica have also been explored for their medical applications. Zhou *et al.* discussed the use of hollow silica nanospheres with magnetic nanoparticles (e.g. Fe_3O_4) within the pores to deliver ibuprofen. When the drug had been stored inside the pores, the openings were encapsulated [17]. As a consequence, the size of the nanospheres was of the order of a few hundred nanometers, while the magnetic Fe_3O_4 nanoparticles were about 5–10 nm. It should be noted here that these nanomaterials were used exclusively for delivery purposes.

Another popular application, almost equivalent to drug delivery, was to use the nanosilica chemically linked to various other labeling agents such as fluorophores to perform imaging tasks. As an example, Tsai *et al.* used mesoporous silica nanorods as a multifunctional cell-imaging probe [47], performing both magnetic resonance imaging (MRI) using a Gd agent and confocal light imaging with a dye

molecule. Because magnetic nanomaterials can also be attached to nanosilica (as has been shown by many groups), these multicomponent nanomaterials can be used in magnetic imaging. Giri *et al*. have shown that it is possible to use magnetic nanoparticles to control the release of substances trapped inside mesoporous silica nanorods [50]. This is similar to the effect described above, where materials trapped inside the host porous silica nanomaterials could be set free when the capping materials were removed. Hu *et al*. develop magnetic-sensitive nanosilica to control the release of drugs remotely [40], by using a high-frequency magnetic field to burst open the magnetic field-sensitive silica nanospheres.

2.4.1.2 Silica Nanomaterials as a Catalyst Host and Sensors

Nanosilica can also be used as a host for catalysis and as a material for separation. Yang *et al*. coated magnetite with silica and showed the product to be a bioactive, mechanically stable and magnetically separable nanomaterial [51] of which the particles were ~50 nm in diameter, with a pore size of 1.5 nm. Peroxidase entrapped in silica-covered porous nanoparticles was shown to possess a high catalytic activity, a direct benefit being that the nanoparticles could easily be separated from solution using an external magnetic field. When using this material, the authors demonstrated a detection limit of 160 ng ml^{-1} for gentamicin.

In another study, Grant *et al*. immobilized the acceptor end of biological donor–acceptor pairs linked via peptides onto the surface of nanosilica [45], such that the silica nanoparticles acted as an optical platform. Upon interacting with a biological molecule (enzyme) that could cleave the peptide bond between the donor and acceptor, the latter pair would separate, thus reducing the fluorescence which originated from fluorescence resonance energy transfer (FRET). The detection limit of this assay (which measured fluorescence intensity or yield) was ~10 μg ml^{-1}.

2.4.1.3 Silica Nanomaterials as Optical Materials

Silica nanomaterials may also have many optical applications, as they themselves can emit light at various wavelengths, as well hosting different fluorophores as sensors. In one study, Elliman *et al*. showed that erbium ions (Er^{3+}) could be excited by light sources to their $^4I_{13/2}$ state where they pass through various energy channels and then relax back to a ground state of $^4I_{15/2}$ [52]. By doping silica nanowires with erbium, the nanowires became optically active, while the duration of the luminescence could be controlled by the nature of the nanowire surface. The decay rate was slower because lower optical density states in the nanowires (the lower the optical density, the higher the light transmittance) caused less quenching of its own fluorescence at high concentrations, and greater thermal quenching due to the closeness of the surface to the site of light emission and large surface area-to-volume ratio for nanostructures. As erbium is so sensitive to the surface of the nanowire, the luminescence could be monitored on the surface as a means of detecting adsorbed molecules.

Bottini *et al*. used luminescent silica nanobeads to investigate the transportation of T lymphocytes [19]. Silica nanobeads are known to be useful for biosensing and

catalysis, due to their easy synthesis, doping capacity/surface functionalization, and large surface area-to-volume ratio. Silica nanobeads can also adopt fluorescent, magnetic and semiconducting properties by linking to molecules that have such properties. Silica nanobeads doped with tris(2,2′-bipyridine) dichlororuthenium(II) hexahydrate [Ru(bpy)$_3$] (RuSNBs) are luminous under a certain pH. To test for luminescence, the cells were incubated with RuSNB, such that luminescence occurred. A momentary luminescence was seen to occur in the cytosol for those nanoparticles capable of leaving the lysosomes. Based on these findings, Bottini *et al.* concluded that nanobeads might be useful for obtaining a specific cytoplasmic effect in target cells, with no cell-toxic effect being observed.

Sekhar *et al.* identified another means of using metal-coated silica nanowires for the detection of cancer [41]. Here, the metal-decorated silica nanowires under study acted as a filter, such that their high selectivity made them effective in the diagnosis of cancers and other diseases. Specifically, the nanowires could detect interleukin-10 (IL-10) and osteopontin (OPN). For a closer examination of the selectivity of the metal nanoclusters, Raman spectroscopy can be used to study the affinity of certain substrate surfaces towards biomarkers. The substrate itself must be chosen carefully as this will affect the Raman scattering from the biomarkers. The applications of these metal-decorated nanowires demonstrate unique functionality compared to uncoated silica nanowires.

In a further study, Wei *et al.* synthesized aligned silica nanowires as fluorophores, where the straight nanowires were shown to emit two bands of green light in the visible range, at 510 and 560 nm [31]. Alignment was important to the photoluminescent properties exhibited at room temperature, while the light emission suggested possible applications in nanoscale optical electronics.

Amorphous silica nanowires have also been tested for their blue light emission properties by Yu *et al.* [53]. Silica nanowires that emit blue light would be applicable in both industry and in research. For example, in scanning near-field optical microscopy (SNOM), the resolution depends on the diameter of the tip and space between the tip and sample. In this respect, silicon nanowires may be used as the optical head in the microscope in order to provide a better resolution. It should also be noted that, aside from applications in industry, silicon nanowires have recently also been of great help in extending our understanding of optical theory and diffraction.

2.4.1.4 Nanosilica in Other Applications

When investigating other uses of nanomaterials, Taylor *et al.* examined the possibility of using MSNs as highly efficient MRI contrast agents [42]. At present, gadolinium functions as an effective contrast agent in MRI studies by enhancing image visibility; however, this can be further enhanced by grafting Gd chelated onto MSNs as carriers, thus enabling the design of highly efficient MRI contrast agents.

Block copolymers with both hydrophilic and hydrophobic properties have been used by Garcia *et al.* in the synthesis of nanoparticles [43]. Reverse block copolymer mesophases have been used to prepare iron oxide-aluminosilicate nanoparticles,

with good control over shape and size, by regulating the amount of inorganic material used. The subsequent decomposition of materials by calcination promotes the formation of crystalline, magnetic gamma ferric oxide in the amorphous phase, which in turn allows the structure and features of the particles to be adjusted, so as to achieve varying functionalities (both magnetic and optical). Moreover, as the silica nanofibers are more structurally flexible, they may have potential applications in nanomechanical, nanoelectronmagnetic devices, resonators and composite materials.

2.4.2 Asymmetric Nanosilica

In recent years, asymmetric nanosilica have not been widely used, most likely due to a lack of convenient ways in which they can be manipulated. Nonetheless, these materials should have an effective application potential in asymmetric catalysis, although their sizes (e.g. nanocoils) must be tightly controlled. The details of asymmetric colloids of many compositions have been discussed. For example, Correa-Duarte *et al.* described the creation of asymmetric functional colloids through selective hemisphere modification [54], a method which could easily be expanded for the modification of silica nanoparticles and asymmetric nanosilica.

2.5 Conclusions

In this chapter, we have reviewed the current state of research into symmetric and asymmetric nanosilica. Although, approximately equal numbers of synthetic methods are available for both types of nanomaterial, a much greater disparity exists between their numbers of application. However, as the development of better synthetic and analytical methods continues to advance, it is foreseeable that both types of nanomaterial will find significantly more applications, especially considering the current lack of applications for the asymmetric forms.

Acknowledgments

The authors thank G.D. Suarez and D.J. Masiel for their assistance in preparing this manuscript.

References

1 Kim, J.W., Kim, L.U. and Kim, C.K. (2007) Size control of silica nanoparticles and their surface treatment for fabrication of dental nanocomposites. *Biomacromolecules*, **8**(1), 215–22.

2 Limmer, S.J., Seraji, S., Wu, Y., Chou, T.P., Nguyen, C. and Cao, G.Z. (2002) Template-based growth of various oxide nanorods by sol-gel electrophoresis. *Advanced Functional Materials*, **12**(1), 59–64.

3 Pan, Z., Dai, Z., Ma, C. and Wang, Z. (2002) Molten gallium as a catalyst for the large-scale growth of highly aligned silica nanowires. *Journal of the American Chemical Society*, **124**(8), 1817–22.

4 Zygmunt, J., Krumeich, F. and Nesper, R. (2003) Novel silica nanotubes with a high aspect ratio – Synthesis and structural characterization. *Advanced Materials*, **15**(18), 1538.

5 Yao, B., Fleming, D., Morris, M.A. and Lawrence, S.E. (2004) Structural control of mesoporous silica nanowire arrays in porous alumina membranes. *Chemistry of Materials*, **16**(24), 4851.

6 Tuan, H., Ghezelbash, A. and Kirgel, B. (2008) Silicon nanowires and silica nanotubes seeded by copper nanoparticles in an organic solvent. *Chemistry of Materials*, **20**, 2306–13.

7 Wu, X.W., Ruan, J.F., Ohsuna, T., Terasaki, O. and Che, S.N. (2007) A novel route for synthesizing silica nanotubes with chiral mesoporous wall structures. *Chemistry of Materials*, **19**(7), 1577–83.

8 Luo, S.D., Zhou, W.Y., Chu, W.G., Shen, J., Zhang, Z.X., Liu, L.F. *et al.* (2007) Batchwise growth of silica cone patterns via self-assembly of aligned nanowires. *Small*, **3**(3), 444–50.

9 Darbandi, M., Thomann, R. and Nann, T. (2007) Hollow silica nanospheres: in situ, semi-in situ, and two-step synthesis. *Chemistry of Materials*, **19**(7), 1700–3.

10 Lee, K.H., Lee, S.W., Vanfleet, R.R. and Sigmund, W. (2003) Amorphous silica nanowires grown by the vapor-solid mechanism. *Chemical Physics Letters*, **376**(3–4), 498–503.

11 Wang, J.C., Zhan, C.Z. and Li, F.G. (2003) The synthesis of silica nanowire arrays. *Solid State Communications*, **125**(11–12), 629–31.

12 Fan, X., Meng, X.M., Zhang, X.H., Lee, C.S. and Lee, S.T. (2007) Template fabrication of SiO_2 nanotubes. *Applied Physics Letters*, **90**(10), 103114-1–103114-3.

13 Yu, Y.T., Qiu, H.B., Wu, X.W., Li, H.C., Li, Y.S., Sakamoto, Y. *et al.* (2008) Synthesis and characterization of silica nanotubes with radially oriented mesopores. *Advanced Functional Materials*, **18**(4), 541–50.

14 Kim, M., Hong, J., Lee, J., Hong, C.K. and Shim, S.E. (2008) Fabrication of silica nanotubes using silica coated multi-walled carbon nanotubes as the template. *Journal of Colloid and Interface Science*, **322**(1), 321–6.

15 Lu, Y.F., Yang, Y., Sellinger, A., Lu, M.C., Huang, J.M., Fan, H.Y. *et al.* (2001) Self-assembly of mesoscopically ordered chromatic polydiacetylene/silica nanocomposites. *Nature*, **411**(6837), 617.

16 Bertone, J.F., Cizeron, J., Wahi, R.K., Bosworth, J.K. and Colvin, V.L. (2003) Hydrothermal synthesis of quartz nanocrystals. *Nano Letters*, **3**(5), 655–9.

17 Zhou, J., Wu, W., Caruntu, D., Yu, M.H., Martin, A., Chen, J.F. *et al.* (2007) Synthesis of porous magnetic hollow silica nanospheres for nanomedicine application. *Journal of Physical Chemistry C*, **111**(47), 17473–7.

18 Trewyn, B.G., Nieweg, J.A., Zhao, Y. and Lin, V.S.Y. (2008) Biocompatible mesoporous silica nanoparticles with different morphologies for animal cell membrane, penetration. *Chemical Engineering Journal*, **137**(1), 23–9.

19 Bottini, M., Cerignoli, F., Mills, D.M., D'Annibale, F., Leone, M., Rosato, N. *et al.* (2007) Luminescent silica nanobeads: characterization and evaluation as efficient cytoplasmatic transporters for T-lymphocytes. *Journal of the American Chemical Society*, **129**(25), 7814–23.

20 Wang, L.D., Major, D., Paga, P., Zhang, D., Norton, M.G. and McIlroy, D.N. (2006) High yield synthesis and lithography of silica-based nanospring mats. *Nanotechnology*, **17**(11), S298–303.

21 Carter, J., Qu, Y., Porter, R., Hoang, L., Masiel, D. and Guo, T. (2005) Silicon-based nanowires from silicon wafers catalyzed by cobalt nanoparticles in a hydrogen environment. *Chemical Communications*, **17**, 2274–6.

22 Zhang, H.F., Wang, C.M., Buck, E.C. and Wang, L.S. (2003) Synthesis, characterization, and manipulation of helical SiO_2 nanosprings. *Nano Letters*, **3**(5), 577–80.

23 Yang, Y.G., Suzuki, M., Owa, S., Shirai, H. and Hanabusa, K. (2006) Control of helical silica nanostructures using a chiral surfactant. *Journal of Materials Chemistry*, **16**(17), 1644–50.

24 Jung, J.H., Yoshida, K. and Shimizu, T. (2002) Creation of novel double-helical silica nanotubes using binary gel system. *Langmuir*, **18**(23), 8724–7.

25 Seddon, A.M., Patel, H.M., Burkett, S.L. and Mann, S. (2002) Chiral templating of silica-lipid lamellar mesophase with helical tubular architecture. *Angewandte Chemie – International Edition in English)*, **41**(16), 2988–91.

26 Zhang, Q.H., Lu, F., Li, C.L., Wang, Y. and Wan, H.L. (2006) An efficient synthesis of helical mesoporous silica nanorods. *Chemistry Letters*, **35**(2), 190–1.

27 Halas, N.J. (2008) Nanoscience under glass: the versatile chemistry of silica nanostructures. *ACS Nano*, **2**(2), 179–83.

28 Qu, Y., Carter, J. and Guo, T. (2006) Silica nanocoils. *Journal of Physical Chemistry B*, **110**(16), 8296–301.

29 Zhang, J.H., Liu, H.Y., Wang, Z.L. and Ming, N.B. (2008) Au-induced polyvinylpyrrolidone aggregates with bound water for the highly shape-selective synthesis of silica nanostructures. *Chemistry*, **14**(14), 4374–80.

30 Jang, J.K. and Yoon, H. (2004) Novel fabrication of size-tunable silica nanotubes using a reverse-microemulsion-mediated sol-gel method. *Advanced Materials*, **16**(9–10), 799.

31 Wei, Q., Meng, G.W., An, X.H., Hao, Y.F. and Zhang, L.D. (2006) Synthesis and photoluminescence of aligned straight silica nanowires on Si substrate. *Solid State Communications*, **138**(7), 325–30.

32 Ma, H., Zhou, J., Caruntu, D., Yu, M.H., Chen, J.F., O'Connor, C.J. *et al.* (2008) Fabrication of magnetic porous hollow silica drug carriers using $CaCO_3/Fe_3O_4$ composite nanoparticles and cationic surfactant double templates. *Journal of Applied Physics*, **103**(7), 07A320.

33 Qu, Y., Masiel, D.J., Cheng, N.N., Sutherland, A.M., Carter, J.D., Browning, N.D. *et al.* (2008) Recognition of melting of nanoparticle catalysts with cubically shaped Co_3O_4 nanoparticles. *Journal of Colloid and Interface Science*, **321**(2), 251–5.

34 Ono, Y., Nakashima, K., Sano, M., Hojo, J. and Shinkai, S. (1999) Template effect of cholesterol-based organogels on sol-gel polymerization creates novel silica with a helical structure. *Chemistry Letters*, **10**, 1119–20.

35 Yang, Y.G., Suzuki, M., Fukui, H., Shirai, H. and Hanabusa, K. (2006) Preparation of helical mesoporous silica and hybrid silica nanofibers using hydrogelator. *Chemistry of Materials*, **18**(5), 1324–9.

36 Li, X.M., Wu, Y.L. and Li, Y. (2007) Surfactant-assisted synthesis of helical silica. *Inorganica Chimica Acta*, **360**(1), 241–5.

37 Yang, Y.G., Fukui, H., Suzuki, M., Shirai, H. and Hanabusa, K. (2005) Preparation of silica nanosprings using cationic gelators as template. *Bulletin of the Chemical Society of Japan*, **78**(11), 2069–74.

38 Sugiyasu, K., Tamaru, S., Takeuchi, M., Berthier, D., Huc, I., Oda, R. *et al.* (2002) Double helical silica fibrils by sol-gel transcription of chiral aggregates of gemini surfactants. *Chemical Communications*, **11**, 1212–13.

39 Yu, D.P., Hang, Q.L., Ding, Y., Zhang, H. Z., Bai, Z.G., Wang, J.J. *et al.* (1998) Amorphous silica nanowires: intensive blue light emitters. *Applied Physics Letters*, **73**(21), 3076–8.

40 Hu, S.H., Liu, T.Y., Huang, H.Y., Liu, D. M. and Chen, S.Y. (2008) Magnetic-sensitive silica nanospheres for controlled drug release. *Langmuir*, **24**(1), 239–44.

41 Sekhar, P.K., Ramgir, N.S. and Bhansali, S. (2008) Metal-decorated silica nanowires: an active surface-enhanced Raman substrate for cancer biomarker detection. *Journal of Physical Chemistry C*, **112**(6), 1729–34.

42 Taylor, K.M.L., Kim, J.S., Rieter, W.J., An, H., Lin, W.L. and Lin, W.B. (2008) Mesoporous silica nanospheres as highly efficient MRI contrast agents. *Journal of*

the American Chemical Society, **130**(7), 2154.

43 Garcia, C.B.W., Zhang, Y.M., Mahajan, S., DiSalvo, F. and Wiesner, U. (2003) Self-assembly approach toward magnetic silica-type nanoparticles of different shapes from reverse block copolymer mesophases. *Journal of the American Chemical Society*, **125**(44), 13310–11.

44 Qu, Y., Porter, R., Shan, F., Carter, J. and Guo, T. (2006) Synthesis of tubular gold and silver nanoshells using silica nanowire core templates. *Langmuir*, **22**(14), 6367–74.

45 Grant, S.A., Weilbaecher, C. and Lichlyter, D. (2007) Development of a protease biosensor utilizing silica nanobeads. *Sensors and Actuators B, Chemical*, **121**(2), 482–9.

46 Liu, Y.Y., Miyoshi, H. and Nakamura, M. (2007) Novel drug delivery system of hollow mesoporous silica nanocapsules with thin shells: preparation and fluorescein isothiocyanate (FITC) release kinetics. *Colloids and Surfaces B, Biointerfaces*, **58**(2), 180–7.

47 Tsai, C.P., Hung, Y., Chou, Y.H., Huang, D.M., Hsiao, J.K., Chang, C. *et al.* (2008) High-contrast paramagnetic fluorescent mesoporous silica nanorods as a multifunctional cell-imaging probe. *Small*, **4**(2), 186–91.

48 Radu, D.R., Lai, C.Y., Jeftinija, K., Rowe, E.W., Jeftinija, S. and Lin, V.S.Y. (2004) A polyamidoamine dendrimer-capped mesoporous silica nanosphere-based gene transfection reagent. *Journal of the American Chemical Society*, **126**(41), 13216–17.

49 Lai, C.Y., Trewyn, B.G., Jeftinija, D.M., Jeftinija, K., Xu, S., Jeftinija, S. *et al.* (2003) A mesoporous silica nanosphere-based carrier system with chemically removable CdS nanoparticle caps for stimuli-responsive controlled release of neurotransmitters and drug molecules. *Journal of the American Chemical Society*, **125**(15), 4451–9.

50 Giri, S., Trewyn, B.G., Stellmaker, M.P. and Lin, V.S.Y. (2005) Stimuli-responsive controlled-release delivery system based on mesoporous silica nanorods capped with magnetic nanoparticles. *Angewandte Chemie - International Edition in English*, **44**(32), 5038–44.

51 Yang, H.H., Zhang, S.Q., Chen, X.L., Zhuang, Z.X., Xu, J.G. and Wang, X.R. (2004) Magnetite-containing spherical silica nanoparticles for biocatalysis and bioseparations. *Analytical Chemistry*, **76**(5), 1316–21.

52 Elliman, R.G., Wilkinson, A.R., Kim, T.H., Sekhar, P.K. and Bhansali, S. (2008) Optical emission from erbium-doped silica nanowires. *Journal of Applied Physics*, **103**(10), 104304–104304-5.

53 Yu, D.P., Hang, Q.L., Ding, Y., Zhang, H. Z., Bai, Z.G., Wang, J.J. *et al.* (1998) Amorphous silica nanowires – intensive blue light emitters. *Applied Physics Letters*, **73**(21), 3076–8.

54 Correa-Duarte, M.A., Salgueirino-Maceira, V., Rodriguez-Gonzalez, B., Liz-Marzan, L. M., Kosiorek, A., Kandulski, W. *et al.* (2005) Asymmetric functional colloids through selective hemisphere modification. *Advanced Materials*, **17**(16), 2014.

Abstract

In this chapter we review the current state of research on symmetric and asymmetric silica nanomaterials, or nanosilica, in terms of their synthesis, characterization and applications. Both, catalytically and noncatalytically grown nanosilica are discussed, and several types of application for these nanomaterials are described. For asymmetric nanosilica, the focus is on helical nanosilica such as silica nanocoils and other helical nanosilica, whereas for symmetric silica nanomaterials the discussion covers more general forms of nanosilica, including nanoparticles, mesoporous nanomaterials and silica nanotubes.

Keywords

silica; nanocoils; nanowires; catalysis; nanoparticles

3
One-Dimensional Silica Structures and Their Applications to the Biological Sciences

Daniel Choi, David McIlroy, James Nagler, Eric Aston, Patrick Hrdlicka, Kurt Gustin, Rod Hill, Deborah Stenkamp and Joshua Branen

3.1
Introduction

One practical reason for the study of nanostructures is the ever-present drive towards smaller sizes in the electronics industry. As features in electronic devices achieve dimensions smaller than the de Bloglie wavelength, it is imperative to explore and understand the physical properties, such as electrical transport, thermal conductivity, mechanical strength, magnetism and light emission, in this regime. During the early years of nanomaterials development, the only types of nanomaterial that could be produced in sufficient quantities for biological research were *nanoparticles*–materials having an aspect ratio of one. However, during the past few years other types of nanomaterial, with high aspect ratios as well as complex shapes (e.g. nanowires, nanorods, nanosprings and carbon nanotubes) have become available. In particular, one-dimensional (1-D) nanomaterials–the so-called *nanowires* and *nanotubes*–have emerged as one of the three types of attractive nanostructure (0-D, 1-D and 2-D) caused by the 1-D quantum confinement that can lead to the enhanced transport of signals along the wires. Moreover, the structure of these materials is more compatible with device design in terms of unique geometry [1, 2], and consequently nanowires have therefore been used for building blocks in electronics [3], optics [4] and sensing technologies, including biomedical applications [5–7].

Today, the most broadly utilized nanowires are formed from silicon, whether pure silicon or silicon oxide (silica; SiO_2), with silicon-based nanowires being used as building blocks for a variety of technologies such as electronics [3], photonics [4] and sensing technology [8, 9]. Given the vast experience of the semiconductor and optics communities while working with silicon and silica, silicon-based nanowires will likely become the most widely utilized family of nanowires. Although many books and reviews have described the details of 1-D silicon or silica nanostructures for a variety of applications, details on their biological applications

Nanomaterials for the Life Sciences Vol. 2: Nanostructured Oxides. Edited by Challa S. S. R. Kumar

ISBN: 978-3-527-32152-0

are sparse. Hence, in this chapter we will focus on the practical biological applications of 1-D silica structures.

3.2 Synthesis of Silica Nanowires and Nanosprings

The vapor–liquid–solid (VLS) mechanism first proposed by Wagner and Ellis [10] is simplistic in nature, yet subtly complex. The VLS model is most readily grasped pictorially; a schematic representation of nanowire formation by to the VLS mechanism is shown in Figure 3.1. The key feature here is a liquid catalyst that is able to absorb material from the surrounding vapor. If the catalyst is not liquid, then material in the vapor will not be absorbed and the nanowire formation will be prohibited. Under the appropriate conditions of temperature and vapor pressure, the liquid will absorb material from the vapor phase, introduced either in elemental form or as a molecular precursor.

In the chemical vapor deposition (CVD) process, a molecular precursor is used [11–13]. Here, as the catalyst absorbs an increasing amount of material it eventually becomes supersaturated, at which point material is deposited at the catalyst–substrate interface (Figure 3.1b), thereby establishing nanowire formation (Figure 3.1c). Extended formation of the nanowire can be maintained as long as a sufficient quantity of reactant is present, and the temperature of the catalyst is maintained above the melting point. If either of these conditions is not met, nanowire formation will cease. Based on the above description of the VLS mechanism, it is clear that the catalyst dictates whether or not nanowire formation will occur.

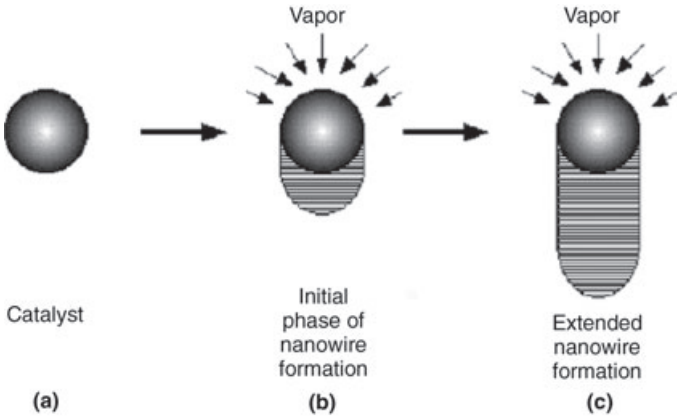

Figure 3.1 A schematic representation of the vapor–liquid–solid (VLS) growth mechanism for nanowire formation.

3.2.1
Catalyst Preparation and Application

A variety of ways exists by which the catalyst may be prepared and introduced into the process, although ultimately the synthesis process will dictate the appropriate methodology. For the laser ablation synthesis of nanowires, the catalyst is introduced directly into the ablation target. This is easily achieved by mixing powders of the catalyst and the nanowire material and then pressing the mixture into a target. In the case of *flow reactors*, the catalyst can either be deposited onto the substrate prior to insertion into the furnace, or placed in a crucible directly in the furnace, upstream from the substrate upon which the nanowires will be deposited, and where transport to the substrate is facilitated by the flow of a background gas. For the CVD synthesis of nanowires, the catalyst is typically applied to the surface prior to nanowire synthesis, this being done either *in situ* or *ex situ*.

An *in situ* application in CVD processes is achieved by first introducing a metallocene precursor (e.g. ferrocene $[(C_5H_5)_2Fe]$) into the deposition chamber for a short period of time, thereby depositing an extremely thin metal film on the order of tens of monolayers onto the substrate. The deposition temperature for the catalyst is typically well below the nanowire synthesis temperature, although again this will depend on the choice of the precursor and the types of nanowire to be synthesized. This step is then followed by nanowire synthesis.

In the case of *ex situ* application of an elemental catalyst, a number of physical vapor deposition techniques can be utilized, including *sputtering* and *molecular beam epitaxy*. In this way, a few to tens of monolayers of the catalyst metal are deposited onto the substrate, which is then inserted into the CVD reactor. For both of these choices the rationale for depositing a few monolayers of the catalyst is twofold. First, an extremely low coverage of the catalyst material will facilitate islanding, which is critical to nanowire formation. Second, the amount of catalyst on the substrate will dictate the size of the metal islands, which in turn will dictate the diameter of the nanowires. The primary drawback to these two approaches is that the size distribution of the islands cannot be readily controlled.

An alternative approach to *ex situ* application of the catalyst is to produce extremely fine powders that can be suspended in a solvent and then applied to the substrate; this method is ideally suited to the use of eutectics as the catalyst. Currently, a number of commercially available sources exist for metallic nanoparticles. In the case of more exotic eutectic materials (e.g. NiB or FeB), powders consisting of particles with diameters of the order of hundreds of microns must be processed to achieve nanoscale particles. The procedure utilized in our laboratory is to grind the purchased powder in a pestle and mortar for 10–12 h, to suspend the fine powder in ethanol, and then to pass the suspension sequentially through a series of polycarbonate membranes in decreasing order of pore size (final pore size 100 nm). The end product is an ethanol-based suspension of particles with a diameter of ≤100 nm. Before applying the catalyst to the substrate surface, the suspension is sonicated for approximately 5 min and then left to stand for 12 h. The latter step allows the larger particles to settle out of suspension, leaving only the smallest

nanoparticles suspended in solution, such that the nanoparticle distribution is in the range of 20 to 100 nm. The solution is then applied to the substrate using a dropper, and the ethanol allowed to evaporate. This procedure is repeated until the desired concentration of nanoparticles is achieved. Unfortunately, a rapid evaporation of the ethanol causes the nanoparticles to agglomerate in patches on the surface; this is undesirable since, upon heating, the small nanoparticles will coalesce into larger particles and produce nanowires with large diameters. An alternative method of applying the ethanol nanoparticle solution would be to spin-coat the solution onto the substrate.

3.2.2 Methods for VLS Synthesis of Nanowires

The VLS synthesis requires only the presence of a metallic catalyst and nanowire material in the vapor. Consequently, a broad spectrum of VLS-based techniques has been developed for synthesizing nanowires. Here, only the three primary techniques will be described, namely, flow reaction, laser ablation and CVD, which includes plasma-enhanced chemical vapor deposition (PECVD). However, the primary focus will be on CVD-based techniques utilized in the authors' laboratory.

3.2.2.1 Flow Reaction Formation of Nanowires

The most common flow reactor consists of a quartz flow tube inside a furnace; a schematic representation of a flow tube is shown in Figure 3.2. The reactor is split into temperature zones, thereby establishing a temperature gradient across the flow tube. A carrier gas is introduced at the high-temperature end, while pumping occurs at the low-temperature end. The source materials are placed in a crucible upstream (zone A) from the nanowire collection (zone B), which is maintained at a lower temperature than zone A. The temperature and pressure in zone A must be balanced such that sublimation or vaporization of the source materials is facilitated. The geometry and temperature differential of the flow reactor lead to the condensation of source materials on the substrate. The temperature in zone B

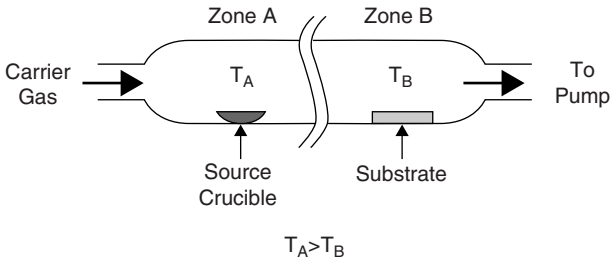

Figure 3.2 A schematic diagram of a flow reactor design used to synthesize nanowires.

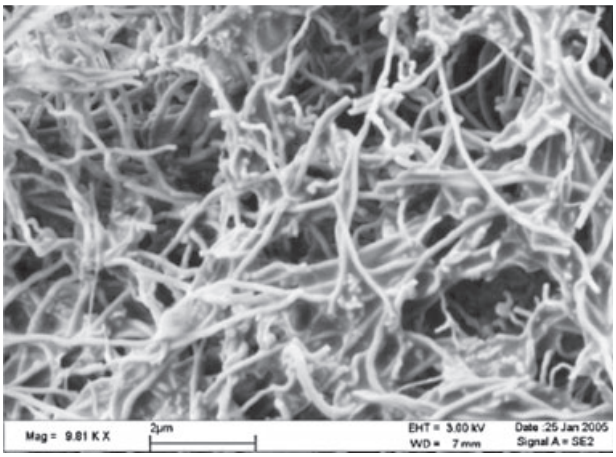

Figure 3.3 Field emission scanning electron microscopy (FESEM) image of fibronectin-coated silica nanowires.

must exceed the melting point of the catalyst, yet be below its sublimation or vaporization temperature.

The catalyst can be introduced either by seeding the substrate prior to insertion into the reactor, or by simultaneously introducing it into the vapor with the source materials for the nanowires. In the latter case, the catalyst is either placed in zone A with the source material, mixed in with the source material, or placed in an intermediate zone. The operating temperatures and gas flow rates are dependent on the geometry of the reactor, the type of nanowires to be synthesized, and the types of source material and catalyst used in the process.

The advantages of these reactors are that they are relatively inexpensive to build, and they are versatile, simple to operate and easy to maintain. In addition, the use of solid, sublimeable precursors in the form of powders simplifies the identification of optimal operating conditions for the synthesis of nanowires. One shortcoming of these systems is that oxygen contamination can be problematic. although if judicious efforts are made to eliminate any oxygen then extremely pure nanowires can be realized.

The heating of a silicon powder using Au as catalyst to 1050 °C for 2 h in argon in this flow reactor, and flowing oxygen during the cool down to 850 °C, can result in the formation of silica nanowires. A field emission scanning electron microscopy (FESEM) image of fibronectin-coated silica nanowire is shown in Figure 3.3.

3.2.3
Laser Ablation of Nanowires

In some ways, the laser ablation of nanowires is very similar to flow reaction synthesis, and fairly straightforward to conduct. First, a target is constructed from

powders of the materials forming the desired nanowire, as well as a metallic catalyst, also in powder form. The powders are combined in the appropriate ratios, mixed, and pressed into a solid target. In the case of Si nanowires, a Si substrate with a metallic catalyst applied to the surface suffices. The target is then placed in a vacuum vessel which is back-filled with an inert gas. The role of the background gas is to facilitate thermalization and condensation of the catalyst, where subsequent nucleation and nanowire formation is due to absorption of materials from the surrounding vapor. Either Nd:YAG lasers [14, 15] or excimer lasers [16–21] are typically used in these ablation processes. Although these two types of laser have the necessary power for ablation, they operate at significantly different wavelengths. The primary factors for the successful laser ablation of nanowires are the choice of catalyst, the correct ratio of nanowire material and catalyst in the target, and background gas pressure.

A hybrid approach to nanowire synthesis developed by Wu *et al.* [22] combines laser ablation with a flow reactor process, and has yielded superlattice nanowires of Si/SiGe. The role of the flow furnace is to produce Si nanowires, while the laser ablation process introduces Ge periodically into the vapor. The Ge is absorbed by the catalyst and incorporated into the forming nanowire. Through judicious control of the process, Wu's group has achieved superlattice periodicities of Si/SiGe of approximately 250 nm. Moreover, the results of this study bode well for superlattice nanowire devices.

3.2.4
Chemical Vapor Deposition and Plasma-Enhanced Chemical Vapor Deposition of Nanowires

The primary distinction between CVD processes for VLS synthesis of nanowires and the preceding processes is that the precursor materials are either gases or vapors. The term CVD is very generic, and therefore encompasses many variants of the same theme. Consequently, a flow reactor could either be used as intended or modified to operate as a CVD reactor. Along these lines, a CVD system could be combined with laser ablation, similar to the system used by Wu *et al.* [22] to grow superlattice nanowires. The construction of a CVD system is fairly simple and straightforward; in fact, the basic reactor is very similar to a flow reactor. What sets CVD apart from a flow reactor is gas handling; in CVD the only requirement of the precursor is that it be a vapor upon introduction into the reactor, and consequently gases, liquids and sublimeable solids are all candidates as CVD precursors. Gaseous precursors are in general the simplest of the three for use in CVD as their introduction into the reactor can be readily metered using mass flow control valve technology.

The use of liquid precursors is more involved than gases, but still easily manageable. Typically, an inert (carrier) gas such as Ar or N_2 is bubbled through a vessel containing the liquid precursor (the vessel is often referred to as a 'bubbler'). Through judicious control of the liquid temperature and carrier gas flow rate, the concentration of the precursor in the gas–vapor mixture can be metered with a

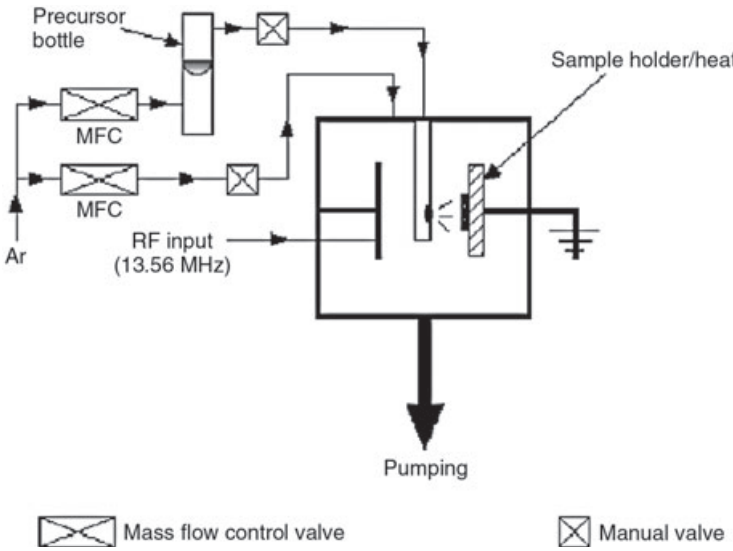

Figure 3.4 A schematic diagram of a parallel plate design of a plasma-enhanced chemical vapor deposition (PECVD) system used to synthesize nanowires.

high degree of precision. It should be noted that, in some cases, a bubbler is not required if very dilute concentrations of the precursor are required. The only disadvantage of using a liquid precursor over gases is the added complexity of the vapor-handling system.

The vapor delivery system for sublimeable solid precursors is similar to liquid precursor delivery systems, specifically in its use of a carrier gas. Heating the solid precursor increases the sublimation rate. Sublimeable solid precursors are the most difficult to handle for the following reasons. The sublimation rate of a solid is a function of temperature, the quantity of the solid precursor in the vessel and the carrier gas flow rate. Consequently, the delivery rate of precursor to the chamber can vary during the course of consecutive experiments unless the quantity and form of the starting material is the same at the start of each experiment. However, if care is taken this is typically not a problem.

The most common difficulty encountered with the use of sublimeable precursors is condensation onto the walls of the delivery lines and valves. Condensation occurs most often in the valve housings, but the effect can be minimized by heating the gas lines and valves to a temperature above that of the precursor vessel.

A schematic of the PECVD system in the authors' laboratory is shown in Figure 3.4. The system can be operated in either the CVD mode (plasma off) or the PECVD mode. The plasma is struck between two 8 cm-diameter circular parallel plates (capacitor design) spaced approximately 2–3 cm apart. The sample is mounted on the grounded anode, which is also the sample heater. The sample

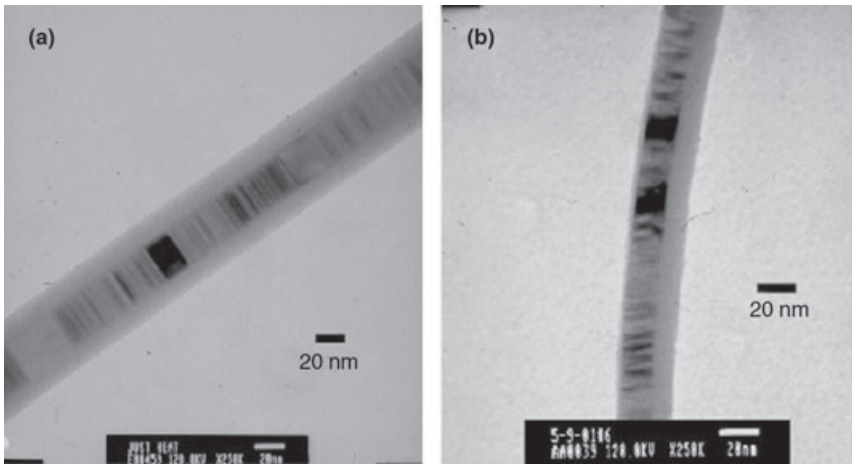

Figure 3.5 (a) Transmission electron microscopy (TEM) image of a biphase coaxial silicon nanowire consisting of a crystalline core and an amorphous sheath; (b) A biphase silicon carbide nanowire, where the amorphous material has grown predominantly on one side of the nanowire. Silica nanowires can result from the oxidation of silicon/silica nanowires.

heater is a boroelectric heater (manufactured by GE Advanced Ceramics), and the plasma frequency is the industry standard of 13.56 MHz. The solid precursor *closo*-1,2-dicarbadodecaborane ($C_2B_{10}H_{12}$) (which from here on will be referred to as *orthocarborane*) is used in the synthesis of boron carbide and silicon carbide nanowires and nanosprings. The system can be broken down into three subsystems: gas handling, reactor, and pumping system. The gas-handling system consists of stainless steel tubing and metal gasket sealed fittings, with the gas flow rates being controlled using mass flow control valves. The reactor consists of a six-way stainless steel cross with metal seal flanges. The system is pumped with a $300 l s^{-1}$ diffusion pump, backed by a mechanical pump, such that the achievable base pressure of the reactor is 5×10^{-5} Torr. A static pressure in the reactor is achieved by balancing the gas-vapor flow rates and the pumping speed, where regulation of the pumping speed is achieved by throttling the valve between the reactor and the diffusion pump. Transmission electron microscopy (TEM) images of silicon nanowires and silicon carbide nanowires are shown in Figure 3.5, and of silicon carbide nanosprings in Figure 3.6.

3.3
Functionalization of Silica 1-D Silica Nanomaterials

Two conceptually different strategies are utilized to attach biomolecules such as proteins, nucleic acids, carbohydrates and lipids to silica surfaces – that is, nonspe-

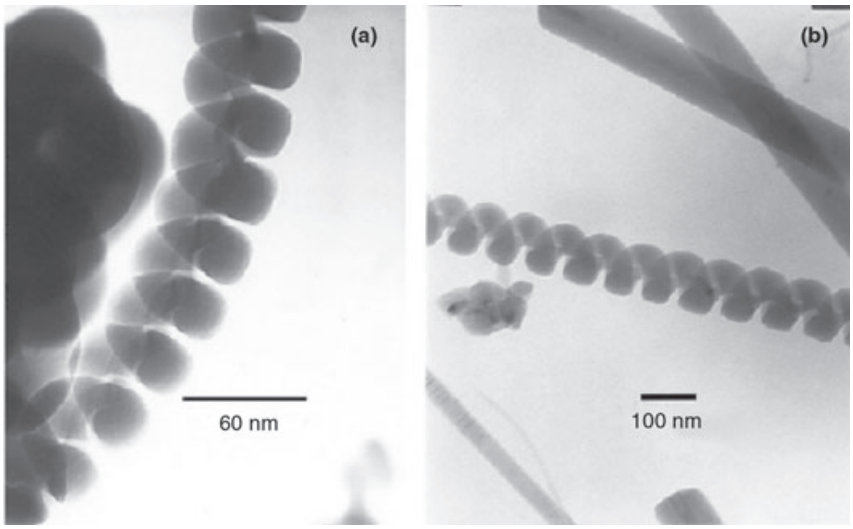

Figure 3.6 Transmission electron microscopy (TEM) images of silicon carbide nanosprings formed from nanowires with circular cross-sections, where the nanospring diameter-to-pitch ratios are (a) 1.8 and (b) 1.23.

cific physiosorption or chemically targeted covalent attachment. Nonspecific physiosorption takes advantage of the chemical properties of the surface, biomolecule and adsorption solution to provide an environment that is conducive to irreversible (or close to irreversible) interactions between the biomolecule and surface. Due to concern over the long-term stability and biological activity of such surfaces, most current techniques tend away from nonspecific adsorption processes. However, the ease and satisfactory attachment that results allows continued use of this technique.

A chemically targeted covalent attachment allows more stable and defined interactions between biomolecules and nanosurfaces. The silanization of oxide surfaces is a common method to provide a handle to a silica surface for further functionalization, for example allowing biological recognition layers to be built [23]. Alternatively, amine, sulfhydryl or epoxide groups have been added to silica surfaces, allowing direct attachment of the biomolecule to the active surface, via chemically reactive linkers such as *N*-hydroxysuccinimide esters (NHS) or succinimidyl 4-(*N*-maleimidomethyl)cyclohexane-1-carboxylate. By using these approaches, the surface chemistry can be tuned to provide a variety of surface environments such as hydrophilicity, biomolecular surface density and electronic/chemical properties, all of which can be important to the specific biological application of the material. The same chemical approaches that have been applied to bulk silica surfaces can also be used for the functionalization of 1-D silica nanomaterials.

The metallization of 1-D silica nanostructures with noble metals provides an alternative method for the attachment of biomolecules. The robust interaction

between sulfhydryl groups and noble metals forms the basis of the formation of self-assembled monolayers (SAMs), which provide a flexible architecture for the design of novel interfaces [24]. This nanoscale tuning of gold surfaces using SAMs is an important component in many recent areas of biosensor development [24, 25]. Two SAM-based architectures can be used to construct the biological recognition interface on gold-coated silicon nanomaterials. The first approach utilizes well-ordered monolayers using bifunctionalized alkane thiols – that is, units where a reactive amine/epoxide/carboxyl is separated by a linker and terminated with a sulfhydryl group. The sulfhydryl is used to directly link the SAM to the metal surface. The biomolecule can subsequently be attached to the nanoconstruct in a similar manner, as described above, such that the biomolecule is attached to the silicon via a SAM on a gold interface.

The second approach for constructing the biological recognition layers on gold-coated silicon nanomaterials utilizes DNA probes modified with alkylthiols, which allows the direct functionalization of gold surfaces [26]. Mercaptohexanol is typically used to passivate the surface and direct the probes in a more constructive orientation for hybridization [27].

Recently, investigations have been started into DNA attachment and hybridization on metallized 1-D silica nanostructures. For this, a process has been developed where nanosprings in a mat can be coated with a sparse or dense layer of Au nanoparticles, to provide 25 to 100% coverage [28]. The process produces uniform nanoparticle size distributions, and has been successfully applied to the metallization of nanowires with Au, Ni and Pt; it can also be used with other metals by identifying a suitable organometallic precursor. The degree of coverage depends on the deposition time, while the particle size and size distribution depend on the chamber pressure and substrate temperature. Supporting the Au nanoparticles on the nanospring scaffold provides an architecture with a high surface area due to the nanoparticle and nanospring mat, along with 3-D, geometric spacing of the nanoparticles; this allows unique interactions between the nanomaterial and solution phases.

In order to allow attachment to the surface, the DNA probes are synthesized with a terminal thiol group. The covalent bond between the sulfur atom of the thiol moiety and the gold is used to link the derivatized molecule to the nanoparticle. In addition to DNA probes, the head group can be designed to provide virtually any desired surface chemistry, either alone or in combination with the DNA. As the nanosprings are physically attached to the substrate, the device can be placed directly into solution, without removing the nanosprings.

For biological activity, the surface must not only be modifiable but also maintain function. In this model system, hybridization is the biological function, and some preliminary studies have been conducted with metallized nanosprings to demonstrate selectivity. Hybridization with biotin-labeled DNA molecules and subsequent enzyme-linked signal enhancement, was used to determine a specific hybridization event. The results of these studies are presented in Figure 3.7. Here, two regions were first pretreated with thiolated oligonucleotide probe sequences. Square sections were then treated with a probe sequence complementary to a

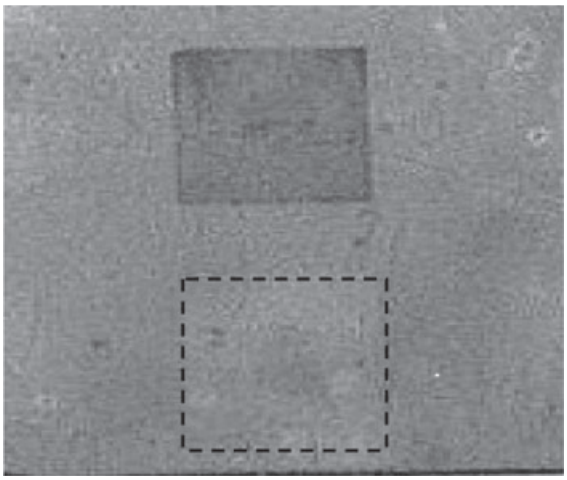

Figure 3.7 An image of sequence-specific hybridization on a gold nanoparticle-decorated nanospring surface. The upper square section was treated with the *E. coli* *hly*A probe sequence, and the lower square (dashed borders) was modified with *Salmonella inv*A probe sequence. Hybridization with a biotin-labeled *hly*A target (10 n*M*) and subsequent enzyme-linked enhancement produced a dark precipitate only in the region of the *E. coli* probe.

genomic sequence (*hly*A) from pathogenic *Escherichia coli* O157:H7 (the upper square in Figure 3.7) or with a probe sequence (*inv*A) for *Salmonella* species (lower, dashed square). A biotin-labeled *hly*A target sequence, complementary to the *E. coli*-specific probe, was introduced to the surface. Following hybridization, enzyme-labeled streptavidin reacted with the biotin sequence, and the surface was developed with a precipitating enzyme substrate. The selective reaction between the *E. coli* probe and the biotin target sequence localized the enzyme to the upper square (causing darkening), while the lower square showed no visually detectable difference from the untreated surface. Further testing confirmed that a biotin-labeled *inv*A sequence could be selectively hybridized to the *Salmonella* probe with no detectable hybridization to the *E. coli* probe. These experiments support the feasibility of introducing DNA sequence-specific selectivity to the Au nanoparticle-decorated nanosprings.

A more quantitative analysis of the available DNA surface probe density is also being investigated. This approach can be used to quantify fluorescently labeled DNA molecules that are specifically bound to the nanosurface [29]. Quantification of the results using a standard curve allows an estimation of active surface area (no. of hybridized molecules/apparent substrate area) and hybridization efficiency (no. of probes hybridized/no. of probes on surface). The preliminary results show that metallized nanospring surfaces can achieve an active surface area of greater than $30\,\mathrm{pmol\,cm^{-2}}$.

3.4 Toxicology Studies on 1-D Silica Nanomaterials

In this section, we provide an overview of the physical characteristics of nanomaterials that enable them to interact with animal cells and cellular compartments. Because they are chemically stable and relatively inert, 1-D nanostructures (1-D NS) have relatively low cell cytotoxicity (as outlined above), while their chemical modification also provides a means for linkage with specific biomolecules. Thus, 1-D NS may interact directly with cellular substructures. In addition, a typical cellular targeted delivery strategy is also discussed that can support the cellular uptake of these nanostructures. Notably, 1-D NS with dimensions of 2 to 100 nm are particularly suited to the adoption of intrinsic cellular transport mechanisms, and can be used for the targeted delivery of specific biomolecules to specific cells and tissues. Moreover, 1-D NS may also provide nanoplatform constructs for the delivery of specific biomolecules through interactions in well-characterized intracellular trafficking pathways.

3.4.1 Intracellular Targeted Delivery

The mechanisms that traffic materials around the cell have enormous potential to be used for the efficient delivery of biomolecules or other therapeutics. However, in order to design delivery strategies that employ these intrinsic cellular transport mechanisms within cells, it is first necessary to understand their functional regulation and mechanism of action. Only then can rigorous approaches be designed for the targeted intracellular delivery of biomolecules and other therapeutics. At least two (partly understood) endocytosis systems exist that can be used in this role, namely clathrin-mediated and caveolin-mediated mechanisms (Figure 3.8). [30, 31] Clathrin-coated pits are typically 200 nm, and caveolin pits approximately 80 nm, in diameter. As any strategy that utilizes 1-D NS as delivery platforms must account for these cellular mechanisms, nanostructures (including the linked biomolecules) should be designed with a maximum diameter of less than 200 nm. It must also be realized that other cellular transport mechanisms might exist that utilize structures which are both larger and smaller than the two mentioned here. Nonetheless, these two mechanisms represent examples of the better-understood systems, and may serve as a reference point when considering the design of 1-D NS to interact with cellular pathways and mechanisms.

3.4.2 A Typical Cellular Targeting Strategy Using 1-D NS-Based Nanostructures

A range of synthetic peptides has been proposed for the delivery of nanostructures bearing cargo molecules through the plasma membrane barrier. These are derived from sequences expressed on viruses, such as HIV transactivator of transcription (TAT) [32–36], for which internalization via a glycosaminoglycan (GAG)-mediated

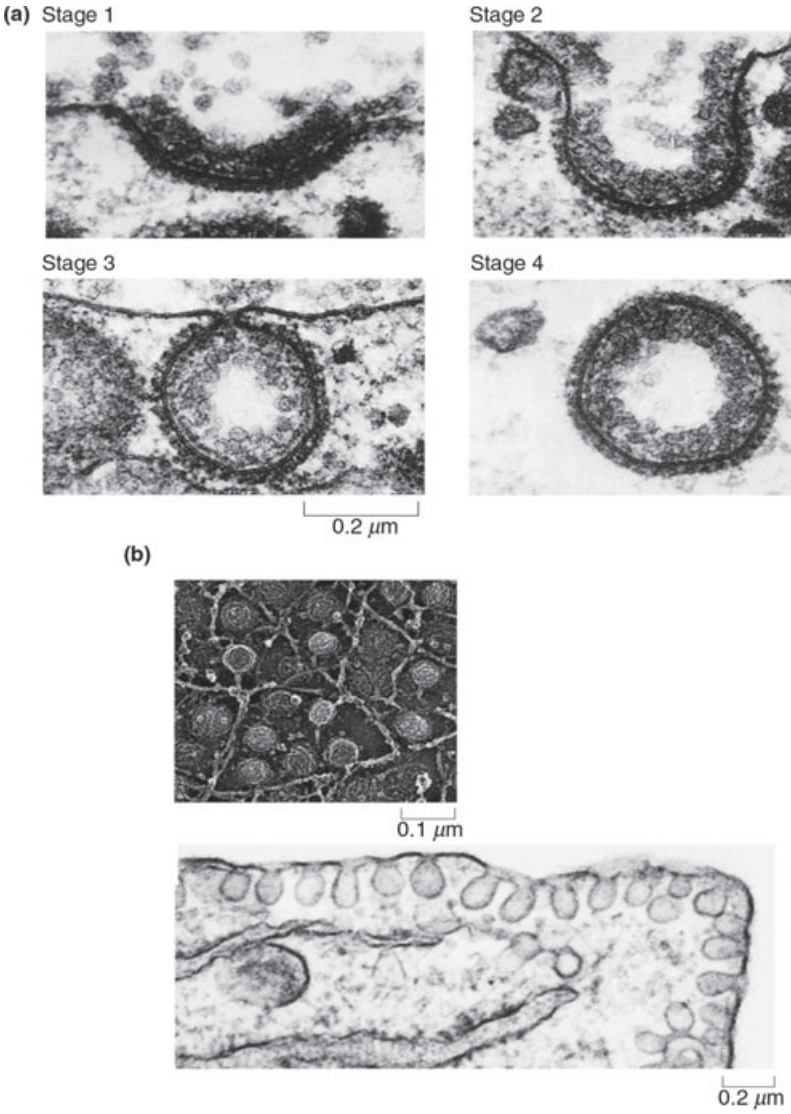

Figure 3.8 (a) Clathrin-mediated endocytosis in which typical vesicles are approximately 200 nm diameter. Reproduced with permission from Ref. [32]; (b) Caveolin-mediated endocytosis in which typical vesicles are approximately 80 nm diameter. Both mechanisms have potential for the uptake of nanostructures. Reproduced with permission from Ref. [33].

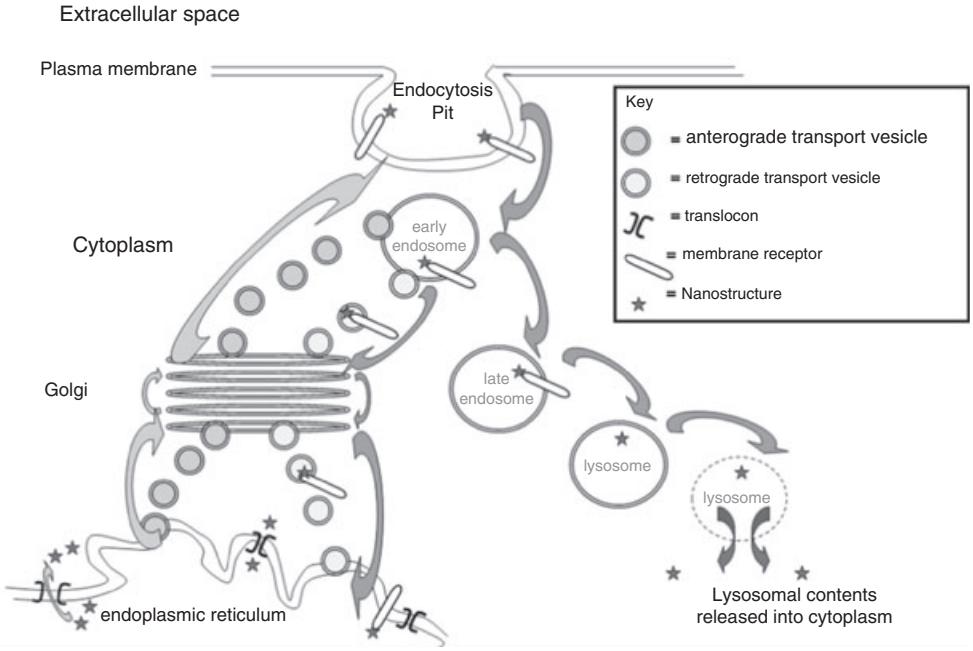

Figure 3.9 Possible pathways for the import and release of nanostructures into the cytoplasm. These include possible receptor-mediated internalization and vesicular transport via either a retrograde transport pathways that leads to the endoplasmic reticulum and cytoplasm through Sec61 translocons, or via the lysosomal pathway. Neither of these mechanisms is well understood. Other, undescribed, pathways may also be involved.

mechanism has been proposed. At least one such mechanism for intracellular uptake via association of GAGs with caveoli has also been described [37].

Despite an incomplete knowledge of the mechanism for the cellular internalization of cationic cell-penetrating peptides (CPPs), they appear to be efficiently internalized, but may be disbursed to different cellular compartments. Antennapedia peptide appeared to colocalize with lysosomes, while TAT remained close to the cell periphery [32]. The potential intracellular pathways that may lead to the transport of specific molecules to the cytoplasm are shown in Figure 3.9.

Thus, an understanding is available of at least some of the mechanisms via which 1-D NS nanostructures can interact directly with cells. In the following text we will discuss the range of biomolecules that can be chemically linked to these structures.

As discussed above, one reason why nanomaterials have generated so much excitement among the research and medical communities is that their small size often provides them with novel chemical and physical properties that are not found in bulk materials composed of the same substances. This may be due to a variety of factors, including the small size of nanomaterials, their composition, their surface chemistry and their ability to aggregate. The use of nanomaterials in the

biological sciences is based on the concept that these novel physico-chemical properties can be exploited for biological applications and, indeed, recent advances in nanotechnology have revolutionized and integrated science disciplines such as biology, chemistry, physics, chemical and mechanical engineering, materials science and clinical medicine. Today, substantial progress has been made in the application of nanotechnology in healthcare and medicine, such that a new term has now evolved, *nanomedicine*. It is clear that this new discipline will provide many exciting developments in the fields of nanomaterials design, and the use of nanomaterials for diagnostics, biosensors and bioactive drug delivery [38–40].

Unfortunately, along with the novel properties exhibited by nanomaterials, come novel interactions with biological systems and the environment that can result in unexpected health and safety issues compared to bulk materials [41–44]. A growing awareness of this issue prompted the U.S. National Science and Technology Council to recommend, among other things, increased funding for research aimed at understanding the interaction between nanomaterials and biological systems, from the molecular level to the level of the whole organism [45]. Similarly, the Royal Society and the Royal Academy of Engineering in the United Kingdom recently recommended that research centers be established where one priority was the development of better methods to study and evaluate the toxicological impact of nanomaterials on human health [46].

3.4.2.1 *In Vitro* Toxicity of 1-D Nanostructures

Currently, very few reports have been made addressing the issue of toxicity as it pertains to 1-D silica nanomaterials. In general, minimal toxicity has been reported for cells in tissue culture exposed to relatively low doses of SiO_2 nanowires. For example, by using a neutral red assay to measure cell viability, Kwon *et al.* showed that the exposure of either human HEp-2 or bovine MAC-T cells to SiO_2 nanowires at a concentration of $40\,\mu g\,ml^{-1}$ for 72 h had no negative effect on cellular survival [47]. These results were in good agreement with those of Qi *et al.* who reported only a modest effect on the viability of a variety of established mouse and human cell lines when exposed to $50\,\mu g\ ml^{-1}$ SiO_2 nanowires for 48 h [48]. However, at the highest concentrations tested ($100\,\mu g\,ml^{-1}$), an approximately 30% reduction in cell viability was observed for all cell lines tested [48]. Another group found that the exposure of HeLa and HEp-2 cells to $190\,\mu g\,ml^{-1}$ SiO_2 nanowires also caused a modest increase in the proportion of dead cells by 48 h, and that this increased to approximately 20% by 72 h [49]. Interestingly, at higher concentrations, the toxicity was increased dramatically. For example, when HeLa or HEp-2 cells were exposed to $1.9\,mg\,ml^{-1}$ SiO_2 nanowires for 72 h, almost 75% of the cell population was killed [49]. When these results were examined together, it appeared that in most tissue culture cell lines examined the SiO_2 nanowires at concentrations of ~100–200 $\mu g\,ml^{-1}$ caused modest (but detectable) toxicity in 10–30% of the cells within 48 h, whereas lower concentrations had a negligible effect on cell viability. Notably, although a 72 h exposure at higher concentrations resulted in extensive cytotoxicity, shorter exposure times (24 h) were tolerated reasonably well, with only 5–15% of the exposed cells showing signs of lysis [49]. Thus, it is possible that

applications requiring exposure to higher levels of SiO_2 nanowires may be feasible, provided that the exposure times are limited.

The mechanisms responsible for this observed toxicity of SiO_2 nanowires at concentrations exceeding ~100 μg ml^{-1} have not yet been determined. In cells treated with high concentrations of SiO_2 nanowires, caspase activity was not elevated and an analysis of low-molecular-weight DNA did not reveal the laddering so characteristic of apoptosis [49]. In fact, the results suggested that such cell death was not due to apoptosis but rather involved necrotic mechanisms. An analysis of HepG2 cells showed that their exposure to 100 μg ml^{-1} SiO_2 nanowires interfered with the attachment and spreading of the cells on tissue culture plates [48]. Subsequently, using energy-dispersive X-ray spectroscopy, it could be shown that the 'rounded-up' HepG2 cells in cultures treated with SiO_2 nanowires had higher surrounding silicon levels than did any neighboring cells that were more spread out [48]. Hence, any impaired cell attachment could be directly attributed to an interaction with the SiO_2 nanowires. An analysis of several cellular messenger RNAs (mRNA)s) in HepG2 cells exposed to SiO_2 nanowires revealed a downregulation of transcripts encoding for focal adhesion kinase (FAK) and type I collagen [48]. FAK is a nonreceptor protein tyrsosine kinase that regulates cell motility and proliferation [50], while type I collagen is a component of the extracellular matrix (ECM) that may also influence cell motility and proliferation by interacting with cell-surface integrin receptors [51]. Although these results were intriguing, it is still not clear whether the downregulation of either FAK or type I collagen is a cause or a consequence of the impaired attachment exhibited by HepG2 cells in the presence of SiO_2 nanowires. It follows that other important experiments must be conducted: (i) to determine whether the downregulation of FAK and type I collagen mRNA results in a decrease in protein levels; and (ii) to identify the extent of downregulation of these factors in cells exposed to high levels of SiO_2 nanowires.

One surprising finding from the study conducted by Adili *et al.* was that SiO_2 nanowires and nanoparticles exhibited differential cytotoxicity towards cells in culture [49]. While neither nanowires nor nanoparticles exhibited significant cytotoxicity on HeLa or HEp-2 cells at concentrations below 100 μg ml^{-1}, this was not the case at higher concentrations. As described above, when cells were exposed to 1.9 mg ml^{-1} nanowires, approximately 75% died within 72 h, whereas the exposure of cells to similar concentrations of nanoparticles resulted in only 10–15% cell death. Thus, SiO_2 nanoparticles and nanowires, despite having the same chemical composition, interact with cells in very different ways. Although the exact nature of these differences is unknown, they can likely be attributed to the different shapes, structures or surface chemistry of nanowires compared to nanoparticles. These results highlight the problems associated with extrapolating toxicity data from bulk materials to nanomaterials, or from one nanomaterial to another, even when their chemical composition is identical. In addition, the findings of Adili *et al.* illustrated a need for the careful evaluation of physico-chemical and biological properties of new nanomaterials as they are developed.

Within the context of developing silica nanoparticles as platforms for drug or biomolecule delivery, it will be important to ascertain the required dose of the

material required to deliver (or carry) the active agent to its site of action. For many biomedical applications, this may require that the material is ultimately delivered to an intracellular compartment. Whilst it is difficult to speculate about what might constitute an effective dose of these (presently hypothetical) delivery platforms, preliminary cell culture studies have provided some hint of the magnitude of the quantity of material required. One of the present authors (RAH) has observed that, both silica and gold nanoparticles, can be effectively used to deliver biomolecules using nanoparticle doses below $5\,ng\,ml^{-1}$ (unpublished results). Others have also reported an enhanced delivery of gene therapeutics using silica nanoparticles [52, 53], although in each of these studies, other transfection strategies were used in concert with the nanostructures, including commercial liposome-forming agents or dendrimers. If only low concentrations (in the picomolar range) are required for the effective delivery of bioactive materials, the present literature – albeit based on *in vitro* studies – indicates that toxic effects on cells will be minimal [47–49]. However, the confirmation of these proposals will require appropriately designed toxicolcogical studies initially in animal models, and eventually in clinical trials.

3.4.2.2 *In Vivo* Toxicity of 1-D Nanostructures

As noted above, all of the toxicological studies conducted to date have focused on the effect of SiO_2 nanowires on cells in various tissue culture systems, and have not explored the consequences of exposure in intact animal models. An extensive search of the available literature revealed that no reports have been made regarding the *in vivo* toxicity of 1-D silica nanomaterials. Here, we will instead briefly summarize the literature on the *in vivo* toxicity of related materials, making predictions based not only on these studies but also on those focusing on particles and 1-D silica nanomaterials in cell culture.

In order to understand the potential impacts of silica nanowires on the body, it is useful briefly to describe how the human body deals with foreign bodies and particulates. These are functions of the immune system, and drugs or particulates that enter the circulation are scavenged and cleared by Kupffer cells and macrophages of the reticuloendothelial system (RES) [54–56]. The RES forms part of the immune system that consists of phagocytic cells located in reticular connective tissue, primarily the monocytes, macrophages and tissue histiocytes. These cells accumulate in the lymph nodes and spleen, whereas the Kupffer cells reside in the liver. Nanoparticles will usually be taken up by the liver, spleen and other parts of the RES, depending on their surface characteristics. Particles with more hydrophobic surfaces will preferentially be taken up by the liver, followed by the spleen and lungs. Hydrophilic nanoparticles (35 nm diameter) appear to be less easily detected and will be scavenged by the spleen and liver and circulate for longer in the bloodstream [56, 57].

Potential exposure routes for silica nanowires include the skin and mucosal membranes, as well as intentional internal exposure for proposed biomedical purposes. The inhalational toxicity of silica and silica-based materials is well known and has been extensively reviewed [58–60]. Crystalline silica, a multidimen-

sional, microscale form of silica, is associated with numerous lung pathologies (including the namesake, silicosis), autoimmune disorders and cancers. Mechanisms for this toxicity remain under investigation, but may include the creation of free radicals, the mechanical disruption of lysosomes, or the modification of lung surfactants [59]. Of additional relevance here is the fate of inhaled crystalline silica, a material which rarely travels outside the pulmonary system and is not metabolized [61]. However, amorphous silica – a particulate, nanoscale form of silica that is also a potential respiratory hazard – causes only transient and moderate lung inflammation and tissue damage in mice [62]. This may be because amorphous silica particles are capable of dispersing beyond the lungs, and therefore do not accumulate in a manner that causes damage to the pulmonary tissues. Nanosized silica particles are, nonetheless, toxic in the mouse model [63], and because they are more widely dispersed can potentially cause damage to multiple organ systems, in addition to the initial exposure route [64, 65]. The target organs involved in toxicological studies should include those also considered as targets for toxic compounds in other (non-nano) forms, such as the vascular endothelium, blood, spleen, liver, nervous system, heart and kidney [44, 66].

While inhalational toxicity may be the most likely threat posed by the use of silica nanowires, the potential consequences of internal exposure may be more relevant, depending upon the proposed biomedical application. In this regard, not only is the route of administration/exposure important but so too is the potential dose and the physico-chemical properties that determine the nanomaterial's mobility, solubility and bioactivity in biological systems. Although it is impossible to predict accurately the exact toxicological profile of SiO_2 nanowires, information derived from inhalational toxicity studies of other microscale and nanoscale silica materials allow speculation regarding potential deleterious effects of silica nanowires *in vivo*. One prediction is that the small size of silica nanowires will permit dispersion and render them less toxic than the larger crystalline silica particles. An alternative prediction is that the high surface area and/or other properties conferred by the high aspect ratio of silica nanowires will result in a high toxicity. The latter, rather simplistic, prediction is supported by the *in vitro* toxicity studies described above, which demonstrate a greater toxicity for silica nanowires than for silica nanoparticles [49]. The present authors' ongoing studies using the zebrafish embryo as a model organism for the study of nanomaterial toxicity and teratology also provide support for this prediction. In these studies, silica nanowires caused extensive embryonic death and deformity, whereas silica nanoparticles (at the same dose) were nontoxic. The use of other animal models will be necessary to determine if silica nanowires affect the development of other organisms, at doses relevant to any proposed biological applications.

Ultimately, the development of silica nanowires or any other nanomaterial for use in biological systems will require a clear demonstration that they do not pose any risks to patients, practitioners, employees at manufacturing facilities, or the general public. As particular applications are developed, a greater and more accurate knowledge of the nanomaterial formulation, including surface modifications, possible dosage and potential administration routes, will become available. This information will need to be used in the design of toxicity studies that can be used

effectively to evaluate the potential harmful effects, if any, of these materials. Such studies should include an analysis of cell lines in tissue culture that are representative of those likely to be encountered by the nanomaterial when delivered *in vivo*. Similarly, animal studies – and, eventually, also clinical trials – should be designed that will provide an assessment of the toxicity associated with relevant tissues and organs. Careful attention to detail in the design, implementation and analysis of these toxicity studies is necessary to ensure that the full potential of using nanomaterials in biological applications is reached as quickly as possible.

3.5 Biological Applications of 1-D Silica Nanomaterials

Nanotechnology for biological applications is initiating a 'Second Industrial Revolution' in the twenty-first century. There are two advantages of 1-D silica nanostructures in situations where interactions with biomolecules (e.g. proteins, DNA), living cells or whole organisms (either prokaryote or eukaryote) are contemplated. The first advantage is the surface geometry of the materials, as a large surface-to-volume ratio provides an increased interaction space. In addition, the dimensions of 1-D silica nanostructures approach those of biological molecules. The second advantage of 1-D silica nanostructures is the ability to tune one or more of the surface characteristics. The surface can easily be modified or functionalized by covalent or adhesive chemical moieties to make it biocompatible. The relatively abundant hydroxyl groups on the surface are readily reacted through various schemes to form amino, carboxyl or thiol units [67], for the conjugation of molecules recognized by biological systems. Silica surfaces will also directly adsorb either proteins [68, 69] or DNA [70]. In the *in vitro* case studied to date, silica nanowires showed no cytotoxic effects below the reported concentration thresholds [49]. The uptake of fibronectin-coated silica nanowires by bacteria showed that these cells can incorporate 1-D silica nanostructures [47]. However, some toxicity has been noted *in vivo*, once silica nanowires have been internalized into eukaryotic organisms (see Sections 3.4.2.1 and 3.4.2.2). Because of the limited number of studies conducted to date, however, broad generalizations regarding the biocompatibility of 1-D silica nanostructures in cells or whole organisms hold little merit at the present time.

3.5.1 Biodetection

The most common application of 1-D silica nanostructures to date has been in electrical sensors to detect small quantities of biomolecules in solution [71–78]. The 1-D nature of these materials provides an enhanced sensitivity to surface charge variations in comparison with bulk 2-D surfaces. The first reported biodetection utilized the well-characterized interaction between biotin and streptavidin [79]. Here, the streptavidin target was detected in solution by covalently immobilizing biotin on the surface of the silicon nanostructure. A single nanowire was then

fabricated to span the gap between two contact electrodes, which allowed the conductivity of the wire to be measured. Binding of streptavidin to the surface-bound biotin resulted in a change in conductance of the wire specific to the biological interaction [79]. Alternate sensor fabrication processes for 1-D silica nanostructures have also been used to detect the biotin–streptavidin interaction [68]. Single protein detection has been extended to the multiplex detection of proteins by fabricating arrays of single nanowire circuits, each specific for a different protein [80]. Other investigators have proposed that a single silica nanofiber might be used as an optical waveguide sensor element, being highly surface-sensitive with respect to changes in the intensity and phase of the evanescent field surrounding the nanowire [81]. As in most other scenarios, the nanowire could be modified to promote specific chemical or biological binding for a target species, and each event would result in a change in the local refractive index that would influence the optical behavior of the device in a measurement fashion.

In addition to protein targets, a number of groups have reported the detection of *nucleic acids* on 1-D silica nanostructures [68, 82–84]. Here, single silica nanowires were used to measure the sequence-specific hybridization of DNA to DNA receptors that were covalently attached to the nanowires [68, 82–84]. DNA was detected by changes in the conductance of the device, and detection limits down to femtomolar DNA concentrations were reported [82].

An alternative to single nanowire biosensor designs is the construction of a mesh, mat or network surface between the contact electrodes. One distinct advantage of extended nanostructures over single nanowire devices is the inherent redundancy in the active material; a single, irreversible material modification or nanowire failure will not render the device useless. These surfaces are fabricated to produce a random network geometry as an extended surface comprised of multiple 1-D silica nanostructures within a single device circuit. This approach has previously been applied to DNA biosensor construction using carbon nanotubes [85]. Recently, 1-D silica nanostructures (silica nanosprings) were integrated into the microfabrication of a DNA sensor. By using this device, which consisted of multiple silica nanosprings (i.e. a nanospring mat) between two contact electrodes [70], it could be shown that DNA would attach to the nanospring surface, after which conductance differences in the mat were measured based on specific DNA hybridization. Metal nanoparticle-coated silica nanowires have also been employed in surface-enhanced Raman detection of the cancer biomarker protein, interleukin-10 [86], again demonstrating the versatility in detection methods (optical versus electrical) for 1-D silica nanostructures networks. The use of 1-D silica nanostructures in sensors to detect small, whole organisms has also been accomplished. For this, a single silica nanowire detection of viruses was based on the cell binding to virus-specific antibodies that were covalently attached to the nanowires [87]. Conductance changes in the circuit caused by a single virus particle binding to the nanowire were then detected, underlining the exceptional sensitivity of this application.

To date, the applications of 1-D silica nanostructures to biological systems have been limited to sensor developments for the detection of biomolecules (e.g. DNA,

proteins) or, in one case, a small, whole organism (e.g. virus). This modest progress in 1-D silica nanostructures applications indicates an enormous potential for device development that could provide the specific, rapid and sensitive detection required for a multitude of applications in the fields of biomedicine, food-safety, environmental monitoring and/or bioterrorism.

References

1 Choi, D., Balandin, A., Leung, M., Stupian, G., Presser, N., Chung, S., Heath, J., Khitun, A. and Wang, K. (2006) Transport study of single bismuth nanowire fabricated by the silver and silicon nanowire shadowmasks. *Applied Physics Letters*, **89**, 141503–5.

2 Cho, J., Min, J., Ko, S., Soh, J., Kim, Y. and Choi, D. (2006) Effect of external magnetic field on anisotropy of Co/Cu multilayer nanowires. *Journal of Applied Physics*, Article no. 08C909.

3 Bilalbegovi, G. (2006) Electronic properties of silica nanowires. *Journal of Physics: Condensed Matter*, **18**, 3829–36.

4 Ton, C., Lin, Y. and Willett, C. (2006) Zebrafish as a model for developmental neurotoxicity testing. *Birth Defects Research. Part A, Clinical and Molecular Teratology*, **76**(7), 553–67.

5 Hultgren, A. and Tanase, M. (2003) Cell manipulation using magnetic nanowires. *Journal of Applied Physics*, **81** (12), 7554.

6 Svizhenko, A., Balandin, A. and Bandyopadhyay, S. (1997) Giant dipole effect and second-harmonic generation in quantum wires biased with a magnetic field. *Journal of Applied Physics*, **81**(12), 7927–33.

7 Wang, L., Major, D., Paga, P., Zhang, D., Norton, M. and McIlroy, D. (2006) High yield synthesis and lithography of silica-based nanospring mats. *Nanotechnology*, **17**, S298–303.

8 Lee, K.J., Nallathamby, P.D., Browning, L.M., Osgood, C.J. and Xu, X.H.N. (2007) In vivo imaging of transport and biocompatibility of single silver nanoparticles in early development of zebrafish embryos. *ACS Nano*, **1**(2), 133–43.

9 McAlpine, M.C., Ahmad, H., Wang, D. and Heath, J.R. (2007) Highly ordered nanowire arrays on plastic substrates for ultrasensitive flexible chemical sensors. *Nature Materials*, **6**, 379.

10 Zhang, H.F., Wang, C.M. and Wang, L.S. (2002) Helical crystalline SiC/SiO_2 core shell nanowire. *Nano Letters*, **2**, 941.

11 Zhang, D., McIlroy, D.N., Geng, Y. and Norton, M.G. (1999) Growth and characterization of boron carbide nanowires. *Journal of Materials Science Letters*, **18**, 349.

12 McIlroy, D.N., Zhang, D., Cohen, R.M., Wharton, J., Geng, Y., Norton, M.G., De Stasio, G., Gilbert, B., Perfetti, L., Streiff, J. H., Broocks, B. and McHale, J.L. (1999) Electronic and dynamic studies of boron carbide nanowires. *Physical Review B.*, **60**, 4874.

13 McIlroy, D.N., Zhang, D., Kranov, Y. and Norton, M.N. (2001) Nanosprings. *Applied Physics Letters*, **79**, 1540.

14 Morales, A.M. and Lieber, C.M. (1998) A laser ablation method for the synthesis of crystalline semiconductor nanowires. *Science*, **279**, 208.

15 Barsotti, R.J., Jr, Fischer J.E., Lee, C.H., Mahmood, J., Adu, C.K.W. and Eklund, P.C. (2002) Imaging, structural, and chemical analysis of silicon nanowires. *Applied Physics Letters*, **81**, 2866.

16 Duan, X. and Lieber, C.M. (2000) Laser-assisted catalytic growth of single crystal GaN nanowires. *Journal of the American Chemical Society*, **122**, 188.

17 Duan, X. and Lieber, C.M. (2000) Laser-assisted catalytic growth of single crystal GaN nanowires. *Advanced Materials*, **12**, 298.

18 Gudiksen, M.S. and Lieber, C.M. (2000) Diameter-selective synthesis of

semiconductor nanowires. *Journal of the American Chemical Society*, **122**, 8801.

19 Gudiksen, M.S., Wang, J. and Lieber, C.M. (2001) Synthetic control of the diameter and length of single crystal semiconductor nanowires. *The Journal of Physical Chemistry B*, **105**, 4062.

20 Zhang, Y.F., Tang, Y.H., Peng, H.Y., Wang, N., Lee, C.S., Bello, I. and Lee, S.T. (1999) Diameter modification of silicon nanowires by ambient gas. *Applied Physics Letters*, **75**, 1842.

21 Wang, R.P., Zhou, G.W., Long, Y.L., Pan, S.H., Zhang, H.Z., Yu, D.P. and Zhang, Z. (2000) Raman spectral study of silicon nanowires: high-order scattering and phonon confinement effects. *Physical Review B*, **61**, 16827.

22 Wu, Y., Fan, R. and Yang, P. (2002) Block-by-block growth of single-crystalline Si/SiGe superlattice nanowires. *Nano Letters*, **2**, 83.

23 Chrisey, L.A., Lee, G.U. and O'Ferrall, C.E. (1996) Covalent attachment of synthetic DNA to self-assembled monolayer films. *Nucleic Acids Research*, **24**, 3031–9.

24 Chaki, N.K. and Vijayamohanan, K. (2002) Self-assembled monolayers as a tunable platform for biosensor applications. *Biosensors and Bioelectronics*, **17**, 1–12.

25 Gau, V., Ma, S.C., Wang, H., Tsukuda, J., Kibler, J. and Haake, D.A. (2005) Electrochemical molecular analysis without nucleic acid amplification. *Methods*, **37**, 73–83.

26 Carpini, G., Lucarelli, F., Marrazza, G. and Mascini, M. (2004) Oligonucleotide-modified screen-printed gold electrodes for enzyme-amplified sensing of nucleic acids. *Biosensors and Bioelectronics*, **20**, 167–75.

27 Herne, T.M. and Tarlov, M.J. (1997) Characterization of DNA probes immobilized on gold surfaces. *Journal of the American Chemical Society*, **119**, 8916–20.

28 LaLonde, A., Norton, M., Zhang, D., Gangadean, D., Alkhateeb, A., Padmanabhan, R. and McIlroy, D. (2006) A rapid method for growth of metal nanoparticles on nanowire substrates. *Journal of Nanoparticle Research*, **8**(1), 99–104.

29 Demers, L.M., Mirkin, C.A., Mucic, R.C., Reynolds, R.A.I, , Letsinger, R.L., Elghanian, R. and Viswanadham, G. (2000) A fluorescence-based method for determining the surface coverage and hybridization efficiency of thiol-capped oligonucleotides bound to gold thin films and nanoparticles. *Analytical Chemistry*, **72**(22), 5535–41.

30 Perry, M.M. and Gilbert, A.B. (1979) Yolk transport in the ovarian follicle of the hen (*Gallus domesticus*): lipoprotein-like particles at the periphery of the oocyte in the rapid growth phase. *Journal of Cell Science*, **39**, 257–72.

31 Cooper, G.M. and Hausman, R.E. (2004) *The Cell: A molecular approach*. 3rd ed. Sinauer-ASM, Washington, DC.

32 Console, S., Marty, C., Garcia-Echeverria, C., Schwendener, R. and Ballmer-Hofer, K. (2003) Antennapedia and HIV transactivator of transcription (TAT) protein transduction domains' promote endocytosis of high molecular weight cargo upon binding to cell surface glycosaminoglycans. *Journal of Biological Chemistry*, **278**(37), 35109–14.

33 Drin, G., Cottin, S., Blanc, E., Rees, A.R. and Temsamani, J. (2003) Studies on the internalization mechanism of cationic cell-penetrating peptides. *Journal of Biological Chemistry*, **278**(33), 31192–201.

34 Foerg, C., Ziegler, U., Fernandez-Carneado, J., Giralt, E., Rennert, R., Beck-Sickinger, A.G. and Merkle, H.P. (2005) Decoding the entry of two novel cell-penetrating peptides in HeLa cells: lipid raft-mediated endocytosis and endosomal escape. *Biochemistry*, **44**(1), 72–81.

35 Kleemann, E., Neu, M., Jekel, N., Fink, L., Schmehl, T., Gessler, T., Seeger, W. and Kissel, T. (2005) Nano-carriers for DNA delivery to the lung based upon a TAT-derived peptide covalently coupled to PEG-PEI. *Journal of Controlled Release*, **109**(1–3), 299–316.

36 Blacklock, J., Handa, H., Soundara Manickam, D., Mao, G., Mukhopadhyay, A. and Oupicky, D. (2007) Disassembly of layer-by-layer films of plasmid DNA and

reducible TAT polypeptide. *Biomaterials*, **28**(1), 117–24.
37 Shigematsu, S., Watson, R.T., Khan, A.H. and Pessin, J.E. (2003) The adipocyte plasma membrane caveolin functional/structural organization is necessary for the efficient endocytosis of GLUT4. *Journal of Biological Chemistry*, **278**(12), 10683–90.
38 Farokhzad, O.C., Teply, B.A., Sherifi, I., Jon, S., Kantoff, P.W., Richie, J.P. and Langer, R. (2006) Targeted nanoparticle-aptamer bioconjugates for cancer chemotherapy in vivo. *Proceedings of the National Academy of Sciences of the United States of America*, **103**(16), 6315–20.
39 Farokhzad, O.C. and Langer, R. (2006) Nanomedicine: developing smarter therapeutic and diagnostic modalities. *Advanced Drug Delivery Reviews*, **58**, 1456–9.
40 Emerich, D.F. and Thanos, C.G. (2006) Targeted nanoparticle-aptamer bioconjugates for cancer chemotherapy in vivo. *Biomolecular Engineering*, **23**(4), 171–84.
41 Nel, A., Xia, T., Madler, L. and Li, N. (2006) Toxic potential of materials at the nanolevel. *Science*, **311**, 622–7.
42 Barnard, A.S. (2006) Nanohazards: knowledge is our first defense. *Nature Materials*, **5**(4), 245–8.
43 Borm, P.J., Robbins, D., Haubold, S. *et al.* (2006) The potential risks of nanomaterials: a review carried out for ECETOC. *Particle and Fibre Toxicology*, **3**, 11.
44 Oberdorster, G., Maynard, A., Donaldson, K. *et al.* (2005) Principles for characterizing the potential human health effects from exposure to nanomaterials: elements of a screening strategy. *Particle and Fibre Toxicology*, **2**, 8.
45 Nanoscale Science, Engineering and Technology Subcommittee (2005) The national nanotechnology initiative: environmental, health and safety research needs for engineered nanoscale materials. 2005 cited; Available from: http://www.nano.gov/html/society/EHS.htm (accessed 28 Nov. 2008).
46 The Royal Society and the Royal Academy of Engineering (2004) Nanoscience and nanotechnologies: opportunities and uncertainties. Available from: http://www.nanotec.org.uk/finalReport.htm (accessed 5 January 2005).
47 Kwon, N.H., Beaux, M. and Ebert, C. (2007) Nanowire-based delivery of *Escherichia coli* O157 shiga toxin 1 A subunit into human and bovine cells. *Nano Letters*, **7**(9), 2718–23.
48 Qi, S., Yi, C., Chem, W., Fong, C.C., Lee, S.T. and Yang, M. (2007) Effects of silicon nanowires on HepG2 cell adhesion and spreading. *Chembiochem*, **8**(10), 1115–18.
49 Adili, A., Crowe, S., Beaux, M., Cantrell, T., Shapiro, P., McIlroy, D. and Gustin, K. (2008) Differential cytotoxicity exhibited by silica nanowires and nanoparticles. *Nanotoxicology*, **2**, 1–8.
50 Cox, B.D., Natarajan, M., Stettner, M.R. and Gladson, C.L. (2006) New concepts regarding focal adhesion kinase promotion of cell migration and proliferation. *Journal of Cellular Biochemistry*, **99**(1), 35–52.
51 O'Toole, E.A. (2001) Extracellular matrix and keratinocyte migration. *Clinical and Experimental Dermatology*, **26**(6), 525–30.
52 Luo, D., Han, E., Belcheva, N. and Saltzman, W.M. (2004) A self-assembled, modular DNA delivery system mediated by silica nanoparticles. *Journal of Controlled Release*, **95**(2), 333–41.
53 Gemeinhart, R.A., Luo, D. and Saltzman, W.M. (2005) Cellular fate of a modular DNA delivery system mediated by silica nanoparticles. *Biotechnology Progress*, **21**(2), 532–7.
54 Rawat, M., Singh, D. and Saraf, S. (2006) Nanocarriers: promising vehicle for bioactive drugs. *Biological & Pharmaceutical Bulletin*, **29**(9), 1790–8.
55 Brigger, I., Dubernet, C. and Couvreur, P. (2002) Nanoparticles in cancer therapy and diagnosis. *Advanced Drug Delivery Reviews*, **54**(5), 631–51.
56 Brannon-Peppas, L. and Blanchette, J.O. (2004) Nanoparticle and targeted systems for cancer therapy. *Advanced Drug Delivery Reviews*, **56**(11), 1649–59.
57 Renoir, J.M., Stella, B., Ameller, T., Connault, E., Opolon, P. and Marsaud, V. (2006) Improved anti-tumoral capacity of

mixed and pure anti-oestrogens in breast cancer cell xenografts after their administration by entrapment in colloidal nanosystems. *The Journal of Steroid Biochemistry and Molecular Biology*, **102**, 114–27.

58 Castranova, V., Vallyathan, V. and Wallace, W.E. (1996) *Silica and Silica Induced Lung Diseases*, CRC Press, Boca Raton, FL.

59 Hamilton, R.F., Jr, Thakur S.A. and Holian, A. (2008) Silica binding and toxicity in alveolar macrophages. *Free Radical Biology and Medicine*, **44**(7), 1246–58.

60 Pelucchi, C., Pira, E., Piolatto, G., Coggiola, M., Carta, P. and La Vecchia, C. (2006) Occupational silica exposure and lung cancer risk: a review of epidemiological studies 1996–2005. *Annals of Oncology*, **17**(7), 1039–50.

61 Thibodeau, M.S., Giardina, C., Knecht, D.A., Helble, J. and Hubbard, A.K. (2004) Silica-induced apoptosis in mouse alveolar macrophages is initiated by lysosomal enzyme activity. *Toxicological Sciences*, **80**(1), 34–48.

62 Cho, W.S., Choi, M., Han, B.S. *et al.* (2007) Inflammatory mediators induced by intratracheal instillation of ultrafine amorphous silica particles. *Toxicology Letters*, **175**(1-3), 24–33.

63 Kaewamatawong, T., Kawamura, N., Okajima, M., Sawada, M., Morita, T. and Shimada, A. (2005) Acute pulmonary toxicity caused by exposure to colloidal silica: particle size dependent pathological changes in mice. *Toxicologic Pathology*, **33**(7), 743–9.

64 Wang, J., Jin, Y.H., Liu, B., Yu, Q.L., Wang, K. and Zhao, C.X. (2008) Comparative study on the acute toxicity of pulmonary caused by nanosized and microsized powders of silicon dioxide. *Zhonghua Yu Fang Yi Xue Za Zhi*, **42**(1), 30–5.

65 Zhao, C., Jin, Y., Zhang, Y. and Liu, B. (2007) Comparative study of effects of nanosized and microsized silicon dioxide dust on mouse embryos. *Wei Sheng Yan Jiu*, **36**(4), 414–16.

66 Hoet, P.H., Bruske-Hohlfeld, I. and Salata, O.V. (2004) Nanoparticles – known and unknown health risks. *Journal of Nanobiotechnology*, **2**(1), 12.

67 Tan, W., Wang, K., He, X., Zhao, X., Drake, T., Wang, L. and Bagwe, R. (2004) Bionanotechnology based on silica nanoparticles. *Medicinal Research Reviews*, **24**, 621–38.

68 Lund, J., Mehta, R. and Parviz, B. (2006) Label-free electronic detection of biomolecules with amorphous silicon nanostructures. *Nanomedicine: Nanotechnology, Biology, and Medicine*, **2**, 230–8.

69 Beaux, M.II, , Wang, L., Zhang, D., Gangadean, D., McIlroy, D., Kwon, N., Dziewanowska, K. and Bohach, G. (2006) Fibronectin bonding to nanowires and subsequent internalization by epithelial cells. *Journal of Biomedicine and Nanotechnology*, **2**, 23–8.

70 Corti, G., Wang, L., Major, D., Branen, J., Jabal, J., Branen, L., Nagler, J., Aston, E., Norton, G. and McIlroy, D. (2007) Nanospring-based biosensors for electrical DNA microarrays. *Materials Research Society Symposium Proceedings*, Paper no. 1010-V05-03.

71 Ramgir, N.S., Sekhar, P.K., Zajac, A., Lee, L., Zhukov, T. and Bhansali, S. (2007) Ultrasensitive voltammetric detection of IL-10, a lung cancer biomarker, in serum using SiO_2 nanowires template. *Sensors Letters*, **5**(3/4), 608–11.

72 Bhansali, S., Sekhar, P.K., Ramgir, N.S., Zhukov, T., Zajac, A. and Lee, L. (2006) Use of silica nanowires on a microfluidics platform for the detection of IL-10. *ECS Transactions*, **3**(10), 249–55.

73 Ramgir, N.S., Zajac, A., Sekhar, P.K., Lee, L., Zhukov, T.A. and Bhansali, S. (2007) Voltammetric detection of cancer biomarkers exemplified by interleukin-10 and osteopontin with silica nanowires. *The Journal of Physical Chemistry C*, **111**(37), 13981–7.

74 Wang, F., Malac, M., Egerton, R.F., Meldrum, A., Li, P., Freeman, M.R. and Veinot, J.G.C. (2007) Controlled growth of silicon oxide nanowires from a patterned reagent. *The Journal of Physical Chemistry C*, **111**(5), 1865–7.

75 McAlpine, M.C., Agnew, H.D., Rohde, R. D., Blanco, M., Ahmad, H., Stuparu, A.D.,

Goddard, W.A., III and Heath, J.R. (2008) Peptide- nanowire hybrid materials for selective sensing of small molecules. *Journal of the American Chemical Society*, **130**(29), 9583–9.

76 Piret, G., Coffinier, Y., Roux, C., Melnyk, O. and Boukherroub, R. (2008) Biomolecule and nanoparticle transfer on patterned and heterogeneously wetted superhydrophobic silicon nanowire surfaces. *Langmuir*, **24**(5), 1670–2.

77 Popat, K.C., Daniels, R.H., Dubrow, R.S., Hardev, V. and Desai, T.A. (2006) Nanostructured surfaces for bone biotemplating applications. *Journal of Orthopaedic Research*, **24**(4), 619–27.

78 Park, I., Li, Z., Li, X., Pisano, A.P. and Williams, R.S. (2007) Towards the silicon nanowire -based sensor for intracellular biochemical detection. *Biosensors and Bioelectronics*, **22**(9-10), 2065–70.

79 Cui, Y., Wei, Q., Park, H. and Lieber, C.M. (2001) Nanowire nanosensors for highly sensitive and selective detection of biological and chemical species. *Science*, **293**, 1289–92.

80 Zheng, G., Patolsky, F., Cui, Y., Wang, W. and Lieber, C. (2004) Multiplexed electrical detection of cancer markers with nanowire sensor arrays. *Nature Biotechnology.*, **23**, 1294–301.

81 Lou, J., Tong, L. and Ye, Z. (2005) Modeling of silica nanowires for optical sensing. *Optics Express*, **13**, 2135–40.

82 Hahm, J. and Lieber, C. (2004) Direct ultrasensitive electrical detection of DNA and DNA sequence variations using nanowire nanosensors. *Nano Letters*, **4**, 51–4.

83 Li, Z., Chen, Y., Li, X., Kamins, T., Nauka, K. and Williams, R. (2004) Sequence specific label-free DNA sensors based on silicon nanowires. *Nano Letters*, **4**, 245–7.

84 Bunimovich, Y.L., Shin, Y.S., Yeo, W.S., Amori, M., Kwong, G. and Heath, J.R. (2006) Quantitative real-time measurements of DNA hybridization with alkylated nonoxidized silicon nanowires in electrolyte solution. *Journal of the American Chemical Society*, **128**, 16323–31.

85 Star, A., Tu, E., Niemann, J., Gabriel, J.C., Joiner, C.S. and Valcke, C. (2006) Label-free detection of DNA hybridization using carbon nanotube network field-effect transistors. *Proceedings of the National Academy of Sciences of the United States of America*, **103**, 921–6.

86 Sekhar, P.K., Ramgir, N.S. and Bhansali, S. (2008) Metal-decorated silica nanowires: an active surface-enhanced Raman substrate for cancer biomarker detection. *The Journal of Physical Chemistry C*, **112**, 1729–34.

87 Patolsky, F., Zheng, G., Hayden, O., Lakadamyali, M., Zhuang, X. and Lieber, C. (2004) Electrical detection of single viruses. *Proceedings of the National Academy of Sciences of the United States of America*, **101**, 14017–22.

Keywords

Silica nanowires; functionalization; biomolecule; protein; toxicology; biosensor

4
Approaches to the Biofunctionalization of Spherical Silica Nanomaterials

Michihiro Nakamura

4.1
Introduction

Nanobiotechnology is an interdisciplinary research area that fuses various scientific fields such as chemistry, physics, materials science, molecular biology, biotechnology and medicine. Functional nanoparticles are at the leading edge of the rapidly evolving field of nanobiotechnology. Indeed, nanoparticles are becoming important components of biomedical applications including bioanalysis, multitarget detection systems, *in vitro* and *in vivo* multimodal imaging and nanomedicine [1–13]. The biofunctionalization of nanoparticles is very important for the progress of nanobiotechnology, as nanoparticles have great potential for bioanalysis and biotechnological applications due to their unique signal properties for imaging, their high surface-to-volume ratio, and other size-dependent qualities. When combined with surface modifications for specific binding and internal biofunctionalization to enhance signal strength, these qualities make nanoparticles excellent probes for the highly specific and ultrasensitive detection of biomolecules. Furthermore, such functional nanoparticles can be tailored to create drug delivery systems through the addition of a pharmacological effect. Therefore, the creation of multifunctional nanoparticles which possess both diagnostic and therapeutic capabilities, has become a major goal of nanobiotechnology.

Various functional nanoparticles such as quantum dots, gold nanoparticles and iron oxide nanoparticles have been developed and utilized in a range of applications. For example, quantum dots have nanocrystalline structures and can be produced from a variety of different compounds, such as cadmium selenide. Quantum dots absorb white light and then emit specific wavelengths of the absorbed light with a delay of a few nanoseconds. Quantum dots can be used to label biological systems for detection by optical or electronic means, both *in vitro* and – to some extent – *in vivo* [14–24]. By varying the size and composition of the quantum dots, this fluorescence emission can be tuned from ultraviolet (UV) to near-infrared wavelengths; thus, these nanosystems have the potential to revolutionize cell, receptor, antigen and enzyme imaging [21–24]. As an example, recent

Nanomaterials for the Life Sciences Vol. 2: Nanostructured Oxides. Edited by Challa S. S. R. Kumar

ISBN: 978-3-527-32152-0

studies have been conducted demonstrating the use of quantum dots for tracking metastatic tumor cell extravasation [22].

Gold nanoparticles are an ideal material for merging nanotechnology with biotechnology because of gold's affinity toward bonding with thiol functional groups, thereby allowing the surface biofunctionalization of gold nanoparticles with thiol-modified molecules. For oligonucleotide detection [25–33], probes have been constructed from gold nanoparticles immobilized with thiol-modified oligonucleotides. These gold nanoparticle probes were used to detect target oligonucleotide hybridization by monitoring changes in the color of the sample solution caused by the formation of polymeric gold nanoparticle/polynucleotide aggregates [20, 21]. Gold nanoparticles have also been used as quenchers in fluorescence resonance energy transfer (FRET) measurements [25, 34]. For example, the distance-dependent optical property of gold nanoparticles has permitted an evaluation of the binding of DNA-conjugated gold nanoparticles to a complementary RNA sequence [25]. The use of gold nanoparticles as highly enhanced photoabsorbing agents (due to their surface plasmon) has also afforded a selective and efficient cancer therapy strategy known as plasmonic photothermal therapy [35]. The synthetic tunability of these optothermal properties, coupled to the biotargeting abilities of the plasmonic gold nanostructures, means that plasmonic photothermal therapy will demonstrate even more promise in this respect.

Iron oxide nanoparticles with superparamagnetic properties are used as contrast agents in magnetic resonance imaging (MRI), based on their ability to cause changes in the spin–spin relaxation times of neighboring water molecules, thereby enabling the monitoring of gene expression or the detection of pathologies such as cancer, brain inflammation, arthritis or atherosclerotic plaques [36–43].

In addition to the three types of functional nanoparticle described above, silica (silicon dioxide) nanoparticles are also used extensively in biological and medical applications. Although many types of silica nanomaterial have been used in these applications, the discussion in this chapter will be limited to silica nanoparticles. Unlike quantum dots or iron oxide nanoparticles, silica nanoparticles do not possess an inherent signal that can be exploited for sensitive imaging applications. However, they can be easily functionalized for a variety of biological applications, for example with stem cells in regenerative medicine. Here, silica nanoparticles are made to fluoresce via an internal biofunctionalization, and can bind with target molecules via surface biofunctionalization. As a result, silica nanoparticles have shown great potential for use as 'stem nanomaterials' for multifunctionalization. Silica nanoparticles can also be adapted to specific applications by controlling the particle diameter; this in turn can be used to induce desirable properties for biological applications, and may also be highly advantageous in biotechnology and bioanalysis.

Silica nanoparticles are highly hydrophilic and easy to prepare, separate and functionalize with biomolecules. The conjugation of various biomolecules such as proteins, enzymes, peptides, drugs and DNA to the surfaces of silica nanoparticles via surface biofunctionalization represents a key technology for various applications, including highly specific and sensitive bioassays, targeted drug delivery and

gene delivery. The incorporation of various bioreagents such as fluorescent dyes into silica nanoparticles is also important for applications such as imaging and multiplexed bioassays.

Although fluorescent silica nanoparticles have been extensively studied and have enabled major advances to be made in imaging, labeling and sensing technologies, they still must overcome a number of challenges before being generally accepted as fluorescent dyes for such applications, and replacing the specialized use of quantum dots. Notably, the dispersion of silica nanoparticles should be improved to prevent their agglomeration, to decrease background noise, and also reduce nonspecific binding. Other challenges include improving the manipulation of the silica nanoparticle surface composition during synthesis, and the subsequent attachment and simultaneous maintenance of the activity of biomolecules. Clearly, until these challenges are addressed, silica nanoparticles cannot achieve their full potential for a variety of biomedical applications.

In order to overcome the above-listed problems, new biofunctionalization routes for silica nanoparticles are currently being explored, and many novel types have recently been developed. The potential for the surface and internal functionalization of silica nanoparticles is determined by their surface and internal structure, and their method of synthesis. Novel silica nanoparticles have been prepared from a variety of organosilicates, and contain modified organic and functional groups (e.g. thiol residues), both inside and on their surfaces. The organosilica silica nanoparticles differ both structurally and functionally from classical silica nanoparticles prepared from tetraethoxysilicate (TEOS; these traditional silica nanoparticles are referred to here as inorganic silica nanoparticles), because they contain both interior and exterior functionalities that allow efficient functionalization with biomolecules. The organic and functional groups on the surface of and inside organosilica nanoparticles continue to reveal innovative effects for silica nanoparticle technology, with the ability of silica nanoparticles to function as 'stem nanoparticles' for multifunctionalization showing excellent progress. Whilst the organosilica nanoparticles have the potential to overcome the above-mentioned challenges, they might also expand the multifunctionalization capabilities of silica nanoparticles. Although several reviews and reports [8–10] have described advances in the synthesis, biofunctionalization and application of silica nanoparticles, none of these has covered the development of novel organic silica nanoparticles.

The main focus of this chapter is to provide an overview of recent developments of novel silica nanoparticles, both inorganic and organic, and their functionalization through both internal and surface processes. The development and classification of silica nanoparticles (again, both inorganic and organic) are summarized in Section 4.2, as are their syntheses and characterizations. As the biofunctionalization of silica nanoparticles depends on their method of synthesis (as mentioned above), clear descriptions of both synthesis and characterization are important in order to understand biofunctionalization capabilities. More recent developments, including the conjugation of biomolecules to the surfaces of silica nanoparticles via surface biofunctionalization, and the addition of bioreagents to nanoparticles

via internal biofunctionalization, are described in Section 4.3. The biofunctionalization of novel organosilica nanoparticles is also emphasized, as this differs substantially from that of inorganic nanoparticles. Finally, in Section 4.4 we review recent biological and biomedical applications of biofunctionalized silica nanoparticles, aiming to promote them as potential 'stem nanomaterials' capable of multifunctionalization.

4.2 Silica Nanoparticles

In 1968, Stöber and coworkers reported a pioneering method for the synthesis of spherical, monodisperse silica nanoparticles from aqueous alcohol solutions of alkoxysilane in the presence of ammonia as catalyst [44]. In this method, the silica nanoparticles were formed through the hydrolysis and condensation of alkoxysilane. In addition to the silica nanoparticles prepared using Stöber's method, various other types have also been prepared and reported (Table 4.1) [44–53]. Although the alkoxysilanes contain carbon, the formed silica nanoparticles do not contain any exposed interior or surface carbons, and therefore can be considered as 'inorganic silica nanoparticles' (and are referred to as such). Recently, novel

Table 4.1 Classification of silica nanoparticles and their source.

Type of silica nanoparticle	Sources
(a) Inorganic silica	Tetraethylorthosilicate (TEOS)
	Tetramethylorthosilicate (TMOS)
(b) Organosilica	
(b-1) Organically modified silane (ORMOSIL)	Octyl triethoxysilane (OTES)
	Vinyl triethoxysilane (VTES)
(b-2) Functional organosilica	
(b-2-1) Thiol-organosilica	3-Mercaptopropyltrimethoxysilane (MPMS)
	3-Mercaptopropyltriethoxysilane (MPES)
	3-Mercaptopropylmethyldimethoxysilane (MPDMS)
(b-2-2) Epoxy-organosilica	2-(3,4-Epoxycyclohexyl)ethyltrimethoxysilane (EpoMS)
(c) Multi-silicate	
(c-1) TEOS-based multi-silicate	Carboxyethylsilanetriol sodium salt
	Octadecyltriethoxysilane
	3-Aminopropyl triethoxysilane
	3-(Trihydroxysilyl)-propylmethylphosphonate
(c-2) ORMOSIL-based multi-silicate	3-Aminopropyltrimethoxysilane and VTES

silica nanoparticles containing exposed interior and surface carbons as well as organic and functional groups were synthesized [45, 46], and these are referred to as 'organosilica nanoparticles'. The latter include various types of nanoparticle such as 'organically modified silane (ORMOSIL) nanoparticles' [46–48] and 'functional organosilica nanoparticles', which include thiol-organosilica and epoxy-organosilica nanoparticles [49–52]. Although ORMOSIL nanoparticles contain carbonaceous moieties (e.g. octyl and vinyl groups), single organosilicate nanoparticles of ORMOSIL do not contain any functional residues (e.g. amines or thiols). Functional organosilica nanoparticles are prepared from organosilica-containing functional residues, such as thiols and epoxies, and when prepared contain interior and surface functional resides as well as organic chains. Organosilica nanoparticles may be classified as either 'single silicate nanoparticles', which comprise only one type of silicate (such as the above-mentioned silica source), or as 'multi-silicate nanoparticles', which comprise at least two types of silicate precursor [53]. The type and extent of possible biofunctionalization of silica nanoparticles are largely controlled by their surface and internal properties, as well as their method of synthesis. Although a wide variety of novel inorganic and organic silica nanoparticles has recently been developed, no reports have been made summarizing their synthesis and characterization. In the following sections, we provide a summary of the surface and internal properties and synthesis of the silica nanoparticles listed in Table 4.1. As different approaches for the biofunctionalization of silica nanoparticles must be developed according to their type, an understanding of their properties is essential in order to realize their role in biofunctionalization.

4.2.1 Inorganic Silica Nanoparticles

Traditionally, inorganic silica nanoparticles have been prepared from either TEOS (**1**) or tetramethoxyorthosilicate (TMOS) (**2**). When prepared, TEOS nanoparticles are composed internally of a simple silica network (—O—Si—O—), and have silanol groups on their surfaces. However, as they lack any exposed organic residues, both inside and on their surfaces (as shown schematically in Figure 4.1), they will require further modification with functional residues (e.g. amine or thiol) prior to their surface biofunctionalization.

TEOS $(CH_3CH_2O)_4$-Si (**1**)

TMOS $(CH_3O)_4$-Si (**2**)

Inorganic silica nanoparticles have been prepared using both the Stöber method [44] and reverse microemulsion [45]. With the Stöber method, submicron-sized TEOS nanoparticles can be obtained, and the synthetic mixtures typically contain ethanol, ammonium hydroxide and water. Although the method is simple and

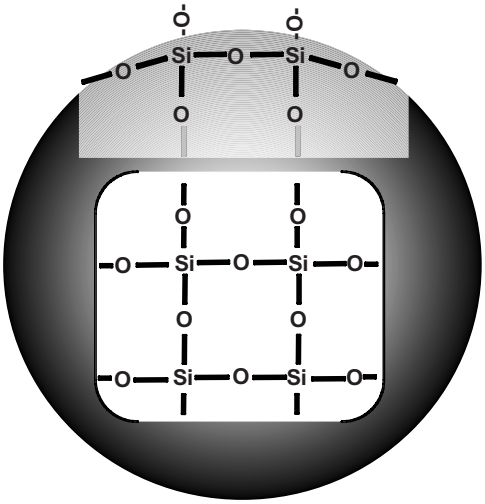

Figure 4.1 Schematic structure of inorganic silica nanoparticles.

requires only a few hours, the silica nanoparticles produced are polydisperse and further separation and purification are required to obtain a monodisperse product. With reverse microemulsion, monodisperse particles in the nanometer size range are obtained. The reverse microemulsions are isotropic and thermodynamically stable single-phase systems which contain water, oil and a surfactant. This method is advantageous because it affords diameter control of silica nanoparticles by varying the water-to-surfactant ratio, and through the dynamic properties of the microemulsion.

4.2.2 Organosilica Nanoparticles

Recently, novel silica nanoparticles made from various organosilica precursors including octyl triethoxysilane (OTES) and 3-mercaptopropyltrimethoxysilane (MPMS) were prepared successfully. These as-prepared organosilica nanoparticles have various exposed organic and functional groups both on their inside and surfaces, depending on the organosilica source, and can be biofunctionalized via these groups. Such organosilica nanoparticles include ORMOSIL nanoparticles, thiol-organosilica nanoparticles and epoxy-organosilica nanoparticles (see below). Multi-silicate nanoparticles containing many types of surface group (e.g. silanols and carbon chains) can also be prepared from two or more types of silicate.

4.2.2.1 **Organically Modified Silane Nanoparticles (ORMOSIL Nanoparticles)**

Single-source ORMOSIL nanoparticles have been prepared with reverse microemulsion using OTES (**3**) [46] and vinyl triethoxysilane (VTES) (**4**) [47]. The as-prepared ORMOSIL nanoparticles contain interior *n*-octyl groups and surface vinyl

groups, and have been prepared from two types of organosilicate [48]. Moreover, the surface vinyl groups of ORMOSIL nanoparticles can be converted to surface carboxylic groups, and then biofunctionalized.

OTES $(CH_3CH_2O)_3$-Si-C_7H_{14}-CH_3 (**3**)

VTES $(CH_3CH_2O)_3$-Si-$CH{=}CH_2$ (**4**)

4.2.2.2 Functional Organosilica Nanoparticles

4.2.2.2.1 **Thiol-Organosilica Nanoparticles** Thiol-organosilica nanoparticles are prepared from MPMS (**5**), 3-mercaptopropyltriethoxysilane (MPES) (**6**) and 3-mercaptopropylmethyldimethoxysilane (MPDMS) (**7**) [49, 50]. The as-prepared nanoparticles contain interior and surface carbon chains as well as interior and surface thiol residues, as shown schematically in Figure 4.2. These thiol residues are useful for direct biofunctionalization of the particles, as the zeta potentials of thiol-organosilica nanoparticles are more negative than those of TEOS nanoparticles [49, 50]. Recently, the synthesis of thiol-organosilica nanoparticles was described [49, 50], in which varying concentrations of MPMS were used under six types of synthetic conditions to prepare particles from a single silicate source (Table 4.2). Here, the condition A and D solutions contained 65% ethanol, 33% water and 2% ammonium hydroxide (traditional Stöber conditions), condition B and E solutions contained 98% water and 2% ammonium hydroxide but no

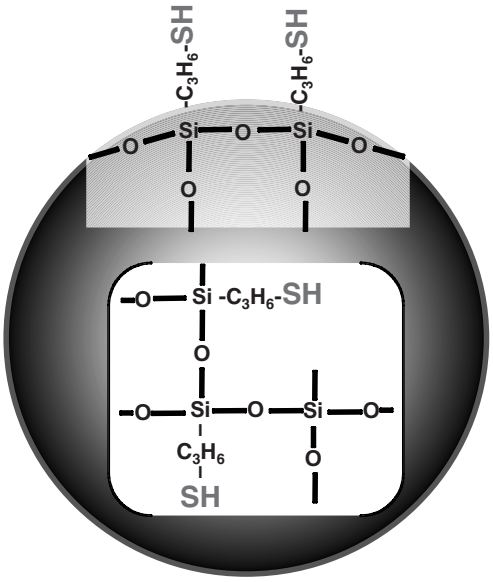

Figure 4.2 Schematic structure of thiol-organosilica nanoparticles.

Table 4.2 Synthetic conditions.

Solvent mixture	RT	100 °C
33% water/2% ammonium hydroxide/65% ethanol	A	D
98% water/2% ammonium hydroxide	B	E
73% water/27% ammonium hydroxide	C	F

RT; room temperature.

ethanol, and condition C and F solutions contained 73% water and 27% ammonium hydroxide. The syntheses conducted under conditions A, B and C were performed at room temperature, and those under conditions D, E and F at 100 °C.

MPMS $(CH_3O)_3\text{-}Si\text{-}C_3H_6\text{-}SH$ (5)

MPES $(CH_3CH_2O)_3\text{-}Si\text{-}C_3H_6\text{-}SH$ (6)

MPDMS $(CH_3O)_2(CH_3)\text{-}Si\text{-}C_3H_6\text{-}SH$ (7)

The results indicated that thiol-organosilica nanoparticles could be prepared via the Stöber method, and also using an entirely aqueous solvent containing ammonium hydroxide, but not ethanol. The formation of thiol-organosilica nanoparticles is dependent on the type and concentration of organosilicate in the synthetic solutions, as well as the synthetic conditions (see Figures 4.3, 4.4 and Table 4.3) [50]. The particle diameter of the formed MPMS nanoparticles was seen to depend on the MPMS concentration used in the reaction mixture, although the average diameters of particles obtained from identical MPMS concentrations varied between different synthetic conditions (see Table 4.4). Size-controlled thiol-organosilica nanoparticles can be obtained under synthetic conditions at high temperature (100 °C). Under conditions D, E and F, the coefficient of variation (CV) of formed MPMS nanoparticles was close to or less than 20%, with an average value of 16.4% for all three synthetic conditions. In contrast, under conditions A, B and C the CVs of MPMS nanoparticles were 21.6–51.9%, with an average for the three conditions of 39.1%. These results indicated that the increased temperature used in conditions D, E and F produced MPMS nanoparticles which possessed a greater monodispersity. The average CVs for conditions D, E and F were 19.6, 16.0 and 13.6%, respectively. The average CVs of MPMS nanoparticles formed at lower MPMS concentrations (from 6.25 to 25 m*M*) were smaller than those for MPMS particles formed at higher MPMS concentrations (from 50 to 200 m*M*) under conditions E and F (see Table 4.4). These results indicate that conditions E and F were suitable for the synthesis of size-controlled MPMS nanoparticles with diameters of a few hundred nanometers from synthetic mixtures containing lower MPMS concentrations.

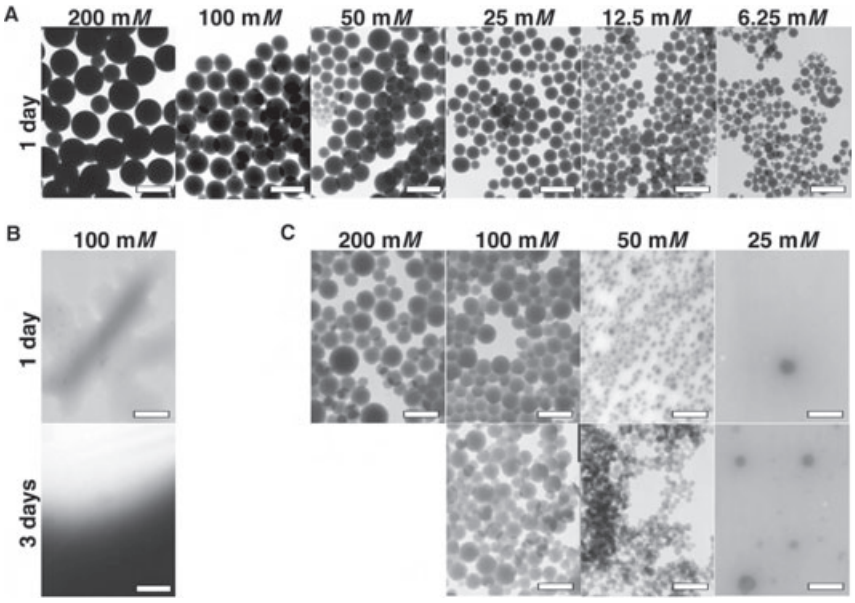

Figure 4.3 Transmission electron microscopy (TEM) images of inorganic silica nanoparticles prepared from TEOS as a function of time and TEOS concentration. TEOS nanoparticles prepared under condition A (a), condition B (b) and condition C (c) were observed after incubation periods of 1 day [(a) and upper row in (b) and (b)] and 3 days [lower row in (b) and (c)]. Scale bars: (a) 500 nm; (b) 5000 nm; (c) 200 nm (Reproduced with permission from Ref. [50]; © 2008, American Chemical Society.).

Thiol-organosilica nanoparticles have also been produced using a two-step process of acid-catalyzed hydrolysis and condensation of MPMS, followed by base-catalyzed condensation; this resulted in a rapid formation of emulsion droplets with a narrow size distribution [51].

4.2.2.2.2 **Epoxy-Organosilica Nanoparticles** Epoxy-organosilica nanoparticles are prepared from 2-(3,4-epoxycyclohexyl)ethyltrimethoxysilane (EpoMS) (**8**) [52]. The as-prepared epoxy-organosilica nanoparticles contain interior and surface epoxy residues that can be used for direct biofunctionalization of the particles, while the zeta potentials are positive [52]. Epoxy-organosilica nanoparticles may be prepared using entirely aqueous solvent methods containing ammonium hydroxide, but not via the Stöber method. A variety of concentrations (from 6.25 to 200 m*M*) of EpoMS was used under synthetic conditions A, B and C (as described above) to prepare particles from a single silicate source (see Figure 4.5 and Table 4.5). No epoxy-organosilica nanoparticles were formed under condition A for any of the EpoMS concentrations, even after incubation for 3 days. However, under conditions B and C, particles were clearly observed after 1 day at all EpoMS concentrations except the lowest (6.25 m*M*) when, even after 3 days, no particles were

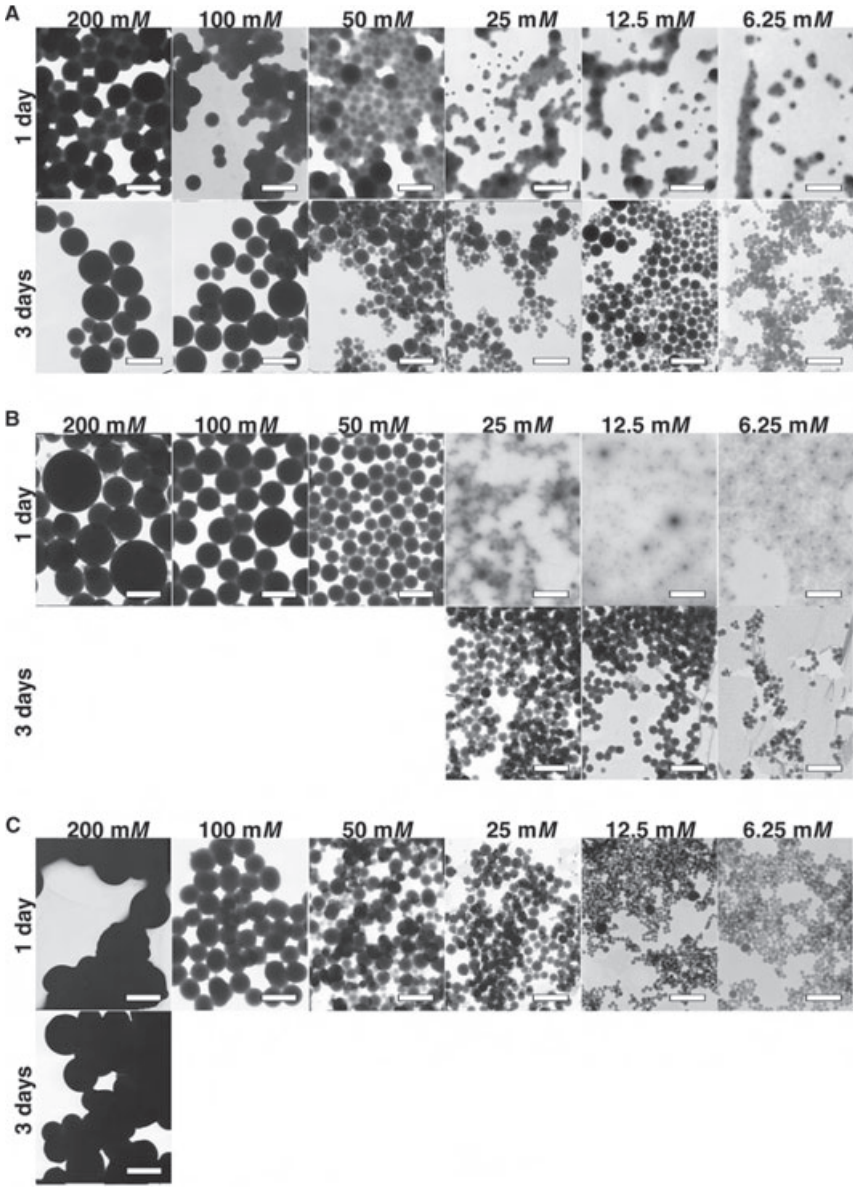

Figure 4.4 TEM images of thiol-organosilica nanoparticles prepared from MPMS as a function of time and MPMS concentration. MPMS nanoparticles prepared under condition A (a), condition B (b) and condition C (c) were observed after incubation periods of 1 day (upper row) and 3 days (lower row). Scale bars: 1000 nm (Reproduced with permission from Ref. [50]; © 2008, American Chemical Society.).

Table 4.3 Formation of silica nanoparticles under conditions A, B and C with incubation periods of 1 day.

	Conc. (m*M*)	Condition A	Condition B	Condition C
TEOS	200	○	×	○
	100	○	×	×
	50	○	×	×
	25	○	×	×
	12.5	○	×	×
	6.25	○	×	×
MPMS	200	○	○	×
	100	×	○	○
	50	×	○	○
	25	×	×	○
	12.5	×	×	○
	6.25	×	×	○

The formation and incomplete formation of nanoparticles are indicated as ○ and ×, respectively. (Reproduced with permission from Ref. [50]; © 2008, American Chemical Society.).

observed. The extent of formation of the epoxy-organosilica nanoparticles depended on the organosilicate concentration and the synthetic conditions. Size-controlled epoxy-organosilica nanoparticles were obtained under synthetic conditions at room temperature, and showed a narrow size distributions (see Table 4.6). The CV were seen to vary with the EpoMS concentration, and at higher concentrations (50–200 m*M*) was less than 20%. The best CV values were obtained at the highest EpoMS concentrations under both conditions B and C.

EpoMS 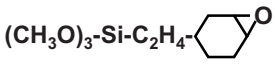 (**8**)

4.2.2.3 **Multisilicate Nanoparticles**

In order to facilitate the surface biofunctionalization of particles, multisilicate nanoparticles are synthesized based either on the synthesis of TEOS nanoparticles (TEOS-based) or of ORMOSIL nanoparticles (ORMOSIL-based). Multisilicate nanoparticles contain surface functional residues (e.g. vinyl or amine groups) that allow biomolecules to be linked to the particles. TEOS-based multi-silicate nanoparticles have been prepared by reverse microemulsion, and are subsequently surface-modified via cohydrolysis with TEOS and various organosilicates such as carboxyethylsilanetriol sodium salt, 3-(aminopropyl)triethoxysilane, 3-(trihydroxysilyl)-propylmethylphosphonate and octadecyltriethoxysilane [53]. TEOS-based multisilicate nanoparticles containing different functional groups, including carboxylate, amine, amine/phosphonate, polyethylene glycol (PEG), octadecyl and carboxylate/octadecyl groups, have also been synthesized [53]. ORMOSIL-

Table 4.4 Size evaluation of silica nanoparticles prepared under conditions A, B, C, D, E and F.

Silica	Condition	Concentration (m*M*)	Average diameter (nm)	CV (%)
TEOS	A	200	447	44.7
TEOS	A	100	381	27.8
TEOS	A	50	314	29.0
TEOS	A	25	192	35.9
TEOS	A	12.5	117	59.8
TEOS	A	6.25	62	72.5
TEOS	C	200	177	34.5
TEOS	C	100	80	40.0
TEOS	C	50	40	40.0
TEOS	D	200	380	20.3
TEOS	D	100	250	20.4
TEOS	D	50	118	30.7
TEOS	D	25	36	26.8
TEOS	D	12.5	29	32.2
TEOS	F	200	78	49.8
TEOS	F	100	100	89.3
TEOS	F	50	98	64.9
TEOS	F	25	77	23.8
MPMS	A	200	705	51.9
MPMS	A	100	484	49.2
MPMS	A	50	380	39.2
MPMS	A	25	333	33.6
MPMS	A	12.5	233	51.1
MPMS	A	6.25	154	43.5
MPMS	B	200	740	50.8
MPMS	B	100	677	42.4
MPMS	B	50	502	24.9
MPMS	B	25	295	25.4
MPMS	B	12.5	234	35.0
MPMS	B	6.25	147	31.3
MPMS	C	100	882	43.3
MPMS	C	50	407	50.1
MPMS	C	25	248	29.8
MPMS	C	12.5	125	21.6
MPMS	C	6.25	66	40.9

(Reproduced with permission from Ref. [50]; © 2008, American Chemical Society.).

Table 4.5 Formation of EpoMS particles under conditions A, B and C with incubation periods of 1 day.

Conc. (m*M*)	Condition A	Condition B	Condition C
200	×	○	○
100	×	○	○
50	×	○	○
25	×	○	○
12.5	×	○	○
6.25	×	×	×

The formation and incomplete formation of EpoMS particles are indicated as ○ and ×, respectively (Reproduced with permission from Ref. [52]; © 2008, American Chemical Society.).

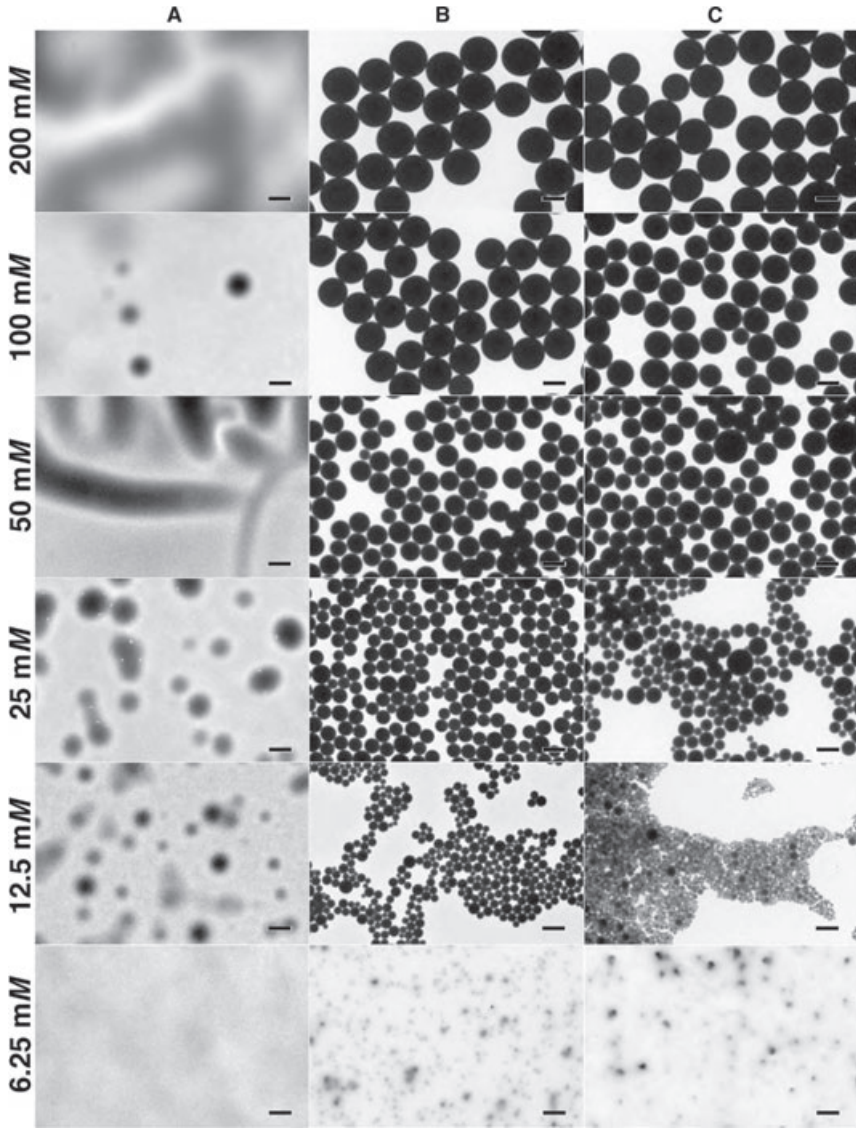

Figure 4.5 TEM images of epoxy-organosilica nanoparticles prepared from EpoMS as a function of EpoMS concentration. Epoxy-organosilica nanoparticles prepared under condition A (a), condition B (b) and condition C (c) were observed after incubation periods of 1 day. Scale bars: 1000 nm (Reproduced with permission from Ref. [52]; © 2008, American Chemical Society.).

Table 4.6 Size evaluation of EpoMS particles prepared using conditions B and C.

Condition	Concentration (m*M*)	Diameter (nm)	CV (%)
B	200	1630	5.7
B	100	1407	8.1
B	50	824	9.5
B	25	512	21.2
B	12.5	362	22.3
C	200	1436	10.9
C	100	1139	13.2
C	50	879	17.0
C	25	533	33.4
C	12.5	92	46.2

(Reproduced with permission from Ref. [52]; © 2008, American Chemical Society)

based multisilicate nanoparticles are prepared from VTES and aminopropyl triethoxysilane (APS) [48], using methods based on reverse microemulsion, and contain surface amine groups as prepared.

4.3 Biofunctionalization of Silica Nanoparticles

The biofunctionalization of silica nanoparticles is very important for biomedical applications such as bioanalysis, multitarget detection systems, *in vitro* and *in vivo* imaging and nanomedicine [8–10, 54–58]. Biofunctionalized silica nanoparticles must be able to provide strong analytical signals, bind targets with high affinity and specificity, and be adaptable for use in systems for the controlled release of drugs or to demonstrate a specific physiological or pharmacological effect. Today, silica nanoparticles are becoming increasingly attractive as the core particles for such applications since they are easily prepared and separated, their surfaces and internal structures can be modified or labeled, they are highly hydrophilic, and they are safe. The biofunctionalization of nanoparticles can be classified as either surface or internal:

- The surface biofunctionalization of silica nanoparticles by conjugation with biomolecules such as proteins, enzymes, peptides and DNA represents a key technology for applications which include bioassays, imaging, and drug or gene delivery systems. The conjugation of biomolecules such as antibodies on the surface of silica nanoparticles can provide specific and sensitive binding and detection of target molecules. Additionally, the attachment of plasmid DNA to the surface of nanoparticles enables gene delivery into cells.

- The internal biofunctionalization of silica nanoparticles with functional molecules, such as fluorescent dyes and drugs, is also very important for bioassays, imaging and drug delivery. Internally biofunctionalized silica nanoparticles that can provide strong and stable signals for imaging are particularly useful.

The optimal fusion of surface and internal biofunctionalization of silica nanoparticles can lead to the creation of useful multifunctional nanoparticles. Although several reviews [8–10] have detailed the advances in biofunctionalization of inorganic silica nanoparticles, none of these has summarized recent developments in this area, such as ORMOSIL and functional organosilica nanoparticles. In the following section we describe both surface and internal biofunctionalization strategies for various types of inorganic silica and organosilica nanoparticles.

4.3.1 Surface Biofunctionalization

Both, inorganic silica and organic silica nanoparticles possess a silica network (—O—Si—O—) within their particles, but have various different reactive groups on their surfaces, depending on the composition of the silicate source. For example, inorganic silica nanoparticles display silanol residues on their surface, while thiol-organosilica nanoparticles display surface thiol residues. The surface charge of silica nanoparticles is also dependent on the type of nanoparticle and their reactive groups on the surface. While inorganic silica and thiol-organosilica nanoparticles both have negative surface charges, epoxy-organosilica nanoparticles have positive surface charges. Hence, a broad spectrum of conjugation chemistry approaches can be applied to the surfaces of these silica nanoparticles, a detailed discussion of which approaches is presented below.

4.3.1.1 Surface Biofunctionalization of Inorganic Silica Nanoparticles

When inorganic silica nanoparticles are prepared from TEOS using either the Stöber method [44] or reverse microemulsion [45], they display surface silanol groups and have negatively charged surfaces. A variety of biofunctionalization methods have been used to conjugate the surface of inorganic silica nanoparticles to biomolecules including nucleic acids, antibodies, enzymes and other proteins, including physical absorption, silanization and chemical coupling [57, 59, 64–77].

4.3.1.1.1 Physical Adsorption Physical adsorption via electrostatic coupling is often used to modify the surface of biofunctionalized TEOS nanoparticles with proteins such as avidin for bioanalysis and biosensing [57, 59, 64]. Avidin, a glycoprotein with four subunits, has a positive charge and binds electrostatically with the negatively charged surface of TEOS nanoparticles, which are then

stabilized by crosslinking with glutaraldehyde. The strong binding affinity of avidin to biotin ($K_d = 10^{-15}$ *M*) [60] is often exploited for biotechnological, diagnostic and therapeutic applications [61–63]. Hence, TEOS nanoparticles coated with avidin can be used to detect biotinylated biomolecules with high sensitivity through avidin–biotin binding. Antibodies may also be used for the surface biofunctionalization of TEOS nanoparticles; for example, immunoglobulin E has been adsorbed to the surface of TEOS nanoparticles and the resultant particles used for cell imaging [64].

4.3.1.1.2 **Silanization** Silanization allows a surface containing silanol groups to be covered with various types of functionalized silicate, and has been well studied and developed in the case of inorganic silica nanoparticles. For example, TEOS nanoparticles containing surface amine, thiol, cyanate ester or carboxyl groups can be prepared by using silanization. As most biomolecules contain amino groups, complementary cyanate ester, amine and carboxyl functionalities are often created at the surface of inorganic silica nanoparticles through surface biofunctionalization.

The amino group is commonly used for the immobilization of enzymes and antibodies; hence, TEOS nanoparticles may be silanized with *N*1-[3-(trimethoxysilyl)-propyl]diethylenetriamine, *N*-(2-amino-ethyl)-3-aminopropyltrimethoxysilane, *N*-(6-amino-hexyl)-3-aminopropyltrimethoxysilane or APS for the direct preparation of amino-modified TEOS nanoparticles [65–75]. Alternatively, an indirect preparation may be carried out through silanization with 3-glycidoxypropyltrimethoxysilane, followed by diamines [76]. Amino-modified TEOS nanoparticles are positively charged due to the cationic amino ($-NH_3^+$) groups on the surface, and further biofunctionalization may be conducted using various methods.

Antibody-conjugated silica nanoparticles have been prepared from amino-modified TEOS nanoparticles. For this, the latter are activated with glutaraldehyde and reacted with anti-rh interleukin-6 (IL-6) antibody [65]. Amino-modified TEOS nanoparticles can also be reacted with biotin–PEG5000–*N*-hydroxysuccinimide (NHS) to conjugate biotin with the surface of the particles via NHS ester–amino linkages. The resulting biotin-modified TEOS nanoparticles are first bound with avidin and then with biotin-labeled antibodies. Such biofunctionalized nanoparticles have been used for the detection of pathogenic bacteria [66]. By using small gold colloids, nanoparticles modified with antibodies have been designed to scatter and absorb light over a broad spectral range, including the near-infrared, a wavelength region that provides maximal penetration of light through tissue. Here, the surface of amino-modified TEOS nanoparticles is bound with small gold colloids, and the antibody attached to a *ortho*-pyridyl disulfide–PEG–NHS linker via NHS. The antibody–PEG linker complex is then attached to gold colloid-modified TEOS nanoparticles via the interaction between a sulfur-containing group located at the distal end of the PEG linker and gold [67].

A peptide has also been conjugated on the surface of amino-modified TEOS nanoparticles. TAT peptide [48–56], an amino acid residue of the HIV-coded TAT regulatory protein, is a cell-penetrating peptide and was conjugated with amino-

modified TEOS nanoparticles through heterobifunctional *N*-hydroxysuccinimidyl 3-(2-pyridyldithio) propionate coupling chemistry. These biofunctionalized amino-modified TEOS nanoparticles were subsequently applied to bioimaging [68].

DNA can also be conjugated with amino-modified TEOS nanoparticles following their activation with 1,2,3-triazine and 1,2,4-triazine, and subsequent reaction with amino-labeled synthetic oligonucleotides [69]. Alternatively, the amino-modified TEOS nanoparticles can be activated with *m*-maleimidobenzoyl-*N*-hydroxysuccinimide ester cross-linkers and then reacted with thiol-labeled synthetic oligonucleotides [70].

A additional surface biofunctionalization procedure for amino-modified TEOS nanoparticles yields carboxyl-modified nanoparticles [54, 56, 71, 72]. The nanoparticles are first treated with succinic anhydride in dimethylformamide (DMF), after which the resulting carboxyl-modified TEOS nanoparticles can be further reacted with carbodiimide hydrochloride before subsequent enzyme conjugation. Enzymes (e.g. glutamate dehydrogenase) conjugated to the surface of the particles have shown excellent enzymatic activity [71]. β-Cyclodextrin, a seven-sugar ring molecule, has also been conjugated to the carboxyl-modified nanoparticles using carbodiimide hydrochloride and NHS [72].

Silanization followed by physical adsorption represents another method for the biofunctionalization of TEOS nanoparticles. The cationic properties of the surfaces of these nanoparticles can be used for biofunctionalization with negatively charged biomolecules, and the formation of a complex consisting of amino-modified TEOS nanoparticles and plasmid DNA has been reported [73–75]. Such a complex is formed simply by mixing amino-modified TEOS nanoparticles and plasmid DNA; the resultant complex is stable and capable of transfecting plasmids into cells *in vitro*.

Thiol-modified TEOS nanoparticles have been prepared by their silanization with 1% MPMS [77]. For this, the nanoparticles were reacted with 1% MPMS in a solution containing ethanol and acetic acid. Disulfide coupling chemistry can also be applied for the immobilization of oligonucleotides onto particles, when thiol-modified silica nanoparticles are conjugated with disulfide-modified oligonucleotides via a thiol/disulfide exchange reaction in carbonate buffer at pH 9.0. Thiol or disulfide coupling is a simple and efficient procedure for the direct immobilization of disulfide-containing biomolecules on the surface of thiol-modified silica nanoparticles through a thiol–disulfide exchange reaction, and the resultant disulfide bond can be severed under strong reducing conditions.

4.3.1.1.3 **Chemical Coupling** By using silanol groups on the surface of inorganic silica nanoparticles, a variety of biofunctionalizations of TEOS nanoparticles with chemical coupling has been reported. The nanoparticles are first surface-modified with sodium carbonate, after which a solution of cyanogen bromide in acetonitrile is added to the suspension to yield surface cyanogen bromide-pretreated nanoparticles [78, 79] that may then bind directly with the free amino groups of biomolecules. For example, anti-human CD10 antibody and

Annexin V (a small protein that binds to phosphatidylserine in the presence of Ca^{2+}) have been conjugated on the surface of cyanogen bromide-treated nanoparticles [79].

Another route for the surface modification of TEOS nanoparticles involves the surface binding of Zr^{4+}, followed by binding with phosphoric acid to form terminal phosphate groups [80]. Oligonucleotide probes modified with amine groups at the 5′-end bind strongly to the phosphate-terminated silica nanoparticles with imidazole in the presence of *N*-ethyl-*N*′-(3-dimethylaminopropyl) carbodiimide, as the phosphate groups are reactive towards amine groups. Silica nanoparticles bound with oligonucleotide probes have been used for the detection of DNA hybridization.

4.3.1.2 Surface Biofunctionalization of Organosilica Nanoparticles

When prepared, organosilica nanoparticles contain a variety of surface and internal carbon chains and functional groups. Fore example, ORMOSIL nanoparticles have carbon chains, while functional organosilica nanoparticles have carbon chains as well as functional groups such as thiol and epoxy residues. When located on organosilica nanoparticle surface, the carbon chains and functional groups provide an easy surface biofunctionalization of the nanoparticles. The presence of functional groups also eliminates some steps in biofunctionalization reactions and reduces the extent of nanoparticle aggregation during modification procedures. Approaches to the biofunctionalization of organosilica nanoparticles depend on their surface properties; these are described below for ORMOSIL, thiol-organosilica and epoxy-organosilica nanoparticles.

4.3.1.2.1 **ORMOSIL Nanoparticles** ORMOSIL nanoparticles composed of vinyl triethoxysilane contain surface vinyl groups that may be oxidized with $KMnO_4$ solution to form surface carboxylic groups. The resultant carboxy-modified ORMOSIL nanoparticles are conjugated with PEG by reaction with ethyl-3-(3-dimethylaminopropyl) carbodiimide [47]. In contrast, ORMOSIL nanoparticles made from VTES and APS are amino-modified [48] and may be biofunctionalized with plasmid DNA by simple mixing, as the plasmid DNA can bind electrostatically to the nanoparticles via the positively charged amino groups on the particle surface. Such nanoparticle–DNA complexes have been used for gene delivery both *in vitro* and *in vivo*.

4.3.1.2.2 **Thiol-Organosilica Nanoparticles** Thiol-organosilica nanoparticles have thiol residues on their surfaces, without requiring any additional procedures. Such nanoparticles are prepared from thiol-organosilicates (MPMS, MPES, MPDMS) which possess one thiol residue per silicate molecule; therefore, thiol-organosilica nanoparticles contain a large proportion of thiol residues. Thiol residues on nanoparticles may be subjected to various surface biofunctionalizations, as shown in Figure 4.6. The zeta potentials of thiol-organosilica nanoparticles are more negative than those of TEOS nanoparticles; typical values for MPMS, MPES and

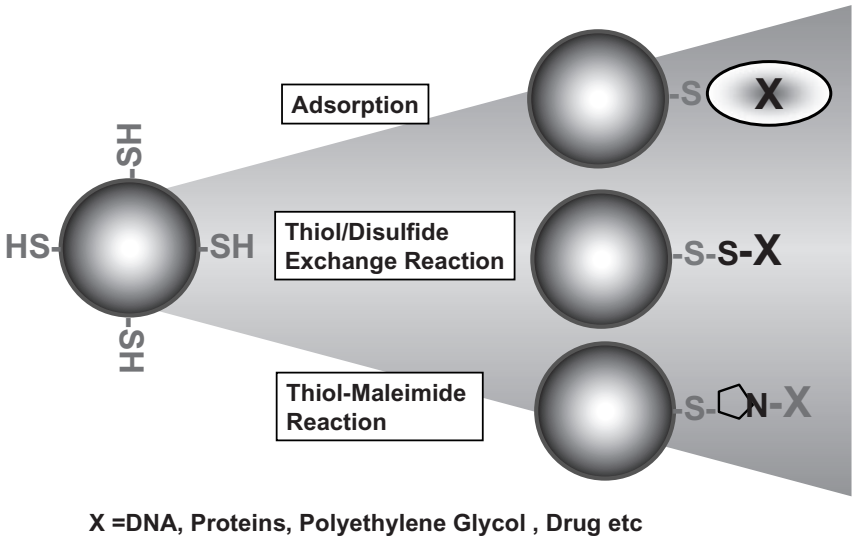

Figure 4.6 Strategies for the conjugation of biomolecules to thiol-organosilica nanoparticles.

MPDMS nanoparticles are −50.2, −49.4 and −50.6 mV, respectively. The zeta potentials of MPMS nanoparticles incorporating fluorescent dye (e.g. rhodamine red) within their interior are not markedly different from those nanoparticles without dye [50].

Recently, the surface properties of biofunctionalized thiol-organosilica nanoparticles were evaluated using methods such as flow cytometry, fluorescence image analysis and fluorescence microscopy, with TEOS nanoparticles as control [49, 50] (M. Nakamura *et al.*, unpublished results). In order to compare the surface properties of MPMS and TEOS nanoparticles, a dot–blot procedure was carried out [49]; when performed on glass slides, this allowed an evaluation of the nanoparticles' ability to adsorb proteins. In this procedure, identical amounts of each nanoparticle were deposited onto glass slides, reacted with a solution containing Cy3-conjugated anti-goat immunoglobulin G (IgG) antibody, and then examined with a fluorescence image analyzer. The MPMS nanoparticles showed a markedly higher intensity derived from Cy3-conjugated anti-goat IgG compared to TEOS nanoparticles, while their fluorescence intensity was threefold higher (Figure 4.7). Hence, *in vitro*, MPMS nanoparticles were able to absorb greater quantities of protein than TEOS nanoparticles. Slides with modified MPMS nanoparticles also demonstrated a substantially improved protein adsorption, making them potentially valuable for chip-based technology.

Flow cytometry was performed to compare the surface properties of MPMS and TEOS nanoparticles in solution. When the nanoparticle solutions were mixed with protein solutions containing either green fluorescent protein (GFP) or phycoery-

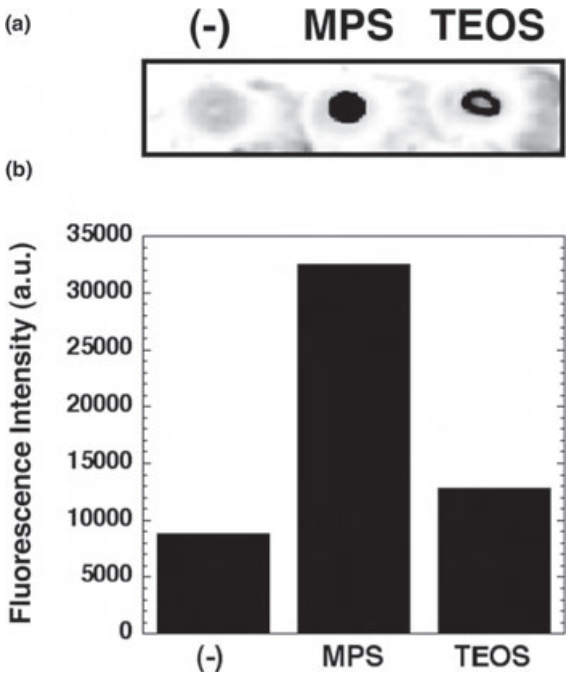

Figure 4.7 Dot–blot analysis of the ability of the silica nanoparticles to bind proteins. Nanoparticles dotted on glass slides were reacted with Cy3-conjugated anti-goat IgG and analyzed with a fluorescence image analyzer (a) and the intensities then plotted (b). The fluorescence intensity of MPMS nanoparticles was higher than that of TEOS nanoparticles (Reproduced with permission from Ref. [49]; © 2007, American Chemical Society.).

thrin-conjugated streptavidin, flow cytometry peaks for the MPMS nanoparticles were markedly shifted due to fluorescence from GFP compared to those of TEOS nanoparticles (Figure 4.8). Thus, in solution, the MPMS nanoparticles appeared to adsorb protein more effectively than the TEOS nanoparticles.

When the dispersion of MPMS nanoparticles modified with surface proteins was observed microscopically, the addition of GFP to a MPMS nanoparticle solution led to well-dispersed nanoparticles with a distinct fluorescence. This indicated that, compared to TEOS nanoparticles, the GFP modified the MPMS nanoparticles very effectively while retaining good dispersion. MPMS nanoparticles modified with GFP were also detected and observed using fluorescence microscopy.

In order to examine the surface modifications of other thiol-organosilica nanoparticles with proteins, the nanoparticle solutions were mixed with GFP/protein solutions and evaluated with fluorescence microscopy. The thiol-organosilica nanoparticles were shown to be well dispersed, with a distinct fluorescence (Figure 4.9), which indicated an effective modification with GFP and retention of dispersion; this contrasted with the TEOS nanoparticles, which showed no clear fluorescence (Figure 4.9).

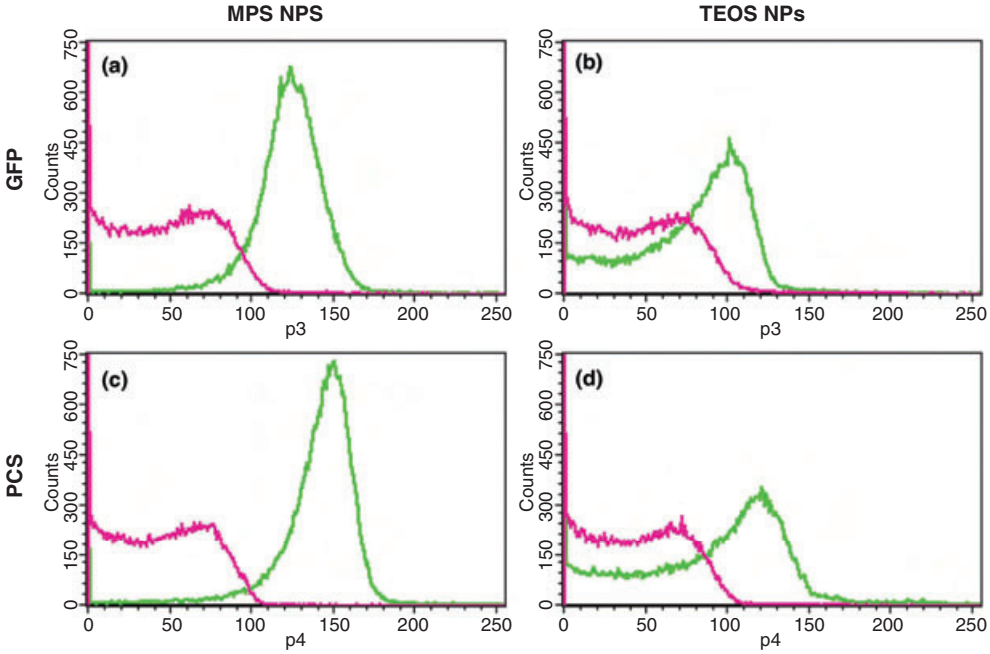

Figure 4.8 Flow cytometry analysis of silica nanoparticles surface-modified with proteins. MPMS nanoparticles (a, c) and TEOS nanoparticles (b, d) modified with GFP (a, b) or phycoerythrin-conjugated streptavidin (PCS) (c, d) were analyzed. Red lines and green lines indicated before and after reaction, respectively (Reproduced with permission from Ref. [49]; © 2007, American Chemical Society.).

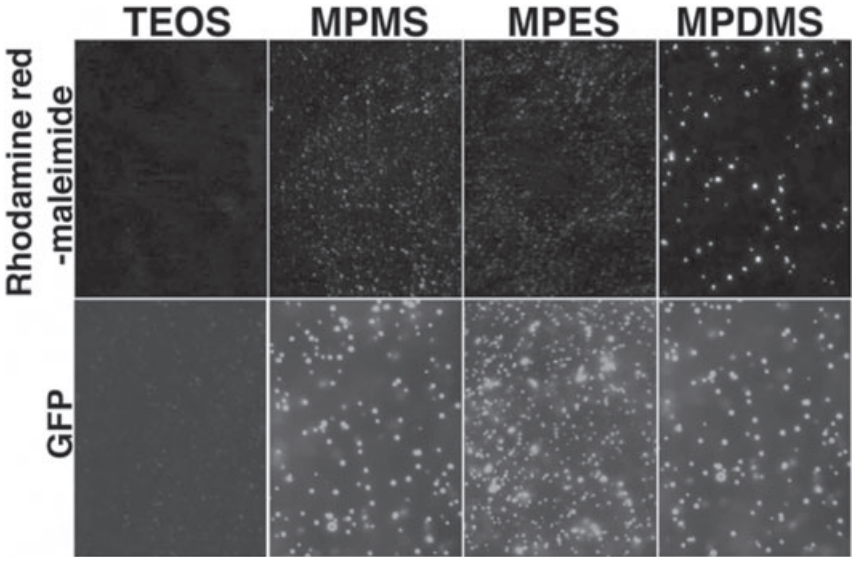

Figure 4.9 Fluorescence microscopy of surface-modified thiol-organosilica and TEOS nanoparticles. Nanoparticles were mixed with rhodamine red–maleimide (upper panels) and with GFP (lower panels) (Reproduced with permission from Ref. [50]; © 2008, American Chemical Society.).

The extent of protein adsorption at MPMS particles was examined using flow cytometry [52]. For this, the size-controlled particle solutions were mixed with different concentrations of fluorescein-conjugated anti-goat antibody solution for 10 min, and the protein concentrations evaluated based on changes in particle fluorescence. As shown in Figure 4.10a, a shift of peaks concurrent with increasing protein concentration was observed. When the geometric mean of each peak was plotted against added protein concentration, a clear concentration dependence was apparent, from 10 pg ml^{-1} to 100 ng ml^{-1} (see Figure 4.13b). These results showed not only that the fluorescent-dye-labeled proteins would bind very effectively and rapidly to the MPMS particles, in concentration-dependent manner, but also that the detection could be achieved with adequate sensitivity. Moreover, the protein concentrations could also be quantified. These properties of MPMS nanoparticles suggest that they might serve as a support for the multiplexed flow-cytometric assays of biological samples, including proteins and DNA.

Thiol residues react with a variety of functionalities (e.g. alkyl halides and maleimides) and easily form covalent bonds with other molecules. Recently, various maleimide-conjugated molecules (e.g. fluorescent dyes, streptavidin and PEG) have become commercially available. The reaction procedures between maleimide-conjugated molecules and the thiol residues of thiol-organosilicates are simple, and the conjugation efficiencies high. The surface biofunctionalization of thiol-organosilica nanoparticles prepared from MPMS, MPES and MPDMS with a maleimide-conjugated fluorescent dye was monitored to determine the ease with which the surface thiol residues could be modified. When the nanoparticles were reacted with rhodamine red–maleimide and characterized using fluorescence microscopy, they showed a prominent fluorescence (see Figure 4.9). As a control, TEOS nanoparticles were reacted with rhodamine red–maleimide, but no fluorescence was observed, suggesting that the surface modification was specific to thiol-organosilica nanoparticles, and that all three types of nanoparticle contained abundant thiol residues on their surfaces that could react with the dye molecules. When the thiol-organosilica nanoparticles were reacted with a NeutrAvidin–maleimide conjugate and characterized, the zeta potential was substantially less than that of unmodified MPMS nanoparticles, indicating the surface binding of NeutrAvidin via a thiol–maleimide reaction.

Thiol/disulfide exchange reactions are also useful for conjugating thiol residues between biomolecules and silica nanoparticles. Thiol-conjugated DNA is commercially available; additionally, some proteins display surface thiols of cysteine residues, while thiol residues can be introduced into proteins by using protein engineering technology. The thiol/disulfide exchange reaction can be applied to the biofunctionalization of thiol-organosilica nanoparticles via disulfide bonds formed by the oxidation of each thiol residue. In addition, the disulfide bonds can be controlled by reduction and oxidation. By using thiol residues on the surface, novel nanoparticle-based drug delivery and release systems have been proposed and, in some cases, demonstrated [81, 82]. The disulfide glutathione (GSH) is the most abundant thiol species in cytoplasm, and may serve as a major reducing

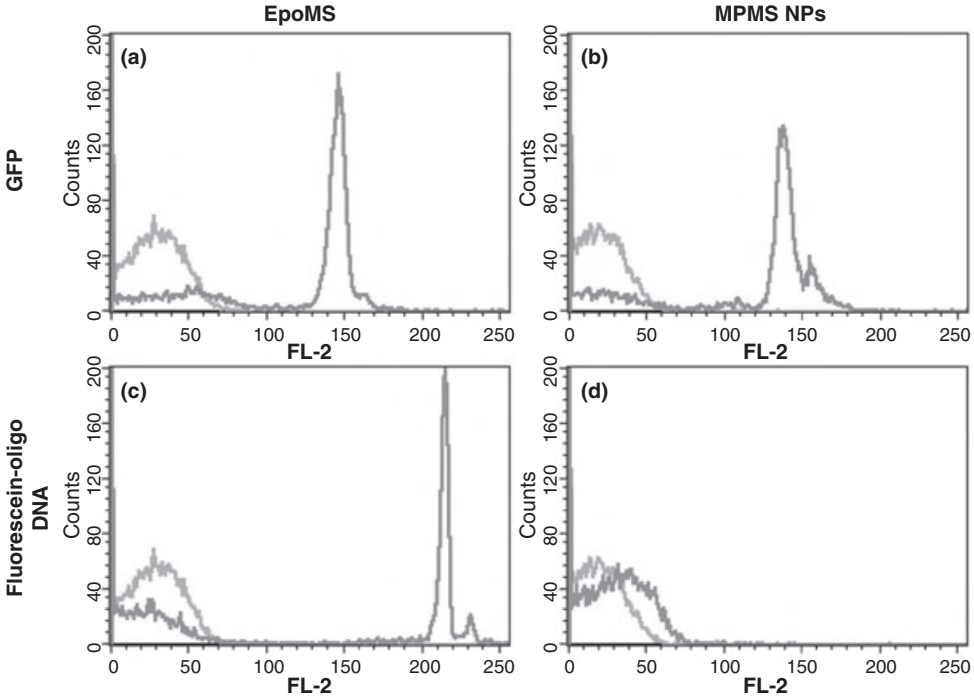

Figure 4.10 Flow cytometry analysis of silica particles surface-modified with protein and DNA. Epoxy-organosilica nanoparticles (a, c) and MPMS particles (b, d) modified with GFP (a, b) or fluorescein-labeled oligonucleotide (c, d) were analyzed. Red lines and green lines indicated before and after reaction, respectively (Reproduced with permission from Ref. [52]; © 2008, American Chemical Society.).

agent. By monitoring differences in the concentration of intracellular (1–10 m*M*) and extracellular GSH (2 μ*M* in plasma), the selective intracellular release of substances has been demonstrated [81–83]. When nanoparticles were coated with plasmid DNA via disulfide bonds, the DNA would be released via dissociation as intracellular disulfide reduction occurred [81]. Gold nanoparticles with layers containing thiolated BODIPY dyes have also been prepared, with the dyes being successfully released in living cells via a GSH-mediated system [82]. The results of studies with MPMS nanoparticles modified with surface thiol residues have suggested that they might be adapted as carriers in nanoparticle-based drug delivery and release systems, using GSH to achieve a selective intracellular release of drugs and biomolecules. Thus, the surface biofunctionalization of thiol-organosilica nanoparticles using thiol/disulfide exchange reactions shows great promise in a variety of biomedical applications.

4.3.1.2.3 **Epoxy-Organosilica Nanoparticles** Epoxy-organosilica nanoparticles prepared from EpoMS [52] contain interior and surface epoxy residues, with the latter being cationic and highly reactive. Biomolecules (including DNA and most proteins) are anionic, and possess amino groups that can form covalent linkages with the epoxy group. The zeta potentials of epoxy-organosilica nanoparticles are positive, indicating that the epoxy groups are present on the particle surface. In addition, the zeta potentials of epoxy-organosilica nanoparticles containing rhodamine B or tris-dichlororuthenium(II) hexahydrate (Rubpy) in their interiors were +44.8 and +46.1 mV respectively, and very similar to those of particles without dye (+46.1 mV); this indicates that incorporation of the dyes did not affect the zeta potential [52]. The epoxy-organosilica nanoparticles were the first to show a positive zeta potential as prepared, and therefore have great potential for surface biofunctionalization with biomolecules.

Flow cytometry was used to investigate the surface biofunctionalization of epoxy-organosilica nanoparticles with proteins and DNA. For this, epoxy-organosilica nanoparticle solutions were mixed with protein solutions containing GFP, or with DNA solutions containing fluorescein-labeled oligonucleotides. After mixing, the flow cytometry peaks for epoxy-organosilica nanoparticles were shifted markedly to the right, due to fluorescence from GFP or fluorescein-labeled oligonucleotides that were bound to the particles (Figure 4.10a and c). As a control experiment, when MPMS particles were treated with GFP the peak was shifted markedly to the right, due to fluorescence from GFP (Figure 4.10b). As reported previously [49, 50], MPMS particles bind with proteins much more strongly than do TEOS particles. The flow cytometry results indicated that both thiol-organosilica particles and epoxy-organosilica nanoparticles could bind strongly with GFP, although when MPMS particles were treated with fluorescein-labeled oligonucleotide no substantial peak shift was observed (Figure 4.10d). These findings indicated that epoxy-organosilica nanoparticles, unlike MPMS particles, would bind with both proteins and DNA, with the ability to bind to DNA seeming to be unique to epoxy-organosilica nanoparticles. Fluorescence microscopy studies were conducted to confirm the surface modification of epoxy-organosilica nanoparticles with protein or DNA, and to evaluate the dispersion of the surface-modified particles. Solutions of epoxy-organosilica nanoparticles mixed with GFP or DNA showed well-dispersed particles with a distinct fluorescence. In addition, the flow cytometry peaks for epoxy-organosilica nanoparticles surface-modified with GFP and fluorescein-labeled oligonucleotides were very sharp, while the peaks characteristic of aggregates were minor (Figure 4.10a and c). Overall, these results indicated that epoxy-organosilica nanoparticles retained good dispersion after surface modification. When such nanoparticles were surface-treated with bovine serum albumin (BSA), the zeta potential was reduced owing to the negative charge of the BSA, while the extent of reduction was increased with increasing BSA dose. These results indicated that the positive charge of the epoxy-organosilica nanoparticles was regulated by surface modification with negatively charged biomolecules.

4.3.2 Internal Biofunctionalization

4.3.2.1 An Overview

Although as-prepared silica nanoparticles appear not to have any unique function, such as the inherent fluorescence of quantum dots, they are easily biofunctionalized internally. Moreover, they may contain various types of functional molecules in their silica matrix, depending on the experimental requirements. For example, fluorescent silica nanoparticles can be prepared with various fluorescent dyes and applied in bioimaging, bioassays and nanomedicine. Traditional fluorescent dyes such as fluorescein, rhodamine, Cy3 and Cy5 have long been used in bioimaging applications, although their low fluorescence intensity and photostability make them unsuitable for high-sensitivity detection and real-time monitoring. Recently, new nanoparticles, including quantum dots, fluorescent latex particles and fluorescent silica nanoparticles, have been developed and shown great utility for these applications.

Quantum dots are composed of atoms of Groups II–IV or II–V of the Periodic Table, and are fluorescent as prepared. They have several advantages over traditional dyes, including broad excitation spectra, size-tunable fluorescence properties, a long fluorescence time and photostability. Quantum dots also have interesting optical properties that can be exploited in a range of photonic applications, including biological fluorescence imaging [9, 10, 17, 18, 84–87] and optoelectronic devices [88–94], and are becoming increasingly popular as a new material in biological fluorescence imaging. Unfortunately, quantum dots are difficult to prepare owing to their poor solubility and agglutination, while their surface-modification chemistry is still being investigated. In addition, the 'blinking' behavior of quantum dots – that is, the 'on'- and 'off'-switching of their luminescence emission by sudden stochastic jumps under continuous excitation – limits their application in bioimaging experiments that require the use of high-speed photography. Quantum dots also have low quantum yields and can be cytotoxic, which is a definite concern for *in vivo* applications. For example, Derfus and coworkers have shown that cadmium selenide quantum dots without a zinc sulfide shell were toxic to liver cells after exposure to UV light [95]. The emission wavelength of quantum dots also depends on the particle diameter – when the diameter of quantum dots becomes larger, the emission peak is shifted to a longer wavelength.

Another type of fluorescent nanoparticle probe is that of nanoparticles containing dyes, such as latex nanoparticles and silica nanoparticles. These nanoparticles contain large quantities of dye molecules inside a latex polymer or silica network, and provide a high intensity of fluorescence signal. Fluorescent latex nanoparticles (e.g. polystyrene nanoparticles) have been used in various biological applications, and are often doped with fluorescent dyes after nanoparticle synthesis. A typical preparation method involves the swelling of polymeric nanoparticles in an organic solvent and fluorescent dye solution. The most common latex polymer matrices include polystyrene, polymethyl methacrylate (PMMA), polylactic acid and polylactic-*co*-polyglycolic acid. The commercialization of fluorescent polymer or latex

nanoparticles and microspheres has facilitated their extensive use in biological applications. For example, fluorescent polymer microspheres have been used as immunofluorescent reagents, cell tracers and standardization reagents for microscopy and flow cytometry. However, because of their hydrophobicity, their tendency to agglomerate in aqueous medium, their large diameter (>100 nm), their observed swelling in organic solvents and their propensity toward dye leakage, latex nanoparticles are not suitable for bioanalysis.

Fluorescent silica nanoparticles possess several advantages over quantum dots and latex nanoparticles, including high fluorescence intensity, good photostability due to the exclusion of oxygen by silica encapsulation, size-independent fluorescence (i.e. nanoparticles of various diameters have the same emission wavelength), fluorescence-independent diameter (i.e. nanoparticles of various emission wavelengths have the same diameter), and good potential for surface biofunctionalization with various biomolecules. Fluorescent silica nanoparticles are highly hydrophilic and easy to prepare, separate, surface-modify and label. Fluorescent silica nanoparticles can be easily prepared through either reverse microemulsion or the Stöber method. Generally, hydrophobic fluorescent dyes are prepared using the latter approach, while hydrophilic fluorescent dyes are prepared using reverse microemulsion.

4.3.2.2 **Preparation of Fluorescent Silica Nanoparticles**

Various types of fluorescent silica nanoparticle have been developed; some details are summarized in Table 4.7. Fluorescent dyes are attached to silica nanoparticles by several means, as indicated in the table. For example, they can be incorporated

Table 4.7 Classification of fluorescent silica nanoparticles.

Method	Type of fluorescent dye	Type of silicates/silica nanoparticle
(a) Incorporation of a fluorescent dye during particle formation.		
(a-1) Doping method:	Various fluorescent dyes	Inorganic silica nanoparticles: TEOS
	Various fluorescent dyes	Organic silica nanoparticles: MPMS, MPES, MPDMS, EpoS
(a-2) Imposition method:	Isothiocyanates–fluorescent dye conjugates	APS
	Succinimidyl esters–fluorescent dye conjugates	APS
	Maleimide–fluorescent dye conjugates	MPMS, MPES, MPDMS
(b) Coupling of fluorescent dye to a particle surface.		
(c) Others; core–shell fluorescent silica nanoparticles.		

(Reproduced with permission from Ref. [52]; © 2008, American Chemical Society.).

during particle formation by simple doping of the dye during particle synthesis (doping method) [96–99], or by imposition of the dye on the silica network via the formation of bonds between the dye and a silane coupling reagent (imposition method) [100–103]. Alternatively, the dye may be coupled to a particle surface [104–107]. Recently, another type of fluorescent silica nanoparticles, core–shell fluorescent silica nanoparticles (CU dots), were reported [64].

4.3.2.2.1 **Imposition Method** Using imposition, silica nanoparticles containing fluorescent dye conjugated with APS have been prepared by means of a two-step reaction between the amino residue of APS and isothiocyanate-conjugated fluorescent dye [100–103]. First, APS is attached to isothiocyanate-conjugated fluorescent dye to form an APS–fluorescent dye conjugate which is then mixed with a synthetic mixture of TEOS nanoparticles. By means of imposition, fluorescent dyes that are difficult to incorporate into silica nanoparticles by doping can be incorporated efficiently into silica nanoparticles. Recently, fluorescent silica nanoparticles using more reactive and stable chemical residues, such as succinimidyl esters conjugated with fluorescent dyes, were prepared using the Stöber method [103]. Multifluorescent silica nanoparticles containing two fluorescent dyes and fluorescent-tuned silica nanoparticles have also been prepared. Fluorescent-tuned TEOS nanoparticles containing various amounts of rhodamine red were attached to a glass slide and observed by fluorescence microscopy to evaluate the intensity of each particle. The fluorescent-tuned TEOS nanoparticles show different fluorescence intensities which depended on the amount of fluorescent dye contained within the nanoparticles. These results suggested that the fluorescence intensities of TEOS nanoparticles could easily be tuned. Moreover, fluorescent-tuned TEOS nanoparticles could be observed clearly by fluorescence microscopy, even when their diameters were <500 nm. Multifluorescent TEOS nanoparticles containing fluorescein and DY-635 showed fluorescence derived from both fluorescent components, whereas fluorescent TEOS nanoparticles containing only fluorescein or DY-635 showed only a single fluorescence [103].

In flow cytometry experiments, fluorescent TEOS nanoparticles containing fluorescein (average diameter 300 nm) were directly detectable by their fluorescence upon excitation at 480/15 nm, had high fluorescence intensity, and were uniform (Figure 4.11a) [103]. Compared to the fluorescence intensities of commercially available nanosized markers (Fluoresbrite Plain YG 0.2 μm microspheres and Fluoresbrite Calibration Grade YG 0.5 μm microspheres), the fluorescence intensity of silica nanoparticles containing fluorescein (GeoMean of intensity 1311) was closer to that of the marker with 0.5 μm diameter (GeoMean of intensity 2322) than to that of the marker with 0.2 μm diameter (GeoMean of intensity 61.8). These results indicated that the specific fluorescence intensity of the TEOS nanoparticles was higher than that of commercial flow cytometry, because the ratio of fluorescence intensity to size of the TEOS nanoparticles was higher than that of the commercial markers.

Flow cytometry analysis was applied to fluorescent-tuned TEOS nanoparticles containing fluorescein, multifluorescent TEOS nanoparticles containing fluores-

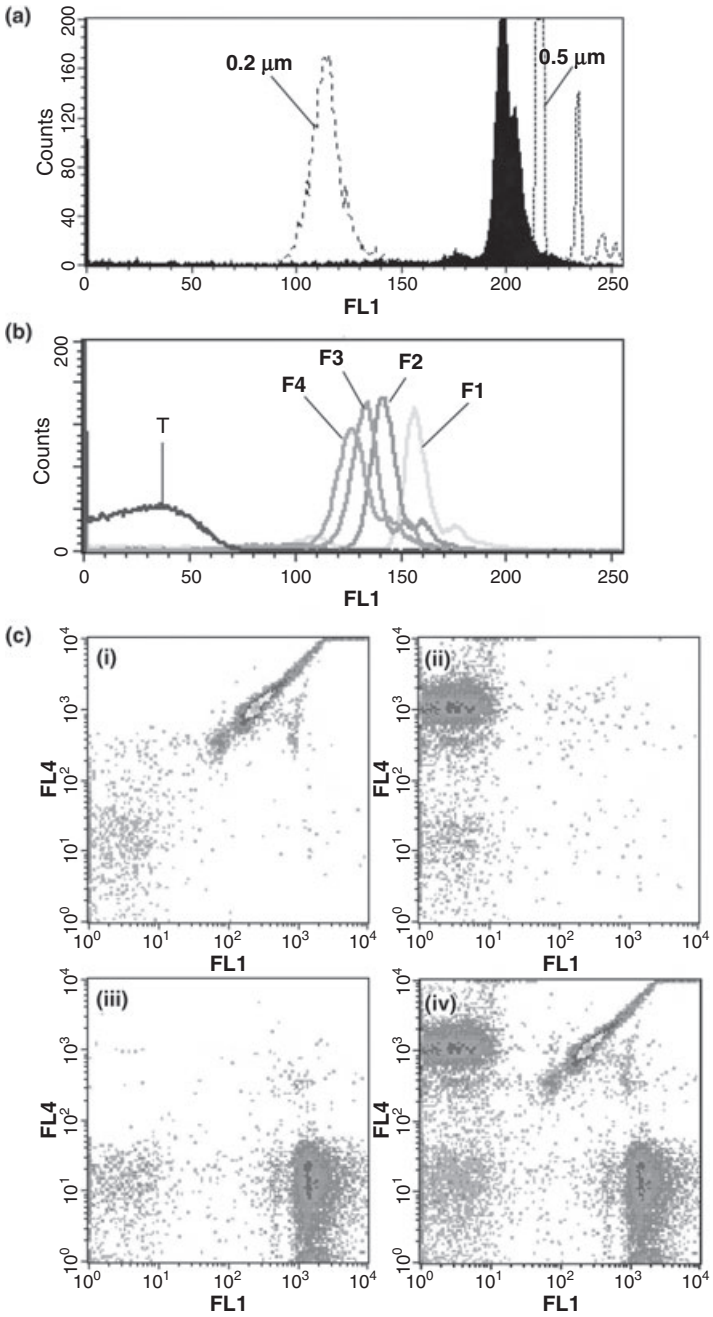

Figure 4.11 Flow cytometry analysis of fluorescent-tuned silica nanoparticles and multifluorescent silica nanoparticles. (a) Fluorescent silica nanoparticles containing fluorescein (shaded peak) were compared with nanosized markers with 0.2 and 0.5 µm diameters (unshaded peaks); (b) Fluorescent-tuned silica nanoparticles containing fluorescein (F1–F4) and nanoparticles without dye (T) were analyzed; (c) Multifluorescent silica nanoparticles containing DY-635 and fluorescein (panel a), DY-635 only (panel b) and fluorescein only (panel c) were analyzed under the same conditions. These findings are superimposed in (panel d) (Reproduced with permission from Ref. [103]; © 2007, American Chemical Society.).

cein and DY-635, and fluorescent TEOS nanoparticles containing just fluorescein or DY-635 [103]. Fluorescent-tuned TEOS nanoparticles containing fluorescein (Figure 4.11b, F1–F4) were detected as peaks with different fluorescence intensities according to the concentrations of fluorescent dye and APS conjugate used to prepare the particles. TEOS nanoparticles containing fluorescein (F1) had almost maximal intensity with the same diameter. These results suggest that the fluorescence intensity of the TEOS nanoparticles could be tuned and detected clearly using flow cytometry analysis. Multifluorescent TEOS nanoparticles (average particle diameter ~360 nm) containing fluorescein and DY-635 show two types of fluorescence signal upon excitations at 480/15 nm (FL1) and 620/30 nm (FL4; Figure 4.11c). Fluorescent TEOS nanoparticles containing only fluorescein showed a peak on FL1 but not FL4, whereas particles containing only DY-635 showed a peak on FL4 but not FL1. These results were the first to indicate that a single multifluorescent TEOS nanoparticle could produce a distinct pair of signals, and that a single fluorescent-tuned nanoparticle produced a single fluorescence signal, on flow cytometry analysis. Multifluorescent nanoparticles and fluorescent-tuned nanoparticles appear to be good candidates for multiplexed flow cytometric assays using nanosized beads to measure proteins and DNA, and also for nanosized calibrators. In addition, fluorescent nanoparticles with high intensity and multiple fluorescence would be useful for the highly sensitive detection and characterization of cells by flow cytometry.

Using fluorescence microscopy, the photostabilities of fluorescent TEOS nanoparticles containing rhodamine red, rhodamine red dye and Q-dot 605 particles were evaluated [103]. The single-particle fluorescence intensity of TEOS nanoparticles (111 351 from 175 889 a.u.) was more photostable than the fluorescence intensity of a fixed area of rhodamine red (116 675 from 1 104 731 a.u.). The Q-dot 605 particles showed high photostability, with occasional intensity changes due to photoblinking. After 250 s, the single-particle fluorescence intensities of Q-dot 605 particles and TEOS nanoparticles containing rhodamine red were 26 288 (from 25 562) and 111 351 (from 175.889) a.u., respectively, and the fluorescence of both Q-dot 605 particles and TEOS nanoparticles was visible. These results indicated that the fluorescent TEOS nanoparticles had high fluorescence intensity and good photostability, and that they exhibited sustained emission without photoblinking. Thus, fluorescent silica nanoparticles may be advantageous for bioimaging experiments requiring high-speed photography.

TEOS nanoparticles doped with three types of dye were prepared for fluorescence-resonance energy transfer (FRET) by means of imposition [55]. The dyes fluorescein, 5-carboxyrhodamine 6G (R6G) and 6-carboxy-X-rhodamine (ROX) were used to prepare these TEOS nanoparticles because their spectral features effectively overlap. In the triple-dye-doped TEOS nanoparticles, fluorescein was used as a common donor for R6G and ROX, whereas R6G acted both as an acceptor for fluorescein isothiocyanate (FITC) and as a donor for ROX. To prepare the nanoparticles, the three types of amine-reactive dye molecule were first covalently linked to APS, 5-(and-6)-carboxyfluorescein succinimidyl ester, 5-carboxyrhodamine 6G succinimidyl ester and 6-carboxy-X-rhodamine succinimidyl ester.

The three APS–dye conjugates were mixed at desired ratios and added to a synthesis mixture of TEOS nanoparticles via a modified Stöber method. The resulting nanoparticles exhibited high, multicolored fluorescence intensity under single-wavelength excitation and excellent photostability [55].

TEOS nanoparticles containing two types of fluorescent dye in a core–shell configuration have been prepared for chemical sensing applications [108]. Tetramethylrhodamine (TMR) isothiocyanate was conjugated to APS in an anhydrous nitrogen environment to create a reference dye. This conjugate was then hydrolyzed with TEOS to form the reference core particle via a modified Stöber method. Following the synthesis of these core particles, FITC was conjugated with APS to create a sensor dye, and then hydrolyzed with TEOS in the presence of the core TEOS particles to form the pH sensor layer on the core particles.

Preparations of thiol-organosilica nanoparticles internally biofunctionalized with fluorescent dye have also been studied [50]. Thiol-organosilica nanoparticles can be internally modified due to the presence of interior thiol residues, permitting the preparation of fluorescent silica nanoparticles using a one-pot synthesis. As described above, the preparations of fluorescent TEOS nanoparticles using APS and amine-reactive fluorescent conjugates are two-step processes. In contrast, the thiol-organosilica nanoparticles retain fluorescent dye–maleimide very well via a maleimide–thiol reaction, and therefore the thiol-organosilica nanoparticles are advantageous for the preparation of fluorescent silica nanoparticles because the preparation process can be reduced to one step.

The high fluorescence intensity of fluorescent thiol-organosilica nanoparticles has been evaluated and compared with that of quantum dots, as summarized in Table 4.8 [49]. The fluorescence intensity of the thiol-organosilica nanoparticles containing rhodamine (average diameter ca. 490 nm) is higher than that of the Q-dot 605 particles because of the larger diameter of the thiol-organosilica nanoparticles (excitation and emission wavelengths were 570 and 590 nm, respectively). The calculated specific fluorescence intensity, which is the theoretical fluorescence intensity divided by the particle volume of the thiol-organosilica nanoparticles, is sevenfold that of the quantum dots under the same conditions, and one fourth that of the quantum dots under optimum conditions (i.e. excitation and emission wavelengths of 350 and 605 nm, respectively). In another study [64], core–shell fluorescent silica nanoparticles (CU dots) were prepared and the fluorescence intensity of CU dots containing TMR isothiocyanate was compared with that of water-soluble CdSe/ZnS quantum dots using two-photon fluorescence correlation spectroscopy. The intensity of the CU dots was one-half to one-third that of the quantum dots. Fluorescent silica nanoparticles were of high fluorescence intensity; the fluorescence intensity of silica nanoparticles may have been enhanced relative to that of quantum dots by an improvement of the synthetic method and the selection of fluorescent dyes. The zeta potentials of thiol-organosilica nanoparticles and TEOS nanoparticles incorporating rhodamine red in their interior were not markedly different from those without dye. However, the value of zeta potential of MPMS nanoparticles surface-treated with rhodamine red–maleimide or NeutrAvidin–maleimide conjugates were substantially lower than that of surface-

Table 4.8 Comparison of fluorescence intensity of rhodamine red-containing silica nanoparticles prepared from MPS (MPSNPs-R) and from TEOS (TEOSNPs-R) and quantum dots 605 (Q-dot 605) under the optimum conditions for rhodamine red and Q-dot 605.

	MPS NPs-R	TEOS NPs-R	Q-dot 605	Q-dot 605
Concentration	$0.10\,mg\,ml^{-1}$	$0.11\,mg\,ml^{-1}$	40 n*M*	40 n*M*
Diameter (average) (nm)	490	200	20	20
Particle counts (counts ml^{-1})[a]	7.1×10^9	2.0×10^9	2.4×10^{13}	2.4×10^{13}
Measurement λ(Ex/Em) (nm)	570/590	570/590	570/590	350/605
Intensity	14.7	13.7	17.3	505.4
Intensity per particle[b]	6.8×10^{-8}	6.8×10^{-9}	7.2×10^{-13}	2.1×10^{-11}
Ratio	1	0.1	1.1×10^{-5}	3.1×10^{-4}
Specific intensity[c]	1.5×10^2	1.2×10^2	2.2×10^1	6.3×10^2
Ratio	1	0.8	0.15	4.2

a Concentration divided by weight of one particle; the weight of one particle was calculated from the volume of one particle: $4\pi(0.000290/2)^3/3$ (mm^3) × 2.3 (specific gravity).
b Intensity divided by the particle count.
c Intensity divided by the particle count and then by the volume of one particle.
(Reproduced with permission from Ref. [49]; © 2007, American Chemical Society.).

untreated particles. These results indicated that nanoparticles incorporating rhodamine red internally did not contain fluorescent dyes on the surface of the particles, and consequently the zeta potential was not affected.

In addition to thiol-organosilica nanoparticles with fluorescent dye, we have prepared fluorescent epoxy-organosilica nanoparticles using chemical crosslinking reagents, such as maleimides and succinimidyl esters, as described above [52]. The epoxy-organosilica nanoparticles containing various types of fluorescent dye–(3-aminopropyl)trimethoxysilane conjugates and fluorescent dye–MPMS conjugates showed high fluorescence. Fluorescent particles could be prepared from EpoMS with crosslinking reagents containing various types of dye.

4.3.2.2.2 **Doping Method** Using doping, fluorescent silica nanoparticles have been prepared by the simple addition of fluorescent dyes during particle synthesis. Rubpy-doped TEOS nanoparticles have been prepared either using reverse microemulsion [96, 98] or with the Stöber method [99]. The resulting Rubpy-doped TEOS nanoparticles were monodisperse, bright and photostable. Additionally, two luminophores – tris(2,2′-bipyridyl)osmium(II)bis(hexafluorophosphate) and Rubpy – were simultaneously entrapped inside TEOS nanoparticles at precisely controlled ratios by reverse microemulsion, and used for multiplexed signaling in bioanalysis [54]. The dual-luminophore-doped TEOS nanoparticles demonstrated specific ratios of luminescence intensities at two well-resolved wavelengths. The preparation of α, β, γ and δ-tetrakis (4-*N*-trimethylaminophenyl)-doped TEOS

nanoparticles and Nile Blue-doped TEOS nanoparticles by the Stöber method have also been reported [109, 110].

The preparation of organic dye-doped silica nanoparticles is difficult due to the highly hydrophobic nature of organic dyes, as compared to the hydrophilic surface of silica nanoparticles. In order to address this problem, TMR-doped TEOS nanoparticles have been prepared using dextran in a reverse microemulsion, and organic dye molecules then were linked to the dextran. This TMR–dextran complex was hydrophilic and could be increased in size and then easily entrapped inside silica pores. Two other organic dye molecules, fluorescein and AlexaFluor 647, have also been doped into TEOS nanoparticles using this method [97].

Organosilica nanoparticles recently were shown to be easily doped with fluorescent dye in the absence of crosslinking reagents [50, 52], and fluorescent dye-doped thiol-organosilica nanoparticles have been prepared via a one-pot synthesis. Thiol-organosilica nanoparticles were synthesized with rhodamine B by adding the fluorescent dye at the start of the nanoparticle synthetic reaction. As a control experiment, TEOS nanoparticles were also prepared with rhodamine B, but no fluorescence was observed from these nanoparticles. As shown in Figure 4.12a (lower panels), rhodamine-B-doped thiol-organosilica nanoparticles show high fluorescence, indicating a successful fluorescent-dye doping of the thiol-organosilica nanoparticles. The results also indicate that the doping of thiol-organosilica nanoparticles differs from that of TEOS nanoparticles. Fluorescent-tuned MPMS nanoparticles were analyzed by means of flow cytometry. MPMS nanoparticles prepared with rhodamine red–maleimide are detected as three peaks with different fluorescence intensities, depending on the concentration between 6.25 and 25 μM of rhodamine red–maleimide used to prepare the particles (emission at 585/42 nm, FL-2; Figure 4.12c). Rhodamine-B-doped thiol-organosilica nanoparticles were detected as six peaks (Figure 4.12d), with the peak at 200 mM being the highest compared to those prepared with rhodamine red–maleimide. These results showed that the fluorescent dye-doped silica nanoparticles could possess fluorescence intensities higher than those of fluorescent silica nanoparticles prepared with chemical crosslinking reagents, such as maleimides and succinimidyl esters. In addition to rhodamine B, Rubpy was also doped into thiol-organosilica nanoparticles very well. As shown in Figure 4.12e, Rubpy-doped thiol-organosilica nanoparticles were also detected as six peaks (emission at above 670 nm; FL-3). These results demonstrated that the cost to prepare fluorescent silica nanoparticles may be reduced by omitting crosslinking reagents and by using a one-pot synthesis. Such fluorescent nanoparticles with higher fluorescence also can be prepared.

The doping of epoxy-organosilica nanoparticles with fluorescent dye also has been studied [52]. Epoxy-organosilica nanoparticles were doped with rhodamine B and Rubpy using a one-pot synthesis. Fluorescent epoxy-organosilica nanoparticles were prepared using the Stöber method, and showed a high fluorescence intensity. Fluorescent-tuned epoxy-organosilica nanoparticles were also prepared and analyzed by means of flow cytometry; those containing rhodamine B were

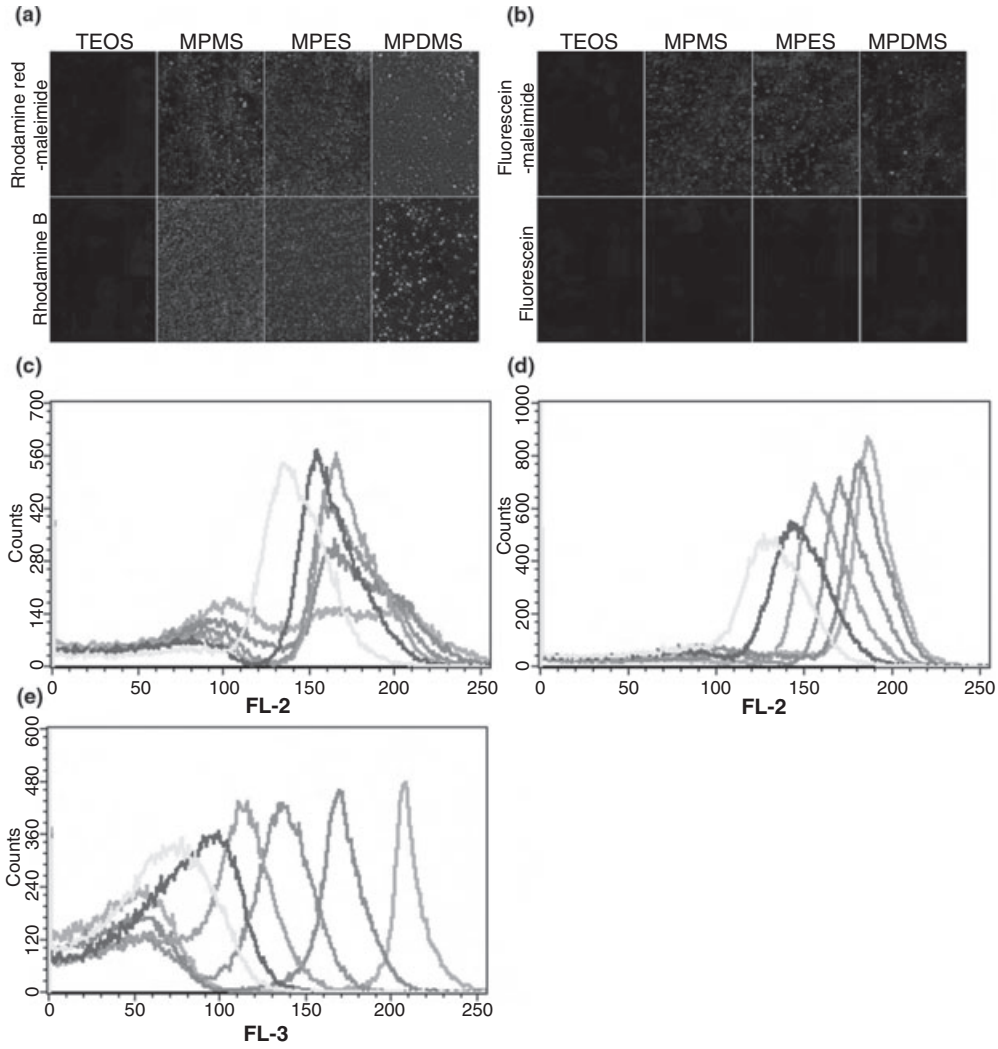

Figure 4.12 Fluorescence microscopy of internally functionalized fluorescent thiol-organosilica and TEOS nanoparticles. (a) Nanoparticles were internally functionalized with rhodamine red–maleimide (upper panels) and with rhodamine B (lower panels); (b) Nanoparticles were internally functionalized with fluorescein–maleimide (upper panels) and with fluorescein (lower panels); Flow cytometry analysis of fluorescent-tuned MPMS nanoparticles prepared with rhodamine red–maleimide (c) and rhodamine B-doped MPMS nanoparticles containing rhodamine B (d) and Rubpy (e). Fluorescent-tuned nanoparticles were prepared with 200 μM (green lines), 100 μM (red lines), 50 μM (light blue lines), 25 μM (orange lines), 12.5 μM (blue lines) and 6.25 μM (yellow lines) rhodamine red–maleimide, rhodamine B or Rubpy, respectively (Reproduced with permission from Ref. [50]; © 2008, American Chemical Society.).

detected as distinct peaks with different fluorescence intensities, depending on the concentration of fluorescent dye used to prepare the particles (emission at 585/42 nm, FL-2; Figure 4.13a). Fluorescent-tuned epoxy-organosilica nanoparticles containing Rubpy were also detected as peaks with different fluorescence intensities (emission above 670 nm, FL-3; Figure 4.13b). The peaks of fluorescent-tuned epoxy-organosilica nanoparticles containing rhodamine and fluorescent-tuned epoxy-organosilica nanoparticles containing Rubpy could be distinguished clearly as 12 spots in a plot of FL-3 versus FL-2 (Figure 4.13c). These results indicated that the fluorescence intensities of epoxy-organosilica nanoparticles could be tuned and clearly detected as distinct peaks by using flow cytometry analysis. The results also indicated that the sizes of fluorescent-tuned epoxy-organosilica nanoparticles were well controlled.

4.3.2.2.3 **Internal Biofunctionalization with Drugs** In addition to fluorescent dyes, anticancer drugs may be used for the internal biofunctionalization of silica nanoparticles to develop novel drug delivery systems and therapeutics. The water-insoluble photosensitizing anticancer drug 2-devinyl-2-(1-hexyloxyethyl) pyropheophorbide (HPPH) has been incorporated into ORMOSIL nanoparticles made from VTES, using reverse microemulsion. The resultant drug-doped nanoparticles were spherical and highly monodisperse, and the entrapped drug was more fluorescent in aqueous medium than was the free drug [48].

Silica nanoparticles also have been developed for two-photon photodynamic therapy. Both, a novel two-photon fluorescent dye, 9,10-bis[4′-(4″-aminostyryl)styryl] anthracene (BDSA) and HPPH, have been incorporated into ORMOSIL nanoparticles made from VTES, using reverse microemulsion. The two-photon-induced intraparticle FRET, based on the use of two-photon fluorescent aggregates as donors and a photosensitizing drug as an acceptor, has been demonstrated [111].

These ORMOSIL nanoparticles are internally biofunctionalized with drugs by simply doping in the drugs during the formation of nanoparticles, although nanoparticles internally biofunctionalized with drugs have also been prepared by imposition. A photodynamic therapy drug, 3-iodobenzyl-pyro, was conjugated with 4-(triethoxysilyl)-aniline using chemical coupling reagents to prepare iodobenzyl-pyro-silane [112]. The latter was then covalently incorporated into ORMOSIL nanoparticles made from VTES by reverse microemulsion, such that highly monodisperse aqueous dispersions of ORMOSIL nanoparticles with covalently incorporated drugs were formed. The spectroscopic and functional properties (i.e. generation of cytotoxic singlet oxygen) of the iodobenzyl-pyro-silane moieties were preserved in the prepared particles [112].

The porous interiors of silica nanoparticles can also be used as reservoirs for storing biomolecules. Some silica nanoparticles contain clear mesoporous structures inside their particles; for example, thiol-modified TEOS-based mesoporous silica nanoparticles have been demonstrated as a novel controlled-release delivery vehicle [113]. These mesoporous silica nanoparticles were used as reservoirs to soak up aqueous solutions of vancomycin and adenosine triphosphate. The

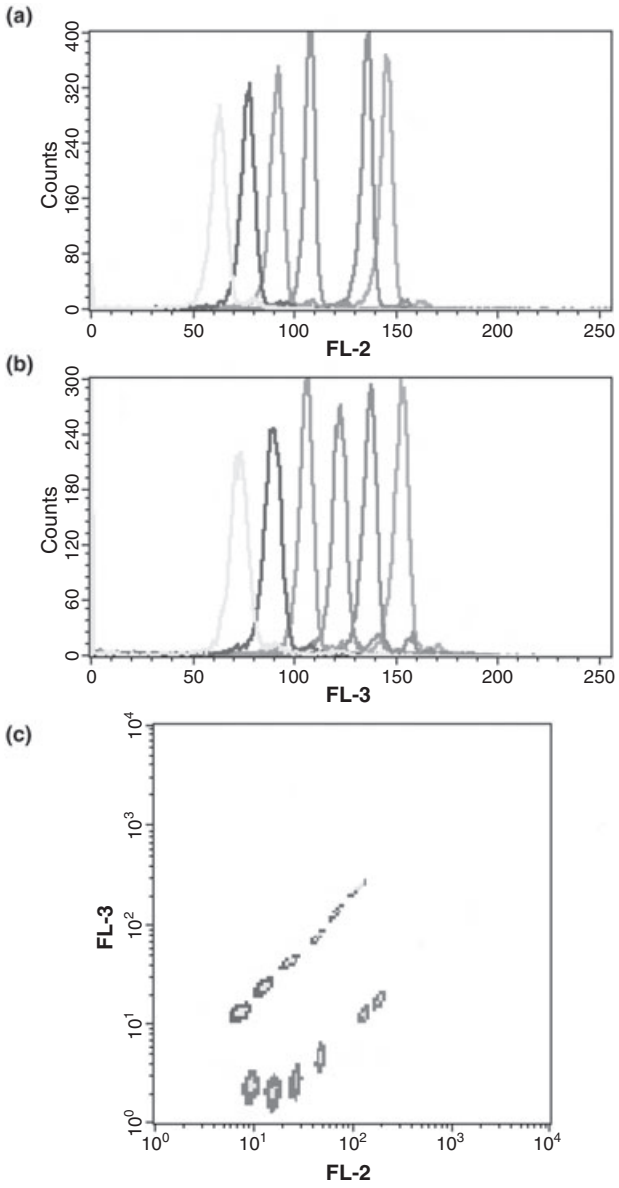

Figure 4.13 Flow cytometry analysis of fluorescent-tuned epoxy-organosilica nanoparticles containing (a) rhodamine B and (b) Rubpy; (c) A plot of FL-3 against FL-2 for epoxy-organosilica nanoparticles containing rhodamine B (red) and epoxy-organosilica nanoparticles containing Rubpy (blue) (Reproduced with permission from Ref. [52]; © 2008, American Chemical Society.).

openings of the mesopores of the drug/neurotransmitter-loaded mesoporous silica nanoparticles were then capped *in situ* by allowing pore surface-bound 2-(propyldisulfanyl) ethylamine functional groups to covalently capture water-soluble, mercaptoacetic acid-derivatized cadmium sulfide nanoparticles [85, 114]. The resulting drug-loaded mesoporous silica nanoparticles were applied to stimuli-responsive, controlled-release drug systems.

Fluorescent silica nanoparticles incorporating a hydrophobic anticancer drug, camptothecin (CPT), have also been reported [115]. Fluorescent silica nanoparticles were prepared from TEOS, FITC–APS conjugates, and 3-trihydroxysilylpropyl methylphosphonate as silica sources under a sol–gel process at high temperature. The resultant silica nanoparticles had mesoporous structures with pores of ~2 nm. After nanoparticle formation, CPT was incorporated into the pores of the particles by soaking the silica nanoparticles in concentrated CPT solution. In this case, the large surface areas and porous interiors of silica nanoparticles could be used as reservoirs for storing hydrophobic drugs.

4.4 Applications

Today, nanoparticles are at the leading edge of the rapidly developing field of nanotechnology, with the unique size-dependent properties of these materials making them both superior and indispensable in many areas. The biofunctionalization and multifunctionalization of nanoparticles has provided new opportunities in bioanalytical, biological imaging and medical applications [1–13]. Currently, fluorescent nanoparticles are used for nanoparticle-based detection and imaging applications due to their excellent fluorescence properties and photostability [4, 5, 8–10]. Yet, because of their size range, nanoparticles are very suitable for manipulations at the molecular level, such as cell–receptor binding for site-selective imaging and targeting, localization of encapsulated therapeutics for delivery, and the decoration of expression systems for substrate-based nanosensing.

Silica nanoparticles are advantageous for biofunctionalization as compared with other fluorescent nanoparticles such as quantum dots and latex nanoparticles, due to their unique properties. Novel organosilica nanoparticles also have many additional advantages for biomedical applications, and high possibilities exist for the further development of novel and advanced applications. To date, no published reports have summarized the advantages and applications of both inorganic and organic silica nanoparticles. Hence, in the following sections we will describe the advantages of biofunctionalized silica nanoparticles for biomedical applications, and also provide a representative overview of the biomedical applications of silica nanoparticles in fields of medical diagnosis, imaging and medical therapy. We will also highlight the possibilities for further development of silica nanoparticles in biomedical applications.

4.4.1
Advantages of Biofunctionalized Silica Nanoparticles

Fluorescence-based detection techniques have been widely used in modern biochemical research and biomedical applications. Primarily, although fluorescent dyes have been used in bioimaging applications, their molecular nature determines their limitations. In most cases, only one or a few fluorescent dyes can signal one biomolecule recognition event, and typically, only a limited number of fluorescent dyes can be attached to a biomolecule without interfering with its binding specificity or causing it to precipitate. Recently, new nanoparticles including quantum dots, fluorescent latex nanoparticles and fluorescent silica nanoparticles have been developed and have shown great utility for fluorescence applications. Whilst quantum dots have several advantages over traditional dyes, they also possess some disadvantages, such as the aforementioned photoblinking, size-dependent fluorescent wavelengths and cytotoxicity. Fluorescent latex nanoparticles have been employed in some biological applications but tend to agglomerate in aqueous medium owing to their hydrophobicity. Additionally, latex nanoparticles incur drawbacks of large size (>100 nm), swelling in organic solvents and dye leakage, thus making them unsuitable for bioanalysis.

Silica nanoparticles containing fluorescent dyes have also been applied as labeling reagents for biological applications. Compared to other fluorescent nanoparticles, silica nanoparticles possess several advantages; notably, they are easy to prepare, separate and biofunctionalize. Silica nanoparticles are more hydrophilic and biocompatible than are quantum dots or latex nanoparticles; they are not subject to microbial attack, and no swelling or porosity change occurs with changes in pH. Fluorescence wavelength and fluorescence intensity are tunable in single silica nanoparticles, and the type of fluorescence is independent of particle diameter. The fluorescence intensity and photostability of fluorescent silica nanoparticles are sufficient for the detection of a single fluorescent particle. Thus, fluorescent silica nanoparticles have shown great promise for use in a variety of biological applications.

The various types of silica nanoparticle, including inorganic and organic, contain a variety of reactive groups internally and on their surface, depending on the source of silicate. The surface charge (zeta potential) of silica nanoparticles is also dependent on the type of nanoparticle and the surface reactive groups. A broad spectrum of conjugation chemistry approaches are amenable to silica nanoparticles, which makes them advantageous for many applications. Some silica nanoparticles also show clear mesoporous structures inside their particles and, indeed, recent advances in the synthesis of mesoporous silica materials can be used to create silica nanoparticles with high surface areas and tunable pore diameters of 2–10 nm. Overall, these advantages have led to the development of a series of new delivery systems, in which various guest molecules such as pharmaceutical drugs can attached onto the silica nanoparticle surface, adsorbed into the mesopores, and later released into solution. Furthermore, novel silica nanoparticles such

as thiol-organosilica nanoparticles have also shown much promise for the improvement of nanoparticle performance in existing applications, as well as the establishment of novel applications. Here, we briefly review current efforts towards biochemical and biomedical applications of biofunctionalized silica nanoparticles.

4.4.2 Applications in Medical Diagnosis

Although very small, fluorescent dyes are of only limited applicability in biological assays because of their poor photostability and limited brightness. In order to improve assays using fluorescence, internally functionalized silica nanoparticles have been synthesized and applied as fluorescent probes for the detection of biological targets such as genes and proteins. In addition, silica nanoparticles can be used in high-throughput assays, as FRET, multifluorescent and fluorescence-tuned silica nanoparticles (barcoding nanoparticles) can be prepared and developed for multiplexed assays. The latter assays, when used for gene and protein arrays, have become an increasingly important tool in genomics and proteomics, since such arrays have great potential in global studies of DNA profiles, single nucleotide polymorphism assays, protein expression, protein profiling and protein–protein interactions.

4.4.2.1 Genes

The intense fluorescence signal of one nanoparticle can be used to great effect in DNA hybridization analysis, and this offers a distinct advantage over traditional, fluorescence-based techniques. Usually, a fluorescent dye molecule is used to signal the hybridization of DNA; however, fluorescent dyes are associated with certain problems such as low signal amplification and poor photostability. A novel assay based on the gold nanoparticle-promoted reduction of silver has been reported to detect target DNA down to a concentration of 50 f*M* [29]. Here, the signal of the single gold nanoparticle was greatly amplified, and an excellent detection limit achieved. However, the system required that the gold nanoparticle be coated with silver, a complicated process that reduces experimental reproducibility.

Alternatively, the application of fluorescent silica nanoparticles for ultrasensitive DNA detection has been reported [57]. Fluorescent TEOS nanoparticles of 60 nm diameter have the fluorescence intensity of thousands of dye molecules, which means that each gene hybridization will be reported by thousands of fluorophores. In this way, an ultrasensitive assay can be achieved by means of fluorescent silica nanoparticles. Typically, a biotinylated capture DNA sequence is immobilized onto a glass slide through an avidin–biotin linkage. This captured DNA sequence is the complement of a portion of the analyte sequence. Hybridization between the captured DNA and the analyte sequence is then carried out while the remaining target sequence hybridizes with a probe DNA sequence conjugated with fluorescent TEOS nanoparticles. One probe DNA hybridizes one target DNA, and thus brings

one fluorescent silica nanoparticle to the surface, leaving a large number of dye molecules on the surface for signaling. By monitoring the fluorescence intensity of these surface-bound fluorescent silica nanoparticles, the target DNA can be detected by probe DNA with high sensitivity. Through this assay, oligonucleotides ranging from 12 to 100 base pairs can be used as capture and detection probes to determine a detection limit. Moreover, a new DNA-sensing strategy incorporating a cationic conjugated polymer and DNA-immobilized silica nanoparticles in the 100 nm size range has also been reported which provides an over 110-fold signal amplification, thereby allowing the detection of target DNA sequences at a concentration of 10 p*M* with a standard fluorimeter [69].

4.4.2.2 **Detection of Proteins**

The application of fluorescent silica nanoparticles for protein detection has been reported. In such detection schemes, microarray slides spotted with serial dilutions of human immunoglobulin G (IgG)–biotin along with regular human IgG are reacted with avidin-labeled fluorescent TEOS nanoparticles. Strong fluorescence signals appear on spots containing IgG–biotin, whereas no signal is detected for human IgG negative controls [10]. The fluorescence intensity from each spot is proportional to the concentration of human IgG–biotin applied, allowing quantification of the amount of target by fluorescence measurement. Compared with experiments using conventional fluorescent dyes, the sensitivity of fluorescent silica nanoparticles increases detection sensitivity [10].

A sensitive fluoroimmunoassay for recombinant human interleukin-6 (IL-6) with functionalized Rubpy-doped fluorescent silica nanoparticles also has been reported [65]. In this strategy, IL-6 is measured from the specific interaction between captured IL-6 antigens and functionalized fluorescent silica nanoparticle-labeled anti-IL-6 monoclonal antibody. The calibration graph for IL-6 is linear over the range 20 to 1250 pg ml^{-1}, with a detection limit of 7 pg ml^{-1} [65].

4.4.2.3 **Detection of Microbes**

A rapid and ultrasensitive immunological method for bacterial detection using fluorescent silica nanoparticles has been developed [55, 66]. On the basis of the synthetic method for preparation of amino-modified fluorescent TEOS nanoparticles, silica nanoparticles are conjugated with antibodies against bacteria. Antibody-conjugated nanoparticles containing Rubpy can be used to detect a single *Escherichia coli* O157 : H7 bacterial cell quickly and accurately, without any signal amplification or enrichment; moreover, the assay takes only ~20 min to complete, thus making real-time detection of bacterial pathogens possible. The accurate enumeration of 1–400 bacterial cells in 1 g of spiked ground-beef samples has been demonstrated [54]. Furthermore, multicolor FRET TEOS nanoparticles have been applied for the multiplexed monitoring of bacteria species [66]. By changing the dye doping ratios of the energy-transfer dye series, a large FRET nanoparticle barcoding library can be built, permitting multiplexed detection of numerous bacterial pathogens. This method can achieve rapid diagnosis through elimination of the sample enrichment and amplification steps required with currently used

cell culture and polymerase chain reaction-based methods. Therefore, FRET silica nanoparticles show much promise for the development of multiplexed bacterial detection methods.

4.4.2.4 Multiplexed Assays

The demand for gene profiling and high-throughput screening has driven the development of novel bioprobes for multiplexed bioassays. Fluorescent silica nanoparticles have recently been used as novel substrates for multiplexed signaling. The type, combination and concentration of the fluorescent dyes in these particles can be changed, and different barcoding nanoparticles, various types of fluorescent silica nanoparticle, multifluorescent silica nanoparticle and fluorescent-tuned silica nanoparticle can be prepared, each of which exhibits a unique optical signature [50, 52, 54, 55, 66]. Figures 4.11 to 4.13 demonstrate the flow cytometry results obtained with multifluorescent nanoparticles and fluorescent-tuned nanoparticles, as well as the multiplexing potential of these probes [50, 52]. The FRET silica nanoparticles exhibited high multicolor fluorescence intensity under a single-wavelength excitation and excellent photostability [55]. Overall, these various types of fluorescent nanoparticle will be useful for multiplexed assay development.

4.4.3 Imaging

Fluorescent silica nanoparticles are very promising for imaging applications, including cellular, tissue and whole-animal fluorescence imaging, because they have high fluorescence intensity and good photostability. Fluorescent silica nanoparticles have been used to image target cells, such as cancer cells, *in vitro*. Anti-human CD10 antibody-conjugated TEOS nanoparticles containing Rubpy were used to label human leukemia cells; a control experiment using bare nanoparticles showed no effective labeling [78]. In addition to antibody-mediated recognition, other affinity reagents, such as receptor ligands and recognition peptides, have also been applied in silica nanoparticle imaging strategies. Folic acid, a small vitamin which is recognized by many cancer cells, has been attached to fluorescent silica nanoparticles and labeled SCC-9 cells [116], while the cell-penetrating peptide TAT, when conjugated to TEOS nanoparticles containing FITC, can be used to label human lung adenocarcinoma (A549) cells *in vitro* [68]. Antibody immunoglobulin E (IgE) and its cell-surface receptor, Fc RI, are known to form a reversible, but tight, complex. The typical labeling of rat basophilic leukemia (RBL) mast cells has been demonstrated with IgE-adsorbed fluorescent TEOS nanoparticles. In equatorial sections of the cells, only the periphery of the cell was labeled, as would be expected for the transmembrane Fc RI receptor. As a control experiment, RBL mast cells were incubated overnight with IgE before incubation with bare silica nanoparticles. In this case, very little peripheral staining is observed, indicating minimal nonspecific interaction between the silica nanoparticles and the cell surface [64].

Moreover, silica nanoparticles have been applied in functional imaging analysis to evaluate apoptosis. Annexin V binds with phosphatidylserine that is externalized from the inner to the outer membrane (this is an early and major event in the apoptotic process). Annexin V-conjugated TEOS nanoparticles containing rhodamine B specifically recognize early-stage apoptotic cells through binding between Annexin V and phosphatidylserine on the outer membrane of apoptotic cells [79]. This method was also used to monitor the increase in the number of early-stage apoptotic cells, along with an extended induction time of apoptosis. Compared to conventional fluorochromes for staining apoptotic cells (such as Cy3-labeled Annexin V), Annexin V-conjugated TEOS nanoparticles containing rhodamine B possess much better photostability.

TEOS nanoparticles containing TMR in their core and fluorescein in their shell have been applied in pH-based imaging and sensing [108]. Fluorescein exists in several protonation states with changing pH, and fluorescence sensing based on the pH-dependent change in quantum efficiency exhibited by fluorescein has been evaluated, using TMR as an internal standard. Intracellular imaging and sensing capabilities of these particles in rat basophilic leukemia mast cells has been demonstrated.

Fluorescence images of culture cells using fluorescent dye derived from photosensitizing photodynamic therapy drugs have been reported. Colon-26 cells treated overnight with ORMOSIL nanoparticles containing 3-iodobenzyl-pyro, an iodinated photosensitizer, show clear fluorescence, indicating substantial uptake of nanoparticles by cells [112]. 2-Devinyl-2-(1-hexyloxyethyl) pyropheophorbide, a water-insoluble photosensitizer, has also been incorporated in ORMOSIL nanoparticles, and the resulting nanoparticles showed confocal fluorescence images of HeLa tumor cells and UCI-107 [48]. ORMOSIL nanoparticles containing both a novel two-photon fluorescent dye, 9,10-bis[4′-(4″-aminostyryl)styryl]anthracene (BDSA), and a photosensitizing photodynamic therapy drug, 2-devinyl-2-(1-hexyloxyethyl) pyropheophorbide (HPPH), have produced two-photon excited fluorescence images of HeLa cells [111].

As preliminary experiments to evaluate the imaging potential toxicity of fluorescent silica nanoparticles *in vivo*, mice were injected intraperitoneally with fluorescent epoxy-organosilica nanoparticles (up to 3 mg per mouse) [52]. Peritoneal cells were harvested and examined by fluorescence and light microscopy, and cells showing fluorescence were observed clearly (Figure 4.14a–c). The peritoneal cells also were examined by electron microscopy. As shown in Figure 4.14b (panel d), cells containing many particles in the cytoplasm were observed. Furthermore, many epoxy-organosilica nanoparticles were contained in a large endosome, as shown in Figure 4.14b (panel e). A single epoxy-organosilica nanoparticle was also observed in one endoplasm (Figure 4.14b, panel f). Epoxy-organosilica nanoparticles located in the cytosol were also observed, but no indications of cell necrosis or apoptosis were observed histologically. These results indicated that fluorescent epoxy-organosilica nanoparticles could be used for labeling cells without risk of toxicity. As shown in Figure 4.14b, panel g, an endosomal membrane was observed around the smaller of the two particles in the figure (right), whereas no endosomal

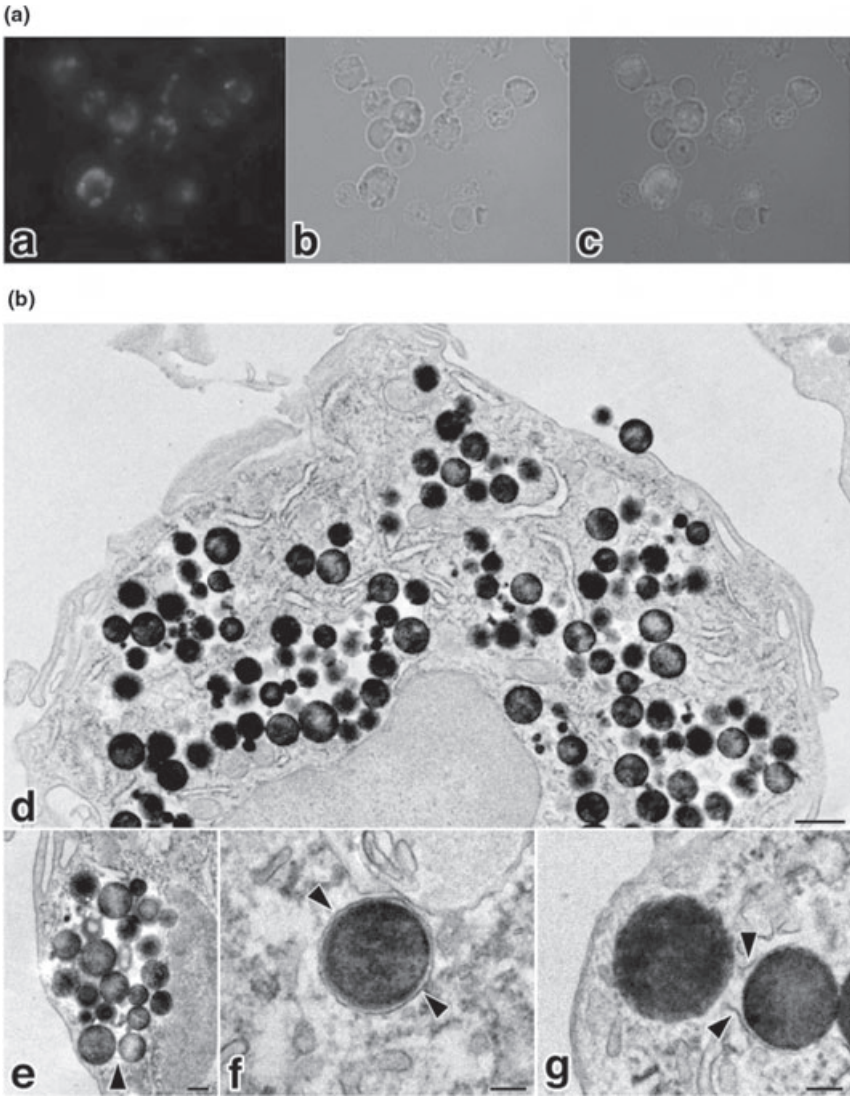

Figure 4.14 Fluorescence microscopy and electron microscopy of mouse peritoneal cells containing fluorescent epoxy-organosilica nanoparticles containing rhodamine B. (a) Peritoneal cells labeled with fluorescent epoxy-organosilica nanoparticles containing rhodamine B were observed with excitation at 520/15 nm (panel a) or under a bright field (panel b); panel c shows the merged image; (b) Electron microscopy images of mouse peritoneal cells containing fluorescent epoxy-organosilica nanoparticles; panel d shows a macrophage containing epoxy-organosilica nanoparticles in the cytoplasm; the particles were observed in either endosomal membranes (arrowheads) (panels e, f and g) or the cytosol (panel g). Scale bars: panel d = 500 nm; panel e = 200 nm; panels f and g = 100 nm (Reproduced with permission from Ref. [52]; © 2008, American Chemical Society.).

membrane was observed around the larger particle (left). These findings indicate that some epoxy-organosilica nanoparticles escaped from the endoplasm to the cytosol [117]. The surface charge of nanoparticles strongly affected the *in vivo* metabolism, distribution, internalization and intracellular localization of the particles. The use of positively or negatively charged nanoparticles to target specific locations has been reported; positively charged nanoparticles were internalized rapidly by means of the clathrin-mediated pathway, whereas negatively charged nanoparticles showed a lower rate of endocytosis and did not utilize the clathrin-mediated endocytosis pathway [118]; that is, the surface charge affected the rate of internalization into cells. The surface charge can also be used to change the intracellular localization: nanoparticles that are positively charged at endosomal pH (pH 4–5) escape from the endosomal compartment to the cytoplasm, whereas those that are negatively charged at pH 4 are retained mostly in the endosomal compartment [119]. The fluorescent epoxy-organosilica nanoparticles were positively charged as prepared, and their surface charge could be regulated by modification with biomolecules. The relationships between the surface properties of nanoparticles (such as their aptitude for modification with biomolecules and their zeta potential) and the interaction of the particles with cells are of major importance for the development of drug delivery systems. Both, epoxy-organosilica nanoparticles (positively charged) and thiol-organosilica nanoparticles (negatively charged), functionalized internally and on their surface, are expected to be useful for such applications.

4.4.4
Applications in Medical Therapy

Nanoparticles offer great potential and a promising approach to deliver therapeutic agents to targeted organs or cells, and have been actively developed for applications in cancer therapy. Micelles, liposomes and polymeric nanoparticles have each been used for effective drug administration, but suffer from substantial limitations such as poor thermal and chemical stability, rapid elimination by the immune system and toxicity [120]. Silica nanoparticles offer a promising alternative because of their intrinsic hydrophilicity, biocompatibility and nontoxicity, as well as the excellent protection they provide for their encapsulated molecules.

4.4.4.1 Drug Delivery

The mesoporous structures of silica nanoparticles have several attractive features for use in the delivery of water-insoluble drugs. These particles have large surface areas and porous interiors that can be used as reservoirs for storing hydrophobic drugs. The pore size and environment can also be tailored to selectively store different molecules of interest [121, 122], while the size and shape of the particles can be tuned to maximize cellular uptake. Unlike polymer-based nanoparticles, these robust inorganic materials can tolerate many organic solvents [123]. Silica-based materials have been successfully used as drug-delivery vectors [124, 125], gene transfection reagents [126], cell markers [127] and carriers of molecules [113].

Thiol-modified, TEOS-based mesoporous silica nanoparticles loaded with drugs in their mesopores and capped with cadmium sulfide nanoparticles have been demonstrated as a stimuli-responsive, novel controlled-release delivery carrier [115]. The linkages between the mesoporous silica nanoparticles and the cadmium sulfide nanoparticles are disulfide bonds, which are chemically labile in nature and can be cleaved with various disulfide-reducing agents, such as dithiothreitol and mercaptoethanol. Hence, the release of the cadmium sulfide nanoparticle caps from the drug-loaded mesoporous silica nanoparticles can be regulated through the introduction of various amounts of release triggers.

Fluorescent, TEOS-based mesoporous silica nanoparticles loaded with CPT have been delivered successfully into a human pancreatic cancer cell line, PANC-1, where they induced cell death. Uptake of the particles by cancer cells was monitored by fluorescence microscopy, and intracellular localization of nanoparticles was suggested, as observed in acidic organelles [115].

4.4.4.2 **Gene Delivery**

Fluorescent silica nanoparticles can also act as nonviral vectors for gene delivery and biophotonics to optically monitor intracellular trafficking and gene transfection. ORMOSIL nanoparticles, encapsulating fluorescent dyes and surface-functionalized by cationic amino groups, have been shown to not only bind and protect plasmid DNA from enzymatic digestion but also transfect cultured cells and deliver DNA to the nucleus [128]. Amino-modified ORMOSIL nanoparticles containing fluorescent dyes bound with DNA on the surface of the nanoparticles through positively charged surface amino groups have been prepared. The resulting particles show FRET between the dye (donor) intercalated in DNA on the surface of nanoparticles and a second dye (acceptor) contained inside the nanoparticles. *In vitro* imaging by fluorescence confocal microscopy shows that cells efficiently uptake the nanoparticles into the cytoplasm, and that the nanoparticles deliver DNA to the nuclei. The use of plasmid-encoding-enhanced GFP allowed the process of gene transfection to be demonstrated in cultured cells, and the development of a multidisciplinary approach for the production of fluorescent ORMOSIL nanoparticles for the gene delivery applications described above.

The amino-modified ORMOSIL nanoparticles have been applied to gene delivery *in vivo* [129]. Here, the intraventricular injection of amino-modified ORMOSIL nanoparticles complexed with plasmid DNA encoding for enhanced GFPs in the mouse brain resulted in the effective transfection and expression of enhanced GFPs in neuronal-like cells in periventricular brain regions, and also in the subventricular zone. In addition, transfection with ORMOSIL nanoparticles complexed with a plasmid expressing the nucleus-targeting fibroblast growth factor receptor type 1 resulted in the modulation of the replication cycle of the stem progenitor cells in the subventricular zone.

These studies provide the groundwork for the use of ORMOSIL nanoparticle formulations for *in vivo* gene transfer into the central nervous system, and demonstrate that ORMOSIL nanoparticles can potentially provide a safe and efficient mechanism for *in vivo* gene therapy. The results of this nanomedicine approach

using ORMOSIL nanoparticles as a nonviral gene delivery platform are promising for the effective therapeutic manipulation of neural stem progenitor cells, as well as for *in vivo* targeted brain therapy.

4.4.4.3 Photodynamic Therapy

Photodynamic therapy (PDT) is based on the concept that photosensitizers (PS) can be localized in malignant tissues and then activated with appropriate wavelength of light, causing the PS to transfer their excess energy to surrounding molecular oxygen, resulting in the generation of reactive oxygen species such as free radicals and singlet oxygen ($^1O_2$), which can damage the malignant cells and tissues [130, 131]. PDT is a noninvasive treatment used for several types of cancer, as well as for cardiovascular, dermatological and ophthalmic conditions. The advantage of PDT lies in its inherent dual selectivity. First, selectivity is achieved by preferential localization of the PS in target tissue (e.g. cancerous tissues); second, the photoirradiation and subsequent photodynamic reactions can be limited to a specific area of interest. Selectivity can be further enhanced by combining the PS with molecular delivery systems, or by conjugating them with targeting agents such as tumor antibodies, integrin antagonists or carbohydrates. Although PDT is emerging as the treatment of choice for many cancer patients, easily injectable formulations of PS have yet to be developed, since most of these are hydrophobic in nature. Silica nanoparticles have been proposed as potential carriers for PS; they are particularly attractive for this application because they provide aqueous stability, are appropriately sized for the passive targeting of tumor tissues by means of the 'enhanced permeability and retention' effect [132, 133], and are amenable to bioconjugation approaches to enhance both bioavailability and tumor targeting [134]. ORMOSIL nanoparticles containing various PS such as 2-devinyl-2-(1-hexyloxyethyl) pyropheophorbide, BDSA, HPPH [111] and 3-iodobenzyl-pyro [112] have been prepared. The nanoparticles containing PS are efficiently taken up by tumor cells *in vitro*, and the light irradiation of such impregnated cells results in substantial cell death *in vitro* [111, 112].

4.5 Summary and Future Perspectives

Recent developments of novel silica nanoparticles, their internal biofunctionalization and surface biofunctionalization and the development of their biomedical applications have been described. Inorganic silica nanoparticles (classical silica nanoparticles prepared from TEOS) are biofunctionalized using various methods, and have advanced greatly in imaging, labeling and sensing applications. ORMOSIL nanoparticles are well developed for gene delivery and PDT applications, whereas functional organosilica nanoparticles such as thiol-organosilica nanoparticles have been developed and characterized only recently. Functional organosilica nanoparticles allow for biofunctionalization using simple strategies, and therefore have great potential for various applications and consequently are under investigation

to optimize their use in unique biomedical applications. Unlike other functional nanoparticles, including quantum dots and iron oxide nanoparticles, silica nanoparticles do not have inherent functionalities such as optical signals for sensitive imaging applications. However, they are easily functionalized through both surface and internal biofunctionalization. Along with the development of novel silica nanoparticles such as organosilica nanoparticles, the ability to multifunctionalize silica nanoparticles has also progressed substantially. Additionally, the inherent unique properties of silica nanoparticles, such as fine-tuning the particle's diameter and nontoxicity, can overcome the limitations of other functional nanoparticles and can be generalized to create excellent nanomaterials that are responsive to various biomedical requirements. Once the safety of silica nanoparticles for humans is confirmed, the intravenous injection of silica nanoparticles into the human body can be envisaged to both image and treat diseased cells, tissues and organs. Moreover, the multifunctionalization capabilities of silica nanoparticles can also be utilized to create silica nanoparticles that possess both diagnostic and therapeutic functions in a single nanoparticle, thus eliminating the barrier between diagnosis and therapy. In addition, novel platforms based on multiplexing with fluorescent silica nanoparticles, such as FRET silica nanoparticles, could enable high-throughput bioassays for protein and gene detection and quantification. When silica nanoparticles are internally and surface-functionalized with the ability to bind to target molecules with specificity and high affinity, and when high photostability and fluorescence intensity of these silica nanoparticles are achieved, in cooperation with the development of bioanalytical instrumentation, then silica nanoparticles will greatly influence the areas of bioanalysis, molecular imaging, nanobiotechnology and nanomedicine.

References

1 Thaxton, C.S., Georganopoulou, D.G. and Mirkin, C.A. (2006) Gold nanoparticle probes for the detection of nucleic acid targets. *Clinica Chimica Acta*, **363**, 120–6.

2 Cheng, M.M., Cuda, G., Bunimovich, Y.L., Gaspari, M., Heath, J.R., Hill, H.D., Mirkin, C.A., Nijdam, A.J., Terracciano, R., Thundat, T. and Ferrari, M. (2006) Nanotechnologies for biomolecular detection and medical diagnostics. *Current Opinion in Chemical Biology*, **10**, 11–19.

3 Thaxton, C.S., Georganopoulou, D.G. and Mirkin, C.A. (2006) Gold nanoparticle probes for the detection of nucleic acid targets. *Clinica Chimica Acta*, **363**, 120–6.

4 Nie, S., Xing, Y., Kim, G.J. and Simons, J.W. (2007) Nanotechnology applications in cancer. *Annual Review of Biomedical Engineering*, **9**, 257–88.

5 Cai, W. and Chen, X. (2007) Nanoplatforms for targeted molecular imaging in living subjects. *Small*, **11**, 1840–54.

6 Gupta, A.K., Naregalkar, R.R., Vaidya, V.D. and Gupta, M. (2007) Recent advances on surface engineering of magnetic iron oxide nanoparticles and their biomedical applications, *Nanomedicine*, **2**, 23–39.

7 Gupta, A.K. and Gupta, M. (2005) Synthesis and surface engineering of iron oxide nanoparticles for biomedical applications. *Biomaterials*, **26**, 3995–4021.

8 Tan, W., Wang, K., He, X., Zhao, J., Drake, T., Wang, L. and Bagwe, R.P. (2004) Biotechnology based on silica nanoparticles. *Medicinal Research Reviews*, **24**, 621–38.

9 Wang, L., Wang, K.M., Santra, S., Zhao, X.J., Hilliard, L.R., Smith, J.E., Wu, J.R. and Tan, W.H. (2006) Watching silica nanoparticles glow in the biological world. *Analytical Chemistry*, **78**, 646–54.

10 Yao, G., Wang, L., Wu, Y., Smith, J., Xu, J., Zhao, W., Lee, E. and Tan, W. (2006) FloDots: luminescent nanoparticles. *Analytical and Bioanalytical Chemistry*, **385**, 518–24.

11 Sinha, R., Kim, G.J., Nie, S. and Shin, D.M. (2006) Nanotechnology in cancer therapeutics: bioconjugated nanoparticles for drug delivery. *Molecular Cancer Therapeutics*, **5**, 1909–17.

12 Moghimi, S.M., Hunter, A.C. and Murray, J.C. (2005) Nanomedicine: current status and future prospects. *FASEB Journal*, **19**, 311–30.

13 Liu, Y., Miyoshi, H. and Nakamura, M. (2007) Nanomedicine for drug delivery and imaging: a promising avenue for cancer therapy and diagnosis using targeted functional nanoparticles. *International Journal of Cancer*, **120**, 2527–37.

14 Watson, A., Wu, X. and Bruchez, M. (2003) Lighting up cells with quantum dots. *Biotechniques*, **34**, 296–303.

15 Chan, W.C., Maxwell, D.J., Gao, X., Bailey, R.E., Han, M. and Nie, S. (2002) Luminescent quantum dots for multiplexed biological detection and imaging. *Current Opinion in Biotechnology*, **13**, 40–6.

16 Jaiswal, J.K., Mattoussi, H., Mauro, J.M. and Simon, S.M. (2003) Long-term multiple color imaging of live cells using quantum dot bioconjugates. *Nature Biotechnology*, **21**, 47–51.

17 Larson, D.R., Zipfel, W.R., Williams, R.M., Clark, S.W., Bruchez, M.P., Wise, F.W. and Webb, W.W. (2003) Watersoluble quantum dots for multiphoton fluorescence imaging in vivo. *Science*, **300**, 1434–6.

18 Dubertert, B., Skourides, P., Norris, D.J., Noireaux, V., Brivanlou, A.H. and Libchaber, A. (2002) In vivo imaging of quantum dots encapsulated in phospholipid micelles. *Science*, **298**, 1759–62.

19 Ballou, B., Lagerholm, B.C., Ernst, L.A., Bruchez, M.P. and Waggoner, A.S. (2004) Noninvasive imaging of quantum dots in mice. *Bioconjugate Chemistry*, **15**, 79–86.

20 Gao, X., Cui, Y., Levenson, R.M., Chung, L.W.K. and Nie, S. (2004) In vivo cancer targeting and imaging with semiconductor quantum dots. *Nature Biotechnology*, **22**, 969–76.

21 Akerman, M.E., Chan, W.C.W., Laakkonen, P., Bhatia, S.N. and Ruoslahti, E. (2002) Nanocrystal targeting in vivo. *Proceedings of the National Academy of Sciences of the United States of America*, 99, 12617–21.

22 Voura, E.B., Jaiswal, J.K., Mattoussi, H. and Simon, S.M. (2004) Tracking metastatic tumor cell extravasation with quantum dot nanocrystals and fluorescence emission-scanning microscopy. *Nature Medicine*, **10**, 993–8.

23 Dahan, M., Levi, S., Luccardini, C., Rostaing, P., Riveau, B. and Triller, A. (2003) Diffusion dynamics of glycine receptors revealed by single-quantum dot tracking. *Science*, **302**, 442–5.

24 Wu, X., Liu, H., Liu, J., Haley, K.N., Treadway, J.A., Larson, J.P., Ge, N., Peale, F. and Bruchez, M.P. (2003) Immunofluorescent labeling of cancer marker Her2 and other cellular targets with semiconductor quantum dots. *Nature Biotechnology*, **21**, 41–6.

25 Taton, T.A., Lu, G. and Mirkin, C.A. (2001) Two-color labeling of oligonucleotide arrays via size-selective scattering of nanoparticle probes. *Journal of the American Chemical Society*, **123**, 5164–5.

26 Elghanian, R., Storhoff, J.J., Mucic, R.C., Letsinger, R.L. and Mirkin, C.A. (1997) Selective colorimetric detection of polynucleotides based on the distance-dependent optical properties of gold nanoparticles. *Science*, **277**, 1078–81.

27 Storhoff, J.J., Elghanian, R., Mucic, R.C., Mirkin, C.A. and Letsinger, R.L. (1998)

One-pot colorimetric differentiation of polynucleotides with single base imperfections using gold nanoparticle probes. *Journal of the American Chemical Society*, **120**, 1959–64.

28 Reynolds, R.A., Mirkin, C.A. and Letsinger, R.L. (2000) A gold nanoparticle/latex microsphere-based colorimetric oligonucleotide detection method. *Pure and Applied Chemistry*, **72**, 229–35.

29 Taton, T.A., Mirkin, C.A. and Letsinger, R.L. (2000) Scanometric DNA array detection with nanoparticle probes. *Science*, **289**, 1757–60.

30 Mucic, R.C., Storhoff, J.J., Mirkin, C.A. and Letsinger, R.L. (1998) DNA-directed synthesis of binary nanoparticle network materials. *Journal of the American Chemical Society*, **120**, 12674–5.

31 Storhoff, J.J., Lazarides, A.A., Mucic, R.C., Mirkin, C.A., Letsinger, R.L. and Schatz, G.C. (2000) What controls the optical properties of DNA-linked gold nanoparticle assemblies. *Journal of the American Chemical Society*, **122**, 4640–50.

32 Reynolds, R.A., Mirkin, C.A. and Letsinger, R.L. (2000) Homogeneous, nanoparticle-based quantitative colorimetric detection of oligonucleotides. *Journal of the American Chemical Society*, **122**, 3795–6.

33 Cao, Y.W., Jin, R. and Mirkin, C.A. (2001) DNA-modified core-shell Ag/Au nanoparticles. *Journal of the American Chemical Society*, **123**, 7961–2.

34 Tyagi, S. and Kramer, F.R. (1996) Molecular beacons: probes that fluoresce upon hybridization. *Nature Biotechnology*, **14**, 303–8.

35 Huang, X., Jain, P.K., El-Sayed, I.H. and El-Sayed, M.A. (2008) Plasmonic photothermal therapy (PPTT) using gold nanoparticles. *Lasers in Medical Science*, **23**, 217–28.

36 Jaffer, F.A. and Weissleder, R. (2004) Seeing within – molecular imaging of the cardiovascular system. *Circulation Research*, **94**, 433–45.

37 Perez, J.M., Josephson, L. and Weissleder, R. (2004) Use of magnetic nanoparticles as nanosensors to probe for molecular interactions. *ChemBioChem*, **5**, 261–4.

38 Saleh, A., Schroeter, M., Jinkmanns, C., Hartung, H.P., Modder, U. and Jander, S. (2004) In vivo MRI of brain inflammation in human ischaemic stroke. *Brain*, **127**, 1670–7.

39 Dousset, V., Ballarino, L., Delalande, C., Coussemacq, M., Canioni, P., Petry, K.G. and Caille, J.M. (1999) Comparison of ultrasmall particles of iron oxide (USIOP)-enhanced T2-weighted, conventional T2-weighted, and gadolinium enhanced T1-weighted MR images in rats with experimental autoimmune encephalomyelitis. *American Journal of Neuroradiology*, **20**, 223–7.

40 Harisinghani, M.G., Barentsz, J., Hahn, P.F., Deserno, W.M. and Tabatabaei, S., Hulsbergen van de Kaa, C., de la Rosette, J. and Weissleder, R. (2003) Noninvasive detection of clinically occult lymph-node metastases in prostate cancer. *The New England Journal of Medicine*, **348**, 2491–9.

41 Dardzinski, B.J., Schmithorst, V.J., Holland, S.K., Boivin, G.P., Imagawa, T., Watanabe, S., Lewis, J.M. and Hirsch, R. (2001) MR imaging of murine arthritis using ultrasmall superparamagnetic iron oxide particles. *Magnetic Resonance Imaging*, **19**, 1209–16.

42 Ruehm, S.G., Corot, C., Vogt, P., Kolb, S. and Debatin, J.F. (2001) Magnetic resonance imaging of atherosclerotic plaque with ultrasmall superparamagnetic particles of iron oxide in hyperlipidemic rabbits. *Circulation*, **103**, 415–22.

43 Kooi, M.E., Cappendijk, V.C., Cleutjens, K.B.J.M., Kessels, A.G.H., Kitslaar, P.J.E.H.M., Borgers, M., Frederik, P.M., Daemen, M.J.A.P. and van Engelshoven, J.M.A. (2003) Accumulation of ultrasmall superparamagnetic particles of iron oxide in human atherosclerotic plaques can be detected by in vivo magnetic resonance imaging. *Circulation*, **107**, 2453–8.

44 Stöber, W., Fink, A. and Bohn, E. (1968) Controlled growth of monodisperse silica spheres in the micron size range. *Journal of Colloid and Interface Science*, **26**, 62–9.

45 Yanagi, M., Asano, Y., Kandori, K. and Kon-no, K.Abs. (1986) 39th Symp. Div. Colloid Interface Chem., Chemical Society of Japan, Tokyo, 386.

46 Das, S., Jain, T.K. and Maitra, A. (2002) Inorganic-organic hybrid nanoparticles from n-octyl triethoxy silane. *Journal of Colloid and Interface Science*, **252**, 82–8.

47 Sharma, R.K., Das, S. and Maitra, A. (2004) Surface modified ormosil nanoparticles. *Journal of Colloid and Interface Science*, **277**, 342–6.

48 Roy, I., Ohulchanskyy, T.Y., Pudavar, H.E., Bergey, E.J., Oseroff, A.R., Morgan, J., Dougherty, T.J. and Prasad, P.N. (2003) Ceramic-based nanoparticles entrapping water-insoluble photosensitizing anticancer drugs: a novel drug-carrier system for photodynamic therapy. *Journal of the American Chemical Society*, **125** (26), 7860–5.

49 Nakamura, M. and Ishimura, K. (2007) Synthesis and characterization of organosilica nanoparticles prepared from 3-mercaptopropyltrimethoxysilane as the single silica source. *The Journal of Physical Chemistry C*, **111**, 18892–8.

50 Nakamura, M. and Ishimura, K. (2008) One-pot synthesis and characterization of three kinds of thiol-organosilica nanoparticles. *Langmuir*, **24**, 5099–108.

51 Vogel, R., Surawski, P.P., Littleton, B. N., Miller, C.R., Lawrie, G.A., Battersby, B.J. and Trau, M. (2007) Fluorescent organosilica micro- and nanoparticles with controllable size. *Journal of Colloid and Interface Science*, **310**, 144–50.

52 Nakamura, M. and Ishimura, K. (2008) Size-controlled, one-pot synthesis, characterization, and biological applications of epoxy-organosilica particles possessing positive zeta potential as prepared. *Langmuir*, **24**, 1228–34.

53 Bagwe, R.P., Hilliard, L.R. and Tan, W. (2006) Surface modification of silica nanoparticles to reduce aggregation and nonspecific binding. *Langmuir*, **22**, 4357–62.

54 Wang, L., Yang, C.Y. and Tan, W.H. (2005) Dual-luminophore-doped silica nanoparticles for multiplexed signaling. *Nano Letters*, **5**, 37–43.

55 Wang, L. and Tan, W.H. (2006) Multicolor FRET silica nanoparticles by single wavelength excitation. *Nano Letters*, **6**, 84–8.

56 Zhao, X., Hilliard, L.R., Mechery, S.J., Wang, Y., Bagwe, R.P., Jin, S. and Tan, W. (2004) A rapid bioassay for single bacterial cell quantitation using bioconjugated nanoparticles. *Proceedings of the National Academy of Sciences of the United States of America*, 101, 15027–32.

57 Zhao, X., Tapec-Dytioco, R. and Tan, W. (2003) Ultrasensitive DNA detection using highly fluorescent bioconjugated nanoparticles. *Journal of the American Chemical Society*, **125**, 11474–5.

58 Santra, S., Bagwe, R.P., Dutta, D., Stanley, J.T., Walters, G.A., Tan, W.H., Moudgil, B.J. and Mericle, R.A. (2005) Synthesis and characterization of fluorescent, radio-opaque, and paramagnetic silica nanoparticles for multimodal bioimaging applications. *Advanced Materials*, **17**, 2165–9.

59 Tapec, R., Zhao, X.J. and Tan, W. (2002) Development of organic dye-doped silica nanoparticles for bioanalysis and biosensors. *Journal of Nanoscience and Nanotechnology*, **2**, 405–9.

60 Green, N.M. (1975) Avidin. *Advances in Protein Chemistry*, **29**, 85–133.

61 Bayer, E.A. and Wilchek, M. (1980) The use of the avidin–biotin complex as a tool in molecular biology. *Methods of Biochemical Analysis*, **26**, 1–45.

62 Wilchek, M. and Bayer, E.A. (1989) Avidin–biotin technology ten years on: has it lived up to its expectations? *Trends in Biochemical Sciences*, **14**, 408–12.

63 Wilchek, M. and Bayer, E.A. (1990) *Methods in Enzymology*, Academic Press, San Diego, p. 746.

64 Ow, H., Larson, D.R., Srivastava, M., Baird, B.A., Webb, W.W. and Wiesner, U. (2005) Bright and stable core-shell fluorescent silica nanoparticles. *Nano Letters*, **5**, 113–17.

65 Hun, X. and Zhang, Z. (2007) Functionalized fluorescent core-shell nanoparticles used as a fluorescent labels

in fluoroimmunoassay for IL-6. *Biosensors & Bioelectronics*, **22**, 2743–8.

66 Wang, L., Zhao, W., O'Donoghue, M.B. and Tan, W. (2007) Fluorescent nanoparticles for multiplexed bacteria monitoring. *Bioconjugate Chemistry*, **18**, 297–30.

67 Loo, C., Lowery, A., Halas, N., West, J. and Drezek, R. (2005) Immunotargeted nanoshells for integrated cancer imaging and therapy. *Nano Letters*, **4**, 709–11.

68 Santra, S., Yang, H., Dutta, D., Stanley, J.T., Holloway, P.H., Tan, W., Moudgil, B.M. and Mericle, R.A. (2004) TAT conjugated, FITC doped silica nanoparticles for bioimaging applications. *Chemical Communications (Cambridge, England)*, **24**, 2810–11.

69 Wang, Y. and Liu, B. (2007) Silica nanoparticle assisted DNA assays for optical signal amplification of conjugated polymer based fluorescent sensors. *Chemical Communications (Cambridge, England)*, **34**, 3553–5.

70 Wu, L., Qiu, L., Shi, C. and Zhu, J.A. (2007) nanoparticle-based solution DNA sandwich assay using ICP-AES for readout. *Biomacromolecules*, **8**, 2795–800.

71 Qhobosheane, M., Santra, S., Zhang, P. and Tan, W. (2001) Biochemically functionalized silica nanoparticles. *Analyst*, **126**, 1274–8.

72 Mahalingam, V., Onclin, S., Péter, M., Ravoo, B.J., Huskens, J. and Reinhoudt, D.N. (2004) Directed self-assembly of functionalized silica nanoparticles on molecular printboards through multivalent supramolecular interactions. *Langmuir*, **20**, 11756–62.

73 Kneuer, C., Sameti, M., Bakowsky, U., Schiestel, T., Schirra, H., Schmidt, H. and Lehr, C.M. (2000) A nonviral DNA delivery system based on surface modified silica-nanoparticles can efficiently transfect cells in vitro. *Bioconjugate Chemistry*, **11**, 926–32.

74 Kneuer, C., Sameti, M., Haltner, E.G., Schiestel, T., Schirra, H., Schmidt, H. and Lehr, C.M. (2000) Silica nanoparticles modified with aminosilanes as carriers for plasmid DNA. *International Journal of Pharmacology*, **196**, 257–61.

75 Sameti, M., Bohr, G., Ravi Kumar, M.N., Kneuer, C., Bakowsky, U., Nacken, M., Schmidt, H. and Lehr, C.M. (2003) Stabilisation by freeze-drying of cationically modified silica nanoparticles for gene delivery. *International Journal of Pharmacology*, **266**, 51–60.

76 Csogor, Z., Nacken, M., Sameti, M., Lehr, C.M. and Schmidt, H. (2003) Modified silica particles for gene delivery. *Materials Science and Engineering C*, **23**, 93–7.

77 Lisa, R.H., Xiaojun, Z. and Tan, W. (2002) Immobilization of oligonucleotides onto silica nanoparticles for DNA hybridization studies. *Analytica Chimica Acta*, **470**, 51–6.

78 Santra, S., Zhang, P., Wang, K., Tapec, R. and Tan, W. (2001) Conjugation of biomolecules with luminophore-doped silica nanoparticles for photostable biomarkers. *Analytical Chemistry*, **73**, 4988–93.

79 Shi, H., He, X., Wang, K., Yuan, Y., Deng, K., Chen, J. and Tan, W. (2007) Rhodamine B isothiocyanate doped silica-coated fluorescent nanoparticles (RBITC-DSFNPs)-based bioprobes conjugated to Annexin V for apoptosis detection and imaging. *Nanomedicine*, **3**, 266–72.

80 Rao, K.S., Rani, S.U., Charyulu, D.K., Kumar, K.N., Lee, B.K., Lee, H.Y. and Kawai, T. (2006) A novel route for immobilization of oligonucleotides onto modified silica nanoparticles. *Analytica Chimica Acta*, **576**, 177–83.

81 Jones, D.P., Carlson, J.L., Samiec, P.S., Sternberg, P., Mody, V.C., Reed, R.L. and Brown, L.A.S. (1998) Glutathione measurement in human plasma: evaluation of sample collection, storage and derivatization conditions for analysis of dansyl derivatives by HPLC. *Clinica Chimica Acta*, **275**, 175–84.

82 Anderson, M.E. (1998) Glutathione: an overview of biosynthesis and modulation. *Chemico-Biological Interactions*, **111**–12, 1–14.

83 Hassan, S.S.M. and Rechnitz, G.A. (1982) Determination of glutathione and glutathione reductase with a silver sulfide

membrane electrode. *Analytical Chemistry*, **54**, 1972–6.
84 Chan, W.C. and Nie, S. (1998) Quantum dot bioconjugates for ultrasensitive nonisotopic detection. *Science*, **281**, 2016–18.
85 Bruchez, M., Moronne, M., Gin, P., Weiss, S. and Alivisatos, A.P. (1998) *Science*, **281**, 2013–16.
86 Green, M. (2004) Semiconductor quantum dots as biological imaging agents. *Angewandte Chemie – International Edition in English*, **43**, 4129–31.
87 Wu, A., Liu, H., Liu, J., Haley, K.N., Tradway, J.A., Larson, J.P., Ge, N., Peale, F. and Bruchez, M.P. (2003) Immunofluorescent labeling of cancer marker Her2 and other cellular targets with semiconductor quantum dots. *Nature Biotechnology*, **21**, 41–5.
88 Bakueva, L., Konstantatos, G., Levina, L., Musikhin, S. and Sargent, E.H. (2004) Luminescence from processible quantum dot-polymer light emitters 1100–1600 nm: tailoring spectral width and shape. *Applied Physics Letters*, **84**, 3459–61.
89 McDonald, S.A., Cyr, P.W., Levina, L. and Sargent, E.H. (2004) Photoconductivity from PbS-nanocrystal/semiconducting polymer composites for solution-processible, quantum-size tunable infrared photodetectors. *Applied Physics Letters*, **85**, 2089–91.
90 Coe, S., Woo, W., Bawendi, M. and Bulovic, V. (2002) Electroluminescence from single monolayers of nanocrystals in molecular organic devices. *Nature*, **420**, 800–3.
91 Tsutsui, T. (2002) Applied physics: a light-emitting sandwich filling. *Nature*, **420**, 752–5;
92 Huynh, W.U., Dittmer, J.J. and Alivisatos, A.P. (2002) Hybrid nanorod-polymer solar cells. *Science*, **295**, 2425–7.
93 Hikmet, R.A.M., Talapin, D.V. and Weller, H. (2003) Study of conduction mechanism and electroluminescence in CdSe/ZnS quantum dot composites. *Journal of Applied Physics*, **93**, 3509–14.
94 Sun, B., Marx, E. and Greenham, N.C. (2003) Photovoltaic devices using blends of branched cdse nanoparticles and conjugated polymers. *Nano Letters*, **3**, 961–3.
95 Derfus, A.M., Chan, W.C.W. and Bhatia, S.N. (2004) Probing the cytotoxicity of semiconductor quantum dots. *Nano Letters*, **4**, 11–8.
96 Santra, S., Zhang, P., Wang, K., Tapec, R. and Tan, W. (2001) Conjugation of biomolecules with luminophore-doped silica nanoparticles for photostable biomarkers. *Analytical Chemistry*, **73**, 4988–93.
97 Zhao, X., Bagwe, R.P. and Tan, W. (2004) Development of organic-dye-doped silica nanoparticles in a reverse microemulsion. *Advanced Materials*, **16**, 173–6.
98 Lian, W., Litherland, S.A., Badrane, H., Tan, W., Wu, D., Baker, H.V., Gulig, P.A., Lim, D.V. and Jin, S. (2004) Ultrasensitive detection of biomolecules with fluorescent dye-doped nanoparticles. *Analytical Biochemistry*, **334**, 135–44.
99 Rossi, L.M., Shi, L., Quina, F.H. and Rosenzweig, Z. (2005) Stöber synthesis of monodispersed luminescent silica nanoparticles for bioanalytical assays. *Langmuir*, **21**, 4277–80.
100 Van Blaaderen, A. and Vrij, A. (1992) Synthesis and characterization of colloidal dispersions of fluorescent, monodisperse silica spheres. *Langmuir*, **8**, 2921–31.
101 Verhaegh, N.A.M. and van Blaaderen, A. (1994) Dispersions of rhodamine-labeled silica spheres : synthesis, characterization, and fluorescence confocal scanning laser microscopy. *Langmuir*, **10**, 1427–38.
102 Imhof, A., Megens, M., Engelberts, J.J., de Lang, D.T.N., Sprik, R. and Vos, W.L. (1999) Spectroscopy of fluorescein (FITC) dyed colloidal silica spheres. *The Journal of Physical Chemistry B*, **103**, 1408–15.
103 Nakamura, M., Shono, M. and Ishimura, K. (2007) Synthesis, characterization, and biological applications of multifluorescent silica nanoparticles. *Analytical Chemistry*, **79**, 6507–14.
104 Schwartz, A., Williams, J. and Stevens, R.D. (1986) Method of preparing

fluorescently labeled microbeads. U.S. Patent 4,609,689.

105 Bele, M., Siiman, O. and Matijevic, E. (2002) Preparation and flow cytometry of uniform silica-fluorescent dye microspheres. *Journal of Colloid and Interface Science*, **254**, 274–82.

106 Eiden-Assmann, S., Lindlar, B. and Maret, G. (2004) Synthesis and characterization of colloidal fluorescent mesoporous silica particles. *Journal of Colloid and Interface Science*, **271**, 120–3.

107 Santra, S., Xu, J., Wang, K. and Tan, W. (2004) Luminescent nanoparticle probes for bioimaging. *Journal of Nanoscience and Nanotechnology*, **4**, 590–9.

108 Burns, A., Sengupta, P., Zedayko, T., Baird, B. and Wiesner, U. (2006) Core/shell fluorescent silica nanoparticles for chemical sensing towards single-particle laboratories. *Small*, **2**, 723–6.

109 Shibata, S., Taniguchi, T., Yano, T. and Yamane, M. (1997) Formation of water-soluble dye-doped silica particles. *Journal of Sol-Gel Science and Technology*, **10**, 263–8.

110 Shibata, S. and Yano T. and Yamane, M. (1998) Formation of dye-doped silica particles. *Japanese Journal of Applied Physics*, **37**, 41–4.

111 Kim, S., Ohulchanskyy, T.Y., Pudavar, H.E., Pandey, R.K. and Prasad, P.N. (2007) Organically modified silica nanoparticles co-encapsulating photosensitizing drug and aggregation-enhanced two-photon absorbing fluorescent dye aggregates for two-photon photodynamic therapy. *Journal of the American Chemical Society*, **129**, 2669–75.

112 Ohulchanskyy, T.Y., Roy, I., Goswami, L.N., Chen, Y., Bergey, E.J., Pandey, R.K., Oseroff, A.R. and Prasad, P.N. (2007) Organically modified silica nanoparticles with covalently incorporated photosensitizer for photodynamic therapy of cancer. *Nano Letters*, **7**, 2835–42.

113 Lai, C.Y., Trewyn, B.G., Jeftinija, D.M., Jeftinija, K., Xu, S., Jeftinija, S. and Lin, V.S. (2003) A mesoporous silica nanosphere-based carrier system with chemically removable CdS nanoparticle caps for stimuli-responsive controlled release of neurotransmitters and drug molecules. *Journal of the American Chemical Society*, **125**, 4451–9.

114 Colvin, V.L., Goldstein, A.N. and Alivisatos, A.P. (1992) Semiconductor nanocrystals covalently bound to metal surfaces with self-assembled monolayers. *Journal of the American Chemical Society*, **114**, 5221–30.

115 Lu, J., Liong, M., Zink, J.I. and Tamanoi, F. (2007) Mesoporous silica nanoparticles as a delivery system for hydrophobic anticancer drugs. *Small*, **3**, 1341–6.

116 Santra, S., Liesenfeld, B., Dutta, D., Chatel, D., Batich, C.D., Tan, W., Moudgil, B.M. and Mericle, R.A. (2005) Folate conjugated fluorescent silica nanoparticles for labeling neoplastic cells. *Journal of Nanoscience and Nanotechnology*, **5**, 899–904.

117 Yessine, M.A. and Leroux, J.C. (2004) Membrane-destabilizing polyanions: interaction with lipid bilayers and endosomal escape of biomacromolecules. *Advanced Drug Delivery Reviews*, **56**, 999–1021.

118 Harush-Frenkel, O., Debotton, N., Benita, S. and Altschuler, Y. (2007) Targeting of nanoparticles to the clathrin-mediated endocytic pathway. *Biochemical and Biophysical Research Communications*, **353**, 26–32.

119 Panyam, J., Zhou, W.Z., Prabha, S., Sahoo, S.K. and Labhasetwar, V. (2002) Rapid endo-lysosomal escape of poly(DL-lactide-co-glycolide) nanoparticles: implications for drug and gene delivery. *FASEB Journal*, **16**, 1217–26.

120 Barbe, C., Bartlett, J., Kong, L., Finnie, K., Lin, H.Q., Larkin, M., Calleja, S., Bush, A., and Calleja, G. (2004) Silica particles: a novel drug-delivery system. *Advanced Materials*, **16** (21), 1959–66.

121 Munoz, B., Ramila, A., Perez-Pariente, J., Diaz, I. and Vallet-Regi, M. (2003) MCM-41 organic modification as drug delivery rate regulator. *Chemistry of Materials*, **15**, 500–3.

122 Han, Y.J., Stucky, G.D. and Butler, A. (1999) Mesoporous silicate sequestration and release of proteins. *Journal of the American Chemical Society*, **121**, 9897–8.

123 Stein, A., Melde, B.J. and Schroden, R.C. (2000) Hybrid inorganic-organic mesoporous silicates–nanoscopic reactors coming of age. *Advanced Materials*, **12**, 1403–19.

124 Arruebo, M., Galan, M., Navascues, N., Tellez, C., Marquina, C., Ibarra, M.R. and Santamaria, J. (2006) Development of magnetic nanostructured silica-based materials as potential vectors for drug-delivery applications. *Chemistry of Materials*, **18**, 1911–19.

125 Arruebo, M., Fernandez-Pacheco, R., Irusta, S., Arbiol, J., Ibarra, M.R. and Santamaria, J. (2006) Sustained release of doxorubicin from zeolite-magnetite nanocomposites prepared by mechanical activation. *Nanotechnology*, **17**, 4057–68.

126 Radu, D.R., Lai, C.Y., Jeftinija, K., Rowe, E.W., Jeftinija, S. and Lin, V.S. (2004) Polyamidoamine dendrimer-capped mesoporous silica nanosphere-based gene transfection reagent. *Journal of the American Chemical Society*, **126**, 13216–17.

127 Lin, Y.S., Tsai, C.P., Huang, H.Y., Kuo, C.T., Hung, Y., Huang, D.M., Chen, Y.C. and Mou, C.Y. (2005) Well-ordered mesoporous silica nanoparticles as cell markers. *Chemistry of Materials*, **17**, 4570–3.

128 Roy, I., Ohulchanskyy, T.Y., Bharali, D.J., Pudavar, H.E., Mistretta, R.A., Kaur, N. and Prasad, P.N. (2005) Optical tracking of organically modified silica nanoparticles as DNA carriers: a nonviral nanomedicine approach for gene delivery. *Proceedings of the National Academy of Sciences of the United States of America*, 102, 279–84.

129 Bharali, D.J., Klejbor, I., Stachowiak, E.K., Dutta, P., Roy, I., Kaur, N., Bergey, E.J., Prasad, P.N. and Stachowiak, M.K. (2005) Organically modified silica nanoparticles: a nonviral vector for in vivo gene delivery and expression in the brain. *Proceedings of the National Academy of Sciences of the United States of America*, 102, 11539–44.

130 Dougherty, T.J. (1987) Photosensitizers: therapy and detection of malignant tumors. *Photochemistry and Photobiology*, **45**, 879–89.

131 Konan, Y.N., Gurny, R. and Allémann, E. (2002) State of the art in the delivery of photosensitizers for photodynamic therapy. *Journal of Photochemistry and Photobiology. B, Biology*, **66**, 89–106.

132 Matsumura, Y. and Maeda, H. (1986) A new concept for macromolecular therapeutics in cancer chemotherapy: mechanism of tumoritropic accumulation of proteins and the antitumor agent smancs. *Cancer Research*, **46**, 6387–92.

133 Maeda, H., Wu, J., Sawa, T., Matsumura, Y. and Hori, K. (2000) Tumor vascular permeability and the EPR effect in macromolecular therapeutics: a review. *Journal of Controlled Release*, **65**, 271–84.

134 Prasad, P.N. (2004) *Introduction to Biophotonics*, John Wiley & Sons, Inc., New York.

Keywords

silica; organosilica; nanoparticles; preparation; biofunctionalization; fluorescent; proteins; applications

5
Mesoporous Cage-Like Silica Monoliths for Optical Sensing of Pollutant Ions

Sherif A. El-Safty, Kohmei Halada and Hirohisa Yamada

5.1
Introduction

The aim of this chapter is to provide details of a new class of nanosensor based on mesoporous silica monoliths with cage-like pores as carriers. Comprehensive up-to-date information is provided regarding the environmental chemistry and toxicity of mercury, antimony, cadmium and lead, in the quest to design simple, eco-friendly and smart sensing systems. A critical review of the literature is also provided in terms of the chemical toxicity of mercury, antimony, cadmium and lead, and their treatments with different processes and under varying environmental conditions.

In order to provide a simple, yet general, design for optical nanosensors based on a dense pattern of immobilized hydrophobic 'neutral' and/or hydrophilic 'charged' chromophores that are both mobile and robust, with three-dimensional (3-D) nanoscale structure, attention was focused on the highly toxic ions of mercury, antimony, cadmium and lead. Initially, the basic concept of optical nanosensor schemes is outlined, in addition to details of the toxicity and deleterious effects of these metal ions. We then describe the sensing methods used to quantify trace elements, and the general design of optical nanosensors based on mesoporous silica monoliths. The optical sensing and one-step visual detection of Hg^{2+}, Sb^{3+}, Cd^{2+} and Pb^{2+} ions, without need for sophisticated instruments and quantitative calibration of nanosensors, are evaluated. The potential of nanosensors in the visual detection of these toxic ions, as well as the advantages of nanosensor designs in terms of the retention of uniformity of nanosensor cage-like sinks, the rapid response of metal ion-sensing systems, the stability of monolithic nanosensors, the reversibility of metal ion-sensing systems and optical selective nanosensor for monitoring trace levels of toxic ions, are each discussed. Ultimately, it is likely that these sensing systems will be employed in basic laboratory set-ups, in field measurements using portable devices, and for household uses as commercial indicators.

Nanomaterials for the Life Sciences Vol. 2: Nanostructured Oxides. Edited by Challa S. S. R. Kumar

ISBN: 978-3-527-32152-0

5.1.1 Basic Concept of Optical Nanosensor Schemes

Chemical sensors are molecular receptors that transform their chemical information into analytically useful signals upon binding to specific guests. Today, such sensors are attracting attention owing to their potential for the easy detection and quantification of pollutant species in many areas of application, including waste management, environmental chemistry, clinical toxicology and the bioremediation of radionuclides [1]. The importance of monitoring and controlling of highly toxic heavy metals such as lead, cadmium, antimony and mercury ions in aquatic samples is unquestionable. Hence, an attractive means of improving the monitoring of these metal ion concentrations would be to use simple, inexpensive, rapidly responding and portable sensors [2]. These sensors, which have the advantage of possessing both high sensitivity and selectivity, as well as providing on-line and real-time analysis, have revolutionized the field of chemical analysis, notably in the analysis of blood and serum samples in critical care [3]. Today, this need has been recognized and several potential methods of measuring specific metal ion concentrations using on-site, inexpensive facilities have been investigated [4]. Although these methods have, in general, utilized electrochemical ion-selective electrodes [5], luminescence [6] and colorimetry [7], they suffer either from high limits of detection or a need to conduct preconcentration procedures, or from the generation of organic wastes. Extensive efforts have also been made to prepare and characterize chemosensors for specific metal ions, with the intent of incorporating these molecules into sensors [8]. Among currently available sensing techniques, optical sensors are perhaps the most effective due to their accurate detection of pollutants at low concentrations, without any equitable control of experimental environments or use of relatively sophisticated equipment [9]. The key components in this sensing method are optical sensors that can efficiently detect toxic ions in terms of sensitivity and selectivity with real-time monitoring [10, 11]. These features are currently required to analyze ultra-trace levels of environmental pollutants [12]. The development of sensing processes entails invention, optimization and commercialization, and remains a significant challenge in materials science [13, 14].

The fabrication of solid-state colorimetric sensors for visual detection is much less advanced, although colorimetric sensors may allow on-site, real-time qualitative/semi-quantitative detection, without the use of complicated analytical instruments [15–17]. Molecular interactions with metal ions in a solid-phase medium often offer interesting results that are diverge conspicuously from those obtained with solution chemistry. Today, such developments – in the form of compact instrumental free ion-sensors – remain at research level and are being investigated by using techniques involving modified sol–gel membranes, molecular imprinted polymers and nano-thin films [18–20]. As these new technologies offer a totally new approach to chemical analysis, pushing these limits can transform technologies into real methods, and in turn often lead to even newer systems. The porous

monolithic architectures provide a robust, open and tunable periodic scaffold on the nanometer scale [21], while nanometer-sized materials with engineered features that include size, shape, composition and function, play a leading role in emerging applications over diverse areas [22, 23]. The ability to control 3-D geometric structures with uniformly shaped cylindrical and cage-like pores is of interest to both potential catalysts and sorbents, as the 3-D morphologies and cage functionalities should allow the efficient transport of guest species to the network sites [24]. Among all 3-D mesostructured materials, ordered cubic mesostructures with cage-like structures perhaps offer the greatest potential, due mainly to the well-defined pore sizes of spherical cavities and connectivity among the pores [25]. Consequently, 3-D cage structures show great promise in many practical applications such as protein separation, electronics, catalytic surfaces and supports, sensing, and inclusion chemistry [24–26]. The mesostructured features have also led to many investigations for the creation of composites with active components embedded inside the pores [27, 28], and the design of high-performance adsorbents for environmental clean-up and heavy metal ion recovery has therefore attracted considerable attention [29]. Because many pollutants in most environments are present at concentrations far below the detection limits of the most commonly used treatment method [15, 24, 29, 30], there is a growing demand worldwide to develop optical chemical sensor materials not only for the accurate and rapid detection but also the selective recognition of, pollutant species. In terms of binding assays, the innovation of nanosized materials has today led to new or vastly improved methods that enable new levels of instrument control and data processing, improved sensitivity and added versatility and selectivity. It is likely that these nanomaterials will, in the near future, bring about substantial improvements in chemical analysis, with their unique characteristics of optical and mass transport properties, their specificity, and the amplification of chemical processes, through microfabrication [15–17, 24, 30, 31].

To date, the development of receptors as 'indicator dyes', and surface-confinement materials as 'carriers', is key to a broadening of the applications of optical chemical sensors for the widespread detection of neutral and ionic analytes [32]. In order to render optical sensors more applicable to high-grade analytical demands, any problems with their visual sensing systems that cause them to be unattractive candidates for the significant detection of analytes, must be solved, such as any nonflexible, intensive design problems, relatively high operating costs and extended real-time detection [1, 10]. Likewise, the development of sensing processes entails not only invention and optimization but also commercialization, and consequently this remains a significant challenge in materials science [14, 15]. The successful design of chemical sensors, in principle, requires the controlled evaluation of the sensors' intrinsic properties (i.e. sensitivity, selectivity, reversibility, stability), as well as their fabrication and operating costs. Yet, for any particular sensing system, the binding character of the probe functional groups and analyte species, the control synthesis and the end-use conditions of sensor materials have often led to a rational design for specific 'real-world' sensing

applications [1–25]. Much of the recent effort in this area has been related to creating optical chemical nanosensors that are both simple and cheap to fabricate, yet retain a high sensitivity and a rapid response for the detection of multiple toxic metal ions [33].

5.1.2 Toxicity and Deleterious Effects of the Metal Ions

Although interest in the biological and environmental effects of toxic metal ions such as lead, cadmium, antimony and mercury have increased during the past decade, large amounts of these materials continue to be released, notably in industrial areas. Due to their extreme toxicity, these metal ions have deleterious effects on the environment and living organisms, even at small doses [1, 34]. Moreover, the adverse health effects of these materials involve not only the nature of the metal species and total dose but also the time of sampling in relation to the original exposure [34]. In the next section, attention is focused on assessing the toxicity of these metals ions, and the need to determine and control their levels in various matrices.

5.1.2.1 Toxicity of Cadmium Ions

Cadmium is a rare element, the average concentration in the Earth's crust being only 0.1–0.2 $mg\,kg^{-1}$ (0.89–1.78 $\mu mol\,kg^{-1}$). The detrimental effects of cadmium on human health are increasingly being recognized; chronic cadmium exposure can cause renal dysfunction, calcium metabolism disorders, and also an increased incidence of certain forms of cancer, possibly due to a direct inhibition by cadmium of DNA mismatch remediation [35–37]. The acute toxicity of cadmium is highly dependent on water hardness, ranging from 1 to 8000 $\mu g\,l^{-1}$ for rainbow trout (at various life stages) and from 1 to almost 500 $\mu g\,l^{-1}$ for daphnids. Other invertebrates display higher levels of toxicity. The free ion (Cd^{2+}) is mainly responsible for aquatic toxicity. Cadmium ions are also deposited intracellularly by binding with a cellular, low-molecular-weight protein, metallothionein; as a result, cadmium accumulates in the liver and kidneys, in turn causing a breakdown of urinary proteins and disturbances of protein metabolism [36]. Chronic cadmium toxicity has long been recognized as the cause of Itai-Itai disease in Japan. Anthropogenic sources of cadmium in the environment include the mining and smelting of metal ores, fossil fuel combustion, and as a waste product of the metal-refining industries [35, 36]. Cadmium is also often found in high concentrations in phosphate fertilizers, and is widely used in the production of nickel–cadmium rechargeable batteries that may become deposited in sewage sludge, thus raising environmental levels of cadmium, with subsequent adverse effects [37]. The discharged metal ions undergo a series of biogeochemical transformations to form toxic chemical species, with extensive accumulations and long residence times. The identification of cadmium-contaminated sewage and fertilizer would prove very useful in limiting human exposure, as would the identification of other environmental sources of cadmium.

5.1.2.2 Toxicity of Antimony Ions

Antimony is a metalloid in Group VB of the Periodic Table – one period below arsenic – with which it shares similar chemical properties. For example, both elements are known to be biomethylated in the environment and appear to act competitively with respect to toxicity [38]. Antimony and its compounds are considered by the United States Environmental Protection Agency (US-EPA) and the European Union Council of the European Communities to be priority pollutants. Typically, the US-EPA recommends that drinking water should contain less than 6 ppb of antimony, although the maximum contaminant level can be substantially elevated (to 100 ppb) in the proximity of anthropogenic sources [38]. The lower oxidation state of antimony, Sb(III), is considerably more toxic and mobile than Sb(V), and the chemical form of its compounds strongly influences its toxicity [38]. Antimony is produced by the metallurgical, alloy and rubber industries, and has also been found in geological, biological and water samples as a result of various anthropogenic activities [39]. Because antimony-containing additives are used in brake linings and tire vulcanization processes, road traffic is also a significant source of antimony pollution [39]. There is a demand for the accurate and specific determination of trace concentrations of Sb(III) ions.

5.1.2.3 Toxicity of Mercury Ions

Mercury ions are more toxic than those of cadmium, antimony and lead, and are also carcinogenic in humans and nonbiodegradable [40]. Mercury waste, which may be emitted either industrially or as a result of natural activities, is accumulated largely through plants and aquatic resources, and ultimately is bioconcentrated through the food chain. When dispersed in the environment, mercury ions undergo a series of biogeochemical transformations to toxic chemical species, and this has provoked intensive studies of their biological effects on humans [40–42]. Organic mercury, such as methylated mercury, has unique chemical characteristics (due to the methyl group) that make it prone to bioaccumulate in animals and plants. Inorganic mercury compounds are expected to be the primary species in mine effluents [41, 42]. The bioavailability and toxicity of inorganic ionic mercury to aquatic life can be influenced by the 'hardness' of the water. Inorganic mercury is a central nervous system and renal toxicant, whereas methyl mercury is well absorbed across the cell membrane and is efficiently accumulated by the biota. The primary target of methyl mercury toxicity is the central nervous system [43]. The acute toxicity thresholds for inorganic mercury (typically as $HgCl_2$) in freshwater organisms vary from 5 to 230 $\mu g l^{-1}$ in crustaceans to 60 to 800 $\mu g l^{-1}$ in fish. Methyl mercury is known to accumulate in muscle tissue, where it binds to the sulfhydryl groups of the muscle proteins. Inorganic mercury is poorly absorbed in comparison to the short-chain alkyl mercurials such as methyl mercury, and accumulates primarily in the liver and kidney [42, 43].

5.1.2.4 Toxicity of Lead Ions

Lead, in the form in which it affects biological systems, has the same +2 charge and is approximately the same physical size as calcium ions. Lead ions are also

similar to zinc and iron ions; in fact, lead ions may replace calcium, zinc and iron ions in many overlapping biochemical pathways. By substituting for essential minerals, lead can effect permanent and severe damage to humans and other animals. Because it is an element, lead does not degrade or lose its toxic effect over time. As lead is toxic on such a basic level, it is important to note that there is no known level at which it is safe [44]. The elemental or ionic forms of lead are bioconcentrated by aquatic organisms as potentially toxic tetraethyl lead and tetramethyl lead species, both of which persist in the life chain through fish and fish-eating animals [45–47]. Lead (Pb^{2+}) is a potential neurotoxin and nephrotoxin and, when exposed to humans beyond its permissible level, can cause chronic inflammatory damage to the kidney and heart. Lead may bind to naturally occurring RNA to create an enzyme-like activation for the cutting of chemical bonds in other RNA strands, thus destroying them [47]. The primary role of RNA is to transport genetic messages from cellular DNA to those parts of the cell where the enzymes and other protein molecules are created. Lead is known to disrupt the normal biochemistry in the kidney, brain and bones by causing the excessive production of some proteins, the role of which is to bind specifically to other molecules [44, 45]. In addition, lead ions can induce nervous and gastrointestinal disorders and also impair the immune and reproductive systems [46]. The regulation and periodic monitoring of these pollutant species are desirable, based on their toxicological significance and greater bioavailability to children than to adults. However, a very recent study conducted at Washington University showed that adult workplace exposure to lead resulted in an ongoing deterioration of verbal memory, visual memory and hand–eye coordination [44]. In the same study, a decrease occurred in brain size, while the numbers of brain tissue abnormalities were increased in direct proportion to the lead exposure. The authors suggested that a cumulative exposure of adults to lead could account for some of the characteristics commonly attributed to old age. The exposure of adults to lead is also known to be related to increases in blood pressure [44]. Lead plays no positive role in human biochemistry, and the considerable complexity of humans and the many factors to which they are exposed to make it difficult to determine the exact effects of very small amounts of lead. Nonetheless, the consequences of low-level exposure to lead have become increasingly clear, and the 'action level' at which lead should be considered dangerous, as suggested by government agencies, has been reduced several times over the years. Within the human body, lead cannot be metabolized to render it less dangerous.

5.2
General Sensing Techniques for Metal Ions

Sensing methods capable of quantifying these trace elements at low levels include atomic absorption spectroscopy (AAS), inductively coupled plasma (ICP) combined with atomic emission spectrometry (ICP-AES) or inductively coupled plasma with mass spectrometry (ICP-MS). The latter technique represents a powerful

technique, owing to its multielement capacity and high sensitivity. Other methods include electrochemical, neutron activation, flame atomic fluorescence spectrometry, molecular absorption spectrometry and X-ray fluorescence. In fact, the majority of these methods have provided analytical devices and assays that are capable of detecting and quantifying trace metal ion concentrations [48, 49]. In turn, these devices are normally restricted to 'wealthier hands', there being limited access to pollution monitoring agencies and other research organizations in the developing countries [50]. A low-cost, easy-to-use and reliable device is still much needed for environmental monitoring and to ensure a 'green chemistry' [1, 2]. The development of optical sensors for the detection of hazardous trace metals is of great interest in environmental and biomedical fields [2]. Optical sensors for Hg^{II} ion detection, for example, have successfully emerged using chromophores [51], fluorophores [52–54], electrochemical methods [55], functionalized polymers and proteins [56, 57] and enzyme inhibition [58], but these were normally associated with certain limitations such as tedious synthesis, organic solvents, complicated analysis, delayed signal response, insufficient selectivity and low sensitivity. Although various concepts in Hg^{II} ion-sensing have been installed to enhance sensitivity, selectivity and the dynamic working range, the recognition of target ions from multi-ion mixtures still poses a major challenge [1–25, 51–58].

5.3
General Designs of Optical Nanosensors Based on Mesoporous Silica Carriers

The quest for simple and smart detection, eco-friendly solid sensors has been limited by few developments, which in recent years have been linked with solid materials, and with the significant progress in nanotechnology [1, 2, 33]. An ideal sensory system with a small molecule-based sensor strips would remain an attractive approach, as nanosensors with such types of probe could ultimately be employed in basic laboratory assays, in field measurement by using portable devices, and in the household as a commercial indicator. Recently, the ability to manipulate matter at the nanoscale level has ked to the development of nanosensors that exhibit high strength, as well as the ability to recognize and signal a broad range of chemical species [15–17]. The advanced functionality of manipulating chromophore probes into nanomaterials as sensing receptors has received much attention in the design of chemical sensor arrays for the responsive recognition of several species such as metal cations [11, 12] and also charged and neutral organic molecules [17, 24, 25, 33]. For the development of such an optical sensor, we recently constructed chromophore probes onto large cage mesostructures, the surfaces of which had been modified by functionalizing agents. The grafting techniques, which are commonly used to control the immobilization of choromogenic receptors on solid materials, leading to fabricate chemosensors for recognition of cation and anion species have been widely discussed [17, 24, 25, 33]. The main challenge in the creation of nanosensors is that, although these grafting techniques of probe-based chemical sensors have included the sophisticated immobi-

lization procedures of the receptor probes, the retention of specific activity and flexibility of the electron acceptor/donor strength of the immobilized probes was evident. Such mobility might lead to the simple generation and transduction of an optical color signal as a response to the events of probe–metal binding. Key to achieving a working design of an optical nanosensor is the ability to immobilize chromophore probes with different functional characteristics (i.e. hydrophobic and hydrophilic) with dense accessibility and intrinsic mobility onto these 3-D high-order monolithic (HOM) pore surfaces, thereby indicating a facile and reliable synthesis design.

Several successful immobilization strategies using direct and indirect post-grafting techniques of hydrophilic and hydrophobic chromophores into the cubic Fm3m cage monoliths (where Fm3m is a face-centered cubic structure with Fm3m space group) were performed to design probe sink-like sensors (see Schemes 5.1 to 5.4). However, the functionalized cage sensors were fabricated through either a direct immobilization for hydrophobic diphenylthiocarbazone (DZ) probe (see Scheme 5.4) or through two-step inclusion procedures for hydrophilic probes (see Schemes 5.1–5.3) via grafted-controlled surface modification of the cage monoliths with amine- or thiol-coupling agents. The experimental results showed that the use of *n*-trimethoxysilylpropyl-*N,N,N*-trimethylammonium chloride (TMAC) or mercaptopropyl trimethoxysilane (MPTS) coupling agents were the most adequate for tuning the polarity of the HOM surfaces on which the high accessibility of the tetraphenylporphine tetrasulfonic acid (TPPS), pyrogallol red (PR), α, β, γ, δ-tetrakis(1-methylpyridinium-4-yl)porphine*p*-toluenesulfonate (TMPyP) moieties were observed [59], and therefore led to generate a long-term stability of sensors for the high selectivity of Hg^{II}, Sb^{III} and Cd^{II} target ions, respectively, with sensitive detection and rapid assessment analysis (≤1 min) (see Schemes 5.1–5.3).

5.3.1
Optical Nanosensor of Cage HOM-TPPS Sink for Hg(II) Ions

Immobilization of the TPPS chromophore into monolithic HOM mesopore geometries led to the creation of optical chemical nanosensors that have efficient sensing functionalities (Scheme 5.1) in terms of sensitivity, selectivity and response time of Hg(II) ions. Due to the potential leaching of the hydrophilic (TPPS) chromophore by the washing cycle, the TPPS probe could not be directly embedded on the silica surface matrices without tuning the surface polarity. Optical TPPS-mediated nanosensors were successfully fabricated by first modifying the HOM silica with the TMAC coupling agent (Scheme 5.1) [24, 59]. With the introduction of TPPS probe molecules, strong ionic interactions successfully occurred between the PR chromophore containing sulfonate acid groups and the carriers charged by the functionalized ammonium ion (Scheme 5.1).

^{29}Si NMR spectroscopy was used to investigate the successful immobilization of the TMAC organic and probe (TPPS) moieties through the elucidation of the molecular environment in the silica materials [60, 61]. First, the ^{29}Si NMR spec-

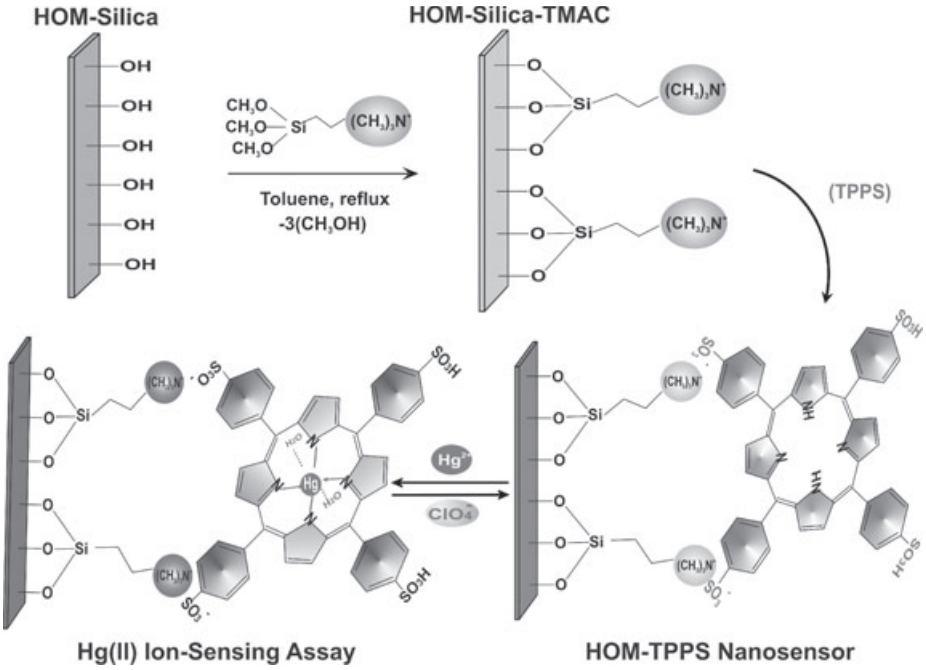

Scheme 5.1 Representative scheme of the Hg(II) ion-sensor design through the post-grafting technique by using TMAC as a coupling agent and TPPS as probe-modified cage HOM structures. Reversibility of the $[Hg–TPPS]^{n+}$ complex was achieved using 0.01 *M* ClO_4^- as stripping agent several times, without causing leaching of the TPPS probe from the HOM pore surface.

trum of HOM-C10 carriers (Figure 5.1a) showed three overlapping signals (Q_n peaks) at –91, –101 and –110 ppm, respectively [61]. Second, ^{29}Si NMR spectra (see, for example, Figure 5.1b) of the silica-TMAC ligand showed signals that were representative of various silicon environments of the T_n and Q_n silane moieties; however, the T_n peaks were representative of a silicon matrix bound directly to organic species. Figure 5.1b shows that, in addition to Q_2, Q_3 and Q_4, three different signals were observed at –53, –61 and –71 ppm, which correspond to three different environments for the siloxane group in functionalized monolayers of T_1 [R–Si$(OH)_2(OSi)_3$], T_2 [R–Si (OH)$(OSi)_3$] and T_3 [R–Si(OSiO)]. This result indicated that the silicon atom in the siloxane matrix was directly incorporated into the organic TMAC moiety. The increase of the intense peak of the siloxane groups (Q_4) with the incorporation of the TMAC ligand or even TPPS, indicated that the Si–OH sites (silanediol and silanol groups) of the silica pore wall had undergone a condensation reaction with the organothiol coupling agent, forming covalent linkages to the silica frameworks. Finally, one signal of T_3 (Figure 5.1c) was the main component with a negligible existence of T_2 dominant with the incorporation

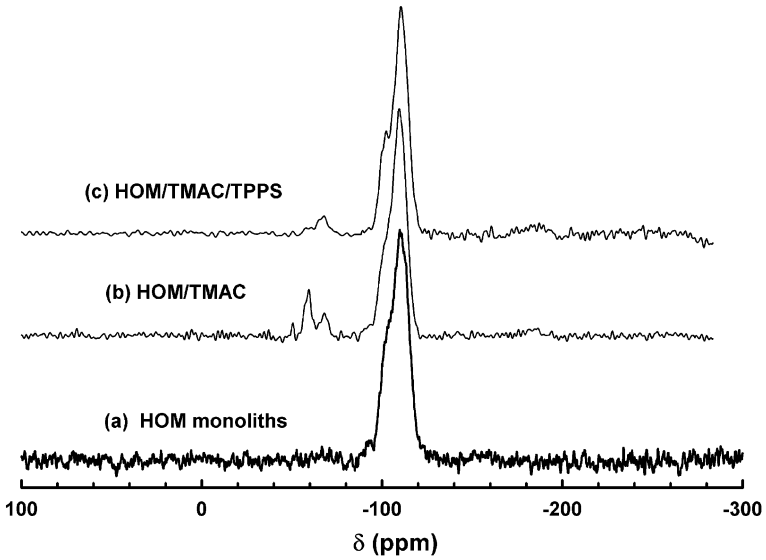

Figure 5.1 ^{29}Si NMR spectra of (a) calcined HOM-C10 monoliths; (b) functionalized TMAC/HOM-C10 monoliths; and (c) HOM/TMAC/TPPS nanosensor.

of TPPS, indicating that the TPPS molecule was loaded closely to another in the functionalized monolayer [60, 61].

5.3.2
Optical Nanosensor of Cage HOM-PR Sink for Sb(III) Ions

The TMAC-functionalized mesoporous HOM materials, in principle, not only led to strongly bound TPPS molecules on the pore surfaces (Scheme 5.1), but also enhanced the loading amount and accessibility of the PR probe (Scheme 5.2) [62]. One of the most exciting aspects of this chemical nanosensor design is that the PR chromophore moieties can be embedded in the pore matrices, without causing any significant alteration of the mesostructured regularity, particle morphology or pore geometry of the two-dimensional (2-D) and 3-D materials. This developed design yielded a sensing response in these chemical nanosensors that was generally linear, as evidenced from the high selectivity and sensitivity of Sb(III) target ions with a rapid response time (Scheme 5.2). With the introduction of PR probe molecules, strong ionic interactions successfully occurred between the PR chromophore containing a sulfonate acid group and the carriers charged by the functionalized ammonium ion (see Scheme 5.1). In addition, the hydrogen bonding between the PR molecules and Si–OH surfaces could also induce retention of the incorporated PR probe during the washing cycle, indicating the successful design of optical nanosensors. ^{29}Si NMR spectroscopy indicated successful tuning of

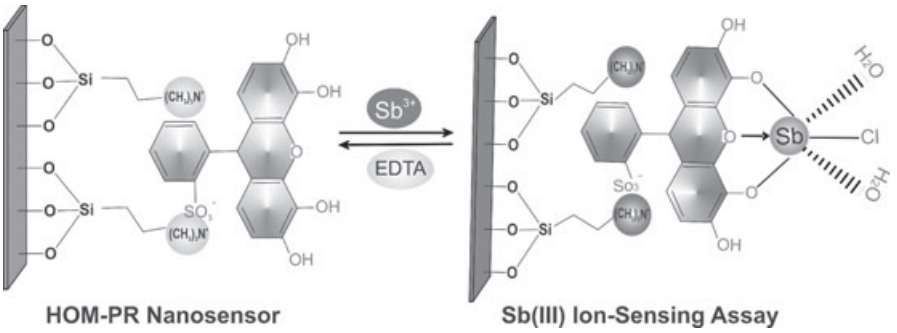

Scheme 5.2 Representative scheme of the Sb(III) ion-sensor design through the post-grafting technique by using TMAC as a coupling agent and PR as probe-modified cage HOM structures. Reversibility of the $[Sb–PR]^{n+}$ complex was achieved using 0.01 *M* EDTA as stripping agent several times, without causing leaching of the PR probe from the HOM pore surface.

the silica surfaces by charged molecules (TMAC) and by the probe moiety (PR) through clarification of the molecular environment in the silica materials (see Figure 5.1).

5.3.3
Optical Nanosensor of Cage HOM-TMPyP Sink for Cd(II) Ions

The results of these synthesis experiments showed that, due to potential leaching of the hydrophilic TMPyP chromophore by the washing cycle, the TMPyP probe could not be directly embedded on the cage (HOM-C10) pore surface matrices, without tuning the surface polarity. Optical nanosensors were successfully fabricated with the TMPyP probe by using a silica-modified MPTS coupling agent (Scheme 5.3), which can be used to create highly tuned and functional nanostructured surfaces [59]. Oxidation of the mercapto group to sulfonic acid occurred by the addition of H_2O_2 solution, leading to the creation of anionic sites on the HOM surfaces. With the introduction of a TMPyP probe, strong ion-pair interactions successfully occurred between the TMPyP chromophore containing a ammonium ion and the negatively charged (SO_3H) carriers (Scheme 5.3). The electrostatic interactions could also induce retention of the incorporated TMPyP probe during the washing cycle, indicating the successful design of cage HOM-TMPyP optical sink.

The Fourier-transform infrared (FTIR) spectra (Figure 5.2) revealed that the MPTS and TMPyP organic moieties were functionalized the HOM carriers. With all samples, the appearance of a broad absorption band in the 3000–3500 cm^{-1} region indicated the presence of Si—OH asymmetric stretching. In addition, two strong bands at 1100 and 960 cm^{-1} were assigned to Si—O—Si and Si—OH stretching vibrations, respectively [45]. The silica-modified MPTS showed additional

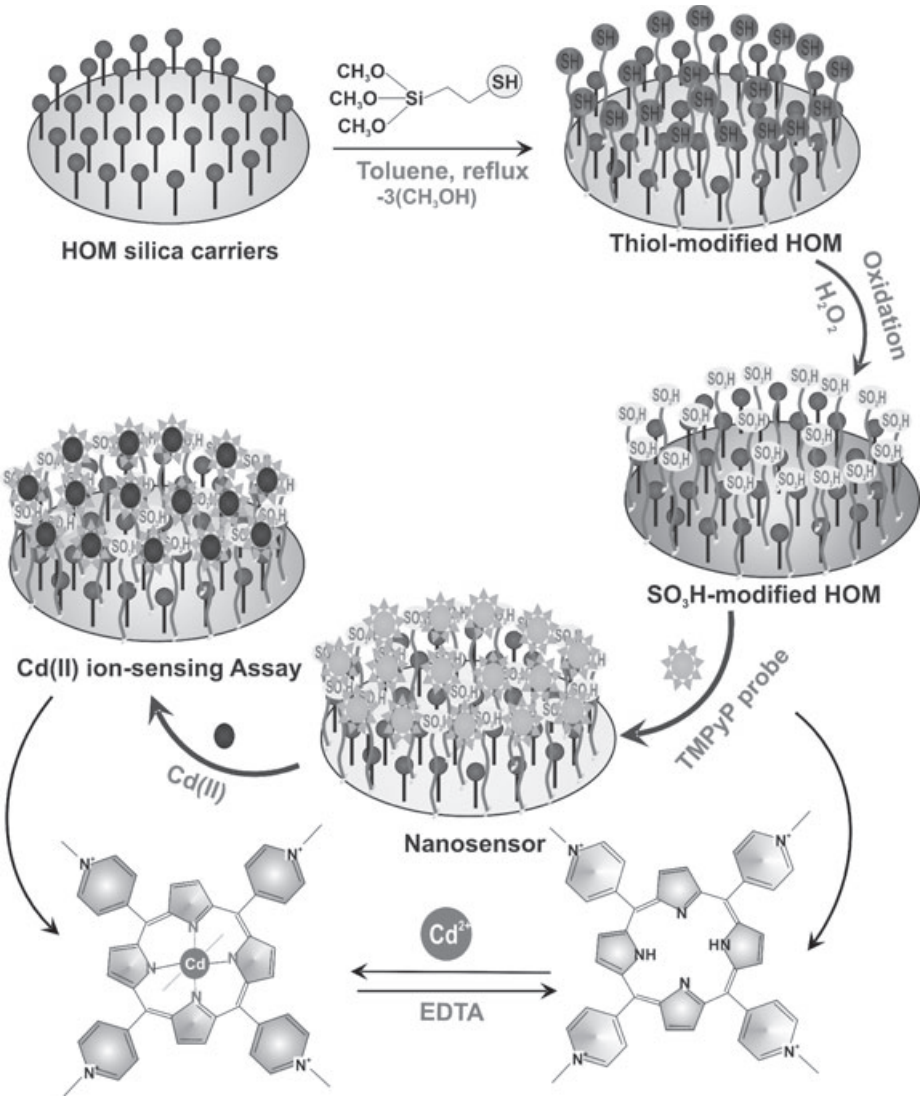

Scheme 5.3 Construction and design of the HOM-TMPyP nanosensor for Cd(II) ion-sensing assay through the modified-silica with thiol group using MPTS as coupling agent and subsequent formation of SO_3H-modified silica, using H_2O_2 as an oxidizing agent and coupling agent. Reversibility of the [Cd–TMPyP]$^{n+}$ complex was achieved using 0.1 *M* EDTA as stripping agent several times, without causing leaching of the TMPyP probe from the HOM pore surface.

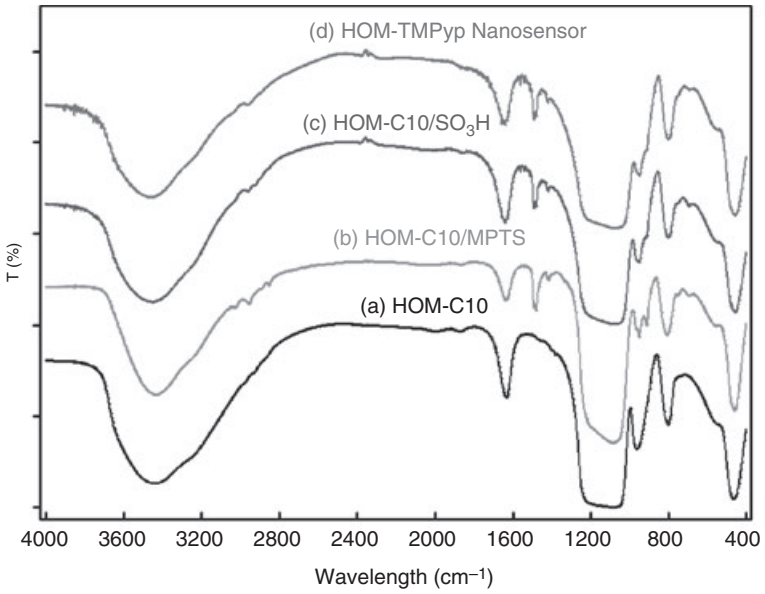

Figure 5.2 FTIR spectra of (a) cage silica monoliths (HOM-C10); (b) functionalized MPTS/HOM-C10; (c) functionalized HSO_3/HOM-C10; and (d) cage HOM-TMPyP nanosensors.

absorption bands at 2960 and 1400 cm^{-1}, which were due to the aliphatic C—H and the stronger C—S bonds, respectively [63]. The FTIR results were consistent with energy-dispersive spectrometry (EDS) X-ray microanalysis of each element. However, the composition contents of nanosensor **1** were estimated by recording an EDS X-ray microanalysis of each element (C, S, O, Si and N contents of 9.01, 6.12, 53.3, 30.14 and 1.02 mass%, respectively). The thermogravimetry-differential thermal analysis (TG-DTA) curves of MPTS-modified HOM monoliths are shown in Figure 5.3, where the TG profile shows a gradual decrease in the weight of HOM-MPTS, although the total weight loss was about 15% between 200 and 700 °C. Two broad exothermic peaks were observed at 320 and 520 °C in the DTA curve, indicating that the MPTS fragments had decomposed between 200 and 700 °C [63]. The data, in general, indicated the successful functionalized of MPTS with the silica carriers; however, the high concentration of nitrogen and sulfur compared to carbon within the cage HOM-TMPyP sensor might have been due to some unreacted functionalities with the probe moieties, consistent with the adsorption amounts (Q) of the TMPyP-probe molecule (Table 5.1).

5.3.4
Optical Nanosensor of Cage HOM-DZ Sink for Pb(II) Ions

The fabrication of cage HOM-DZ sink sensors was successfully fabricated by using the direct grafting process in which the DZ-probe was immobilized into HOM

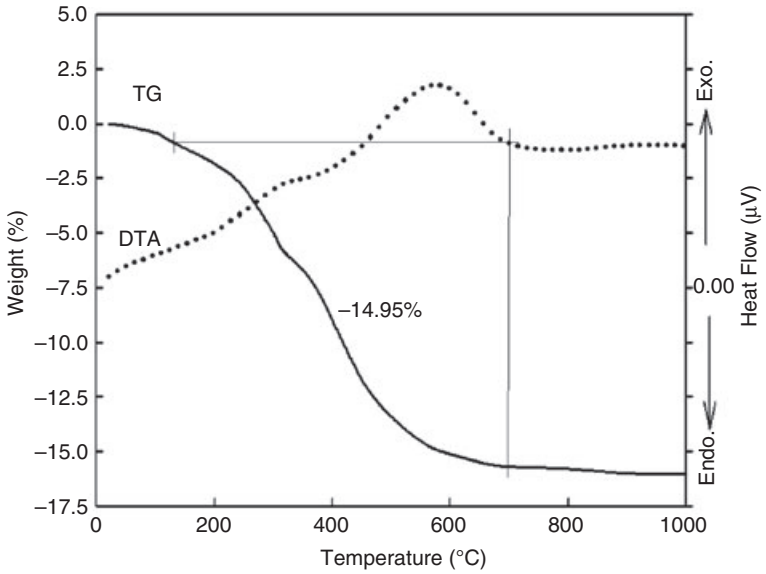

Figure 5.3 Thermogravimetric (TG) analysis and differential thermal analysis (DTA) of MPTS-modified monoliths.

Table 5.1 Metal ion-sensing assays and sensing performance of monolithic cage nanosenors during the recognition of Hg^{2+}, Sb^{3+}, Cd^{2+} and Pb^{2+} analyte ions at pH 9, 3, 9.5 and 7, respectively. The sensor amount, total volumes and temperature of the sensing systems were maintained at 4 mg, 20 cm^3 and 25 °C, respectively.

Metal ion-sensing assays						Nanosensor performance				
HOM sensor	**Analyte**	**pH range**	***Q*** **(mmol g^{-1})**	**Log *Ks***	***S***	**$10^9.L_D$ (mol dm^{-3})**	**D_R (mol dm^{-3})**	**$10^8.L_Q$ (mol dm^{-3})**	**Storage (months)**	**t_R (s)**
TPPS	Hg^{2+}	8–10	0.0054	14.8	1:1	6.34	9.9×10^{-9} to 1.5×10^{-6}	2.11	10	60
PR	Sb^{3+}	2.7–3.6	0.019	8.9	1:1	33.7	4.1×10^{-8} to 1.6×10^{-6}	11.2	7	60
TMPyP	Cd^{2+}	7–10	0.0031	13.52	1:1	13.5	1.78×10^{-8} to 4.4×10^{-6}	4.5	8	60
DZ	Pb^{2+}	6–7.5	0.12	8.87	1:1	2.38	9.7×10^{-9} to 4.8×10^{-6}	7.93	4	150

Adsorption amount (Q) of the probes, detection (L_D) and quantification (L_Q) limits and range (D_R), response times (t_R), stoichiometry of metal ions/probes complex formation (S) and effective pH range used and stability constant (log K_s) of the complexes.Adapted with permission from Ref. [24]; © 2006, Wiley-VCH.

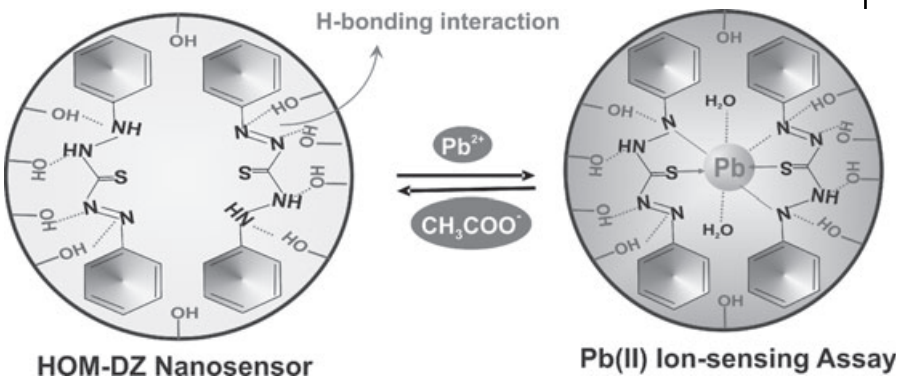

Scheme 5.4 Fabrication of HOM-DZ sensor via direct immobilization of DZ probe into HOM monoliths via H-bonding interaction under vacuum. Reversibility of the $[Pb–(DZ)_2]^{n+}$ complex was achieved using 0.1 *M* CH_3COO^- as stripping agent several times, without causing leaching of the DZ probe from the HOM pore surface.

monoliths without previous modification of their pore surfaces (Scheme 5.4). In fact, the direct grafting of DZ chromophore molecules with high adsorption capacity (Q) led to the design of optical molecular sensors for the simple detection of Pb(II) ions (Table 5.1). However, the amount (q) of DZ probe adsorbed at saturation was calculated by Equation 5.1:

$$Q = (C_o - C_t)V/m\,(\mathrm{mmol\,g^{-1}}) \tag{5.1}$$

where Q_t is the adsorbed amount at contact time t, V is the solution volume (in liters), m is the mass of HOM carriers (in grams), and C_o and C_t are the initial concentration and the concentration at saturation time t, respectively (see Table 5.1). In general, the variation in the loading capacity (Q) of probes for the cage sink nanosensor (Table 5.1) was attributed to the interaction characteristics of the TPPS, PR, TMPyP and DZ probes with HOM cage monoliths [24].

The functional use of the mesoporous silica HOM monoliths with large particle morphology (size ≥ 150 μm) and 3-D nanoscale cubic structures as modal carriers enhanced the potential sensing of Pb(II) ions. These results revealed that the direct immobilization of a DZ-probe into HOM monoliths occurred mainly through the physical 'short-range' interactions (i.e. van der Waals and H-bonding interactions) between the abundant hydroxyl groups of pore surface silicates and the three-centered heteroatoms of DZ (Scheme 5.4). Such interactions led to the stability of mesocaged chemosensors during the washing cycle and potential sensing detection of Pb(II) ions. Compared to the indirect immobilization of a probe in which commonly used silane or thiol coupling agents were used to tune the surface polarity of HOM-, SBA- and MCM-silicas [24, 61], the direct immobilization enabled the design of chemosensors without pore blockage that commonly

occurred with the grafting of silane and thiol moieties [25]. Furthermore, such a direct incorporation process not only led to a strongly bound DZ probe with a higher loading capacity onto the pore surfaces, but also enhanced the accessibility of the DZ probe to Pb(II) ions, without any increase in kinetic hindrance compared to that of an indirect grafting process [25]. In fact, the ability to achieve flexibility on the specific activity of the electron acceptor/donor strength of the DZ molecular probe might lead to the easy generation and transduction of an optical color signal in response to the DZ–Pb(II) analyte binding events, as evidenced from the cubic chemosensor responses (see Table 5.1).

5.4 Optical Sensing Assays of Metal Ions Using Nanosensors

Although, in general, the successful design of optical sensors based on nanostructures enabled the selective and sensitive detection of Pb(II), Hg(II), Cd(II) and Sb(III) ions to subnanomolar concentrations (see Table 5.1), the high performance of the sensors was dependent on key factors such as the contact-time 'signal response time', the amount of support-based sensor, the reaction temperature [1–17] and the pH [18–20]. In order to control the sensing assays, it I necessary to understand that these key factors strongly affected the homogeneity in the color map distribution and intensity, even at low loading level of metal ions during the visual detection process in the laboratory experiments. In general, changes in these key factors can play significant roles involving redistribution of the charge polarity and electron and energy transfer within the probe molecule into the pore surfaces. Therefore, the chemical sensing system is extremely sensitive to such changes which, in turn, acutely affects the accuracy and precision in the determination and visual detection of the target ions [24].

In order to control the sensing assays of the chemical nanosensors for Hg(II), Sb (III), Cd(II) and Pb(II) ions, they were studied as a function of the HOM-nanosensor amount, temperature, pH solution and contact-time 'signal response time' (Figures 5.4 and 5.5). In this study, a series of experiments was carried out to systematically define and evaluate the relative importance of these factors in a HOM-probe nanosensor for the detection of Pb(II), Hg(II), Cd(II) and Sb(III) ions. In general, the extent of metal ion chelation with the receptor-immobilized HOM was monitored quantitatively after equilibration at a real-time response (i.e. $\geq R_t$), in which the prominent color change and signal saturation of the $[Hg–TPPS]^{n+}$, $[Sb–PR]^{n+}$, $[Cd–TMPyP]^{n+}$ and $[Pb–(DZ)_2]^{n+}$ complex equilibrium of binding were achieved (see Figures 5.4 and 5.5). In such a quantification procedure, R_t can be considered as a reference signal with practically no metal analyte ion remaining (see Table 5.1) [24, 25]. The pH response was also studied by continuously monitoring the signal sensing response of the nanosensors for [0.5 ppm] Hg^{2+}, [0.5 ppm] Sb^{3+}, [0.3 ppm] Cd^{2+} and [1.0 ppm] Pb^{2+} analyte ions at different pH-values of the solution (from 1 to 11) and at 25 °C. It should be noted that the effect of pH on the visual detection of Hg(II), Sb(III), Cd(II) and Pb(II) ions was studied by adding

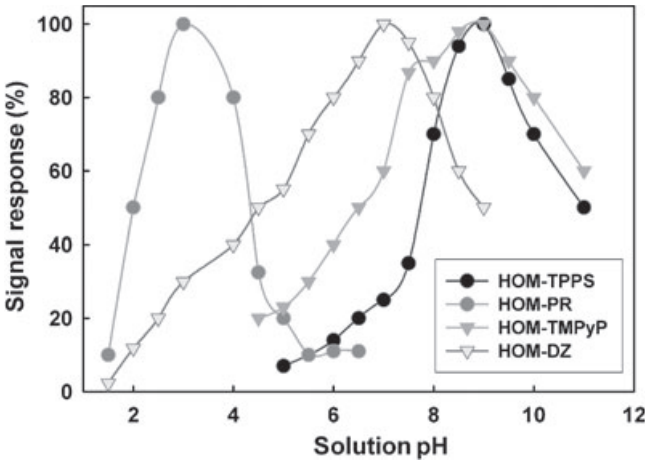

Figure 5.4 The pH-dependent signal response of HOM-TPPS, HOM-PR, HOM-TMPyP and HOM-DZ nanosensors during the recognition of [0.5 ppm] Hg^{2+}, [0.5 ppm] Sb^{3+}, [0.3 ppm] Cd^{2+} and [1.0 ppm] Pb^{2+} analyte ions at λ of 447, 534, 453 and 501 nm, respectively. The amount of solid sensors, response time, total volume and temperature of the sensing systems were maintained at 4 mg, 3.0 min, 20 cm^3 and 25 °C, respectively.

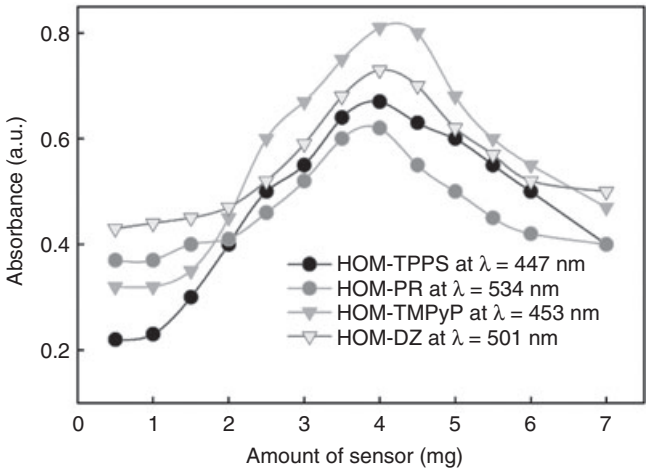

Figure 5.5 Effect of the amount of monolithic HOM-TPPS, HOM-PR, HOM-TMPyP and HOM-DZ nanosensors on the signal response of $[Hg–TPPS]^{n+}$, $[Sb–PR]^{n+}$, $[Cd–TMPyP]^{n+}$ and $[Pb–(DZ)_2]^{n+}$ complexes during the recognition of [0.5 ppm] Hg^{2+}, [0.5 ppm] Sb^{3+}, [0.3 ppm] Cd^{2+} and [1.0 ppm] Pb^{2+} analyte ions at pH 9, 3, 9.5 and 7, respectively. The response time, total volumes and temperature of the sensing systems were maintained at 3 min, 20 cm^3 and 25 °C, respectively.

a mixture containing a specific concentration of Hg(II), Sb(III), Cd(II) and Pb(II) ions adjusted to a pH between 1 and 3 (by using 0.2 *M* KCl/HCl), to 4–6 (by using 0.2 *M* CH_3COOH-CH_3COONa), to 7–8 (by using 0.2 *M* 3-morpholinopropane sulfonic acid, MOPS) and to 9–11 (by using 0.2 *M* 2-cyclohexylamino ethane sulfonic acid; CHES), respectively, under the same conditions. The results of this pH study showed that the maximum absorbance intensity of the metal-to-ligand complex was exhibited at pH 9.0, 3.0, 9.5 and 7.0, respectively (see Figure 5.4).

In fact, not only a high surface area and porosity but also the particle-size morphology of the materials proved advantageous by allowing a high adsorption capacity of the chromophore probe, with fast kinetics. While the amount adsorbed onto the probe significantly influenced the creation of a significant sensing system, the results also showed that the quality of the sensing system depended on the amount of solid support-probe used; however, the probe concentration substantially affected the sensitivity in ordinary spectrophotometric methods. Based on the results of these recent studies, the amount of adsorbed probe was seen to significantly affect the metal ion-sensing systems. The data in Figure 5.5 show that the signal response of the $[Hg–TPPS]^{n+}$, $[Sb–PR]^{n+}$, $[Cd–TMPyP]^{n+}$ and $[Pb–(DZ)_2]^{n+}$ complexes at λ-values of 447, 534, 453 and 501 nm, respectively and at the specific pH solutions, were also dependent on the amount of solid HOM-probe nanosensor used; however, the probe concentration also had a significant effect on complex formation (see Figure 5.5). These findings revealed that ~4 mg of solid HOM-probe was sufficient to achieve a good color separation between the blank and the Hg(II), Sb(III), Cd(II) and Pb(II) ion samples, even at a low metal concentration.

5.5
One-Step and Simple Ion-Sensing Procedures

Despite the feasible use of these commercial receptor TPPS, PR, TMPyP and DZ probes for the sensitive determination of Hg^{2+}, Sb^{3+}, Cd^{2+} and Pb^{2+} ions up to 10^{-7} mol dm^{-3} [64], the solid cage materials immobilized by the indicator dyes could, in principle, be used as preconcentrators to yield a high adsorption capacity and preconcentration efficiency. This would lead to a simultaneous visual inspection and simple detection over a wide, adjustable range of Hg^{2+}, Sb^{3+}, Cd^{2+} and Pb^{2+} ion concentrations, even at trace levels (~10^{-9} mol dm^{-3}). No elution of the probe molecules was evident with the addition of Hg^{2+}, Sb^{3+}, Cd^{2+} and Pb^{2+} ions during the sensing process. The binding of these ions with probes led to a color change of nanosensors which corresponded to formation of the metal–chelate $[Hg–TPPS]^{n+}$, $[Sb–PR]^{n+}$, $[Cd–TMPyP]^{n+}$ and $[Pb–(DZ)_2]^{n+}$ complexes (Schemes 5.1–5.4). The results (Figures 5.6–5.9) indicated that chemical nanosensors offered one-step, simple sensing procedures for both the quantification and visual detection of Hg^{2+}, Sb^{3+}, Cd^{2+} and Pb^{2+} ions, without the need for sophisticated instrumentation [33].

Key to the success of these nanosensors was that the colorimetric determination using UV-visible reflectance spectroscopy could be used to quantitatively validate

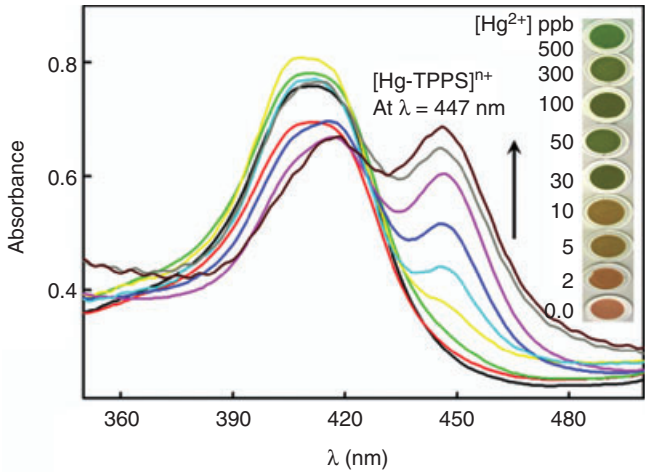

Figure 5.6 Representative concentration-dependent changes of HOM-TPPS cage chemosensor sink in the color map and in UV-visible reflection spectra of $[Hg–TPPS]^{n+}$ complex formation at $\lambda = 447$ nm, with the addition of various concentrations of Hg(II) ions. The signal responses of the optical sink were monitored at specific sensing conditions (pH 9, 4.0 mg, 60 s, 25 °C). Adapted with permission from Ref. [24]; © 2006, Wiley-VCH.

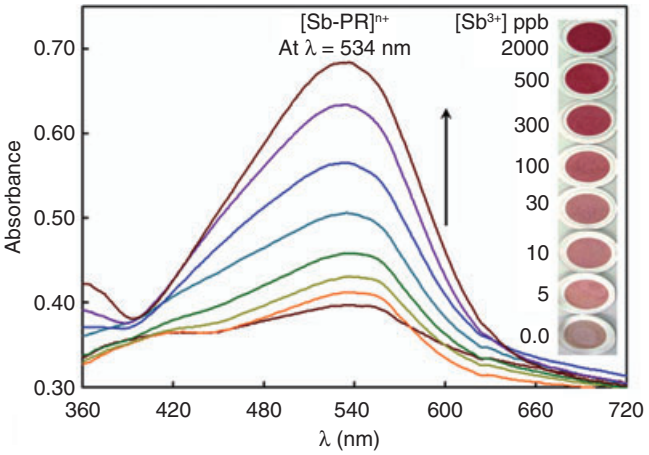

Figure 5.7 Representative concentration-dependent changes of HOM-PR cage chemosensor sink in the color map and in UV-visible reflection spectra of $[Sb–PR]^{n+}$ complex formation at $\lambda = 534$ nm, with the addition of various concentrations of Sb(III) ions. The signal responses of optical sink were monitored at specific sensing conditions (pH 3, 4.0 mg, 60 s, 25 °C). Adapted with permission from Ref. [24]; © 2006, Wiley-VCH.

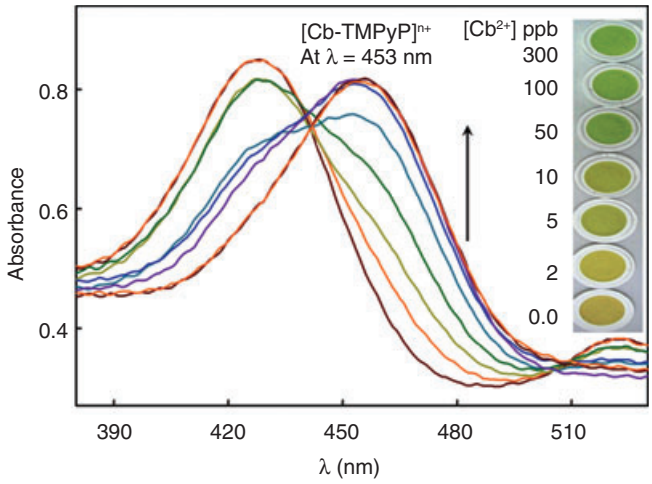

Figure 5.8 Representative concentration-dependent changes of HOM-TMPyP cage chemosensor sink in the color map and in UV-visible reflection spectra of $[Cd–TMPyP]^{n+}$ complex formation at $\lambda = 453$ nm, with the addition of various concentrations of Cd(II) ions. The signal responses of optical sink were monitored at specific sensing conditions (pH 9.5, 4.0 mg, 60 s, 25 °C). Adapted with permission from Ref. [24]; © 2006, Wiley-VCH.

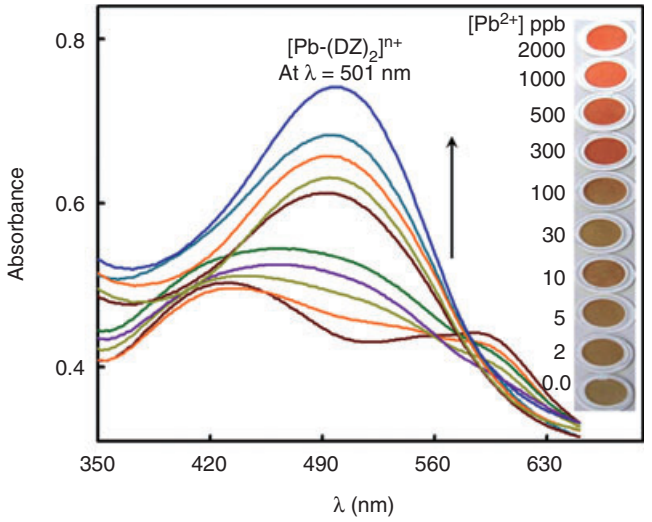

Figure 5.9 Representative concentration-dependent changes of HOM-DZ cage chemosensor sink in the color map and in UV-visible reflection spectra of $[Pb–(DZ)_2]^{n+}$ complex formation at $\lambda = 501$ nm, with the addition of various concentrations of Pb(II) ions. The signal responses of optical sink were monitored at specific sensing conditions (pH 7, 4.0 mg, 150 s, 25 °C). Adapted with permission from Ref. [24]; © 2006, Wiley-VCH.

the wider concentration range of the Hg^{2+}, Sb^{3+}, Cd^{2+} and Pb^{2+} ions (see Table 5.1); this could be achieved by monitoring the signaling change in the reflectance spectra of nanosensors during the formation of $[Hg–TPPS]^{n+}$, $[Sb–PR]^{n+}$, $[Cd–TMPyP]^{n+}$ and $[Pb–(DZ)_2]^{n+}$ complexes (Figures 5.6–5.9). However, in general, the reflectance spectra of HOM-TPPS and HOM-TMPyP nanosensors exhibited a bathochromic shift, from 410 and 429 nm to 447 and 453 nm, during recognition of the Hg^{II} and Cd^{II} ions, respectively. In turn, the reflectance spectra of the HOM-PR sensor showed a hyperchromic effect at 534 nm upon the addition of Sb^{III} ions. In the Pb^{II} ion-sensing system, the HOM-DZ sensor at 596 nm exhibited a blue shift to 501 nm after the addition of Pb^{II} ions. These results indicated the formation of charge–transfer complexes between the metal ions and the probes (as shown in Schemes 5.1–5.4).

Successful visual detection of Hg^{2+}, Sb^{3+}, Cd^{2+} and Pb^{2+} ions over wide detection ranges (D_Rs) of 2 to 500 ppb, 5 to 2000 ppb, 2 to 300 ppb and 2 to 2000 ppb was clearly achieved by using HOM-TPPS, HOM-PR, HOM-TMPyP and HOM-DZ nanosensors, respectively. The color of the nanosensors (see insets in Figures 5.6 to 5.9) changed with increasing $[Cd^{2+}]$ ions. The color reaction was stable, and no elution of the probe molecules occurred with addition of the Hg^{2+}, Sb^{3+}, Cd^{2+} and Pb^{2+} analyte ions [24, 25, 33, 63]. The rapid, sensitive detection of Hg^{2+}, Sb^{3+}, Cd^{2+} and Pb^{2+} ions at nanomolar concentrations by using the naked eye, without any instrumentation, indicated the high performance and reliability of these sensing systems, as evidenced by the results of UV-visible spectroscopy (see Figures 5.6–5.9).

5.6 The Calibration Graphs and Analytical Parameters of Nanosensors

The reflectance bands of the $[Hg–TPPS]^{n+}$, $[Sb–PR]^{n+}$, $[Cd–TMPyP]^{n+}$ and $[Pb–(DZ)_2]^{n+}$ complexes were recorded after correction of the baseline of the reflection spectra between the nanosensor signal of the blank and the concentration-dependence for Hg^{2+}, Sb^{3+}, Cd^{2+} and Pb^{2+} ions at λ-values of 447, 534, 453 and 501 nm, respectively. A linear calibration at low-level concentrations of Hg^{2+}, Sb^{3+}, Cd^{2+} and Pb^{2+} ions with a correlation coefficient range of ~0.998 was characteristic of the calibration curve for the 3-D cubic cage nanosensors (Figure 5.10). Due to saturation effects, however, a nonlinear correlation at the inflection point was observed with high concentrations of Hg^{2+}, Sb^{3+}, Cd^{2+} and Pb^{2+} ions (≥0.049, 0.024, 0.088 and 0.014, respectively) [24]. The nonlinear curves indicated that the Hg^{2+}, Sb^{3+}, Cd^{2+} and Pb^{2+} analytes could be detected with highest sensitivity at low concentrations. To ensure both accuracy and precision of the metal ion-sensing systems, several quantification measurements (10 or more times) were carried out over a wide range of concentrations of 'standard' solutions of Hg^{2+}, Sb^{3+}, Cd^{2+} and Pb^{2+} analytes at the specific sensing conditions (see Figures 5.4 and 5.5). The calculated standard deviation for the analysis, using all monolithic nanosensors, was in the range of 0.1–0.3%, as evidenced by the fitting plot of the calibration graphs.

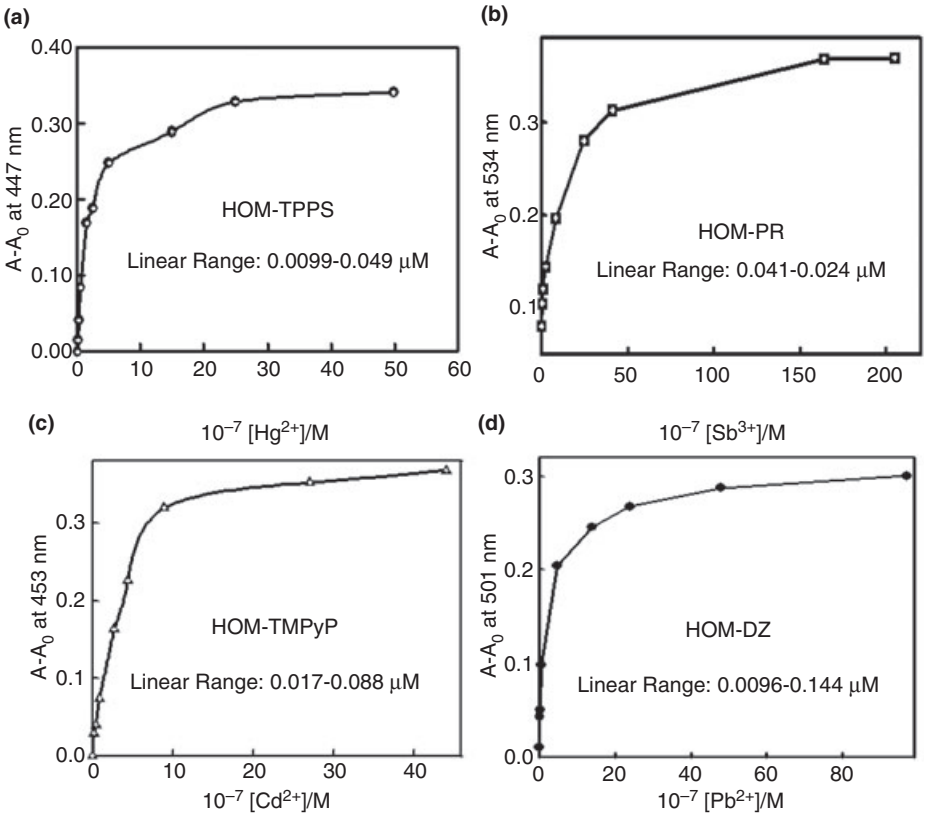

Figure 5.10 Calibration plots (A-A_o [metal ion] concentration, where A_o and A_c is the absorbance of HOM-probe (blank) of (a) HOM-TPPS; (b) HOM-PR; (c) HOM-TMPyP; and (d) HOM-DZ nanosensors and the signal response of $[Hg–TPPS]^{n+}$, $[Sb–PR]^{n+}$, $[Cd–TMPyP]^{n+}$ and $[Pb–(DZ)_2]^{n+}$ complexes during the recognition of Hg^{2+}, Sb^{3+}, Cd^{2+} and Pb^{2+} analyte ions at pH 9, 3, 9.5 and 7, respectively. The sensor amount, total volumes and temperature of the sensing systems were maintained at 4 mg, 20 cm^3 and 25 °C, respectively.

Both, the detection (L_D) and quantification (L_Q) limits of Bi(III) ions, using the mesocaged nanosensors, were estimated from the linear portion of the calibration plot (Figure 5.10) [34, 64], according to Equations 5.2 and 5.3:

$$L_D = k_1 S_b / m \tag{5.2}$$

$$L_Q = k_2 S_b / m \tag{5.3}$$

where the constants of k_1 and k_2 are equal to 3 and 10, respectively, S_b is the standard deviation for the blank, and m is the slope of the calibration graph in the linear range (Figure 5.10). The L_D value (Table 5.1) indicated that the cubic nano-

sensors enabled an effective detection of Hg^{2+}, Sb^{3+}, Cd^{2+} and Pb^{2+} target ions at concentrations up to ~10^{-9} mol dm^{-3} by using these simple ion-sensing systems. Furthermore, the quantification limit (L_Q) signifies the precise correlation of the experimental sensing procedure of Hg^{2+}, Sb^{3+}, Cd^{2+} and Pb^{2+} ion-sensing data obtained from the fabricated nanosensors (see Table 5.1).

Furthermore, at the inflection points in the calibration curves (see Figure 5.10), the stoichiometry of the $[Hg–TPPS]^{n+}$, $[Sb–PR]^{n+}$, $[Cd–TMPyP]^{n+}$ and $[Pb–(DZ)_2]^{n+}$ complexes was 1:1 (Hg^{II}:TPPS), 1:1 (Sb^{III}:PR), 1:1 (Cd^{II}:TMPyP) and 1:2 (Pb^{II}:DZ) for HOM-probe nanosensors (see Schemes 5.1–5.4). Further evidence for the stoichiometric $[Hg–TPPS]^{n+}$, $[Sb–PR]^{n+}$, $[Cd–TMPyP]^{n+}$ and $[Pb–(DZ)_2]^{n+}$ complexes was revealed from Job's plot (data not shown), where changes in the absorbance of the complex formation in solution under experimental conditions were monitored. The results indicated a 1:1 binding for TPPS with Hg^{II}, PR with Sb^{III} and TMPyP with Cd^{II} ions, respectively (see Schemes 5.1–5.3). However, a 1:2 binding for DZ with Pb^{II} ion was characteristic for formation of the $[Pb–(DZ)_2]^{n+}$ complex (see Scheme 5.4).

The stability constant (log K_s) of the formed $[Hg–TPPS]^{n+}$, $[Sb–PR]^{n+}$, $[Cd–TMPyP]^{n+}$ and $[Pb–(DZ)_2]^{n+}$ complexes with the nanosensors, at specific pH values of 9.0, 3.0, 9.5 and 7.0, was estimated according to Equation 5.4:

$$\log K_s = [ML]_S/[L]_S \times [M] \tag{5.4}$$

where [M] refers to the concentration of metal ions in solution that have not reacted with the chelating agent, [L] represents not only the concentration of free DZ ligand but also the concentration of all ligands not bound to the metal, and the subscript S refers to the total concentration and the species in the solid phase [64]. Values of the binding constants (log *Ks*) indicated that the nitrogen-containing TPPS and TMPyP ligands typically bound tightly to Hg^{II} and Cd^{II} ions of the fabricated nanosensors. In general, the high analyte-to-receptor binding affinity was due to an intrinsic mobility of the probe-based nanosensors to bind the Hg^{2+}, Sb^{3+}, Cd^{2+} and Pb^{2+} ions efficiently in these sensing systems (see Table 5.1).

5.7
The Advantages of Nanosensor Designs

5.7.1
Retention of Uniformity of Nanosensor Cage-Like Sinks

The X-ray diffraction (XRD) profiles (Figure 5.11) provide evidence that the ordered face-centered cubic Fm3m structures (HOM-C10) were characteristic of the fabricated monolithic carriers and nanosensors [21b, d]. Despite the high loading level of the organic-probe moieties into the necked pore channels, or onto the pore surface, finely resolved Bragg diffraction peaks were clearly evident for the cubic Fm3m nanosensor geometries. This finding indicated the successful immobiliza-

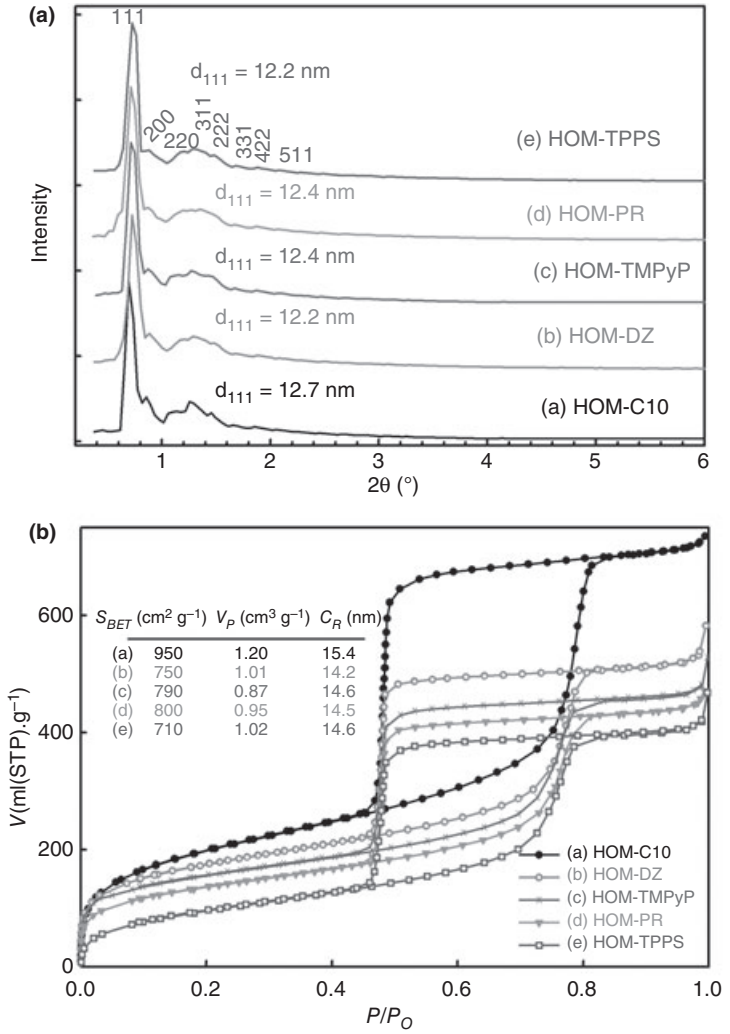

Figure 5.11 (a) X-ray diffraction pattern and (b) N_2 adsorption/desorption isotherms at 77 K of cubic Fm3m cage carriers (HOM-C10) (curve a) and HOM-DZ (curve b); HOM-TMPyP (curve c); HOM-PR (curve d) and HOM-TPPS (curve e) nanosensors. The inserts are the texture parameters of the HOM carriers and sensors: Mesopore (V_p) volumes, BET surface area (S_{BET}) and pore cavity (C_R). Adapted with permission from Ref. [25]; © 2006, Wiley-VCH.

tion of the hydrophilic TPPS, TMPyP and PR probes and hydrophobic DZ chromophore into the rigid condensed framework of the matrices, while retaining the mesoscopically orientational order (Figure 5.11a and b, curves b to e) of cubic Fm3m mesostructures. These rigid matrices with such order led to a high flux and transport of Hg^{2+}, Sb^{3+}, Cd^{2+} and Pb^{2+} analyte ions during the detection process [24].

The N_2 isotherms revealed a uniformity and regularity of the 3-D cubic cage nanosensors, as evidenced from a well-known sharp inflection of the adsorption/desorption branches (Figure 5.11b). However, H_2-type hysteresis loop and the well-defined steepness of the isotherms (Figure 5.11b, curves a to e) indicated that uniform cage-like pore structures were characteristic of the cubic Fm3m nanosensors [21, 65]. The adsorption branches were slightly shifted to a lower relative pressure (P/P_o) when the organic probe moieties were immobilized (Figure 5.11b), indicating an inclusion of the organic moieties (to some extent) into the spherical mesopore cavity, without any significant effect on the uniformly sized structures. In turn, no shift in the desorption branches of the nanosensors was evident. The latter aspect, in particular, indicated a retention of the entrance of cage structures and an accessibility and retainability of the probes in the spherical cavity. Further evidence of this inclusion inside the pore cavity was that, first, the width of the hysteresis loop was decreased with embedding of the organic moieties, which in turn indicated a decrease in the nanoscale pore length for all of the fabricated nanosensors (see Figure 5.11b, inset). Second, a decrease in the surface area and pore volume with the functionalization of cubic nanosensors provided further evidence that the organic moieties were embedded inside the mesopore. The retention of physical characteristics of nanosensors, such as large porosity, surface area and pore volume, allowed the Hg^{2+}, Sb^{3+}, Cd^{2+} and Pb^{2+} ions to access the functional active sites of the probe-based nanosensor [65]. In fact, homogeneous diffusion and rapid transport of analyte ions onto the ordered pore networks of materials led to an excellent sensitivity with a rapid response-time of detection (see t_R in Table 5.1).

Transmission electron microscopy (TEM) images (Figure 5.12) revealed well-organized mesopore arrays over a large area of the cubic Fm3m lattices of nanosensors, despite an immobilization of the loading coverage of bulky chromophore molecules such as the TPPS, PR, TMPyP and DZ probes. The TEM images (Figure 5.12) show uniformly sized, cage-like pores and continuous spherical arrangements along all directions of the nanosensors [21], despite the slight defects, as indicated by arrows. The topological defect surfaces for these fabricated nanosensors were also evident from the 3-D TEM images (Figures 5.12c and d). Both sets of images, in general, indicated the retention of uniformly sized order structures, which in turn facilitated receptor–metal binding events during the sensing response systems, as evidenced by the rapid response times for Hg^{2+}, Sb^{3+}, Cd^{2+} and Pb^{2+} ion detection (see Table 5.1).

5.7.2
Rapid Time-Response of Metal Ion-Sensing Systems

The rapid metal-to-ligand binding kinetics with formation of the $[Hg–TPPS]^{n+}$, $[Sb–PR]^{n+}$, $[Cd–TMPyP]^{n+}$ and $[Pb–(DZ)_2]^{n+}$ complexes was investigated by continuously monitoring the UV-visible reflectance spectra (Figure 5.13) and the color change of the nanosensors after addition of Hg^{2+}, Sb^{3+}, Cd^{2+} and Pb^{2+} ions as a function of time. The results showed that charge transfer between the TPPS, PR,

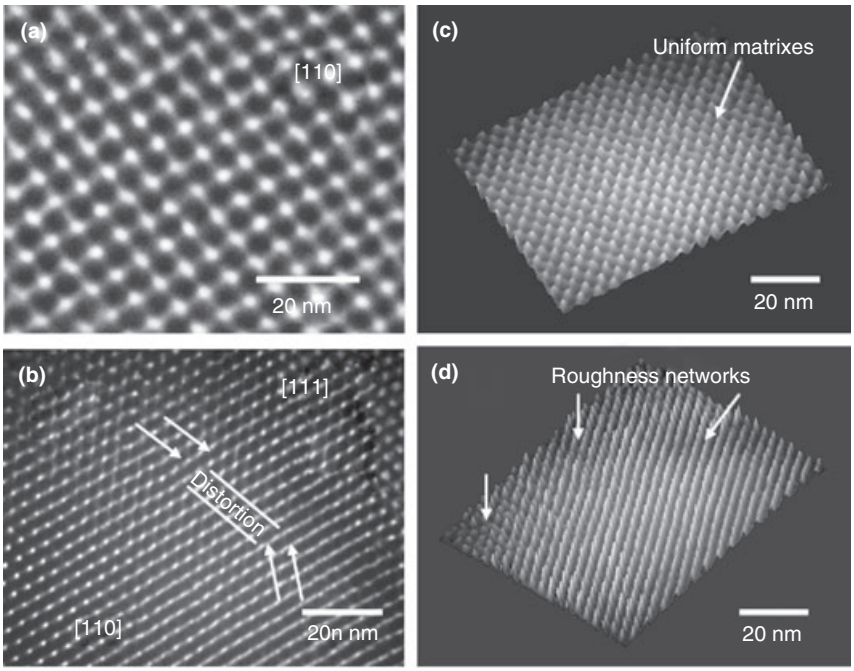

Figure 5.12 Representative transmission electron microscopy (TEM) images of uniformly shaped cage mesochannels of the optical (a) HOM-DZ and (b) HOM-PR sensors recorded along the [110] (a); distorted [110]/[111] (b). The 3-D surfaces of these TEM micrographs (c and d, respectively) with a tilt of 45° revealed, in general, smooth and well-ordered network surfaces over wide-range domains. However, TEM image (b) showed that grafting of the cage monoliths during batch embedding experiments might induce an orientationally distorted portion, though this did not lead to significant collapse in the mesoscopic frameworks. Adapted with permission from Ref. [24]; © 2006, Wiley-VCH.

TMPyP and DZ probes and Hg^{2+}, Sb^{3+}, Cd^{2+} and Pb^{2+}, respectively, occurred within a short time period ($60\,s \leq t_R \leq 3\,min$), due to the ability of the nanostructures with large, open, uniform pore architectures to efficiently bind the Hg^{2+}, Sb^{3+}, Cd^{2+} and Pb^{2+} ions to the grafted TPPS, PR, TMPyP and DZ probes (Figure 5.13). Despite a low, or even high, concentration of analyte ions used during the detection process, no significant change in nanosensor response time was evident. The results indicated a high availability and affinity of the probe ligands for Hg^{2+}, Sb^{3+}, Cd^{2+} and Pb^{2+} ions binding at all metal–ion loading levels. In fact, the high metal flux – namely, ion transport and the affinity of the metal–ligand binding – were significantly affected by the mesopore shape and by the structural geometry and morphology of fabricated nanosensors, as clearly evidenced by the t_R value (Table 5.1). The results also indicated that the cage nanosensors 'sink-like' exhibited an easy accessibility of Hg^{2+}, Sb^{3+}, Cd^{2+} and Pb^{2+} ions, and rapid binding of TPPS with Hg^{II}, PR with Sb^{III}, TMPyP with Cd^{II}, and DZ with Pb^{II}.

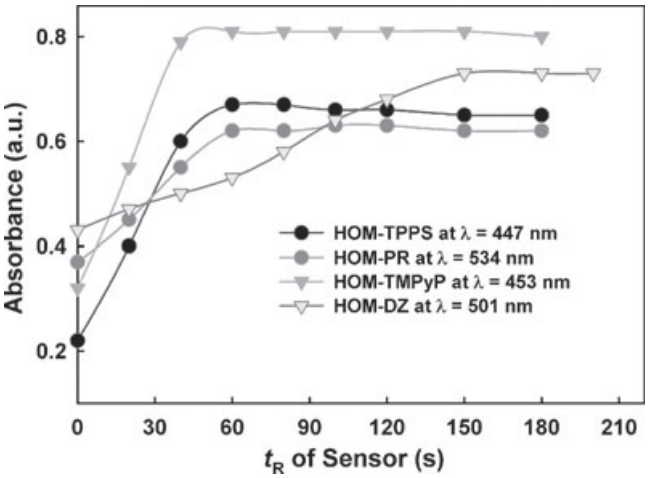

Figure 5.13 Kinetic response-time of the signal response of $[Hg–TPPS]^{n+}$, $[Sb–PR]^{n+}$, $[Cd–TMPyP]^{n+}$ and $[Pb–(DZ)_2]^{n+}$ complexes during the recognition of [0.5 ppm] Hg^{2+}, [0.5 ppm] Sb^{3+}, [0.3 ppm] Cd^{2+} and [1.0 ppm] Pb^{2+} analyte ions using the monolithic HOM-TPPS, HOM-PR, HOM-TMPyP and HOM-DZ nanosensors at pH 9, 3, 9.5 and 7, respectively. The sensor amount, total volumes and temperature of the sensing systems were maintained at 4 mg, 20 cm^3 and 25 °C, respectively.

5.7.3
Stability of the Monolithic Nanosensors

The stability of the grafted PR-probe based nanosensors was examined for 2-D and 3-D mesostructured traps. The long-term retention of the electron acceptor/donor strength of the probe functional group bestows great technological promise on these optical sensing systems [1–17]. Among the developed sensor-based nanostructure materials, the robustness in sensor design (see Schemes 5.1–5.4) provided control over any potential leaching of the hydrophilic TPPS, TMPyP and PR chromophores and hydrophobic DZ probe during any washing cycles, or after long-term storage (see Table 5.1). However, the strong (coulombic) electrostatic interactions of the hydrophilic TPPS, TMPyP and PR chromophores with charged grafted surfaces by TMAC and MPTS ligands led to stable, confined sensors. The study results showed that only a slight change in the optically colored density of the 'absorption spectra' for the HOM-TPPS, HOM-TMPyP and HOM-PR nanosensors was evident, even after long-term storage (on the order of months), which provided further evidence of an efficient sensing functionality (see Table 5.1). Although, direct immobilization of the DZ-probe into HOM monoliths, without the use of silane or a thiol coupling agent, led to a high-mobility ion-sensing system during the Pb(II)–DZ binding events, although limitations were observed in the retention of sensor activity during storage. This effect might have been due to the grafting design of DZ into HOM carrier, which occurred through the

physical 'short-range' interactions (i.e. van der Waals and H-bonding interactions). In both designs of optical nanosensor, the tailored nanostructures achieved by tuning the surface characteristics with charge carrier groups enabled the sensing systems to acquire long-term stability in their functionalities, despite the longer storage time (see Table 5.1). Such long-term stability makes these sensing systems particularly applicable for the detection of other toxic metal ions [1–3].

5.7.4 Reversibility of the Metal Ion-Sensing Systems

One major advantage of nanostructured sensors is their retention of functionality in terms of sensitivity with a rapid response time, even after multiple regeneration/reuse cycles of the $[Hg–TPPS]^{n+}$, $[Sb–PR]^{n+}$, $[Cd–TMPyP]^{n+}$ and $[Pb–(DZ)_2]^{n+}$ complexes in the materials [1–3, 24, 25, 33]. Although improvements in the reducibility and reversibility of the chemical sensors represent a major challenge, the nanostructured sensor can extend control of the Hg^{2+}, Sb^{3+}, Cd^{2+} and Pb^{2+} ion detection, even after several cycles of decomplexation in which an appropriate stripping agent is used, such as 0.01–0.1 *M* ethylenediaminetetraacetic acid (EDTA), 0.01 *M* ClO_4^- or 0.1 *M* $CH_3COO_3^-$ (see Schemes 5.1–5.4). After multiple regeneration/reuse cycles (i.e. six, or more), although the regenerated nanosensors showed a relatively lower sensitivity (Figure 5.14) with greater metal-to-ligand kinetic hindrances (see t_R values), they also showed a well-controlled signaling for their visual detection (see Table 5.2).

As a consequence of the recycle process, the effective binding and signaling of the metal ion targets to the probe functional sites might become significantly degraded due to the substantial influence of the stripping agents (Figure 5.14) upon cycling. Although the time-response of such regenerated sensors was generally influenced by the extensive cycling process, the binding and signaling remained relatively rapid (on the order of minutes), and fully reversible [24]. In order to understand the differences in sensing efficiency among the various regenerated nanosensors, textural parameters were examined for all of the nanostructured sensors after the reuse cycles (Table 5.2). The results revealed that, in particular, all of the sensing systems experienced a significant reduction in surface area and pore volume. Compared to the powder sensors [15–17], the meso/macroporous surfaces of monolith-based nanosensors showed a greater reversibility, due to the open interconnectivity macropore grains. These large-pore surface grains may induce characteristics of high adsorption in the probe, and increase accessibility for analyte ion transport, leading to large amounts of the probe being retained. A high probe loading may result in a selective and sensitive sensor, without increased kinetic hindrance, despite the probe potentially leaching from the pore surface during decomplexation. In this way, the nanosensors will achieve the high performance required for use in the environmental clean-up of toxic heavy metal ions.

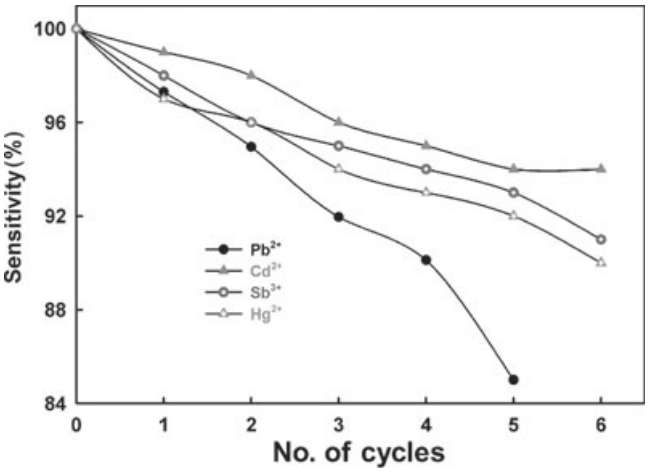

Figure 5.14 Reversibility graph of the cage HOM-DZ (a); HOM-TMPyP (b); HOM-PR (c); and HOM-TPPS (d) nanosensors after regeneration cycles 'decomplexation process' of analyte ions using [0.1 *M*] CH_3COO^-, [0.1 *M*] EDTA, [0.01 *M*] EDTA and [0.01 *M*] ClO_4^- stripping agents, respectively. Note the calculated percent variability regarding efficiency of the optical sensors after cycling of 0.3 ppm analyte ions. Adapted with permission from Ref. [24]; © 2006, Wiley-VCH.

Table 5.2 Textural parameters (V_p and S_{BET}) and sensing features of optical HOM nanosensors after several decomplexation processes of $[Hg–TPPS]^{n+}$, $[Sb–PR]^{n+}$, $[Cd–TMPyP]^{n+}$ and $[Pb–(DZ)_2]^{n+}$ complexes using various eluants and the reuse cycles and during the recognition of 0.3 ppm analyte ions.

HOM sensor	Eluant (*M*)	Analyte	V_p ($cm^3 g^{-1}$)	S_{BET} ($m^2 g^{-1}$)	Cycle no.	t_R (min)	E[a] (%)
TPPS	[0.02] ClO_4^-	Hg^{2+}	0.99	700	2	1.5	96
			0.96	680	4	2.0	94
			0.94	670	6	2.5	90
PR	[0.01] EDTA	Sb^{3+}	0.93	790	2	1.5	96
			0.9	770	4	2.0	95
			0.88	740	6	2.5	92
TMPyP	[0.1] EDTA	Cd^{2+}	0.86	780	2	1.0	98
			0.84	760	4	1.5	96
			0.83	750	6	2.0	95
DZ	[0.1] CH_3COO^-	Pb^{2+}	1.0	740	2	3.0	95
			0.98	690	4	3.5	90
			0.96	680	6	3.5	86

a Efficiency (E) of cage HOM sensors within the regeneration/reuse cycle numbers was estimated based on sensor sensitivity during detection of analytes ions compared with the original data in Table 5.1.

5.7.5
Optically Selective Nanosensors for Trace-Level Toxic Ions

The practical utility of the nanoscale-structured sensors described here is the ability to fine-tune highly selective sensing systems, when combined with actively diverse ions (interfering components), under experimentally controlled conditions (Figures 5.15 and 5.16). In order to investigate the effect of extraneous ions in the

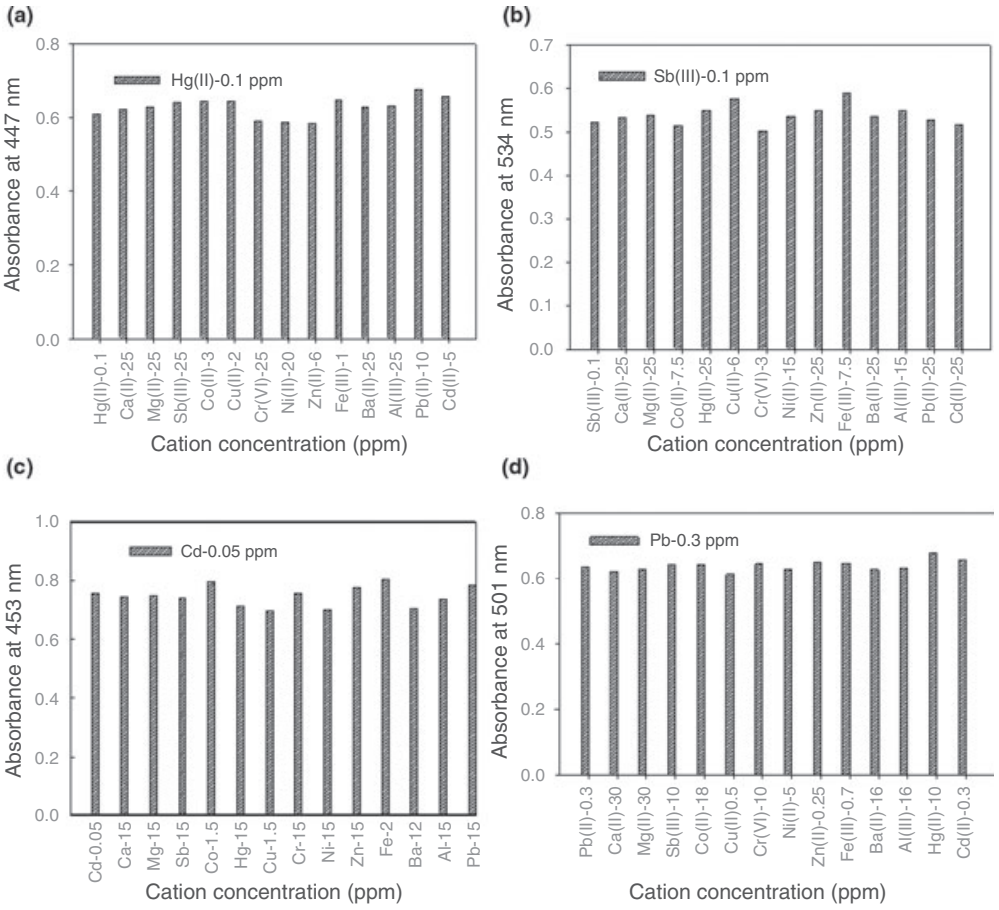

Figure 5.15 Selectivity profiles of (a) HOM-TPPS; (b) HOM-PR; (c) HOM-TMPyP; and (d) HOM-DZ nanosensors using the simultaneously selective recognition method, in which the effect of various cations on the signal response of $[Hg–TPPS]^{n+}$, $[Sb–PR]^{n+}$, $[Cd–TMPyP]^{n+}$ and $[Pb–(DZ)_2]^{n+}$ complexes during the recognition of [0.1 ppm] Hg^{2+}, [0.1 ppm] Sb^{3+}, [0.05 ppm] Cd^{2+} and [0.3 ppm] Pb^{2+} analyte ions at pH 9, 3, 9.5 and 7, respectively. Note: the concentration of diverse ions was in ppm, and given with the notations of interfered ions (x-axis). The inferred species were also first mixed with the monolithic sensors before addition of the analytes under working sensing conditions of 4 mg sensor, 20 ml volume and 25 °C.

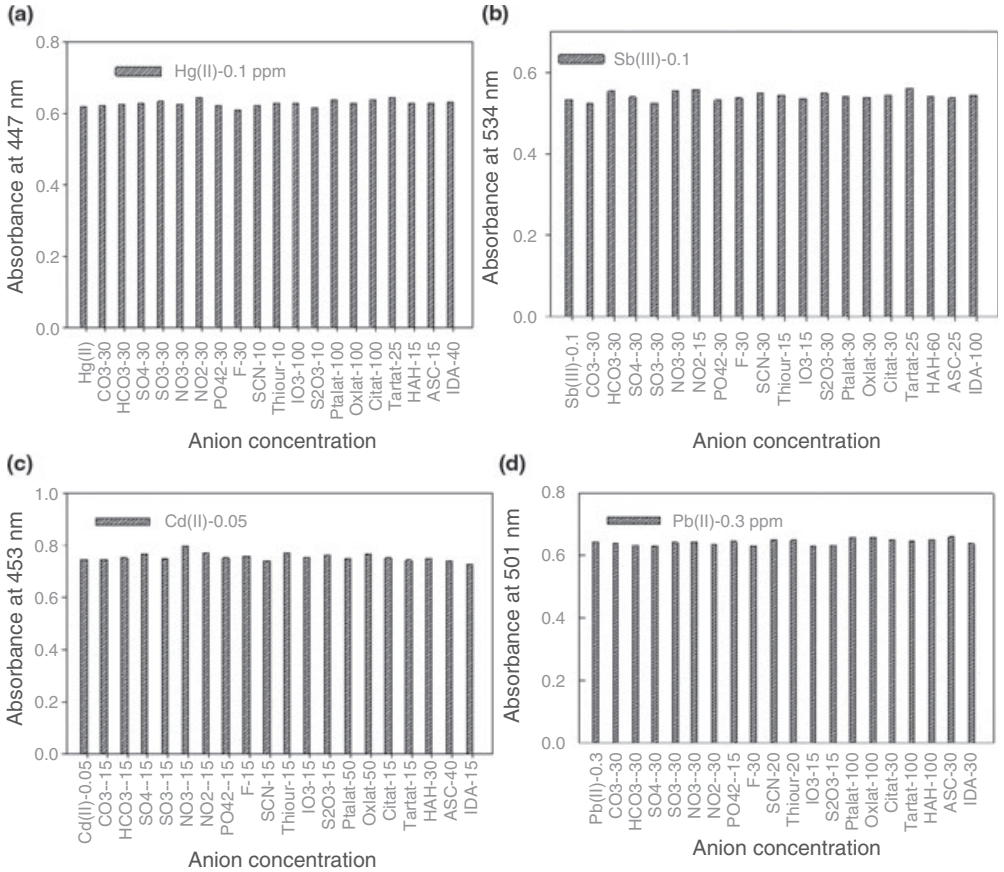

Figure 5.16 Selectivity profiles of (a) HOM-TPPS; (b) HOM-PR; (c) HOM-TMPyP; and (d) and HOM-DZ nanosensors using the simultaneously selective recognition method, in which the effect of various anions and complexing agents on the signal response of $[Hg–TPPS]^{n+}$, $[Sb–PR]^{n+}$, $[Cd–TMPyP]^{n+}$ and $[Pb–(DZ)_2]^{n+}$ complexes during the recognition of [0.1 ppm] Hg^{2+}, [0.1 ppm] Sb^{3+}, [0.05 ppm] Cd^{2+} and [0.3 ppm] Pb^{2+} analyte ions at pH 9, 3, 9.5 and 7, respectively. Note: the concentration of diverse ions was in ppm, and given with the notations of interfered ions (x-axis). In addition, the inferred species were first mixed with the monolithic sensors before addition of the analytes at the working sensing conditions of 4 mg sensor amount, 20 ml volume and 25 °C. The abbreviation of anions were as follows: CO_3^{2-} = carbonate; HCO_3^- = bicarbonate; SO_4^{2-} = sulfate; SO_3^{2-} = sulfite; NO_3^- = nitrate; NO_2^- = nitrite; PO_4^{3-} = phosphate; F^- = fluoride; SCN^- = thiocyanate; Thiour = thiourea; IO_3^- = iodate; $S_2O_3^{2-}$ = thiosulfate; Ptalat = phthalate; Oxlat = oxalate; Citat = citrate; Tartat = tartrate; HAH = hydroxylamine hydrochloride; ASC = ascorbic acid; IDA = iminodiacetic acid.

simultaneous selective detection of Hg^{2+}, Sb^{3+}, Cd^{2+} and Pb^{2+} ions (particularly at low concentration), a series of controlled sensing experiments was conducted in which known amounts of cations and anions were added to the Hg^{2+}, Sb^{3+}, Cd^{2+} and Pb^{2+} ion-sensing systems (Figures 5.15 and 5.16). The results showed the sensing system for Hg^{2+}, Sb^{3+}, Cd^{2+} and Pb^{2+} target ions to be affected by oppositely and potentially charged species of the interfering anions and cations. These extraneous ions could actually bind or interact, detrimentally, with the HOM-TPPS, HOM-PR, HOM-TMPyP and HOM-DZ nanosensors. However, despite such interactions the optical signal of the $[Hg–TPPS]^{n+}$, $[Sb–PR]^{n+}$, $[Cd–TMPyP]^{n+}$ and $[Pb–(DZ)_2]^{n+}$ complexes varied within a permissible tolerance limit of ±5%; this indicated that the sensing system for Hg^{2+}, Sb^{3+}, Cd^{2+} and Pb^{2+} target ions was highly tuned, functional and selective, even at nanomolar-level detection (Figures 5.15 and 5.16) [33]. In general, no significant changes in either the developed color or the reflectance intensities of the $[Hg–TPPS]^{n+}$, $[Sb–PR]^{n+}$, $[Cd–TMPyP]^{n+}$ and $[Pb–(DZ)_2]^{n+}$ complexes were observed (Figures 5.15 and 5.16), despite the addition of cations, which are effective disturbance species at concentrations ranging from 1- to 100-fold higher than that of the target ions.

In this respect, the nanostructured hydrophilic- and hydrophobic-based sensors exhibited a high selectivity for Hg^{2+}, Sb^{3+}, Cd^{2+} and Pb^{2} target ions, permitting the accurate and specific detection of analyte ions, without significant interference by the active component species [15–17]. Under specific sensing conditions, two key factors affect the selectivity of the nanostructured sensing systems. First, nanostructured sensors exhibit selectivity even at a low concentration of target ions (nanomolar scale); however, active interfering species and multicomponents at much higher concentrations can be introduced into these nanostructured sensors without affecting either significant physical characteristics or chemical properties. This retention in nanosensor features allowed an efficient binding of multifunction components with probe molecule-based sensors, without causing distortion in the octahedral $[Hg–TPPS]^{n+}$, $[Sb–PR]^{n+}$, $[Cd–TMPyP]^{n+}$ and $[Pb–(DZ)_2]^{n+}$ complexes. Second, the 3-D-ordered sensor with nanoscale open-pore arrays, high surface areas and high pore volumes might enhance the rapid, homogeneous distribution of multi-ion transport species onto the modified probes, leading to a durable signal in response to metal-to-probe binding events in toxic environmental and wastewater samples.

5.8 Conclusions and Outlook

In this chapter we have defined the key factors for the development of receptors as ‘indicator dyes’, and surface-confined nanomaterials as ‘carriers’, for the creation of optical chemical sensors capable of selectively discriminating trace levels of toxic analytes. Our aim was to widen the knowledge base with regards to the causes of – and solutions to – metal-ion toxicity. A key factor when designing optical nanosensors to sense mercury, cadmium, lead and antimony is the stable immo-

bilization of molecular probes on 3-D-ordered cubic monoliths. Hence, we have reviewed the published information relating to these four metals, in terms of their chemical behavior in various processes and environmental conditions, their contributions to toxicity, and applicable sensing technologies.

The nanosensor designs were aimed at identifying and evaluating metal-treatment technologies for reducing – or even eliminating – the toxicity of these four metals. Hence, a simple, generalized nanosensor design was described, based on a dense pattern of immobilized hydrophobic 'neutral' and hydrophilic 'charged' chromophores, but with an intrinsic mobility and robust construction based on 3-D nanoscale structures. The flexibility of electron acceptor/donor strength of the receptor molecules might lead to the creation and transduction of optical color signals in response to receptor–metal analyte binding events. Thus, potential nanosensor designs in the area of environmental sensing for toxic analytes has been emphasized.

Today, the invention, optimization and commercialization of sensing processes represents a significant challenge in materials science and nanotechnology. Whilst, at present, these properties are difficult to monitor with chemical-oriented sensors – and, indeed, progress has been made in this direction – the need for simple, effective and eco-friendly solid sensors persists and, in recent years, this has led to the emergence of solid-material sensors. Today, nanosensors with probes can be utilized not only for basic laboratory assays, but also for field measurements using portable devices and in the domestic situation as commercial indicators.

References

1 (a) Miyawaki, A., Lopis, J., Helm, R., McCaffery, J.M., Adams, J.A., Ikura, M. and Tsien, R.Y. (1997) Fluorescent indicators for Ca^{2+} based on green fluorescent proteins and calmodulin. *Nature*, **388**, 882;
(b) Wolfbeis, O.S. (2005) Materials for fluorescence-based optical chemical sensors. *Journal of Materials Chemistry*, **15**, 2657;
(c) Oehme, I. and Wolfbeis, O.S. (1997) Optical Sensors for determination of heavy metal ions. *Mikrochimica Acta*, **126**, 177.

2 (a) Buhlmann, P., Pretsch, E. and Bakker, E. (1998) Carrier-based ion-selective electrodes and bulk optodes. 2. Ionophores for potentiometric and optical sensors. *Chemical Reviews*, **98**, 1593–687;
(b) Pretsch, E., Buhlmann, P. and Bakker, E. (1997) Carrier-based ion-selective electrodes and bulk optodes. 1. General characteristics. *Chemical Reviews*, **97**, 3083–132;
(c) Keith, L.H., Gron, L.U. and Young, J.L. (2007) Green analytical methodologies. *Chemical Reviews*, **107**, 2695–708.

3 Spichiger-Keller, U.S. (1998) *Chemical Sensors and Biosensors for Medical and Biological Applications*, Wiley-VCH Verlag GmbH, Weinheim, Germany.

4 Gupta, V.K. and Kumar, P. (1999) Cadmium (II)-selective sensors based on dibenzo-24-crown-8 in PVC matrix. *Analytica Chimica Acta*, **389**, 205.

5 (a) Gupta, V.K., Singh, A.K. and Gupta, B. (2007) Schiff bases as cadmium(II) selective ionophores in polymeric membrane electrodes. *Analytica Chimica Acta*, **583**, 340;
(b) Zheng, H., Yan, Z., Dong, H. and Ye, B. (2007) Simultaneous determination of lead and cadmium at a glassy carbon

electrode modified with Langmuir–Blodgett film of *p-tert*-butylthiacalix[4]arene. *Sensors and Actuators. B, Chemical*, **120**, 603;
(c) Shtoyko, T., Conklin, S., Maghasi, A. T., Piruska, A., Richardson, J.N., Seliskar, C.J. and Heineman, W.R. (2004) Spectroelectrochemical sensing based on attenuated total internal reflectance stripping voltammetry. 3. Determination of cadmium and copper. *Analytical Chemistry*, **76**, 1466.

6 (a) Peng, X., Du, J., Fan, J., Wang, J., Wu, Y., Zhao, J., Sun, S. and Xu, T. (2007) A selective fluorescent sensor for imaging Cd^{2+} in living cells. *Journal of the American Chemical Society*, **129**, 1500;
(b) Bronson, R.T., Michaelis, D.J., Lamb, R.D., Husseini, G.A., Farnsworth, P.B., Linford, M.R., Izatt, R.M., Bradshaw, J.S. and Savage, P.B. (2005) Efficient immobilization of a cadmium chemosensor in a thin film: Generation of a cadmium sensor prototype. *Organic Letters*, **7**, 1105;
(c) Grandini, P., Mancin, F., Tecilla, P., Scrimin, P. and Tonellato, U. (1999) Exploiting the self-assembly strategy for the design of selective Cu^{II} ion chemosensors, *Angewandte Chemie – International Edition*, **38**, 3061;
(d) Cho, E.J., Moon, J.W., Ko, S.W., Lee, J.Y., Kim, S.K., Yoon, J. and Nam, K.C. (2003) A new fluoride selective fluorescent as well as chromogenic chemosensor containing a naphthalene urea derivative. *Journal of the American Chemical Society*, **125**, 12376.

7 (a) Kolusheva, S., Shahal, T. and Jelinek, R. (2000) Cation-selective color sensors composed of ionophore-phospholipid-polydiacetylene mixed vesicles. *Journal of the American Chemical Society*, **122**, 776;
(b) Zhang, C. and Suslick, K.S. (2005) A colorimetric sensor array for organics in water. *Journal of the American Chemical Society*, **127**, 11548;
(c) Han, M.S. and Kim, D.H. (2002) Naked-eye detection of phosphate ions in water at physiological pH: a remarkably selective and easy-to-assemble colorimetric phosphate-sensing probe. *Angewandte Chemie – International Edition*, **41**, 3809;
(d) Miyaji, H., Sato, W. and Sessler, J.L. (2000) Naked-eye detection of anions in dichloromethane: Colorimetric anion sensors based on calix[4]pyrrole. *Angewandte Chemie – International Edition*, **39**, 1777.

8 (a) Nam, J-M., Thaxton, C.S. and Mirkin, C.A. (2003) Nanoparticle-based bio-bar codes for the ultrasensitive detection of proteins. *Science*, **301**, 1884;
(b) Prodi, L., Bolletta, F., Montalti, M. and Zaccheroni, N. (2000) Luminescent chemosensors for transition metal ions. *Coordination Chemical Reviews*, **205**, 59.

9 Ho, H-A. and Leclerc, M. (2004) Optical sensors based on hybrid aptamer/conjugated polymer complexes. *Journal of the American Chemical Society*, **126**, 1384.

10 (a) Resendiz, M.J.E., Noveron, J.C., Disteldorf, H., Fischer, S. and Stang, P.J. (2004) A self-assembled supramolecular optical sensor for Ni(II), Cd(II) and Cr(III). *Organic Letters*, **6**, 651;
(b) Wolfbeis, O.S. (2006) Fiber-optic chemical sensors and biosensors. *Analytical Chemistry*, **78**, 3859–74.

11 Hagleitner, C., Hierlemann, A., Brand, O. and Baltes, H. (2002) *Sensors Update*, Vol. 11, Wiley-VCH Verlag GmbH, Weinheim, pp. 101–55.

12 Desacalzo, A.B., Rurack, K., Weisshoff, H., Mártinez-Mánez, R.M., Marcos, M.D., Amoros, P., Hoffmann, K. and Soto, J. (2005) Rational design of a chromo- and fluorogenic hybrid chemosensor material for the detection of long-Chain Carboxylates. *Journal of the American Chemical Society*, **127**, 184.

13 (a) Liu, J. and Lu, Y. (2004) Accelerated color change of gold nanoparticles assembled by DNAzymes for simple and fast colorimetric Pb^{2+} detection. *Journal of the American Chemical Society*, **126**, 12298;
(b) Coronado, E., Galán-Mascarós, J.R., Martí-Gastaldo, C., Palomares, E., Durrant, J.R., Vilar, R., Gratzel, M. and Nazeeruddin, Md K. (2005) Reversible colorimetric probes for mercury sensing. *Journal of the American Chemical Society*, **127**, 12351.

14 (a) Deo, S. and Godwin, H.A. (2000) A selective, ratiometric fluorescent sensor for Pb^{2+}. *Journal of the American Chemical Society*, **122**, 174;
(b) Rex, M., Hernandez, F.E. and Campiglia, A.D. (2006) Pushing the limits of mercury sensors with gold nanorods. *Analytical Chemistry*, **78**, 445;
(c) Woodroofe, C.C. and Lippard, S.J. (2003) A novel two-fluorophore approach to ratiometric sensing of Zn^{2+}. *Journal of the American Chemical Society*, **125**, 11458.

15 (a) Wirnsberger, G., Scott, B.J., Stucky, G.D., Wirnsberger, G., Scott, B.J. and Stucky, G.D. (2001) pH sensing with mesoporous thin films. *Chemical Communications*, 119;
(b) Nicole, L., Boissiere, C., Grosso, D., Hesemann, P., Moreau, J. and Sanchez, C. (2004) Advanced selective optical sensors based on periodically organized mesoporous hybrid silica thin films. *Chemical Communications*, 2312;
(c) Lee, S.J., Lee, S.S., Lee, J.Y. and Jung, J.H. (2006) A functionalized inorganic nanotube for the selective detection of copper(II) ion. *Chemistry of Materials*, **18**, 4713.

16 (a) Palomares, E., Vilar, R., Green, A. and Durrant, J.R. (2004) Alizarin complexone on nanocrystalline TiO_2: a heterogeneous approach to anion sensing, *Advanced Functional Materials*. **14**, 111;
(b) Wolfbeis, O.S. (2004) Fiber-optic chemical sensors and biosensors. *Analytical Chemistry*, **76**, 3269–84;
(c) Liu, J. and Lu, Y. (2004) Optimization of a Pb^{2+}-directed gold nanoparticle/ DNAzyme assembly and its application as a colorimetric biosensor for Pb^{2+}. *Chemistry of Materials*, **16**, 3231.

17 Comes, M., Marcos, M.D., Sancenon, F., Soto, J., Villaescusa, L.A., Amoros, P. and Beltran, D. (2004) Chromogenic discrimination of primary aliphatic amines in water with functionalized mesoporous silica. *Advanced Materials*, **16**, 1783.

18 (a) Capitan-Vallvey, L.F., Raya, C.C., Lopez, E.L. and Ramos, M.D.F. (2004) Irreversible optical test strip for mercury determination based on neutral ionophore. *Analytica Chimica Acta*, **524**, 365;
(b) Kalinina, M.A., Golubev, N.V., Raitman, O.A., Selector, S.L. and Arslanov, V.V. (2006) A novel ultra-sensing composed Langmuir–Blodgett membrane for selective calcium determination in aqueous solutions. *Sensors and Actuators. B, Chemical*, **114**, 19;
(c) Rodman, D.L., Pan, H., Clarier, C.W., Feng, W. and Xue, Z.L. (2005) Optical metal ion sensor based on diffusion followed by an immobilizing reaction: quantitative analysis by a mesoporous monolith containing functional groups. *Analytical Chemistry*, **77**, 3231.

19 Seiler, K. (1993) *Ion-Selective Optode Membrane*, Fluka, Buchs, Switzerland.

20 (a) Potyrailo, A.R. (2006) Polymeric sensor materials: toward an alliance of combinational and rational design tools? *Angewandte Chemie – International Edition*, **45**, 702;
(b) Heng, L.Y. and Hall, E.A.H. (2000) Producing 'self-plasticizing' ion-selective membranes. *Analytical Chemistry*, **72**, 42.

21 (a) El-Safty, S.A. and Hanaoka, T. (2004) Microemulsion liquid crystal templates for highly ordered three-dimensional mesoporous silica monoliths with controllable mesopore structures. *Chemistry of Materials*, **16**, 384–400;
(b) El-Safty, S.A., Mizukami, F. and Hanaoka, T. (2005) General and simple approach for control cage and cylindrical mesopores and thermal/ hydrothermal stable frameworks. *The Journal of Physical Chemistry B*, **109**, 9255–64;
(c) El-Safty, S.A., Mizukami, F. and Hanaoka, T. (2005) Transparent cubic Fd3m mesoporous silica monoliths with highly controllable pore architectures. *Journal of Materials Chemistry*, **15**, 2590–8;
(d) El-Safty, S.A., Hanaoka, T. and Mizukami, F. (2005) Design of highly stable, ordered cage mesostructured monoliths with controllable pore geometries and sizes. *Chemistry of Materials*, **17**, 3137–45;
(e) El-Safty, S.A., Hanaoka, T. and Mizukami, F. (2005) Large scale design of cubic Ia3d mesoporous silica monoliths with high order, controlled pores and

hydrothermal stability. *Advanced Materials*, **17**, 47–53;
(f) El-Safty, S.A., Hanaoka, T. and Mizukami, F. (2006) Stability of highly ordered nanostructures with uniformly cylindrical mesochannels. *Acta Materialia*, **54**, 899–908;
(g) El-Safty, S.A. (2008) A review of key controls in design of copolymer-silica mesophase monoliths with large particle morphology and uniform three-dimensional pore geometry. *Journal of Porous Materials*, **15**, 369–87;
(h) El-Safty, S.A. and Evans, J. (2002) Formation of highly ordered mesoporous silica materials adopting lyotropic liquid crystal mesophases. *Journal of Materials Chemistry*, **12**, 117;
(i) El-Safty, S.A. and Hanaoka, T. (2003) Fabrication of crystalline, highly ordered three-dimensional silica monoliths (HOM-n) with large, morphological mesopore structures. *Advanced Materials*, **15**, 1893;
(j) El-Safty, S.A. and Hanaoka, T. (2003) Monolithic nanostructured silicate family templated by lyotropic liquid-crystalline nonionic surfactant mesophases. *Chemistry of Materials*, **15**, 2892.

22 (a) Jaroniec, M. (2006) Organosilica the conciliator. *Nature*, **442**, 638;
(b) Lu, Y., Yang, Y., Sellinger, A., Lu, M., Huang, J., Fan, H., Haddad, R., Lopez, G., Burns, A.R., Sasaki, D.Y., Shelnutt, J. and Brinker, C.J. (2001) Self-assembly of mesoscopically ordered chromatic polydiacetylene/silica nanocomposites. *Nature*, **410**, 913;
(c) Corma, A. (1997) From microporous to mesoporous molecular sieve materials and their use in catalysis. *Chemical Reviews*, **97**, 2373;
(d) Clark, J.H., Macquarrie, D.J. and Tavener, S.J. (2006) The application of modified-silicas in liquid phase catalysis. *Dalton Transactions*, 4297–309.

23 (a) El-Safty, S.A. (2003) Sorption and diffusion of phenols onto well-defined ordered nanoporous monolithic silicas. *Journal of Colloid and Interface Science*, **260**, 184–94;
(b) El-Safty, S.A., Hanaoka, T. and Mizukami, F. (2008) *Applied Catalysis A: General*, **337**, 121–9;
(c) El-Safty, S.A. (2008) Synthesis, characterization and catalytic activity of highly ordered hexagonal and cubic composite monoliths. *Journal of Colloid and Interface Science*, **319**, 477–88;
(d) El-Safty, S.A., Kiyozumi, Y., Hanaoka, T. and Mizukami, F. (2008) Heterogeneous catalytic activity of NiO-silica composites designated with cubic Pm3n cage nanostructures. *Applied Catalysis B – Environmental*, **82**, 169–79;
(e) El-Safty, S.A., Kiyozumi, Y., Hanaoka, T. and Mizukami, F. (2008) Nanosized NiO particles wrapped onto uniformly mesocaged silica structures as efficient catalysts. *Applied Catalysis A: General*, **337**, 121–9.

24 El-Safty, S.A., Balaji, T., Matsunaga, H., Hanaoka, T. and Muzukami, F. (2006) Optical sensors based on nanostructured cage materials for the detection of toxic metal ions. *Angewandte Chemie – International Edition*, **45**, 7202.

25 El-Safty, S.A., Ismail, D. Prabhakaran. A. A., Matsunaga, H. and Muzukami, F. (2007) Nanosensor design packages: a smart and compact development for metal ions sensing responses. *Advanced Functional Materials*, **17**, 3731.

26 (a) Matos, J.R., Kruk, M., Mercuri, L.P., Jaroniec, M., Zhao, L., Kamiyama, T., Terasaki, O., Pinnavaia, T.J. and Liu, Y. (2003) Ordered mesoporous silica with large cage-like pores: structural identification and pore connectivity design by controlling the synthesis temperature and time. *Journal of the American Chemical Society*, **125**, 821;
(b) Kleitz, F., Liu, D., Anilkumar, G.M., Park, I., Solovyov, L.A., Shmakov, A.N. and Ryoo, R. (2003) Large cage face-centered-cubic Fm3m mesoporous silica: synthesis and structure. *The Journal of Physical Chemistry B*, **107**, 14296.

27 (a) Turner, A.P.F. (2000) Biosensors-sense and sensitivity. *Science*, **290**, 1315–17;
(b) Stein, A. (2003) Advances in microporous and mesoporous solids – highlights of recent progress. *Advanced Materials*, **15**, 763;
(c) Fan, J., Yu, C., Lei, J., Tian, B., Wang, L., Luo, Q., Tu, B., Zhou, W. and Zhao, D. (2003) Cubic mesoporous silica with large controllable entrance sizes and advanced

adsorption properties. *Angewandte Chemie – International Edition*, **42**, 3146.

28 Fukuoka, A., Araki, H., Sakamoto, Y., Sugimoto, N., Tsukada, H., Kumai, Y., Akimoto, Y. and Ichikawa, M. (2002) Template synthesis of nanoparticle arrays of gold and platinum in mesoporous silica films. *Nano Letters*, **2**, 793.

29 Feng, X., Fryxell, G.E., Wang, L.-Q., Kim, A.Y., Liu, J. and Kemner, K.M. (1997) Functionalized monolayers on ordered mesoporous supports. *Science*, **276**, 92.

30 (a) Metivier, R., Leray, I., Lebeau, B.D. and Valeur, B. (2005) A mesoporous silica functionalized by a covalently bound calixarene-based fluoroionophore for selective optical sensing of mercury(II) in water. *Journal of Materials Chemistry*, **15**, 2965;
(b) Balaji, T., Sasidrharan, M. and Matsunaga, H. (2005) Optical sensor for the visual detection of mercury using mesoporous silica anchoring porphyrin moiety. *Analyst*, **130**, 1162–7.

31 (a) Ensafi, A.A. and Fouladgar, M. (2006) Development of a mercury optical sensor based on immobilization of 4-(2-pyridylazo)-resorcinol on a triacetylcellulose membrane. *Sensors and Actuators. B, Chemical*, **113**, 88;
(b) Carrington, N.A., Thomasa, G.H., Rodmana, D.L., Beach, D.B. and Xue, Z-L. (2007) Optical determination of Cr(VI) using regenerable, functionalized sol–gel monoliths. *Analytica Chimica Acta*, **581**, 232.

32 (a) Mohr, G.J. (2006) New chromogenic and fluorogenic reagents and sensors for neutral and ionic analytes based on covalent bond formation–a review of recent developments. *Analytical and Bioanalytical Chemistry*, **386**, 1201;
(b) Umemura, T., Hotta, H., Abe, T., Takahashi, Y., Takiguchi, H., Uehara, M., Odake, T. and Tsunoda, K. (2006) Slab optical waveguide high-acidity sensor based on an absorbance change of protoporphyrin IX. *Analytical Chemistry*, **78**, 7511;
(c) Narayanaswamy, S.R. (2006) Fluorescence sensor using a molecularly imprinted polymer as a recognition receptor for the detection of aluminium ions in aqueous media. *Analytical and Bioanalytical Chemistry*, **386**, 1235.

33 (a) El-Safty, S.A., Prabhakaran, D., Ismail, A.A., Matsunaga, H. and Muzukami, F. (2008) Simple control of three-dimensional worm-like and ordered mesostructures and their applicability as optically ion-sensitive carriers. *Chemistry of Materials*, **20**, 2644;
(b) El-Safty, S.A., Ismail, A.A., Matsunaga, H. and Muzukami, F. (2008) Uniformly mesocaged cubic Fd3m silica monoliths as optical sensors for Bi(III) ions. *The Journal of Physical Chemistry C*, **112**, 4825.

34 Christian, G.D. (2003) *Analytical Chemistry*, 6th edn, John Wiley & Sons, Inc., New York.

35 McMurray, C.T. and Tainer, J.A. (2003) Cancer, cadmium and genome integrity. *Nature Genetics*, **34**, 239.

36 Goel, J., Kadirvelu, K., Rajagopal, C. and Garg, V.K. (2006) Cadmium(II) uptake from aqueous solution by adsorption onto carbon aerogel using a response surface methodological approach. *Industrial and Engineering Chemistry Research*, **45**, 6531.

37 (a) Gunnlaugsson, T., Lee, T.C. and Parkesh, R. (2003) Cd(II) sensing in water using novel aromatic iminodiacetate-based fluorescent chemosensors. *Organic Letters*, **5**, 4065;
(b) Lee, M.H., Cho, K.K., Shah, A.P. and Biswas, P. (2005) Nanostructured sorbents for capture of cadmium species in combustion environments. *Environmental Science & Technology*, **39**, 8481.

38 Keith, L.H. and Telliard, W.A. (1979) ES&T special report: priority pollutants: I-a perspective view. *Environmental Science & Technology*, **13**, 416.

39 Andrewes, P., Cullen, W.R. and Polishchuk, E. (2000) Arsenic and antimony biomethylation by *Scopulariopsis brevicaulis*: interaction of arsenic and antimony compounds. *Environmental Science & Technology*, **34**, 2249–53.

40 Benounis, M., Jaffrezic-Renault, N., Halouani, H., Lamartine, R. and Dumazet-Bonnamour, I. (2006) Detection of heavy metals by an optical fiber sensor with a sensitive cladding including a new chromogenic calix[4]arene molecule. *Materials Science and Engineering C*, **26**, 364–8.

41 Harris, H.H., Pickering, I. and George, G.N. (2003) The chemical form of mercury in fish. *Science*, **301**, 1203.

42 Tag, K., Riedel, K., Bauer, H.J., Hanke, G., Baronian, K.H.R. and Kunze, G. (2007) Development of a mercury optical sensor based on immobilization of 4-(2-pyridylazo)-resorcinol on a triacetylcellulose membrane. *Sensors and Actuators. B, Chemical*, **122**, 403–9.

43 Kaiser, G. and Tolg, G. (1980) *The Handbook of Environmental Chemistry*, Vol. 3, Part A, Springer-Verlag, NY, pp. 1–58.

44 Francesconi, K.A. (2007) Toxic metal species and food regulations – making a healthy choice. *Analyst*, **132**, 17.

45 Manahan, S.E. (1994) *Environmental Chemistry*, 6th edn, Lewis Publishers, New York, p. 677.

46 Derelanko, M.J. and Hollinger, M.A. (1995) *CRC Handbook of Toxicology*, CRC Press, Boca Raton, FL, p. 550.

47 Yang, L. and Saavedra, S.S. (1995) Chemical sensing using sol-gel derived planar waveguides and indicator phases. *Analytical Chemistry*, **67**, 1307.

48 Wagner, E.P., Smith, B.W. and Winefordner, J.D. (1996) Ultratrace determination of lead in whole blood using electrothermal atomization laser-excited atomic fluorescence spectrometry. *Analytical Chemistry*, **68**, 3199.

49 Wang, Y., Wang, Y.H. and Fang, Z.L. (2005) Octadecyl immobilized surface for precipitate collection with a renewable microcolumn in a lab-on-valve coupled to an electrothermal atomic absorption spectrometer for ultratrace cadmium determination. *Analytical Chemistry*, **77**, 5396–401.

50 Simpson, N.J.K. (2000) *Solid Phase Extraction, Principle, Techniques and Applications*, Marcel Dekker, Inc., New York.

51 Tatay, S., Gavina, P., Coronado, E. and Palomares, E. (2006) Optical mercury sensing using a benzothiazolium hemicyanine dye. *Organic Letters*, **8**, 3857.

52 (a) Ros-Lis, J.V., Marcos, M.D., Mártinez-Mánez, R., Rurack, K. and Soto, J. (2005) A regenerative chemodosimeter based on metal-induced dye formation for the highly selective and sensitive optical determination of Hg^{2+} ions. *Angewandte Chemie – International Edition*, **44**, 4405;
(b) Kim, S.H., Kim, J.S., Park, S.M. and Chang, S-K. (2006) Hg^{2+}-selective off-on and Cu^{2+}-selective on-off type fluoroionophore based upon cyclam. *Organic Letters*, **8**, 371;
(c) Guo, Z., Zhu, W., Shen, L. and Tian, H. (2007) A fluorophore capable of crossword puzzles and logic memory. *Angewandte Chemie – International Edition*, **46**, 5549;
(d) Liu, J. and Lu, Y. (2005) Stimuli-responsive disassembly of nanoparticle aggregates for light-up colorimetric sensing. *Journal of the American Chemical Society*, **127**, 12677.

53 (a) Mello, J.V. and Finney, N.S. (2005) Reversing the discovery paradigm: a new approach to the combinatorial discovery of fluorescent chemosensors. *Journal of the American Chemical Society*, **127**, 10124–5;
(b) Guo, X.G., Qian, X. and Jia, L. (2004) A highly selective and sensitive fluorescent chemosensor for Hg^{2+} in neutral buffer aqueous solution. *Journal of the American Chemical Society*, **126**, 2272–3;
(c) Moon, S.-Y., Youn, N.J., Park, S.M. and Chang, S.-K. (2005) *Journal of Organic Chemistry*, **70**, 2394–7;
(d) Ono, A. and Togashi, H. (2004) Highly selective oligonucleotide-based sensor for mercury(II) in aqueous solutions. *Angewandte Chemie – International Edition*, **43**, 4300–2;
(e) Kim, J.S., Choi, M.G., Song, K.C., No, K.T., Ahn, S.A. and Chang, S-K. (2007) Ratiometric determination of Hg^{2+} ions based on simple molecular motifs of pyrene and dioxaoctanediamide. *Organic Letters*, **9**, 1129;
(f) Mu, H., Gong, R., Ma, Q., Sun, Y. and Fu, E. (2007) *Tetrahedron Letters*, **48**, 5525;

54 (a) Lee, M.H., Wu, J-S., Lee, J.W., Jung, J. H. and Kim, J.S. (2007) Highly sensitive and selective chemosensor for Hg^{2+} based on the rhodamine fluorophore. *Organic Letters*, **9**, 2502;
(b) Yuan, M., Li, Y., Li, J., Li, C., Liu, X., Lv, J., Xu, J., Liu, H., Wang, S. and Zhu, D. (2007) A colorimetric and fluorometric

dual-modal assay for mercury ion by a molecule. *Organic Letters*, **9**, 2313.

55 Maghasi, A.T., Conklin, S.D., Shtoyko, T., Pirucka, A., Richardson, J.H., Seliskar, C.J. and Heineman, W.R. (2004) Spectroelectrochemical sensing based on attenuated total internal reflectance stripping voltammetry. 2. Determination of mercury and lead. *Analytical Chemistry*, **76**, 1458.

56 (a) Fakhari, A.R., Ganjali, M.R. and Shamsipur, M. (1997) PVC-based hexathia-18-crown-6-tetraone sensor for mercury(II) ions. *Analytical Chemistry*, **69**, 3693;
(b) Zhao, Y. and Zhong, Z. (2006) Tuning the sensitivity of a foldamer-based mercury sensor by its folding energy. *Journal of the American Chemical Society*, **128**, 9988;
(c) Chen, P. and He, C. (2004) A general strategy to convert the MerR family proteins into highly sensitive and selective fluorescent biosensors for metal ions. *Journal of the American Chemical Society*, **126**, 728.

57 Lee, J-S., Han, M.S. and Mirkin, C.A. (2007) Colorimetric detection of mercuric ion (Hg^{2+}) in aqueous media using DNA-functionalized gold nanoparticles. *Angewandte Chemie–International Edition*, **46**, 4093.

58 Yantasee, W., Timchalk, C., Weitz, K.K., Moore, D.A. and Lin, Y. (2004) Optimization of a portable microanalytical system to reduce electrode fouling from proteins associated with biomonitoring of lead (Pb) in saliva. *Talanta*, **67**, 617.

59 Liu, A.M., Hidajat, K., Kawi, S. and Zhao, D.Y. (2000) A new class of hybrid mesoporous materials with functionalized organic monolayers for selective adsorption of heavy metal ions, *Chemical Communications*, 1145.

60 Engelhardt, G. and Michel, D. (1987) *High Resolution Solid-State NMR of Silicates and Zeolites*, John Wiley & Sons, Inc., New York.

61 Liu, Y-H., Lin, H-P. and Mou, C-H. (2004) Direct method for surface silyl functionalization of mesoporous silica. *Langmuir*, **20**, 3231.

62 El-Safty, S.A., Ismail, A.A., Matsunaga, H. and Muzukami, F. (2007) Optical nanosensor design with uniform pore geometry and large particle morphology. *Chemistry–A European Journal*, **13**, 9245.

63 Ji, X., Hu, Q., Hampsey, J.E., Qiu, X., Gao, L., He, J. and Lu, Y. (2006) Synthesis and characterization of functionalized mesoporous silica by aerosol-assisted self-assembly. *Chemistry of Materials*, **18**, 2265.

64 Sandell, E.B. (1959) *Determination of Traces of Metals*, 3rd edn, Interscience Publisher, INC., NY.

65 (a) Kruk, M. and Jaroniec, M. (2003) Argon adsorption at 77 K as a useful tool for the elucidation of pore connectivity in ordered materials with large cagelike mesopores. *Chemistry of Materials*, **15**, 2942;
(b) Ravikovitch, P.I. and Neimark, A.V. (2002) Density functional theory of adsorption in spherical cavities and pore size characterization of templated nanoporous silicas with cubic and three-dimensional hexagonal structures. *Langmuir*, **18**, 1550.

Abstract

An attractive means of improving pollution monitoring would be the use of simple, inexpensive, rapidly responsive and portable sensors. In this respect, selective optical sensing attracts much interest due to the use of 'low-tech' spectroscopic instrumentation to detect relevant chemical species in biological and environmental processes. With recent advances in mesostructured materials and nanotechnologies, new methods are emerging to design optical sensors and biosensors and develop highly sensitive solid sensors. Recent developments have focused on tailoring specific sensors for the naked-eye detection of highly toxic heavy metal ions such as lead, cadmium, antimony and mercury in aquatic samples. Sensitive, low-cost, simple nanosensor designs have been successfully developed by the immobilization of hydrophobic and hydrophilic chromophore molecules into spherically nanosized cage cavities and surfaces. A rational strategy was crucial to the development of optical nanosensors that can be used to control the accurate recognition and signaling abilities of analyte species for ion-sensing purposes. In this chapter, we report evidence of significant key factors in the development of receptors as 'indicator dyes' and surface-confined materials as 'carriers' to broaden the applicability of optical chemical sensors for the selective discrimination of trace levels of toxic analytes. For the nanosensor design techniques described here, a dense pattern of immobilized hydrophobic 'neutral' and hydrophilic 'charged' chromophores with intrinsic mobility via extremely robust constructed sequences onto nanoscale structures was key to enhancing the sensing functionality of optical nanosensors. These nanosensor designs can be used as cage probe sinks with reliable control, for the first time, over the colorimetric recognition of highly toxic metal ions to low levels of ~10^{-9} *M*. Control sensing assays were established to achieve enhanced signal response and color intensities. Moreover, these new classes of optical cage sensor exhibited long-term stability of signaling and recognition functionalities that provided extraordinary sensitivity, selectivity, reusability and rapid kinetic detection and quantification of deleterious metal ions in the environment. This chapter details recent developments in the efficient design of optical nanosensors that employ mesoporous materials as model carriers to control the accurate recognition and signaling abilities of analyte species for ion-sensing purposes.

Keywords

nanosensor; cage; monoliths; chromophores; lead; cadmium; antimony; mercury ions

6
Nanoscale Bioactive Silicate Glasses in Biomedical Applications

Tobias J. Brunner, Wendelin J. Stark and Aldo R. Boccaccini

6.1
Introduction

Biomaterials for medical applications have a long history. The demand for synthetic biomaterials and better treatments for the patient pushes science to improve existing or exploit novel materials. Bioactive glasses represent a group of surface-reactive materials which are able to bond to bone in a physiological environment, and were first developed by Hench and coworkers in 1969 [1]. The traditional bioactive glasses described in biomedical science consist of a silicate network incorporating sodium, calcium and phosphorus at different ratios (SiO_2–Na_2O–CaO–P_2O_5 system). Other glass compositions contain either no sodium or have additional elements in the silicate network such as fluorine, magnesium or zinc [2–5]. The common characteristic of all bioactive glasses is their ability to interact with living tissue (bioactivity). The bonding to bone is established by the precipitation of a calcium-deficient, carbonated apatite surface layer on the bioactive glass surface when in contact with body fluids. Although some details of this process remain unknown, it is clearly recognized that for a bond with bone tissue to occur, a layer of biologically active apatite must be formed at the interface. This conclusion is based on the fact that the apatite layer is the common characteristic of all known bioactive materials used for orthopedic implants, bone replacement and bone filler [6]. *In vivo*, the apatite crystals precipitate in the vicinity of collagen fibrils, thereby allowing interfacial bonding and cell attachment. An interesting finding for the development of bone regeneration strategies was that the dissolution products from bioactive glasses upregulate the expression of genes that control osteogenesis [7]. The range of bioactive glasses which exhibit these properties has been extended over the years as new methods of preparation have become available, for example, sol–gel techniques. Thus, variations of silicate compositions still exhibiting bioactivity have been considered [8, 9]. The classical 45S5 composition of bioactive glass, known as Bioglass (in wt%: 45% SiO_2, 24.5% Na_2O, 24.5% CaO and 6% P_2O_5) has received approval from the US Food and Drug Administration (FDA), and is

Nanomaterials for the Life Sciences Vol. 2: Nanostructured Oxides. Edited by Challa S. S. R. Kumar

ISBN: 978-3-527-32152-0

currently used in the clinical treatment of periodontal diseases as a bone filler as well as in middle ear surgery [6].

The traditional synthesis method for bioactive glasses is very similar to the preparation of conventional glasses, such as window glass. The process involves melting of the correct mixture of metal oxides at elevated temperatures. The glass components in the form of grains of oxides or carbonates are mixed, melted and homogenized, and the glass forms at temperatures of 1200–1400 °C. Subsequently, the melt is either quenched and cast into a mold, or the liquid glass is poured into a liquid cooling medium to prepare glass frit. In order to form glass particles of a size below 100 μm, the material is subsequently milled (e.g. ball-milled) to the preferred size. Such top-down approaches are straightforward and simple, but of low energy efficiency. Although they often result in a dense material, a particle size reduction to the submicron size range to enhance glass particle reactivity is, in most cases, not possible. Moreover, the milling process often requires additives or provokes contamination by wear debris – both of which are undesirable factors when producing a material for implantation into the human body. As a result, other approaches are necessary to scale down the particle size of bioactive glass powders to the nanometric range, and thus to extend the applications of bioactive glasses to the domain of nanomaterials and nanotechnology.

In Section 6.2, different synthesis methods to produce bioactive glasses with nanometric dimensions, including nanoparticles and nanofibers, will be described, while in Section 6.3 some possible applications of such novel nanomaterials in medicine, with attention focused on dentistry, orthopedic implants and tissue engineering, are presented and discussed. The subject of the development of composites consisting of combinations of nanoparticulate bioactive glasses and biodegradable polymers for use in bone tissue engineering will also be introduced. Finally, in Section 6.4 a summary of the topic is presented, together with some details of future research developments in the field.

6.2
Fabrication of Nanoscale Bioactive Glass Particles and Fibers

The two processes used to prepare nanostructures of bioactive glass are the sol–gel technique and the flame spray synthesis method. The processes are rather different, as one is performed in liquid phase at room temperature, and the other in gas phase at high temperature. An overview of both schemes, and their characteristics, is provided in the following sections.

6.2.1
Liquid-Phase Synthesis Method (Sol–Gel Technique)

Liquid-phase preparation methods use metal–organic precursors which are converted to inorganic materials, either in water or in an organic solvent. The sol–gel process has a long history in the preparation of silicate systems and other oxides,

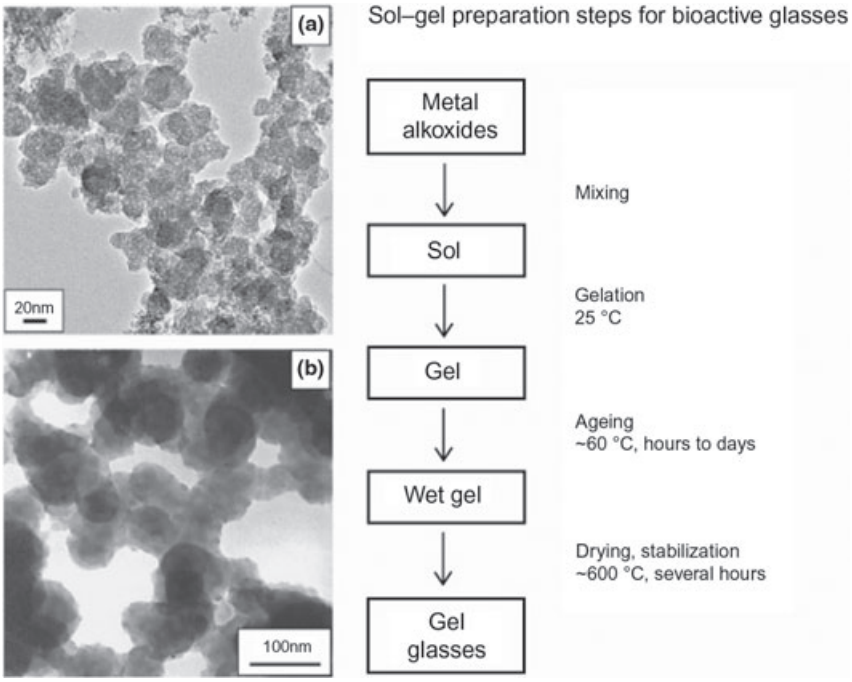

Figure 6.1 Production steps for the preparation of bioactive glasses by the sol–gel technique. (a,b) Electron microscopy images of nanoparticulate products [12]. Reprinted in part from Ref. [12] with permission.

and has become widespread in the research field with a high technological relevance, for example in the fabrication of thin films, coatings, nanoparticles and fibers [10]. The synthesis of specific bioactive glasses using the sol–gel technique at low temperatures, and using metal alkoxides as precursors, was first demonstrated in 1991 by Li *et al.* [11]. For bioactive glasses, chemicals such as tetraethyl orthosilicate, calcium nitrate and triethylphosphate are used. Following hydrolysis and polycondensation reactions, a gel is formed which subsequently is calcined at 600–700 °C to form the glass. Based on the preparation method, sol–gel derived products – such as thin films or particles – are highly porous and exhibit a high specific surface area [8, 10, 11]. The production steps to fabricate bioactive glass nanoparticles using the sol–gel method, as presented in Ref. [12], are shown schematically in Figure 6.1, together with some electron microscopy images of the typical nanoparticles produced.

Further investigations into the fabrication of bioactive silicate glass nanoparticles using sol–gel have been carried out recently by Hong *et al.* [13].

For some applications, such as in tissue engineering, it is advantageous to use anisotropic structures such as fibers, and for this purpose a combination of the sol–gel and electrospinning techniques is applied [14]. Additives such as polyvinyl

butyral are necessary to adjust the rheological properties of the sol for electrospinning. As for the normal sol–gel preparation, the electrospun fibers need to undergo a heat-treatment step in order to remove organic residues. This process can result in fibers with diameters less than 100 nm [14, 15], although the diameter and morphology of the nanofibers can be controlled to some extent by the amount and type of additive and the applied electric field. The resulting nanofiber mats are initially flexible, but become fragile when immersed in a simulated body fluid. Some scanning electron microscopy images of bioactive glass nanofibers prepared by the electrospinning of a sol [15], and the distribution of fiber diameters, are shown in Figure 6.2.

Although the sol–gel technique is versatile, it has limitations in terms of the composition and a high residual water or solvent content; indeed, in some cases a high-temperature calcination step is required. Sol–gel processing is also relatively time-consuming and, as it is not a continuous process, batch-to-batch variations may occur among the products.

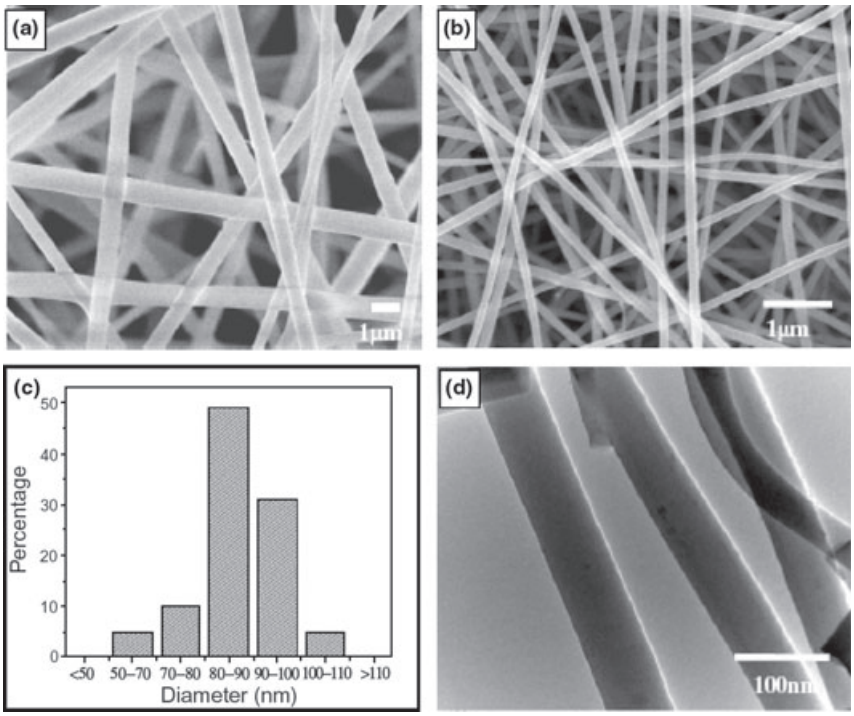

Figure 6.2 Scanning electron microscopy images of bioactive glass nanofibers. (a) Prepared by electrospinning of a sol as electrospun fibers; (b) After calcination at 600 °C; (c) Distribution of the fiber diameter; (d) Transmission electron microscopy image after calcination at 600 °C. Reprinted from Ref. [15] with permission.

6.2.2
Gas-Phase Synthesis Method (Flame Spray Synthesis)

In gas-phase synthesis routes, an inorganic or metal–organic precursor compound is used which is then converted to the nanoscale product at very high temperatures, typically above 1000 °C. One of the most successful gas-phase synthesis methods is flame spray synthesis, where the precursor is combusted in a flame [16]. One advantage of this process compared to other gas-phase processes is that no additional source of energy is required for the precursor conversion, such as plasma, lasers or electrically heated walls [16]. Flame synthesis has its roots in the manufacture of carbon black, which today is prepared in megaton quantities each year for use in tire and rubber production, and also as a pigment in inks. Although the process was later adapted for the preparation of titania and fumed silica, it was still very limited in terms of accessible materials. A subsequent adaptation of the process precursors away from gaseous towards organic liquids loaded with metals proved to be very successful [17–19]. In this re-engineered system, the liquid precursor is dispersed by oxygen over a nozzle and thereby forms a spray, which is ignited. As the spray burns, the organic constituents of the liquid precursor combust completely and the metal constituents oxidize to form the nanoparticles. The basic principle of all gas-phase synthesis methods is the formation of molecular nuclei from either condensation or chemical reactions, and subsequent growth by coalescence in high-temperature regions during the process. The process dynamics is well understood and can be controlled [17–19]. A scheme representing the flame spray synthesis process, together with some electron microscopy images of nanoparticulate bioactive glass (NBG) prepared in this way, are shown in Figure 6.3.

The metal carboxylate system is most prominent because it allows the synthesis of oxide nanoparticles of almost any composition [17–19]. In addition, the metal–organic salts are considerably stable in air, tolerate humidity and, most importantly, are fully miscible among each other. Consequently, the process allows the production of nanoparticulate mixed-oxides and even salts with high chemical homogeneity. As a result, the preparation of different bioactive glasses has become possible by employing corresponding mixtures of 2-ethylhexanoic acid salts of calcium and sodium, hexamethyldisiloxane, tributyl phosphate and fluorobenzene to introduce fluorine [20]. In addition, the preparation of a highly amorphous calcium phosphate material – that is, calcium phosphate glass with different Ca/P ratios – has become possible [21].

The high-temperature environment in the flame reactor, as well as short residence times and rapid cooling directly after production of the particles, often result in the formation of metastable phases or polymorphs which are not easily accessible by conventional techniques. Depending on the composition, the rapid quenching can preserve the amorphous state of the material [20, 21]. As a result of the process characteristics and parameters, the primary particles produced are spherically shaped with different degrees of agglomeration [22, 23]. Based on models and experimental data, the primary particles have a log normal particle size distribution [24, 25].

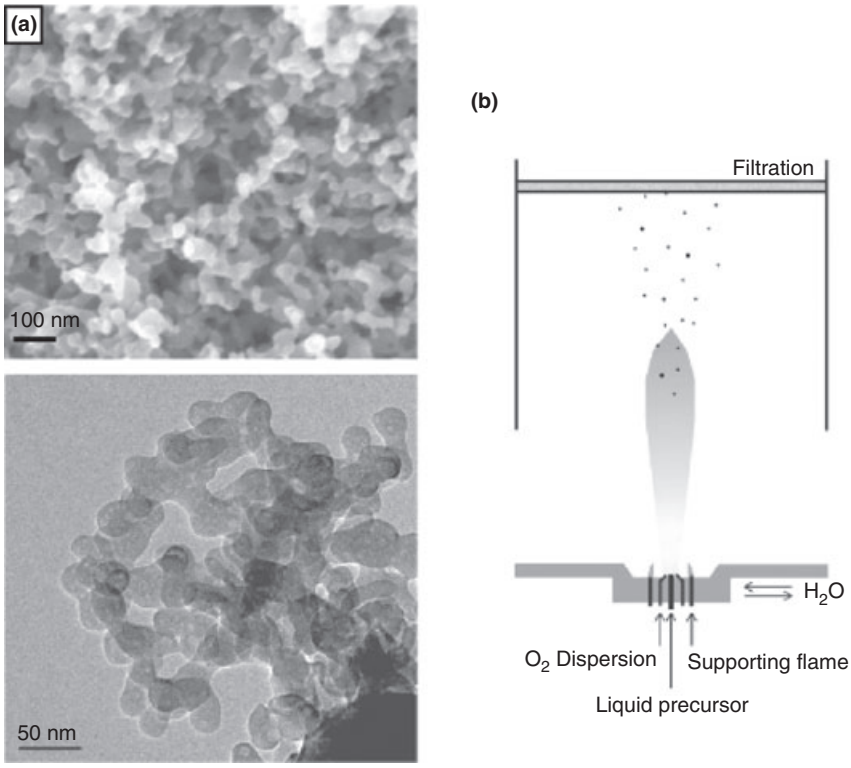

Figure 6.3 (a) Electron microscopy images of nanoparticulate bioactive glass (NBG) as prepared by flame spray synthesis. Upper: Partial agglomeration of the nanoparticles; Lower: Primary nanoparticles with <50 nm diameter; (b) Schematic representation of the flame spray synthesis process [20].

In summary, the advantages of flame spray synthesis lie in the ready accessibility of a wide range of nanoparticle compositions, as well as the facile introduction of dopants and the proven scalability of the technique. However, the process is very energy-intensive when compared to wet synthesis methods, which are conducted at room temperature.

6.3 Applications of Nanoscale Bioactive Glasses

6.3.1 Conventional Bioactive Glasses

Since its clearance by the FDA, 45S5 bioactive glass (Bioglass®) has been used in biomedical applications such as middle ear surgery (Ceravital®) or in the clinical

treatment of periodontal diseases (PerioGlas®, NovaMin®). Bioactive glass can also be applied as bone filler for different osseous defects, or for the coating of a variety of implants or devices. Here, a brief overview will be provided of the applications of bioactive glasses in medicine.

The early applications of bioactive glasses were in the form of solid shapes for small bone replacement, typically in middle ear surgery [6]. If the middle ear cannot perform its function as an acoustic impedance transformer, the cochlear input signal is diminished and so-called conduction deafness results. The reconstruction of an osseous part of the middle ear is possible and, by fitting a prosthesis, the patient's hearing can be regained. Cochlear implants have been prepared from porous polyethylene or biocompatible bioactive glass ceramic (Ceravital) [26, 27]. Although the implants prepared from bioactive glasses showed good tolerance and compatibility in the middle ear space, today they find only limited use because of the difficulties encountered when trimming the glass prostheses [28].

Later, other clinical applications of bioactive glasses (e.g. in periodontology) have become evident. The discipline of periodontology deals with the supporting structures of teeth and dental implants, as well as diseases and conditions that affect them. When teeth are extracted, an extraction socket is formed and the jawbone begins to be resorbed, resulting in bone loss, and the subsequent placing of a metallic dental implant becomes difficult, or even impossible. In this respect, bioactive glass (PerioGlas) can act as a scaffold around and through which new bone in an osseous defect can form. Once the new bone is built up and/or enough mechanical stability is achieved, a dental implant can be placed in position [29, 30]. Another traditional application of bioactive glasses is in the form of coatings; here, orthopedic implants or medical devices are covered with bioactive glass in order to establish a bioactive surface for better bonding to bone tissue and to improve adherence [31–34].

More recently, great potential has been attributed to the application of bioactive glasses in tissue engineering and regenerative medicine [7, 35, 36]. Tissue engineering combines the action of mammalian cells, engineering and materials methods, and suitable biochemical and physico-chemical factors to repair or replace tissues such as bone [7, 36–42]. As indicated by an ever-increasing number of reports, bone tissue engineering possibly represents one of the most exciting future clinical applications of bioactive glasses, for example, in the design and fabrication of optimal scaffolds [43]. Both, micron-sized and nanoscale particles are considered in this application field, which includes also the fabrication of composite materials, such as a combination of biodegradable polymers and bioactive glass [37] (see below).

6.3.2
Advantages of Nanometric Bioactive Glasses

A reduction in size to the nanometer scale has been suggested to develop a new family of nanostructured materials that should not only enhance the performance of bioactive glasses in existing applications, but also open new application opportunities. The higher specific surface area of nanostructured bioactive glasses allows

not only for a faster release of ions but also a higher protein adsorption; hence, an enhanced bioactivity can be expected. As a consequence, a faster deposition or mineralization of tissues such as bone or tooth is possible when they are in contact with nanoscale bioactive glass particles, as opposed to micron-sized particles.

Another advantage of bioactive glass nanoparticles is that their small size could enable passage into smaller domains within the body, when compared to micron-sized particles. For example, tooth matrix contains dentinal tubules with a diameter of 2–3 μm [44]. In order to regenerate dentine it would be advantageous for the active ingredient to penetrate these tubules. However, whereas micron-sized particles of bioactive glass are incapable of doing so, nanoparticles should be able to infiltrate dentinal tubules and be active within them.

For bone tissue engineering purposes, nanostructured bioactive glasses can improve the microstructural, mechanical and biological properties of the degradable biopolymer/bioactive glass composites used to fabricate scaffolds. For example, nanoscale bioactive glass particles will induce nanotopographic features on scaffold surfaces, and this is likely to improve osteoblast cell attachment [45]. Bone has nanostructured features consisting of a tailored mixture of collagen and hydroxyapatite, and most current orthopedic implant materials are smooth at the nanoscale. Mimicking the nanofeatures of bone on the surface of a synthetic implant material has been shown to increase bone-forming cell adhesion and proliferation [45].

6.3.3 Applications in Dentistry

As mentioned above, bioactive glasses are known for their specific *in vivo* responses, including osteoconductivity and bonding to bone via the release of relevant ions and formation of an apatite layer [6, 46, 47]. Therefore, while these materials are used for bone reconstitution and tissue engineering, they are also interesting candidates for mineralization in dentistry [48]. Dentin accounts for the greatest part of the dental hard substance but, unlike enamel, is very much like bone, having an organic matrix of collagen and other proteins in which crystalline apatite mineral is embedded. A well-defined system of tubules stretches from the pulp space towards the dentin–enamel and dentin–cementum junctions. Dentinal tubules contain projections of odontoblast cells that line the inside of the pulpodentinal junction. Dental plaque – that is, the biofilm adhering to the teeth – contains numerous bacteria which produce organic acids that can dissolve the dental hard tissues enamel and dentin. This demineralization or loss of mineral from these tissues is counterbalanced by the deposition of minerals from saliva or oral fluid (remineralization), and the relative magnitude of these two actions determines whether destruction by caries or regeneration occurs [49]. Odontoblasts orchestrate mineralization processes in dentin not only during dentinogenesis, but also after the teeth have been formed. Mineralizing processes are conveyed via a liquid similar to extracellular fluid [50]. *In vitro* studies using micron-sized bioactive glasses have been reported to induce the mineralization of dentin disc

surfaces [48, 51, 52]. These results suggest that bioactive glass could be instrumental for the remineralization of human dentin, and that it has potential as a filler component in mineralizing restorative materials [53]. Unfortunately, relatively long reaction times have limited or inhibited the application of micron-sized bioactive glass as a remineralization agent in dental practice.

6.3.3.1 **Remineralization**

The remineralization potential of NBG of the 45S5 composition (Bioglass), as prepared by flame spray synthesis, compared to a micron-sized reference material was investigated by Vollenweider *et al.* [54]. The results showed a substantially higher dentin remineralization rate induced by NBG compared to the conventional, micron-sized material. The results of studies monitoring ion release in suspension showed that NBG releases more ions into its environment than does its micron-sized counterpart (Figure 6.4). Thus, bioactive glass in nanoparticulate form can be considered a more efficient calcium and silicon source for remineralization. The measured ion release profiles reflected the critical role of particle size and specific surface area, which were in agreement with reports made by Sepulveda *et al.* [55]. Biomechanical testing, however, indicated that remineralization did not restore the original mechanical properties of dentin; although a possible explanation for this might be that no proper interconnection with the collagen matrix took place. If newly precipitated apatite mineral does not form a composite material with the collagen matrix of demineralized dentin bars, then no mechanically stable composite material will be formed.

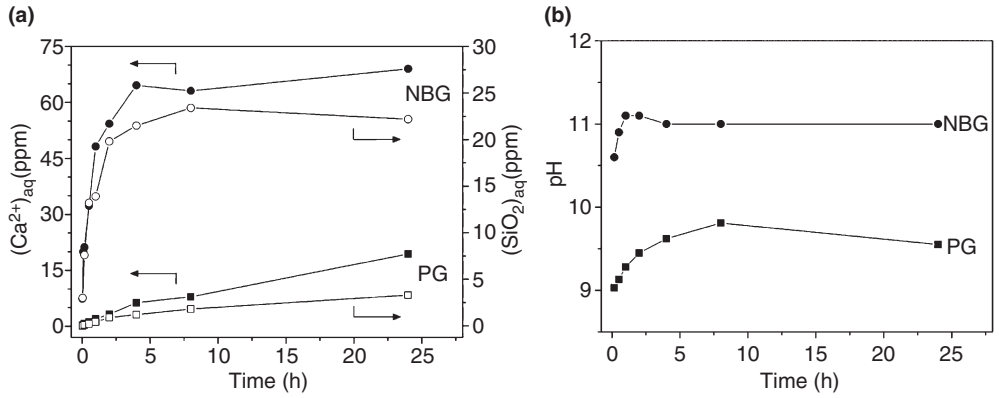

Figure 6.4 (a) Release of ions from NBG and a commercial micron-sized bioactive glass (Perioglass, PG) in buffered saline solution. The nanoparticles showed a much faster release of silica and calcium when compared to PG; (b) The basicity (pH) of NBG dispersions caused an up to 10-fold higher OH^- concentration than corresponding micron-sized particles. Reprinted from Ref. [54] with permission.

6.3.3.2 Antimicrobial Effects

Besides their potential for promoting mineralization, bioactive glasses are also of interest because they may possess a certain antimicrobial effect in closed systems [56, 57]. An important issue in dentistry – and especially in endodontics – is the disinfection of infected tissue. Microorganisms are omnipresent in the oral environment, and can cause pathological situations such as root canal infections. Root canals are filled with a highly vascularized, loose connective tissue ('dental pulp' which may become infected and inflamed, generally as a result of caries or tooth fractures that allow microorganisms (mostly bacteria from the oral flora, or their byproducts) to access the pulp chamber or root canals. The infected tissue is removed by a surgical intervention known as endodontic therapy or root canal treatment. Following the removal of as much of the infected pulp as possible, the root canals are often temporarily filled with a calcium hydroxide slurry, which is not tolerated by microorganisms. This strong alkaline biocide is left in position for a week or more to disinfect and therefore reduce inflammation in the surrounding tissues. At a subsequent consultation, the disinfectant must be removed and the root canal system sealed with epoxy resin or silicon sealer, in conjunction with gutta percha points. The tooth may then be restored either by placing a crown or a coronal filling. If any remaining infected tissue is left in the tooth, or leakage of the crown occurs, then the root canal treatment may fail, causing a reinfection.

As bioactive glasses also cause an increase in pH [57], they may potentially be used as topical endodontic disinfectants, without the reported negative side effects of calcium hydroxide on dentin stability [58]. Therefore, a treatment using bioactive glass would be less harsh, in part also due to the bioactivity of the glass, which may be beneficial in terms of dentin remineralization. The bioactive glass can also be left in the root canal, making a second treatment session unnecessary. However, the antibacterial efficacy of a conventional bioactive glass in human teeth is inferior to that of calcium hydroxide [59]. Flame spray synthesis-derived bioactive glass nanoparticles of the 45S5 composition showed a higher dissolution rate of alkaline species, and thus an elevated antimicrobial efficacy *in vitro* when compared to currently available melt-derived, micron-sized bioactive glass, yet having the same chemical composition [60]. When the antimicrobial efficacy of nanoscale bioactive glass particles was assessed against the *Enterococcus faecalis*-type strain clinical isolates of enterococci from persistent root canal infections, the shift from micron-sized to nanoscale treatment materials led to a 10-fold increase in silica release, while the solution pH values changed by four units. The key results of these experiments are summarized in Figure 6.5.

The short-term antimicrobial effect of these glasses has been attributed exclusively to their ability to raise the pH in an aqueous environment [57, 61]. This pH increase results from the release of alkali ions, mainly Na^+, and the incorporation of protons (H^+) into the corroding material [55, 62]. A secondary effect explaining the antimicrobial behavior has been identified, which is believed to be related to the release of specific ions from the glass [61].

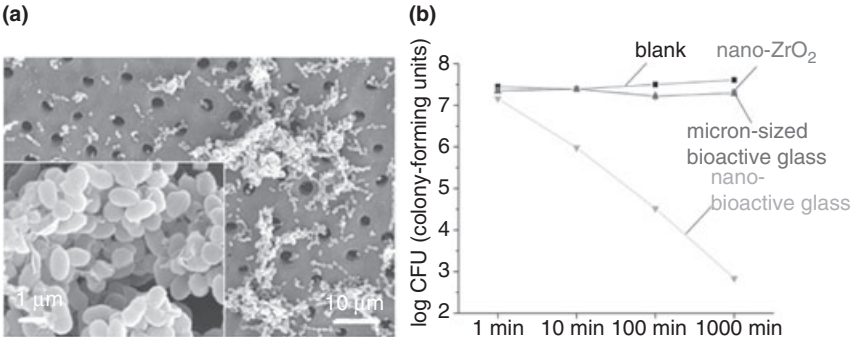

Figure 6.5 (a) Bovine dentin surface with dentinal tubules covered with *E. faecalis* bacteria; (b) Reduction of viability of *E. faecalis* bacteria after treatment with nanoparticulate and micron-sized bioactive glass, with nanometric zirconia as an inert reference. Reprinted in part from Refs [60, 61] with permission.

6.3.4 Applications in Tissue Engineering

The combination of biodegradable polymers and bioactive ceramics has resulted in a new group of composite materials which can act as hard tissue regeneration materials, or as biocompatible scaffolds in the field of tissue engineering [37]. The goal of these composite materials is to impart strength and bioactivity by an inorganic bioactive filler while retaining the positive properties of the polymer such as flexibility and capacity to deform under loads.

Various composites of biodegradable polymers and bioactive inorganic phases have been reported. Among these polymeric compounds, both natural materials such as collagen [63–65] and chitosan [66, 67] and synthetic polymers such as poly(lactic acid), poly(lactic acid-*co*-glycolic acid) (PLGA), polycaprolactone (PCL) [68, 69] (to name only a few) have been considered. Inorganic materials for the production of bioactive composites range from calcium phosphates such as hydroxyapatite [65, 70] and tricalcium phosphate [66, 71] to bioactive silicate glasses [37, 42, 72, 73].

Inorganic phases can be added to the different polymer matrices in the form of micron-sized or nanoscale particles or fibers. The size of the filler particles is an important parameter that affects the mechanical properties of composite materials. This is due to the marked microstructural differences introduced by the micron-sized or nanoscale fillers that contribute towards different interactions between the filler particles and the polymer matrix. In general, the introduction of nanoscale fillers with a desired morphology can increase the mechanical strength and stiffness of the composites in comparison to the properties of the neat polymer. The use of nanoscale degradable fillers such as bioactive glass or

calcium phosphate nanoparticles might result therefore in improved orthopedic implants and tissue engineering scaffolds. Additionally, in the case of bioactive silicate glass nanoparticles, they can produce a higher alkalinity when compared to commercially available (micron-sized) 45S5 Bioglass [54]. This effect could buffer to a greater extent the acidic degradation of some polymers when nanoscale bioactive glass particles are used as filler in a composite.

The larger specific surface area of the nanoparticles should lead to increased interface effects, and it should also contribute to improved bioactivity, when compared to standard (micron-sized) particles. Additionally, the use of nanoparticles in a polymeric matrix mimics more closely the structure of natural bone, which contains nanoscale hydroxyapatite crystallites combined with the polymeric phase of collagen, being responsible for the desirable mechanical properties of bone. Moreover, Webster *et al.* [74] have reported that a significant increase in protein adsorption and osteoblast adhesion has been observed on nanoscale ceramic materials compared to micron-sized ceramic materials and composites. Related results were achieved by Loher *et al.* [75] who showed that the bioactivity, degradation and mechanical properties of PLGA doped with nanoscale amorphous calcium phosphate are strongly improved by the addition of nanoscale amorphous calcium phosphate particles when compared to the pure polymer [75]. In recent investigations, Misra *et al.* [76] have described the successful preparation of poly(3-hydroxybutyrate) (P(3HB))/NBG composites with different filler concentrations by solvent casting. The thermal, mechanical and microstructural properties of these new composites were compared to their counterparts prepared with micron-sized bioactive glass. Similar to other reported studies [75], the addition of nanoparticles was shown to have a stiffening effect on the modulus of the composites, as shown in Figure 6.6. The systematic addition of nanoparticles of bioactive glass induced a nanostructured topography on the surface of the composites, which was not visible on their micron-sized bioactive glass particle-containing counterparts. This surface effect induced by the nanoparticles considerably improved the total protein adsorption on the composites compared to the unfilled polymer and composites containing micron-sized bioactive glass particles. A short-term *in vitro* degradation (30 days) study in a simulated body fluid showed a high level of bioactivity as well as a higher water absorption for the nanoparticle-containing composites. A preliminary cell proliferation study using osteoblast-like cells also highlighted the excellent biocompatibility of both types of P(3HB)/bioactive glass composite system [76]. Hong *et al.* [77] investigated a similar system using poly(L-lactic acid) as the biodegradable polymer and sol–gel-derived bioactive glass ceramic nanoparticles, and prepared porous scaffolds by thermally induced phase-separation; the structure and porosity of the foams produced are depicted in Figure 6.7. The most striking effect of adding nanoparticles to the scaffolds, however, was an improved mechanical stability when compared to neat polymer foams.

Thus, the introduction of bioactive glass nanoparticles as fillers in biodegradable polymers adds many interesting features, and represents a promising step towards the development of improved biomaterials for bone regeneration, as well as engineered scaffolds for tissue engineering applications.

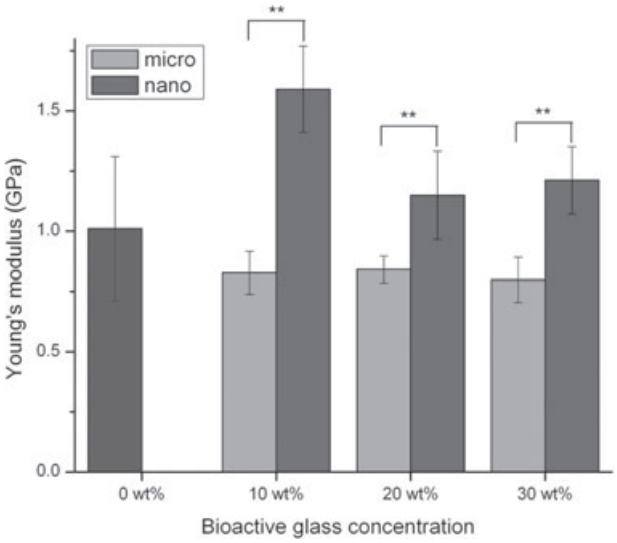

Figure 6.6 Young's modulus of composites consisting of different concentrations of micron- or nanosized bioactive glass particles in poly(3-hydroxybutyrate) compared to the neat polymer [76].

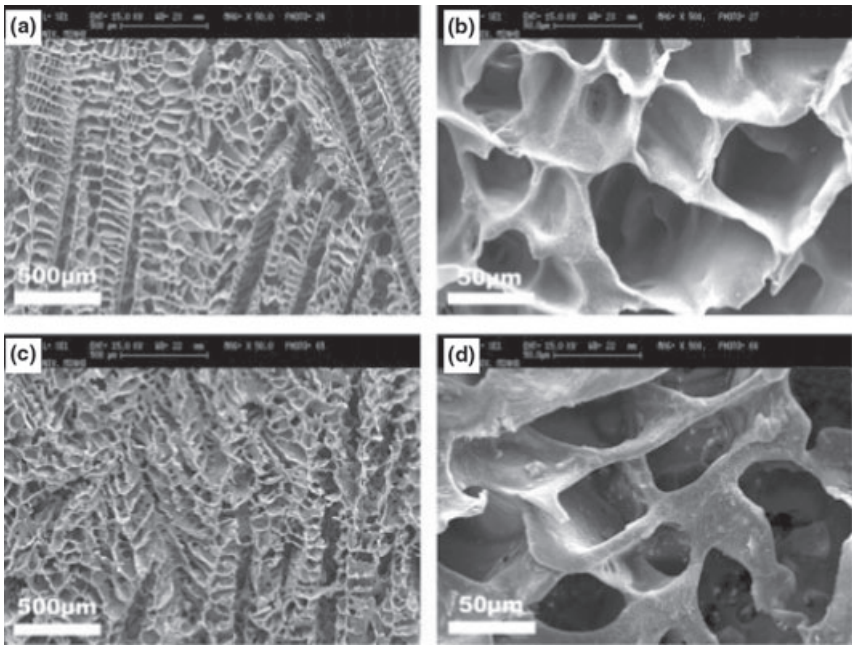

Figure 6.7 (a,b) Scanning electron microscopy images of poly(L-lactic acid) scaffolds without nanoparticles; (c,d) Scaffolds containing 25 wt% bioactive glass-ceramic nanoparticles. Reprinted from Refs [13, 77] with permission.

6.4 Summary and Future Perspective

The preparation of bioactive glasses in nanoparticle and nanofiber form has recently been made feasible by advances in wet and dry synthesis methods. Both, nanoscale particulate and nanofiber bioactive glasses, have demonstrated advantages over conventional (micron-sized) glasses due to their large surface area and enhanced solubility, coupled with the possibility of inducing nanotopographic surface features. As a consequence, these nanomaterials have inspired research groups to investigate new applications of bioactive glasses in biomedical engineering. A minor drawback here is that, whilst all studies to date have been performed *in vitro*, their clinical efficacy must be tested and validated *in vivo*. In conclusion, the great potential of nanometric bioactive glass systems lies in the field of bone tissue engineering and dentistry, notably in dentin regeneration and the reconstruction of critical bone defects.

References

1 Hench, L.L., Splinter, R.J., Allen, W.C. and Greenlee, T.K. (1971) Bonding mechanisms at the interface of ceramic prosthetic materials. *Journal of Biomedical Materials Research*, **5**(6), 117–41.

2 Sepulveda, P., Jones, J.R. and Hench, L.L. (2001) Characterization of melt-derived 45S5 and sol-gel-derived 58S bioactive glasses. *Journal of Biomedical Materials Research*, **58**(6), 734–40.

3 Saravanapavan, P., Jones, J.R., Pryce, R.S. and Hench, L.L. (2003) Bioactivity of gel-glass powders in the CaO-SiO_2 system: a comparison with ternary (CaO-P_2O_5-SiO_2) and quaternary glasses (SiO_2-CaO-P_2O_5-Na_2O). *Journal of Biomedical Materials Research Part A*, **66A**(1), 110–19.

4 Oki, A., Parveen, B., Hossain, S., Adeniji, S. and Donahue, H. (2004) Preparation and in vitro bioactivity of zinc containing sol-gel-derived bioglass materials. *Journal of Biomedical Materials Research Part A*, **69A**(2), 216–21.

5 Vallet-Regi, M., Salinas, A.J., Roman, J. and Gil, M. (1999) Effect of magnesium content on the in vitro bioactivity of CaO-MgO-SiO_2-P_2O_5 sol-gel glasses. *Journal of Materials Chemistry*, **9**(2), 515–18.

6 Hench, L.L. (1998) Bioceramics. *Journal of the American Ceramic Society*, **81**(7), 1705–28.

7 Xynos, I.D., Hukkanen, M.V.J., Batten, J.J., Buttery, L.D., Hench, L.L. and Polak, J.M. (2000) Bioglass (R) 45S5 stimulates osteoblast turnover and enhances bone formation in vitro: implications and applications for bone tissue engineering. *Calcified Tissue International*, **67**(4), 321–9.

8 Carta, D., Pickup, D.M., Knowles, J.C., Smith, M.E. and Newport, R.J. (2005) Sol-gel synthesis of the P_2O_5-CaO-Na_2O-SiO_2 system as a novel bioresorbable glass. *Journal of Materials Chemistry*, **15**(21), 2134–40.

9 Saravanapavan, P. and Hench, L.L. (2001) Low-temperature synthesis, structure, and bioactivity of gel-derived glasses in the binary CaO-SiO_2 system. *Journal of Biomedical Materials Research*, **54**(4), 608–18.

10 Scherrer, G.W. and Brinker, C.J. (1990) *Sol–Gel Science: The Physics and Chemistry of Sol-Gel*, Academic Press, Boston, MA.

11 Li, R., Clark, A.E. and Hench, L.L. (1991) An investigation of bioactive glass powders by sol-gel processing. *Journal of Applied Biomaterials*, **2**(4), 231–9.

12 Xia, W. and Chang, J. (2007) Preparation and characterization of nano-bioactive-

glasses (NBG) by a quick alkali-mediated sol-gel method. *Materials Letters*, **61**(14-15), 3251–3.

13 Hong, Z., Reis, R.L. and Mano, J.F. (2008) Preparation and in vitro characterization of novel bioactive glass ceramic nanoparticles. *Journal of Biomedical Materials Research Part A*, doi: 10.1002/jbm.a.31848.

14 Kim, H.W., Kim, H.E. and Knowles, J.C. (2006) Production and potential of bioactive glass nanofibers as a next-generation biomaterial. *Advanced Functional Materials*, **16**(12), 1529–35.

15 Xia, W., Zhang, D.M. and Chang, J. (2007) Fabrication and in vitro biomineralization of bioactive glass (BG) nanofibres. *Nanotechnology*, **18**(13), Article 135601.

16 Pratsinis, S.E. (1998) Flame aerosol synthesis of ceramic powders. *Progress in Energy and Combustion Science*, **24**(3), 197–219.

17 Stark, W.J., Madler, L., Maciejewski, M., Pratsinis, S.E. and Baiker, A. (2003) Flame synthesis of nanocrystalline ceria-zirconia: effect of carrier liquid. *Chemical Communications*, **5**, 588–9.

18 Stark, W.J., Mädler, L. and Pratsinis, S.E. (2004) Metal oxides prepared by flame spray pyrolysis. WO 2004/005184.

19 Stark, W.J. and Pratsinis, S.E. (2004) Metal delivery system for nanoparticle manufacture. WO 2004/103900A1.

20 Brunner, T.J., Grass, R.N. and Stark, W.J. (2006) Glass and bioglass nanopowders by flame synthesis. *Chemical Communications*, **13**, 1384–6.

21 Loher, S., Stark, W.J., Maciejewski, M., Baiker, A., Pratsinis, S.E., Reichardt, D., Maspero, F., Krumeich, F. and Günther, D. (2005) Fluoro-apatite and calcium phosphate nanoparticles by flame synthesis. *Chemistry of Materials*, **17**(1), 36–42.

22 Tsantilis, S. and Pratsinis, S.E. (2004) Soft- and hard-agglomerate aerosols made at high temperatures. *Langmuir*, **20**(14), 5933–9.

23 Grass, R.N., Tsantilis, S. and Pratsinis, S.E. (2006) Design of high-temperature, gas-phase synthesis of hard or soft TiO_2 agglomerates. *AIChE Journal*, **52**(4), 1318–25.

24 Dekkers, P.J. and Friedlander, S.K. (2002) The self-preserving size distribution theory I. Effects of the Knudsen number on aerosol agglomerate growth. *Journal of Colloid and Interface Science*, **248**(2), 295–305.

25 Vemury, S., Kusters, K.A. and Pratsinis, S.E. (1994) Time-lag for attainment of the self-preserving particle-size distribution by coagulation. *Journal of Colloid and Interface Science*, **165**(1), 53–9.

26 Reck, R., Storkel, S. and Meyer, A. (1988) Bioactive glass-ceramics in middle ear surgery. An 8-year review. *Annals of the New York Academy of Sciences*, **523**(1), 100–6.

27 Gersdorff, M. and Ear, M. (1988) Prosthesis. US patent 4728327.

28 Battista, R. (2008) *Middle Ear, Ossiculoplasty*, eMedicine, http://www.emedicine.com (accessed 24 September 2008).

29 Zamet, J.S., Darbar, U.R., Griffiths, G.S., Bulman, J.S., Brägger, U., Bürgin, W. and Newman, H.N. (1997) Particulate Bioglass® as a grafting material in the treatment of periodontal intrabony defects. *Journal of Clinical Periodontology*, **24**(6), 410–18.

30 Gatti, A.M., Simonetti, L.A., Monari, E., Guidi, S. and Greenspan, D. (2006) Bone augmentation with bioactive glass in three cases of dental implant placement. *Journal of Biomaterials Applications*, **20**(4), 325–39.

31 Boccaccini, A.R., Stamboulis, A.G., Rashid, A. and Roether, J.A. (2003) Composite surgical sutures with bioactive glass coating. *Journal of Biomedical Materials Research Part B-Applied Biomaterials*, **67B**(1), 618–26.

32 Gomez-Vega, J.M., Saiz, E., Tomsia, A.P., Marshall, G.W. and Marshall, S.J. (2000) Bioactive glass coatings with hydroxyapatite and Bioglass® particles on Ti-based implants. 1. Processing. *Biomaterials*, **21**(2), 105–11.

33 Kitsugi, T., Nakamura, T., Oka, M., Senaha, Y., Goto, T. and Shibuya, T. (1996) Bone-bonding behavior of plasma-sprayed coatings of Bioglass®, AW-glass ceramic, and tricalcium phosphate on

titanium alloy. *Journal of Biomedical Materials Research*, **30**(2), 261–9.

34 Ducheyne, P. and Cuckler, J.M. (1992) Bioactive ceramic prosthetic coatings. *Clinical Orthopaedics and Related Research*, **276**, 102–14.

35 Yao, J., Radin, S., Leboy, S. and Duchey, P. (2005) The effect of bioactive glass content on synthesis and bioactivity of composite poly(lactic-*co*-glycolic acid)/bioactive glass substrate for tissue engineering. *Biomaterials*, **26**(14), 1935–45.

36 Hench, L.L. and Polak, J.M. (2002) Third-generation biomedical materials. *Science*, **295**(5557), 1014–17.

37 Rezwan, K., Chen, Q.Z., Blaker, J.J. and Boccaccini, A.R. (2006) Biodegradable and bioactive porous polymer/inorganic composite scaffolds for bone tissue engineering. *Biomaterials*, **27**(18), 3413–31.

38 Hutmacher, D.W. (2000) Scaffolds in tissue engineering bone and cartilage. *Biomaterials*, **21**(24), 2529–43.

39 Burg, K.J.L., Porter, S. and Kellam, J.F. (2000) Biomaterial developments for bone tissue engineering. *Biomaterials*, **21**(23), 2347–59.

40 Petite, H., Viateau, V., Bensaid, W., Meunier, A., de Pollak, C., Bourguignon, M., Oudina, K., Sedel, L. and Guillemin, G. (2000) Tissue-engineered bone regeneration. *Nature Biotechnology*, **18**(9), 959–63.

41 Laurencin, C.T., Ambrosio, A.M.A., Borden, M.D. and Cooper, J.A. (1999) Tissue engineering: orthopedic applications. *Annual Review of Biomedical Engineering*, **1**, 19–46.

42 Boccaccini, A.R. and Maquet, V. (2003) Bioresorbable and bioactive polymer/Bioglass® composites with tailored pore structure for tissue engineering applications. *Composites Science and Technology*, **63**(16), 2417–29.

43 Chen, Q.Z.Z., Thompson, I.D. and Boccaccini, A.R. (2006) 45S5 Bioglass®-derived glass-ceramic scaffolds for bone tissue engineering. *Biomaterials*, **27**(11), 2414–25.

44 Schilke, R., Lisson, J.A., Bau, O. and Geurtsen, W. (2000) Comparison of the number and diameter of dentinal tubules in human and bovine dentine by scanning electron microscopic investigation. *Archives of Oral Biology*, **45**(5), 355–61.

45 Palin, E., Liu, H.N. and Webster, T.J. (2005) Mimicking the nanofeatures of bone increases bone-forming cell adhesion and proliferation. *Nanotechnology*, **16**(9), 1828–35.

46 Hench, L.L. (1991) Bioceramics – from concept to clinic. *Journal of the American Ceramic Society*, **74**(7), 1487–510.

47 Silver, I.A., Deas, J. and Erecinska, M. (2001) Interactions of bioactive glasses with osteoblasts in vitro: effects of 45S5 Bioglass®, and 58S and 77S bioactive glasses on metabolism, intracellular ion concentrations and cell viability. *Biomaterials*, **22**(2), 175–85.

48 Forsback, A.P., Areva, S. and Salonen, J.I. (2004) Mineralization of dentin induced by treatment with bioactive glass S53P4 in vitro. *Acta Odontologica Scandinavica*, **62**(1), 14–20.

49 Suga, S. and Watabe, N. (1992) *Hard Tissue Mineralization and Demineralization*, Springer, Tokyo.

50 Coffey, C.T., Ingram, M.J. and Bjorndal, A.M. (1970) Analysis of human dentinal fluid. *Oral Surgery Oral Medicine Oral Pathology Oral Radiology and Endodontics*, **30**, 835.

51 Gillam, D.G., Tang, J.Y., Mordan, N.J. and Newman, H.N. (2002) The effects of a novel Bioglass dentifrice on dentine sensitivity: a scanning electron microscopy investigation. *Journal of Oral Rehabilitation*, **29**(4), 305–13.

52 Efflandt, S.E., Magne, P., Douglas, W.H. and Francis, L.F. (2002) Interaction between bioactive glasses and human dentin. *Journal of Materials Science–Materials in Medicine*, **13**(6), 557–65.

53 Yli-Urpo, H., Narhi, M. and Narhi, T. (2005) Compound changes and tooth mineralization effects of glass ionomer cements containing bioactive glass (S53P4), an in vivo study. *Biomaterials*, **26**(30), 5934–41.

54 Vollenweider, M., Brunner, T.J., Knecht, S., Grass, R.N., Zehnder, M., Imfeld, T. and Stark, W.J. (2007) Remineralization of human dentin using ultrafine bioactive

glass particles. *Acta Biomaterialia*, **3**(6), 936–43.

55 Sepulveda, P., Jones, J.R. and Hench, L.L. (2002) In vitro dissolution of melt-derived 45S5 and sol-gel derived 58S bioactive glasses. *Journal of Biomedical Materials Research*, **61**(2), 301–11.

56 Stoor, P., Soderling, E. and Salonen, J.I. (1998) Antibacterial effects of a bioactive glass paste on oral microorganisms. *Acta Odontologica Scandinavica*, **56**(3), 161–5.

57 Allan, I., Newman, H. and Wilson, M. (2001) Antibacterial activity of particulate Bioglass® against supra- and subgingival bacteria. *Biomaterials*, **22**(12), 1683–7.

58 Doyon, G.E., Dumsha, T. and von Fraunhofer, J.A. (2005) Fracture resistance of human root dentin exposed to intracanal calcium hydroxide. *Journal of Endodontics*, **31**(12), 895–7.

59 Zehnder, M., Luder, H.U., Schatzle, M., Kerosuo, E. and Waltimo, T. (2006) A comparative study on the disinfection potentials of bioactive glass S53P4 and calcium hydroxide in contra-lateral human premolars ex vivo. *International Endodontic Journal*, **39**(12), 952–8.

60 Waltimo, T., Brunner, T.J., Vollenweider, M., Stark, W.J. and Zehnder, M. (2007) Antimicrobial effect of nanometric bioactive glass 45S5. *Journal of Dental Research*, **86**(8), 754–7.

61 Gubler, M., Brunner, T.J., Zehnder, M., Waltimo, T., Sener, B., and Stark, W.J. (2008) Do bioactive glasses convey a disinfecting mechanism beyond a mere increase in pH? *International Endodontic Journal*, **41**(8), 670–8.

62 Ratner, B. (2004) *Biomaterials Science: An Introduction to Materials in Medicine*, 2nd edn, Elsevier Academic Press, San Diego, CA.

63 Pohunkova, H. and Adam, M. (1995) Reactivity and the fate of some composite bioimplants based on collagen in connective-tissue. *Biomaterials*, **16**(1), 67–71.

64 Dunn, M.G., Bellincampi, L.D., Tria, A.J. and Zawadsky, J.P. (1997) Preliminary development of a collagen-PLA composite for ACL reconstruction. *Journal of Applied Polymer Science*, **63**(11), 1423–8.

65 Rodrigues, C.V.M., Serricella, P., Linhares, A.B.R., Guerdes, R.M., Borojevic, R., Rossi, M.A., Duarte, M.E.L. and Farina, M. (2003) Characterization of a bovine collagen-hydroxyapatite composite scaffold for bone tissue engineering. *Biomaterials*, **24**(27), 4987–97.

66 Zhang, Y. and Zhang, M.Q. (2001) Synthesis and characterization of macroporous chitosan/calcium phosphate composite scaffolds for tissue engineering. *Journal of Biomedical Materials Research*, **55**(3), 304–12.

67 Di Martino, A., Sittinger, M. and Risbud, M.V. (2005) Chitosan: a versatile biopolymer for orthopaedic tissue-engineering. *Biomaterials*, **26**(30), 5983–90.

68 Lutolf, M.P. and Hubbell, J.A. (2005) Synthetic biomaterials as instructive extracellular microenvironments for morphogenesis in tissue engineering. *Nature Biotechnology*, **23**(1), 47–55.

69 Griffith, L.G. (2000) Polymeric biomaterials. *Acta Materialia*, **48**(1), 263–77.

70 Kim, S.S., Park, M.S., Jeon, O., Choi, C.Y. and Kim, B.S. (2006) Poly(lactide-*co*-glycolide)/hydroxyapatite composite scaffolds for bone tissue engineering. *Biomaterials*, **27**(8), 1399–409.

71 Peter, S.J., Miller, S.T., Zhu, G.M., Yasko, A.W. and Mikos, A.G. (1998) In vivo degradation of a poly(propylene fumarate) beta-tricalcium phosphate injectable composite scaffold. *Journal of Biomedical Materials Research*, **41**(1), 1–7.

72 Helen, W., Merry, C.L., Blaker, J.J. and Gough, J.E. (2008) Three-dimensional culture of annulus fibrosus cells within PDLLA/Bioglass composite foam scaffolds: assessment of cell attachment, proliferation and extracellular matrix production. *Biomaterials*, **28**(11), 2010–20.

73 Roether, J.A., Boccaccini, A.R., Hench, L.L., Maquet, V., Gautier, S. and Jerome, R. (2002) Development and in vitro characterisation of novel bioresorbable and bioactive composite materials based on polylactide foams and Bioglass (R) for tissue engineering applications. *Biomaterials*, **23**(18), 3871–8.

74 Webster, T.J., Siegel, R.W. and Bizios, R. (1999) Osteoblast adhesion on nanophase ceramics. *Biomaterials*, **20**(13), 1221–7.

75 Loher, S., Reboul, V., Brunner, T.J., Simonet, M., Dora, C., Neuenschwander, P. and Stark, W.J. (2006) Improved degradation and bioactivity of amorphous aerosol derived tricalcium phosphate nanoparticles in poly(lactide-*co*-glycolide). *Nanotechnology*, **17**(8), 2054–61.

76 Misra, S.K., Mohn, D., Brunner, T.J., Stark, W.J., Philip, S.E., Roy, I., Salih, V., Knowles, J.C. and Boccaccini, A.R. (2008) Comparison of nanoscale and microscale bioactive glass on the properties of P(3HB)/Bioglass® composites. *Biomaterials*, **29**(12), 1750–61.

77 Hong, Z., Reis, R.L. and Mano, J.F. (2008) Preparation and in vitro characterization of scaffolds of poly(L-lactic acid) containing bioactive glass ceramic nanoparticles. *Acta Biomaterialia*, **4**, 1297–306.

Keywords

bioactive glass; inorganic nanoparticles; nanofibers; tissue engineering; electrospinning; sol–gel; flame spray synthesis

7
Toxicity of Spherical and Anisotropic Nanosilica

Yuhui Jin, Samuel Lohstreter and Julia Xiaojun Zhao

7.1
Introduction

A wide variety of engineered nanomaterials has been extensively developed in recent years. Among these, certain photoactive engineered nanomaterials have become highly attractive and widely used, including quantum dots, gold (Au) nanoparticles, carbon nanotubes and silica-based fluorescent nanoparticles. One of the major applications of these photoactive nanomaterials is the labeling of biological samples for the detection and imaging of trace amounts of biological targets [1–12]. At the same time, these nanomaterials have also been used for gene and drug delivery [13–22], as well as cancer diagnosis and therapy [23–27]. The performances of these nanomaterials are remarkable due to their unique physical, chemical and electrical properties [28–31]. However, the question of whether they would exert any toxic effect(s) on living systems is starting to become a major concern [25, 32–36].

In order to address this possible problem, the toxicity of a variety of engineered nanomaterials towards biological systems has been studied both *in vitro* and *in vivo* [33–35, 37–50]. Based on the results of current studies, several properties of nanomaterials – including their size, shape, composition, form, coating material and surface properties – may affect their toxicity [33, 35, 51, 52]. The mechanism of toxicity for these nanomaterials was also investigated, and pointed towards oxidative stress as being an important factor in nanomaterials-induced toxicity [32, 33, 35]. For example, cadmium-containing quantum dots – for example, cadmium selenide quantum dots and cadmium telluride quantum dots – were each shown to generate reactive oxygen species (ROS) which mutate and break DNA strands, oxidize proteins and phospholipids, trigger oxidative stress, and also cause cell apoptosis [40, 42, 47, 49, 50]. The generation of ROS during the application of photoactive nanomaterials has also been demonstrated for metallic nanoparticles and carbon nanotubes [35]. The accepted mechanism in toxicity for these nanomaterials has been detailed in several recent reviews [14, 32, 33, 35, 51, 53, 54].

Nanomaterials for the Life Sciences Vol. 2: Nanostructured Oxides. Edited by Challa S. S. R. Kumar

ISBN: 978-3-527-32152-0

Today, colloidal and/or amorphous silica nanomaterials represent the most widely studied engineered nanomaterials [6–11, 15, 17, 21, 24, 26, 28–31, 37, 43, 48, 55–81]. Silica nanomaterials are frequently used as supporting or entrapping nanomatrices to engineer a variety of functionalized nanomaterials. Such wide use is based on two major advantages which make silica a useful matrix, and particularly relevant in bioapplications:

- The surface of silica nanomaterials is easily modified, based on well-established chemistry. With appropriate surface and internal functionality, the nanomaterials can be linked to a variety of biorecognition agents in many different ways (e.g. antibodies, protein complexes, nucleic acids, aptamers).
- The negatively charged silica matrix itself provides numerous electrostatic binding sites to physically dope (i.e. adsorb) a wide variety of positively charged molecules. When doped with bioactive molecules, these nanomaterials can serve as drug delivery vehicles capable of controlling the quantity and time of release. When doped with dye molecules, the nanoparticles become intensely luminescent reagents that are capable of sensitively signaling biological targets.

Today, silica-based fluorescent nanomaterials have an important role as fluorescent labeling reagents for bioanalysis, having been used for the ultrasensitive detection of trace amounts of DNA strands and bacterial cells [10–12]. The exceptionally strong and stable fluorescence signals of silica nanomaterials are the driving forces behind their high detection sensitivity. In addition to being an effective photoactive nanomaterial, silica nanomaterials are also promising matrices for drug delivery, with anticancer drugs having been doped into the porous structure of silica nanomaterials. Upon modification with antibodies or aptamers, the silica nanomaterials are 'driven' to cancer cells, which are then killed either by photodynamic therapy or by the anticancer drugs doped inside the nanomaterial [23].

Such extensive use of colloidal silica-based nanomaterials in biological systems brought about further safety concerns with regards to the rapidly developing fields of nanoscience and nanotechnology. Thus, a clear and basic understanding of the toxicity of silica nanomaterials might further improve their use in the biological arena. Although the toxicity of engineered silica nanomaterials has not been extensively studied, several research reports and reviews [25, 32–36] have suggested possible mechanisms for silica nanomaterials-induced toxicity. Whilst most of these reports have focused on the toxicity of airborne particulate matter, some have also discussed the direct toxicity of engineered nanomaterials such as quantum dots and metal-containing nanomaterials. In this chapter, attention will center on the toxicity of engineered amorphous silica nanomaterials and, in order to more clearly understand these structures, the current methods used for their production will be introduced. The three important pathways by which nanomaterials invade living systems will also be discussed, providing essential information for avoiding the toxic effects of nanomaterials in humans. The toxic effects and mechanisms of toxicity of amorphous silica nanomaterials on living systems will be reviewed

in detail. It has long been recognized that the properties of silica nanomaterials may have an impact on their own toxicity, and these so-called 'property effects' will be addressed. The chapter will conclude with a brief summary and perspective of the silica nanomaterials field.

7.2
Synthesis of Amorphous Silica Nanoparticles

With amorphous silica having been employed in industry for many years, the methods for its synthesis and its properties – including its toxicity – have been well documented. However, as the dimension of amorphous silica moves down to the nanometer level, not only have some of the properties of silica materials changed, but different synthetic methods have also been developed for the preparation of suitable sizes of silica nanoparticles [28–30, 59]. Currently, the most common methods used to create silica nanoparticles are the Stöber method and the water-in-oil (w/o) microemulsion method (also known as reverse microemulsion) [6–9, 28–30, 56, 58, 59, 63, 64, 70, 71, 75, 78, 82]. Moreover, on the basis of the very narrow size-distribution of the products, the w/o microemulsion method is the preferred approach (Figure 7.1).

The Stöber method, which was developed in 1968, is a simple and convenient method for producing silica nanoparticles, in which a mixture of water and alcohol (e.g. methanol, ethanol, propanol) is employed as a hydrolysis reaction medium [59]. The hydrolysis of tetraethylorthosilicate (TEOS) leads to the formation of silica nanoparticles, with ammonia being used to catalyze the hydrolysis. The resultant

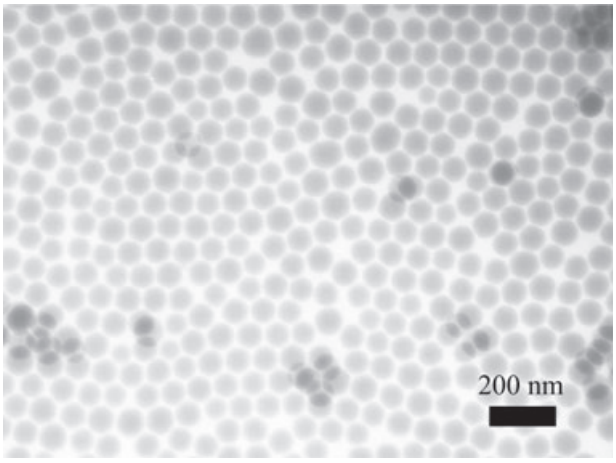

Figure 7.1 Transmission electron microscopy image of silica nanoparticles synthesized via the reverse microemulsion method.

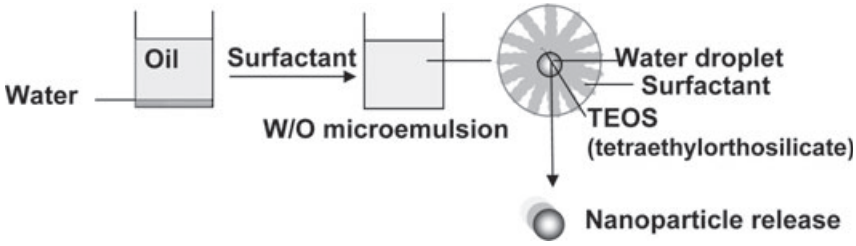

Figure 7.2 Schematic diagram of the reverse microemulsion method for the synthesis of silica nanoparticles.

size of the silica nanoparticles can be easily controlled, from tens of nanometers to several micrometers, by changing the amount of TEOS and varying the reaction time [6, 9, 10, 30, 56, 59, 70, 76, 77]. Unfortunately, the method is limited by the relatively wide size distribution of the silica nanoparticle product. In addition, the method has not been optimized to produce functionalized silica nanoparticles by doping functional molecules inside the silica matrix.

In overcoming the limitations of the Stöber method, the w/o microemulsion method represents an ideal alternative [7, 8, 12, 28, 30, 58, 60, 63, 67, 71, 78]. A w/o microemulsion is an isotropic and thermodynamically stable single-phase solution which consists of a small amount of water, a large volume of organic solvent (oil), and a surfactant. The surfactant molecules reduce the interfacial tension between water and the organic solvent, and this results in the formation of a transparent solution (Figure 7.2). The water droplets which are formed in the bulk organic solvent serve as nanoreactors for the synthesis of nanoparticles from various silane precursors, and with a variety of dopants. TEOS is a typical water-soluble precursor for the synthesis of silica nanoparticles. Upon the polymerization of TEOS, a silica core is formed in the water droplet and, as the polymerization progresses, the silica core grows in size. Ultimately, a stable silica nanoparticle is produced in the water droplet. Several factors that affect the size of the silica nanoparticle product have been extensively studied, including the type of surfactant, the water-to-surfactant ratio, the dimension of organic solvents, and the amount of TEOS present.

In addition to the Stöber and w/o microemulsion methods, a new technique was recently developed which produces organically modified silica nanoparticles that contain a hydrophobic core and a hydrophilic shell [15, 21, 24, 26]. In order to synthesize such a core–shell structure, an organic solvent, surfactant and water were first mixed to form a micellar solution, after which a special precursor – triethoxyvinylsilane – was used to provide amphiphilic characteristics to the organically modified silica nanoparticles. By using this method, water-insoluble molecules can be doped *in situ* within the silica core during the synthesis. This new approach has broadened the applications of silica nanoparticles such that, today, water-insoluble anticancer drug molecules and photodynamic therapy reagents can be doped inside the silica core, without affecting their functions.

Each of the above three methods produces amorphous silica nanoparticles of various sizes and with varying properties, the versatility being obtained mainly through doping and surface modifications. The Stöber method is simple and fast (a few hours), but the size of products is not uniform. In contrast, the w/o microemulsion method results in uniform and small-sized silica nanoparticles, but only allows hydrophilic dopants to be embedded in the silica matrix, as does the Stöber method. The triethoxyvinylsilane method, on the other hand, allows hydrophobic molecules to be doped inside the silica matrix, while the properties of the hydrophobic molecules remain stable. In this way, both hydrophilic and hydrophobic dopants can be readily engulfed in the silica matrix by combining multiples of the above-described methods. Consequently, silica nanoparticles rather resemble nanoscale vessels that load and deliver cargo, or an assembly of single molecules that exhibit a group behavior. Today, the biological applications of silica nanoparticles show much promise due to the novel physical and chemical properties of the dopants, with a wide variety of applications having been demonstrated in areas of biosensing and bioimaging [7–12, 28], gene, protein and drug delivery [6, 15, 17–19, 21], cancer diagnosis, and photodynamic therapy [23, 24, 26].

7.3 Invasion Pathways of Silica Nanomaterials into Living Systems

In order to understand the toxicity of silica nanomaterials, we must first be made aware of the exposure routes that silica nanomaterials might take to penetrate living systems. Previous studies of particle toxicity have shown that the size, shape and surface properties of the particles are the key factors that eventually determine whether, or not, the particles can enter and remain inside living systems [14, 32, 35, 51, 83, 84]. As the interior properties and composition of the particle have a negligible effect on its penetrance of biological systems, similar investigations of invasion routes for other nanomaterials can be used to study silica nanomaterial invasion. In general, foreign materials invade the human body through one of three pathways, namely the respiratory tract, the gastrointestinal tract, and by skin contact. The invasion routes used by nanomaterials to access living systems will be detailed in the following sections.

7.3.1 Exposure via the Respiratory Tract

Respiratory tract exposure is the most common and widely studied pathway of particulate matter invasion [14, 32, 35, 51, 84], and the same is true for nanomaterials. The inhalation of airborne natural particulate matter or engineered nanomaterials may lead to serious toxic effects; for example, the prolonged exposure and uptake of these materials in the human lung can cause chronic obstructive pulmonary disease and pulmonary morbidity, both of which may lead to death [32]. Therefore, it is crucial to understand how these materials enter and reside in

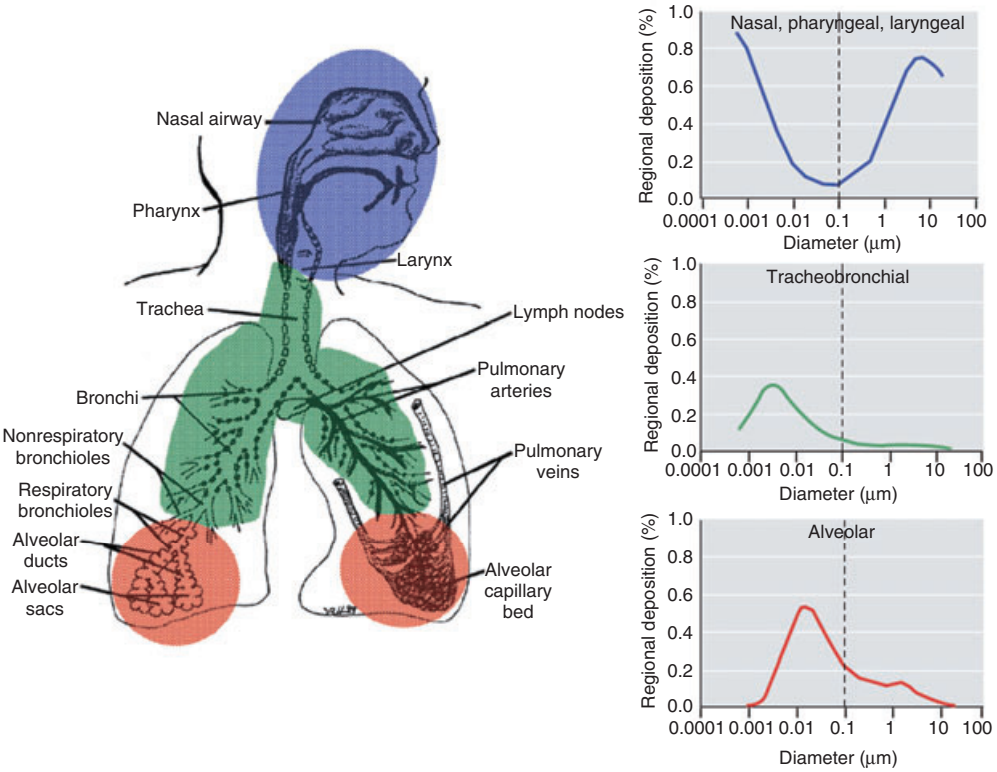

Figure 7.3 Prediction of site-selective deposition of nanomaterials in the respiratory tract during nose breathing. Reprinted with from Ref. [51] with permission from *Environmental Health Perspectives*.

the respiratory system, and whether the human body can detoxify them and/or translocate them to other organs.

Particulate matters, when inhaled into the respiratory system, may remain unchanged in the nasopharyngeal, tracheobronchial and alveolar regions [14, 51, 85]. Previously, the suggested model of how particulate matters exist in the respiratory system was widely accepted (Figure 7.3) [51, 85], with the preferential region of particle distribution being essentially size-dependent. Such a prediction is valid for single, unattached particles (i.e. without aggregation), and most micrometer-sized particles are more likely to be deposited in the nasopharyngeal region. However, as the size falls to nanometer scale the particles can move deeper into the tracheobronchial and alveolar regions. When the diameter reaches about 20 nm, the particles show the highest theoretical deposition efficiency in the alveolar region (50%). Surprisingly, however, it is not the smallest nanomaterials that are deposited in the deepest region of the respiratory tract. For example, over 90% of particles with a diameter <1 nm will remain in the nasopharyngeal region, and

10% in the tracheobronchial region. None of these nanomaterials can reach the alveolar region, as the smallest nanomaterials can easily be exhaled from the alveolar interstitial region, without deposition. Although the size-related deposition efficiency is complicated, the evidence is clear that it is particle size that determines the rates of decomposition and consequent particle-induced toxicity. In addition to size, the solubility of particles is also important with regards to their deposition site. Typically, water-soluble particles are readily absorbed in all parts of the respiratory tract, whereas insoluble particles will remain inside the lung, due to their long retention time [85].

Any particulate matter and nanomaterials which invades the respiratory system will be disposed of by macrophages and the 'mucociliary escalator', before they reach the epithelial cells [35]. Macrophages will engulf and relocate particles via the process of phagocytosis and, indeed, following the instillation of amorphous silica particles in the lung the concentration of macrophages and neutrophils in the bronchoalveolar lavage increases dramatically [38, 44–46]. Moreover, the numbers of these cells kept increasing until 15 days after exposure [38, 45, 46]. Biodegradable particles can be decomposed after being trapped inside macrophages. Here, the water-soluble debris is either evacuated by the mucociliary escalator, or translocated into the blood circulation or lymphatic drainage. Although amorphous silica may not be easily degraded by macrophages, the silica particles can still be ejected from the body or translocated to other organs.

As particulate matters and synthetic nanomaterials are deposited in the respiratory system, they are further translocated to other organs via several pathways. The first step for the translocation is endocytosis or transcytosis [35], after which particulate matters and nanomaterials will be further transported to other organs via the blood, lymphatic drainage or, in very rare cases, the sensory nervous system [86]. The particle size, shape and surface properties greatly affect these processes. First, the endocytosis of particulate matters and nanomaterials is size- dependent, with smaller particles more easily taken up by epithelial cells than larger particles. Thus, nanomaterials are more readily translocated via endocytosis or transcytosis. As an example, the uptake efficiency of polystyrene microbeads was quite different from that of nanobeads [51]. Whereas, the large majority (80%) of microbeads was located in macrophages (by phagocytosis), only 20% of the nanoparticles were in macrophages, with the other 80% either being located in epithelial cells or further transported to other organs via the blood or lymphatic circulation. In nonphagocytic cells, the smaller nanomaterials were engulfed through caveolae sites, while larger particles were transported by clathrin-coated pits [35, 87, 88].

The rate of uptake is also affected by the nanomaterials' surface properties. Whilst, in theory, water-soluble materials are easier to translocate to other organs than their insoluble counterparts, an effective surface coating, such as albumin, lecithin or polyethylene glycol (PEG), can enhance the process of endocytosis [35].

The shape of nanomaterials is also a considerable factor in the process of endocytosis. The macrophages find greater difficulty in phagocytosing fiber- or acicular-like nanomaterials than spherical shapes [68, 89]. The large dimension of fibers

also greatly hinders the uptake process, with a comparison among single-walled and multiwalled carbon nanotubes and fullerenes showing a comparative uptake rate in the order fullerene > multiwalled carbon nanotube > single-walled carbon nanotube [25]. The same trend was also recently reported for nanosized amorphous silica nanomaterials [68].

Finally, nanomaterials can be deposited ('settle') in different organs, such as the liver, spleen, vasculature, heart and bone marrow [14, 35, 51, 84]. Most nanomaterials deposited in the liver were engulfed by Kupffer cells [51]. The deposition location appears to be affected by the nanomaterials' surface coating; for example, a PEG surface coating can prevent the uptake of nanoparticles by hepatic and splenic cells [90]. On occasion, for drug delivery purposes, an intentional surface coating is required. For example, the delivery of nanomaterials to the brain is extremely difficult, although a specific receptor, *apolipoprotein*, has been used to facilitate such translocation [16, 20, 91, 92].

Typically, the translocation of synthetic nanomaterials leads to a reduction in the pulmonary symptoms, although diseases and symptoms may appear in other organs due to the redeposition of nanomaterials. For example, cardiovascular events such as heart attacks and cardiac rhythm disturbances have been observed after pulmonary exposure to ultrafine particles [93]. The relationship between toxicity and the impact on a patient's health will be discussed later in the chapter.

7.3.2 Exposure via the Gastrointestinal Tract

Exposure to nanomaterials via the gastrointestinal tract is inevitable as food products may be contaminated by synthetic nanomaterials present in the environment. In addition, nanomaterials or particulate matter cleared through the mucociliary escalator in the respiratory system will relocate to the gastrointestinal tract [14, 35, 51, 84]. Thus, it is important to understand particulate invasion via the gastrointestinal tract, and the factors that dominate the tract's absorption processes.

Hagens *et al.* have summarized details of the different routes of uptake of particulate matters and nanomaterials via the gastrointestinal tract [84], noting that micrometer-sized particles may be transported to the lymphatic and circulatory systems through a persorption process. The absorption routes via the Peyer's patches in the small intestine, and also by intestinal enterocytes, have been observed previously. Similar to the respiratory tract, absorption in the gastrointestinal tract first requires nanomaterials to be absorbed, and then transferred to the circulatory and lymphatic systems. Finally, the nanomaterials will be deposited in other organs such as the liver, spleen, bone marrow and kidneys. As nanomaterials enter the blood or lymphatic circulations, the procedure is similar to that in the respiratory tract, and therefore only the initial step of gastrointestinal uptake is discussed in detail. The translocation step mostly demonstrates the same phenomena; for example, the liver is the primary target organ of translocation, with studies

of the gastrointestinal uptake of titanium particles (150–500 nm) having shown the particles to be deposited primarily in the liver. Likewise, gastrointestinal exposure to fullerene resulted in a 73–80% hepatic deposition of the nanomaterial [51].

The uptake of nanomaterials in the gastrointestinal tract is greatly affected by the nanomaterials' size and surface properties [32, 51, 94], with small nanoparticles being more easily absorbed than larger nanoparticles. The rate of uptake for different-sized polystyrene particles showed a distinctive pattern of efficiencies, with 6.6% and 5.8% of small particles (50 and 100 nm) being absorbed, respectively, but almost none of the micrometer-sized particles (0.8% and 0% for 1 μm and 3 μm particles, respectively) [94].

The surface charges of the nanomaterials can also affect their rate of uptake. Typically, positively charged particles are absorbed more efficiently than neutral and negatively charged particles. although most particles in the gastrointestinal tract will be quickly expelled via the feces [84].

7.3.3 Skin Contact

As nanomaterials may invade living systems by penetrating the epidermal layer of the skin, the handling of engineered nanomaterials and the use of cosmetic products containing nanomaterials will increase the threat of epidermal exposure. Since large, micrometer-sized particles cannot penetrate healthy skin, their only route is through open wounds and cuts [35]. However, as the size of particles reduces to the nanometer scale, the chance of particle penetration is increased dramatically, and consequently nanometer-sized particles will be more harmful than their micrometer-sized counterparts in the case of skin contact.

It has been shown that 0.5 μm fluorescent dextran beads may penetrate the stratum corneum within 60 min under flexing, whereas 1 μm beads could not penetrate [95]. Small-sized nanomaterials, such as fullerene, metal nanoparticles and quantum dots, were able to penetrate the intact skin [83, 96–99], with small-sized quantum dots (15 nm) penetrating deeper (observed in the epidermal region) than the larger (40 nm) quantum dots (observed only in the stratum corneum) during the same period (8 h) [98]. Aside from the size of the quantum dots, their shape also seems have a role in skin penetrance, as spherical quantum dots were seen to penetrate the epidermal barrier more easily than ellipsoids [98].

The surface properties of the nanomaterials may also affect skin penetration. In a study of metal nanoparticles in which the skin pH was varied [83], a tetramethylammonium hydroxide-coated metal nanoparticle (TMAOH-nanoparticle) with an isoelectric point of 6.3 was used. Changing the skin pH caused a change in the surface charge of the nanoparticles; this in turn led to aggregation such that the hydrodynamic diameter of the nanoparticles expanded. These changes led directly to a slower rate of penetration. However, in a study using quantum dots, whether the surface charges were negative, positive or neutral, a passive penetration dominated, which meant that the surface charge had no effect on the

penetration rate of quantum dots [99]. Besides the effect of surface charges, other types of coating (e.g. surfactant coating) also affect the penetration rate of nanoparticles. For example, Aerosol OT (AOT)-nanoparticles might compromise the integrity of skin due to the amphiphilic property of AOT, which assisted in the nanoparticle penetration [83]. As in the case of nanomaterials which enter living systems via other routes, foreign nanomaterials that penetrate via skin contact may further translocate to other organs, assisted by the circulatory or lymphatic systems.

7.3.4 A Brief Summary

Although most studies of the exposure routes of nanomaterials in living systems have not been conducted with silica nanomaterials, the same general principles should still be applied. Because the size, shape and surface properties of nanomaterials are key factors not only during the exposure but also following their translocation and deposition, the chemical composition of nanomaterials serves only a minor role in this respect. Therefore, amorphous silica nanomaterials may invade living systems by all three of the above-mentioned routes. Importantly, intravenous injection may represent an additional, minor route for the invasion of silica nanomaterials, due to their potential use as drug delivery vessels or cancer therapeutic reagents. In theory, the penetration, translocation and deposition of amorphous silica nanomaterials are all affected by their properties, such as size, shape and surface characteristics.

7.4 Mechanism of Nanomaterials-Induced Toxicity

In the past, the toxicity of airborne ultrafine particles and certain engineered nanomaterials have been well documented [32, 33, 35, 51, 53, 54, 93], with colloidal silica generally being accepted as either a nontoxic or low-toxicity material [44, 53]. However, when the structure is changed to a crystallized analogue – an ultrafine quartz particle – the previously inert silica becomes acutely toxic [44]. If the amorphous structure remains constant while the size of amorphous silica particles is reduced to nanometer scale, then the changes will mainly be physical and chemical and capable of generating many fantastic applications of nanomaterials in the field of biology. Meanwhile, however, the toxicity of silica particles must be re-evaluated.

In general, when living systems come into direct contact with amorphous silica nanomaterials, the result may be a series of negative effects including chronic pulmonary changes during inflammation, ROS generation, and damage to intracellular DNA, RNA and proteins [37, 38, 43–46, 48, 100]. The following section provides some introductory details of the mechanism of toxicity for photoactive and silica nanomaterials.

7.4.1 Photoactive Nanomaterials-Induced Toxicity

Recently, the toxic effects of engineered photoactive nanomaterials have undergone extensive investigation, notably the toxicity of quantum dots [14, 32, 33, 35]. The proposed essential mechanism for nanomaterials-induced toxicity has focused on the generation of ROS and the induction of oxidative stress [35, 54]. The ROS were generated via different pathways as a result of stimulation by nanomaterials [54]; an example was the generation of ROS by cadmium-containing quantum dots irradiated with UV light [40]. The oxidation of metals, or the catalysis of redox cycles (e.g. Fenton chemistry) led to the production of intracellular ROS [35, 54], as did the direct interaction of nanomaterials with cells, since nanomaterials are capable of activating a phagocytic oxidative burst. When nanomaterials interact directly with intracellular molecules – such as DNA, RNA, enzymes and other types of protein – the damage or malfunction of these molecules may cause the generation of ROS. With genomic contamination the cells may repair their damaged DNA, but if the cell defense mechanism does not function correctly, then mutagenesis or cancer may occur. In general, nanomaterials can induce ROS generation through both acellular and cellular pathways, although the characteristics of the nanomaterials, such as size, shape, composition, solubility and surface properties, will each have an effect on such generation.

7.4.2 Toxicity of Silica Nanoparticles

The mechanisms of engineered photoactive nanomaterials-induced toxicity apply only partially to amorphous silica nanoparticles, mainly because their composition and structure differ from those of quantum dots, metal nanoparticles, carbon nanotubes and quartz nanoparticles. The amorphous structure and nontoxic composition provide amorphous silica nanoparticles with a significant advantage – that is, the nanoparticle has a relatively low toxicity compared to the above-mentioned photoactive nanomaterials. Until now, studies on the toxicity of silica nanoparticles have been reported both *in vitro* and *in vivo*, as discussed below.

7.4.2.1 *In Vitro* Studies of Silica Nanomaterials-Induced Toxicity

In vitro toxicity studies of amorphous silica nanomaterials are mostly focused on the reaction of nanomaterials with cells from organs included in the three nanomaterials exposure routes (respiratory tract, gastrointestinal tract and skin contact). Until now, a variety of different cell lines have been studied, including mesothelial cells (MET-5A, skin), WS1 (skin), CCD-966sk (skin), A549 cells (lung), alveolar macrophage cells (lung) and MKN-28 (gastric).

The MTT [3-(4,5-dimethylthiazol-2-yl)-2,5-diphenyltetrazolium bromide] and LDH (lactate dehydrogenase) assays are commonly used to evaluate the cytotoxicity of nanomaterials, while measurements of ROS, glutathione (GSH) and hOgg1 are used to evaluate nanomaterial-induced oxidative stress. The different cell lines

showed varied resistance to the nanomaterials-induced toxicity. In the study by Chang, cancer cell lines (A549, MKN-28) had a higher viability and resistance to silica nanoparticles than did normal cell lines (MRC-5, WS1 and CCD-966sk) [37]. Similarly, a previous study showed that A549 cells were more resistant to the treatment of silica nanoparticles than were macrophages [43]. When Lin *et al*. examined the size- and time-dependence of silica nanoparticle-induced toxicity [48], a 48 h treatment of cells with silica nanoparticles caused a reduction in GSH level, indicating that the silica nanoparticles had induced the generation of ROS. Levels of the hOgg1 protein (a DNA repair protein produced in response to oxidative stress) were also increased when cells were exposed to silica nanoparticles, although no increase in DNA damage was observed. Again, these findings suggested that the silica nanoparticles had induced oxidative stress, in response to which the cells had produced more hOgg1 to prevent further DNA damage and cell death [43].

7.4.2.2 *In Vivo* Studies of Silica Nanomaterials-Induced Toxicity

Although the toxicities of silica nanomaterials have been investigated widely *in vitro*, these studies may not reflect the true scenario, as would occur with *in vivo* exposure. For example, a low efficiency of endocytosis might lead to a low cytotoxicity *in vitro*, while severe chronic toxicity may be induced in the evacuation process. Therefore, *in vivo* studies are necessary in order to evaluate silica nanomaterials-induced toxicity.

Pulmonary exposure is the most popular route for *in vivo* investigations of nanomaterials-induced toxicity. In order to better understand the toxic effect of amorphous silica nanomaterials, the nanomaterials were instilled into the respiratory tract [38, 44–46, 100] and, after a period of treatment, the acute and subacute pulmonary toxic effects were monitored. However, this phenomenon was an induced transient toxicity, and pulmonary function was fully recovered after several days post-exposure. Compared to the persistent pulmonary inflammation caused by crystalline silica nanomaterials, the negative effect of amorphous silica nanomaterials was considered insignificant.

Under pulmonary exposure, silica nanomaterials can be taken up via phagocytosis and endocytosis. In response to the instillation of silica nanomaterials, various cytokines [including interleukin (IL)-1β, IL-6, IL-8 and tumor necrosis factor-α (TNF-α)] and chemokines [monocyte chemoattractant protein-1 (MCP-1) and macrophage inflammatory protein-2 (MIP-2)] were expressed to regulate the pulmonary inflammation [38]. While the increase in IL-1β mediated the process of inflammation, the levels of other cytokines such as IL-6 and IL-8 were also increased, even after one week of instillation of the silica nanomaterials. Meanwhile, MIP-2 (which can direct neutrophils to the inflammation sites) was also expressed as a result of silica nanomaterial-induced oxidative stress. Thus, it appeared that the inflammation and phagocytic 'oxidative burst' had occurred as a result of exposure to silica nanomaterials.

Upon the uptake of the silica nanomaterials in the respiratory tract, the cell counts of both neutrophils and macrophages were transiently increased [38, 44–46]. Cho and coworkers reported an increase in neutrophil count in the bronchoalveolar lavage fluid following the instillation of 14 nm silica nanomaterials, at different

doses [38]. The symptoms (which included inflammation and an increased expressions of both cytokines and chemokines) were acute, but resolved as the post-instillation time was prolonged. The rapid recovery was most likely due to the small size of the silica nanomaterials, which had facilitated endocytosis and transcytosis to aid in the rapid translocation of nanomaterials and their evacuation from the lung. However, at times the macrophage population may have decreased.

In *in vivo* studies, the induced toxicity of silica nanomaterials is transient, with the level of apoptosis, neutrophil and macrophage counts and cytokine/chemokine expressions returning to normal between one week and one month of recovery.

7.4.2.3 Mechanism of Silica Nanomaterials-Induced Toxicity

Most engineered photoactive nanomaterials contain metal components. Metals can generate ROS without interacting with cells; for example, quantum dots can generate ROS under UV irradiation, while iron-containing nanomaterials can catalyze redox reactions through Fenton chemistry. The crystallized metal oxide nanomaterials can also produce ROS through an acellular approach [35, 40]. In contrast, amorphous silica nanomaterials contain no metal components, and the direct generation of ROS is unlikely to occur. However, an intracellular presence of ROS was observed in the *in vitro* treatment of silica nanomaterials [37, 43, 48], which suggests that a different mechanism might be involved in the generation of ROS.

Based on previously proposed mechanisms, the cellular-based generation of ROS is most likely the case for the silica nanomaterial-induced ROS and oxidative stress. In the cellular mechanism, interactions between intracellular nanomaterials and the cells are dominant, and an uptake of silica nanomaterials has been demonstrated in both *in vitro* and *in vivo* studies [43, 45, 46]. Furthermore, small-sized nanomaterials have been found in the mitochondria and nuclear regions, where damage to the cellular structure and biomolecules is possible [101]. Proteins, such as human carbonic anhydrase I (HCAI), could be absorbed and denatured on the surface of nanomaterials [72], while DNA strands were shown to interact easily with the surface of amine-modified silica nanomaterials [55]. Therefore, a strong binding and interactions of silica nanomaterials with intracellular biomolecules led to incorrect functions of these molecules and nanomaterial-engulfed cells [55, 69, 72, 74, 80, 102]. It is possible that these processes might trigger the inflammation and generation of ROS and oxidative stress, and that apoptosis and necrosis may also occur during the treatment of silica nanomaterials [37, 38, 43–46, 48].

7.5 Effects of Silica Nanomaterial Properties on Toxicity

Many factors influence the toxicity of silica nanomaterials, including their size, shape and surface and core properties, as well as the concentration of the nanomaterial, the treatment time and the type of targeted cell line. Thus, a knowledge of these factors might help in the reduction and/or control of the toxicity associated with silica nanomaterials.

7.5.1 Effect of Silica Nanomaterial Size

The size of the nanomaterial greatly influences its toxicity; typically, as the nanomaterial's size decreases, certain of its parameters are changed [28–31]. Many studies have shown that variations in the size of nanomaterials account for the different toxicity levels between nanosized and micrometer-sized materials [32, 35, 51]. It is known that a reduction in size can increase the rate of uptake and translocation of silica nanomaterials *in vitro* and *in vivo*, thereby inducing a more severe and transient toxicity (Figure 7.4) [82]. For example, Kaewamatawong *et al*. reported that, with the same treatment dose ($mg\,ml^{-1}$) *in vivo*, small silica nanoparticles (14 nm) showed a more severe toxicity than did large nanoparticles (213 nm) [45]. A similar phenomenon was observed by Jin *et al*. in an *in vitro* study, when smaller silica nanoparticles (23 nm) proved to be more toxic than larger ones (85 nm) following a three-day treatment of A549 cells (Figure 7.5) [82]. In contrast, when *similar* toxicities were observed *in vitro* for 15 nm and 46 nm amorphous silica nanoparticles [48], this was considered due to the similarity of the nanoparticles' hydrodynamic diameters. Thus, the state of the conjugate and the hydrodynamic size of the silica nanomaterial, rather than its physical diameter, are more representative of the differences in size-induced toxicity [48].

A smaller size not only facilitates the cellular uptake and translocation of nanomaterials but also alters the interaction between nanomaterials and the cellular components. Changes in particle–protein interaction appear to influence silica nanomaterial-induced toxicity [69, 72, 74, 80, 102], as demonstrated in the pioneer studies reported in 2004 of the interaction between silica nanoparticles and pro-

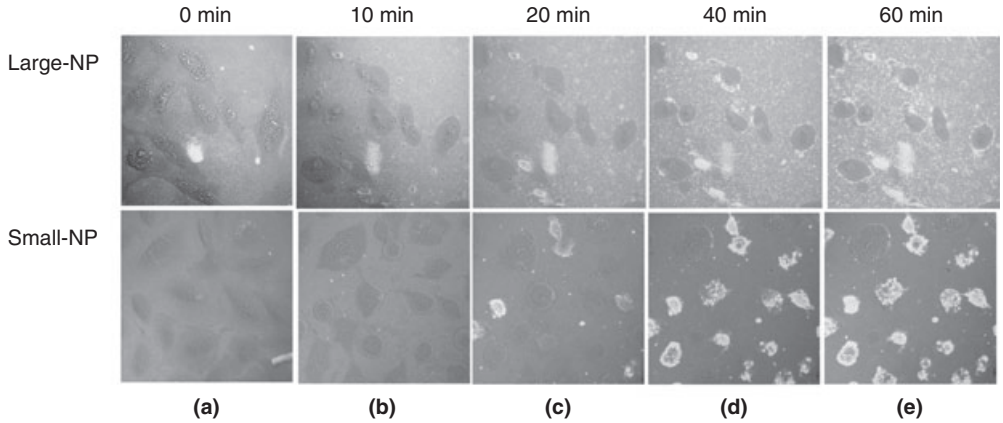

Figure 7.4 Penetration of different-sized silica nanoparticles (NP) through the membranes of A549 cells. Large-NP: 85 nm; small-NP: 23 nm. Both NPs are fluorescent and monitored by their fluorescent color (yellow) under the confocal fluorescence microscope. Reprinted with permission from Ref. [82]; © 2007, American Chemical Society.

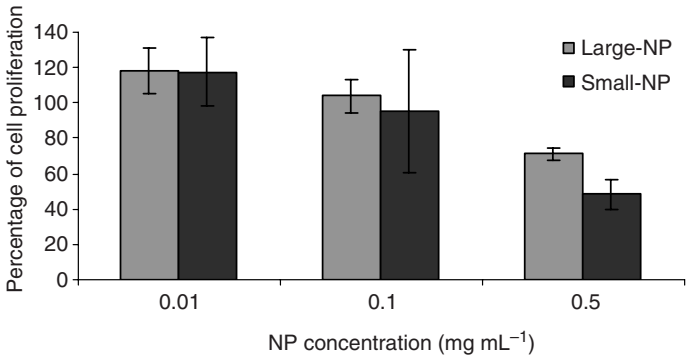

Figure 7.5 Comparison of cytotoxicity induced by different-sized nanoparticles (NP) using the cell proliferation assay. Reprinted with permission from Ref. [82]; © 2007, American Chemical Society.

teins. In studies conducted by both Vertegel and Lundqvist and colleagues, proteins were seen to be denatured when they were adsorbed onto the surface of silica nanoparticles [72, 74], with larger nanoparticles (15 nm) inducing a more severe (ca. sixfold) denaturation than their smaller counterparts (6 nm). As an example, ribonuclease A, when adsorbed to the silica surface, could be unfolded to different extents based on the curvature of the silica nanoparticles. In overall terms, however, it is the size of silica nanoparticles that affects their toxicity.

7.5.2
Effect of Silica Nanomaterial Shape

Although, until now, investigations into the effect of nanomaterial shape on toxicity have been limited in number, currently available information suggests that the shape of a nanomaterial can affect its toxicity in two ways. First, the shape of a nanomaterial has an effect on the rate of its cellular uptake; and second, the shape of a nanomaterial can affect the extent of its aggregation, and hence alter its cytotoxic properties.

An initial study of the toxicity of carbon nanotubes and fullerene implied that fiber-shaped nanomaterials were more toxic than spherical nanomaterials [25]. In the case of the carbon nanotube, its shape appeared to hamper the processes of endocytosis and phagocytosis, such that chronic pulmonary toxicity occurred. However, a recent *in vitro* toxicity study using different sizes of silica nanomaterials showed spherical nanomaterials be more toxic than rods [68]. The suggested reason for this was that the silica nanorod aggregated much more easily than the spherical silica nanomaterials; consequently, the large aggregates not only reduced the surface area-to-volume ratio of the nanomaterials but also slowed their rate of cellular uptake. It was also shown to be more difficult for elliptical nanomaterials to penetrate the skin layer than spherical ones [98]. Overall, however, the results of these studies indicated that the shape of nanomaterials could indeed affect their toxicity.

7.5.3 Effects of Silica Nanomaterial Surface Properties

The surface properties of nanomaterials include their chemical reactivity, water solubility, charge, functional groups and biocompatibility, In general, the surface properties of nanomaterials have a profound effect on their toxicity. Pure silica nanomaterials show low levels of toxicity as:

- the inert nature of silica surface is resistant to the direct generation of ROS, which greatly reduces the silica nanomaterials-induced toxicity
- the surface of silica nanomaterials is hydrophilic; hence, a high water solubility reduces the aggregation of silica nanomaterials and facilitates endocytosis, transcytosis and the translocation of silica nanomaterials [78]. Such a rapid translocation may reduce the chronic pulmonary burden.

Based on well established silica chemistry, the surface of silica nanomaterials can be modified to introduce a variety of functionalizations [28–30]. The toxicity of surface-modified nanomaterials is largely determined by their surface functional groups. For example, when quantum dots were coated with three different functional groups of amine, carboxyl and PEG [99], their endocytotic processes became significantly different. The surfactant (AOT)-coated nanomaterials, which had detergent-like surface properties, were able to break the skin structure such that skin penetration was much easier [83]. The amine group-modified silica nanoparticles exhibited a strong DNA binding capability to prevent DNA cleavage [55], while a specific PEG coating on the nanoparticles dramatically reduced their hepatic and splenic deposition from the blood circulation [90]. A specific antibody coating on silica nanomaterials may cause the nanomaterials to be 'driven' to a specific location in the living system, thus having less effect on other organs. As an example, Kreuter reported that an apolipoprotein coating on silica nanoparticles aided their endocytosis in brain capillaries through the LDL-receptor [16, 91, 92]. Overall, silica nanomaterials are low-toxicity materials, although their toxicity can be altered if surface modifications are applied to them.

7.5.4 Effect of Dopants

Although a wide variety of molecules can be doped inside a silica matrix, the dopants, in general, have little effect on the toxicity of silica nanomaterials because they are isolated from the environment [28–30, 63]. However, if the dopants are photosensitizers or some other specialized molecule, they can have an effect on the toxicity of the silica nanomaterial. For example, when a hydrophobic photosensitizer, PS HPPH [2-devinyl-2-(1-hexyloxyethyl) pyropheophorbide], was doped inside organically modified silica nanoparticles [23], and the nanoparticles were delivered into cells (under irradiation), ROS were produced by the doped photosensitizers such that the cells were killed.

Dopants may also leak from the silica matrix, and if this occurs then the toxicity of the silica nanomaterials will be altered. However, under certain circumstances, leakage can be deliberately induced, an example being in the case of drug delivery. Here, anticancer drugs can be doped inside a silica matrix and then delivered to target cells [15, 21, 26]; the subsequent intracellular release of the drug molecules would then result in death of the cancer cells.

7.5.5
Effects of Dose and Interaction Time

Dose-dependent toxicity has frequently been observed in the study of nanomaterials [37, 38, 43–46, 48], with increasing doses of silica nanomaterials invariably worsening their toxicity. Both, cell proliferation and viability were greatly hampered at higher doses in *in vitro* studies [37, 43, 48], whereas acute pulmonary toxicity and inflammation were both prolonged as higher concentrations of silica nanomaterials were instilled *in vivo* [38, 44–46]. Thus, it would appear that there was a dose 'safety limit' for the application of variable-sized silica nanomaterials [43, 82]. Interactions between nanomaterials and environmental materials generally occur on the surface of nanomaterials, and indeed the release of ROS and interactions of nanomaterials with protein and DNA molecules are all surface-related. Therefore, the effective surface area of a nanomaterial is an important factor when determining dose-related toxicity. However, similar dose-dependencies have also been observed in toxicity studies of other materials.

The duration of treatment with nanomaterials in living systems is another important factor that affects silica nanomaterial-induced toxicity. Whilst for *in vitro* studies a greater toxicity was observed with a prolonged treatment (several days) [37, 43, 48], for *in vivo* studies the pulmonary toxicity and inflammation regressed and recovered with a prolonged post exposure time (one to several weeks) [38, 44–46]. However, this difference might be due to differences in methodology since, for the *in vivo* study the nanomaterials could be evacuated or translocated via several mechanisms. In contrast, in the *in vitro* studies the nanomaterials could not be excluded from the culture environment, which in turn would induce chronic toxicity. Nonetheless, a longer experimental time for *in vivo* studies would allow observations to be made of any slow regression.

7.6
Toxicity of Silica Nanomaterials: A Summary

The toxicity of amorphous silica nanomaterials has been investigated both in *in vitro* and *in vivo*. Although the severity of the toxic reaction increases as the size of the amorphous silica is reduced to the nanometer scale, compared to metal-containing nanomaterials silica nanomaterials exhibit a relatively lower toxicity, due to their amorphous silica structure. Among *in vitro* studies, no significant toxic effect was observed for silica nanomaterials at concentrations up to $100\,\mu g\,ml^{-1}$

[37, 43, 48]. A low toxicity was also observed in *in vivo* studies, where the amorphous silica nanomaterials can only cause transient toxicity, and no chronic affect was found [38, 44–46]. However, a significant toxicity of silica nanomaterials was observed at high doses; this may be caused by the generation of intracellular ROS as the nanomaterials penetrate and interact with cells and organelles. Increased ROS levels have been observed by monitoring the ratio of GSH:GSSH, DNA damage and the level of DNA repair proteins. Following treatment with silica nanomaterials, both cytokines and chemokines have been detected, some of which are responsible for the regulation of apoptosis and necrosis of the invaded cells. The hampered proliferation and low viability were observed using the MTT and LDH assays.

In summary, whilst the toxicity of silica nanomaterials is generally low – and even more so at lower concentrations – a variety of factors which include the nanomaterials' size, shape, surface properties, dopants, treatment dose and time, all affect their toxicity to similar degrees. Although such toxicity is a relatively recently investigated topic, and many studies are still at the experimental stages, the above-described factors are crucial for the safe use of silica nanomaterials in a variety of biological applications.

7.7 Perspectives on Silica Nanomaterials

In their role as engineered nanomaterials, amorphous silica nanomaterials possess several attractive properties for bioapplications. First, a minimal toxicity not only permits their wide and safe use in biological fields, but also ensures that their environmental impact will be insignificant. Second, the unique amorphous silica matrix provides large intraparticle spaces and numerous docking sites for dopants, such as fluorophores and anti-cancer drugs. Third, amorphous silica nanomaterials can be engineered with different sizes, shapes and properties. Until now, the biological uses of silica nanomaterials have involved bioimaging, analyte determination at trace levels, drug delivery and cancer therapy. In addition, due to their low toxicity, silica materials may be used as a protective outer shell to reduce the toxicity of other nanomaterials, such as Au nanoparticles and quantum dots. Nevertheless, the correct use of engineered silica nanomaterials among a wide variety of fields will require the use of a standard protocol for their handling and disposal, which has yet to be completed.

Acknowledgments

These studies were supported by the National Science Foundation (NSF) Grant CHE-0616878, NSF REU grant CHE-0552762. North Dakota Water Resource Research Institute, and North Dakota DOE EPSCoR Seed Awards. The authors thank Mr Ke Xu at Harvard University for editing the manuscript.

References

1 Bruchez, M., Moronne, M., Gin, P., Weiss, S. and Alivisatos, A.P. (1998) Semiconductor nanocrystals as fluorescent biological labels. *Science*, **281**, 2013–16.

2 Cao, Y., Jin, R. and Mirkin, C.A. (2002) Nanoparticles with Raman spectroscopic fingerprints for DNA and RNA detection. *Science*, **297**(5586), 1536–40.

3 Chan, W.C.W. and Nie, S.M. (1998) Quantum dot bioconjugates for ultrasensitive nonisotopic detection. *Science*, **281**(5385), 2016–18.

4 Esch, M.B., Locascio, L.E., Tarlov, M.J. and Durst, R.A. (2001) Detection of viable cryptosporidium parvum using DNA-modified liposomes in a microfluidic chip. *Analytical Chemistry*, **73**(13), 2952–8.

5 Han, M., Gao, X., Su, J.Z. and Nie, S.M. (2001) Quantum-dot-tagged microbeads for multiplexed optical coding of biomolecules. *Nature Biotechnology*, **19**(7), 631–5.

6 Rossi, L.M., Shi, L., Quina, F.H. and Rosenzweig, Z. (2005) Stöber synthesis of monodispersed luminescent silica nanoparticles for bioanalytical assays. *Langmuir*, **21**, 4277–80.

7 Santra, S., Wang, K., Tapec, R. and Tan, W. (2001) Development of novel dye-doped silica nanoparticles for biomarker application. *Journal of Biomedical Optics*, **6**(2), 160–6.

8 Santra, S., Zhang, P., Wang, K., Tapec, R. and Tan, W. (2001) Conjugation of biomolecules with luminophore-doped silica nanoparticles for photostable biomarkers. *Analytical Chemistry*, **73**(20), 4988–93.

9 Wang, L., Yang, C. and Tan, W. (2005) Dual-luminophore-doped silica nanoparticles for multiplexed signaling. *Nano Letters*, **5**, 37–43.

10 Wang, L., Zhao, W., O'Donoghue, M.B. and Tan, W. (2007) Fluorescent nanoparticles for multiplexed bacteria monitoring. *Bioconjugate Chemistry*, **18**, 297–301.

11 Zhao, X., Hilliard, L.R., Mechery, S.J., Wang, Y., Bagwe, R.P., Jin, S. and Tan, W. (2004) A rapid bioassay for single bacterial cell quantitation using bioconjugated nanoparticles. *Proceedings of the National Academy of Sciences of the United States of America*, **101**(42), 15027–32.

12 Zhao, X., Tapec-Dytioco, R. and Tan, W. (2003) Ultrasensitive DNA detection using highly fluorescent bioconjugated nanoparticles. *Journal of the American Chemical Society*, **125**(38), 11474–5.

13 Vallet-Regí, M., Balas, F. and Arcos, D. (2007) Mesoporous materials for drug delivery. *Angewandte Chemie – International Edition in English*, **46**, 7548–58.

14 Vega-Villa, K.R., Takemoto, J.K., Yáñez, J.A., Remsberg, C.M., Forrest, M.L. and Davies, N.M. (2008) Clinical toxicities of nanocarrier systems. *Advanced Drug Delivery Reviews*, **60**, 929–38.

15 Roy, I., Ohulchanskyy, T.Y., Bharali, D.J., Pudavar, H.E., Mistretta, R.A., Kaur, N. and Prasad, P.N. (2005) Optical tracking of organically modified silica nanoparticles as DNA carriers: a nonviral, nanomedicine approach for gene delivery. *Proceedings of the National Academy of Sciences of the United States of America*, **102**(2), 279–84.

16 Michaelis, K., Hoffmann, M.M., Dreis, S., Herbert, E., Alyautdin, R.N., Michaelis, M., Kreuter, J. and Langer, K. (2006) Covalent linkage of apolipoprotein e to albumin nanoparticles strongly enhances drug transport into the brain. *The Journal of Pharmacology and Experimental Therapeutics*, **317**(3), 1246–53.

17 Luo, D., Han, E., Belcheva, N. and Saltzman, W.M. (2004) A self-assembled, modular DNA delivery system mediated by silica nanoparticles. *Journal of Controlled Release*, **95**(2), 333–41.

18 Luo, D. and Saltzman, W.M. (2000) Enhancement of transfection by physical concentration of DNA at the cell surface. *Nature Biotechnology*, **18**, 893–5.

19 Luo, D. and Saltzman, W.M. (2006) Nonviral gene delivery: thinking of silica. *Gene Therapy*, **13**, 585–6.

20 Jones, A.R. and Shusta, E.V. (2007) Blood-brain barrier transport of therapeutics via receptor-mediation. *Pharmaceutical Research*, **24**(9), 1759–71.

21 Bharali, D.J., Klejbor, I., Stachowiak, E.K., Dutta, P., Roy, I., Kaur, N., Bergey, E.J., Prasad, P.N. and Stachowiak, M.K. (2005) Organically modified silica nanoparticles: a nonviral vector for in vivo gene delivery and expression in the brain. *Proceedings of the National Academy of Sciences of the United States of America*, **102**(32), 11539–44.

22 Kwon, N.H., Beaux, M.F.I., Ebert, C., Wang, L., Lassiter, B.E., Park, Y.H., McIlroy, D.N., Hovde, C.J. and Bohach, G.A. (2007) Nanowire-based delivery of *Escherichia coli* O157 shiga toxin 1 A subunit into human and bovine cells. *Nano Letters*, **7**(9), 2718–23.

23 Smith, J.E., Medley, C.D., Tang, Z., Shangguan, D., Lofton, C. and Tan, W. (2007) Aptamer-conjugated nanoparticles for the collection and detection of multiple cancer cells. *Analytical Chemistry*, **79**(8), 3075–82.

24 Ohulchanskyy, T.Y., Roy, I., Goswami, L.N., Chen, Y., Bergey, E.J., Pandey, R.K., Oseroff, A.R. and Prasad, P.N. (2007) Organically modified silica nanoparticles with covalently incorporated photosensitizer for photodynamic therapy of cancer. *Nano Letters*, **7**(9), 2835–42.

25 Kagan, V.E., Bayir, H. and Shvedova, A.A. (2005) *Nanomedicine* and nanotoxicology: two sides of the same coin. *Nanomedicine*, **1**(4), 313–16.

26 Kim, S., Ohulchanskyy, T.Y., Pudavar, H.E., Pandey, R.K. and Prasad, P.N. (2007) Organically modified silica nanoparticles co-encapsulating photosensitizing drug and aggregation-enhanced two-photon absorbing fluorescent dye aggregates for two-photon photodynamic therapy. *Journal of the American Chemical Society*, **129**(9), 2669–75.

27 Taylor, K.M.L., Kim, J.S., Rieter, W.J., An, H., Lin, W. and Lin, W. (2008) Mesoporous silica nanospheres as highly efficient MRI contrast agents. *Journal of the American Chemical Society*, **130**(7), 2154–5.

28 Zhao, X., Hilliard, L.R., Wang, K. and Tan, W. (2004) Bioconjugated silica nanoparticles for bioanalysis, in *Encyclopedia of Nanoscience And Nanotechnology* (ed. H.S. Nalwa), American Scientific Publishers, Stevenson Ranch, pp. 255–68.

29 Yao, G., Wang, L., Wu, Y., Smith, J., Xu, J., Zhao, W., Lee, E. and Tan, W. (2006) FloDots: luminescent nanoparticles. *Analytical and Bioanalytical Chemistry*, **385**, 518–24.

30 Wang, L., Wang, K., Santra, S., Zhao, X., Hilliard, L.R., Smith, J., Wu, Y. and Tan, W. (2006) Watching silica nanoparticles glow in the biological world. *Analytical Chemistry – A Pages*, **78**, 646–54.

31 Rosi, N.L. and Mirkin, C.A. (2005) Nanostructures in biodiagnostics. *Chemical Reviews*, **105**, 1547–62.

32 Gwinn, M.R. and Vallyathan, V. (2006) Nanoparticles: health effects – pros and cons. *Environmental Health Perspectives*, **114**(12), 1818–25.

33 Lewinski, N., Colvin, V. and Drezek, R. (2008) Cytotoxicity of nanoparticles. *Small*, **4**(1), 26–49.

34 Medina, C., Santos-Martinez, M.J., Radomski, A., Corrigan, O.I. and Radomski, M.W. (2007) Nanoparticles: pharmacological and toxicological significance. *British Journal of Pharmacology*, **150**(5), 552–8.

35 Nel, A., Xia, T., Mädler, L. and Li, N. (2006) Toxic potential of materials at the nanolevel. *Science*, **311**, 622–7.

36 Hess, H. and Tseng, Y. (2007) Active intracellular transport of nanoparticles: opportunity or threat? *ACS Nano*, **1**(5), 390–2.

37 Chang, J.S., Chang, K.L., Hwang, D.F. and Kong, Z.L. (2007) In vitro cytotoxicity of silica nanoparticles at high concentrations strongly depends on the metabolic activity type of the cell line. *Environmental Science & Technology*, **41**(6), 2064–8.

38 Cho, W.S., Choi, M., Han, B.S., Cho, M., Oh, J., Park, K., Kim, S.J., Kim, S.H. and Jeong, J. (2007) Inflammatory mediators induced by intratracheal instillation of ultrafine amorphous silica particles. *Toxicology Letters*, **175**(1–3), 24–33.

39 Cui, D., Tian, F., Ozkan, C.S., Wang, M. and Gao, H. (2005) Effect of single wall carbon nanotubes on human HEK293 cells. *Toxicology Letters*, **155**(1), 73–85.

40 Derfus, A.M., Chan, W.C.W. and Bhatia, S.N. (2004) Probing the cytotoxicity of semiconductor quantum dots. *Nano Letters*, **4**(1), 11–18.

41 Goodman, C.M., McCusker, C.D., Yilmaz, T. and Rotello, V.M. (2004) Toxicity of gold nanoparticles functionalized with cationic and anionic side chains. *Bioconjugate Chemistry*, **15**(4), 897–900.

42 Hoshino, A., Fujioka, K., Oku, T., Suga, M., Sasaki, Y.F., Ohta, T., Yasuhara, M., Suzuki, K. and Yamamoto, K. (2004) Physicochemical properties and cellular toxicity of nanocrystal quantum dots depend on their surface modification. *Nano Letters*, **4**(11), 2163–9.

43 Jin, Y., Kannan, S., Wu, M. and Zhao, J.X. (2007) Toxicity of luminescent silica nanoparticles to living cells. *Chemical Research in Toxicology*, **20**(8), 1126–33.

44 Johnston, C.J., Driscoll, K.E., Finkelstein, J.N., Baggs, R., O'Reilly, M.A., Carter, J., Gelein, R. and Oberdörster, G. (2000) Pulmonary chemokine and mutagenic responses in rats after subchronic inhalation of amorphous and crystalline silica. *Toxicological Science*, **56**(2), 405–13.

45 Kaewamatawong, T., Kawamura, N., Okajima, M., Sawada, M., Morita, T. and Shimada, A. (2005) Acute pulmonary toxicity caused by exposure to colloidal silica: particle size dependent pathological changes in mice. *Toxicologic Pathology*, **33**(7), 743–9.

46 Kaewamatawong, T., Shimada, A., Okajima, M., Inoue, H., Morita, T., Inoue, K. and Takano, H. (2006) Acute and subacute pulmonary toxicity of low dose of ultrafine colloidal silica particles in mice after intratracheal instillation. *Toxicologic Pathology*, **34**(7), 958–65.

47 Kirchner, C., Liedl, T., Kudera, S., Pellegrino, T., Javier, A.M., Gaub, H.E., Stoelzle, S., Fertig, N. and Parak, W.J. (2005) Cytotoxicity of colloidal CdSe and CdSe/ZnS nanoparticles. *Nano Letters*, **5**(2), 331–8.

48 Lin, W., Huang, Y.W., Zhou, X.D. and Ma, Y. (2006) In vitro toxicity of silica nanoparticles in human lung cancer cells. *Toxicology and Applied Pharmacology*, **217**(3), 252–9.

49 Lovric, J., Bazzi, H.S., Cuie, Y., Fortin, G.R.A., Winnik, F.M. and Maysinger, D. (2005) Differences in subcellular distribution and toxicity of green and red emitting CdTe quantum dots. *Journal of Molecular Medicine*, **83**(5), 377–85.

50 Shiohara, A., Hoshino, A., Hanaki, K., Suzuki, K. and Yamamoto, K. (2004) On the cytotoxicity caused by quantum dots. *Microbiology and Immunology*, **48**(9), 669–75.

51 Oberdörster, G., Oberdörster, E. and Oberdörster, J. (2005) Nanotoxicology: an emerging discipline evolving from studies of ultrafine particles. *Environmental Health Perspectives*, **113**(7), 823–39.

52 Fujiwara, K., Suematsu, H., Kiyomiya, E., Aoki, M., Sato, M. and Moritoki, N. (2008) Size-dependent toxicity of silica nano-particles to *Chlorella kessleri*. *Journal of Environmental Science and Health. Part A, Toxic/Hazardous Substances & Environmental Engineering*, **43**(10), 1167–73.

53 Borm, P.J.A., Schins, R.P.F. and Albrecht, C. (2004) Mini review: inhaled particles and lung cancer, Part B: paradigms and risk assessment. *International Journal of Cancer*, **110**, 3–14.

54 Knaapen, A.M., Borm, P.J.A., Albrecht, C. and Schins, R.P.F. (2004) Mini review: inhaled particles and lung cancer. Part A: mechanisms. *International Journal of Cancer*, **109**, 799–809.

55 He, X.X., Wang, K., Tan, W., Liu, B., Lin, X., He, C., Li, D., Huang, S. and Li, J. (2003) Bioconjugated nanoparticles for

DNA protection from cleavage. *Journal of the American Chemical Society*, **125**, 7168–9.

56 Ow, H., Larson, D., Srivastava, M., Baird, B., Webb, W. and Wiesner, U. (2005) Bright and stable core-shell fluorescent silica nanoparticles. *Nano Letters*, **5**, 113–17.

57 Zhang, T., Stilwell, J.L., Gerion, D., Ding, L., Elboudwarej, O., Cooke, P.A., Gray, J.W., Alivisatos, A.P. and Chen, F.F. (2006) Cellular effect of high doses of silica-coated quantum dot profiled with high throughput gene expression analysis and high content cellomics measurements. *Nano Letters*, **6**(4), 800–8.

58 Chang, C. and Fogler, H. (1997) Controlled formation of silica particles from tetraethyl orthosilicate in nonionic water-in-oil microemulsions. *Langmuir*, **13**, 3295–307.

59 Stöber, W. and Fink, A. (1968) Controlled growth of monodisperse silica spheres in the micron size range. *Journal of Colloid and Interface Science*, **26**, 62–9.

60 Arriagada, F. and Osseo-Asare, K. (1999) Controlled hydrolysis of tetraethoxysilane in a nonionic water-in-oil microemulsion: a statistical model of silica nucleation. *Colloids and Surfaces*, **154**, 311–26.

61 Di Pasqua, A.J., Sharma, K.K., Shi, Y.L., Toms, B.B., Ouellette, W., Dabrowiak, J.C. and Asefa, T. (2008) Cytotoxicity of mesoporous silica nanomaterials. *Journal of Inorganic Biochemistry*, **102**(7), 1416–23.

62 Li, D., He, X., Wang, K. and He, C. (2002) Detecting on toxicity of series silica shell inorganic nanoparticles to cells. *Hunan Daxue Xuebao, Ziran Kexueban*, **29**(6), 1–6.

63 Zhao, X., Bagwe, R.P. and Tan, W. (2004) Development of organic-dye-doped silica nanoparticles in a reverse microemulsion. *Advanced Materials*, **16**(2), 173–6.

64 Montalti, M., Prodi, L., Zaccheroni, N., Zattoni, A., Reschiglian, P. and Falini, G. (2004) Energy transfer in fluorescent silica nanoparticles. *Langmuir*, **20**, 2989–91.

65 Wang, L., Estévez, M.C., O'Donoghue, M. and Tan, W. (2008) Fluorophore-free luminescent organosilica nanoparticles. *Langmuir*, **24**, 1635–9.

66 Chen, M. and von Mikecz, A. (2005) Formation of nucleoplasmic protein aggregates impairs nuclear function in response to SiO_2 nanoparticles. *Experimental Cell Research*, **305**(1), 51–62.

67 Finnie, K.S., Bartlett, J.R., Barbé, C.J. and Kong, L. (2007) Formation of silica nanoparticles in microemulsions. *Langmuir*, **23**(6), 3017–24.

68 Brown, S.C., Kamal, M., Nasreen, N., Baumuratov, A., Sharma, P., Antony, V. and Moudgil, B.M. (2007) Influence of shape, adhesion and simulated lung mechanics on amorphous silica nanoparticle toxicity. *Advanced Powder Technology*, **18**(1), 69–79.

69 Roiter, Y., Ornatska, M., Rammohan, A.R., Balakrishnan, J., Heine, D.R. and Minko, S. (2008) Interaction of nanoparticles with lipid membrane. *Nano Letters*, **8**(3), 941–4.

70 Wang, L. and Tan, W. (2006) Multicolor FRET silica nanoparticles by single wavelength excitation. *Nano Letters*, **6**, 84–8.

71 Bagwe, R.P., Yang, C., Hilliard, L.R. and Tan, W. (2004) Optimization of dye-doped silica nanoparticles prepared using a reverse microemulsion method. *Langmuir*, **20**, 8336–42.

72 Lundqvist, M., Sethson, I. and Jonsson, B.H. (2004) Protein adsorption onto silica nanoparticles: conformational changes depend on the particles' curvature and the protein stability. *Langmuir*, **20**(24), 10639–47.

73 Rampazzo, E., Bonacchi, S., Montalti, M., Prodi, L. and Zaccheroni, N. (2007) Self-organizing core-shell nanostructures: spontaneous accumulation of dye in the core of doped silica nanoparticles. *Journal of the American Chemical Society*, **129**(46), 14251–6.

74 Vertegel, A.A., Siegel, R.W. and Dordick, J.S. (2004) Silica nanoparticle size influences the structure and enzymatic activity of adsorbed lysozyme. *Langmuir*, **20**(16), 6800–7.

75 Montalti, M., Prodi, L., Zaccheroni, N., Battistini, G., Marcuz, S., Mancin, F., Rampazzo, E. and Tonellato, U. (2006) Size effect on the fluorescence properties of dansyl-doped silica nanoparticles. *Langmuir*, **22**, 5877–81.

76 Green, D.L., Lin, J.S., Lam, Y.F., Hu, M.Z., Schaefer, D.W. and Harris, M.T. (2003) Size, volume fraction, and nucleation of Stöber silica nanoparticles. *Journal of Colloid and Interface Science*, **266**, 346–58.

77 Nozawa, K., Gailhanou, H., Raison, L., Panizza, P., Ushiki, H., Sellier, E., Delville, J.P. and Delville, M.H. (2005) Smart control of monodisperse Stöber silica particles: effect of reactant addition rate on growth process. *Langmuir*, **21**, 1516–23.

78 Bagwe, R.P., Hilliard, L.R. and Tan, W. (2006) Surface modification of silica nanoparticles to reduce aggregation and nonspecific binding. *Langmuir*, **22**, 4357–62.

79 Nakamura, M., Shono, M. and Ishimura, K. (2007) Synthesis, characterization, and biological applications of multifluorescent silica nanoparticles. *Analytical Chemistry*, **79**, 6507–14.

80 Shang, W., Nuffer, J.H., Dordick, J.S. and Siegel, R.W. (2007) Unfolding of ribonuclease A on silica nanoparticle surfaces. *Nano Letters*, **7**(7), 1991–5.

81 Orr, G., Panther, D.J., Phillips, J.L., Tarasevich, B.J., Dohnalkova, A., Hu, D., Teeguarden, J.G. and Pounds, J.G. (2007) Submicrometer and nanoscale inorganic particles exploit the actin machinery to be propelled along microvilli-like structures into alveolar cells. *ACS Nano*, **1**(5), 463–75.

82 Jin, Y., Lohstreter, S., Pierce, D.T., Parisien, J., Wu, M., Hall, C.III, and Zhao, J.X. (2008) Silica nanoparticles with continuously tunable sizes: synthesis and size effects on cellular contrast imaging. *Chemistry of Materials*, **20**(13), 4411–19.

83 Baroli, B., Ennas, M.G., Loffredo, F., Isola, M., Pinna, R. and López-Quintela, M.A. (2007) Penetration of metallic nanoparticles in human full-thickness skin. *The Journal of Investigative Dermatology*, **127**(7), 1701–12.

84 Hagens, W.I., Oomen, A.G., de Jong, W.H., Cassee, F.R. and Sips, A.J. (2007) What do we (need to) know about the kinetic properties of nanoparticles in the body? *Regulatory Toxicology and Pharmacology*, **49**(3), 217–29.

85 International Commission on Radiological Protection (1994) *Annals of the ICRP*, **24**, 1–300.

86 Oberdörster, G., Sharp, Z., Atudorei, V., Elder, A., Gelein, R., Kreyling, W. and Cox, C. (2004) Translocation of inhaled ultrafine particles to the brain. *Inhalation Toxicology*, **16**(6–7), 437–45.

87 Rejman, J., Oberle, V., Zuhorn, I.S. and Hoekstra, D. (2004) Size-dependent internalization of particles via the pathways of clathrin- and caveolae-mediated endocytosis. *The Biochemical Journal*, **377**, 159–69.

88 Raynal, I., Prigent, P., Peyramaure, S., Najid, A., Rebuzzi, C. and Corot, C. (2004) Macrophage endocytosis of superparamagnetic iron oxide nanoparticles: mechanisms and comparison of ferumoxides and ferumoxtran-10. *Investigative Radiology*, **39**(1), 56–63.

89 Mossman, B.T. and Churg, A. (1998) Mechanisms in the pathogenesis of asbestosis and silicosis. *American Journal of Respiratory and Critical Care medicine*, **157**, 1666–80.

90 Akerman, M.E., Chan, W.C., Laakkonen, P., Bhatia, S.N. and Ruoslahti, E. (2002) Nanocrystal targeting in vivo. *Proceedings of the National Academy of Sciences of the United States of America*, **99**(20), 12617–21.

91 Kreuter, J. (2001) Nanoparticulate systems for brain delivery of drugs. *Advanced Drug Delivery Reviews*, **47**(1), 65–81.

92 Kreuter, J., Shamenkov, D., Petrov, V., Ramge, P., Cychutek, K., Koch-Brandt, C. and Alyautdin, R. (2002) Apolipoprotein-mediated transport of nanoparticle-bound drugs across the blood-brain barrier. *Journal of Drug Targeting*, **10**(4), 317–25.

93 Nel, A. (2005) Atmosphere. Air pollution-related illness: effects of particles. *Science*, **308**, 804–6.

94 Jani, P., Halbert, G.W., Langridge, J. and Florence, A.T. (1990) Nanoparticle uptake by the rat gastrointestinal mucosa: quantitation and particle size dependency. *The Journal of Pharmacy and Pharmacology*, **42**(12), 821–6.

95 Tinkle, S.S., Antonini, J.M., Rich, B.A., Roberts, J.R., Salmen, R., DePree, K. and Adkins, E.J. (2003) Skin as a route of exposure and sensitization in chronic Beryllium disease. *Environmental Health Perspectives*, **111**(9), 1202–8.

96 Lee, H.A., Imran, M., Monteiro-Riviere, N.A., Colvin, V.L., Yu, W.W. and Riviere, J.E. (2007) Biodistribution of quantum dot nanoparticles in perfused skin: evidence of coating dependency and periodicity in arterial extraction. *Nano Letters*, **7**(9), 2865–70.

97 Rouse, J.G., Yang, J., Ryman-Rasmussen, J.P., Barron, A.R. and Monteiro-Riviere, N.A. (2007) Effects of mechanical flexion on the penetration of fullerene amino acid-derivatized peptide nanoparticles through skin. *Nano Letters*, **7**(1), 155–60.

98 Ryman-Rasmussen, J.P., Riviere, J.E. and Monteiro-Riviere, N.A. (2006) Penetration of intact skin by quantum dots with diverse physicochemical properties. *Toxicological Sciences*, **91**(1), 159–65.

99 Ryman-Rasmussen, J.P., Riviere, J.E. and Monteiro-Riviere, N.A. (2007) Variables influencing interactions of untargeted quantum dot nanoparticles with skin cells and identification of biochemical modulators. *Nano Letters*, **7**(5), 1344–8.

100 Sayes, C.M., Reed, K.L. and Warheit, D.B. (2007) Assessing toxicity of fine and nanoparticles: comparing in vitro measurements to in vivo pulmonary toxicity profiles. *Toxicological Sciences*, **97**(1), 163–80.

101 Li, N., Sioutas, C., Cho, A., Schmitz, D., Misra, C., Sempf, J., Wang, M., Oberley, T., Froines, J. and Nel, A. (2003) Ultrafine particulate pollutants induce oxidative stress and mitochondrial damage. *Environmental Health Perspectives*, **111**(4), 455–60.

102 Asuri, P., Bale, S.S., Karajanagi, S.S. and Kane, R.S. (2006) The protein-nanomaterial interface. *Current Opinion in Biotechnology*, **17**(6), 562–8.

Keywords

silica nanomaterials; toxicity; exposure route; morphology of silica nanomaterials; protein denaturation; reactive oxygen species

8
Zirconia Nanomaterials: Synthesis and Biomedical Application

Georg Garnweitner

8.1
Introduction

Today, zirconia nanomaterials are attracting great interest for applications in the fields of catalysis and sensing [1–8], as filler materials in organic–inorganic nanocomposites with enhanced mechanical or optical properties [9–13], and as solid electrolytes [14]. Their development and application in the biomedical field, however, has not yet received much attention, this being in stark contrast to other metal oxides such as magnetite or silica. The reasons for this surely include the greater difficulty of synthesis and manipulation of zirconia nanostructures with defined and highly controlled properties, and the fact that, as a hard nonmagnetic ceramic material, zirconia is not *a priori* suited for tasks such as drug delivery or diagnostic imaging that currently represent the backbone of the – arbitrarily defined – new area of 'nanomedicine' [15, 16]. Although zirconia-based materials are usually not considered for such applications [17, 18], this does not imply that they are *not* highly suited for use in the biomedical field. On the contrary, they possess great potential due to their outstanding material properties in terms of mechanical behavior, especially their high tensile strength and toughness, good corrosion and abrasion resistance [19] and superplasticity [20], as well as their nontoxicity [21] and oncological safety [22, 23].

The relatively low profile that zirconia nanomaterials have found stems from the fact that very diverse research areas, from ceramic engineering to biochemistry, are currently involved in the development of nanostructured or nanoengineered zirconia biomaterials. However, as yet no strong impetus of any one combined research goal has emerged that would create a multidisciplinary, but unified and more interactive, research community – as has been the case for example in the field of magnetic nanomaterials for diagnostic imaging. Until now, no single specialized review article dedicated to zirconia-based nanostructured materials has been prepared. Hence, the aim of this chapter is to fill that gap and to report on the development of zirconia-based nanomaterials from a totally new perspective of applications in the life sciences, attempting to combine the so-far

Nanomaterials for the Life Sciences Vol. 2: Nanostructured Oxides. Edited by Challa S. S. R. Kumar

ISBN: 978-3-527-32152-0

diverse approaches pursued by scientists with diverse backgrounds. Ultimately, this chapter may even provide a 'bridge' by helping to define research goals and leading to a more focused research on this area.

The chapter incorporates a comprehensive overview of the synthesis and use of zirconia nanomaterials in the life sciences today. First, an overview is provided of the synthetic schemes for nanoparticles and anisotropic nanostructures, with the most frequently used strategies being discussed, together with examples. In general, the syntheses are described with no specific application in mind; rather, the discussion will center on synthetic approaches for nanomaterials used in biomedical applications, or which may be further processed to materials capable of use in the life sciences.

Details will then be presented of the current applications of nanostructured zirconia, not only in the life sciences but also of biolabeling and biosensing that might lead to future biomedical applications. Today, whilst the zirconia-based and -reinforced ceramics that are used widely as bioceramic implants involve the use of nanopowders to produce materials with optimum mechanical stability and biocompatibility, further processing mainly uses conventional ceramic methods. As yet, the use of nanoengineered materials, with the control of structure at the nanoscale, or the production of individual zirconia nanocrystals, have shown promise at the laboratory scale but must still be proven for biotechnological and *in vivo* use. Examples are provided for both fields, with recent developments in bioceramics indicating the current uses and benefits of nanostructured and nanocomposite materials, and introducing conceptual approaches and initial reports on novel applications for zirconia nanomaterials, notably in diagnostics, biosensing and bioelectronics.

Finally, a concise summary is provided of the synthetic strategies towards zirconia nanoparticles and their applications in the life sciences, as well as an outlook of anticipated future trends in this area. Despite their unobtrusive – almost hesitant – introduction into the biomedical field, these materials can expect a bright future, most likely leading to completely novel applications. There are, however, many challenges to face and risks to overcome!

8.2 Synthesis of Zirconia Nanomaterials

8.2.1 Historical Overview

Among the earliest driving forces of research into nanocrystalline materials was the observation of their lower sintering temperature compared to coarsely grained powders [24–26]. In view of the importance of zirconia ceramics, it is no surprise that research into ZrO_2 nanomaterials began in the area of ceramics research, the main incentive being to prepare ceramic bodies with high density and fine microstructure that possessed advantageous properties [27, 28]. Much of this early inter-

est was triggered by the fact that zirconia appears in several polymorphs, namely in monoclinic, cubic and tetragonal modifications. Whilst, the monoclinic form is normally stable at temperatures up to 1170 °C, Ruff and Ebert demonstrated in 1929 that the cubic phase of zirconia could be stabilized at room temperature by doping with certain metal oxides [29]. A few years later, it was also noted that, whilst normally being stable only above 1000 °C, the tetragonal polymorph of zirconia was metastable at room temperature for 'extremely fine-grained' powders [30]. During the next few decades these ultrafine zirconia particles (often <10 nm in size) were prepared by the thermal decomposition of suitable precursors, especially zirconium salts such as hydrous $ZrOCl_2$ [30, 31], $ZrO(NO_3)_2$ [32, 33] or alkoxides [34], or by their precipitation from aqueous salts followed by calcination [32, 35]. In 1983, Tani, Yoshimuri and Somiya described the hydrothermal synthesis of zirconia nanoparticles under high pressure (100 MPa), and this resulted in highly crystalline nanoparticles [36]. This report attracted a great deal of attention because the crystalline ZrO_2 powders in the tetragonal modification were obtained at temperatures as low as 200 °C. The influence of alkaline metal salts on mineralization was also investigated, and resulted in a high control over the polymorph and particle size; in fact, the particle size could be tuned within a range of 16 to 30 nm by varying the reaction temperature [36].

Four years later, Komarneni and coworkers reported the use of zirconia nanoparticles of approximately 10 nm diameter as seeds for the sol–gel-based preparation of zircon [37]. The hydrothermal treatment of zirconyl oxynitrate and zirconium oxychloride thereby enabled these authors to prepare stable sols of crystalline zirconia nanoparticles of 70 nm and 10 nm in size, respectively. Some transmission electron microscopy (TEM) images of the nanoparticles obtained are shown in Figure 8.1.

During the two decades that have passed since the above-described studies were conducted, the synthesis of nanomaterials has attracted enormous attention, and the synthesis of nanostructured zirconia has become a focus of research. Whereas, during the early days research into nanoscale particles was carried out mainly by those active in the field of ceramics, today the major investigations into nanostruc-

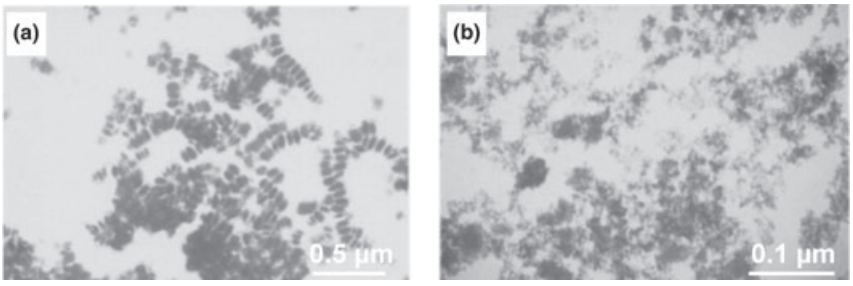

Figure 8.1 Zirconia nanoparticles prepared via a hydrothermal method. (a) Monoclinic ZrO_2 of 70 nm diameter; (b) cubic ZrO_2 of 10 nm particle size [37]. (Reproduced from Ref. [37], with kind permission of Springer Science + Business Media).

tured materials are conducted by materials chemists, physicists and, to an increasing extent, also engineers. Especially during the past decade, research into zirconia nanomaterials has led to the publication of numerous reports, often strongly focused on specific aspects of the synthesis or processing. Thus, whilst the aim of this chapter is to place the individual research strategies into a more general context, the extremely large number of reports means that only a selection of articles describing the various strategies and methods can be discussed. It is also important to focus on approaches that lead to nanostructured materials in their stabilized or isolated form, or to composites that are suitable for biomedical applications. For a more complete overview, the reader is referred to a growing number of books describing nanomaterials syntheses [38, 39], to an encompassing general review on metal oxide nanomaterials by Cushing *et al.* [40], and to other reviews of selected areas, notably those of Omata [14] (an overview of zirconia-based nanomaterials suitable as solid electrolytes) and Di Monte and Kašpar [41] (which focuses on CeO_2-ZrO_2 composites).

Today, both chemical and physical synthesis routes to zirconia are employed. Most chemical methods are performed in solvents at rather moderate temperatures, and offer advantages such as the possibility of utilizing organic surface modifiers in the synthesis mixture that can act to stabilize the formed particles against agglomeration. However, for highly covalent metal oxides such as zirconia, many of these methods do not result in crystalline materials, and therefore must be succeeded by a calcination treatment. Unfortunately, this poses several disadvantages, including decomposition of the organic modifiers and uncontrolled grain growth. Both drawbacks render these methods unattractive for advanced biomedical applications, where specific surface functionality with organic ligands is required to ensure stability and biocompatibility. Gas-phase chemical methods are capable of high throughputs, and result in materials of high crystallinity. However, their often rather rigid conditions, involving low pressures or high temperatures, as well as the strong tendency of the obtained products to agglomerate, severely hamper their potential in the production of biocompatible nanomaterials. In addition, most physical methods are often capable of only low production rates, and normally operate under nonstandard conditions, which renders them rather unsuitable for large-scale production. As the distinction between chemical and physical synthesis methods is sometimes ambiguous, we will in the following sections attempt to classify the synthesis routes to zirconia nanostructures as solvent-based and gas-phase strategies. We will also briefly discuss the 'top-down' approaches to nanoscale zirconia powders that are, to some extent, becoming an attractive alternative to 'bottom-up' methods.

8.2.2
Solvent-Based Synthesis of Zirconia Nanoparticles

The main advantage of the chemical solution-based methods used to prepare metal oxide nanoparticles is the excellent homogeneity of the resultant particles, even when a complex metal oxide system is the target rather than a pure oxide. Espe-

cially for ceramic applications (but also in the biomedical field; see Section 8.3), the desired properties can often only be realized by doping or by the fabrication of composite materials which sometimes consist of three or more phases. Whilst most ceramic nanocomposites consist of individual grains of pure metal oxides sintered together, in doped oxides a mixing of the metals is desired on the atomic level in order to achieve optimum homogeneity. This is especially relevant for the synthesis of zirconia, where doping is usually desirable in order to achieve stabilization against phase transformation; the most common dopant used is Y_2O_3 (yttria-stabilized zirconia; YSZ). Chemical solution-based methods, in principle, ensure homogeneity of the doped materials on a molecular scale, as the individual components are dissolved and homogenized in solution [42, 43]. However, inhomogeneous materials might still be obtained if the subsequent reactions leading to the formation of solids do not proceed in a controlled manner at similar reaction rates. This constitutes a major difficulty that must be overcome in order to successfully establish versatile and reliable synthesis strategies.

8.2.2.1 Hydrothermal Synthesis Strategies

Due to the generally good crystallinity of the obtained materials, and the usually high homogeneity (even in the case of systems with a complex composition), the hydrothermal synthesis strategy is still receiving considerable attention today [44]. Both, pure and doped zirconia, as well as mixed ceria–zirconia and zirconia–alumina nanocrystals, have been prepared via the hydrothermal strategy. A variety of precursors and reaction media has been employed, and the older developments in this field are described in a review produced by Somiya and Akiba [45]. During the past few years, a number of novel approaches have been reported which employ reagents that lead to a substantially improved product quality and/or a potential for lowering the reaction temperature. For example, Zhu *et al.* described the synthesis of zirconia nanocrystals of 5 nm in size by the treatment of zirconium salts in aqueous hydrazine solutions at only 150 °C [46]. Some TEM images of the obtained nanoparticles are shown in Figure 8.2. The overview image (panel a) illustrates some weak agglomeration of the nanoparticles, whereas in the high-resolution image (panel b) the lattice fringes of the individual zirconia crystals are clearly visible, evidencing the high crystallinity of the nanoparticles. For comparison, hydrothermal treatment was also carried out in sodium hydroxide, and the resulting particles are shown in Figure 8.2c. These are substantially larger than the particles obtained in the presence of hydrazine and, based on additional spectroscopic analysis, the authors inferred that hydrazine would act as mineralizer in the former system, interacting with the zirconium precursor salts to form clusters which transform to ZrO_2 in a controlled fashion under hydrothermal conditions [46].

A comparative study of the influence of the mineralizing agent on the product quality was performed by Su *et al.* By using conductivity measurements, these authors showed that nanopowders prepared in ammonia possessed a higher purity than when other mineralizers such as urea were used, and that hydrothermally prepared nanopowders exhibited less agglomeration than nanoparticles prepared

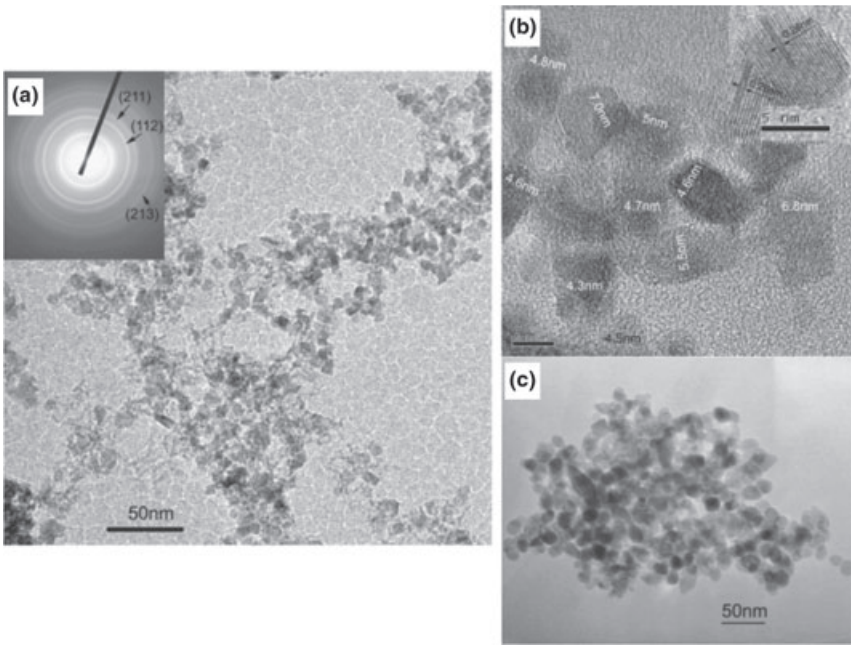

Figure 8.2 (a,c) Overview transmission electron microscopy images and (b) high-resolution micrograph of crystalline ZrO_2 nanoparticles obtained via the hydrothermal treatment of zirconium salts [46]. (Reproduced from Ref. [46], with kind permission of the American Ceramic Society).

by precipitation [47]. Zirconia-based, mixed-metal oxide and doped-zirconia nanoparticles were prepared by several research groups. For example, Walton and coworkers prepared ceria–zirconia in nanocrystalline form from $CeCl_3$ and $ZrOCl_2$ in the presence of bases, additionally using H_2O_2 as an oxidizing agent for the ceria [48]. The influence of various mineralizers on the hydrothermal synthesis of yttria-doped zirconia nanoparticles was investigated by Yueming *et al.*, and suggested certain advantages of bivalent mineralizers [49]. Hydrothermal treatment, however, is not only suitable for the direct reaction of molecular zirconia precursors to the oxide; it has also been shown to be effective in the conversion of amorphous zirconia gels to crystalline nanoparticles [50, 51]. Qin and Song thereby studied the influence of various alcohol additives on the zirconia product, and showed that the addition of monohydric and dihydric alcohols (e.g. *n*-propanol and glycol) resulted in formation of the monoclinic ZrO_2 polymorph, whereas polyhydric alcohols (e.g. trimethylolpropane) led to pure-phase tetragonal zirconia [50]. Some interesting variations of the hydrothermal synthesis have also been applied, such as the sonochemically assisted hydrothermal synthesis reported by Meskin *et al.* [52], and the microwave-assisted hydrothermal technique described by Bondioli *et al.* [53]. The latter method was shown to allow the rapid synthesis of nanoparticles of praseodymium-doped ZrO_2 with narrow size distributions; a representative

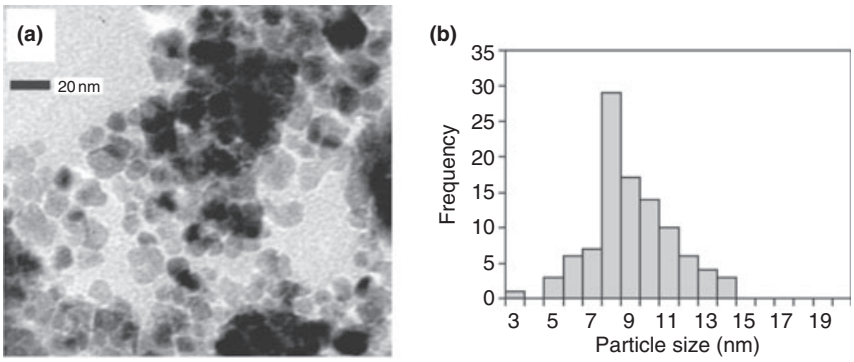

Figure 8.3 Synthesis of zirconia nanoparticles by sonochemically assisted hydrothermal synthesis. (a) TEM image of the obtained particles; (b) Size evaluation of the particles [53]. (Reproduced from Ref. [53], with kind permission of the American Ceramic Society).

TEM image and its evaluation are shown in Figure 8.3. The respective metal salts were simply dissolved and the neutralized solution subjected to the hydrothermal treatment for 2 h using a microwave digestion system [53]. Another variant of the hydrothermal synthesis, which has been considered a 'green-chemistry' strategy, is the so-called supercritical water method, as proposed by Sue *et al.* [54]. Here, the synthesis is carried out in a flow-through reactor under higher temperatures and pressures than are usually employed in hydrothermal synthesis (400 °C, pressures of 25–40 MPa), leading directly to crystalline oxide nanoparticles of several metals, including zirconium.

As an alternative to water, alcohols may also be used as solvents, notably ethanol and isopropanol. This solvothermal treatment was proposed to result in less-agglomerated nanoparticles [55]. Mixtures of water and organic solvents have also been employed, and it was observed that, by varying the nature of the organic solvents, the particle morphology would be strongly influenced [56], as would the stability of the particles against agglomeration [57]. Whilst all of these studies employed soluble zirconium salts, which can only be subjected to solvothermal treatment at low concentrations due to problems of corrosion and aggregation, a commercially more promising method was recently presented that utilizes metal hydroxides as precursors [58]. Whereas, the hydrothermal treatment of zirconium hydroxide normally results in amorphous, agglomerated powders, its solvothermal treatment would be capable of a high-yield production of crystalline ZrO_2 nanoparticles (10–40 g powder per 100 ml reactant mixture), although the addition of NaOH would be required as a mineralizer [58].

8.2.2.2 **Precipitation Techniques**

The quickest – and most straightforward – strategy for the preparation of inorganic materials is the precipitation technique, although in the case of metal oxides this often results in amorphous materials that require extensive calcination treatment.

In order to prepare ZrO_2, zirconium oxychloride ($ZrOCl_2$) is normally used as the precursor, with its aqueous solution being added to an ammonia solution for precipitation. Following the addition of other metal salts to the precursor solution, doped or composite materials can be achieved via coprecipitation. However, the precipitates obtained must first be washed extensively to remove unwanted impurities (notably chloride), dried, and finally calcined to obtain crystalline particles. By varying the calcination temperature it is possible to tune the particle size to a great extent [59]. Due to its simplicity, the precipitation method is still widely used. Additionally, by varying the precipitation agent and the processing conditions, improved product properties can be achieved. For example, YSZ nanoparticles with a crystallite size of 7 nm were obtained in a highly dispersed state after precipitation with urea and heat treatment at moderate temperatures of 500 °C [60]. Otherwise, the addition of cetyltrimethylammonium bromide (CTAB) as surfactant allowed the synthesis of zirconia nanoparticles with a narrow size dispersion from zirconium nitrate [61]. As an alternative to calcination, a hydrothermal processing of the obtained precipitates can also be carried out to obtain crystalline nanoparticles. Shevchenko *et al.*, for example, recently prepared mixed nanopowders of the ZrO_2—Y_2O_3—CeO_2 system by precipitation, starting from the respective metal nitrates, followed by hydrothermal treatment at 210 °C [62]. Whereas, after precipitation, an amorphous gel resulted, following the hydrothermal treatment a sol of nanoparticles with the cubic zirconia modification was obtained.

Microemulsions consist of nanometer-sized droplets that can be used as microreactors in which the synthesis of nanoparticles, for example by precipitation, is carried out. As the liquid–liquid interface acts as boundary where the reaction is stopped, the particle sizes and morphologies obtained are highly controlled and uniform. The microemulsion-based synthesis of zirconia nanoparticles has been investigated in very few studies [5, 63], but in all cases the nanoparticles were obtained in amorphous form and needed to be subjected to a calcination treatment. This limited the most prominent advantages of microemulsion-based synthesis, as the grain growth processes during high-temperature treatments are uncontrolled and result in random particle morphologies. Directly, crystalline zirconia nanoparticles were obtained by the liquid–solid–solution phase-transfer method described by Li and coworkers. This astonishingly general strategy allowed the synthesis of 4 nm-sized ZrO_2 nanocrystals via dehydration of the acetate at 180 °C [64], and exhibited some similarities to the nonhydrolytic sol–gel synthesis discussed below.

8.2.2.3 **The Pechini Method**

Another common strategy for the synthesis of nanoparticles is the so-called Pechini method. Originally developed during the 1960s for thin ceramic films [65], this method – which originated from the field of ceramics – is today used for the synthesis of fine particles of many metal oxides, including zirconia. Although, normally an aqueous salt solution is prepared, dilute acid starting mixtures can also be utilized; this allows the direct use of metal oxides as precursors that, prior to mixing, are dissolved in a mineral acid. The characteristic feature of this method

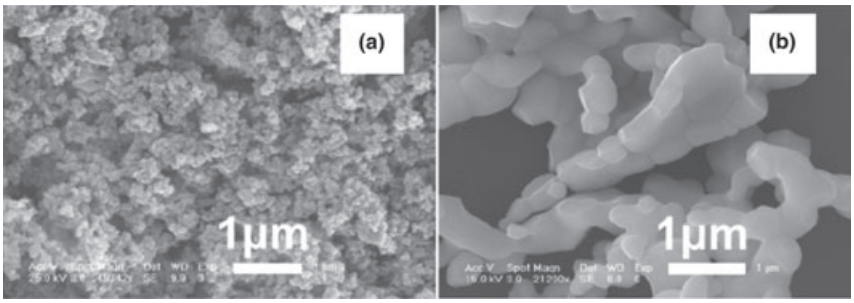

Figure 8.4 Scanning electron microscopy images illustrating the effect of calcination treatment on nanopowders. (a) Zirconia nanoparticles obtained after Pechini synthesis at 500 °C; (b) The same particles transformed into large micrograins after annealing at 1000 °C [68]. (Reproduced from Ref. [68], with kind permission of the American Chemical Society).

is the addition of an α-hydroxycarboxylic acid (often citric acid) and a multifunctional alcohol which, upon heating, undergo polyesterification leading to a viscous resin. The mixture is heated further until eventually a fine oxide powder is obtained. This strategy allows the preparation of metal oxides at significantly lower temperatures than are required for conventional solid-state reactions, and also permits the synthesis of complex multicomponent oxides with good homogeneity [66]. Thulium-doped zirconia nanocrystals were, for example, prepared by dissolving zirconium nitrate and thulia in dilute nitric acid, followed by the addition of citric acid and ethylenediaminetetraacetic acid (EDTA) and calcination [67]. In another study, Lin *et al*. prepared ZrO_2 nanocrystals of various sizes via the Pechini method, starting from zirconium oxychloride, and characterized their phase stability and photoluminescent properties [68]. Scanning electron microscopy (SEM) images of the products showed grain growth effects which occurred during calcination (Figure 8.4). The sample prepared via the Pechini strategy at 500 °C was composed of aggregated nanoparticles of approximately 80 nm in size (Figure 8.4a) whereas, after an additional annealing treatment at 1000 °C (as required in conventional solid-state synthesis) the nanoparticles were completely sintered together to form micrometer-sized grains (Figure 8.4b). In contrast to this calcined sample, the zirconia powders obtained directly after a Pechini-type synthesis exhibited strong luminescence, which the authors attributed to carbon impurities [68]. Unfortunately, this risk of carbon impurities at the single-atom level constitutes one of the main disadvantages of the Pechini method.

8.2.2.4 **Combustion Synthesis/Auto-Ignition**

Somewhat similar to the Pechini method is the combustion synthesis, or auto-ignition technique, that was presented by Kingsley and Patil in 1988 [69]. Here, metal nitrate salts are reacted with an organic fuel (usually urea, glycine or citric acid) in a strongly exothermic reaction to form the crystalline oxides at

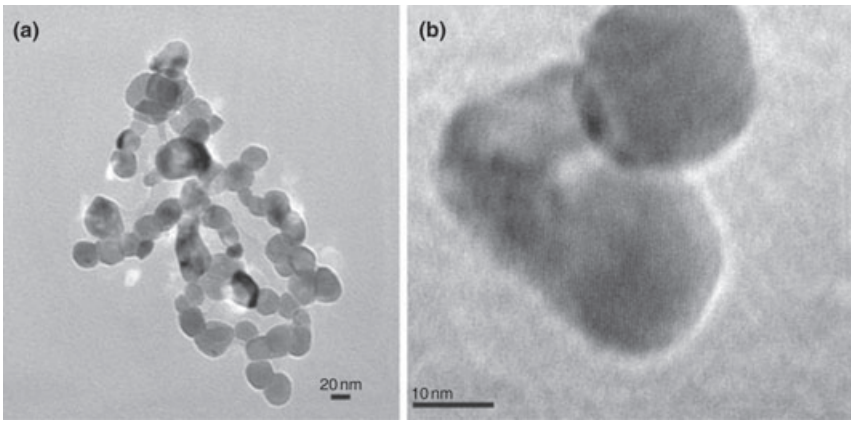

Figure 8.5 (a) Transmission electron microscopy image and (b) high-resolution image of zirconia nanoparticles prepared by combustion synthesis from zirconyl nitrate and glycine [72]. (Reproduced from Ref. [72], with kind permission of Springer Science + Business Media).

substantially lower temperatures than otherwise required. This method has been used for the synthesis of zirconia nanoparticles [70–72] as well as for composite materials, especially mixed alumina–zirconia powders [73, 74] and ceria-doped zirconia [75]. Depending on both the precursor–fuel ratio and the composition, particle sizes between 10 and 100 nm are usually obtained with this method, although an additional calcination treatment is often required to ensure high crystallinity and complete removal of any nitrate impurities. When using a glycine-to-nitrate ratio of 1.0, Das *et al.* obtained only loosely agglomerated particles with single crystalline nature (Figure 8.5) [72].

8.2.2.5 **Sol–Gel Methods**

Sol–gel methods, on the other hand, have proven their potential for the controlled synthesis of nanomaterials in numerous examples, and consequently they have been studied extensively also for the preparation of zirconia nanoparticles [76–78]. The synthesis of monodisperse ZrO_2 nanoparticles was achieved by Livage *et al.*, using acetylacetone as a capping agent to reduce the reactivity of the zirconium alkoxides [79]. However, these conventional aqueous sol–gel strategies result in amorphous zirconia nanomaterials that can only be crystallized by an additional thermal treatment [79]. Recently, an interesting study on the crystallization kinetics of yttria-stabilized zirconia nanomaterials was presented by Shih *et al.*, who showed that the crystallization of zirconia stabilized with 8 mol% of yttria, and obtained by aqueous sol–gel processing, commenced at temperatures of approximately 475 °C [80].

In order to circumvent the calcination treatment that may lead to desorption and decomposition of the organic stabilizers and uncontrolled grain growth, some more elaborate combined approaches were developed. Schmidt *et al.*, for example,

performed the sol–gel reaction of zirconium *n*-propoxide in a mixture of isobutanol, propionic acid and water. The resulting transparent sol was subjected to hydrothermal processing, which produced crystalline zirconia nanoparticles of 3–4 nm in size at 250 °C [81]. Recently, Mizuno and coworkers reported the synthesis of stabilized zirconia nanocrystals by performing a controlled sol–gel reaction in a mixed organic environment, followed by extraction and annealing at 280 °C [82]. Another strategy is the so-called aerogel processing technique, where zirconia (or YSZ) precursors are dissolved in water and the solutions transformed into gels upon the addition of propylene oxide or other epoxy monomers. After aging, washing and supercritical drying, aerogels are obtained that can easily be ground and calcined to obtain nanocrystalline powders with good homogeneity and uniform particle size and morphology [83–85].

8.2.2.6 **Nonaqueous/Nonhydrolytic Sol–Gel Technique**

One alternative to conventional sol–gel synthesis which is attracting an increasing amount of attention is the nonaqueous or nonhydrolytic sol–gel technique, which allows the simple fabrication of metal oxide nanostructures under high control and straightforward conditions [86–88]. Although these approaches have been developed from aqueous sol–gel chemistry and employ the same precursor species, water is not added to the reaction medium as a catalyst, but rather is provided via organic reactions that may follow complex mechanisms and are often catalyzed by the precursor species [89]. Strictly speaking, the term 'nonhydrolytic' may only be applied if no hydroxyl groups are present in the reaction medium; otherwise, for example when using alcohols as solvents, the term 'nonaqueous' will apply. Often, the materials obtained are highly crystalline even when employing comparably mild reaction conditions, and stabilization of the product particles against agglomeration is achieved with excellent results. Although the nonaqueous method has received much more attention in the past few years, similar methods had already been applied by Inoue and coworkers a decade earlier [90]. In this reaction, using toluene or glycols as solvents, the decomposition of zirconium alkoxides resulted in crystalline nanomaterials at 300 °C, although they were heavily agglomerated due to a lack of stabilizers. In 2003, the synthesis of highly crystalline and well-stabilized ZrO_2 nanocrystals in high yield was achieved via a nonhydrolytic approach by Hyeon's group [91]. When these authors reacted stoichiometric amounts of zirconium chloride and zirconium isopropoxide at 340 °C in high-boiling organic solvents, the result was the production of monodisperse nanoparticles (see Figure 8.6). The function of the organic reaction medium thereby is manifold: it not only serves as solvent, but is also capable of binding to the particle surface, thus acting as a stabilizer. An analogous procedure allowed the synthesis of binary $Hf_xZr_{1-x}O_2$ nanocrystals within a broad range of compositions [92]. In these approaches, trioctylphosphine oxide (TOPO) was used as the organic reaction medium and stabilizer, but zirconia nanocrystals were also prepared via similar nonhydrolytic approaches using long-chain amines [93].

Alternatively, alcohols can be used as solvents for water-free sol–gel processing and, in contrast to the media mentioned above, they are actively involved in the

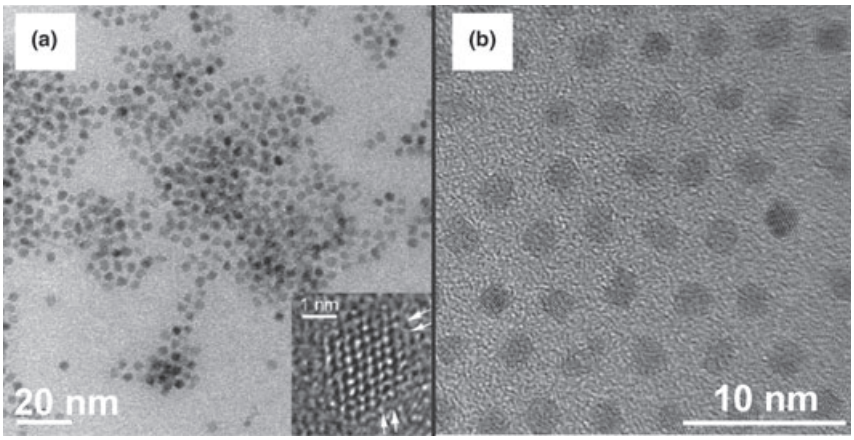

Figure 8.6 Zirconia nanoparticles obtained via the nonhydrolytic sol–gel synthesis. (a) Overview TEM image; (b) High-resolution TEM image proving the high crystallinity of the nanoparticles [91].

particle formation process. Benzyl alcohol in particular has shown great potential for the formation of a variety of metal oxides [94–97], and has also been used for the synthesis of zirconia nanoparticles [12, 98]. The use of a very simple experimental protocol, simply adding benzyl alcohol to zirconium isopropoxide, followed by thermal treatment at 200 °C, led to the production of monodisperse zirconia nanocrystals about 3 nm in size. These crystals could be stabilized such that they were totally nonagglomerated by the addition of fatty acids (the pronounced effect of this stabilization treatment is shown in Figure 8.7). As the zirconia precursors can be used in a quite concentrated fashion, these synthesis methods represent a highly promising strategy for the future large-scale production of high-quality ZrO_2 nanomaterials [12].

8.2.3
Gas-Phase Synthesis of Zirconia Nanoparticles

Gas-phase synthesis techniques used to prepare metal oxide nanoparticles are capable of high throughputs, and generally lead to well-crystallized materials of high purity. Hence, they have become the main industrial techniques for the bulk production of nanomaterials today [99]. Zirconia nanoparticles can be obtained in high throughput via the flame spray pyrolysis of alkoxide precursors, with the particle properties being tuned by the precise control of processing parameters [100, 101]. The main disadvantage of the pyrolysis route is that the particle stabilization cannot be achieved to a degree possible with solvent-based routes; consequently, some degree of agglomeration always occurs, although by optimizing the process conditions it is possible to obtain only 'soft' agglomerates [100]. Whereas in many cases, the preparation of mixed oxides via the gas-phase synthesis is dif-

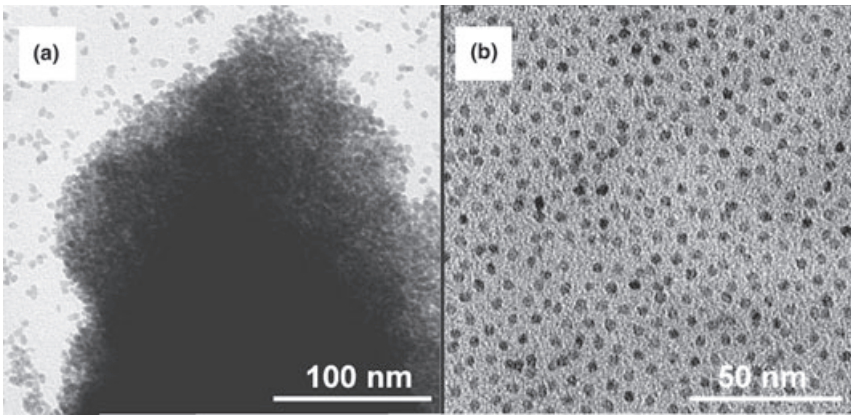

Figure 8.7 Transmission electron microscopy images of ZrO_2 nanoparticles prepared by the benzyl alcohol-based nonaqueous strategy. (a) The particles were agglomerated after the synthesis; (b) Particles were easily stabilized by the addition of fatty acids [12]. Image (a) reproduced courtesy of the author; image (b) reproduced from Ref. [12], with kind permission of Wiley-VCH).

ficult to achieve due to the short reaction times, the synthesis of yttria-doped zirconia with high homogeneity of the resulting nanoparticles can be realized by using flame-spray pyrolysis, as demonstrated by the Pratsinis group [102]. Whilst mixtures of inorganic precursors and metal organic precursors lead to poor mixing, a high degree of homogeneity was achieved by using either metal organic precursors for both metal oxides, or inorganic precursors in the solvent 2-ethylhexanoic acid. TEM images of nanoparticles of zirconia doped with 10 mol% yttria prepared from metal alkoxide precursors are shown in Figure 8.8. Whereas, a quite narrow particle size distribution could be achieved at low production rates (Figure 8.8a), rather broad distributions were obtained at higher production rates (Figure 8.8b). However, in both cases the particles exhibited soft agglomeration [102].

A better control over particle size is achieved with the inert gas condensation (IGC) method [103]. This laboratory-scale method is based on the thermal evaporation of a volatile precursor into an inert gas atmosphere, at reduced pressure. At a cold surface (usually the wall of the reaction chamber, which is cooled by liquid N_2), the substance is condensed and crystalline nanoparticles form [104]. For zirconia synthesis, zirconium monoxide is used as precursor, followed by post-deposition oxidation to the dioxide [103]. In this way, highly crystalline, defect-free ZrO_2 nanoparticles were obtained, with the particle size being tunable to some extent through the cooling rate [104]. As an alternative to conventional evaporation by Joule heating, sputtering – using metallic zirconium as the sputter source – can be carried out; this results in ZrO_2 nanoparticles of very high purity and good crystallinity, as shown by Hahn *et al.* using DC magnetron sputtering [105].

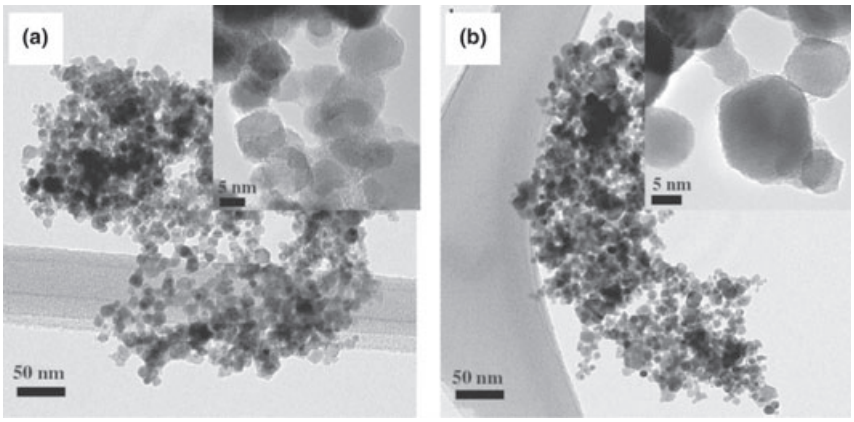

Figure 8.8 Transmission electron microscopy images of YSZ nanoparticles (containing 10 mol% yttria) by flame spray pyrolysis at (a) low and (b) high production rates [102]. Reproduced from Ref. [37]; © Institute of Physics Publishing.

8.2.4
Top-Down Methods to Zirconia Nanoparticles

Top-down strategies to metal oxide nanomaterials often offer not only complementary benefits but also disadvantages, compared to the chemical synthesis. Previously, comminution has been employed to prepare nanosized zirconia particles as precursors for high-performance ceramics, this procedure being capable of high throughput at a much lower cost than solution-based chemical routes. Often, however, the resultant nanoparticles feature a broad size distribution, random shapes and, due to the high energy input required to obtain small nanoparticles, the crystal lattice may become severely distorted, especially on the particle surface. Yet, in the case of zirconia, the necessary ball-milling treatment had no detrimental effect on the crystallinity and phase changes during subsequent ceramic processing [106]. On the contrary, such treatment can even be utilized to introduce dopants by mechanical alloying, as investigated extensively during the 1990s [107]. Kumagai *et al*. also showed that it is even possible to induce crystallization during the attrition-milling of amorphous yttria-partially stabilized zirconia composites, leading to stable tetragonal zirconia solid solutions as the particle sizes were decreased to the 10 nm region [108]. One recent trend which has evolved in the field of nanogrinding in recent years is that of 'combined grinding'; this is an ultrasonic processing method which has been reported to result in nano-ZrO_2, with high efficiency [109].

In addition to purely mechanical comminution, mechanochemical processing has been employed for the preparation of nanoscale zirconia. Here, McCormick and coworkers obtained nanoparticles of 4–6 nm by the reaction of $ZrCl_4$ with Li_2O or MgO in a vibratory mill under an argon atmosphere to afford ZrO_2 and LiCl/$MgCl_2$, which could be crystallized at moderate temperatures [110, 111].

8.2.5
Synthesis of Zirconia Nanorods and Nanowires

Metal oxide nanorods and nanotubes constitute a promising special class of nanostructured materials with high potential in the field of biotechnology [112, 113]. Reports of the synthesis of anisotropic zirconia nanocrystals so far are scarce, however, due mainly to the intrinsic properties of the zirconia polymorphs not exhibiting any significantly preferred direction of growth. Only recently have the first reports on morphological control over zirconia nanostructures in solution-based systems been published. For example, Li and coworkers performed a hydrothermal treatment of zirconyl nitrate hydrate in the presence of NaOH as mineralizer, and observed a changing morphology of the resultant monoclinic ZrO_2 nanostructures as a function of the hydrothermal treatment time (see Figure 8.9). While, after 3 h, the structure remained ill-defined (Figure 8.9a), after 24–48 h a rice grain-like structure could be seen (Figure 8.9b,c), which transformed after further treatment into a fibrous structure (Figure 8.9d) [114]. The synthesis of zirconia nanocrystals via a two-phase solvothermal reaction was reported by Ji *et al.*, who used fatty acids as surface capping agents to induce the formation of anisotropic nanostructures [115]. Also in this case, the morphology of the obtained

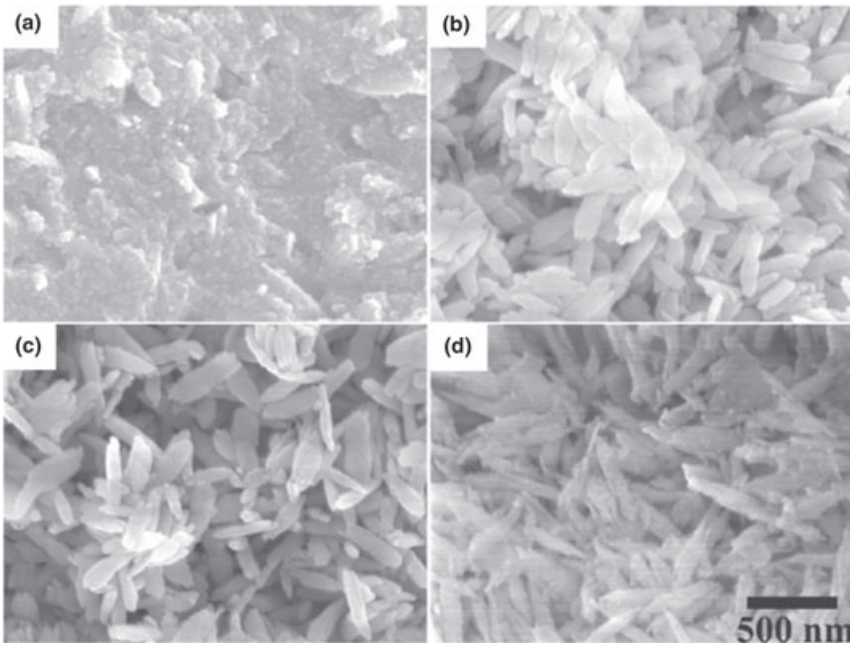

Figure 8.9 Scanning electron microscopy images of zirconia nanostructures obtained by hydrothermal treatment in presence of NaOH after 3 h (a), 24 h (b), 48 h (c) and 72 h (d) [114]. (Reproduced from Ref. [114], with kind permission of Institute of Physics Publishing).

nanocrystals changed over reaction time: whereas initially, spherical particles were observed, after 42 h mainly anisotropic crystals were observed. The authors attributed this change to the low reactivity of the zirconium(IV) *n*-propoxide precursor, which formed only a small number of nuclei that tended to anisotropic growth along one axis as the monomer concentration decreased below a critical value [115].

Template-based methods have so far been the only successful strategies to obtain zirconia nanorods or nanotubes with high aspect ratios. Hollow zirconia nanotubes were first prepared by Rao *et al.*, using carbon nanotubes as templates [116], subjected to acid treatment for the creation of acidic surface functions, and then immersed in a zirconium alkoxide. For zirconia formation, the material was calcined after the removal of excess alkoxide by washing; this had the extra benefit of concurrent removal of the carbon nanotubes [116]. Rao and coworkers also showed that organic hydrogel gelators could be used successfully as templates [117]. Similarly, Ueda and colleagues utilized carbon nanofibers as templates, although this required multiple coating with a solution of an alkoxide precursor in organic solvents to achieve stable zirconia structures after calcination. On the other hand, by using carbon nanocoil templates, even coiled structures could be prepared, as shown in Figure 8.10 [118].

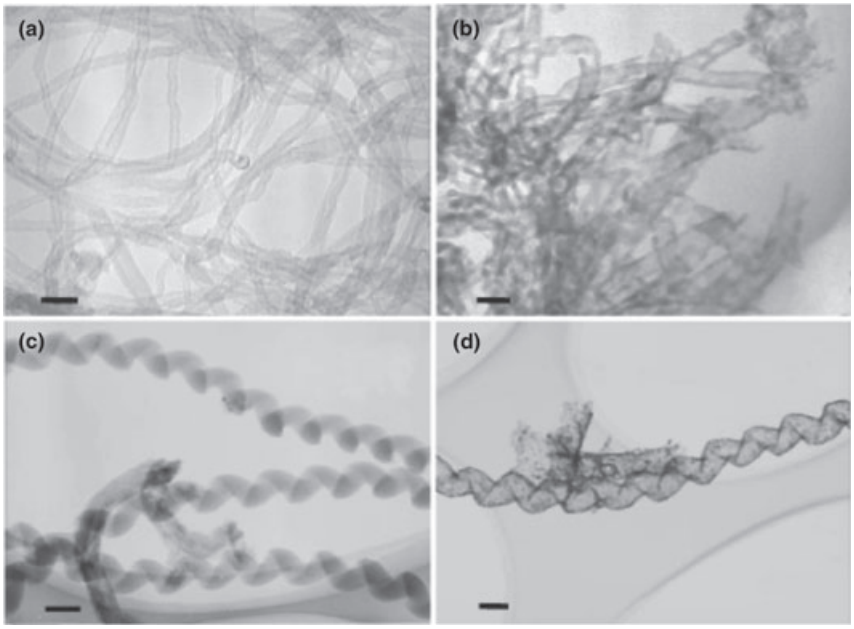

Figure 8.10 One-dimensional zirconia nanostructures (b) and (d) prepared from carbon nanofiber templates (a) and (c) after multiple coating. Scale bars: (a,b) = 30 nm; (c,d) = 200 nm. Reproduced from Ref. [118], with kind permission of the American Chemical Society.

Hollow zirconia nanotubes were also prepared by the immersion of porous alumina membranes in sols prepared from hydrous $ZrOCl_2$, and it was even possible to fill the nanowires with nickel or copper metal wires by electrodeposition [119]. Anodic aluminum oxide (AAO) was used as a template by Lee and coworkers, who were able to tune the wall thickness of the resulting ZrO_2 nanotubes by varying the precursor concentration in the immersion solution (see Figure 8.11). Whilst low precursor concentrations resulted in thin rods, at higher concentrations predominantly nanowires were obtained [120]. Li *et al.* obtained ordered arrays of ZrO_2 nanowires via a similar method [121]. Another strategy was recently presented by Cochran *et al.*, who prepared crystalline metal oxide nanotubes from fluorine-based precursors, without any need for calcination treatment [122]. Formation of the metal oxides was achieved using an interesting strategy: boric acid was added and acted as a scavenger for fluoride ions, thereby promoting hydrolysis of the precursors and resulting in the formation of crystalline metal oxides. For ZrO_2, ammonium hexafluorozirconate was used as precursor, and nanorods of 60 and 250 nm diameter consisting of 6 nm tetragonal ZrO_2 grains were obtained,

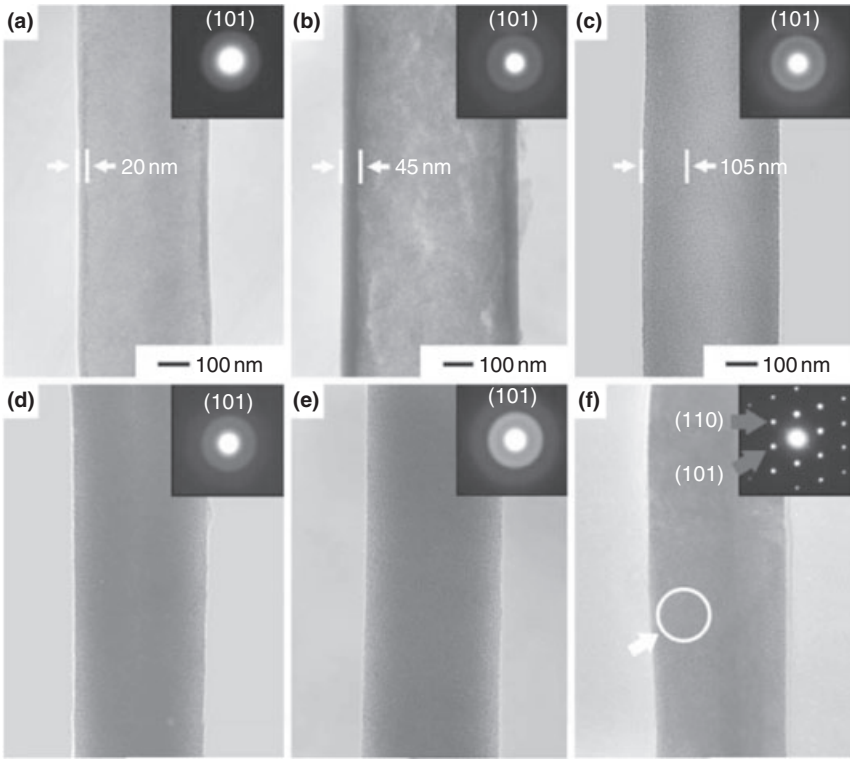

Figure 8.11 Zirconia nanotubes with tunable wall thicknesses (a–e) and nanorods (f) obtained using anodic alumina templates [120]. Reproduced from Ref. [120], with kind permission of Springer Science + Business Media.

depending on the template pore size. By sequential immersion of the template in the titania and zirconia precursor solutions, even coaxial TiO_2/ZrO_2 nanotubes could be prepared [122].

Recently, solid ZrO_2 nanorods were grown in track-etched membrane templates by Palmese and coworkers [123]. Here, a plasma treatment was performed on the template membranes (featuring various pore sizes of ca. 50–500 nm) before infiltration to ensure good affinity of the membrane pore surface to the prehydrolyzed zirconia precursor solution. After infiltration, the composite was subjected to calcination treatment at 600 °C, which resulted in the removal of the polymer membrane. The resulting zirconia nanorods (see Figure 8.12) ranged from about 50 nm to 500 nm in size, depending on the membrane pore size. Another strategy used here was the electrochemical anodization of zirconium, which can result in the formation of a layer of ZrO_2 nanorods on the metal electrode [124, 125].

Alternatively, gas-phase methods can be used for the growth of zirconia nanorods, enabling the synthesis of highly crystalline structures at comparatively low processing temperatures. In particular, the atomic layer deposition technique has been used to fabricate zirconia nanorods in porous polycarbonate templates [126, 127]. Kim *et al.* presented an interesting strategy to facilitate the preparation process (see Figure 8.13): prior to the deposition, a microcontact printing step was carried out in order to apply a hydrophobic layer of octadecyltrichlorosilane

Figure 8.12 ZrO_2 nanorods obtained from track-etched membranes [123]. (Reproduced from Ref. [123], with kind permission of the Royal Society of Chemistry).

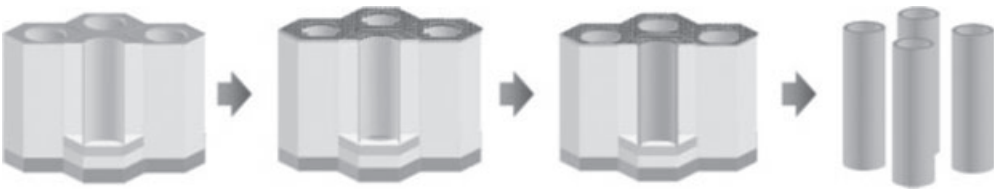

Figure 8.13 Schematic illustration of the fabrication for metal oxide nanotubes. The template is coated with a passivation layer that enables selective deposition onto the inner pore walls; after chemical etching, the free-standing nanotubes are obtained [126]. Reproduced from Ref. [126], with kind permission of Wiley-VCH.

onto the template outer surface. This resulted in a selective deposition of the metal oxide inside the pores, and directly resulted in free-standing nanotubes without any need to remove any excess material from the membrane surface [126]. In addition to polycarbonate membranes, the authors also investigated the use of AAO as a template. Whilst this has an advantage of a much higher pore density, the authors also emphasized the substantially higher difficulty in template removal. Whereas, polycarbonate is simply dissolved in organic solvents, AAO can only be removed by etching at either high or low pH. Although etching with KOH or NaOH proved effective for the selective removal of alumina in the presence of zirconia nanostructures, this led concurrently to the formation of nanowire bundles (see Figure 8.14). A solid–gas-phase reaction method was also reported to enable the synthesis of boron nitride nanotubes filled with zirconia nanorods. The formation of these composite nanotubes was achieved simply from zirconium diboride and ammonium chloride as solid-state precursors [128].

8.3
Biomedical Applications of Zirconia Nanomaterials

8.3.1
Nanostructured Zirconia-Based Bioceramics

Currently, zirconia is undergoing extensive investigation as a bioinert ceramic material for the repair and reconstruction of diseased or damaged parts of the human musculoskeletal system [129]. ZrO_2-based bioceramics are commonly used in the form of yttria-stabilized polycrystalline bodies (these are known as tetragonal zirconia polycrystals; TZP or Y-TZP), in order to make use of the transformation–toughening mechanism. This effect was first reported by Garvie *et al.*, who observed that metastable tetragonal zirconia grains finely dispersed within the matrix of cubic zirconia led to a major enhancement in toughness [130]. Here, the tensile stress in the tip of an advancing crack in the material induces a phase transformation of the tetragonal zirconia grains, which results in a stress field acting in opposition to the stress field propagating the crack; additional energy is then required to advance the crack further [131, 132]. A visualization of the transformation process, using atomic force microscopy (AFM), was recently presented by Deville and Chevalier, and is included in the illustration of the transformation-toughening effect in Figure 8.15 [133, 134]. Garvie *et al.* had already recognized that the tetragonal grains need to be less than 100 nm in size to be metastable, and therefore TZP bioceramics may be regarded as nanostructured materials. The ultrafine grain structure is, however, normally obtained via conventional techniques of colloidal processing rather than deliberate nanoengineering. Here, attention is focused on application examples where nanostructured materials are deliberately used or applied to achieve special properties and effects.

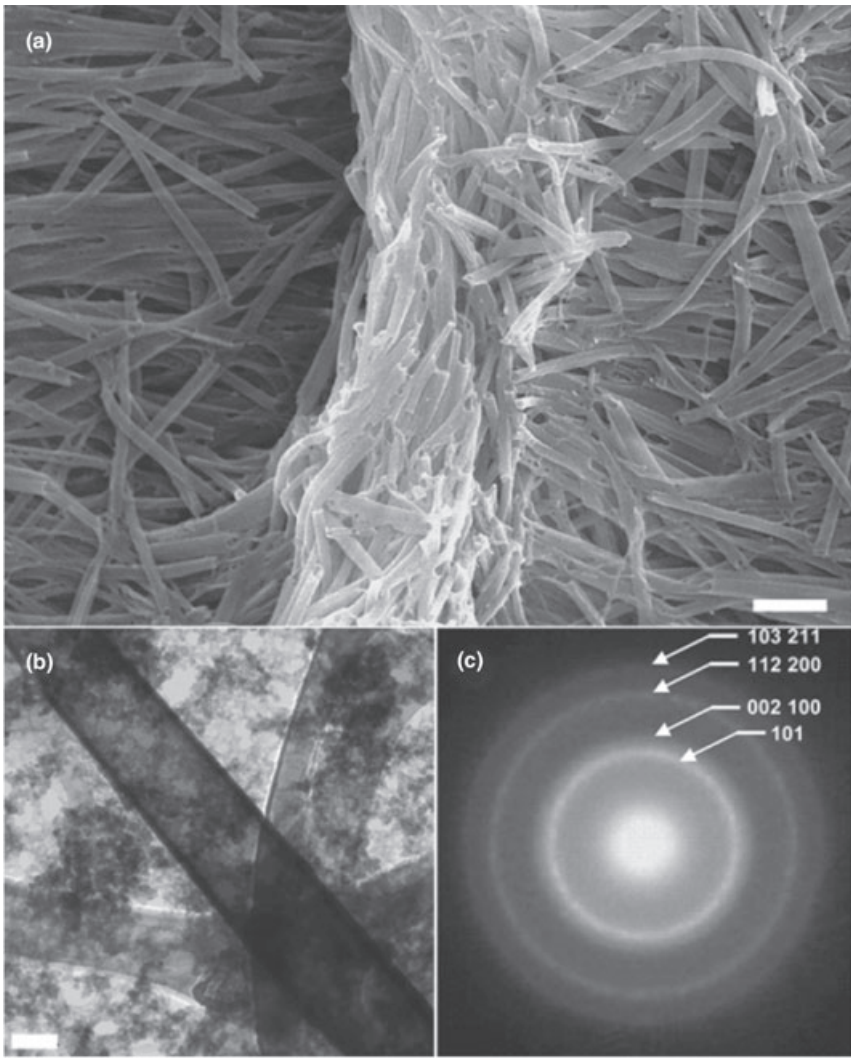

Figure 8.14 (a) Scanning electron microscopy and (b) transmission electron microscopy images of ZrO_2 nanorods obtained via atomic layer deposition within AAO membranes; (c) The electron diffraction pattern corroborates the high crystallinity of the obtained nanotubes [127]. The scale bars correspond to 1000 nm (a) and 100 nm (b), respectively. Reproduced from Ref. [127], with kind permission of the Royal Society of Chemistry.

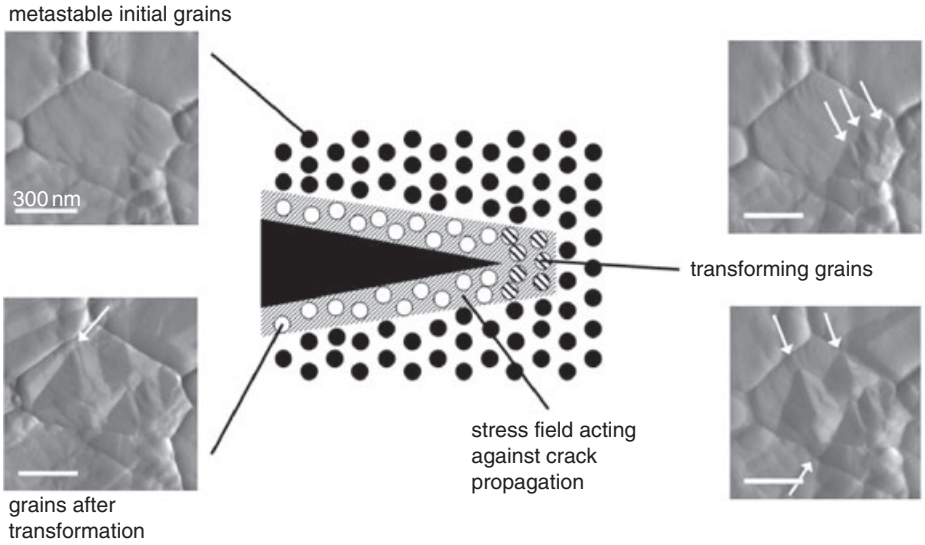

Figure 8.15 Schematic illustration of the transformation-toughening mechanism in tetragonal zirconia polycrystal (TZP) ceramics, as visualized by atomic force microscopy. (AFM images reproduced from Ref. [133] with kind permission of Wiley-Blackwell Publishing.)

8.3.1.1 Joint Replacements

In the years after Garvie's reports were published, TZP ceramics were investigated extensively and soon began to be used commercially, notably as ball heads in total hip replacements [19]. However, the very complexity of the zirconia mechanical properties that was utilized for phase toughening began to cause serious problems in 2001–2002, when a high proportion of zirconia implants failed within a short period due to aging processes [135]. It became clear that these failures were triggered by a steam sterilization procedure performed prior to surgery – a finding which had a major impact on the use of zirconia as bioceramic material [135]. Unfortunately, as no clear alternative to zirconia could be identified, the decision was taken to develop an 'aging-free zirconia' as a possible solution to the risk of failure.

Several possibilities emerged for the production of 'aging-free' zirconia polycrystalline ceramics with a longer *in vivo* lifetime. Primarily, it was suggested that ceria could be used as a stabilizer instead of yttria, as the aging phenomenon arose from yttrium oxygen vacancies that aided the nucleation of transformation by a stress corrosion-type mechanism [135]. Other solutions included the use of alumina–zirconia composites [134] or the application of an yttria coating rather than doping of the zirconia [136]. The development of alumina–zirconia composites has been promoted by major ceramic manufacturers, and thus has received the greatest attention. Although alumina is the most common material for hip

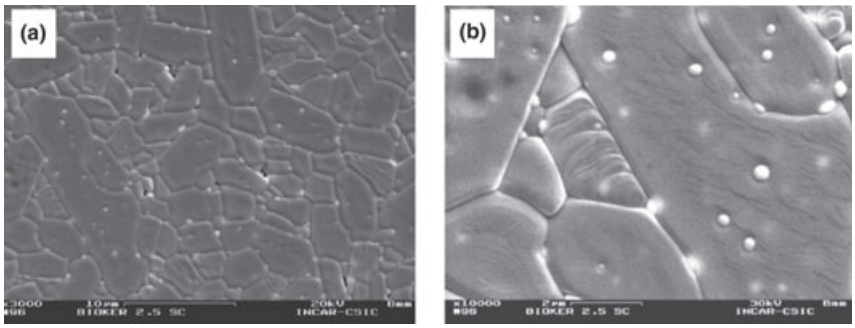

Figure 8.16 (a) Scanning electron microscopy image of the microstructure of an Al_2O_3–ZrO_2 nanocomposite. (b) A magnified view showing the nanosized ZrO_2 particles embedded within the alumina matrix [145]. (Reproduced from Ref. [145], with kind permission of the American Chemical Society).

and knee joint replacements, it exhibits only a low fracture toughness. Hence, alumina–TZP composites, known as zirconia-toughened alumina (ZTA), have been investigated with the aim of obtaining materials that exhibit both good aging behavior and high fracture toughness for orthopedic implants with an extended lifetime [134, 137, 138]. It turned out, however, that the formation of micrometer-sized phases was not effective and thus, the deliberate dispersion of nanometer-sized particles of the second phase within the matrix was investigated [139–142]. These composites have been mainly prepared through ceramic processing emanating from conventional powders for the matrix and commercial pyrogenic nanopowders [141] for the zirconia filler phase. A combined process has also been used, where a zirconium alkoxide is added to an aqueous or ethanolic suspension of Al_2O_3 particles, followed by drying and calcination steps [137, 143, 144]. Chevalier *et al.* showed that these nanocomposite ceramics, which consisted of nanosized TZP phases distributed within a microcrystalline alumina matrix (see Figure 8.16) were far less prone to degradation phenomena such as the slow crack growth that normally cause the deterioration of ceramic implants [145]. An improved lifetime was demonstrated by Affatato *et al.* in a comparative, long-term *in vitro* wear study [146].

Whilst the aforementioned strategies employ nanosized zirconia filler particles, the alumina matrix is composed of micrograins. Composites of zirconia nanoparticles within nanocrystalline alumina, however, might exhibit different – and possibly even enhanced – mechanical properties [147]. Until now, their fabrication has barely been reported due to difficulties of preserving the nanocrystalline matrix in fully consolidated ceramics. One viable strategy was presented by Bhaduri and Bhaduri, who used a combustion synthesis to prepare composites consisting of 10% ZrO_2 nanograins distributed within a nanocrystalline alumina matrix that possessed an ultra-high fracture toughness [148].

8.3.1.2 Dental Implants

Another field of application for zirconia-based ceramics is that of dental crown implants [149]. Here, the use of zirconia is highly attractive due to the high shear stresses that occur during chewing processes [150, 151], although pure zirconia ceramics are not suitable for dental implants due to their bright white color. The rapid development for applications began only after the introduction of colored zirconia ceramics a decade ago [152]. Today, a CAD/CAM (computer-aided design/manufacturing) technique is regularly applied [153], where the surface structure of the tooth stump is recorded and the crown or bridge is virtually reconstructed using CAD software [151]. In the next step, a CAM milling machine is used to carve the calculated structure either from a ceramic green body or from a predensified material. The final step comprises a high-temperature sintering to ensure mechanical stability which, however, also involves a major shrinkage of green bodies that must be compensated. Although the predensified ceramic body allows a higher geometric precision, its milling is complicated and costly due to its hardness, requiring the use of diamond tools. Therefore, it is generally preferred to use green body ceramics for the forming process, though these must show a high homogeneity to ensure good control of the shrinkage during sintering [154]. Only zirconia nanoparticles of <10 nm grain size allow the sintering of dense bodies at moderate temperatures [155], and these are therefore frequently used as starting materials. Recently, Oetzel and Clasen presented an interesting alternative to the CAD/CAM technique which involved an electrophoretic deposition (EPD), which is believed to be more cost-efficient [154]. For this, the authors first prepared an aqueous dispersion of commercial Ce-doped zirconia and alumina powders by ultrasonic dispersion, and then adjusted the pH value to achieve the desired basic conditions. Additional nanosized zirconia particles were added to enhance the green body density. EPD was then performed, as shown schematically in Figure 8.17a. The deposition of zirconia and alumina particles onto the mold, for which a cast of the dental stump is used, followed by calcination treatment, resulted in ceramic cups (Figure 8.17b) of transformation-toughened zirconia. The particle size distribution of the powders used is shown in Figure 8.17c; it appears that the highest green density was achieved at a weight content of ZrO_2 nanoparticles of 8% (Figure 8.17d). The role of alumina in these composites is to stop the growth of zirconia crystallites during the calcination, thus preventing their phase transition towards the monoclinic polymorph [154].

8.3.2 Nanostructured Zirconia in Bioactive Apatite-Based Ceramics

In contrast to early approaches involving purely bioinert materials, the concept of bioactive ceramics was founded on the assumption that optimum biocompatibility can only be achieved by promoting the formation of normal tissue on the surface of ceramic implants [129, 156]. Such biologically active implants are interfacially bonded to the surrounding tissue, and therefore provide optimum fixation, preventing phenomena such as micromovements that might lead either to deteriora-

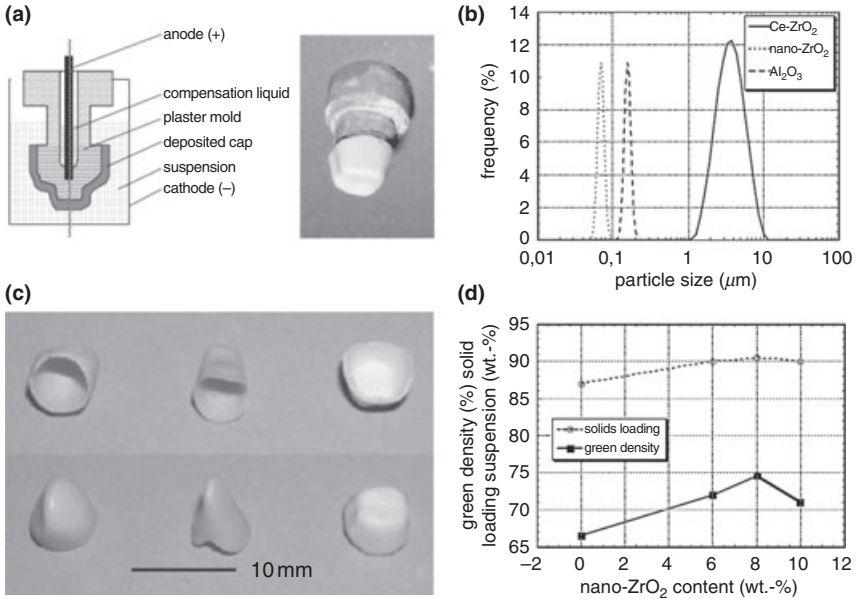

Figure 8.17 (a) Schematic of an electrophoretic deposition cell and photographic image of the cell with a deposited cap on the plaster mold; (b) Photographic images of the obtained ceramic cups; (c) Particle size of the starting powders used; (d) Dependence of solids loading and obtained green density on the nano-ZrO_2 content. (Reproduced from Ref. [154] with kind permission of Springer Science + Business Media).

tion in function of the implant, or to inflammation of the surrounding tissue [129]. Hydroxyapatite (HA) possesses excellent bioactivity, and is thus highly attractive as a ceramic material for orthopedic and dental implants. Unfortunately, however, its application is strongly limited by its poor mechanical properties and processing difficulties, which in turn has prompted the development of ceramic composites and bioglasses as materials to overcome these limitations [157]. In particular, bioceramic composites consisting of HA and zirconia have shown great promise, being both mechanically strong and biologically active [158]. The fabrication of dense HA–zirconia composites however is difficult, because HA decomposes at the temperatures above 1200 °C that are needed for the densification of conventional ZrO_2 powders. One solution to this problem was to use nanoscale powders of HA and zirconia, as was first suggested by Silva and Domingues [159] and later investigated by several other groups [160, 161]. Novel sintering techniques have also been explored that allow densification at lower temperatures [162]. By combining nanostructure processing with pressure-assisted sintering, Ying and coworkers developed a feasible method to obtain HA–zirconia composites with high mechanical strength [163]. In this case, a step-wise chemical precipitation approach was employed where YSZ was first precipitated by the addition of ethanolic zirconia and yttria salt solutions to an ammonia solution. The resultant sol was then

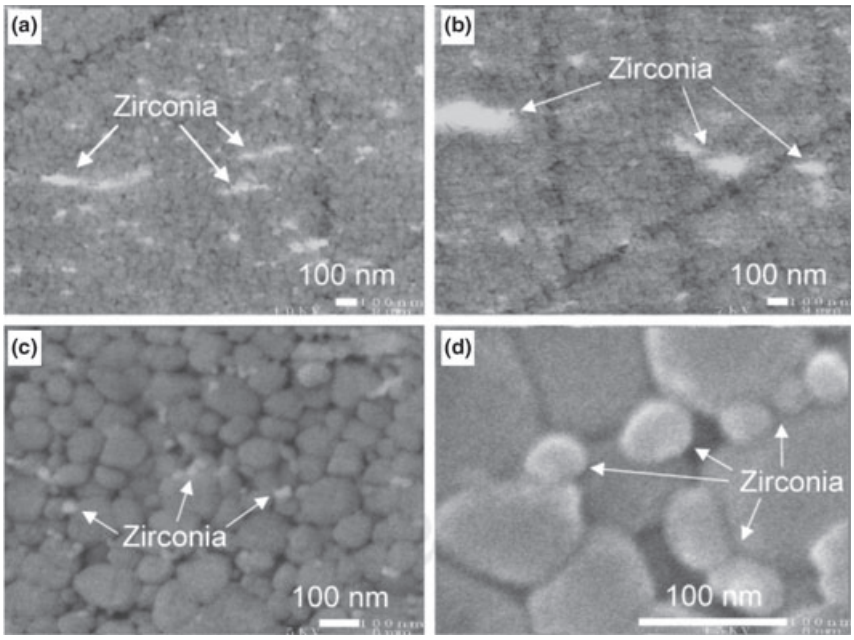

Figure 8.18 Scanning electron microscopy images of hydroxyapatite–zirconia composites obtained via a gel mixing strategy, using (a) zirconium hydroxide and (b) crystalline zirconia, compared to composites obtained after colloidal addition of crystalline zirconia nanoparticles (c, d) [164]. (Reproduced from Ref. [164], with kind permission of the American Ceramic Society).

aged before hydroxyapatite precipitation was performed by adding the HA precursors. In this way, a homogeneous distribution of YSZ nanoparticles of approximately 20 nm in size within a nanocrystalline HA matrix was achieved after pressure-assisted sintering at 900–1000 °C. Even though the YSZ content did not exceed 3 wt%, the fracture toughness was increased substantially, approaching that of compact bone [163]. In a later study, the same group reported a substantially improved distribution of zirconia nanoparticles within the nanocrystalline HA matrix after performing colloidal processing. This involved the hydrothermal synthesis of YSZ, followed by the addition and precipitation of HA, as compared to a gel-mixing synthesis route (see Figure 8.18), the consequence being a material with much better mechanical properties [164].

8.3.3
Nanostructured Zirconia Coatings on Non-Zirconia Bioceramics

Another approach for bioactive medical implants that has been pursued for several years is the use of hydroxyapatite thin-film coatings on load-bearing bodies [165]. For load-bearing applications, metallic alloys are commonly used, and thermal

spraying is the coating technique mainly applied today. Although plasma-sprayed HA coatings on titanium alloy substrates have been used extensively, the erratic bond strength between HA and Ti alloy has raised serious concerns over the long-term reliability of these implants. It was shown by Khor and colleagues that the use of an intermediate layer of YSZ would result in composite coatings with superior mechanical properties as compared to conventional plasma-sprayed HA coatings [166]. Such coatings can also be accomplished by using sol–gel techniques, resulting in nanostructured ZrO_2–HA composite coatings. The strategy employed here normally involves the preparation of a zirconia–yttria sol, which is mixed with a solution of the HA precursors, and then subjected to aging, coating and annealing treatment at about 1000 °C. In this way, Balamurugan *et al.* obtained coatings with a grain structure of approximately 30 nm that led to easy adherence and spreading of osteoblastic cells on stainless steel substrates [167].

8.3.4
Doped Zirconia Nanostructures for Biolabeling

Luminescent nanomaterials show great promise for biolabeling purposes, due to their generally high photochemical stability, narrow emission spectra and tunable fluorescence emission [168, 169]. The most prominent materials are the so-called semiconductor quantum dots, which have been studied for use in biomedical studies, clinical diagnostics and photodynamic therapy [170]. These materials are composed of toxic metal and chalcogenide components such as Cd, Pb, Se and Te, however, and so their biological safety remains the subject of much controversy [171]. Consequently, the use of fluorescent metal oxides that show bioinertness represent a promising alternative. Within this context, the use of lanthanide-doped zirconia nanoparticles is attracting an increasing amount of attention, mainly because the high chemical stability and bioinertness of ZrO_2 render it a highly suitable host lattice material. Thus, a number of studies on the synthesis and properties of fluorescent rare-earth-doped zirconia materials have been reported during the past few years [67, 172–178], with the synthesis mainly being achieved via sol–gel or precipitation methods. Nevertheless, reports concerning the application of these materials in the biomedical field are very few in number. Among the few studies, Yuan and coworkers examined the use of terbium complex-doped zirconia nanoparticles as biosensors [179], having prepared the nanoparticles via a sol–gel method in microemulsions, and functionalizing them with streptavidin via a bovine serum albumin linkage. The biofunctional particles were then successfully used for time-resolved fluoroimmunoassay of human prostate-specific antigen [179].

Additionally, some lanthanide-doped zirconia materials present up-conversion behavior, and therefore have received special attention. Up-converting luminescent materials emit light in the visible range when excited with near-infrared (IR) radiation. This represents an interesting prospect for biomedical applications, as IR light exhibits a higher tissue penetration than does ultraviolet light, with the result being superior sensitivity [180, 181]. Until now, ZrO_2 nanomaterials doped

with several rare earth ions have been prepared and investigated, notably the up-conversion systems of Yb^{3+} plus Er^{3+}-doped zirconia [182, 183] and Er^{3+}-doped zirconia nanoparticles [184–187]. All of these were prepared via solution-based approaches and consequently required calcination at 1000 °C to achieve crystallinity.

An important prerequisite for the use of doped zirconia nanomaterials in biolabeling is their successful stabilization against agglomeration. In general, very few strategies are recognized for the stabilization of zirconia nanoparticles, with most studies presented to date being aimed at the optimum stabilization of zirconia in organic systems. Previously, fatty acids were used successfully to individually stabilize ZrO_2 nanoparticles, both in hydrophobic solvents and acrylate-based polymers [12]. For the incorporation of zirconia nanocrystals into acrylate polymer matrices, vinyl group-containing ligands are highly suitable and promise a covalent linkage of the filler particles to the matrix [188, 189]. However, much less is known about the stabilization of zirconia nanostructures in aqueous media, which would be a prerequisite for their use as biolabeling agents in biological media, or even *in vivo*. Schmidt *et al*. prepared transparent aqueous dispersions of zirconia nanoparticles during a two-step synthesis following the addition of a methacrylsilane ligand, although at this stage the nanoparticles were still amorphous [81]. Elsewhere, TODA [(2-(2-(2-methoxy)ethoxy)ethoxy)acetic acid] was used as a dispersant for zirconia nanoparticles in mixtures of water and 1,2-propanediol, in which colloidal probe investigations of the surface forces acting on the nanoparticles were performed. Unfortunately, however, the agent did not suffice to achieve stable aqueous dispersions in higher solid contents at neutral pH [190]. Subsequently, Lü *et al*. showed that the stabilization of zirconia nanoparticles could be achieved by providing a silica shell around the nanoparticles with TEOS (tetraethyl orthosilicate), thereby also enhancing the optical properties. The silica shell is then modified with an aminosilane stabilizer [3-aminopropyltriethoxysilane (APTES); see Figure 8.19a] to render amine surface groups as hydrophilic surface functions and result in an efficient stabilization of the nanoparticles in aqueous systems. This situation can be seen in the TEM images of Figure 8.19b and c, which show multicore-shell spherical particles of about 100 nm diameter. In addition, the surface functionalities can be altered to feature carboxylic acid functions by simple amide coupling reactions with succinic acid (SA) (Figure 8.19a and c) [191].

8.3.5
Other Applications of Zirconia Nanomaterials in the Life Sciences

The immobilization of biomolecules on solid surfaces represents one of the most important problems in the field of bioelectronics and biosensing, where attempts are made to utilize biomolecules as active components to assemble novel hybrid devices [192]. In particular, the immobilization of enzymes and proteins under conditions that preserve their native structure has triggered considerable research efforts, with the layer-by-layer self-assembly method being one of the most promising techniques due to its simplicity, preciseness of layer thickness,

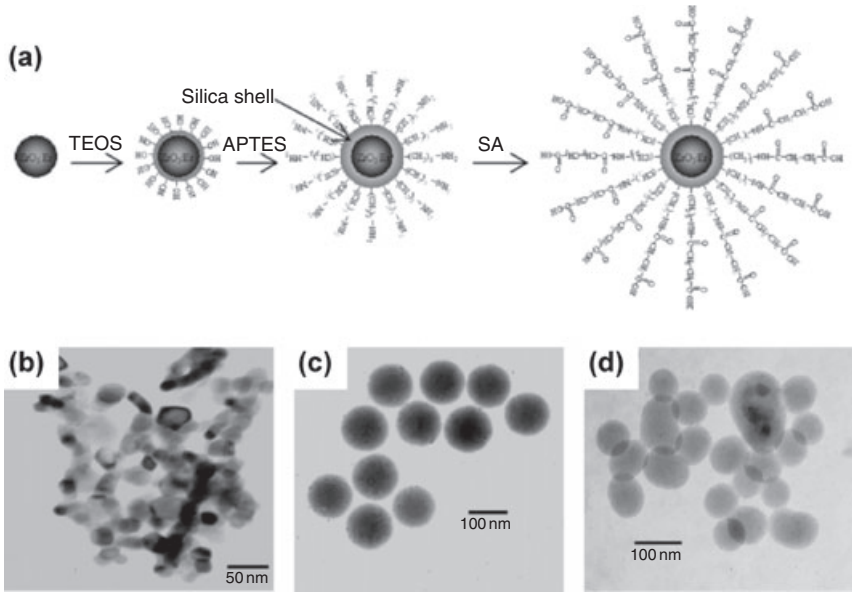

Figure 8.19 (a) Stabilization of fluorescent erbium-doped ZrO_2 nanoparticles via a versatile silica–aminosilane–carboxylic acid strategy; (b–d) TEM images of unstabilized (b) and stabilized (c,d) nanoparticles [191]. (Reproduced from Ref. [191], with kind permission of the American Chemical Society).

and broad choice of available materials [193]. Recently, Hu and coworkers investigated the use of zirconia multilayers and zirconia nanoparticles for protein immobilization, using myoglobin as an electrochemically active protein [194, 195]. The zirconia layers were synthesized by the vapor-surface sol–gel deposition method, where an alkoxide precursor is vaporized into thin water layers, where it reacts to form thin layers of zirconia. As a second system, alternating layers of poly(diallyldimethylammonium) (PDDA) and zirconia nanoparticles were fabricated. Following the incorporation of myoglobin into the layers, which was achieved by simple immersion in suitable solutions of the protein, the electrochemical and electrocatalytic properties of the composites were compared to evaluate not only the myoglobin uptake but also the permeability and porosity of the films. It transpired that the zirconia multilayers exhibited a higher electrochemical/electrocatalytic activity than the nanoparticle-containing multilayers, although the latter still showed a higher activity than the purely organic multilayers used as reference [195].

Biosensors have also been fabricated and tested by the immobilization of proteins on suitable electrode substrates coated with zirconia nanoparticles to provide an adhesion-promoting, bioinert layer that would still allow electron transfer. Ju *et al*. immobilized hemoglobin on a graphite electrode that had been modified with ZrO_2 nanoparticles, and showed that the device could be used as sensor for hydro-

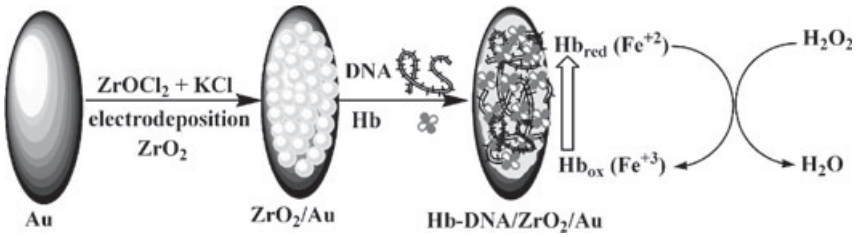

Figure 8.20 Step-wise fabrication of a biosensor consisting of Au–ZrO_2–DNA–hemoglobin structure. (Reproduced from Ref. [199], with kind permission of Springer Science + Business Media).

gen peroxide [196]. Similar devices were also obtained by the immobilization of heme protein [197] and horseradish peroxidase [198] on zirconia-modified carbon electrodes. Recently, Liang and Mu reported the details of a biosensor which possessed a gold–ZrO_2–DNA-derivatized polyion complex composition [199]. These devices were fabricated as illustrated in Figure 8.20. First, the polished Au electrodes were subjected to electrodeposition of zirconia nanoparticles from an aqueous solution of zirconium oxychloride, thereby creating a thin zirconia film on the electrode surface. After drying, the coated electrode was simply incubated with an aqueous solution of DNA and hemoglobin to form the biosensor, which showed high sensitivity and good reproducibility towards H_2O_2 detection [199].

8.4 Summary and Conclusions

Although zirconia was among the first materials to be prepared deliberately and studied in their nanocrystalline form, its synthesis on the nanoscale in a controlled and precise manner has attracted broader attention only within the past two decades. Nowadays, the synthesis and investigation of zirconia nanomaterials is carried out by materials chemists, solid-state chemists, physicists and engineers, as well as by more application-oriented groups in the fields of catalysis and biomedicine. Research groups with such diverse backgrounds naturally also focus on diverse aspects, and the fact that the synthesis of these materials is performed with very diverse intentions – on the one hand, the development of novel ceramics with improved mechanical properties, and on the other hand the fabrication of devices potentially useful as biosensors, but in the most cases, the pure investigation of novel materials by itself – has led to the development of a very broad and diversified research field. In fact, due to its interdisciplinary character, this tendency is a general problem for nanotechnology, although it appears to be more pronounced for the synthesis and application of zirconia-based oxides than for other classes of materials, such as magnetic nanoparticles or semiconductor nanocrystals, where close interaction between experts in the areas of synthesis and the application has resulted in a more unified research field and has thus promoted a more rapid

development. This aim of this chapter was to provide a review for research teams working in the more basic fields of nanomaterials synthesis, as well as for more application-oriented teams. In this way, it is hoped that an increased interaction and exchange of knowledge between these two groups, and between the various disciplines, will result.

The first sections of the chapter provided a review of current synthetic strategies for zirconia nanomaterials, detailing both solution phase and gas-phase techniques, as well as comminution to nanoscale ZrO_2 powders. For biomedical applications, solution-based strategies appear especially suitable, providing homogeneity and control of particle size and facilitating stabilization against agglomeration and aggregation. Unfortunately, these methods require calcination to achieve crystalline materials, which often results in the decomposition of organic stabilizers, grain growth and phase transformation processes, all of which are accepted as being required to fabricate (bio)ceramics, but lead to a loss of control and stabilization for most other applications. Recently, strategies have been developed to ensure control during high-temperature calcination, including the Pechini or combustion synthesis techniques, both of which allow the preparation of crystalline products at low temperature. To prepare highly defined nanostructured zirconia, however, crystallization in a liquid medium is preferred, with its optimum control and stabilization. The liquid-phase synthesis of crystalline zirconia nanomaterials can be accomplished by novel methods, notably improved hydrothermal and solvothermal routes, as well as nonaqueous and nonhydrolytic sol–gel synthesis that allow the simple, low-temperature preparation of crystalline zirconia nanomaterials that can be isolated and manipulated as single nonagglomerated particles.

Gas-phase methods are widely used for the industrial production of the metal oxide nanopowders with diverse particle sizes that are often used as feedstocks in the preparation of ceramics. The stabilization of such powders has provend difficult task, however, and many of today's *in vivo* applications of nanomaterials rely on solution-based methods, based on much better possibilities of functionalization and manipulation. Comminution has also begun to be accepted for the production of nanoscale powders, although its use for high-purity zirconia nanomaterials, as required for biomedical use, is severely hampered by the extreme hardness of ZrO_2.

Unlike zirconia nanoparticle synthesis, the preparation of anisotropic zirconia nanomaterials has been rarely reported, with the preparation of nanoparticles with a rice- or fiber-like morphology having been achieved in solution-based processes, and the underlying mechanisms not yet understood. Template-based processes, both in solution and in gas phase, have however been successfully employed to prepare nanorods and nanotubes, using common polymer-based membranes and anodic alumina as templates.

With regards to the application of zirconia nanomaterials in the life sciences, ceramics based on transformation-toughened zirconia are today widely used in joint replacement surgery, due to their bioinertness and excellent mechanical properties, although the complex structural and mechanical properties of zirconia, and the long-term mechanical behavior of these ceramics *in vivo* are still not

understood. A case in hand is the spectacular multiple failure of zirconia implants some years ago which, though rapidly identified, triggered an intensive search for alternatives. In this respect, and due to their unrivaled toughness, zirconia-based bioceramics will undoubtedly be used widely in the future, although there is a strong trend towards 'aging-free' materials created from composites, notably alumina–zirconia ceramics. Today, nanostructural control is exerted solely by the use of nanopowders as starting materials for these bioceramics, without precise control of particle or grain size and shape during the course of further processing. Efforts are currently being directed towards achieving control on a more elaborate level via novel processing methods such as 'nanostructure processing', as has recently been proposed. This integration of nanotechnology into ceramic processing will go hand in hand with further optimizations of the composition, leading to a higher complexity and superior ceramic materials with enhanced stability and toughness.

A further trend in bioceramics is that bioactivity rather than bioinertness should serve as the concept for the optimal integration of implants in surrounding tissues. Today, extensive studies are conducted on the development of HA-based composites that combine biocompatibility with the mechanical stability (notably toughness) of metal oxides, with zirconia being a primary candidate for this role. It has already been proven, that the integration of zirconia nanoparticles into the HA matrix leads to composites with high mechanical strength and excellent biocompatibility, despite levels of control being low. Although such materials bring us closer to what may be referred to as 'artificial bone', there is still a long way to go to reach the 'biomimetic dream' of a biologically controlled, laboratory-based bone fabrication. It can certainly be expected, however, that research into organic–inorganic hybrid materials will intensify over the next few years, with the biologically controlled fabrication of metal oxide nanostructures gaining momentum. This will especially be the case for the synthesis of crystalline ceramics such as zirconia, long times being the domain of solid-state chemists, operating well above 1000 °C, which will become feasible in reaction systems quite closely related to biological conditions. In parallel with this development, bioceramics will become bioactive in the long term, with an elaborate strategy employing both chemical and biological efforts to ensure the rapid integration of implants into the host tissues.

With regards to the biomedical applications of zirconia, aside from bioceramic implants research into the potential and limitations of nanoparticles, nanorods, nanowires and other nanostructures has just begun. In many areas, the biological inertness and chemical stability of zirconia make it an interesting and promising alternative to the more established materials, that may pose biological risks. Uses such as fluorescent biolabels will become feasible when the stabilization and efficient functionalization of zirconia nanostructures is achieved by scalable methods, yet the benefits – especially if up-conversion luminescent properties are taken into account – are already evident today. In nanobiotechnology in general, and nanoelectronics in particular, whilst nanostructured zirconia may not emerge as a key component, its advantageous properties will surely render it indispensable for many applications.

References

1 Yamaguchi, T. (1994) Application of ZrO_2 as a catalyst and a catalyst support. *Catalysis Today*, **20**, 199–217.

2 Stichert, W. and Schüth, F. (1998) Synthesis of catalytically active high surface area monoclinic sulfated zirconia. *Journal of Catalysis*, **174**, 242–5.

3 Benfer, S. and Knözinger, E. (1999) Structure, morphology and surface properties of nanostructured ZrO_2 particles. *Journal of Material Chemistry*, **9**, 1203–9.

4 Cioffi, N., Faticanti, M., Ditaranto, N., De Rossi, S., Traversa, L., Monopoli, A., Nacci, A., Torsi, L. and Sabbatini, L. (2007) Analytical characterisation of Pd/ZrO_2 composite nanoparticles employed in heterogeneous catalysis. *Current Nanoscience*, **3**, 121–7.

5 Sun, W., Xu, L., Chu, Y. and Shi, W. (2003) Controllable synthesis, characterization and catalytic properties of WO_3/ZrO_2 mixed oxides nanoparticles. *Journal of Colloid and Interface Science*, **266**, 99–106.

6 Landau, M.V., Vradman, L., Wolfson, A., Rao, P.M. and Herskowitz, M. (2005) Dispersions of transition-metal-based phases in mesostructured silica matrixes: Preparation of high-performance catalytic materials. *Comptes Rendus Chimie*, **8**, 679–91.

7 Reddy, B.M. and Khan, A. (2005) Recent advances on TiO_2-ZrO_2 mixed oxides as catalysts and catalyst supports. *Catalysis Reviews Science and Engineering*, **47**, 257–96.

8 Zhang, Z., Zhang, C. and Zhang, X. (2002) Development of a chemiluminescence ethanol sensor based on nanosized ZrO_2. *Analyst*, **127**, 792–6.

9 Wang, Q., Xue, Q., Liu, H., Shen, W. and Xu, J. (1996) The effect of particle size of nanometer ZrO_2 on the tribological behaviour of PEEK. *Wear*, **198**, 216–19.

10 Song, H.-J. and Zhang, Z.-Z. (2006) Investigation of the tribological properties of polyfluo wax/polyurethane composite coating filled with nano-SiC or nano-ZrO_2. *Materials Science and Engineering A*, **426**, 59–65.

11 Beecroft, L.L. and Ober, C.K. (1997) Nanocomposite materials for optical applications. *Chemistry of Materials*, **9**, 1302–17.

12 Garnweitner, G., Goldenberg, L.M., Sakhno, O.V., Antonietti, M., Niederberger, M. and Stumpe, J. (2007) Large-scale synthesis of organophilic zirconia nanoparticles and their application in organic-inorganic nanocomposites for efficient volume holography. *Small*, **3**, 1626–32.

13 Wang, Y., Zhang, D., Shi, L., Li, L. and Zhang, J. (2008) Novel transparent ternary nanocomposite films of trialkoxysilane-capped poly(methyl methacrylate)/zirconia/titania with incorporating networks. *Materials Chemistry and Physics*, **110**, 463–70.

14 Omata, T. (2007) Nanocrystals of zirconia- and ceria-based solid electrolytes: Syntheses. *Science and Technology of Advanced Materials*, **8**, 524–30.

15 Hasirci, V., Vrana, E., Zorlutuna, Z., Ndreu, A., Yilgor, P., Basmanav, F.B. and Aydin, E. (2006) Nanobiomaterials: a review of existing science and technology, and new approaches. *Journal of Biomaterials Science. Polymer Edition*, **17**, 1241–68.

16 Caruthers, S.D., Wickline, S.A. and Lanza, G.M. (2007) Nanotechnological applications in medicine. *Current Opinion in Biotechnology*, **18**, 26–30.

17 Narayan, R.J., Kumta, P.N., Sfeir, C., Lee, D.-H., Olton, D. and Choi, D. (2004) Nanostructured ceramics in medical devices: applications and prospects. *Journal of the Minerals, Metals and Materials Society*, **56**, 38–43.

18 Ying, J.Y. (2005) Research in bioengineering and nanotechnology. *AIChE Journal*, **51**, 2382–5.

19 Piconi, C. and Maccauro, G. (1999) Zirconia as a ceramic biomaterial. *Biomaterials*, **20**, 1–25.

20 Maehara, Y. and Langdon, T.G. (1990) Superplasticity in ceramics. *Journal of Materials Science*, **25**, 2275–86.

21 Brunner, T., Wick, P., Manser, P., Spohn, P., Grass, R.N., Limbach, L.K., Bruinink, A. and Stark, W.J. (2006) In vitro cytotoxicity of oxide nanoparticles: comparison to asbestos, silica, and the effect of particle solubility. *Environmental Science & Technology*, **40**, 4374–81.

22 Covacci, V., Bruzzese, N., Maccauro, G., Andreassi, C., Ricci, G.A., Piconi, C., Marmo, E., Burger, W. and Cittadini, A. (1999) In vitro evaluation of the mutagenic and carcinogenic power of high purity zirconia ceramic. *Biomaterials*, **20**, 371–6.

23 Takamura, K., Hayashi, K., Ishinishi, N., Yamada, T. and Sugioka, Y. (2004) Evaluation of carcinogenicity and chronic toxicity associated with orthopedic implants in mice. *Journal of Biomedical Materials Research*, **28**, 583–9.

24 Kingery, W.D., Bowen, H.K. and Uhlmann, D.R. (1976) *Introduction to Ceramics*, 2nd edn, John Wiley & Sons, Inc., New York.

25 Reed, J.S. (1995) *Introduction to the Principles of Ceramic Processing*, John Wiley & Sons, Inc., New York.

26 Groza, J.R. (1999) *Nanosintering. Nanostructured Materials*, **12**, 987–92.

27 Hoch, M., Thompson, A.L., Houck, J. and Nair, K.M. (1977) Sintering of ultrafine (<100 Å). *Journal Bulk Solids and Powder Science and Technology*, **1**, 34–8.

28 King, A.G. (2002) *Ceramic Technology and Processing*, William Andrew Publishing, Norwich, NY.

29 Ruff, O. and Ebert, F. (1929) Beiträge zur Keramik hochfeuerfester Stoffe I: Die Formen des Zirkondioxyds. *Zeitschrift für Anorganische und Allgemeine Chemie*, **180**, 19–41.

30 Clark, G.L. and Reynolds, D.H. (1937) Chemistry of zirconium dioxide: X-ray diffraction studies. *Industrial and Engineering Chemistry*, **29**, 711–15.

31 Whitney, E.D. (1965) Kinetics and mechanism of the transition of metastable tetragonal to monoclinic zirconia. *Transactions of the Faraday Society*, **61**, 1991–2000.

32 Garvie, R.C. (1965) The occurrence of metastable tetragonal zirconia as a crystallite size effect. *Journal of Physical Chemistry*, **69**, 1238–43.

33 Garvie, R.C. (1978) Stabilization of the tetragonal structure in zirconia microcrystals. *Journal of Physical Chemistry*, **82**, 218–24.

34 Mazdiyasni, K.S., Lynch, C.T. and Smith, J.S.I. (1965) Preparation of ultra-high-purity submicron refractory oxides. *Journal of the American Ceramic Society*, **48**, 372–5.

35 Haberko, K. (1979) Characteristics and sintering behaviour of zirconia ultrafine powders. *Ceramics International*, **5**, 148–54.

36 Tani, E., Yoshimura, M. and Somiya, S. (1983) Formation of ultrafine tetragonal ZrO_2 powder under hydrothermal conditions. *Journal of the American Ceramic Society*, **66**, 11–14.

37 Vilmin, G., Komarneni, S. and Roy, R. (1987) Lowering crystallization temperature of zircon by nanoheterogeneous sol-gel processing. *Journal of Materials Science*, **22**, 3556–60.

38 Edelstein, A.S. and Cammarata, R.C.E. (1996) *Nanomaterials: Synthesis, Properties and Applications*, Institute of Physics Publishing, Bristol.

39 Rodríguez, J.A. and Fernández-García, M.E. (2007) *Synthesis, Properties, and Applications of Oxide Nanomaterials*, John Wiley & Sons, Inc., New York.

40 Cushing, B.L., Kolesnichenko, V.L. and O'Connor, C.J. (2004) Recent advances in the liquid-phase syntheses of inorganic nanoparticles. *Chemical Reviews*, **104**, 3893–946.

41 Di Monte, R. and Kaspar, J. (2005) Nanostructured CeO_2-ZrO_2 mixed oxides. *Journal of Materials Chemistry*, **15**, 633–48.

42 Livage, J. and Sanchez, C. (1992) Sol-gel chemistry. *Journal of Non-Crystalline Solids*, **145**, 11–19.

43 Corriu, R.J.P. and Leclercq, D. (1997) Solution chemistry for the elaboration of solids. *Comments on Inorganic Chemistry*, **19**, 245–62.

44 Piticescu, R., Monty, C. and Millers, D. (2005) Hydrothermal synthesis of

nanostructured zirconia materials: present state and future prospects. *Sensors and Actuators. B, Chemical*, **109**, 102–6.

45 Somiya, S. and Akiba, T. (1999) Hydrothermal zirconia powders: a bibliography. *Journal of the European Ceramic Society*, **19**, 81–7.

46 Zhu, H., Yang, D., Xi, Z. and Zhu, L. (2007) Hydrothermal synthesis and characterization of zirconia nanocrystallites. *Journal of the American Ceramic Society*, **90**, 1334–8.

47 Xin, X., Lü, Z., Huang, X., Sha, X., Zhang, Y. and Su, W. (2006) Influence of synthesis routes on the performance from weakly agglomerated yttria-stabilized zirconia nanomaterials. *Materials Research Bulletin*, **41**, 1319–29.

48 Wright, C.S., Walton, R.I., Thompsett, D., Fisher, J. and Ashbrook, S.E. (2007) One-step hydrothermal synthesis of nanocrystalline ceria-zirconia mixed oxides: the beneficial effect of sodium inclusion on redox properties. *Advanced Materials*, **19**, 4500–4.

49 Xingyong, G., Xia, L., Qi, L., Yunxia, C. and Yueming, L. (2007) Effect of novel bivalent mineralizers on the synthesis of nano-sized Y_2O_3 doped ZrO_2 powder by hydrothermal method. *Key Engineering Materials*, **336–338**, 2065–7.

50 Qin, D. and Chen, H. (2006) The influence of alcohol additives on the crystallization of ZrO_2 under hydrothermal conditions. *Journal of Materials Science*, **41**, 7059–63.

51 Chen, F., Zhu, K., Gan, G.J., Shen, S. and Kooli, F. (2007) Hydrothermal processing of amorphous hydrous zirconia gels in the presence of 1,12-diaminododecane. *Materials Research Bulletin*, **42**, 1128–36.

52 Meskin, P.E., Ivanov, V.K., Barantchikov, A.E., Churagulov, B.R. and Tretyakov, Y.D. (2006) Ultrasonically assisted hydrothermal synthesis of nanocrystalline ZrO_2, TiO_2, $NiFe_2O_4$ and $Ni_{0.5}Zn_{0.5}Fe_2O_4$ powders. *Ultrasonics Sonochemistry*, **13**, 47–53.

53 Bondioli, F., Leonelli, C., Manfredini, T., Ferrari, A.M., Caracoche, M.C., Rivas, P.C. and Rodríguez, A.M. (2005) Microwave-hydrothermal synthesis and hyperfine characterization of praseodymium-doped nanometric zirconia powders. *Journal of the American Ceramic Society*, **88**, 633–8.

54 Sue, K., Suzuki, M., Arai, K., Ohashi, T., Ura, H., Matsui, K., Hakuta, Y., Hayashi, H., Watanabe, M. and Hiaki, T. (2006) Size-controlled synthesis of metal oxide nanoparticles with a flow-through supercritical water method. *Green Chemistry*, **8**, 634–8.

55 Wang, X.M., Xiao, P. and Lorimer, G. (2005) Highly dispersed suspension of YSZ and zirconia nanoparticles by solvothermal processing. *Advances in Applied Ceramics*, **104**, 135–41.

56 Moon, Y.T., Park, H.K., Kim, D.K., Kim, C.H. and Seog, I.-S. (1995) Preparation of monodisperse and spherical zirconia powders by heating of alcohol-aqueous salt solutions. *Journal of the American Ceramic Society*, **78**, 2690–4.

57 Zile, H., Wang, X.M., Xiao, P. and Shi, J. (2006) Solvent effect on microstructure of yttria-stabilized zirconia (YSZ) particles in solvothermal synthesis. *Journal of the European Ceramic Society*, **26**, 2257–64.

58 Wang, X.M. and Xiao, P. (2007) Solvothermal synthesis of zirconia and yttria-stabilized zirconia nanocrystalline particles. *Journal of Materials Research*, **22**, 46–55.

59 Qian, Z. and Shi, J.L. (1998) Characterization of pure and doped zirconia nanoparticles with infrared transmission spectroscopy. *Nanostructured Materials*, **10**, 235–44.

60 Xin, X., Lü, Z., Ding, Z., Huang, X., Liu, Z., Sha, X., Zhang, Y. and Su, W. (2006) Synthesis and characteristics of nanocrystalline YSZ by homogeneous precipitation and its electrical properties. *Journal of Alloys and Compounds*, **425**, 69–75.

61 Zhou, L., Xu, J., Li, X. and Wang, F. (2006) Metal oxide nanoparticles from inorganic sources via a simple and general method. *Materials Chemistry and Physics*, **97**, 137–42.

62 Shevchenko, A.V., Dudnik, E.V., Ruban, A.K., Vereschaka, V.M., Red'ko, V.P. and Lopato, L.M. (2007) Hydrothermal

synthesis of nanocrystalline powders in the ZrO_2-Y_2O_3-CeO_2 system. *Powder Metallurgy and Metal Ceramics*, **46**, 18–24.

63 Duan, G.-R., Yang, X.-J., Huang, G.-H., Lu, L.-D. and Wang, X. (2006) Water/Span80/Triton X-100/n-hexyl alcohol/*n*-octane microemulsion system and the study of its application for preparing nanosized zirconia. *Materials Letters*, **60**, 1582–7.

64 Wang, X., Zhuang, J., Peng, Q. and Li, Y. (2005) A general strategy for nanocrystal synthesis. *Nature*, **437**, 121–4.

65 Pechini M.P. (1967) US Patent 3,330,697.

66 Segal, D. (1997) Chemical synthesis of ceramic materials. *Journal of Materials Chemistry*, **7**, 1297–305.

67 Zhang, H., Fu, X., Niu, S. and Xin, Q. (2008) Blue emission of ZrO_2:Tm nanocrystals with different crystal structure under UV excitation. *Journal of Non-Crystalline Solids*, **354**, 1559–63.

68 Lin, C., Zhang, C. and Lin, J. (2007) Phase transformation and photoluminescence properties of nanocrystalline ZrO_2 powders prepared via the Pechini-type sol-gel process. *Journal of Physical Chemistry C*, **111**, 3300–7.

69 Kingsley, J.J. and Patil, K.C. (1988) A novel combustion process for the synthesis of fine particle alpha-alumina and related oxide materials. *Materials Letters*, **6**, 427–32.

70 Kaus, I., Dahl, P.I., Mastin, J., Grande, T. and Einarsrud, M.-A. (2006) Synthesis and characterization of nanocrystalline YSZ powders by smoldering combustion synthesis. *Journal of Nanomaterials*, Article ID 49283.

71 Purohit, R.D., Saha, S. and Tyagi, A.K. (2006) Combustion synthesis of nanocrystalline ZrO_2 powder: XRD, Raman spectroscopy and TEM studies. *Materials Science and Engineering B*, **130**, 57–60.

72 Reddy, B.S.B., Mal, I., Tewari, S., Das, K. and Das, S. (2007) Aqueous combustion synthesis and characterization of nanosized tetragonal zirconia single crystals. *Metallurgical and Materials Transactions A*, **38**, 1786–93.

73 Biamino, S., Fino, P., Pavese, M. and Badini, C. (2006) Alumina-zirconia-yttria nanocomposites prepared by solution combustion synthesis. *Ceramics International*, **32**, 509–13.

74 Deb, A., Chatterjee, P. and Sen Gupta, S.P. (2007) Synthesis and microstructural characterization of α-Al_2O_3 t-ZrO_2 composite powders prepared by combustion technique. *Materials Science and Engineering A*, **459**, 124–31.

75 Grover, V., Chavan, S.V., Sastry, P.U. and Tyagi, A.K. (2008) Combustion synthesis of nanocrystalline $Zr_{0.80}Ce_{0.20}O_2$: detailed investigations of the powder properties. *Journal of Alloys and Compounds*, **457**, 498–505.

76 Shukla, S., Seal, S. and Vanfleet, R. (2003) Sol-gel synthesis and phase evolution behavior of sterically stabilized nanocrystalline zirconia. *Journal of Sol-Gel Science and Technology*, **27**, 119–36.

77 Khimich, N.N., Semashko, O.V., Khimich, E.N. and Voronkov, M.G. (2006) Sol-gel synthesis of dispersed ZrO_2 nanoparticles. *Russian Journal of Applied Chemistry*, **79**, 351–5.

78 Suciu, C., Gagea, L., Hoffmann, A.C. and Mocean, M. (2006) Sol-gel production of zirconia nanoparticles with a new organic precursor. *Chemical Engineering Science*, **61**, 7831–5.

79 Livage, J., Beteille, F., Roux, C., Chatry, M. and Davidson, P. (1998) Sol-gel synthesis of oxide materials. *Acta Materialia*, **46**, 743–50.

80 Kuo, C.-W., Lee, Y.-H., Hung, I.-M., Wang, M.-C., Wen, S.-B., Fung, K.-Z. and Shih, C.-J. (2008) Crystallization kinetics and growth mechanism of 8 mol% yttria-stabilized zirconia (8YSZ) nano-powders prepared by a sol-gel process. *Journal of Alloys and Compounds*, **453**, 470–5.

81 Schmidt, T., Mennig, M. and Schmidt, H. (2007) New method for the preparation and stabilization of nanoparticulate t-ZrO_2 by a combined sol–gel and solvothermal process. *Journal of the American Ceramic Society*, **90**, 1401–5.

82 Mizuno, M., Sasaki, Y., Lee, S. and Katakura, H. (2006) High-yield sol-gel synthesis of well-dispersed, colorless ZrO_2 nanocrystals. *Langmuir*, **22**, 7137–40.

83 Ward, D.A. and Ko, E.I. (1993) Synthesis and structural transformation of zirconia aerogels. *Chemistry of Materials*, **5**, 956–69.

84 Chervin, C.N., Clapsaddle, B.J., Chiu, H.W., Gash, A.E., Satcher, J.H. and Kauzlarich, S.M. (2005) Aerogel synthesis of yttria-stabilized zirconia by a non-alkoxide sol-gel route. *Chemistry of Materials*, **17**, 3345–51.

85 Chervin, C.N., Clapsaddle, B.J., Chiu, H.W., Gash, A.E., Satcher, J.H. and Kauzlarich, S.M. (2006) Role of cyclic ether and solvent in a non-alkoxide sol-gel synthesis of yttria-stabilized zirconia nanoparticles. *Chemistry of Materials*, **18**, 4865–74.

86 Park, J., Joo, J., Kwon, S.G., Jang, Y. and Hyeon, T. (2007) Synthesis of monodisperse spherical nanocrystals. *Angewandte Chemie – International Edition*, **46**, 4630–60.

87 Niederberger, M. (2007) Nonaqueous sol-gel routes to metal oxide nanoparticles. *Accounts of Chemical Research*, **40**, 793–800.

88 Garnweitner, G. and Niederberger, M. (2008) Organic chemistry in inorganic nanomaterials synthesis. *Journal of Materials Chemistry*, **18**, 1171–82.

89 Niederberger, M. and Garnweitner, G. (2006) Organic reaction pathways in the nonaqueous synthesis of metal oxide nanoparticles. *Chemistry – A European Journal*, **12**, 7282–302.

90 Inoue, M., Kominami, H. and Inui, T. (1993) Novel synthetic method for the catalytic use of thermally stable zirconia: thermal decomposition of zirconium alkoxides in organic media. *Applied Catalysis A*, **97**, L25–30.

91 Joo, J., Yu, T., Kim, Y.W., Park, H.M., Wu, F.X., Zhang, J.Z. and Hyeon, T. (2003) Multigram scale synthesis and characterization of monodisperse tetragonal zirconia nanocrystals. *Journal of the American Chemical Society*, **125**, 6553–7.

92 Tang, J., Fabbri, J., Robinson, R.D., Zhu, Y.M., Herman, I.P., Steigerwald, M.L. and Brus, L.E. (2004) Solid-solution nanoparticles: use of a nonhydrolytic sol-gel synthesis to prepare HfO_2 and $Hf_xZr_{1-x}O_2$ nanocrystals. *Chemistry of Materials*, **16**, 1336–42.

93 Omata, T., Sasai, S., Goto, Y., Ueda, M. and Otsuka-Yao-Matsuo, S. (2006) Synthesis of CeO_2, ZrO_2 nanocrystals, and core-shell type nanocomposites. *The Journal of the Electrochemical Society*, **153**, A2269–73.

94 Niederberger, M., Bartl, M.H. and Stucky, G.D. (2002) Benzyl alcohol and transition metal chlorides as a versatile reaction system for the nonaqueous and low-temperature synthesis of crystalline nano-objects with controlled dimensionality. *Journal of the American Chemical Society*, **124**, 13642–3.

95 Niederberger, M., Pinna, N., Polleux, J. and Antonietti, M. (2004) A general soft chemistry route to perovskites and related materials: synthesis of $BaTiO_3$, $BaZrO_3$ and $LiNbO_3$ nanoparticles. *Angewandte Chemie – International Edition*, **43**, 2270.

96 Garnweitner, G. and Niederberger, M. (2006) Nonaqueous and surfactant-free synthesis routes to metal oxide nanoparticles. *Journal of the American Ceramic Society*, **89**, 1801–8.

97 Garnweitner, G., Ninjbadgar, T., Dierke, H. and Niederberger, M. (2008) Benzylamines as versatile agents for the one-pot synthesis and highly ordered stacking of anatase nanoparticles. *European Journal of Inorganic Chemistry*, **2008**, 890–5.

98 Niederberger, M., Garnweitner, G., Buha, J., Polleux, J., Ba, J. and Pinna, N. (2006) Nonaqueous synthesis of metal oxide nanoparticles: review and indium oxide as case study for the dependence of particle morphology on precursors and solvents. *Journal of Sol-Gel Science and Technology*, **40**, 259–66.

99 Gutsch, A., Mühlenweg, H. and Krämer, M. (2004) Tailor-made nanoparticles via gas-phase synthesis. *Small*, **1**, 30–46.

100 Mueller, R., Jossen, R., Pratsinis, S.E., Watson, M. and Akhtar, M.K. (2004) Zirconia nanoparticles made in spray

flames at high production rates. *Journal of the American Ceramic Society*, **87**, 197–202.

101 Mueller, R., Jossen, R., Kammler, H.K., Pratsinis, S.E. and Akhtar, M.K. (2005) Growth of zirconia particles made by flame spray pyrolysis. *AIChE Journal*, **50**, 3085–94.

102 Jossen, R., Mueller, R., Pratsinis, S.E., Watson, M. and Akhtar, M.K. (2005) Morphology and composition of spray-flame-made yttria-stabilized zirconia nanoparticles. *Nanotechnology*, **16**, S609–17.

103 Skandan, G. (1995) Processing of nanostructured zirconia ceramics. *Nanostructured Materials*, **5**, 111–26.

104 Nitsche, R., Rodewald, M., Skandan, G., Fuess, H. and Hahn, H. (1996) HRTEM study of nanocrystalline zirconia powders. *Nanostructured Materials*, **7**, 535–46.

105 Hahn, H. and Averback, R.S. (1990) The production of nanocrystalline powders by magnetron sputtering. *Journal of Applied Physics*, **67**, 1113–15.

106 Gajovic, A., Furic, K., Stefanic, G. and Music, S. (2004) In situ high temperature study of ZrO_2 ball-milled to nanometer sizes. *Journal of Molecular Structure*, **744–747**, 127–33.

107 Michel, D., Faudot, F., Gaffet, E. and Mazerolles, L. (1993) Stabilized zirconias prepared by mechanical alloying. *Journal of the American Ceramic Society*, **76**, 2884–8.

108 Kumagai, T., Hongo, K. and Kimura, H. (2004) Phase transformation and densification of an attrition-milled amorphous yttria-partially stabilized zirconia-20 mol% alumina powder. *Journal of the American Ceramic Society*, **87**, 644–50.

109 Xiang, D.H., Ma, Y.P., Zhao, B. and Chen, M. (2006) Study on surface quality of nano ZrO_2 ceramics in grinding by the aid of ultrasonic vibration. *Key Engineering Materials*, **315–316**, 190–4.

110 Dodd, A.C. and McCormick, P.G. (2001) Solid-state chemical synthesis of nanoparticulate zirconia. *Acta Materialia*, **49**, 4215–20.

111 Dodd, A.C., Raviprasad, K. and McCormick, P.G. (2001) Synthesis of ultrafine zirconia powders by mechanochemical processing. *Scripta Materialia*, **44**, 689–94.

112 Mitchell, D.T., Lee, S.B., Trofin, L., Li, N., Nevanen, T.K., Söderlund, H. and Martin, C.R. (2002) Smart nanotubes for bioseparations and biocatalysis. *Journal of the American Chemical Society*, **124**, 11864–5.

113 Martin, C.R. and Kohli, P. (2003) The emerging field of nanotube biotechnology. *Nature Reviews Drug Discovery*, **2**, 29–37.

114 Kumari, L., Li, W. and Wang, D. (2008) Monoclinic zirconium oxide nanostructures synthesized by a hydrothermal route. *Nanotechnology*, **19**, Article no. 195602.

115 Zhao, N., Pan, D., Nie, W. and Ji, X. (2006) Two-phase synthesis of shape-controlled colloidal zirconia nanocrystals and their characterization. *Journal of the American Chemical Society*, **128**, 10118–24.

116 Rao, C.N.R., Satishkumar, B.C. and Govindaraj, A. (1997) Zirconia nanotubes. *Chemical Communications*, 1581–2.

117 Gundiah, G., Mukhopadhyay, S., Tumkurkar, U.G., Govindaraj, A., Maitra, U. and Rao, C.N.R. (2003) Hydrogel route to nanotubes of metal oxides and sulfates. *Journal of Materials Chemistry*, **13**, 2118–22.

118 Ogihara, H., Sadakane, M., Nodasaka, Y. and Ueda, W. (2006) Shape-controlled synthesis of ZrO_2, Al_2O_3, and SiO_2 nanotubes using carbon nanofibers as templates. *Chemistry of Materials*, **18**, 4981–3.

119 Bao, J., Xu, D., Zhou, Q. and Xu, Z. (2002) An array of concentric composite nanostructure of metal nanowires encapsulated in zirconia nanotubes: preparation, characterization, and magnetic properties. *Chemistry of Materials*, **14**, 4709–13.

120 Tsai, M.C., Lin, G.T., Chiu, H.T. and Lee, C.Y. (2008) Synthesis of zirconium dioxide nanotubes, nanowires, and nanocables by concentration dependent

solution deposition. *Journal of Nanoparticle Research*, **10**, 863–9.

121 Xu, H., Qin, D.-H., Yang, Z. and Li, H.-L. (2003) Fabrication and characterization of highly ordered zirconia nanowire arrays by sol-gel template method. *Materials Chemistry and Physics*, **80**, 524–8.

122 Cochran, R.E., Shyue, J.-J. and Padture, N.P. (2007) Template-based, near-ambient synthesis of crystalline metal-oxide nanotubes, nanowires and coaxial nanotubes. *Acta Materialia*, **55**, 3007–14.

123 Chen, H., Elabd, Y.A. and Palmese, G.R. (2007) Plasma-aided template synthesis of inorganic nanotubes and nanorods. *Journal of Materials Chemistry*, **17**, 1593–6.

124 Tsuchiya, T., Macak, J.M., Taveira, L. and Schmuki, P. (2005) Fabrication and characterization of smooth high aspect ratio zirconia nanotubes. *Chemical Physics Letters*, **410**, 188–91.

125 Lee, W.-J. and Smyrl, W.H. (2005) Zirconium oxide nanotubes synthesized via direct electrochemical anodization. *Electrochemical and Solid State Letters*, **8**, B7–9.

126 Shin, H., Jeong, D.-K., Lee, J., Sung, M.M. and Kim, J. (2004) Formation of TiO_2 and ZrO_2 nanotubes using atomic layer deposition with ultraprecise control of the wall thickness. *Advanced Materials*, **16**, 1197–200.

127 Bae, C., Kim, S., Ahn, B., Kim, J., Sung, M.M. and Shin, H. (2008) Template-directed gas-phase fabrication of oxide nanotubes. *Journal of Materials Chemistry*, **18**, 1362–7.

128 Shen, Z.Q., He, L.L., Wu, E.D., Fan, Y.Y., He, J.F., Cheng, H.M., Li, D.X. and Ye, H.Q. (2002) Boron nitride nanotubes filled with zirconium oxide nanorods. *Journal of Materials Research*, **17**, 2761–4.

129 Hench, L.L. (1998) Bioceramics. *Journal of the American Ceramic Society*, **81**, 1705–28.

130 Garvie, R.C., Hannink, R.H. and Pascoe, R.T. (1975) Ceramic steel? *Nature*, **258**, 703–4.

131 Rieu, J. and Goeuriot, P. (1993) Ceramic composites of biomedical applications. *Clinical Materials*, **12**, 211–17.

132 Butler, E.P. (1985) Transformation-toughened zirconia ceramics. *Materials Science and Technology*, **1**, 417–32.

133 Deville, S. and Chavalier, J. (2003) Martensitic relief observation by atomic force microscopy in yttria-stabilized zirconia. *Journal of the American Ceramic Society*, **86**, 2225–7.

134 Rahaman, M.N., Yao, A., Sonny Bal, B., Garino, J.P. and Ries, M.D. (2007) Ceramics for prosthetic hip and knee joint replacement. *Journal of the American Ceramic Society*, **90**, 1965–88.

135 Chevalier, J. (2006) What future for zirconia as a biomaterial? *Biomaterials*, **27**, 535–43.

136 Piconi, C., Burger, W., Richter, H.G., Cittadini, A., Maccauro, G., Covacci, V., Bruzzese, N., Ricci, G.A. and Marmo, E. (1998) Y-TZP ceramics for artificial joint replacements. *Biomaterials*, **19**, 1489–94.

137 Chevalier, J., De Aza, A.H., Fantozzi, G., Schehl, M. and Torrecillas, R. (2000) Extending the lifetime of ceramic orthopaedic implants. *Advanced Materials*, **12**, 1619–21.

138 Nawa, M., Yamada, K. and Pezzotti, G. (2008) Microscopic mechanisms behind the toughening behavior of ceria stabilized tetragonal zirconia/alumina nanocomposite for biomedical applications. *Key Engineering Materials*, **361–363**, 813–16.

139 Nawa, M., Nakamoto, S., Sekino, T. and Niihara, K. (1998) Tough and strong Ce-TZP/alumina nanocomposite doped with titania. *Ceramics International*, **24**, 497–506.

140 Tanaka, K., Tamura, J., Kawanabe, K., Nawa, M., Oka, M., Uchida, M., Kokubo, T. and Nakamura, T. (2002) Ce-TZP/Al_2O_3 nanocomposite as a bearing material in total joint replacement. *Journal of Biomedical Materials Research*, **63**, 262–70.

141 Gadow, R. and Kern, F. (2006) Pressureless sintering of injection molded zirconia toughened alumina nanocrystals. *Journal of the Ceramic Society of Japan*, **114**, 958–62.

142 Gutknecht, D., Chevalier, J., Garnier, V. and Fantozzi, G. (2007) Key role of

processing to avoid low temperature ageing in aluminia zirconia composites for orthopaedic application. *Journal of the European Ceramic Society*, **27**, 1547–52.

143 Schehl, M., Díaz, L.A. and Torrecillas, R. (2002) Alumina nanocomposites from powder-alkoxide mixtures. *Acta Materialia*, **50**, 1125–39.

144 Bartolome, J.F., De Aza, A.H., Martin, A., Pastor, J.Y., Llorca, J., Torrecillas, R. and Brunoz, G. (2007) Alumina/zirconia micro/nanocomposites: a new material for biomedical applications with superior sliding wear resistance. *Journal of the American Ceramic Society*, **90**, 3177–84.

145 Chevalier, J., Deville, S., Fantozzi, G., Bartolomé, J.F., Pecharroman, C., Moya, J.S., Diaz, L.A. and Torrecillas, R. (2005) Nanostructured ceramic oxides with a slow crack growth resistance close to covalent materials. *Nano Letters*, **5**, 1297–301.

146 Affatato, S., Torrecillas, R., Taddei, P., Rocchi, M., Fagnano, C., Ciapetti, G. and Toni, A. (2006) Advanced nanocomposite materials for orthopaedic applications. I. A long-term in vitro wear study of zirconia-toughened alumina. *Journal of Biomedical Materials Research, Part B*, **78B**, 76–82.

147 Kuntz, J.D., Zhan, G.-D. and Mukherjee, A.K. (2004) Nanocrystalline-matrix ceramic composites for improved fracture toughness. *MRS Bulletin*, **29**, 22–7.

148 Bhaduri, S. and Bhaduri, S.B. (1997) Enhanced low temperature toughness of Al_2O_3-ZrO_2 nano/nano composites. *Nanostructured Materials*, **8**, 755–63.

149 Wenz, H.J., Bartsch, J., Wolfart, S. and Kern, M. (2008) Osseointegration and clinical success of zirconia dental implants: a systematic review. *International Journal of Prosthodontics*, **21**, 27–36.

150 Yin, L., Jahanmir, S. and Ives, L.K. (2003) Abrasive machining of porcelain and zirconia with a dental handpiece. *Wear*, **255**, 975–89.

151 Pilathadka, S., Vahalová, D. and Vosáhlo, T. (2007) The zirconia: a new dental ceramic material. An overview. *Prague Medical Report*, **108**, 5–12.

152 Cales, B. (1998) Colored zirconia ceramics for dental applications. *Bioceramics*, **11**, 591–4.

153 Kelly, J.R. (2007) Developing meaningful systematic review of CAD/CAM reconstructions and fiber-reinforced composites. *Clinical Oral Implants Research*, **18**, 205–17.

154 Oetzel, C. and Clasen, R. (2006) Preparation of zirconia dental crowns via electrophoretic deposition. *Journal of Materials Science*, **41**, 8130–7.

155 Trunec, M. and Maca, K. (2007) Nanocomposite as a bearing material in total joint replacement. *Journal of the American Ceramic Society*, **90**, 2735–40.

156 Hench, L.L. (1998) Biomaterials: a forecast for the future. *Biomaterials*, **19**, 1419–23.

157 Dujardin, E. and Mann, S. (2002) Bio-inspired materials chemistry. *Advanced Materials*, **14**, 775–88.

158 Zhang, J., Iwasa, M., Kotobuki, N., Tanaka, T., Hirose, M., Ohgushi, H. and Jiang, D. (2006) Fabrication of hydroxyapatite–zirconia composites for orthopedic applications. *Journal of the American Ceramic Society*, **89**, 3348–55.

159 Silva, V.V. and Domingues, R.Z. (1997) Hydroxyapatite–zirconia composites prepared by precipitation method. *Journal of Materials Science: Materials in Medicine*, **8**, 907–10.

160 Wang, Q., Ge, S. and Zhang, D. (2005) Nano-mechanical properties and biotribological behaviors of nanosized HA/partially-stabilized zirconia composites. *Wear*, **259**, 952–7.

161 Khalil, K.A., Kim, S.W. and Kim, H.Y. (2007) Consolidation and mechanical properties of nanostructured hydroxyapatite-(ZrO_2 + 3 mol% Y_2O_3) bioceramics by high-frequency induction heat sintering. *Materials Science and Engineering A*, **456**, 368–72.

162 Shen, L., Adolfsson, E., Nygren, M., Gao, G., Kawaoka, H. and Niihara, K. (2001) Dense hydroxyapatite-zirconia ceramic composites with high strength for biological applications. *Advanced Materials*, **13**, 214–16.

163 Ahn, E.S., Gleason, N.J., Nakahira, A. and Ying, J.Y. (2001) Nanostructure processing of hydroxyapatite-based bioceramics. *Nano Letters*, **1**, 149–53.

164 Ahn, E.S., Gleason, N.J. and Ying, J.Y. (2005) The effect of zirconia reinforcing agents on the microstructure and mechanical properties of hydroxyapatite-based nanocomposites. *Journal of the American Ceramic Society*, **88**, 3374–9.

165 Ben-Nissan, B. (2004) Nanoceramics in biomedical applications. *MRS Bulletin*, **29**, 28–32.

166 Khor, K.A., Gu, Y., Pan, D. and Cheang, P. (2004) Microstructure and mechanical properties of plasma sprayed HA/YSZ/Ti-6Al-4V composite coatings. *Biomaterials*, **25**, 4009–17.

167 Balamurugan, A., Balossier, G., Kannan, S., Michel, J., Faure, J. and Rajeswari, S. (2007) Electrochemical structural characterisation of zirconia reinforced hydroxyapatite bioceramic sol-gel coatings on surgical grade 316L SS for biomedical application. *Ceramics International*, **33**, 605–14.

168 Wang, F., Tan, W.B., Zhang, Y., Fan, X. and Wang, M. (2006) Luminescent nanomaterials for biological labelling. *Nanotechnology*, **17**, R1–13.

169 Michalet, X., Pinaud, F., Lacoste, T.D., Dahan, M., Bruchez, M.P., Alivisatos, A.P. and Weiss, S. (2001) Properties of fluorescent semiconductor nanocrystals and their application to biological labeling. *Single Molecules*, **2**, 261–76.

170 Weng, J. and Ren, J. (2006) Luminescent quantum dots: a very attractive and promising tool in biomedicine. *Current Medicinal Chemistry*, **13**, 897–909.

171 Hardman, R. (2006) A toxicologic review of quantum dots: toxicity depends on physicochemical and environmental factors. *Environmental Health Perspectives*, **114**, 165–72.

172 De la Rosa-Cruz, E., Diaz-Torres, L.A., Salas, P., Rodríguez, J.A., Kumar, G.A., Meneses, M.A., Mosino, J.F., Hernández, J.M. and Barbosa-García, O. (2003) Luminescent properties and energy transfer in ZrO_2:Sm^{3+} nanocrystals. *Journal of Applied Physics*, **94**, 3509–15.

173 Chen, L., Liu, Y. and Li, Y. (2004) Preparation and characterization of ZrO_2:Eu^{3+} phosphors. *Journal of Alloys and Compounds*, **381**, 266–71.

174 Julián, B., Corberán, R., Cordoncillo, E., Escribano, P., Viana, B. and Sanchez, C. (2005) One-pot synthesis and optical properties of Eu^{3+}-doped nanocrystalline TiO_2 and ZrO_2. *Nanotechnology*, **16**, 2707–13.

175 Speghini, A., Bettinelli, M., Riello, P., Bucella, S. and Benedetti, A. (2005) Preparation, structural characterization, and luminescence properties of Eu^{3+}-doped nanocrystalline ZrO_2. *Journal of Materials Research*, **20**, 2780–91.

176 Ghosh, P. and Patra, A. (2006) Role of surface coating in ZrO_2/Eu^{3+} nanocrystals. *Langmuir*, **22**, 6321–7.

177 Diaz-Torres, L.A., De la Rosa, E., Salas, P., Romero, V.H. and Angeles-Chavez, C. (2008) Efficient photoluminescence of Dy^{3+} at low concentrations in nanocrystalline ZrO_2. *Journal of Solid State Chemistry*, **181**, 75–80.

178 Liu, H.-Q., Wang, L.-L., Chen, S.-G. and Zou, B.-S. (2008) Optical properties of nanocrystal and bulk ZrO_2:Eu^{3+}. *Journal of Alloys and Compounds*, **448**, 336–9.

179 Ye, Z., Tan, M., Wang, G. and Yuan, J. (2005) Preparation, characterization and application of fluorescent terbium complex-doped zirconia nanoparticles. *Journal of Fluorescence*, **15**, 499–505.

180 van de Rijke, F., Zijlmans, H., Li, S., Vail, T., Raap, A.K., Niedbala, R.S. and Tanke, H.J. (2001) Up-converting phosphor reporters for nucleic acid microarrays. *Nature Biotechnology*, **19**, 273–6.

181 Corstjens, P.L.A.M., Li, S., Zuiderwijk, M., Kardos, K., Abrams, W.R., Niedbala, R.S. and Tanke, H.J. (2005) Infrared up-converting phosphors for bioassays. *IEE Proceedings: Nanobiotechnology*, **152**, 64–72.

182 Salas, P., Angeles-Chavez, C., Montoya, J.A., De La Rosa, E., Diaz-Torres, L.A., Desirena, H., Martinez, A., Romero-Romo, M.A. and Morales, J. (2005) Synthesis, characterization and luminescence properties of ZrO_2:Yb^{3+}-Er^{3+} nanophosphor. *Optical Materials*, **27**, 1295–300.

183 Hyppänen, I., Hölsä, J., Kankare, J., Lastusaari, M. and Pihlgren, L. (2007) Upconversion properties of nanocrystalline ZrO_2:Yb^{3+}, Er^{3+} phosphors. *Journal of Nanomaterials*, Article no. 16391.

184 Patra, A., Friend, C.S., Kapoor, R. and Prasad, P.N. (2002) Upconversion in Er^{3+}:ZrO_2 nanocrystals. *The Journal of Physical Chemistry B*, **106**, 1909–12.

185 De la Rosa-Cruz, E., Diaz-Torres, L.A., Rodriguez-Rojas, R.A., Meneses-Nava, M.A. and Salas, P. (2003) Luminescence and visible upconversion in nanocrystalline ZrO_2:Er^{3+}. *Applied Physics Letters*, **83**, 4903–5.

186 Chen, G.Y., Zhang, Y.G., Somesfalean, G., Zhang, Z.G., Sun, Q. and Wang, F.P. (2006) Two-color upconversion in rare-earth-ion-doped ZrO_2 nanocrystals. *Applied Physics Letters*, **89**, Article no. 163105.

187 López-Luke, T., De la Rosa, E., Salas, P., Angeles-Chavez, C., Díaz-Torres, L.A. and Bribiesca, S. (2007) Enhancing the up-conversion emission of ZrO_2:Er^{3+} nanocrystals prepared by a micelle process. *Journal of Physical Chemistry C*, **111**, 17110–17.

188 Zhou, S., Garnweitner, G., Niederberger, M. and Antonietti, M. (2007) Dispersion behavior of zirconia nanocrystals and their surface functionalization with vinyl group-containing ligands. *Langmuir*, **23**, 9178–87.

189 Scholz, S. and Kaskel, S. (2008) Surface functionalization of ZrO_2 nanocrystallites for the integration into acrylate nanocomposite films. *Journal of Colloid and Interface Science*, **323**, 84–91.

190 Renger, C., Kuschel, P., Kristoffersson, A., Clauss, B., Oppermann, W. and Sigmund, W. (2004) Colloid probe investigation of the stabilization mechanism in aqueous 1,2-propanediol nano-zirconia dispersions. *Physical Chemistry Chemical Physics*, **6**, 1467–74.

191 Lü, Q., Guo, F.-Y., Sun, L., Li, A. and Zhao, L.-C. (2008) Surface modification of ZrO_2:Er^{3+} nanoparticles to attenuate aggregation and enhance upconversion fluorescence. *Journal of Physical Chemistry C*, **112**, 2836–44.

192 Willner, I. and Katz, E. (2000) Integration of layered redox proteins and conductive supports for bioelectronic applications. *Angewandte Chemie – International Edition*, **39**, 1180–218.

193 Cooper, C.L., Dubin, P.L., Kayitmazer, A.B. and Turksen, S. (2005) Polyelectrolyte-protein complexes. *Current Opinion in Colloid and Interface Science*, **10**, 52–78.

194 Wang, G., Lu, H. and Hu, N. (2007) Electrochemically and catalytically active layer-by-layer films of myoglobin with zirconia formed by vapor-surface sol-gel deposition. *Journal of Electroanalytical Chemistry*, **599**, 91–9.

195 Wang, G., Liu, Y. and Hu, N. (2007) Comparative electrochemical study of myoglobin loaded in different types of layer-by-layer assembly films. *Electrochimica Acta*, **53**, 2071–9.

196 Liu, S., Dai, Z., Chen, H. and Ju, H. (2004) Immobilization of hemoglobin on zirconium dioxide nanoparticles for preparation of a novel hydrogen peroxide biosensor. *Biosensors and Bioelectronics*, **19**, 963–9.

197 Zhao, G., Feng, J.-J., Xu, J.-J. and Chen, H.-Y. (2005) Direct electrochemistry and electrocatalysis of heme proteins immobilized on self-assembled ZrO_2 film. *Electrochemistry Communications*, **7**, 724–9.

198 Zong, S., Cao, Y., Zhou, Y. and Ju, H. (2006) Zirconia nanoparticles enhanced grafted collagen tri-helix scaffold for unmediated biosensing of hydrogen peroxidase. *Langmuir*, **22**, 8915–19.

199 Liang, K.-Z. and Mu, W.-J. (2008) ZrO_2/DNA-derivated polyion hybrid complex membrane for the determination of hydrogen peroxide in milk. *Ionics*, **14**, 533–9.

Keywords

zirconia; nanoparticles; nanotubes; synthesis; sol–gel; bioceramics; implants

9
Metal Oxide Nanomaterials for Water Treatment

Jinbo Fei and Junbai Li

9.1
Introduction

In today's world, approximately 20% of the population has no access to safe water, 40% suffers the consequences of unacceptable sanitary conditions, and millions of people die every year from diseases transmitted through unsafe water [1]. Moreover, the situation will undoubtedly worsen, in both developing and developed countries, as materials ranging from heavy metals and distillates to microorganisms continue to attack water supplies as contaminants, mainly as a result of human activities. Very recently, Shannon *et al.* claimed that during the coming decades, water scarcity and water stress may become watchwords that prompt action ranging from wholesale population migration to war, unless new, rapid, more effective, low-cost and robust procedures to supply clean water are identified [2].

Fortunately, nanotechnology – with its emerging opportunities – can provide powerful solutions for some environmental problems. Due to their unique activity towards recalcitrant contaminants and the flexibility of their applications, many nanomaterials are currently being examined for the treatment of ground water, surface water and drinking water contaminated by toxic metal ions, organic and inorganic solutes and microorganisms. In particular, metal oxide nanomaterials are undergoing development for environmental monitoring, remediation and pollution prevention, in addition to the effective saving of resources. These properties are based on the rich valence states, vast surfaces and varying electronic structures of nanomaterials. Previously, Theron *et al.* prepared an excellent general review on nanotechnology and water treatment, which described a variety of nanomaterials and their applications for water treatment, purification and disinfection [3]. In this chapter, our intention is to highlight the details of current research investigations into typical metal oxide nanomaterials (TiO_2, Fe_3O_4/Fe_2O_3, MnO_2, CeO_2, MgO and Al_2O_3) and their applications in water treatment.

Nanomaterials for the Life Sciences Vol. 2: Nanostructured Oxides. Edited by Challa S. S. R. Kumar

ISBN: 978-3-527-32152-0

9.2 Titanium Dioxide (TiO_2)

Since the initial discovery of photocatalytic water splitting on titanium dioxide (TiO_2) electrodes [4], much attention has been paid to applying TiO_2 as a high-quality photocatalyst for water treatment. This proposal is based not only on the potential of TiO_2 to degrade a wide range of organic and inorganic compounds, but also on its physical and chemical stability, lower cost and resistance to corrosion [5]. The decrease of TiO_2 particle size into nanoscale will result in a measure of selectivity in the photoreactions and the presence of crystal defects, which in turn will allow the electron-hole separation yield to be maximized [6–8]. During the past few years, many TiO_2 nanostructures – such as nanoparticles, nanotubes/nanorods, nanofilms and nanocomposites – have been synthesized in various ways and used widely in the treatment of water.

9.2.1 TiO_2 Nanoparticles

9.2.1.1 Degradation of Organic Pollutants

From laboratory to plant, the commercially available TiO_2 named Degussa P-25 (30 nm) has been widely used in the treatment of contaminated water, and has indeed become a research standard reference [9, 10]. This two-phase composite (anatase and rutile) has been considered to have a synergy effect for photocatalytic reactions [11].

A smaller titanium dioxide was also used for the degradation of certain organic pollutants. For example, TiO_2 with diameters of 6 to 10 nm were prepared for the photocatalytic degradation of hexahydro-1,3,5-trinitro-1,3,5-triazine (RDX) wastewater under simulated sunlight [12]. The result showed that the RDX degradation percentage of the photocatalytic process was higher than that of Fenton oxidation before 80 min, equivalent after 80 min, and reached 95% or above after 120 min.

During recent years, the synthesis of doped TiO_2 nanoparticles has attracted increasing attention in organic wastewater treatment [13–17]. For example, Liu *et al.* introduced a low-cost and high-efficiency approach for preparing nitrogen-doped TiO_2 with a lower band-gap energy which can be responsive to visible light [18]. The N-doped TiO_2 showed superior photocatalytic activities in both chemical compound degradation and bactericidal reactions over commercially available Degussa P25 power, under identical solar light exposure.

As well as nonmetal-doped TiO_2 nanoparticles, metal-doped TiO_2 nanoparticles have also been developed for the degradation of organic pollutants. As an example, Fe(III)-doped TiO_2 nanoparticles have been prepared to degrade phenol in water under solar light irradiation [19]. Furthermore, Oh *et al.* studied the effect of additives (Si, Fe) on the photocatalytic activity of titanium dioxide powders prepared by thermal plasma [20]. Similarly, the photocatalytic degradation of 2-chlorophenol (2-CP) in aqueous solution was evaluated using a Co-doped TiO_2 nanoparticulate catalyst [21]. Specifically, rare earth metal Pr-doped TiO_2 showed a high activity for

the photocatalytic degradation of phenol [22], the degradation process having been optimized using 1 g l^{-1} Pr-doped TiO_2 with a Pr(III) concentration of 0.072 mol% after 2 h irradiation. As a systemic study, Shah *et al.* reported that the metallo-organic chemical vapor deposition (MOCVD) method could be used successfully to synthesize pure TiO_2 and Nd^{3+}-, Pd^{2+}-, Pt^{4+}- and Fe^{3+}-doped TiO_2 nanoparticles [23]. When the effects of different types of dopant on the photocatalytic activity were investigated by the degradation of 2-CPs in UV light, it was suggested that the negative and positive effects could be ascribed to the position of the dopants in the nanoparticles and the difference in their ionic radii with respect to that of Ti^{4+}. There is no general way to guide and evaluate the TiO_2-doped photocatalytic activity associated with the relationships of the category, quantity and position of dopant, since doping is referred to as a very complex processes.

9.2.1.2 Catalysis and Adsorption of Inorganic Anions

Arsenic has, for many centuries, been considered as one of the most toxic elemental contaminants. In the presence of sunlight and dissolved oxygen, Pena *et al.* investigated the effectiveness of nanocrystalline TiO_2 in removing arsenate [As(V)], arsenite [As(III)] and the photocatalytic oxidation of As(III) [24]. These studies revealed that the TiO_2 was effective for arsenic removal at pH 8, and had a maximum removal quantity for As(III) at pH approximately 7.5 in the challenging water. Moreover, the adsorption capacity of the TiO_2 for As(V) and As(III) was much higher than that of the commercial TiO_2 (Degussa P-25) and granular ferric oxide.

Cr(VI) represents another typical (and also carcinogenic) pollutant that is found in the wastewater from industrial processes, such as mining, leather tanning and paint-making. In a typical treatment process, Cr(VI) can be reduced to less toxic Cr(III) by reducing agents, although this usually leads to a much larger dosage of the reducing agent than the stoichiometric amount. To overcome this drawback, photocatalytic reduction – as an environment-friendly treatment process – has been developed and proven effective in the reduction of Cr(VI) to Cr(III). For example, when TiO_2 and sulfated TiO_2 (SO_4^{2-}/TiO_2) catalysts with different textural properties were prepared for the photocatalytic reduction of Cr(VI) to Cr(III) [25], the calcination temperature was shown to be a key factor that affected the catalytic activities. Consequently, the research group involved suggested that SO_4^{2-} on the surface could provide an acid environment over the catalyst surface and in turn promote the photoreduction of Cr(VI).

9.2.1.3 Disinfection of Microorganisms

When titanium dioxide nanoparticles and nanocrystallines are irradiated with UV-visible light, this semiconductor can exhibit strong bactericidal activity. For instance, Chang *et al.* showed that the irradiation of suspensions of *Escherichia coli* and TiO_2 (P-25) with of wavelengths longer than 380 nm led to bactericidal action within minutes [26]. Furthermore, the trends in these simulated laboratory experiments were mimicked in outdoor tests conducted under the summer, noonday sun [27]. Elsewhere, Maness *et al.* presented the first evidence that lipid peroxida-

tion reaction was the underlying mechanism of cell death of *E. coli* K-12 irradiated in the presence of a TiO_2 photocatalyst [28]. These authors claimed that the TiO_2 photocatalysis initiated peroxidation of the unsaturated phospholipid component of the lipid membrane, thus inducing a major disorder in the *E. coli* cell membrane and killing the cells.

TiO_2 nanoparticles, as-doped, could also be used for the disinfection of wastewater. For example, Yu *et al.* reported that sulfur-doped titanium dioxide exhibited a strong visible-light-induced antibacterial effect [29], while Egerton *et al.* found that the photoelectrocatalytic disinfection of *E. coli* by an iron-doped TiO_2 sol–gel electrode was more efficient than disinfection by the corresponding electrode when undoped [30].

9.2.2
TiO_2 Nanotubes and Nanorods

The band-gap of aqueous colloids of titanate nanotubes at room temperature has been estimated at approximately 3.87 eV, which is close to the value of about 3.84 eV in two-dimensional (2-D) titanate nanosheets, but much higher than the value of about 3.2 eV in bulk TiO_2 [31, 32]. Three general approaches – namely alkaline hydrothermal [33], template-assisted [34] and anodic oxidation [35] – for the preparation of nanostructured titanate and TiO_2 have been reviewed by Bavykin [36]. TiO_2 nanotubes have potential applications in solar cells and hydrogen production [37–41], although the details of TiO_2 nanotubes, which were developed directly for the photocatalytic removal of organic pollutants, have been rarely reported.

As a typical study, the synthesis of TiO_2-based p-n junction nanotubes has been described [42]. The outside of the tubes was comprised of TiO_2, and the inside platinum. The nature of the p-n junction allowed the outside of the tube to act as an oxidizing surface, while the inside of the tube acted as a reductive surface. When exposed to UV light, these catalysts were able to degrade toluene, with experimental results showing that the photocatalytic destruction rates of these catalysts were higher than those of non-nanotube-structured material and nanotubes without a p-n junction.

Moreover, titanate nanotubes can adsorb functional cations from aqueous solution, which may in turn provide a strategy for the deposition of active catalysts on the surface of nanotubes [43]. In addition, when nanoparticles and titanate nanotubes have good electrical contacts, it can provide an efficient interfacial charge-transfer region, which makes this binary system also suitable for photocatalysis. In photocatalytic processes, the photosensibilizer could be either wide-bandgap titanate nanotubes [44] or narrow-bandgap semiconductor nanoparticles [45, 46]. At present, these studies are still in the early stages of research, but will undoubtedly find applications in nanofiltration membranes for water treatment.

As in the case of TiO_2 nanotubes, TiO_2 nanorods – as another one-dimensional (1-D) nanostructure – have also been developed for water purification. By using a nonhydrolytic sol–gel reaction between titanium(IV) isopropoxide and oleic acid,

large-scale TiO_2 nanorods with a narrow distribution of diameters were prepared (see Figure 9.1) [47]. The anisotropic naked TiO_2 nanorods exhibited a higher photocatalytic activity than the P-25 photocatalyst for the photocatalytic inactivation of *E. coli* (see Figure 9.1c).

9.2.3 TiO_2 Nanofilms

Yu *et al.* reported that transparent anatase mesoporous TiO_2 ($MTiO_2$) and TiO_2 nanometer thin films were prepared on soda-lime glass and fused quartz by the reverse-micelle and sol–gel methods, respectively [48]. $MTiO_2$ thin films showed a higher photocatalytic activity than that of the TiO_2 thin films, because of their higher specific surface areas. Shieh and coworkers developed a new photocatalyst thin film that has strong antibacterial action in visible light [49]. In this study, the radiofrequency (RF) sputter technique was used to deposit a defective titanium dioxide (TiO_x, $x < 2$) photocatalyst thin film on glass and steel substrates. Subsequently, it was demonstrated that the antibacterial performance rate against *E. coli* could reach 99.99% in visible light.

Furthermore, in order to illustrate the mechanism for the photokilling of *E. coli* cells on TiO_2 thin film, the survival of intact cells and spheroplasts was investigated as a function of photoillumination time [50]. Recently, on TiO_2 porous films, attenuated total reflectance (ATR)-FTIR spectroscopy was used to study the photocatalytic peroxidation of *E. coli* cells, lipopolysaccharide (LPS), phosphatidylethanolamine (PE) and peptidoglycan (PGN) of the *E. coli* membrane wall [51].

9.2.4 TiO_2 Nanocomposites

Nanocomposites can combine many advantages from single components. In the case of water treatment, by using conventional grafting, precipitation or impregnation, TiO_2 nanoparticles and nanocrystals can be deposited and incorporated to form suitable nanocomposites [52–54]. For example, López-Munoz *et al.* reported the use of tubular arrays of mesoporous and microporous molecular sieves composed of TiO_2 nanoparticles, supported by mesoporous silica, for the water remediation of aromatic pollutants in the presence of UV light [55]. In another report, a novel biocidal photocatalytic nanocomposite, composed of TiO_2 and multi-walled carbon nanotubes (MWNTs) showed a threefold higher photocatalytic specific surface area than commercial TiO_2 nanoparticles (P-25) when dispersed in water. The irradiation of bacterial endospores (*Bacillus cereus*) with solar UV lamps in the presence of novel photocatalyst led to the successful inactivation of the spores, whereas solar UV lamps only or solar UV lamps with Degussa P-25 showed no significant inactivating behavior [56]. Photocatalysts composed of nanostructured TiO_2 and Fe_2O_3, have also been prepared and used for removal of colored humic acids from wastewater in a UV bubble photocatalytic reactor [57]. Here, Shephard *et al.* introduced an experimental laboratory-scale 'falling film' reactor which

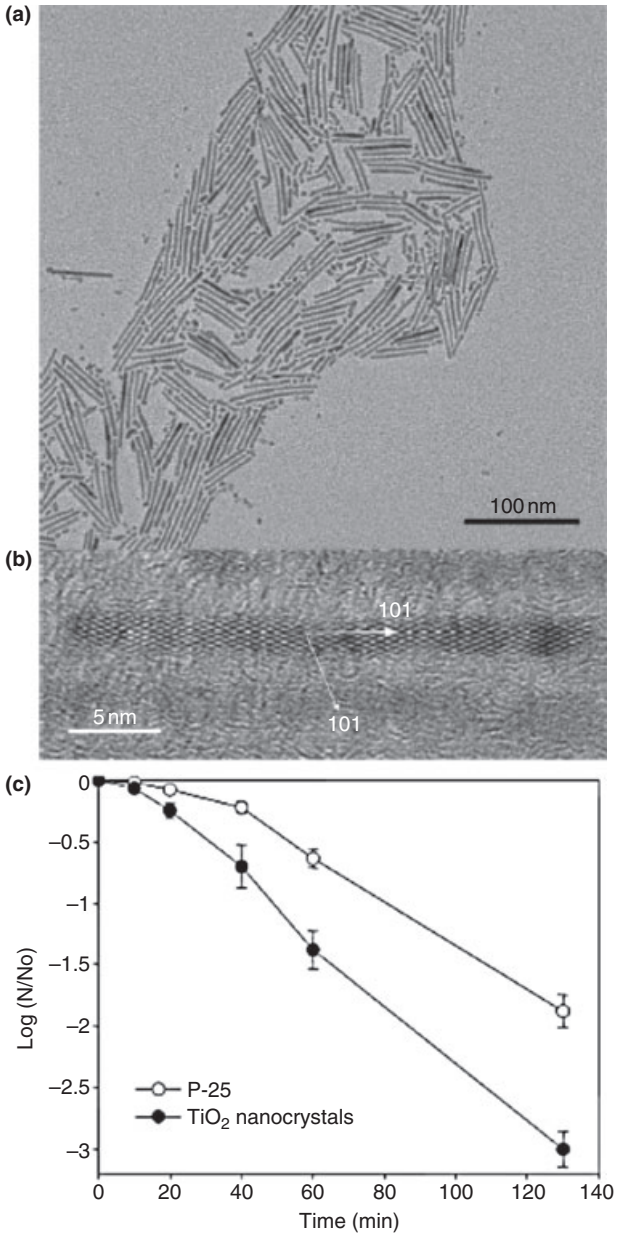

Figure 9.1 (a) Transmission electron microscopy (TEM) image of as-synthesized TiO_2 nanocrystals; (b) High-resolution (HR) TEM image of TiO_2 nanorods; (c) The photocatalytic inactivation of *E. coli* using naked TiO_2 nanocrystals and Degussa P-25 as photocatalysts. Reproduced with kind permission from Ref. [47]; © American Chemical Society.

involved TiO_2 nanoparticles for studying the photocatalytic degradation of microcystins in aqueous solution [58].

Several methods have been developed to lower the band-gap energy of TiO_2 nanocomposites, examples being sensitizing by dyes or by having semiconductors with lower band-gaps [59]. For instance, Bae *et al*. reported an example of a visible-light photocatalyst based on TiO_2 modified by ruthenium-complex sensitizers and noble metal deposits such as Pt, Au, Ag and Pd [60]. These authors discussed the effects of metal loading on the visible light activity, and its implications for the efficient visible-light photocatalyst development. CdSe-modified rutile TiO_2 nanocrystals were synthesized by the hydrothermal method, while the photoactivities of the new photocatalyst under visible light illumination were demonstrated by the degradation of methylene blue (MB) [61]. As expected, after sensitization TiO_2 was significantly responsive to visible light illumination, which resulted in the visible light photoactivities increasing. Similarly, nanosized CdS-coupled TiO_2 nanocrystals with an enhanced activity were prepared using a microemulsion-mediated solvothermal method [62]. However, the toxicity and environmental impact was on major concern due to the heavy metal Cd(II) content of these two TiO_2 nanocomposites.

9.3 Iron Oxides

As a typical magnetic material, iron oxides are of major interest in a wide range of fields, including magnetic fluids [63], catalysis [64–66], magnetic resonance imaging (MRI) [67–69], biological cell labeling and sorting [70] and high-density information storage [71]. Whilst many suitable methods such as coprecipitation, thermal decomposition and/or reduction, micelle synthesis and hydrothermal synthesis have been developed for the synthesis of iron oxide nanoparticles, the successful application of such magnetic nanoparticles in these areas is heavily dependent on the stability of the particles under a range of different conditions. Most recently, Lu *et al*. have reviewed the synthesis, protection, functionalization and application of magnetic nanoparticles (including iron oxides), as well as the magnetic properties of nanostructured systems [72]. However, as yet there are no details of iron oxides nanomaterials being used for applications in water treatment.

Many research groups have used iron oxide nanomaterials, including Fe_2O_3 and Fe_3O_4, as cheap adsorbents to remove toxic ions and organic pollutants from water, and indeed these materials have demonstrated more effective removal capabilities than have bulk materials [73–80]. Typically, Yavuz *et al*. reported that using the high specific surface area of Fe_3O_4 NCs with a diameter of 12 nm, the mass of waste associated with arsenic was removed from water by orders of magnitude [81]. These processes are often the most effective – or perhaps the only – possible approaches for building a good model quantitatively in water treatment [82]. However, iron oxides were shown to act as low arsenic adsorption capacitor, slow

adsorption processes and with narrow optimum pH ranges [83, 84], all of which compromised their applicability. Thus, it is likely that certain protection strategies will be developed, including metal doping, surfactant/polymer coating, silica/carbon coating and embedding them in a matrix/support [85]. For instance, Zhang *et al*. reported that Fe oxide materials doped by the metals (Ce, La, Zr) were used for the removal of anions from groundwater [86]. The maximum adsorption capacity of the Fe—Ce materials for As (V) ions was significantly higher that of the other adsorbents reported, and the preparation and adsorption properties of the Fe—Ce system have been investigated [87, 88].

Iron oxides nanoparticles with surfaces modified by some photocatalysts, functional polymers or special molecules, have also been used as various functional systems for targeted water treatment, including remediation and disinfection. Sun *et al*. reported a novel photocatalysts composed of nanostructured TiO_2 in the anatase phase, which was uniformly deposited onto porous Fe_2O_3 [89]. The experimental results showed the suspended TiO_2/Fe_2O_3 photocatalyst to be effective for the removal of total organic carbon at 61.58% and $color_{400}$ (i.e. absorbance at 400 nm selected for quantitative analysis of color) at 93.25% at 180 min illumination time, under a 0.4 $g\,l^{-1}$ catalyst loading and at pH 7.

Poly (1-vinylimidazole) (Im18) with a reactive silane terminal group was grafted directly onto nanosized magnetic particles (maghemite, $ç$-Fe_2O_3) through siloxane bonds to produce polymer-grafted magnetic nanocomposite particles (Mag-Im18). The Mag-Im18 showed a selective binding of divalent heavy metal ions with a binding strength in the order of $Cu^{2+} > Ni^{2+} > Co^{2+}$. Selective separation/recovery of Cu^{2+} ions from a Cu^{2+}/Co^{2+} aqueous solution was demonstrated over a pH range of 3 to 7 [90].

Interestingly, based on the high affinity between the bisphosphonate and uranyl ions (due to a chelating effect), Xu group reported that bisphosphonate-modified magnetite nanoparticles could be used to remove the radioactive metal toxins UO_2^{2+} with high efficiency from water [91]. This simple procedure proved capable of removing 99% of UO_2^{2+} from the sample. In addition, the principle demonstrated in these studies allowed the detection, recovery and decorporation of other heavy metal toxins from biological systems, either by choosing the ligands or utilizing other novel nanomaterials.

Today, there is a growing threat of water-borne infectious diseases in the developing and developed countries, with *E. coli* contaminations of food products and *Bacillus anthracis* attacks frequently reported in recent headline news bulletins. Hence, an urgent task would be to develop effective methods not only for microbial decontamination but also for their rapid detection, without involving time-consuming cell culture. A photokilling approach for pathogenic bacteria was demonstrated using a new type of magnetic nanoprobe which comprised iron oxide/titania (Fe_3O_4@TiO_2) core/shell magnetic nanoparticles as the photokilling agent [92]. This group demonstrated that the IgG—Fe_3O_4@TiO_2 magnetic nanoparticles had the capacity to target several pathogenic bacteria, and could effectively inhibit the cell growth of bacteria targeted by the nanoparticles under irradiation of a low-power UV lamp within a short time period. In another disinfection study,

bifunctional Fe_3O_4@Ag nanoparticles with both superparamagnetic and antibacterial properties were prepared by reducing silver nitrate on the surface of Fe_3O_4 nanoparticles using a water-in-oil microemulsion method [93]. The nanoparticles presented a good antibacterial performance against *E. coli* (Gram-negative bacterium), *Staphylococcus epidermidis* (Gram-positive) and *Bacillus subtilis* (spores). Moreover, Fe_3O_4@Ag nanoparticles could easily be reclaimed from water by using a magnetic field, thus avoiding any contamination of the surroundings.

Very recently, Huang group developed a magnetic glyco-nanoparticle (MGNP)-based system to rapidly detect *E. coli* in just 5 min by the unique combination of magnetic nanoparticles and diverse carbohydrate bioactivities [94]. Capture efficiencies achieved were up to 88%, and much higher than the 10–30% range typically observed with antibody- or lectin-functionalized magnetic particles [95, 96]. Moreover, the response patterns of the MGNPs were utilized to explain the pathogen identity for accurately differentiating between three *E. coli* strains. This was the first time that MGNPs had been used to detect, quantify and differentiate *E. coli* cells. Decontamination and diagnostic applications can be further developed by this strategy.

Not only zero-dimensional iron oxides nanoparticles can be engineered for water treatment, but novel 3-D or even more complex nanostructures of iron oxides also have excellent abilities to remove heavy metal ions and other pollutants from wastewater. Series of iron oxides with 3-D flowerlike nanostructures have been obtained by a simple calcinations procedure following an ethylene glycol-mediated self-assembly process (see Figure 9.2) [97]. The nanostructures as-prepared are used to adsorb the As(V), Cr(VI) and Orange II, respectively. The maximum capacity of the α-Fe_2O_3 sample was found to be 7.6 mg g^{-1} for As(V), 5.4 mg g^{-1} for Cr(VI) and 43.5 mg g^{-1} for Orange II, which was higher than those of commercial TiO_2 and Fe_2O_3. Moreover, the solid/liquid separation should be straightforward because the sizes of the iron oxide structures were several micrometers (see Table 9.1 and Figure 9.3).

9.4 Manganese Oxides

Manganese oxide species (including MnO, Mn_3O_4, Mn_2O_3 and MnO_2) are of considerable importance in technological applications, including molecular adsorption, catalysis and electrochemical supercapacitors, owing to their structural flexibility combined with novel chemical and physical properties [98–102]. In particular, the many polymorphic forms of manganese dioxide, such as α, β, γ and δ-types, have distinctive properties and now are widely used as ion-sieves and especially as electrode materials in Li/MnO_2 batteries [103]. Bulk MnO_2 and its composites also could be used to remove Cd(II), copper(II), lead(II), uranium(VI), As(III), As(V), Se(IV) and organic waste from water by adsorption and subsequent catalytic combustion at relatively low temperature [104–120]. During the past few years, various nanostructures of MnO_2, including nanoparticles [121], nanorods/

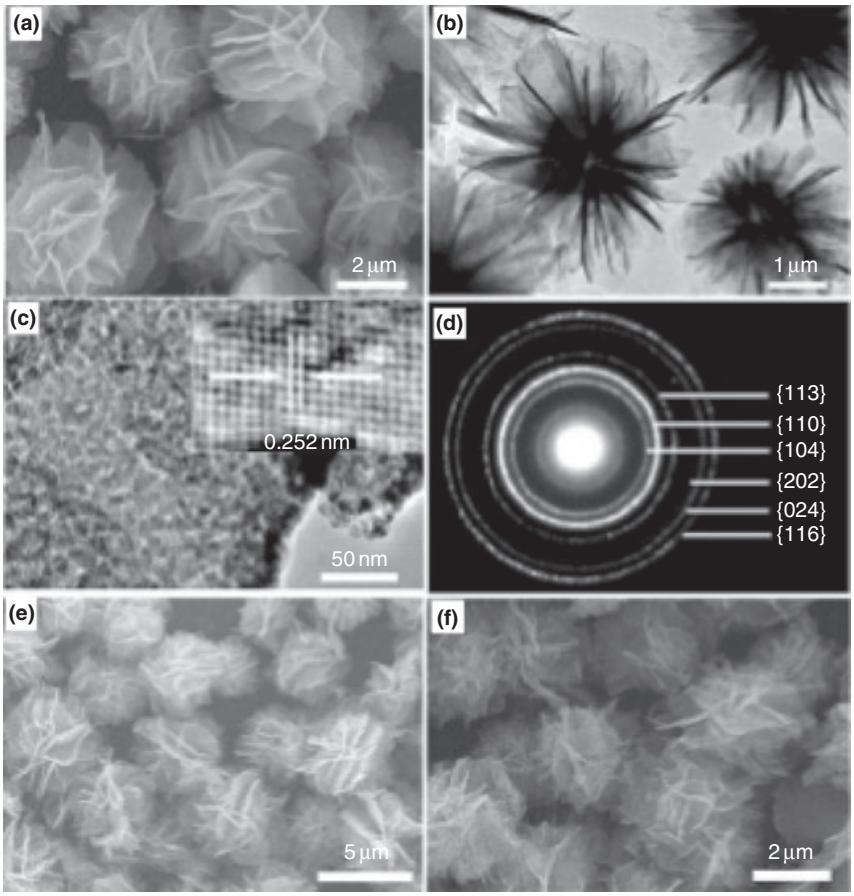

Figure 9.2 (a) Scanning electron microscopy (SEM) and (b) TEM images of the as-obtained α-Fe_2O_3; (c) High-magnification TEM image of the petal of the flower-like structure of the as-obtained α-Fe_2O_3. Inset: High-resolution TEM (HRTEM) image taken from the as-obtained α-Fe_2O_3 nanoparticle; (d) Selected-area electron diffraction (SAED) pattern of the as-obtained α-Fe_2O_3; (e) SEM image of the as-obtained Fe_3O_4; (f) SEM image of the as-obtained c-Fe_2O_3. Reproduced with kind permission from Ref. [97]; © John Wiley & Sons, Inc.

-belts/-wires/-tubes/-fibers [122–126], nanosheets [127], mesoporous/molecular sieves and branched structures [128–132], urchins/orchids and other hierarchical structures [133–136], have been synthesized by different methods. However, to our knowledge, there are few reports in existence concerning the MnO_2 nanostructures used in water treatment.

Among the anisotropic nanostructures, 1-D nanostructures appear as an exciting research field for the great potential of addressing space-confined transport phenomena, as well as applications [137–139]. β-MnO_2 has been used as a catalyst for H_2O_2 decomposition, which would assist when taking advantage of this process

Table 9.1 BET surface area and removal capacity of different types of adsorbent sample. The initial concentration of both As(V) and Cr(VI) was 10.63 mg l^{-1}.

Absorbent sample	BET surface area ($m^2 g^{-1}$)	Removal capacity for As ($mg g^{-1}$)	Removal capacity for Cr ($mg g^{-1}$)
α-Fe_2O_3	40	5.31	4.47
γ-Fe_2O_3	56	4.75	3.86
Fe_3O_4	34	4.65	4.38
Commercial α-Fe_2O_3	2	0.46	0.68
Commercial TiO_2	45	4.11	2.42

Reproduced with kind permission from Ref. [97]; © John Wiley & Sons, Inc.

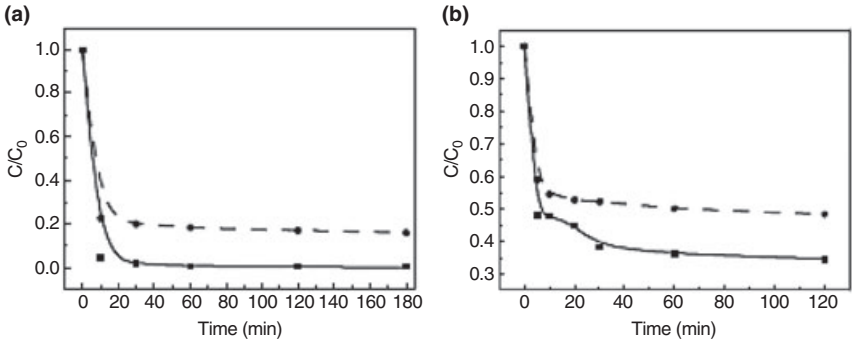

Figure 9.3 (a) Adsorption rate of As(V) (solid line) and Cr(VI) (dashed line) on the as-prepared α-Fe_2O_3; (b) Adsorption rate of the azo-dye Orange II on new as-prepared α-Fe_2O_3 (solid line) and regenerated α-Fe_2O_3 (dashed line). Reproduced with kind permission from Ref. [97]; © John Wiley & Sons, Inc.

to accelerate the decoloration and mineralization of organic dyes [140–142]. Recently, Zhang *et al*. reported that β-MnO_2 nanorods have been synthesized by the thermal decomposition of a template precursor of MnOOH, which was obtained by hydrothermal treatments of $KMnO_4$ in an aqueous ethanol solution (Figure 9.4) [143]. As shown in Figure 9.5, the catalytic activity is much higher than that of commercial microsized MnO_2 powders, due to the larger surface area and more active surface sites of the β-MnO_2 nanorods.

More recently, our group has shown that MnO_2 with intricate and well-controlled 3-D morphologies are synthesized by combining the Kirkendall effect with a sacrificial crystalline template [144]. In detail, the hierarchical hollow manganese dioxide can be successfully synthesized by shape-preserving $KMnO_4$ oxidation of micrometer-scale manganese carbonate structures at room temperature, followed by the selective removal of $MnCO_3$ with HCl. This created a novel route to the synthesis of MnO_2 superstructures with unique morphologies and complex

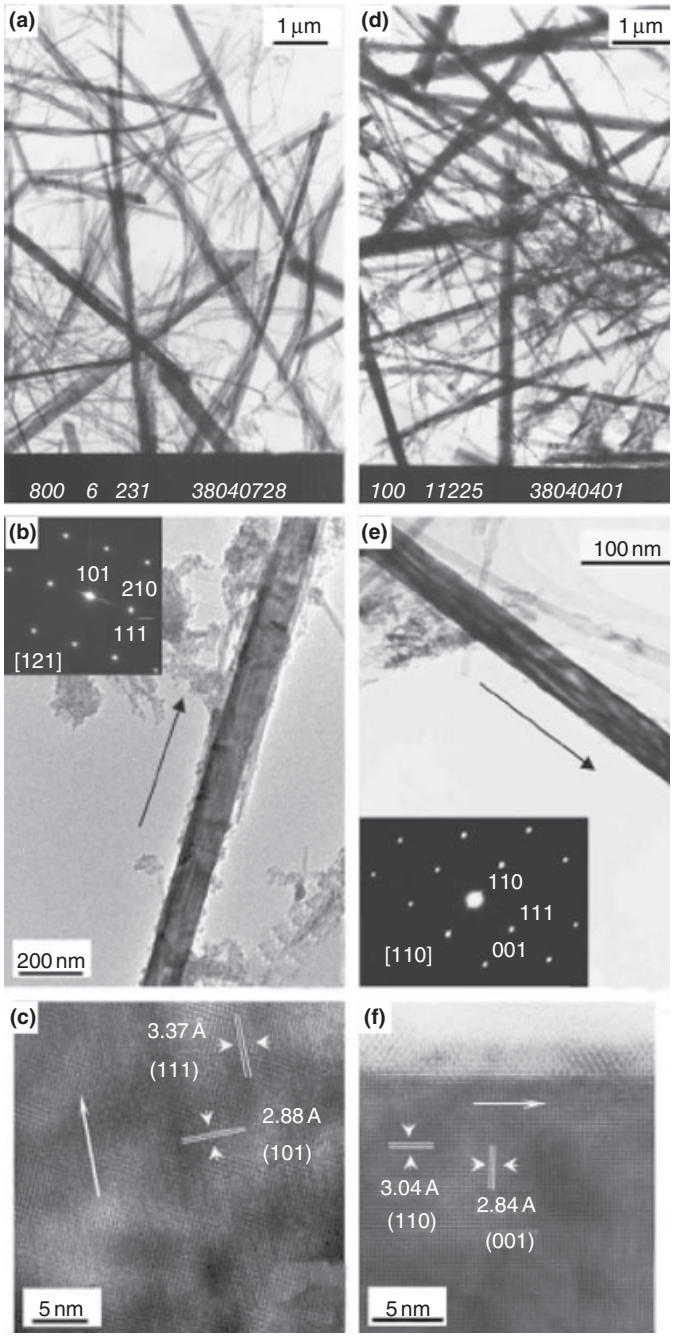

Figure 9.4 TEM/HRTEM images or SAED patterns. (a) MnOOH nanorods; (b) A single MnOOH nanorod (inset: SAED pattern); (c) MnOOH nanorod (HRTEM); (d) β-MnO_2 nanorods; (E) A single β-MnO_2 nanorod (inset: SAED pattern); (f) β-MnO_2 nanorod (HRTEM). Reproduced from Ref. [143]; © Elsevier B.V.

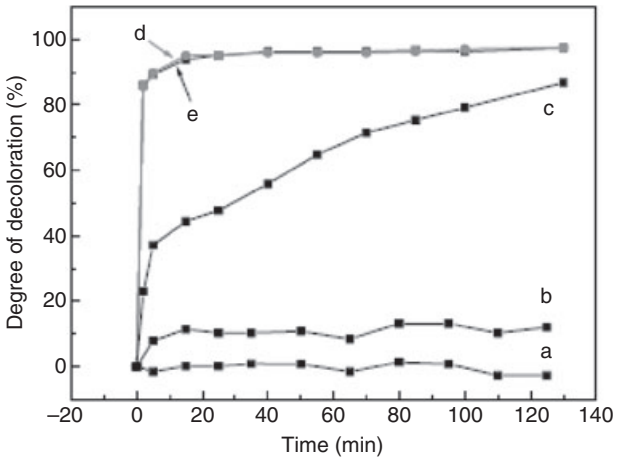

Figure 9.5 Time profiles of methylene blue (MB) degradation. (a) MB + H_2O_2; (b) MB + β-MnO_2 nanorods; (c) MB + H_2O_2 + commercial β-MnO_2 powder; (d) MB + H_2O_2 + MnO_2 nanorods; (e) MB + H_2O_2 + β-MnO_2 nanorods (dark). Reproduced with kind permission from Ref. [143]; © Elsevier B.V.

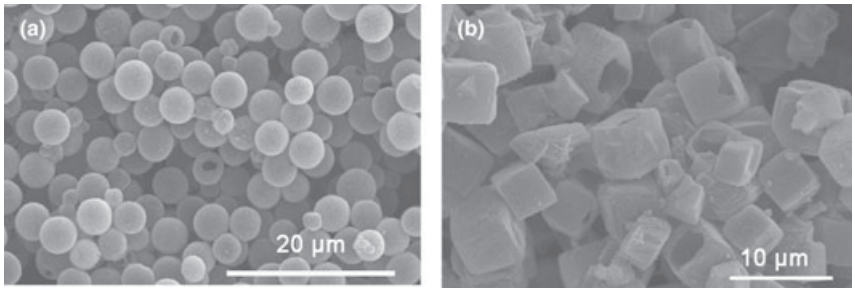

Figure 9.6 The SEM images of (a) MnO_2 microspheres and (b) MnO_2 microcubes. Reproduced with kind permission from Ref. [144]; © John Wiley & Sons, Inc.

hierarchies at the microscale and nanoscale. Based on the novel nanostructures, the as-prepared MnO_2 nanomaterials were used as an adsorbent for the removal of organic pollutant in waste water (see Figure 9.6). Based on the data shown in Figures 9.7 and 9.8, the maximum adsorption capacitor of the nanostructures is about 60 mg g^{-1} for Congo red, which is higher than those of commercial micro-sized MnO_2 and γ-Fe_2O_3 with an average size of 20–30 nm. This might be ascribed to the special hierarchical hollow microstructure of as-obtained MnO_2, which provided a new and more efficient material for applications in organic wastewater treatment. After adsorption, the solid–liquid separation can be achieved very easily because of the relatively higher density, while the MnO_2 nanostructures in water treatment can be reused many times.

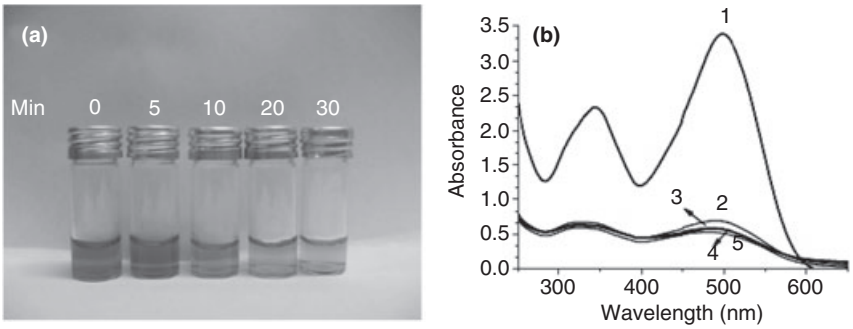

Figure 9.7 (a) Absorption of Congo red with time by new MnO_2 microspherical hollow hierarchical nanostructures; (b) Absorption spectra of a solution of Congo red (100 mg l^{-1}, 20 ml) in the presence of MnO_2 hierarchical hollow microspheres (0.03 g) at different time intervals (min) of: (1) 0; (2) 5; (3) 10; (4) 20; and (5) 30. Reproduced with kind permission from Ref. [144]; © John Wiley & Sons, Inc.

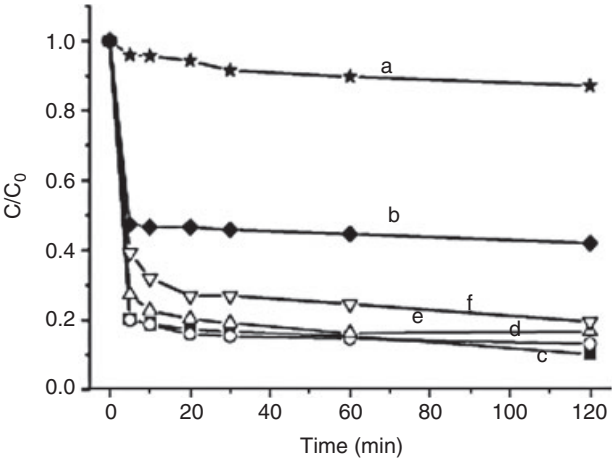

Figure 9.8 Adsorption rate of the azo-dye Congo red on (a) commercial MnO_2; (b) commercial γ-Fe_2O_3; (c) new as-prepared MnO_2 hierarchical hollow microspheres; (d) secondary; (e) third; and (f) fourth regenerated particles. C_0 (mg l^{-1}) is the initial concentration of the Congo red solution; C (mg l^{-1}) is the dye concentration at different intervals during the adsorption. Reproduced with kind permission from Ref. [144]; © John Wiley & Sons, Inc.

9.5 Cerium Oxide (CeO_2)

Hydrous rare earth oxides have been proposed as a new adsorbent for the removal of aqueous hazardous anions such as arsenate, fluoride and phosphate, because of their relatively higher adsorption capacitors [145, 146]. The relatively small ionic potential and strong basicity of rare earth ions bring a strong tendency to dissociate OH groups into hydroxyl ions [147, 148].

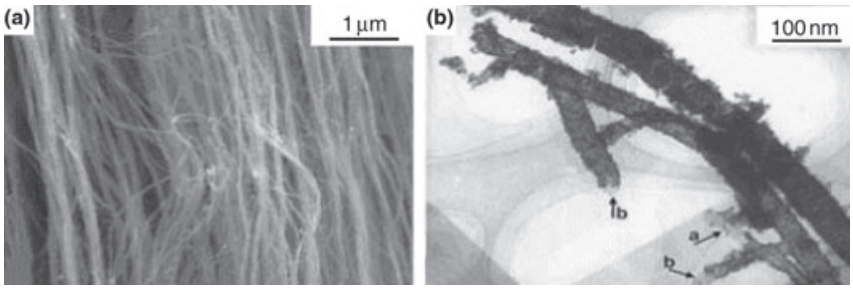

Figure 9.9 (a) SEM images of aligned carbon nanotubes (ACNTs); (b) TEM image of CeO_2/ACNTs. Reproduced with kind permission from Ref. [164]; © Elsevier B.V.

As a typical form of rare earth oxide, ceria has been given wide attention because of its unique physical and chemical properties, including oxygen ion conductivity and oxygen storage capacity [149, 150]. Because of these characteristics, ceria has been widely used for fuel cell [151–153], sensor [154] and chemical–mechanical polishing for microelectronics [155], phosphor/luminescence [156] and catalysts [157, 158]. Until now, the various nanostructures of ceria such as nanoparticles [159], nanorods/ nanowires/ nanotubes [160–162] and nanopolyhedrons [163] have been synthesized using different methods. However, the application of ceria nanostructures for water treatment is rare, mainly because of the high costs involved when using rare earth compounds. Many research groups have attempted to develop new adsorbents with a high adsorption capacity and relatively low cost. For example, cerium oxide nanoparticles supported on carbon nanotubes (CeO_2-CNT) or on aligned carbon nanotubes (CeO_2-ACNTs) have been developed as effective adsorbents for As(V) (see Figure 9.9) [164]. Surprisingly, correct addition of the divalent cations Ca(II) and Mg(II) was found to increase the amount of adsorbed As(V), from 10 to 82 $mg\,g^{-1}$. The largest Cr(VI) adsorption capacity was 30.2 $mg\,g^{-1}$ at pH 7.0, which was twofold higher than those of activated carbon and Al_2O_3 (see Figure 9.10) [165].

Novel nanostructures can expand the advanced applications of nanomaterials. More recently, Wan and coworkers showed that the as-prepared ceria 3-D nanomaterial could be used as a good adsorbent for the removal of As(V) and Cr(VI) in wastewater treatment (Figure 9.11) [166]. The maximum adsorption capacity of the ceria as-prepared was found to be 14.4 $mg\,g^{-1}$ for As(V) and 5.9 $mg\,g^{-1}$ for Cr(VI), respectively. After adsorption, the solid/liquid separation in suspension was performed very easily by using centrifugation. Moreover, this new adsorbent could be recovered and reused, which proved to be very useful for real applications when cutting operational costs. The main advantages of the 3-D nanostructure, which it was claimed made CeO_2 particularly attractive for environmental remediation and other applications, were that: (i) separation and recycle were easier compared with common nanoparticles, as the total size of the structure was on the micrometer scale; (ii) the as-obtained CeO_2 retained a high specific surface area as the micropetal of the composite structure was composed of interconnected nanoparticles; and (iii) the flowerlike structure could effectively prevent further

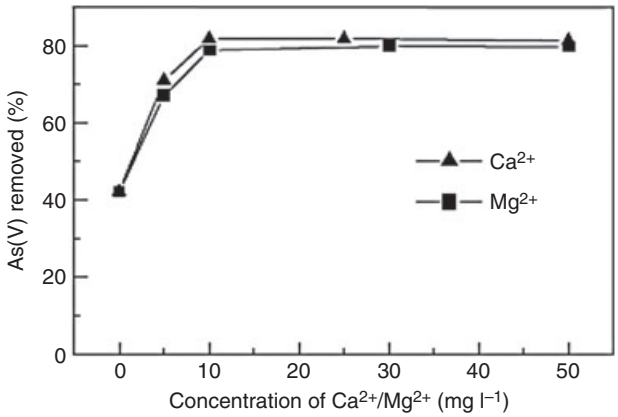

Figure 9.10 The effect of Ca^{2+} and Mg^{2+} on adsorption ($C_0 = 20\,mg\,l^{-1}$; m = 0.025 g; t = 24 h). Reproduced with kind permission from Ref. [165]; © Elsevier B.V.

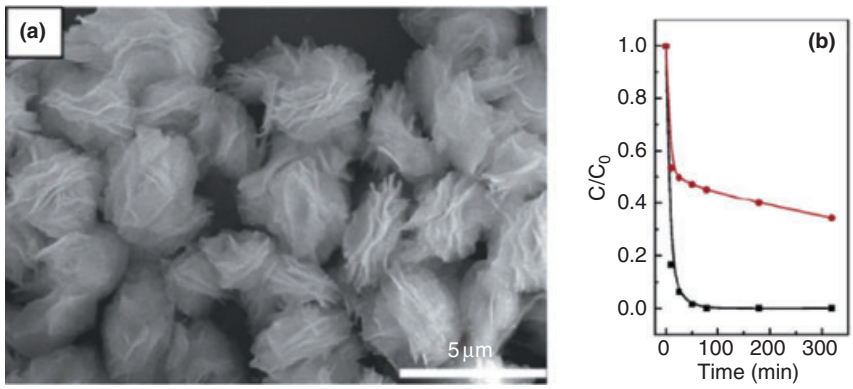

Figure 9.11 (a) SEM image of the as-obtained ceria; (b) Adsorption rate of As(V) (black line, initial concentration of 12.9 mg g^{-1}) and Cr(VI) (red line, initial concentration of 17.2 mg g^{-1}) on the as-prepared ceria. Reproduced with kind permission from Ref. [166]; © American Chemical Society.

aggregation, so that an unblocked mass transfer and high catalytic activity could be retained.

9.6 Magnesium Oxide (MgO)

As far as magnesium oxide (MgO) is concerned, very few reports have been made to date regarding the use of its nanostructures for water treatment. Stoimenov *et al.* reported that reactive magnesium oxide nanoparticles and halogen (Cl_2, Br_2)

adducts of the MgO particles were prepared to contact certain bacteria and spore cells [167]. Bacteriological test data subsequently showed that these materials were very effective against Gram-positive *Staphylococcus aureus* and Gram-negative *E. coli, Klebsiella pneumoniae* and *Pseudomonas aeruginosa*) bacteria, as well as spores. It was suggested that the material's abrasiveness, basic character, electrostatic attraction and oxidizing power (due to the presence of active halogen) combine to promote these biocidal properties. Subsequently, Koper and coworkers described the size effect of the antibacterial activities of MgO nanoparticles [168]. More details indicated that smaller MgO nanoparticles with a diameter of 8 nm had the highest activity in killing *E. coli* and *S. aureus*, while a gradual decrease in antibacterial activity was observed with increase in particle size (from 11 to 23 nm) [169].

9.7 Alumina (Al_2O_3)

Membrane processes are considered as important components of advanced water purification and desalination technologies. Alumina (Al_2O_3) nanoparticles, when used as robust ceramic membranes for supporting functional substances, are applied for water treatment. In recent years, several reactive and functionalized Al_2O_3 membranes have been developed for use in water filtration processes. For example, when using alumina (A-alumoxane) nanoparticles, DeFriend *et al.* reported the fabrication of alumina ultrafilter (UF) membranes which showed selectivity toward three different synthetic dyes [170]. By using a layer-by-layer technique, positive poly(allylamine hydrochloride) (PAH) and negative poly(styrene sulfonate) (PSS) were assembled onto porous alumina for the fabrication of novel nanofilter (NF) membranes [171]. These NF membranes exhibited a high water flux, a high retention of divalent cations (Ca^{2+} and Mg^{2+}), and Cl^-/SO_4^{2-} selectivity ratios of up to 80. Moreover, based on the good catalysis of gold nanoparticles, through layer-by-layer adsorption of polyelectrolytes and citrate-stabilized gold nanoparticles, a composite membrane composed of alumina and polymers was prepared by Dotzauer *et al.* [172]. The result in this study showed that the membranes could reduce more than 99% of 0.4% m*M* 4-nitrophenol to 4-aminophenol. Such studies have been extended through the use of ceramic membranes made from alumina (Al_2O_3) impregnated with crosslinked, silylated dendritic or cyclodextrin polymers [173].

Pd-Cu/γ-alumina, a bimetallic active catalyst, was prepared for the reduction of NO_3^- [174]. It should be noted here that this design can be regarded as one of the futuristic remediation strategies for mineralizing the brine, because this nanocomposite can convert organic compounds into innocuous N_2 without any deleterious brine.

Conventional activated alumina (AA) has certain disadvantages, including ill-defined pore structures, low adsorption capacities and subsequently slow kinetics. In order to overcome these difficulties, through a post-hydrolysis, mesoporous alumina (MA) with a large surface area and uniform pore size was prepared for

arsenic removal [175]. The maximum As(V) uptake by MA was sevenfold higher (121 mg of As(V) g^{-1} and 47 mg of As(III) g^{-1}) than that of conventional AA. Meanwhile, more than 85% of the adsorbed arsenic could be desorbed in less than 1 h using 0.05 *M* NaOH. Thus, it was suggested that MA, as-prepared, could be easily reusable and reclaimable.

In addition, as a relatively mature technique, Al_2O_3 nanomembranes can be obtained by electrochemical anodic oxidation, and their thicknesses, pore diameters and densities adjusted by operational conditions such as electrolytes, voltages and temperatures. Under the assistance of porous aluminum, nanowires, nanotubes and more complex nanostructures can be prepared controllably [176], and this may open the door to the preparation of functional anisotropic NF membranes for high throughput in real applications.

9.8 Summary

Water has a major impact on every facet of human activity, including health, energy and food production, industrial output and the quality of the environment. In recent years, as a result of extended droughts, population growth, more stringent health-based regulations and increasing demands from a variety of users, water is today becoming a competitive resource – indeed, in many parts of the world it is regarded as the 'oil of the twenty-first century'. Metal oxide nanomaterials have many important physico-chemical and biological properties that make them particularly attractive for water treatment. Due to their large surface areas and their size-, shape- and dimension-dependent catalytic properties, considerable efforts have driven exploration into the uses of metal oxide nanomaterials for applications such as catalysis, adsorption and membrane separations. In addition, metal oxide nanomaterials can be functionalized with various chemical groups to increase their affinity towards many interesting compounds. This may result in ligands that are not only recyclable but also have a high capacity and selectivity for toxic metal ions and inorganic anions, as well as for bacteria and viruses in aqueous solutions. Today, we envision metal oxide nanomaterials as being engineered to remove current and emerging pathogens without any toxic byproducts, to realize targeted sensing and detection, transformation and the removal of low-concentration or trace contaminations in high backgrounds at lower cost, and to be reusable, reclaimable and recyclable [177, 178].

It is, therefore, very important that a systematic overview of water treatments be undertaken since, even when efficient metal oxide nanomaterials have been prepared for the treatment of water it is also vital to consider the subject from an engineering aspect. Indeed, in some cases this may be more important than the unique nature of the materials themselves. Likewise, it should be noted – from a precautionary angle – that the very properties of these nanomaterials which render them attractive for water treatment might also cause them to become eco-toxic [179–181].

Acknowledgments

The authors would like to acknowledge the financial support provided by the National Nature Science foundation of China (No. 20574077) and, the Chinese Academy of Sciences (No. Kjcx2-sw-h12).

References

1 Schwarzenbach, R.P., Escher, B.I., Fenner, K., Hofstetter, T.B., Johnson, C.A., Gunten, U.V. and Wehrli, B. (2006) The challenge of micropollutants in aquatic systems. *Science*, **303**, 1072–7.

2 Shannon, M.A., Bohn, P.W., Elimelech, M., Georgiadis, J.G., Marina, B.J. and Mayers, A.M. (2008) Science and technology for water purification in the coming decades. *Nature*, **452**, 301–10.

3 Theron, J., Walker, J.A. and Cloete, T.E. (2008) Nanotechnology and water treatment: applications and emerging opportunities. *Critical Reviews in Microbiology*, **34**, 43–69.

4 Fujishima, A. and Honda, K. (1972) Electrochemical photolysis of water at a semiconductor electrode. *Nature*, **238**, 37–8.

5 Linsebigler, A.L., Lu, G. and Yates, J.T. (1995) Photocatalysis on TiO_2 surfaces: principles, mechanisms, and selected results. *Chemical Reviews*, **95**, 735–58.

6 Zhang, Z., Wang, C.C., Zakaria, R. and Ying, J.Y. (1998) Role of particle size in nanocrystalline TiO_2-based photocatalysts. *Journal of Physical Chemistry B*, **102**, 10871–8.

7 Rao, C.N.R., Kulkarni, G.U., Thomas, P.J. and Edwards, P.P. (2002) Size-dependent chemistry: properties of nanocrystals. *Chemistry – A European Journal*, **8**, 28–35.

8 Amal, R., McEvoy, S., Beydoun, D. and Low, G. (1999) Role of nanoparticles in photocatalysis. *Journal of Nanoparticle Research*, **1**, 439–58.

9 Ohno, T., Sarukawa, K., Tokieda, K. and Matsumura, M. (2001) Morphology of a TiO_2 photocatalyst (Degussa P-25) consisting of anatase and rutile crystalline phases. *Journal of Catalysis*, **203**, 82–6.

10 Zhang, J., Xu, Q., Feng, Z.C., Li, M.J. and Li, C. (2008) Importance of the relationship between surface phases and photocatalytic activity of TiO_2. *Angewandte Chemie – International Edition*, **47**, 1766–9.

11 Prieto, O., Fermoso, J., Nuez, Y., Del Valle, J.L. and Irusta, R. (2005) Decoloration of textile dyes in wastewaters by photocatalysis with TiO_2. *Solar Energy*, **79**, 376–83.

12 Liu, Z., He, Y., Li, F. and Liu, Y. (2006) Photocatalytic treatment of RDX wastewater with nano-sized titanium dioxide. *Environmental Science and Pollution Research International*, **13**, 328–32.

13 Dvoranova, D., Brezova, V. and Malati, M.A. (2002) Investigations of metal-doped titanium dioxide photocatalysts. *Applied Catalysis B: Environmental*, **37**, 91–105.

14 Yang, M.C., Yang, T.S. and Wong, M.S. (2004) Nitrogen-doped titanium oxide films as visible light photocatalyst by vapor deposition. *Thin Solid Films*, **469**, 1–5.

15 Ohno, T., Mitsui, T. and Matsumura, M. (2003) Photocatalytic activity of S-doped photocatalyst under visible light. *Chemistry Letters*, **32**, 364–5.

16 Hirano, K., Suzuki, E., Ishikawa, A., Moroi, T., Shiroishi, H. and Kaneko, M. (2000) Sensitization of TiO_2 particles by dyes to achieve H_2 evolution by visible light. *Journal of Photochemistry and Photobiology A: Chemistry*, **136**, 157–61.

17 Irie, H., Watanabe, Y. and Hashimoto, K. (2003) Carbon-doped anatase as a visible light-sensitive photocatalyst. *Chemistry Letters*, **32**, 772–3.

18 Liu, Y., Li, J., Qiu, X. and Burda, C. (2006) Novel TiO_2 nanocatalysts for wastewater purification – tapping energy

from the sun. *Water Practice and Technology*, **1** doi: 10.2166/wpt.2006.073.

19 Nahar, S., Hasegawa, K. and Kagaya, S. (2006) Photocatalytic degradation of phenol by visible light-responsive iron-doped TiO_2 and spontaneous sedimentation of the TiO_2 particles. *Chemosphere*, **65**, 1976–82.

20 Oh, S.M., Kim, S.S., Lee, J.E., Ishigaki, T. and Park, D.W. (2003) Effect of additives on photocatalytic activity of titanium dioxide powders synthesized by thermal plasma. *Thin Solid Films*, **435**, 252–8.

21 Barakat, M.A., Schaeffer, H., Hayes, G. and Ismat-Shah, S. (2005) Photocatalytic degradation of 2-chlorophenol by Co-doped TiO_2 nanoparticles. *Applied Catalysis B: Environmental*, **57**, 23–30.

22 Chiou, C.H. and Juang, R.S. (2007) Photocatalytic degradation of phenol in aqueous solutions by Pr-doped TiO_2 nanoparticles. *Journal of Hazardous Materials*, **149**, 1–7.

23 Shah, S.I., Li, W., Huang, C.P., Jung, O. and Ni, C. (2002) Study of Nd^{3+}, Pd^{2+}, Pt^{4+} and Fe^{3+} dopant effect on photoreactivity of TiO_2 nanoparticles. *Proceedings of the National Academy of Sciences of the United States of America*, **99**, 6482–6.

24 Pena, M.E., Korfiatis, G.P., Patel, M., Lippincott, L. and Meng, X. (2005) Adsorption of As(V) and As(III) by nanocrystalline titanium dioxide. *Water Research*, **39**, 2327–37.

25 Jiang, F., Zheng, Z., Xu, Z., Zheng, S., Guo, Z. and Chen, L. (2006) Aqueous Cr(VI) photo-reduction catalyzed by TiO_2 and sulfated TiO_2. *Journal of Hazardous Materials*, **134**, 94–103.

26 Wei, C., Lin, W.Y., Zainal, Z., Nathan, T., Williams, E., Zhu, K., Krurlc, A.P., Smith, R.L. and Rajeshwar, K. (1994) Bactericidal activity of TiO_2 photocatalyst in aqueous media: toward a solar-assisted water disinfection system. *Environmental Science & Technology*, **28**, 934–8.

27 Bekbolet, M. and Araz, C. (1996) Inactivation of *Escherichia coli* by photocatalytic oxidation. *Chemosphere*, **32**, 959–65.

28 Maness, P.-C., Smolinski, S., Blake, D.M., Huang, Z., Wolfrum, E.J. and Jacoby, W.A. (1999) Bactericidal activity of photocatalytic TiO_2 reaction: toward an understanding of its killing mechanism. *Applied and Environmental Microbiology*, **65**, 4094–8.

29 Yu, J.C., Ho, W., Yu, J., Yip, H., Wong, P.K. and Zhao, J. (2005) Efficient visible light-induced photocatalytic disinfection on sulfur-doped nanocrystalline titania. *Environmental Science & Technology*, **39**, 1175–9.

30 Egerton, T.A., Kosa, S.A. and Christensen, P.A. (2006) Photoelectrocatalytic disinfection of *E. coli* suspensions by iron doped TiO_2. *Physical Chemistry Chemical Physics: PCCP*, **8**, 398–406.

31 Bavykin, D.V., Gordeev, S.N., Moskalenko, A.V., Lapkin, A.A. and Walsh, F.C. (2005) Apparent two-dimensional behavior of TiO_2 nanotubes revealed by light absorption and luminescence. *Journal of Physical Chemistry B*, **109**, 8565–9.

32 Sakai, N., Ebina, Y., Takada, K. and Sasaki, T. (2004) Electronic band structure of titania semiconductor nanosheets revealed by electrochemical and photoelectrochemical studies. *Journal of the American Chemical Society*, **126**, 5851–8.

33 Kasuga, T., Hiramatsu, M., Hoson, A., Sekino, T. and Niihara, K. (1998) Formation of titanium oxide nanotube. *Langmuir*, **14**, 3160–3.

34 Sander, M.S., Coete, M.J., Gu, W., Kile, B.M. and Tripp, C.P. (2004) Template-assisted fabrication of dense, aligned arrays of titania nanotubes with well-controlled dimensions on substrates. *Advanced Materials*, **22**, 2052–7.

35 Gong, D., Grimes, C.A., Varghese, O.K., Hu, W., Singh, R.S., Chen, Z. and Dickey, E.C. (2001) Titanium oxide nanotube arrays prepared by anodic oxidation. *Journal of Materials Research*, **16**, 3331–4.

36 Bavykin, D.V., Friedrich, J.M. and Walsh, F.C. (2006) Protonated titanates and TiO_2 nanostructured materials: synthesis, properties, and applications. *Advanced Materials*, **18**, 2807–24.

37 Adachi, M., Murata, Y., Okada, I. and Yoshikawa, S. (2003) Formation of titania nanotubes and applications for dye-sensitized solar cells. *Journal of the Electrochemical Society*, **150**, G488.

38 Ngamsinlapasathian, S., Sakulkhaemaruethai, S., Pavasupree, S., Kitiyanan, A., Sreethawong, T., Suzuki, Y. and Yoshikawa, S. (2004) Highly efficient dye-sensitized solar cell using nanocrystalline titania containing nanotube structure. *Journal of Photochemistry and Photobiology A*, **164**, 145–51.

39 Varghese, O.K., Gong, D., Paulose, M., Ong, K.O., Dickey, E.C. and Grimes, C.A. (2003) Extreme changes in the electrical resistance of titania nanotubes with hydrogen exposure. *Advanced Materials*, **15**, 624–7.

40 Mor, G.K., Carvalho, M.A., Varghese, O.K., Pishko, M.V. and Grimes, C.A. (2004) A room temperature TiO_2-nanotube hydrogen sensor able to self-clean photoactively from environmental contamination. *Journal of Materials Research*, **19**, 628–34.

41 Mor, G.K., Shankar, K., Paulose, M., Varghese, O.K. and Grimes, C.A. (2005) Enhanced photocleavage of water using titania nanotube arrays. *Nano Letters*, **5**, 191–5.

42 Chen, Y., Crittenden, J., Hackney, S., Sutter, L. and Hand, D. (2005) Preparation of a novel TiO_2-based p-n junction nanotube photocatalyst. *Environmental Science & Technology*, **39**, 1201–8.

43 Bavykin, D.V., Lapkin, A.A., Plucinski, P.K., Torrente-Murciano, L., Friedrich, J.M. and Walsh, F.C. (2006) Deposition of Pt, Pd, Ru and Au on the surfaces of titanate nanotubes. *Topics in Catalysis*, **39**, 151–60.

44 Lin, C.H., Lee, C.H., Chao, J.H., Kuo, C.Y., Cheng, Y.C., Huang, W.N., Chang, H.W., Huang, Y.M. and Shih, M.K. (2004) Photocatalytic generation of H_2 gas from neat ethanol over Pt/TiO_2 nanotube catalysts. *Catalysis Letters*, **98**, 61–6.

45 Cao, J., Sun, J.Z., Li, H.Y., Hong, J. and Wang, M. (2004) A facile room-temperature chemical reduction method to TiO_2@CdS core/sheath heterostructure nanowires. *Journal of Materials Chemistry*, **14**, 1203–6.

46 Hodos, M., Horvath, E., Haspel, H., Kukovecz, A., Konya, Z. and Kiricsi, I. (2004) Photosensitization of ion-exchangeable titanate nanotubes by CdS nanoparticles. *Chemical Physics*, **399**, 512–15.

47 Joo, J., Kwon, S.G., Yu, T., Cho, M., Lee, J., Yoon, J. and Hyeon, T. (2005) Large-scale synthesis of TiO_2 nanorods via nonhydrolytic sol-gel ester elimination reaction and their application to photocatalytic inactivation of *E. coli*. *The Journal of Physical Chemistry B*, **109**, 15297–302.

48 Yu, J.C., Yu, J.G. and Zhao, J.C. (2002) Enhanced photocatalytic activity of mesoporous and ordinary TiO_2 thin films by sulfuric acid treatment. *Applied Catalysis B: Environmental*, **36**, 31–43.

49 Shieh, K.J., Li, M., Lee, Y.H., Sheu, S.D., Liu, Y.T. and Wang, Y.C. (2006) Antibacterial performance of photocatalyst thin film fabricated by defection effect in visible light. *Nanomedicine: Nanotechnology, Biology and Medicine*, **2**, 121–6.

50 Sunada, K., Watanabe, T. and Hashimoto, K. (2003) Studies on photokilling of bacteria on TiO_2 thin film. *Journal of Photochemistry and Photobiology A: Chemistry*, **156**, 227–33.

51 Kiwi, J. and Nadtochenko, V. (2005) Evidence for the mechanism of photocatalytic degradation of the bacterial wall membrane at the TiO_2 interface by ATR-FTIR and laser kinetic spectroscopy. *Langmuir*, **21**, 4631–41.

52 Tuel, A. and Hubert-Pfalzgraf, L.G. (2003) Nanometric monodispersed titanium oxide particles on mesoporous silica: synthesis, characterization, and catalytic activity in oxidation reactions in the liquid phase. *Journal of Catalysis*, **217**, 343–53.

53 Reddy, M.P., Venugopal, A. and Subrahmanyam, M. (2007) Hydroxyapatite-supported $Ag\text{-}TiO_2$ as *Escherichia coli* disinfection photocatalysts. *Water Research*, **41**, 379–86.

54 Zhang, X., Zhang, F. and Chan, K.Y. (2005) Synthesis of titania-silica mixed

oxide mesoporous materials, characterization and photocatalytic properties. *Applied Catalysis A*, **284**, 193–8.

55 López-Munoz, M.J., Van Grieken, R., Aguado, J. and Marugán, J. (2005) Role of the support on the activity of silica-supported TiO_2 photocatalysts: structure of the TiO_2/SBA-15 photocatalysts. *Catalysis Today*, **101**, 307–14.

56 Lee, S.H., Pumprueg, S., Moudgil, B. and Sigmund, W. (2005) Inactivation of bacterial endospores by photocatalytic nanocomposites. *Colloids and Surfaces B: Biointerfaces*, **40**, 93–8.

57 Qiao, S., Sun, D.D., Tay, J.H. and Easton, C. (2003) Photocatalytic oxidation technology for humic acid removal using a nano-structured TiO_2/Fe_2O_3 catalyst. *Water Science and Technology*, **47**, 211–17.

58 Shephard, G.S., Stockenstrom, S., de Villiers, D., Engelbrecht, W.J. and Wessels, G.F.S. (2002) Degradation of microcystin toxins in a falling film photocatalytic reactor with immobilized titanium dioxide catalyst. *Water Research*, **36**, 140–6.

59 Wu, L., Yu, J.C. and Fu, X.Z. (2006) Characterization and photocatalytic mechanism of nanosized CdS coupled TiO_2 nanocrystals under visible light irradiation. *Journal of Molecular Catalysis A: Chemical*, **244**, 25–32.

60 Bae, E. and Choi, W. (2003) Highly enhanced photoreductive degradation of perchlorinated compounds on dye-sensitized metal/TiO_2 under visible light. *Environmental Science & Technology*, **37**, 147–52.

61 Liu, H.Y. and Gao, L. (2005) Synthesis and properties of CdSe-sensitized rutile TiO_2 nanocrystals as a visible light-responsive photocatalyst. *Journal of the American Ceramic Society*, **88**, 1020–2.

62 Yu, J.C., Wu, L., Lin, J., Li, P. and Li, Q. (2003) Microemulsion-mediated solvo-thermal synthesis of nanosized CdS-sensitized TiO_2 crystalline photocatalyst. *Chemical Communications*, **8**, 1552–3.

63 Chikazumi, S., Taketomi, S., Ukita, M., Mizukami, M., Miyajima, H., Setogawa, M. and Kurihara, Y. (1987) Physics of magnetic fluids. *Journal of Magnetism and Magnetic Materials*, **65**, 245–51.

64 Lu, A.H., Schmidt, W., Matoussevitch, N., Bennermann, H., Spliethoff, B., Tesche, B., Bill, E., Kiefer, W. and Schüth, F. (2004) Nanoengineering of a magnetically separable hydrogenation catalyst. *Angewandte Chemie–International Edition*, **43**, 4303–6.

65 Tsang, S.C., Caps, V., Paraskevas, I., Chadwick, D. and Thompsett, D. (2004) Magnetically separable, carbon-supported nanocatalysts for the manufacture of fine chemicals. *Angewandte Chemie–International Edition*, **43**, 5645–9.

66 Shokouhimehr, M., Piao, Y.Z., Kim, J.Y., Jang, Y.J. and Hyeon, T. (2007) A magnetically recyclable nanocomposite catalyst for olefin epoxidation. *Angewandte Chemie–International Edition*, **46**, 7039–43.

67 Gupta, A.K. and Gupta, M. (2005) Synthesis and surface engineering of iron oxide nanoparticles for biomedical applications. *Biomaterials*, **26**, 3995–4021.

68 Mornet, S., Vasseur, S., Grasset, F., Verveka, P., Goglio, G., Demourgues, A., Portier, J., Pollert, E. and Duguet, E. (2006) Magnetic nanoparticle design for medical applications. *Progress in Solid State Chemistry*, **34**, 237–47.

69 Li, Z., Wei, L., Gao, M.Y. and Lei, H. (2005) One-pot reaction to synthesize biocompatible magnetite nanoparticles. *Advanced Materials*, **17**, 1001–5.

70 Chemla, Y.R., Grossman, H.L., Poon, Y., McDermott, R., Stevensi, R., Alper, M.D. and Clarke, J. (2000) Ultrasensitive magnetic biosensor for homogeneous immunoassay. *Proceedings of the National Academy of Sciences of the United States of America*, **97**, 14268–72.

71 Hyeon, T. (2003) Chemical synthesis of magnetic nanoparticles. *Chemical Communications*, 927–34.

72 Lu, A.H., Salabas, E.L. and Schüth, F. (2007) Magnetic nanoparticles: synthesis, protection, functionalization, and application. *Angewandte Chemie–International Edition*. **46**, 1222–44.

73 Li, P., Miser, D.E., Babier, S., Yadav, R.T. and Hajaligol, M.R. (2003) The removal of carbon monoxide by iron oxide

nanoparticles. *Applied Catalysis B*, **43**, 151–62.

74 Oliveira, L.C.A., Petkowicz, D.I., Smaniotto, A. and Pergher, S.B.C. (2004) Magnetic zeolites: a new adsorbent for removal of metallic contaminants from water. *Water Research*, **38**, 3699–704.

75 Hai, C.H. and Chen, C.Y. (2001) Removal of metal ions and humic acid from water by iron-coated filter media. *Chemosphere*, **44**, 1177–84.

76 Onyango, M.S., Kojima, Y., Matsuda, H. and Ochieng, A. (2003) Adsorption kinetics of arsenic removal from groundwater by iron-modified zeolite. *Journal of Chemical Engineering of Japan*, **36**, 1516–22.

77 Wu, R.C., Qu, J.H. and Chen, Y.S. (2005) Magnetic powder $MnO–Fe_2O_3$ composite–a novel material for the removal of azo-dye from water. *Water Research*, **39**, 630–8.

78 Wu, R.C., Qu, H.H., He, H. and Yu, Y.B. (2004) Removal of azo-dye Acid Red B (ARB) by adsorption and catalytic combustion using magnetic $CuFe_2O_4$ powder. *Applied Catalysis B*, **48**, 49–56.

79 Herrera, F., Lopez, A., Mascolo, G., Albers, E. and Kiwi, J. (2001) Catalytic combustion of Orange II on hematite: surface species responsible for the dye degradation. *Applied Catalysis B*, **29**, 147–62.

80 Takafuji, M., Ide, S., Ihara, H. and Xu, Z. (2004) Preparation of poly (1-vinylimidazole)-grafted magnetic nanoparticles and their application for removal of metal ions. *Chemistry of Materials*, **16**, 1977–83.

81 Yavuz, C.T., Mayo, J.T., Yu, W.W., Parkash, A., Falkner, J.C., Yean, S.J., Cong, L.L., Shipey, H.J., Kan, A., Tomson, M., Nateson, D. and Colvin, V.L. (2006) Low-field magnetic separation of monodisperse Fe_3O_4 nanocrystals. *Science*, **314**, 964–7.

82 Magnuson, M.L. and Speth, T.F. (2005) Quantitative structure-property relationships for enhancing predictions of synthetic organic chemical removal from drinking water by granular activated carbon. *Environmental Science & Technology*, **39**, 7706–11.

83 Cornell, F.H. and Schwertmann, U. (1996) *The Iron Oxide*, 1st edn, John Wiley & Sons, Inc., New York.

84 Hsia, T.H., Lo, S.L., Lin, C.F. and Lee, D.Y. (1994) Characterization of arsenate adsorption on hydrous iron oxide using chemical and physical methods. *Colloids and Surfaces A*, **85**, 1–7.

85 Munoz, J.A., Gonzalo, A. and Valiente, M. (2002) Arsenate adsorption by Fe(III)-loaded open-celled cellulose sponge: thermodynamic and selectively aspect. *Environmental Science & Technology*, **36**, 3405–11.

86 Zhang, Y., Yang, M. and Huang, X. (2003) Arsenic(V) removal with a Ce(IV)-doped iron oxide adsorbent. *Chemosphere*, **51**, 945–52.

87 Zhang, Y., Yang, M., Gao, Y.X., Wang, F. and Huang, X. (2003) Preparation and adsorption mechanism of rare earth-doped adsorbent for arsenic (V) removal from groundwater. *Science in China Series B*, **46**, 252–8.

88 Zhang, Y., Yang, M., Dou, X.M., He, H. and Wang, D.S. (2005) Arsenate adsorption on a Fe—Ce bimetal oxide adsorbent: role of surface properties. *Environmental Science & Technology*, **39**, 7246–53.

89 Sun, D., Meng, T.T., Loong, T.H. and Hwa, T.J. (2004) Removal of natural organic matter from water using a nano-structured photocatalyst coupled with filtration membrane. *Water Science and Technology*, **49**, 103–10.

90 Takafuji, M., Ide, S., Ihara, H. and Xu, Z. (2004) Preparation of poly(1-vinylimidazole)-grafted magnetic nanoparticles and their application for removal of metal ions. *Chemistry of Materials*, **16**, 1977–83.

91 Wang, L., Yang, Z.M., Gao, J.H., Xu, K.M., Gu, H.W., Zhang, B., Zhang, X.X. and Xu, B. (2006) A biocompatible method of decorporation: bisphosphonate-modified magnetite nanoparticles to remove uranyl ions from blood. *Journal of the American Chemical Society*, **128**, 13358–9.

92 Chen, W.J., Tsai, P.J. and Chen, Y.J. (2008) Functional Fe_3O_4/TiO_2 core/shell magnetic nanoparticles as photokilling

agents for pathogenic bacteria. *Small*, **4**, 485–91.

93 Gong, P., Li, H.M., He, X.X., Wang, K.M., Hu, J.B., Tan, W.H., Zhang, S.C. and Yang, X.H. (2007) Preparation and antibacterial activity of Fe_3O_4@Ag nanoparticles. *Nanotechnology*, **18**, 285604.

94 El-Boubbou, K., Gruden, C. and Huang, X.F. (2007) Magnetic glyco-nanoparticles: a unique tool for rapid pathogen detection, decontamination, and strain differentiation. *Journal of the American Chemical Society*, **129**, 13392–3.

95 Chang, S.C. and Adriaens, P. (2007) Nano-immunodetection and quantification of mycobacteria in metalworking fluids. *Environmental Engineering Science*, **24**, 58–72.

96 Porter, J., Robinson, J., Pickup, R. and Edwards, C.J. (1998) An evaluation of lectin-mediated magnetic bead cell sorting for the targeted separation of enteric bacteria. *Journal of Applied Microbiology*, **84**, 722–32.

97 Zhong, L.S., Hu, J.S., Liang, H.P., Cao, A.M., Song, W.G. and Wan, L.J. (2006) Self-assembled 3D flowerlike iron oxide nanostructures and their application in water treatment. *Advanced Materials*, **18**, 2426–31.

98 Thackeray, M.M. (1997) Manganese oxides for lithium batteries. *Progress in Solid State Chemistry*, **25**, 1–71.

99 Armstrong, A.R. and Bruce, P.G. (1996) Synthesis of layered $LiMnO_2$ as an electrode for rechargeable lithium batteries. *Nature*, **381**, 499–500.

100 Morales, A.M. and Lieber, C.M. (1998) A laser ablation method for the synthesis of crystalline semiconductor nanowires. *Science*, **279**, 208–11.

101 Li, Y.D., Li, X.L., Deng, Z.X., Zhou, B.C., Fan, S.S., Wang, J.W. and Sun, X.M. (2002) From surfactant-inorganic mesostructures to tungsten nanowires. *Angewandte Chemie – International Edition*, **41**, 333–5.

102 Benaissa, M., José-Yacamán, M., Xiao, T.D. and Strutt, P.R. (1997) Microstructural study of hollandite-type MnO_2 nano-fibers. *Applied Physics Letters*, **70**, 2120–2.

103 Fischer, A.E., Pettigrew, K.A., Rolison, D.R., Stroud, R.M. and Long, J.W. (2007) Incorporation of homogeneous, nanoscale MnO_2 within ultraporous carbon structures via self-limiting electroless deposition: implications for electrochemical capacitors. *Nano Letters*, **7**, 281–6.

104 Driehaus, W., Seith, R. and Jekel, M. (1995) Oxidation of arsenite (III) with manganese oxides in water treatment. *Water Research*, **29**, 297–305.

105 Bajpai, S. and Chaudhuri, M. (1999) Removal of arsenic from ground water by manganese dioxide-coated sand. *Journal of Environmental Engineering*, **125**, 782–4.

106 Foster, A.L., Brown, G.E. and Parks, G.A. (2003) X-Ray absorption fine structure study of As(V) and Se(IV) sorption complexes on hydrous Mn oxides. *Geochimica et Cosmochimica Acta*, **67**, 1937–53.

107 Oscarson, D.W., Huang, P.M., Defosse, C. and Herbillon, A. (1981) Oxidative power of Mn(IV) and Fe(III) oxides with respect to As(III) in terrestrial and aquatic environments. *Nature*, **291**, 50–1.

108 Tournassat, C., Charlet, L., Bosbach, D. and Manceau, A. (2002) Arsenic(III) oxidation by birnessite and precipitation of manganese(II) arsenate. *Environmental Science & Technology*, **36**, 493–500.

109 Scott, M.J. and Morgan, J.J. (1995) Reactions at oxide surfaces. 1, Oxidation of As(III) by synthetic birnessite. *Environmental Science & Technology*, **29**, 1898–905.

110 Chiu, V.Q. and Hering, J.G. (2000) Arsenic adsorption and oxidation at manganite surfaces 1. Method for simultaneous determination of adsorbed and dissolved arsenic species. *Environmental Science & Technology*, **34**, 2029–34.

111 Tripathy, S.S. and Kanungo, S.B. (2005) Adsorption of Co^{2+}, Ni^{2+}, Cu^{2+} and Zn^{2+} from 0.5 M NaCl and major ion sea water on a mixture of δ-MnO_2 and amorphous FeOOH. *Journal of Colloid and Interface Science*, **284**, 30–8.

112 Lenoble, V., Laclautre, C., Serpaud, B., Deluchat, V. and Bollinger, J.C. (2004) As (V) retention and As(III) simultaneous oxidation and removal on a MnO_2-loaded

polystyrene resin. *Science of the Total Environment*, **326**, 197–207.

113 Zhu, Z.L., Ma, H.M., Zhang, R.H., Ge, Y.X. and Zhao, J.F. (2007) Removal of cadmium using MnO_2 loaded D301 resin. *Journal of Environmental Sciences*, **19**, 652–6.

114 Han, R.P., Zou, W.H., Wang, Y. and Zhu, L. (2007) Removal of uranium(VI) from aqueous solutions by manganese oxide coated zeolite: discussion of adsorption isotherms and pH effect. *Journal of Environmental Sciences*, **93**, 127–43.

115 Manning, B.A., Fendorf, S.E., Bostick, B. and Suarez, D.L. (2002) Arsenic(III) oxidation and arsenic(V) adsorption reactions on synthetic birnessite. *Environmental Science & Technology*, **36**, 976–81.

116 Ouvrard, S., Simonnot, M.O. and Sardin, M. (2002) Reactive behavior of natural manganese oxides towards the adsorption of phosphate and arsenate. *Industrial & Engineering Chemistry Research*, **41**, 2785–91.

117 Katsoyiannis, I.A., Zouboulis, A.I. and Jekel, M. (2004) Kinetics of bacterial As(III) oxidation and subsequent As(V) removal by sorption onto biogenic manganese oxides during groundwater treatment. *Industrial & Engineering Chemistry Research*, **43**, 486–93.

118 Ouvrard, S., Simonnot, M.O., Donato, P. and Sardin, M. (2002) Diffusion-controlled adsorption of arsenate on a natural manganese oxide. *Industrial & Engineering Chemistry Research*, **41**, 6194–9.

119 Han, R.P., Zou, W.H., Zhang, Z.P., Shi, J. and Yang, J.J. (2006) Removal of copper (II) and lead (II) from aqueous solution by manganese oxide coated sand I. Characterization and kinetic study. *Journal of Hazardous Materials*, **137**, 384–95.

120 Maity, S., Chakravarty, S., Bhattacharjee, S. and Roy, B.C. (2005) A study on arsenic adsorption on polymetallic sea nodule in aqueous medium. *Water Research*, **39**, 2579–90.

121 Espinal, L., Suib, S.L. and Rusling, J.F. (2004) Electrochemical catalysis of styrene epoxidation with films of MnO_2 nanoparticles and H_2O_2. *Journal of the American Chemical Society*, **126**, 7676–82.

122 Wang, X. and Li, Y.D. (2002) Rational synthesis of a-MnO_2 single-crystal nanorods. *Chemical Communications*, 764–5.

123 Li, G.C., Jiang, L.H., Pang, T. and Peng, H.R. (2007) Synthesis of γ-MnO_2 single-crystalline nanobelts. *Materials Letters*, **61**, 3319–22.

124 Li, Q., Olson, J.B. and Penner, R.M. (2004) Nanocrystalline α-MnO_2 nanowires by electrochemical step-edge decoration. *Chemistry of Materials*, **16**, 3402–5.

125 Zheng, D.S., Sun, S.X., Fan, W.L., Yu, H.Y., Fan, C.H., Cao, G.X., Yin, Z.L. and Song, X.Y. (2005) One-step preparation of single-crystalline β-MnO_2 nanotubes. *Journal of Physical Chemistry B*, **109**, 16439–43.

126 Zheng, Y.H., Cheng, Y., Bao, F., Wang, Y. and Qin, S.Y. (2006) Multiple branched a-MnO_2 nanofibers: a two-step epitaxial growth. *Journal of Crystal Growth*, **286**, 156–61.

127 Omomo, Y., Sasaki, T., Wang, L.Z. and Watanabe, M. (2003) Redoxable nanosheet crystallites of MnO_2 derived via delamination of a layered manganese oxide. *Journal of the American Chemical Society*, **125**, 3568–75.

128 Zhao, L.L. and Wang, R.S. (2004) γ-MnO_2 nano-sieve membrane: preparation, characterization and reaction studies. *Applied Surface Science*, **236**, 217–22.

129 Li, W.N., Yuan, J., Shen, X.F., Gomez-Mower, S., Xu, L.P., Sithambaram, S., Aindow, M. and Suib, S.L. (2006) Hydrothermal synthesis of structure- and shape-controlled manganese oxide octahedral molecular sieve nanomaterials. *Advanced Functional Materials*, **16**, 1247–53.

130 Luo, J.Y., Zhang, J.J. and Xia, Y.-Y. (2006) Highly electrochemical reaction of lithium in the ordered mesoporous β-MnO_2. *Chemistry of Materials*, **18**, 5618–23.

131 Suzuki, N., Sasaki, H., Morinaga, Y. and Yamada, Y. (2005) Nano-porous manganese oxide formed by self-assembled agglomeration of nanocrystallites. *Applied Surface Science*, **252**, 1498–501.

132 Jiao, F. and Bruce, P.G. (2007) Mesoporous crystalline β-MnO_2 – a reversible positive electrode for rechargeable lithium batteries. *Advanced Materials*, **19**, 657–60.

133 Cheng, F.Y., Zhao, J.Z., Song, W.N., Li, C.S., Chen, J. and Shen, P.W. (2006) Facile controlled synthesis of MnO_2 nanostructures of novel shapes and their application in batteries. *Inorganic Chemistry*, **45**, 2038–44.

134 Zheng, D.S., Yin, Z.L., Zhang, W.M. and Tan, X.J. and Sun, S.X. (2006) Novel branched γ-MnOOH and β-MnO_2 multipod nanostructures. *Crystal Growth & Design*, **6**, 1733–5.

135 Li, B.X., Rong, G.X., Xie, Y., Huang, L.F. and Feng, C.Q. (2006) Low-temperature synthesis of α-MnO_2 hollow urchins and their application in rechargeable Li^+ batteries. *Inorganic Chemistry*, **45**, 6404–10.

136 Li, Z.Q., Ding, Y.Y., Xiong, J., Yang, Q. and Xie, Y. (2005) One-step solution-based catalytic route to fabricate novel α-MnO_2 hierarchical structures on a large scale. *Chemical Communications*, 918–20.

137 Dekker, C. (1999) Carbon nanotubes as molecular quantum wires. *Physics Today*, **52**, 22–8.

138 Huang, M.H., Mao, S., Feick, H., Yan, H.Q., Wu, Y.Y., Kind, H., Weber, E., Russo, R. and Yang, P.D. (2001) Room-temperature ultraviolet nanowire nanolasers. *Science*, **292**, 1897–9.

139 Hu, J., Odom, T.W. and Lieber, C.M. (1999) Chemistry and physics in one dimension: synthesis and properties of nanowires and nanotubes. *Accounts of Chemical Research*, **32**, 435–45.

140 Selim, M.M., El-Aiashi, M.K., Mazhar, H.S. and Kanal, S.M. (1996) Decomposition of H_2O_2 over manganese-chromium oxide catalyst in aqueous and alkaline solutions. *Materials Letters*, **28**, 417–21.

141 Hasan, M.A., Zaki, M.I., Pasupulety, L. and Kumari, K. (1999) Promotion of the hydrogen peroxide decomposition activity of manganese oxide catalysts. *Applied Catalysis A*, **181**, 171–9.

142 Espinal, L., Suib, S.L. and Rusling, J.F. (2004) Electrochemical catalysis of styrene epoxidation with films of MnO_2 nanoparticles and H_2O_2. *Journal of the American Chemical Society*, **126**, 7676–82.

143 Zhang, W.X., Yang, Z.H., Wang, X., Zhang, Y.C., Wen, X.G. and Yang, S.H. (2006) Large-scale synthesis of β-MnO_2 nanorods and their rapid and efficient catalytic oxidation of methylene blue dye. *Catalysis Communications*, **7**, 408–12.

144 Fei, J.B., Cui, Y., Yan, X.H., Qi, W., Yang, Y., Wang, K.W., He, Q. and Li, J.B. (2008) Controlled preparation of MnO_2 hierarchical hollow nanostructures and their application in water treatment. *Advanced Materials*, **20**, 452–6.

145 Hideaki, I., Junji, N., Yuzuru, I. and Tokuzo, K. (1987) Anion adsorption behavior of rare earth oxide hydrates. *The Chemical Society of Japan*, **5**, 807–13.

146 Tokunaga, S., Hardon, M.J. and Wasay, S.A. (1995) Removal of fluoride ions from aqueous solution by multivalent metal compounds. *International Journal of Environmental Studies*, **48**, 17–28.

147 British Geological Survey (2000) *Arsenic in Groundwater from Major Aquifers: Sources, Effects and Potential Mitigation*, British Geological Survey, London.

148 Zhang, Y., Yang, M. and Huang, X. (2003) Arsenic (V) removal with a Ce (IV)-doped iron oxide adsorbent. *Chemosphere*, **51**, 945–52.

149 Trovarelli, A. (1996) Catalytic properties of ceria and CeO_2-containing materials. *Catalysis Reviews – Science and Engineering*, **38**, 439–520.

150 Inaba, H. and Tagawa, H. (1996) Ceria-based solid electrolytes. *Solid State Ionics*, **83**, 1–16.

151 Trovarelli, A., de Leitenburg, C., Boaro, M. and Dolcetti, G. (1999) The utilization of ceria in industrial catalysis. *Catalysis Today*, **50**, 353–67.

152 Park, S.D., Vohs, J.M. and Gorte, R.J. (2000) Direct oxidation of hydrocarbons in a solid-oxide fuel cell. *Nature*, **404**, 265–7.

153 Kang, Z.C. and Wang, Z.L. (2003) Novel oxides for cycled hydrogen production from methane and water using a temperature swing. *Advanced Materials*, **15**, 521–6.

154 Brosha, E.L., Mukundan, R., Brown, D.R., Garzon, F.H. and Visser, J.H.

(2002) Development of ceramic mixed potential sensors for automotive applications. *Solid State Ionics*, **148**, 61–9.

155 Feng, X.D., Sayle, D.C., Wang, Z.L., Paras, M.S., Santora, B., Sutorik, A.C., Sayle, T.X.T., Yang, Y., Ding, Y., Wang, X.D. and Her, Y.S. (2006) Converting ceria polyhedral nanoparticles into single-crystal nanospheres. *Science*, **312**, 1504–8.

156 Yu, X.J., Xie, P.B. and Su, Q.D. (2001) Size-dependent optical properties of nanocrystalline CeO_2: Er obtained by combustion synthesis. *Physical Chemistry Chemical Physics*, **3**, 5266–9.

157 Bera, P. and Hegde, M.S. (2002) Characterization and catalytic properties of combustion synthesized Au/CeO_2 catalyst. *Catalysis Letters*, **79**, 75–81.

158 Valenzuela, R.X., Bueno, G., Solbes, A., Sapina, F., Martinez, E. and Corberan, V.C. (2001) Nanostructured ceria-based catalysts for oxydehydrogenation of ethane with CO_2. *Topics in Catalysis*, **15**, 181–8.

159 Yin, L.X., Wang, Y.Q., Pang, G.S., Koltypin, Y. and Gedanken, A.J. (2002) Sonochemical synthesis of cerium oxide nanoparticles–effect of additives and quantum size effect. *Journal of Colloid and Interface Science*, **246**, 78–84.

160 Huang, W.P., Wu, S.H. and Song, D.Y. (2005) CeO_2 nanorods and gold nanocrystals supported on CeO_2 nanorods as catalyst. *Journal of Physical Chemistry B*, **109**, 19169.

161 Yu, T.Y., Joo, J., Park, Y.I. and Hyeon, T. (2005) Large-scale nonhydrolytic sol-gel synthesis of uniform-sized ceria nanocrystals with spherical, wire, and tadpole shapes. *Angewandte Chemie–International Edition*, **44**, 7411–14.

162 Tang, C.C., Bando, Y., Liu, B.D. and Golberg, D. (2005) Cerium oxide nanotubes prepared from cerium hydroxide nanotubes. *Advanced Materials*, **17**, 3005–9.

163 Si, R., Zhang, Y.W., You, L.P. and Yan, C.H. (2005) Rare-earth oxide nanopolyhedra, nanoplates, and nanodisks. *Angewandte Chemie–International Edition*, **44**, 3256–60.

164 Di, Z.C., Ding, J., Peng, X.J., Li, Y.H., Luan, Z.K. and Liang, J. (2006) Chromium adsorption by aligned carbon nanotubes supported ceria nanoparticles. *Chemosphere*, **62**, 861–5.

165 Peng, X.J., Luan, Z.K., Ding, J., Di, Z.C., Li, Y.H. and Tian, B.H. (2005) Ceria nanoparticles supported nanotubes for the removal of arsenate from water. *Materials Letters*, **59**, 399–403.

166 Zhong, L.S., Hu, J.S., Cao, A.M., Liu, Q., Song, W.G. and Wan, L.J. (2007) 3D flowerlike ceria micro/nanocomposite structure and its application for water treatment and CO removal. *Chemistry of Materials*, **19**, 1648–55.

167 Stoimenov, P.K., Klinger, R.L., Marchin, G.L. and Klabunde, K.J. (2002) Metal oxide nanoparticles as bactericidal agents. *Langmuir*, **18**, 6679–86.

168 Koper, O.B., Klabunde, J.S., Marchin, G.L., Klabunde, K.J., Stoimenov, P. and Bohra, L. (2002) Nanoscale powders and formulations with biocidal activity towards spores and vegetative cells of *Bacillus* species, viruses, and toxins. *Current Microbiology*, **44**, 49–55.

169 Makkhluf, S., Dror, R., Nitzan, Y., Abramovich, A., Jelinek, R. and Gedanken, A. (2005) Microwave-assisted synthesis of nanocrystalline MgO and its use as a bacteriocide. *Advanced Functional Materials*, **15**, 1708–15.

170 DeFriend, K.A., Wiesner, M.R. and Barron, A.R. (2003) Alumina and aluminate ultrafiltration membranes derived from alumina nanoparticles. *Journal of Membrane Science*, **224**, 11–28.

171 Stanton, B.W., Harris, J.J., Miller, M.D. and Bruening, M.L. (2003) Ultrathin, multilayered polyelectrolyte films as nanofiltration membranes. *Langmuir*, **19**, 7038–42.

172 Dotzauer, D.M., Dai, J., Sun, L. and Bruening, M.L. (2006) Catalytic membrane prepared using layer-by-layer adsorption of polyelectrolyte/metal nanoparticle films in porous supports. *Nano Letters*, **6**, 2268–72.

173 Allabashi, R., Aekas, M., Hormann, G. and Tsiouvas, D. (2007) Removal of some organic pollutants in water employing ceramic membranes impregnated with cross-linked silylated dendritic and

cyclodextrin polymers. *Water Research*, **41**, 476–86.

174 Chaplin, B.P., Roundy, E., Guy, K.A., Shaply, J.R. and Werth, C.J. (2006) Effects of natural water ions and humid acid on catalytic nitrate reduction kinetics using an alumina supported Pd-Cu catalyst. *Environmental Science & Technology*, **40**, 3075–81.

175 Kim, Y., Kim, C., Choi, I., Rengaraj, S. and Yi, J. (2004) Arsenic removal using mesoporous alumina prepared via a templating method. *Environmental Science & Technology*, **38**, 924–31.

176 Meng, G.W., Jung, Y.J., Cao, A.Y., Vajtai, R. and Ajayan, P.M. (2005) Controlled fabrication of hierarchically branched nanopores, nanotubes, and nanowires. *Proceedings of the National Academy of Sciences of the United States of America*, **102**, 7474–8.

177 Rickerby, D.G. and Morrison, M. (2007) Nanotechnology and the environment: A European perspective. *Science and Technology of Advanced Materials*, **8**, 19–24.

178 Riu, J., Maroto, A. and Rius, F.X. (2006) Nanosensors in environmental analysis. *Talanta*, **69**, 288–301.

179 Hillie, T. and Hlophe, M. (2007) Nanotechnology and the challenge of clean water. *Nature Nanotechnology*, **2**, 663–4.

180 *Strategy for Nanotechnology-related Environmental, Health, and Safety Research: National Nanotechnology Initiative*, http://www.nano.gov/NNI_EHS_Research_Strategy.pdf (accessed 11 Dec. 2008).

181 Oberdörster, G., Oberdörster, E. and Oberdörster, J. (2005) Nanotoxicology: an emerging discipline evolving from studies of ultrafine particles. *Environmental Health Perspectives*, **113**, 823–39.

Abstract

In today's world, nanotechnology is becoming increasingly popular for water treatment. In this chapter, we will summarize recent advances in the development of typical metal oxide materials (TiO_2, Fe_3O_4/Fe_2O_3, MnO_2, CeO_2, MgO and Al_2O_3) and the related processes for the treatment of various water resources which have been contaminated by organic solutes, inorganic anions, radionuclides, bacteria and viruses.

Keywords

nanotechnology; nanomaterials; metal oxides; water treatment; degradation; absorption

10
Approaches to Mesoscale Modeling of Nanoparticle–Cell Membrane Interactions

Valeriy V. Ginzburg, Sudhakar Balijepalli, Kurt A. Smith and Anna C. Balazs

10.1
Introduction

In recent years, inorganic – and, to a lesser extent, polymeric – nanoparticles have become ubiquitous in advanced technologies, pharmaceuticals and medicine [1–27]. When used as additives in polymers, nanoparticles can improve various physical properties, including electrical conductivity, mechanical strength and the gas permeability of membranes [1–3]. Even more promising is the potential use of nanoparticles in the health care industry [4–10]. Because of their small size (sometimes <5 nm radius), nanoparticles might conceivably penetrate cell membranes, and consequently could be used for drug delivery or for intracellular imaging. Indeed, numerous clinical trials are ongoing in which nanoparticles are being tested for cancer treatment or to image various tumors. In contrast, the same ability of the nanoparticles to nonselectively breach the membranes has resulted in significant concerns regarding the environmental [11] and health [12–19] effects of the new nanoparticle-containing products.

One of the crucial difficulties in understanding the specifics of nanoparticle–cell interactions is our limited knowledge of the molecular or biochemical mechanisms behind them. Let us consider a specific case of the interaction between a nanoparticle and a cell membrane. One would naturally expect that the chemical nature of the particle (whether gold, silver, silicon dioxide, etc.) is important for determining how the membrane would react to its proximity; this proximity could activate specific receptors and cause, for example, endocytosis of the particle. Yet, from experiments which have been conducted it is now known that the chemical nature of the particle is only one of many factors that influence its interaction with cell membranes. The other factors include particle size [17, 20], the chemical nature of the ligands grafted onto the particle surface [17–19], the effective charge of the particle surface [17–19], and perhaps the particle shape anisotropy. On the other hand, a typical cell membrane contains regions of different chemical and physical nature [21–26], and a nanoparticle could potentially 'choose' to interact

Nanomaterials for the Life Sciences Vol. 2: Nanostructured Oxides. Edited by Challa S. S. R. Kumar

ISBN: 978-3-527-32152-0

with any of these. It is very difficult to probe such interactions experimentally because of the small scales and high speeds of the processes involved.

The importance of understanding of these processes at a fundamental level cannot be overestimated, however. As recent studies have shown, gold and silver nanoparticles can easily penetrate inside various human cells, including red blood cells [13, 15, 20]. These studies have strongly elevated the question about the safety of nanoparticle-related products or processes (one of many reports describing these studies was entitled: 'Nanoparticle interaction with biological membranes: does nanotechnology present a Janus face?' [19]). Today, government agencies and chemical industry councils worldwide are rapidly developing new programs and protocols to address these issues and establish new safety rules and regulations for nanotechnology. Similarly, in nanomedicine, the use of nanoparticles for drug delivery or tumor imaging can only be fully successful when the selectivity of the interactions – that is, whether nanoparticles target diseased, but not healthy, cells – can be determined.

Based on the preliminary results from some of these studies, it might be suggested that in many cases, the interaction between nanoparticles and cell membranes is governed not only by biochemical (receptor–ligand interaction) but also by nonselective, biophysical factors. Following the studies of Banazsak Holl and coworkers [17–19], it is now known that functionalized, strongly charged nanoparticles can produce nanosized holes in various phospholipid membranes, including model membranes that contain no receptors. If it is assumed that the interaction between nanoparticles and cell membranes can often be understood based on simple biophysical – or even simple physico-chemical – arguments, then it becomes possible to develop meaningful models to simulate and understand this interaction in more detail. Then, both theory and modeling can be used to predict the probability of a nanoparticle penetrating through a membrane, as a function of the nanoparticle size, surface chemistry, surface charge density and shape anisotropy. This information can then be utilized to help understand nanoparticle cytotoxicity and/or to design better agents for drug delivery.

The question is, therefore, what are the appropriate modeling methods to investigate nanoparticle–membrane interaction? As shown in Figure 10.1, modeling methods in soft matter (including polymer science and biophysics) may be divided schematically into atomistic, mesoscale and continuum or large-scale [27]. Atomistic methods [most often, atomistic molecular dynamics (MD) or Monte Carlo (MC)] have been utilized in biological sciences quite often in recent years, especially as the speed and power of modern computers continues to increase. Thus, various research groups, including Klein and coworkers [28–32], Voth and coworkers [33–35], Chang and Violi [36] and Tian [37], have successfully used atomistic MD to study the conformations, elastic properties and thermodynamics of biological membranes. Most recently, Chang and Violi [36] demonstrated the use of atomistic MD in predicting the structure of a lipid bilayer in the presence of carbon nanoparticles (see Figure 10.2). Other successful applications of atomistic MD have included calculation of the structure of ion channels in membranes, the partitioning of anesthetics in membranes, and the interaction of membranes with

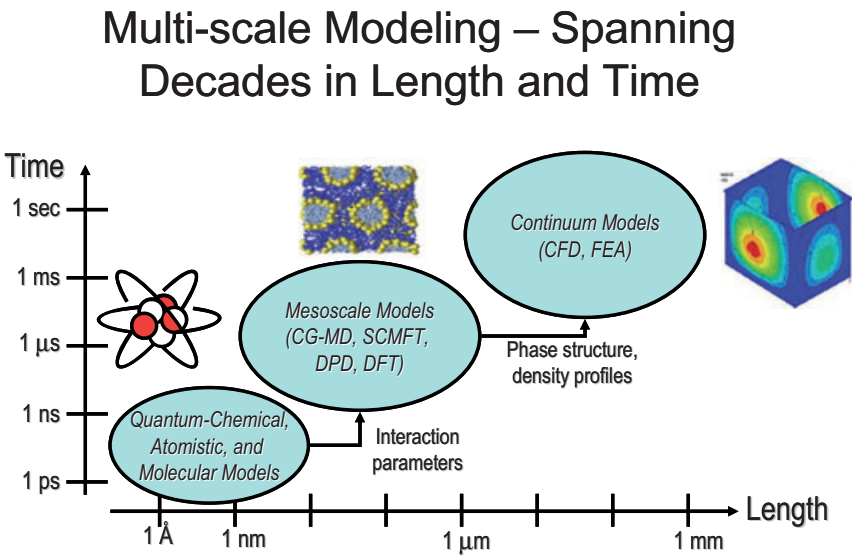

Figure 10.1 Schematic representation of length and time scales involved in various types of physical models of polymeric and biological systems. CFD = computational fluid dynamics; CG-MD = coarse-grained molecular dynamics; DPD = dissipative particle dynamics; FEA = finite element analysis; SCMFT = self-consistent mean field theory; DFT = density functional theory.

inserted proteins. (A detailed overview of atomistic simulations of membranes and nanoparticles is beyond the scope of this chapter; hence, the reader is referred to the review by Saiz and Klein [30] for more details.) At the same time, even today, fully atomistic simulations are extremely time-consuming. Accordingly, one would often choose to employ mesoscale [or coarse-grained (CG)] methods instead. In mesoscale models, although the level of detail is somewhat sacrificed the speed of the calculation is improved substantially compared to the full atomistic models. A large number of mesoscale modeling studies have been conducted of lipid bilayers, polymersomes and vesicles using coarse-grained MD [38–45], self-consistent mean-field theory (SCMFT) [46–49], density functional theory (DFT) [50, 51] and dissipative particle dynamics (DPD) [52–65]. These studies addressed a variety of problems, from vesicle fusion to pore formation to intra-membrane phase separation and line tension. Because of these proven successes of mesoscale approaches, it is reasonable to employ similar methods for the description of nanoparticle–membrane interactions, and indeed, coarse-grained Monte Carlo [66] and Brownian dynamics [67] had been used to study the adsorption of nanoparticles onto membranes. (It has also been noted that, in many cases, interactions between particles and membranes could be described by employing even further coarse-graining and analyzing elastic deformations of the membranes in the presence of the particle within the framework of Helfrich [68] elasticity theory; this approach

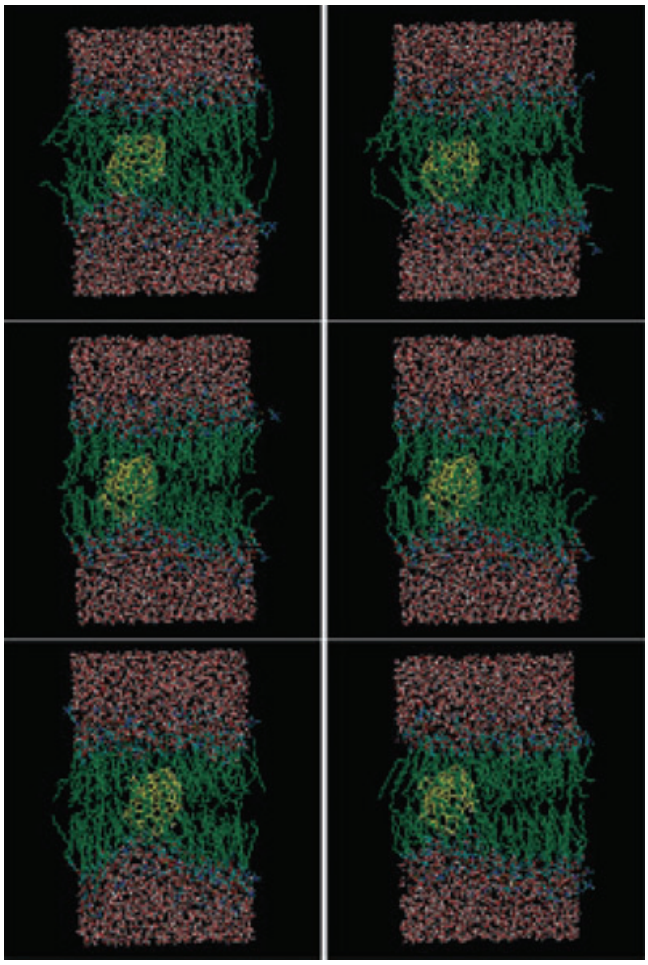

Figure 10.2 Snapshots of configurations of round carbon nanoparticles in a DMPC bilayer membrane (from atomistic molecular dynamics simulations). The time elapsed between frames is 2 ns. Reprinted from Ref. [36], with permission from the American Chemical Society.

was successfully employed by Deserno and coworkers [69–72] and provided excellent insights into thermodynamics of colloid adhesion onto membranes.)

In this chapter, we describe our recent mesoscale modeling studies of the interactions between spherical nanoparticles and model cell membranes [73–75]. Although these studies are not comprehensive, they demonstrate the techniques that could be used to further explore the mechanisms of nanoparticle–membrane interactions. Initially, we describe the use of hybrid self-consistent field theory to study the phase behavior of small (radius $R_p < 10$ nm) spherical nanoparticles near a lipid bilayer. Depending on the nanoparticle size and interaction parameters

between the nanoparticle and the hydrophilic head-group, various responses of the membrane are observed, ranging from endocytosis-like behavior (for hydrophobic particles) to membrane break-up and hole formation (for charged or hydrophilic particles). In the case of larger nanoparticles ($R_p > 10\,\mathrm{nm}$), more coarse-grained DPD simulations were used to identify the various scenarios of endocytosis and/or membrane break-up and hole formation. Finally, the extension of modeling to more complex systems ('Janus' particles, anisotropic particles, etc.) is discussed.

10.2
Field-Theoretical Modeling of Nanoparticle – Membrane Interactions

10.2.1
Background and Theoretical Formalism

As mentioned above, many previous studies have been targeted at examining and understanding the interactions between nanoparticles and human cells [1–20, 76]. In some cases, nanoparticles can result in cytotoxicity which may be either beneficial (e.g. when nanoparticles are used for cancer therapy [4–10]) or harmful [11–20]. Interestingly, several studies have shown that the effect of nanoparticles on cells often differs from that of microparticles, even when chemical nature of the particulates is very similar [15, 16]. It was further shown that nanoparticles can strongly interact with the cell membrane, either adsorbing onto it or compromising the membrane's integrity to result in the formation of holes, with the resultant morphology depending on the nanoparticle size and surface charge [17–19].

In order to explain these observations on a qualitative basis, Ginzburg and Balijepalli [73] recently proposed that the changes in the membrane structure as a result of interaction with nanoparticles can be ascribed to changes in the thermodynamics of the nanoparticle/water/membrane system. It is notable that the nature of nanoparticle–polymer interactions has been at the forefront of extensive research within the polymer community in recent years [1–3, 77–92]. Here, theoretical, computational and experimental studies have demonstrated conclusively that nanoparticles can influence the thermodynamics and phase behavior of multicomponent polymer melts or solutions. For example, when nanoparticles are incorporated into a block copolymer melt, new thermodynamically stable, equilibrium microphase separated structures are formed [83]. These phenomena typically occur when the nanoparticle size is on the order of the characteristic polymer length-scale (e.g. radius of gyration or characteristic lamellar thickness). In the case of nanoparticle–membrane interactions, it can be similarly hypothesized that the system can potentially lower its free energy by forming hybrid nanoparticle–lipid micellar structures. To describe these new structures theoretically, we use the Thompson–Ginzburg–Matsen–Balazs (TGMB) self-consistent field/density functional theory of block copolymer/nanoparticle mixtures [83, 84], adapting it to describe lipid bilayers (simplified representation of cell membranes) and

nanoparticles in solution. We then map the new hybrid structures as a function of nanoparticle radius and surface treatment, and qualitatively explain the observed trends.

First, we write down the free energy of a three-component mixture of water (W), diblock surfactant (D) and particle (P). Each diblock surfactant consists of a hydrophilic (H) block and lipophilic (L) block. Following the TGMB mean-field formalism, we write:

$$\frac{FN_D}{k_BT\rho_0V} = f_1 + f_2 + f_3 + f_4 \tag{10.1}$$

$$f_1 = -\frac{\varphi_P}{\alpha}\ln\left(\frac{Q_P}{V}\right) - \varphi_D \ln\left(\frac{Q_D}{V}\right) - N_D\varphi_W \ln\left(\frac{Q_W}{V}\right)$$

$$f_2 = \frac{1}{V}\int \mathbf{dr}\left[\sum_{\alpha,\beta}(\chi_{\alpha\beta}N_D)\phi_\alpha(\mathbf{r})\phi_\beta(\mathbf{r}) - \xi(\mathbf{r})\left(1 - \sum_\alpha \phi_\alpha(\mathbf{r})\right)\right]$$

$$f_3 = \frac{1}{V}\int \mathbf{dr}\left[-\sum_{\alpha(\neq P)} w_\alpha(\mathbf{r})\phi_\alpha(\mathbf{r}) - w_P(\mathbf{r})\rho_P(\mathbf{r})\right]$$

$$f_4 = \frac{1}{V}\int \mathbf{dr}\left[\rho_{\mathbf{P}}(\mathbf{r})\Psi_{CS}\left(\bar{\bar{\phi}}_P(\mathbf{r})\right)\right] \tag{10.2}$$

Here, the first term, f_1, describes the 'ideal mean-field' free energies of each component given external chemical potential fields w. The overall volume fractions of the components, φ_P, φ_D and φ_W add up to 1. The partition functions of individual components, Q_P, Q_D, and Q_W, are given below. The second term, f_2, contains the (local) interactions among various species, described in a traditional Flory–Huggins [93, 94] fashion, as well as the incompressibility constraint. The third term, f_3, contains the terms with chemical potential fields w; it should be noted that, as in the original TGMB report, the chemical potential fields are conjugate to the local volume fractions, $\phi_\alpha(\mathbf{r})$; the exception is the 'particle' field, W_P, which is conjugate to the particle center density probability, $\rho_{\mathbf{P}}(\mathbf{r})$. Finally, the fourth term, f_4, contains the nonideal hard-sphere interactions, summed up via the 'smoothed density approximation' of the hard sphere DFT due to Tarazona [95]. In the Tarazona DFT, the nonideal free energy of the hard-sphere fluid is given by the Carnahan–Starling [96] equation of state:

$$\Psi_{CS}(x) = \frac{4x - 3x^2}{(1-x)^2} \tag{10.3}$$

The particles are, in a sense, described by three interrelated 'densities': center probability function, $\rho_{\mathbf{P}}(\mathbf{r})$; local volume fraction, $\phi_P(\mathbf{r})$; and the 'smoothed density' function, $\bar{\bar{\phi}}_P(\mathbf{r})$. The relationship between these three functions is as follows:

$$\phi_P(\mathbf{r}) = \frac{1}{N_D}\int \mathbf{dr}'\rho_P(\mathbf{r}')\Theta\left(1-\frac{|\mathbf{r}-\mathbf{r}'|}{(R_P/R_{gD})}\right) \tag{10.4a}$$

$$\bar{\bar{\phi}}_P(\mathbf{r}) = \frac{1}{2^d N_D}\int \mathbf{dr}'\rho_P(\mathbf{r}')\Theta\left(1-\frac{|\mathbf{r}-\mathbf{r}'|}{(2R_P/R_{gD})}\right) \tag{10.4b}$$

Note that the spatial integration is in dimensionless coordinates scaled by the diblock radius of gyration, $R_{gD} = a(N_D/6)^{1/2}$. In introducing this scaling, we follow the formalism of Drolet and Fredrickson [97], whose real-space method of free energy minimization is adopted both in the TGMB report and in this study. The power exponent d in Equation 10.4b is space dimensionality, and Θ is the Heaviside step function ($\Theta(x) = 1$ if $x > 0$ and 0 otherwise).

Partition functions of individual components are given by:

$$Q_W = \int \exp\{-w_W(\mathbf{r})\}\mathbf{dr} \tag{10.5}$$

$$Q_P = \int \exp\{-w_P(\mathbf{r})\}\mathbf{dr} \tag{10.6}$$

$$Q_D = \int q(\mathbf{r},1)\mathbf{dr} \tag{10.7}$$

Here, the propagator $q(\mathbf{r}, s)$ (where $0 < s < 1$ is the index denoting the position along the diblock chain) and its counterpart $q\dagger(\mathbf{r}, s)$ are given by the modified diffusion equations:

$$\frac{\partial q(\mathbf{r},s)}{\partial s} = [\nabla^2 - w_{t(s)}]q(\mathbf{r},s) \tag{10.8a}$$

$$\frac{\partial q\dagger(\mathrm{r},\mathrm{s})}{\partial s} = -[\nabla^2 - w_{t(s)}]q\dagger(\mathrm{r},\mathrm{s}) \tag{10.8b}$$

Here, $t(s) = L$ if $s < f$, and H otherwise. Equations 10.8a and 10.8b must be solved subject to boundary conditions $q(\mathbf{r}, 0) = q\dagger(\mathbf{r}, 1) = 1$.

Equation 10.1 determines the overall free energy of the system as a function of the local densities [$\phi_\alpha(\mathbf{r})$ for nonparticle species and $\rho_P(\mathbf{r})$ for the particles], local chemical potentials $w_\alpha(\mathbf{r})$, and the incompressibility constraint field $\xi(\mathbf{r})$. Minimization of Equation 10.1 with respect to all of these functions results in a set of self-consistency equations; these equations are then solved on a lattice using an iterative procedure until the specified convergence is achieved. The self-consistency equations are as follows:

$$w_H(\mathbf{r}) = \chi_{HL}N_D\phi_L(\mathbf{r}) + \chi_{HP}N_D\phi_P(\mathbf{r}) + \xi(\mathbf{r}) \tag{10.9a}$$

$$w_L(\mathbf{r}) = \chi_{HL}N_D\phi_H(\mathbf{r}) + \chi_{WL}N_D\phi_W(\mathbf{r}) + \xi(\mathbf{r}) \tag{10.9b}$$

$$w_W(\mathbf{r}) = \chi_{WL}N_D\phi_L(\mathbf{r}) + \chi_{WP}N_D\phi_P(\mathbf{r}) + \xi(\mathbf{r}) \tag{10.9c}$$

$$w_P(\mathbf{r}) = \Psi_{CS}\left(\bar{\bar{\phi}}_P(\mathbf{r})\right) + \frac{1}{N_D}\int \mathbf{dr}'\Theta\left(1 - \frac{|\mathbf{r}-\mathbf{r}'|}{(R_P/R_{gD})}\right)\times [\chi_{HP}N_D\phi_H(\mathbf{r}') + \chi_{WP}N_D\phi_W(\mathbf{r}') + \xi(\mathbf{r}')] + \frac{1}{2^d N_D}\int \mathbf{dr}'\Theta\left(1 - \frac{|\mathbf{r}-\mathbf{r}'|}{(2R_P/R_{gD})}\right)\times\left[\rho_P(\mathbf{r}')\Psi'_{CS}\left(\bar{\bar{\phi}}_P(\mathbf{r}')\right)\right] \tag{10.9d}$$

$$\rho_P(\mathbf{r}) = \frac{\varphi_P}{\alpha}\frac{V}{Q_P}\exp[-w_P(\mathbf{r})] \tag{10.9e}$$

$$\phi_W(\mathbf{r}) = \varphi_W\frac{V}{Q_W}\exp[-w_W(\mathbf{r})] \tag{10.9f}$$

$$\phi_L(\mathbf{r}) = \varphi_D\frac{V}{Q_D}\int_0^f q(\mathbf{r},s)q^{\dagger}(\mathbf{r},s)\mathrm{d}s \tag{10.9g}$$

$$\phi_H(\mathbf{r}) = \varphi_D\frac{V}{Q_D}\int_f^1 q(\mathbf{r},s)q^{\dagger}(\mathbf{r},s)\mathrm{d}s \tag{10.9h}$$

$$\phi_H(\mathbf{r}) + \phi_L(\mathbf{r}) + \phi_P(\mathbf{r}) + \phi_W(\mathbf{r}) = 1 \tag{10.9i}$$

Equations 10.9a–10.9i, together with definitions of functions $\phi_P(\mathbf{r})$ and $\bar{\bar{\phi}}_P(\mathbf{r})$ (Equations 10.4a and 10.4b), constitute a full set of self-consistency equations that need to be solved iteratively. The solution algorithm (as adapted from the approach of Drolet and Fredrickson [97] and the original TGMB report [83]) is as follows. First, the chemical potential and pressure fields are initialized. Next, using Equations 10.9e–10.9i, together with Equations 10.4a and 10.4b, density fields for all species are calculated. Then, new chemical potential fields are generated using the Drolet–Fredrickson prescription,

$$w_i^{t+1}(\mathbf{r}) = (1-\lambda_i)w_i^t(\mathbf{r}) + \lambda_i\mu_i(\mathbf{r}) \tag{10.10}$$

where t is the iteration number ('effective time'), $i = H, L, W$ or P, λ_t is the 'timestep' and μ_i are the 'new chemical potentials' calculated using Equations 10.9a–10.9d. Finally, we update the pressure field, ξ, using the following formula:

$$\xi(\mathbf{r}) = \hat{F}^{-1}(P(\mathbf{q})) + \varepsilon(\phi_P(\mathbf{r}) + \phi_W(\mathbf{r}) + \phi_H(\mathbf{r}) + \phi_L(\mathbf{r}) - 1) \tag{10.11a}$$

$$P(\mathbf{q}) = \frac{H_W(\mathbf{q}) + H_P(\mathbf{q}) + H_H(\mathbf{q}) + H_L(\mathbf{q})}{3 + N_D^{-1}\hat{F}\left(\Theta\left(1 - \frac{\mathbf{r}}{[R_P/R_{gD}]}\right)\right)} \tag{10.11b}$$

Functions $H_H(\boldsymbol{q})$, $H_L(\boldsymbol{q})$, $H_W(\boldsymbol{q})$, and $H_P(\boldsymbol{q})$ are Fourier transforms of the right-hand sides of Equations 10.9a–10.9d, respectively, except for the terms containing ξ (see Rasmussen and Kalosakas [98] for the derivation of a similar formula in a particle-free case). Operators $\hat{F}$ and $\hat{F}^{-1}$ denote the standard (either two- or three-dimensional) Fourier transforms. (Note that Equations 10.11a and 10.11b can be used only in conjunction with periodic boundary conditions.)

In the original TGMB reports, as well as in a recent study of hybrid nanoparticle/block copolymer micelles by Zhang *et al.* [85], simulations began with random initial conditions. Here, we start from the field configuration representing a bilayer and a nanoparticle touching it on one side. Also, in this study, we consider the case of a single 'stationary' nanoparticle, whereas the other reports dealt with an ensemble of nanoparticles. The particle is 'created' by setting $w_P(\mathbf{r})$ as a sharp Gaussian (almost a delta-function) with maximum at the particle center:

$$w_P(i,\, j) = -A \exp\left\lfloor -B\left\{(i-I)^2 + (j-J)^2\right\}\right\rfloor, \tag{10.12}$$

where (i, j) are local coordinates of a given point $\boldsymbol{r}$, (I,J) are coordinates of the particle center, and A and B are large numbers so that Equation 10.12 effectively represents a delta-function (we used $A = 10.0$, $B = 10.0$). Because of Equation 10.4a and the incompressibility constraint, $\phi_P(\mathbf{r}) \approx 1$ within the d-dimensional sphere of radius R_P ($d = 2$ or 3 is the space-dimensionality of the simulation box; in our system, $d = 2$).

Over the course of the simulation, $w_P(\mathbf{r})$ is kept constant ($\lambda_p = 0$), while all other variables are driven towards the state corresponding to the local free energy minimum. In addition, Equation 10.11 is modified as follows:

$$\xi(\mathbf{r}) = P(\mathbf{r}) + \varepsilon\left(\phi_P(\mathbf{r}) + \phi_W(\mathbf{r}) + \phi_H(\mathbf{r}) + \phi_L(\mathbf{r}) - 1\right) \tag{10.13a}$$

$$P(\mathbf{r}) = \frac{H_W(\mathbf{r}) + H_H(\mathbf{r}) + H_L(\mathbf{r})}{3} \tag{10.13b}$$

where $H_H(\boldsymbol{r})$, $H_L(\boldsymbol{r})$ and $H_W(\boldsymbol{r})$ are the right-hand sides of Equations 10.9a–10.9c, respectively, except for the terms containing ξ.

We set $\lambda = 0.025$, and $\varepsilon = 60$. With these parameters, we obtained a reliable convergence for all particle radii in the range $4a < R_p < 8a$; the average deviation from the incompressibility, $|\Sigma\phi - 1|$, was less than 10^{-3} in all cases.

10.2.2
Simulation Results: Small Nanoparticle Near a Lipid Bilayer

We begin by simulating a particle-free solution of phospholipids in water, starting from the uniform initial condition. Our goal is to obtain a phospholipid bilayer that would give a reasonable representation of a cell membrane (see Figure 10.3a). A typical phospholipid surfactant has a hydrophilic head-group and one or two lipophilic tails; we model this as a simple diblock, with hydrophilic (H) and lipo-

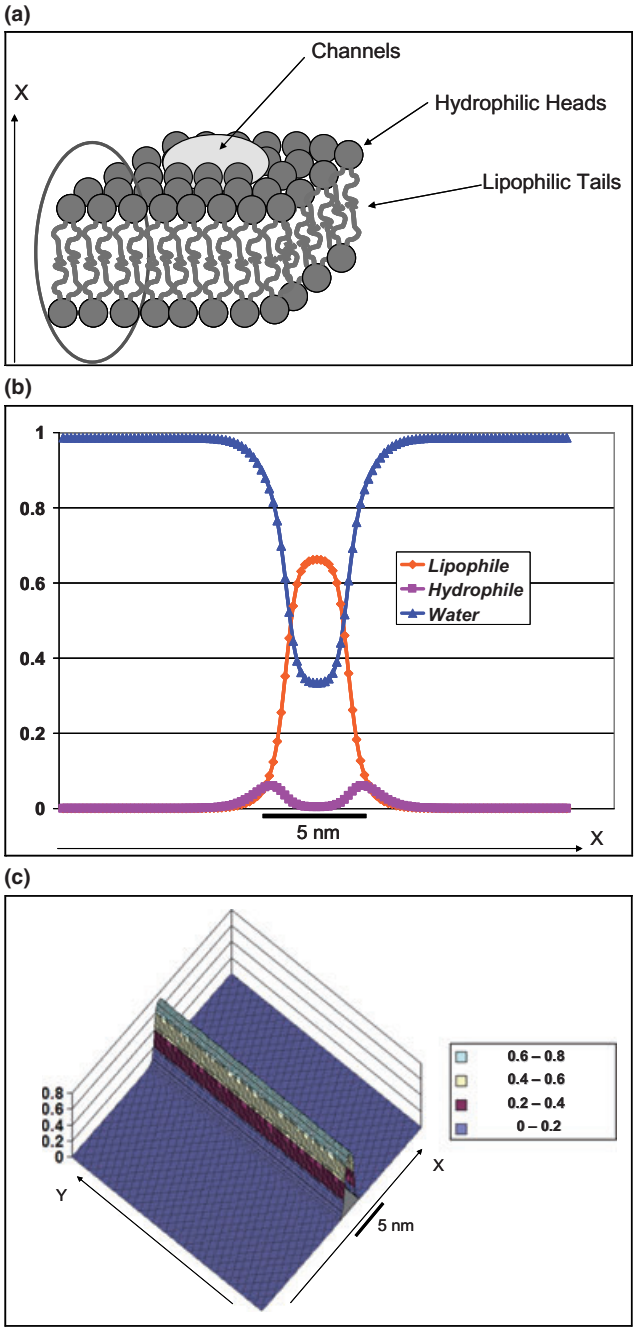

Figure 10.3 Simplified representation of a cell membrane. (a) Sketch of the membrane structure; (b) Simulated density profiles of various species as function of the distance from the center of the bilayer; (c) Simulated density map of the lipophilic part of the bilayer. The x-axis represents the normal to the membrane plane.

philic (L) blocks. The total degree of polymerization is denoted N_D, and the fraction of lipophilic block is denoted f. We assume that each segment has Kuhn length $a = 0.4\,\text{nm}$, and volume $(\rho_0)^{-1} = 0.064\,\text{nm}$ [3]. The volume fraction of the diblock is denoted φ_D, while the rest of the system is water (W). The morphology of the membrane is determined by N_D and φ_D, as well as by the pairwise Flory–Huggins interaction parameters, χ_{HL}, χ_{WL} and χ_{HL}. Here, we take $\chi_{HL} = \chi_{WL} = 1.0$, $\chi_{HL} = 0.0$, $N_D = 50$, $f = 0.88$ and $\varphi_D = 0.05$. Simulated density profiles (local volume fractions) of hydrophilic (H) and lipophilic (L) blocks, as well as water (W) are shown in Figure 10.3b. It can be seen that our model successfully captures many features of a typical cell membrane; a slight drawback is that it somewhat overestimates the fraction of water inside the bilayer. The thickness of the membrane that 'self-assembles' in this simulation is approximately 16 lattice cells = $14.4a \sim 5.6\,\text{nm}$, which is consistent with the thickness of, for example a dimyristoylphosphatidylcholine (DMPC) membrane [19]. In Figure 10.3c, the density map of the lipophilic block is plotted; as the volume fraction of lipophiles in the membrane is almost 90%, it is a good indication of the morphology of the whole membrane, and will form the basis of a comparison as the changes brought about by the particle are evaluated.

It is now possible to model the thermodynamics of the nanoparticle–membrane interaction. To do this, we save all fields from the final configuration representing the bilayer, and then add the new field describing the particle. The particle field is set up as a sharp Gaussian, with the maximum being exactly one particle radius away from the outer edge of the bilayer. We then use the new fields as the starting point for the simulations. To facilitate comparison with experimental studies (e.g. recent studies by Banaszak Holl, Orr *et al.* [17–19]), we fix the Flory–Huggins interaction parameters between the particle and water, $\chi_{PW} = 1.0$, and particle and lipid, $\chi_{PL} = 0.0$, while varying the interaction parameter between the particle and the head-group, χ_{PH}, from +1.0 (repulsive) to −3.0 (strongly attractive). This variation is expected to mimic the role of the nanoparticle surface charges. The uncharged particles (χ_{PH}, of +1.0) should show hydrophobic tendencies, while strongly charged particles (χ_{PH}, of −3.0) should have attractive interactions with the zwitterionic (dipolar) head-groups.

We first consider uncharged ('hydrophobic') nanoparticles. In this case, the particle is likely to be absorbed into the membrane, swelling it and effectively 'cleaving' its internal hydrophobic bilayer into two. This mechanism is somewhat similar to the selective swelling of block copolymer lamellar domains by nanoparticles [83–84, 88, 91, 92]. Because of the hydrophobic nature of the particle surface, the particle breaks up the bilayer to increase its contacts with the lipophilic surfactant tails, and thereby minimize its surface tension. Such behavior is consistent with the results of recent experiments conducted Banaszak Holl, Orr *et al.* [17–19], which showed that charge-neutral PAMAM dendrimers G5-Ac adsorb to the existing supported lipid bilayers – the layers thicken, but no new holes are formed.

The behavior of the membrane changes completely in the presence of strongly charged nanoparticles. Because of the strong attraction of the head-groups to the particle surface, the preferential phospholipid arrangement now would be to form

a bilayer around the particle. As a result of this, large numbers of phospholipid molecules are pulled away from the original membrane. The membrane, then, can thin or even rupture. This model is consistent with the hole formation observed by Banaszak Holl, Orr *et al.* [17–19] in the systems where supported lipid bilayers were exposed to charged PAMAM dendrimers G7-NH_2. Indeed, Banaszak Holl and coworkers speculated that the hole formation in the bilayers was caused by a migration of phospholipids onto the dendrimer – or other charged nanoparticle – surface and the formation of 'dendrimer-filled vesicles' [17].

From the above analysis, it follows that uncharged or hydrophobically modified nanoparticles can incorporate into cell membranes, resulting in membrane swelling. On the other hand, strongly charged or more hydrophilic nanoparticles can pull the phospholipids away from the membrane, forming a hybrid micelle (particle as core, phospholipid bilayer as shell). This process can lead to the rupture of the original membrane and formation of nanosized holes.

In order to qualitatively understand the dependence of the particle–membrane interaction on particle size and surface treatment type, several simulations were carried out with various particle radii (R_p = 1.6, 2.0, 2.4, 2.8 and 3.2 nm) and particle–hydrophile interaction parameters (χ_{PH} = 1.0, 0.0, −1.0, −2.0, −3.0). The results of these simulations are summarized in the phase diagram shown in Figure 10.4. It can be seen that, as the charge density of the particle surface is increased, the particle is attracting more and more phospholipid molecules away from the membrane so that they could adsorb on the particle surface. In particular, while the neutral particles surround themselves with a monolayer of phospholipids, the strongly charged particles must surround themselves with a bilayer, thus taking away twice as much phospholipids as the neutral particles. This qualitative picture is also supported by the analysis of density profiles across the particle and the

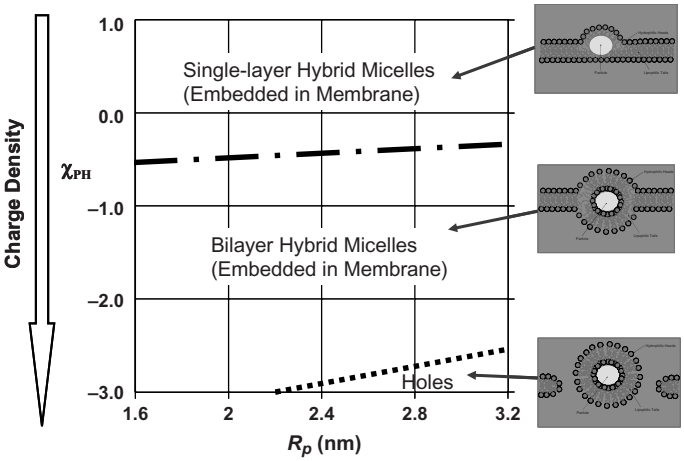

Figure 10.4 Phase diagram illustrating the nature of membrane–nanoparticle interaction as a function of particle surface treatment and particle size.

membrane in the X-direction (perpendicular to the membrane surface), as plotted in Figure 10.5. It can be seen that while for the 'neutral' ($\chi_{PH} = 1.0$) nanoparticles (Figure 10.5a, c, e), there are only two maxima in the head-group (H) density profile (pink curves), indicating that the particle goes inside the bilayer and swells it. On the other hand, for the 'charged' ($\chi_{PH} = -3.0$) particles (Figure 10.5b, d, f), there are four maxima for the head-group density profile. This indicates that the

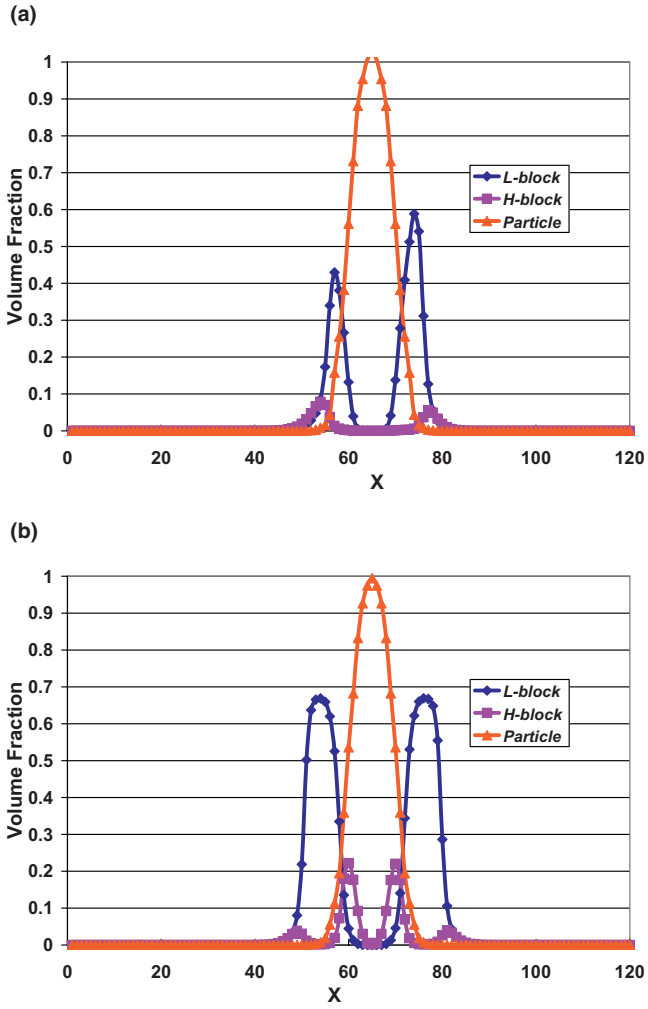

Figure 10.5 Density profiles for hydrophilic (H) and lipophilic (L) blocks of the membrane surfactant, as well as particles, along the line normal to the original membrane surface and passing through the nanoparticle center. Cases considered: (a) $R_P = 1.6$ nm, $\chi_{PH} = 1.0$; (b) $R_P = 1.6$ nm, $\chi_{PH} = -3.0$; (c) $R_P = 2.4$ nm, $\chi_{PH} = 1.0$; (d) $R_P = 2.4$ nm, $\chi_{PH} = -3.0$; (e) $R_P = 3.2$ nm, $\chi_{PH} = 1.0$; (f) $R_P = 3.2$ nm, $\chi_{PH} = -3.0$.

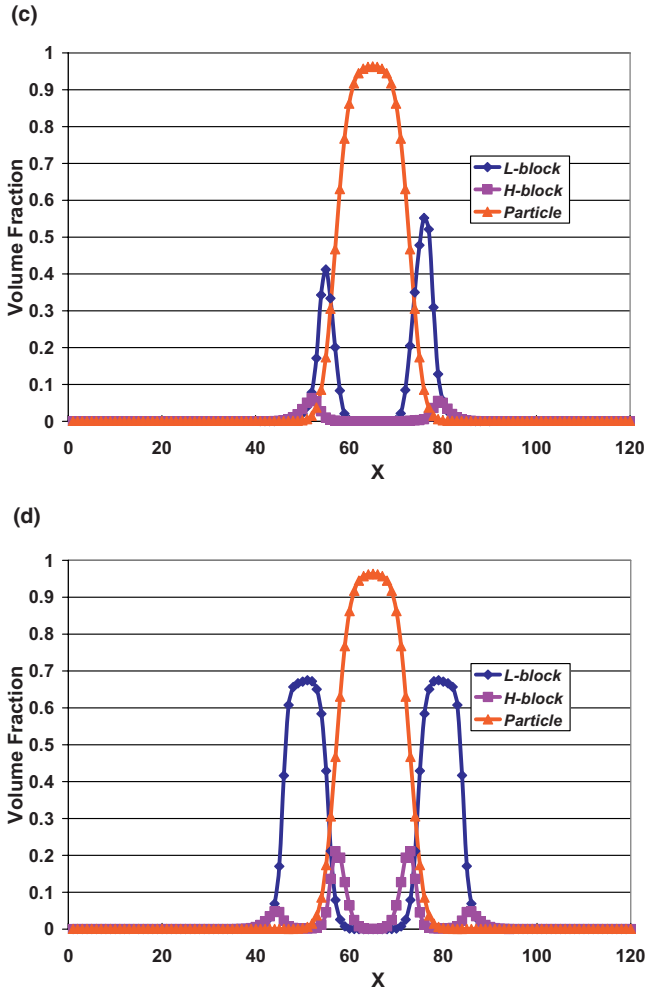

Figure 10.5 *Continued*

particles attract the head-groups and cause the phospholipids to attempt to create a curved bilayer around the particle. Ultimately, if the particles are sufficiently large, they attract so much phospholipid that the membrane can no longer sustain its flat morphology, and reduces its free energy by making a hole. Thus, one can observe the creation of holes in the case of strongly charged particles, the diameter of which is comparable or larger than the membrane thickness, as demonstrated by Banaszak Holl, Orr *et al.* [17–19].

Until now, this analysis has focused on nanoparticles with $R_p \sim 1$–4 nm. But what might be expected if the nanoparticle size were to be increased? We believe that the same trends would be observed for slightly larger sizes ($R_p \sim 5$–10 nm), where particle size is still comparable to the membrane thickness. It could be

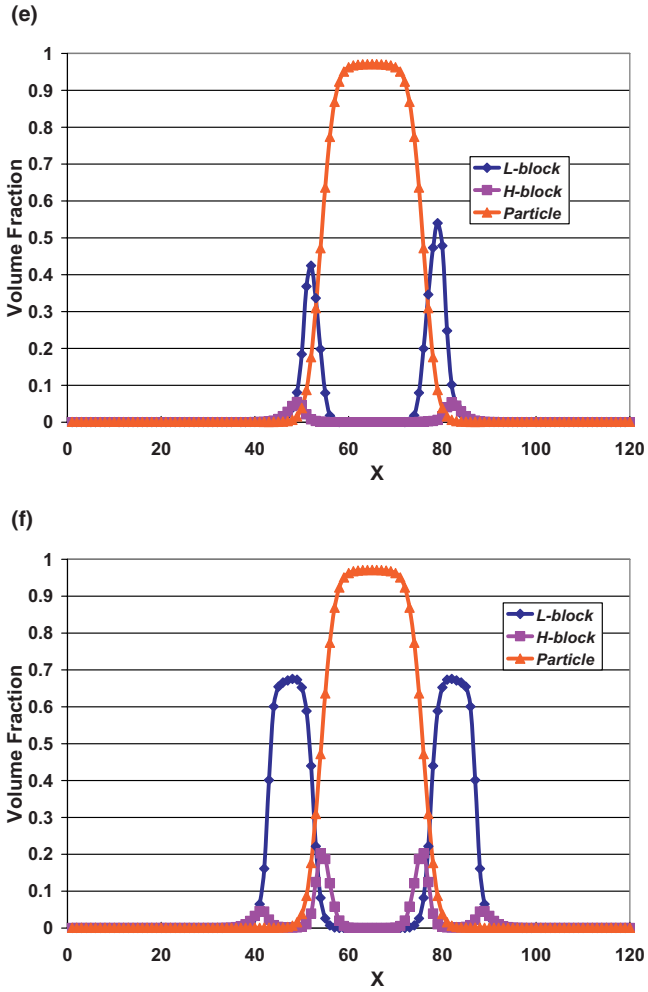

Figure 10.5 *Continued*

imagined that, within this range, neutral nanoparticles would still be able to incorporate into the membrane, while charged ones would force hole formation. Then, as the particle size becomes larger, the activation barriers for these processes (due to the disruption of the bilayer) would be likely to increase substantially (in proportion to the particle surface area). It is still possible that strongly charged particles could overcome those barriers and pull the phospholipids away from the membrane, as discussed above. To better understand these events, however, we should consider the DPD model. In the following, we describe a recent DPD study [74] in which the dynamics of phagocytosis (the envelopment of particles by membranes) were addressed.

10.3
Dissipative Particle Dynamic Simulations of Nanoparticle–Cell Membrane Interactions

10.3.1
Background and Theoretical Formalism

An intriguing challenge that is currently engaging the combined efforts of materials scientists and biologists alike is to determine the extent to which artificial membranes and vesicles can be induced to perform 'life-like' functions that resemble those performed by living cells. One of the functions critical to cell survival is the selective uptake of 'targets' into the cell interior, via phagocytosis. Cells have evolved a variety of specialized mechanisms to accomplish this vital function. In particular, specialized receptor molecules in the membrane first adhere to the target or particle, after which the membrane wraps completely around the particle. The membrane-coated particle, known as a lysosome, then separates from the outer cell membrane and is free to interact with the internal components of the cell. While an understanding of the physical processes involved in phagocytosis is far from complete, recent models have provided significant insight into the structural evolution of the cell as it engulfs the particles [99, 100]. Such studies are also useful for suggesting design rules for creating synthetic vesicles that can perform a similar function – that is, the controlled intake of nanoscopic particles.

Here, we examine the interactions between solid nanoparticles and bilayer membranes, which are formed from short-chain amphiphiles. The goal is to identify the conditions where the particle is wrapped by, and subsequently becomes detached from, the membrane. In order to more closely mimic phagocytosis, and to design robust systems that could be used in various technological applications, attention is focused on determining conditions that permit the membrane to remain intact throughout most of the process. If the particle wrapping proceeds smoothly, then rupture of the membrane could potentially occur only at the final pinch-off, and thus, the integrity of the membrane would not be significantly disrupted. A final aspect of the mechanisms of interest is that the membrane should coat particles entering the vesicle; in this case, the interaction between the engulfed particle and the vesicle contents could potentially be inhibited or controlled.

Synthetic vesicles that exhibit such robust biomimetic behavior can ultimately be utilized in a variety of technological applications. For example, these vesicles could be useful in waste remediation, where they could selectively remove pollutant particles. Both, vesicles [101–104] and microcapsules [105, 106] are increasingly being used in microfluidic systems as microreactors, which provide a controlled environment for chemical reactions to occur. In this situation, the engulfing process could be harnessed to regulate the entry of specific chemical species into the vesicle.

In order to carry out this study, a DPD approach was used. As discussed above, DPD has been proved useful in studies of the thermodynamics and dynamics of

lipid bilayers and many other systems. In the following, we first describe this computational technique and then present results for a particle in contact with an adhesive, homogeneous membrane and for a particle in contact with an adhesive domain in a multicomponent membrane. Through studies involving the homogeneous membrane, we investigate how the strength of the particle–membrane adhesive interaction affects the ability of the membrane to envelop the particle. For this range of adhesive energies, we also examine whether a particle wrapped by this single-component bilayer can become detached from the membrane. Turning to membranes that contain a chemically distinct domain, which is phase-separated from the remainder of the bilayer, we examine the potential advantages offered by this multicomponent system. In the ensuing discussions, we attempt to relate the results of our simulations to the forces that control the curvature of membranes and the available theoretical calculations on analogous systems. We conclude by summarizing our results and discussing their relevance to vesicle design.

As the DPD method has been detailed extensively elsewhere [55], here we provide only a brief description of the technique. Similar to MD simulations, DPD captures the time evolution of a many-body system through the numerical integration of Newton's equation of motion, $d\mathbf{v}_i/dt = \mathbf{f}_i$, where the mass m of a bead of any species is set to 1. (We use the term 'bead' to refer to a single point particle in the numerical simulation, and the term 'particle' to refer to a nanoparticle, the interaction of which with a membrane is studied here.) Unlike MD simulations, DPD involves the use of soft, repulsive interactions and a momentum-conserving thermostat. The force acting on a bead contains three parts, each of which is pairwise additive: $\mathbf{f}_i(t) = \sum (\mathbf{F}_{ij}^C + \mathbf{F}_{ij}^D + \mathbf{F}_{ij}^R)$, where the sum runs over all beads j within a certain cutoff radius r_c. The conservative force is a soft, repulsive force given by $\mathbf{F}_{ij}^C = a_{ij}(1 - r_{ij})\hat{\mathbf{r}}_{ij}$, where α_{ij} is the maximum repulsion between beads i and j, $\mathbf{r}_{ij} = |\mathbf{r}_i - \mathbf{r}_j|/r_c$, and $\hat{\mathbf{r}}_{ij} = \mathbf{r}_{ij}/|\mathbf{r}_{ij}|$. The drag force is $\mathbf{F}_{ij}^D = -\gamma\omega_D(r_{ij})(\hat{\mathbf{r}}_{ij} \cdot \mathbf{v}_{ij})\hat{\mathbf{r}}_{ij}$, where γ is a simulation parameter related to viscosity, ω_D is a weight function that goes to zero at r_c, and $\mathbf{v}_{ij} = \mathbf{v}_i - \mathbf{v}_j$. The random force is $\mathbf{F}_{ij}^R = \sigma\omega_R(r_{ij})\xi_{ij}\hat{\mathbf{r}}_{ij}$, where ξ_{ij} is a zero-mean Gaussian random variable of unit variance and $\sigma^2 = 2k_B T\gamma$. Finally, we use $\omega_D(r_{ij}) = \omega_R(r_{ij})^2 = (1 - r_{ij})^2$ for $r_{ij} < r_c$. The equations of motion are integrated in time with a modified velocity-Verlet algorithm [55]. (We use the nomenclature σ here for consistency with the literature on DPD. In the latter sections of this chapter, σ is used to refer to a line tension.) All simulations are performed using the LAMMPS package [107].

10.3.2 Simulation Details

The system contains amphiphilic 'lipid' molecules, each of which consists of a head-group containing three linearly connected hydrophilic beads (H) and two tails, connected to adjacent head beads, of three hydrophobic beads (T). The lipids are immersed in solvent (S). The amphiphilic nature of the lipids derives from the repulsive interactions. For any two beads of the same type, we take the repulsion

parameter to be $a_{ij} = 25$ and for the remaining interactions, we set $a_{HS} = 25$, $a_{HT} = 100$, and $a_{ST} = 100$. At these values, we find that lipids spontaneously self-assemble into bilayers, as has previously been observed for similar values [108]. In certain cases, we examine the role of membrane rafts by introducing two different lipid species, the head and tail beads of which are labeled H_1, T_1 and H_2, T_2, respectively. We set $a_{H_1H_2} = a_{T_1T_2} > 25$, which causes the lipids to phase separate within the membrane. All interactions between similar lipids, and between head and tail beads, are the same as described above. In general, for real lipid membranes, at least three components (including cholesterol) must be present for phase separation to occur [109]. However, in order to focus on mesoscale phenomena, it is preferable to use this simpler two-component model. Here, we take r_c as the characteristic length scale and k_BT as the characteristic energy scale in the simulations. A characteristic time scale is then defined as $\tau = \sqrt{mr_c^2/k_BT}$. The remaining simulation parameters are $\sigma = 3$ and $\Delta t = 0.02\tau$, with a total bead number density of $\rho = 3/r_c^3$.

Bonds are represented by the harmonic spring potential $E_{bond} = K_{bond}((r - b)/r_c)^2$, where K_{bond} is the bond constant and b the equilibrium bond length; here, we use $K_{bond} = 64$ and $b = 0.5$. We also insert a weaker bond ($K'_{bond} = 10$) between the first beads on the two tails to keep the tails oriented in the same direction. Additionally, we include a three-body stiffness potential along the tails of the form $E_{angle} = K_{angle}(1 + \cos\theta)$, where θ is the angle formed by three adjacent beads, and set the coefficient to $K_{angle} = 10$. This stiffness term increases the stability and bending rigidity of the bilayers.

We use the settings and procedures described above to 'prepare' a lipid bilayer membrane in a solvent. The membrane has a near-zero interfacial tension, as will be discussed below. The membrane thickness h is defined as the distance between the two peaks in the lipid head density profile; here, $h \approx 4r_c$.

A solid, near-spherical nanoparticle is formed from particle beads (P) arranged on an FCC lattice with a number density of $\rho = 3/r_c^3$. The beads comprising a single particle are constrained to move as a rigid body. It has been verified that the solvent and lipid beads do not penetrate the interior of the particle under these conditions. The particle is chosen to have a hydrophilic surface, so the interaction between the beads composing the particle (P) and the lipid tail beads is taken to be $a_{PT} = 100$. To induce an adhesive interaction between the particle and the membrane, we make the particle compatible with the lipid head beads by setting $a_{PH} = 25$, and vary the particle–solvent interaction in the range $25 \le a_{PS} \le 60$.

For situations in which a membrane undergoes only continuous transformations (i.e. excluding changes in topology, such as pore formation), the equilibrium conformation can be determined by minimizing the macroscopic free energy functional, under a given set of constraints. This approach was used by Deserno *et al.* [69–72] to determine equilibrium conformations for a membrane in contact with a particle. The free energy of the membrane depends upon the mean and Gaussian curvatures (the Helfrich functional [68]), the membrane tension and the contact area with the particle.

Below, we describe both the free energy functional and how we extracted the relevant macroscopic parameters from our simulations. We then verify that our chosen simulation parameters represent physically realistic values and estimate the length and time scales that characterize our system. Finally, we compare our simulation results for the case involving the partial wrapping of the particle with the theoretical predictions made by Deserno [70]. We stress that the macroscopic analytical approach determines only the lowest energy conformation. In general, changes between partially wrapped states can occur through continuous deformation of the membrane, so that the system can always reach an equilibrium partially wrapped conformation when the membrane is in contact with the particle. However, the transition from partial to complete wrapping is not a smooth, continuous process, but necessarily involves a change in the membrane topology. This will potentially require the surmounting of a free energy barrier that is not captured by the macroscopic analysis. Thus, the strength of the numerical simulation is that it allows us to explore both the partially and fully wrapped regimes.

The free energy of a membrane formed from self-assembled lipids includes contributions from a number of different factors. In general, the area per lipid a_l within the membrane is close to the equilibrium value $a_{l,0}$. For small deviations of a_l, the membrane is accurately modeled as a linear elastic material. Then, the elastic free energy term is:

$$F_{elastic} = f_{elastic} A, \tag{10.14}$$

where $f_{elastic} = \frac{K}{2}\left(\frac{a_l - a_{l,0}}{a_{l,0}}\right)^2$ is the energy per unit area, K is the elastic modulus and $A = Na_l/2$ is the total membrane area. The membrane tension is defined as

$$\Sigma = \frac{\partial f_{elastic}}{\partial a} = K\left(\frac{a_l - a_{l,0}}{a_{l,0}}\right) \tag{10.15}$$

If the membrane is not flat, there is a bending free energy given by the Helfrich functional [68]:

$$F_{bend} = \int dA\left[\frac{\kappa}{2}(C_1 + C_2)^2 + \kappa_G C_1 C_2\right] \tag{10.16}$$

where C_1 and C_2 are the two principal curvatures, κ is the mean curvature bending modulus, and κ_G is the Gaussian curvature modulus. From the Gauss–Bonnet theorem [110], the integral of Gaussian curvature over a surface is constant under any deformation that does not change the surface topology or boundary. Thus, the second term in the integral does not contribute to a change in energy, prior to complete wrapping of the particle or some other topology change. A correct description of the transition to complete wrapping requires a more detailed examination of lipid rearrangements, which is discussed below.

We assume that the total energy is decreased by an amount e_{adh} per unit area of membrane adhered to an attractive surface, so that the free energy contribution associated with this binding is given by:

$$F_{adh} = -A_{adh} e_{adh} \tag{10.17}$$

where A_{adh} is the area of contact. The total free energy of a membrane is then

$$F = F_{elastic} + F_{bend} + F_{adh} \tag{10.18}$$

To compare theoretically predicted equilibrium shapes with the results of numerical simulations, it is necessary to determine the values of the macroscopic parameters K, Σ, $a_{l,0}$, κ and e_{adh} that are implied by the simulations. To estimate K and κ, we must first measure the membrane tension Σ for a flat membrane spanning a periodic box. Following the procedure described by Goetz and Lipowsky [111] (which builds on the results of Schofield and Henderson [112]), we measure the stress tensor $\Sigma^{\alpha\beta}$, which is diagonal for a homogeneous membrane in a translationally invariant fluid and has the form $\Sigma^{\alpha\beta} = \begin{pmatrix} \Sigma_T & 0 & 0 \\ 0 & \Sigma_T & 0 \\ 0 & 0 & \Sigma_N \end{pmatrix}$. Here, Σ_N is the normal stress and Σ_T is the tangential stress. Σ_N and Σ_T are determined as a function of z, the distance from the bilayer membrane plane. We then calculate the interfacial tension as $\Sigma = \int_{-\infty}^{\infty} (\Sigma_T(z) - \Sigma_N(z)) dz$. We measure Σ for several values of a_l. We now describe the manner in which a_l is varied. The system is periodic with dimensions L_x, L_y and L_z. The membrane spans the system in the x and y directions, for which the cross-sectional area of the system is $A_C = L_x L_y$. The area per lipid is defined as $a_l = 2A_C/N$, where N is the total number of lipids and the factor of 2 accounts for the two sides of the bilayer. It is important to note that, for small values of A_C, the membrane buckles, and the true membrane surface area is greater than A_C. However, we are mainly interested in situations in which the membrane is flat, outside the vicinity of a particle or raft, so we use the definition of area per lipid based on A_C. To vary a_l for a given system, we increase or decrease L_x and L_y, while varying L_z as necessary to maintain a constant system volume.

From our simulations, we find that $\Sigma \approx 0$ at $a_l = a_{l,0} \approx 1.28 r_c^2$. From a linear fit of $\Sigma(a_l)$ at low membrane tension, we then evaluate $K \approx 33.2 k_B T / r_c^2$. An analysis of thin elastic films [18] shows that κ can be estimated as $\kappa = Kh^2/48$, where h is the membrane thickness, in good agreement with direct numerical [113] and experimental [114] measurements. Substituting in our value for K, we obtain $\kappa = 11 K_B T$ for our system.

We next measure the energy change per unit area associated with a membrane binding to an attractive surface, e_{adh}. The difference in energy exists because, microscopically, the repulsive force between a particle bead and a lipid head bead is weaker than the repulsive force between a particle bead and a solvent bead. To

measure e_{adh}, we prepare a system consisting of solvent bounded by two flat solid walls in the z direction and periodic in the x and y directions. Each wall is comprised of three layers of beads arranged on an FCC lattice with a number density of $\rho = 3/r_c^3$, similar to how the nanoparticle is constructed. To prevent the passage of fluid particles through the wall, we impose an additional bounce-back boundary condition on the fluid particles, as discussed by others [115–117]. We first measure the surface tension of the wall–solvent interface when the repulsion coefficient α between wall and solvent beads is equal to the repulsion coefficient between particle beads and lipid head beads, $a = a_{\mathrm{PH}} = 25$. This value of the surface tension is taken as a measure of the energy of interaction between the particle and the membrane per unit area of contact, e_{coated}. We then measure the surface tension of the wall–solvent interface when the repulsion coefficient a is equal to the repulsion coefficient between particle beads and solvent beads $a = a_{PS}$. As described above, we consider the range $30 \leq a_{\mathrm{PS}} \leq 60$. This value is taken as a measure of the energy of interaction per unit area of particle surface that is not coated by the membrane, $e_{uncoated}$. Then, the energy of adhesion is given by the energy difference between an uncoated and a coated surface:

$$e_{adh} = e_{uncoated} - e_{coated} \tag{10.19}$$

For the values of a_{PS} considered, we find e_{adh} to be on the order of $1 - 14 k_B T / r_c^2$.

The simulation results can be related to physical length and time scales by examining the properties of a tensionless membrane. Typical experimental measurements of dipalmitoylphosphatidylcholine (DPPC) membranes [108] in a tensionless state yield $a_{l,0} \approx 0.6\,\mathrm{nm}^2$, from which we take the length scale in our simulations to be $r_c = 0.67\,\mathrm{nm}$. We estimate the DPD time scale τ from the in-plane diffusion constant of lipids which, for a flat DPPC membrane, has been measured [108] as $D = 5\,\mu\mathrm{m}^2\,\mathrm{s}^{-1}$. Matching this to the diffusion constant in a simulation yields $\tau = 7.2\,\mathrm{ns}$ and, for a single timestep, $\Delta t = 0.02\tau = 0.14\,\mathrm{ns}$.

10.3.3 DPD Simulation Results: Engulfing Nanoparticles with Membranes

10.3.3.1 Engulfing a Small Particle with a Homogeneous Membrane

In the previous section, we defined the membrane free energy and extracted the relevant parameters from our numerical model. We will now use these results to make a comparison of our simulations for the partial wrapping of a particle with theoretical predictions. There are three relevant length scales for the interaction of a vesicle and a particle: the size of the particle; the size of the vesicle; and the thickness of the membrane, h. When the radius of the vesicle is within an order of magnitude of h, it is computationally feasible to represent the entire vesicle. For a much larger vesicle, it is reasonable to represent the portion of the vesicle that interacts with the particle by a flat membrane patch. We consider the case of a large vesicle and take the particle size to be larger than, but within an order of magnitude of, the membrane thickness.

When the particle is brought into contact with the membrane, the membrane will deform in order to increase the amount of its surface area that adheres to the particle. This is driven by the decrease in energy upon adhesion, e_{adh}, and is opposed by the increase in bending energy, which depends upon κ, and the increase in stretching energy, which depends upon the stretching modulus K and the membrane tension Σ.

To understand particle wrapping behavior, we prepare a flat membrane under a small positive tension, containing 12 390 lipids. We bring the membrane in contact with a particle of radius $R_p = 12r_c$ and an adhesion energy in the range of $0k_BT/r_c^2 \leq e_{adh} \leq 14.2k_BT/r_c^2$ and allow the system to equilibrate. The total number of beads in the system (including lipid, particle and solvent) is 1 022 208. Typical values of the box dimensions are $L_x = L_y = 88r_c$ and $L_z = 44r_c$, though we will vary box dimensions to change membrane tension. Holding the membrane lipid properties constant, there are two controlling parameters, the area per lipid a_l (determined from the cross-sectional area A_C as described above), and the adhesion energy e_{adh}. Upon setting $a_l = 1.25r_c^2$, we allow the system to equilibrate and observe the shape of the membrane. We then reduce A_C incrementally, without varying e_{adh}, so that at each step there is more excess membrane area. We observe the extent to which the membrane wraps the particle at each stage. A series of images for equilibrium particle/membrane conformations is shown in Figure 10.6 for different adhesion strengths and different cross-sectional areas.

For coverage greater than one-half of the particle surface, there is a noticeable sharp kink in the membrane where it meets the particle surface. For adhesion energies of $e_{adh} \leq 11.9k_BT/r_c^2$, there is a limit in the extent to which the membrane wraps the particle, and a further decrease of a_l does not lead to increased adhesion beyond a certain point. For example, Figure 10.6e shows the maximum wrapping

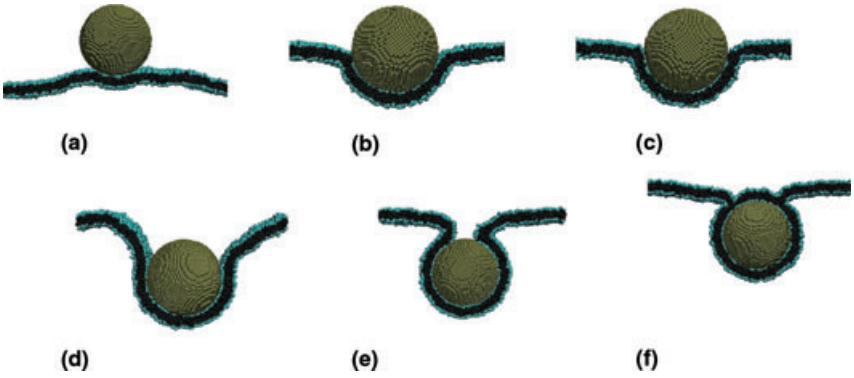

Figure 10.6 Cross-sectional images of equilibrium membrane wrapping around particle at various values of adhesion energy e_{adh} and excess membrane area A_{excess}. Images (a–c) represent $A_{excess} = 0.08$; images (d–f) represent $A_{excess} = 0.87$. The adhesion energy is $e_{adh} = 0$ for images (a) and (d), $e_{adh} \approx 11.9k_BT/r_c$ for (b) and (e), and $e_{adh} \approx 14.2k_BT/r_c$ for (c) and (f).

obtained for $e_{adh} \approx 11.9 k_B T / r_c^2$. The particle is almost completely covered and a small membrane neck exists near the unwrapped portion of the particle surface. A long simulation of this system was run and the neck was observed to be stable for 100 000 time steps.

At a higher adhesion energy, $e_{adh} \approx 14.2 k_B T / r_c^2$, it is possible for the membrane to completely wrap the particle. Initially, one might expect to observe a narrow neck, as in the $e_{adh} \approx 11.9 k_B T / r_c^2$ case, which could eventually undergo fission, allowing the wrapped particle to detach from the flat membrane. However, apparently this does not occur; instead, the membrane forms a film (or 'eyelid'), which spreads across the remaining surface of the particle, as shown in Figure 10.6c. To the best of our knowledge, such a process has not yet been seen in the context of particle wrapping. When the particle is entirely coated, the membrane assumes a new topology, with a closed loop where the flat membrane comes into contact with the bilayer that coats the particle. The membrane structure in a cross-section of this loop is shown in Figure 10.7. The topology of the 'eyelid' closely resembles that of the inverted hexagonal (H_{II}) phase of lipid assemblies. In particular, the junction where the outer membrane contacts the membrane that coats the particle (see Figure 10.7d) bears a close resemblance to a 'trilaterally symmetric void' (TSV), which has been analyzed by Siegel [118, 119] and others [120]. Siegel derived the following relation for g_{TSV}, the free energy per unit length of TSV:

$$g_{TSV} = \pi \kappa_{mono} / 2 R_{mono} \tag{10.20}$$

where κ_{mono} is the mean curvature bending modulus and R_{mono} is the radius of monolayer curvature (equivalent to the radius of the monolayer tubes in the H_{II} phase). Taking $\kappa_{mono} = \kappa/2$ and $R_{mono} = R_p$, we obtain $g_{TSY} \approx k_B T / r_c$. As the 'eyelid' spreads across the particle, the length of the TSV is on the order of $10 r_c$ and thus,

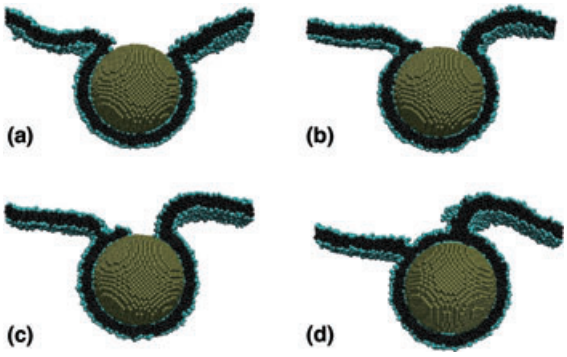

Figure 10.7 Time sequence showing a cross-section of the membrane 'eyelid' which wraps the particle for $e_{adh} \approx 14.2 k_B T / r_c$. Image (d) shows the fully wrapped particle that remains attached to the membrane.

the free energy cost of creating the TSV is commensurate with the free energy reduction due to increased particle wrapping.

The theoretical analysis of this system is typically made for the limit of a large membrane. In this case, the particle is in contact with an infinite reservoir of membrane, so that any stretching of the membrane has an infinitesimal effect on Σ. In this limit, the behavior is independent of the elastic modulus, K. For the finite size system in our simulation, it is necessary to include the change in a_l in the analysis. If this change is not too large, then the linear relationship between Σ and K is preserved.

To compare our simulation results with the theoretical findings, we take the following approach. All simulations are performed in an NVT (constant particle number N, constant volume V and constant temperature T) ensemble, where the box size and dimensions are fixed. If the membrane is essentially flat, under a positive tension, then in order to wrap the particle the total membrane area must increase (excluding situations where the membrane rips). In this case, wrapping is resisted by the increase in the membrane stretching energy. To simplify our analysis, we allow the system dimensions to vary so that the membrane always has a near-zero tension away from the particle. The remaining components of the free energy are then due to the adhesive interaction between the particle and the membrane and the bending rigidity of the membrane.

For a given set of interaction parameters, we allow the membrane and particle to reach an equilibrium conformation for given box dimensions. We repeat this process over a range of the cross-sectional area A_C, keeping the system volume constant. We find that in each case, the area per lipid a_l far from the particle is very close to the zero membrane tension value. We thus take the case with the lowest system energy to be representative of the equilibrium state for a particle in contact with an infinitely large membrane under zero tension.

When the adhesion energy is negligible, the free energy is dominated by membrane bending and stretching. In this case, the minimum free energy is for a flat membrane with the equilibrium area per lipid, $A_C = \frac{N}{2} a_{l,0}$. For larger adhesion energies, as A_C is reduced, there is an 'excess membrane area' $\frac{N}{2} a_{l,0} - A_C$, which is available to wrap the particle, while the remaining free portion of the membrane is flat and at zero tension. The total excess area needed to wrap the particle is $4\pi\left(R_p + \frac{h}{2}\right)^2$, where we take into account the membrane thickness. In this case, the minimum free energy is expected to occur at $A_C + 4\pi\left(R_p + \frac{h}{2}\right)^2 = \frac{N}{2} a_{l,0}$, for a fully wrapped particle. It is convenient to discuss the variation in A_C in terms of a relative excess membrane area $A_{excess} = \left(\frac{N}{2} a_{l,0} - A_C\right) \Big/ \left(4\pi\left(R_P + \frac{h}{2}\right)^2\right)$. For $A_{excess} = 0$, the membrane cannot wrap the particle without increasing its tension. For $A_{excess} = 1$, there is exactly enough excess membrane area to fully wrap the particle while minimizing the membrane stretching and bending energies. Finally, a

negative value of A_{excess} simply means that the flat membrane is under positive tension ($a_l > a_{l,0}$).

We evaluated the energy of the system as function of A_{excess} for multiple values of e_{adh}. This energy has a minimum at a certain value, A^*_{excess}. As A_{excess} is decreased below this value, the contact between the membrane is peeled away from the particle, such that more of the particle surface is exposed to solvent. As A_{excess} is increased above this value, the membrane is unable to further wrap the particle. Instead, the free (unadhered) portion of the membrane takes on increased curvature, in order to fit into the box dimensions. The conformation at A^*_{excess} is taken as a representation of the equilibrium state for a particle in contact with a large, low-tension membrane.

Particle wrapping should occur when the free energy gain due to adhesion exceeds the cost of bending. Following Deserno [70], and using the energies defined in Equations 10.16 and 10.17, the wrapping transition is predicted to occur at $e_{adh}R_p^2/2\kappa = 1$, or $e_{adh} = 0.2k_BT/r_c^2$. Deserno estimates a necessary binding energy for a viral capsid containing 80 adhesive spikes on its surface to be on the order of $6k_BT$ per spike. This is in close agreement with our prediction, where the particle surface can be divided into 80 regions, each of area $22.6r_c^2$ with a necessary binding energy of $0.2k_BT/r_c^2 \times 22.6r_c^2 = 4.5k_BT$ per region.

To determine whether the observed wrapping in our simulations matches these predictions, we calculated the system energy as a function of A_{excess} for different values of e_{adh} (see Ref. [74] for a more in-depth discussion). For low values of e_{adh}, we expect no decrease in energy due to wrapping of the particle. In this case, the system energy appears to have a shallow minimum near $A_{excess} = 0$ (i.e. $a_l = a_{l,0}$). This is the expected behavior when the dominant contributions to the energy are the stretching and bending of the membrane. When $A_{excess} < 0$ the membrane is stretched and the energy rises rapidly with decreasing A_{excess}. For $A_{excess} = 0$, the membrane is forced to wrap around the particle, due to the reduced cross-section. However, this does not lower the energy and the total energy instead increases with decreasing A_{excess}, due to the increased bending of the membrane. At larger values of the adhesion energy, we find that the system energy decreases monotonically with A_{excess}, up to $A_{excess} \approx 1$, since the energy gain of adhesion overcomes the cost of bending. As discussed above, this indicates the tendency of membrane to fully wrap the particle. From our results, it is difficult to measure the precise value of e_{adh} at which the wrapping transition occurs, and the energy minimum at $A_{excess} \approx 0$ disappears. However, we can estimate that it is in the range of $0.9k_BT/r_c^2 \leq e_{adh} \leq 3.6k_BT/r_c^2$, which is somewhat larger than the value predicted by Deserno [70].

There are several factors that might help to explain the larger value. In the first case, the simulation includes thermal effects. The particle surface has a discrete representation, consisting of a large number of beads interacting with the surrounding solvent and membrane. While the value of e_{adh} needed to overcome bending rigidity is quite small, it is likely that thermal fluctuations at the boundary between the adhered and unadhered regions of the membrane would inhibit it from further wrapping the particle. It is also important to note that, in wrapping

the particle, the membrane forms a neck which is a region of high local Gaussian curvature. The Gauss–Bonet theorem, as mentioned above, states that the surface integral of Gaussian curvature is constant with respect to deformations of the membrane. However, it is conceivable that higher-order terms in Gaussian curvature could be important in the free energy, in the region of the neck [121].

10.3.3.2 Engulfing a Small Particle with a Membrane Raft

We next consider the situation where the particle adheres only to a phase-separated membrane domain, or 'raft'. This case has two important differences from the homogeneous adhesive membrane. First, the finite size of the raft implies that particle size plays an important role in determining the outcome. Second, line tension at the raft boundary, or the interface, can alter the dynamics that the membrane goes through as it reaches the point of complete wrapping of the particle.

When a raft is present in the membrane, we must also take into account the interfacial energy between the raft and the bulk of the membrane. Additionally, during fission, a pore can appear in the membrane (as will be discussed in the following section), and there will be an energy per unit length of the pore edge. These two line energy terms can be written as:

$$F_{\text{int}} = \int dl_{\text{int}} \sigma_{\text{int}} \tag{10.21}$$

$$F_{edge} = \int dl_{edge} \sigma_{edge} \tag{10.22}$$

where σ_{int} and σ_{adge} are the line tensions of a domain interface and a free edge, respectively. To determine the line tensions, we measure the stress tensor for a flat membrane containing two domains separated by a linear interface (for σ_{int}), or, in the case of edge tension, a flat homogeneous membrane that spans a periodic box in one direction and has free edges in another (for σ_{edge}), at $\Sigma \approx 0$. Let z be the coordinate normal to the membrane, y the coordinate normal to the interface, or free edge, in the plane of the membrane, and x the remaining, invariant coordinate. The stress tensor is diagonal and has two components, Σ_x and Σ_y in the plane of the membrane. (For the above case of a homogeneous flat membrane, these components are equivalent, $\Sigma_x = \Sigma_y = \Sigma_T$.) Then $\int_{-\infty}^{\infty} (\Sigma_X - \Sigma_Y) dy$ is the 'surface tension' of a plane that is normal to the membrane and intersects it at the domain interface. This is converted to a line tension by integrating over z, so that $\sigma_i = \int_{-\infty}^{\infty} \int_{-\infty}^{\infty} (\Sigma_X - \Sigma_Y) dy dz$, where σ_i has the correct dimensions of energy/length. We measure σ_{edge} in much the same manner, where the line in this case is the free edge of the membrane. The line tension of a free edge was found to be $\sigma_{edge} \approx 4.9 k_B T / r_c$. As both types of lipids have the same interaction with solvent, σ_{edge} is the same for either type.

In this section, we will demonstrate the ability of a membrane raft to enhance particle encapsulation and fission. This is largely due to the reduction in the

interface energy F_{int} that is obtained by allowing the raft to wrap the particle and then separate from the membrane. Fission requires the creation of a pore in the membrane, and so the edge energy F_{edge} also plays a role.

It is well known that membrane rafts can be unstable, deforming into buds, in order to reduce their interfacial energy, potentially causing the bud to separate completely from the rest of the membrane [53, 122, 123]. In order for particle adhesion to be feasible, it is necessary that the raft be stable in the absence of the particle. Before turning to the interaction of particle and raft, we study the behavior of the raft alone. We prepare a flat membrane as described above, but label all lipids as type 2 within a circular region. After allowing the membrane to equilibrate under high tension, we reduce the cross-sectional area of the box to determine whether the raft will form a bud.

To determine the stability of a raft, we initially allow the system to equilibrate while the membrane is held under a small positive tension. In this case, the membrane tension resists budding. We then decrease the cross-section area slightly, so that there is an excess of membrane in the system; this creates ripples across the membrane. Following Julicher and Lipowsky [122], we predict that the lowest energy state is one where the majority phase of the membrane is flat and all excess area is contained in a partially budded raft. In this state, the raft forms a cup- or bowl-like surface. However, the dynamics to reach this state can be quite slow, as fluctuations inevitably cause ripples to develop in the raft and, in particular, near the raft interface. Thus, it can take some time for the raft to settle on one side of the membrane on which it might bud. To speed up this process, we apply a small upwards force on the raft, and an equivalent downwards force on the rest of the membrane. This causes the raft to bud above (rather than below) the membrane in a reasonable time. Once the raft has selected a side, in the initial stages of budding, this force can be turned off. We then continue to reduce the cross-sectional area A_C in small increments, observing the equilibrium state at each step. For values of interfacial tensions up to $\sigma_{\text{int}} \approx 6.2 k_B T / r_c$ we find that the raft becomes partially budded when A_c is reduced. However, it is unable to form a narrow neck (of the type shown in Figure 10.6e) and the partially budded raft appears to be a stable conformation, remaining attached to the membrane for a run of 100 000 time steps.

We now examine the interaction of a particle with a membrane raft. We prepare a flat membrane under a small positive tension, as above, but containing a raft of radius $R_r = 28 r_c$ that has line tension of $\sigma_{\text{int}} \approx 3.7 k_B T / r_c$. We place a particle of radius $R_p = 12 r_c$ at the center of the raft with an adhesion energy of $e_{adh} \approx 11.9 k_B T / r_c^2$. The raft's radius is chosen such that its area is approximately that needed to exactly cover the particle. (Assuming the raft will deform into a spherical shape, still having a membrane thickness of h, then we choose R_r to satisfy $\pi R_r^2 = 4\pi (R_p + h/2)^2$.) First, we allow the system to equilibrate so that the membrane partially wraps the particle. We then reduce A_c such that $A_{excess} = 1$. The raft wraps the particle in such a way that, when the particle is nearly completely covered, the raft interface lies very close to the membrane neck. What happens after this point is illustrated in Figure 10.8. In this figure, the particle is represented by brown beads. A portion

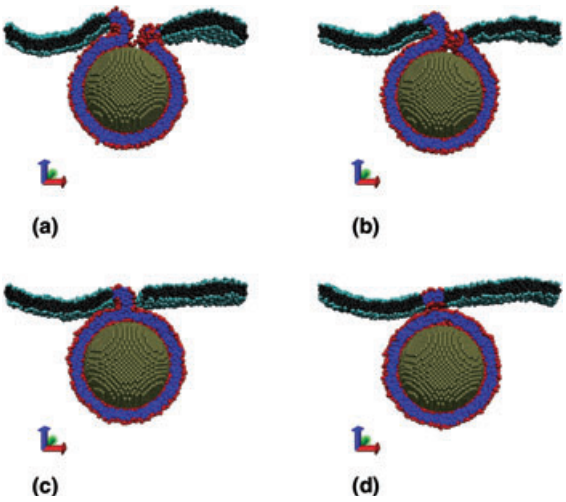

Figure 10.8 Time sequence of membrane neck structure during fission (cross-sectional view). (a) Neck formation and the appearance of a rip; (b) The neck size decreases; (c) The rip spreads across the interface; (d) The raft fully coats the particle. See text for more details.

of the raft, near the membrane neck, is shown with red head beads and dark blue tail beads. In order to illustrate the location of the raft interface, only the bulk phase lipids which lie in close proximity to the raft lipids (within a distance of $1.5r_c$) are shown. These lipids have light blue head beads and black tail beads.

As the particle wrapping proceeds, a rip eventually appears at the raft interface (Figure 10.8a). The rip eventually grows, which has the effect of both reducing the interfacial energy and allowing the raft to completely coat the particle (Figure 10.8b–d). This finally leads to a complete detachment of the coated particle from the flat membrane, or fission.

We repeat this process for different values of e_{adh} and σ_{int} in the range of $3.6k_BT/r_c^2 \le e_{adh} \le 11.9k_BT/r_c^2$ and $1.5k_BT/r_c \le \sigma_{\text{int}} \le 6.2k_BT/r_c$, where the raft is stable in the absence of a particle. The results are summarized in Figure 10.9. Here, circles represent cases in which the membrane remained open and did not fully wrap the particle. The 'plusses' represent cases in which the particle becomes fully wrapped but does not detach from the particle. The diagonal crosses represent cases where the particle is wrapped by the raft, which then undergoes fission, detaching from the membrane. The adhesion energy e_{adh} and the interfacial line tension σ_{int} are varied. The raft radius is $R_R = 28$ and the particle radius is $R_p = 12$. For low adhesion energy $(e_{adh} \approx 3.6k_BT/r_c^2)$, there is only a small area of contact between the particle and the membrane. The particle does not induce sufficient curvature of the membrane to drive the raft to form a bud. As a result, the particle remains partially wrapped and the raft is unable to detach from the membrane. At larger adhesion energies $(e_{adh} \ge 8.5k_BT/r_c^2)$, the reduction in energy due to

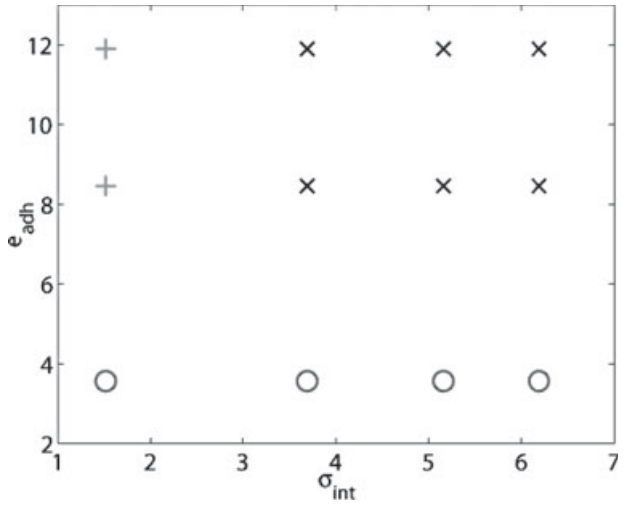

Figure 10.9 Phase diagram describing the equilibrium state of a membrane raft interacting with a particle (see text for details).

particle–membrane contact is sufficient to overcome the increase in membrane bending energy, as was true for the homogeneous membrane. The raft continues to cover the particle until the particle is fully wrapped. However, the final state of the system depends upon σ_{int}. When σ_{int} is low ($\sigma_{int} \approx 1.5 k_B T/r_c$), it is unable to drive fission and the raft spreads across the particle following the same 'eyelid' mechanism that was observed for the homogeneous membrane. In this case, the particle remains attached to the membrane. At larger line tensions ($\sigma_{int} \geq 3.7 k_B T/r_c$), the fission illustrated in Figure 10.8 occurs, allowing the wrapped particle to completely detach from the membrane.

10.3.4
Overall Trends Observed in DPD Simulations

In order to design synthetic vesicles that can uptake nanoscale particles (and thereby mimic the biological function of phagocytosis), we used DPD simulations to model the interactions between lipid membranes and solid spheres, of size greater than – but within an order of magnitude of – the membrane thickness. We considered both a uniformly adhesive, homogeneous membrane and a nonadhesive membrane containing an adhesive raft. The raft in the latter system is composed of a region of distinct amphiphiles, which have phase-separated from the bulk of the lipids making up the majority of the membrane.

For the homogeneous membrane, we find that the particle always remains attached to the vesicle membrane. When the energy of adhesion is below a threshold value, this behavior arises because the membrane remains stable to any rip or change in its topology. Even when the particle is almost fully wrapped, it remains

attached to the bulk membrane by a stable, long-lasting neck. When the energy of adhesion is above the threshold value, the membrane partially wraps the particle, and then grows an 'eyelid' across the remaining particle surface. The result is a new membrane topology, for which the particle is completely wrapped but remains trapped at the membrane.

For the heterogeneous membrane, however, we find that when a particle is in contact with an adhesive raft of comparable size, it is possible for the particle to pass across the membrane, thus entering the vesicle. In this situation, when the particle is almost fully wrapped, the raft's interfacial energy drives a fission process at the membrane neck, thus freeing the wrapped particle from the flat membrane.

The studies on the heterogeneous membranes provide design rules for creating vesicles that can engulf and intake certain nanoscopic particles in their environment. Such 'active' structures can find applications in a number of technologies. For example, the vesicles can be used in waste remediation to selectively remove specific contaminants in a solution. Additionally, synthetic vesicles can be utilized as microscopic 'reaction flasks'; the ability to controllably introduce nanoparticles into these containers could enhance the utility of the heterogeneous vesicles as effective 'tools' for microscale analyses.

10.4
The Next Steps, and Future Opportunities

Until now, theoretical models of nanoparticle interactions with cell membranes have dealt primarily with the simplest cases of spherical nanoparticles with uniform surface chemistry. Within both field-theory and particle-based approaches, one could naturally develop extensions to include more complex cases. For example, it is reasonably straightforward to generalize either model to consider anisotropic nanoparticles. In that case, the main challenge would be not simply to write equations of motion or self-consistency, but to efficiently sample both translational and orientational degrees of freedom. Several research groups have already investigated the interaction of membranes with nanotubes [45] or carbon 'nanoflakes' [36] using atomistic molecular dynamics. Within the next few years, we can expect to see the development of new mesoscale models (both field- and particle-based), and this could be especially useful in analyzing the cytotoxicity of various nanofibers and carbon nanotubes.

Another interesting challenge remains in the area of describing the interactions. In the above studies, all interactions between particles and lipids were parameterized via their short-range potential. Moreover, particle surface chemistry was assumed to be uniform. It is possible to envision a variety of more interesting possibilities. One such possibility would include 'Janus' or 'patchy' particles, where the surface chemistry is nonuniform (there is a lateral phase separation into more hydrophobic and more hydrophilic areas). Very recently, Alexeev, Uspal and Balazs [75] used DPD simulations to study this problem, and some representative results of their

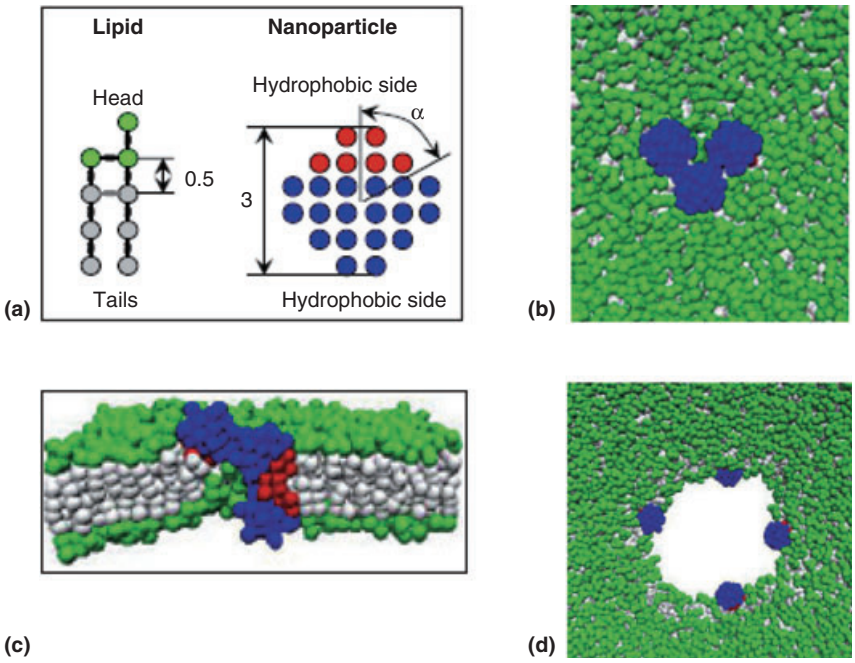

Figure 10.10 Simulation of a lipid bilayer membrane in the presence of four nanoparticles with $\alpha = 60°$. (a) The definition of α and the architecture of the particles and lipids used in the simulation; (b) Nanoparticles assembled in a cluster that perforates the stretched membrane (top view); (c) The same cluster, side view; (d) Pore with nanoparticles in the stretched membrane (top view).

simulations are shown in Figure 10.10. Here, the green beads mark the hydrophilic head groups in the lipid, while the gray particles indicate the hydrophobic tails. The blue beads mark the hydrophilic portion of the nanoparticles and the red beads indicate the hydrophobic portion. The solvent is not shown.

The results of the study showed that the presence of 'Janus' particles can substantially impact the pore ('channel') opening or closing in the membrane. In the simulation of Alexeev, Uspal and Balazs, particles were initially attached to the membrane surface with their hydrophobic patches, leaving the hydrophilic portions exposed to water. Subsequently, a membrane was stretched by some external means (mechanical or chemical) and a pore or channel was formed. Once the channel was formed, the particles quickly diffused towards it and ended up stabilizing its walls. Even when the stress was released, the channel could not fully close. The next stretching-unloading cycles would then be fully reversible, in a sense that the membrane would always open and close the particle-decorated pore, instead of nucleating a new one. When the authors investigated the conditions (particle concentration and the fraction of hydrophobic moieties on the surface) that enabled such behavior, it was found, for example, that if the hydrophobic

fraction of the surface was too low, the particles do not prevent complete closing of the pores; rather, they are expelled to form a cluster attached to the membrane surface. On the other hand, when the hydrophobic portion was too high, the particles were unable to form stable clusters. According to the authors, the results of this study could help to '... establish optimal conditions for harnessing the Janus nanoparticles to act as "artificial proteins", which would allow us to create gateways and regulate the trafficking of molecules into and out of synthetic membranes and vesicles.'

Another interesting possibility might include particles covered with 'loosely bound' ligands that could move around the particle, depending on its surroundings. As shown by Kramer and coworkers [124, 125], such mobile ligands could be used to guide nanoparticles into various domains or towards the surfaces or interfaces. Even more intriguing and challenging scenarios could include the studies of drug delivery with nanoparticles as carriers (how a nanoparticle can move through a membrane intact but release its content upon entering a cell). All of these – and many other – phenomena could be studied within the framework of field- or particle-based mesoscale theories.

10.5 Summary and Outlook

In this chapter, we have reviewed recent developments in the area of theory and modeling of nanoparticle–cell membrane interaction. It has been shown that, depending on their size and surface chemistry, small spherical nanoparticles can either 'lodge themselves' in the membrane or 'pull' some of the phospholipids off the membrane, thus creating a nanosized hole. Larger particles could either 'wrap themselves' in the membrane or 'peel off' a portion of the membrane, once again creating small holes. These effects take place even when the particle surface is homogeneous; particles with 'Janus'-like or 'patchy' surfaces could result in a variety of even more complex behaviors. These results are consistent with those of several recent studies, and illustrate at least some potential mechanisms of nanoparticle cytotoxicity. It is important to realize that the mechanisms described here are purely physical – not biochemical – as the particles penetrate into or through the membranes not because of ligand–receptor interactions but purely because of weaker screened electrostatic or hydrophobic or van der Waals interactions. (It is important to realize, however, that particles have many sites of those interactions, acting in unison!) Thus, unlike simple molecules, nanoparticles can often penetrate through cell membranes nonselectively.

It is expected that, in the future, mesoscale simulations of nanoparticle–cell membrane interactions will become an important tool in the design of nanoparticle-based tools in medicine, agriculture and other areas. As nanoparticle-based drug delivery, cancer treatment, or imaging methods are proposed, particular attention must be paid to ensure selectivity (i.e. that tumor cells are targeted, while all other cells are left alone). This, in turn, requires not only the correct addition

of receptors or ligands to target the tumor cells, but also the design of nanoparticles in such a way that their nonselective adsorption into other cells is prevented. Simulation techniques described in this review could, indeed, be used to help accomplish this second goal.

One could also expect that mesoscale simulations will become important tool in studies of nanoparticle cytotoxicity. Over the past decade, the number of products containing 'nanoparticles' (i.e. dimensions <100 nm) has increased dramatically. As these nanoparticles are introduced into various media (mainly polymer matrices), they are functionalized with different ligands and surfactants to achieve better dispersions. The simulation techniques discussed in this chapter may help to understand, from a qualitative aspect, how the interaction of nanoparticles with cell membranes will depend not only on the type of surface modification but also on the particle size and shape.

One major challenge in applying mesoscale models to predict the behavior of real systems is the question of estimating various interaction parameters based on the chemistry of the particles and/or ligands. In particular, how can we estimate the interaction parameter between a particle and a phospholipid head-group, and how might this parameter depend on whether the particle is metallic (gold, silver, etc.), carbon or ceramic? What is the role of ligands? And how can one properly evaluate the charge density on the particle surface? These types of question cannot be fully answered without atomistic simulations which, as discussed above, are often computationally expensive and difficult. Nonetheless, it is still possible to make some educated guesses simply by examining the relative hydrophobicity or hydrophilicity of various materials, and using these data to 'order' different particles on appropriate phase maps. Thus, for example, small carbon ('more hydrophobic') nanoparticles might lodge themselves in the membrane, whereas gold ('more hydrophilic') nanoparticles of similar size would most likely create holes in a similar membrane. Yet, in most cases, the transition from one type of nanoparticle to another requires simultaneous changes in a number of variables (e.g. size, surface charge, ligand chemistry); hence, direct comparisons will most likely not be straightforward.

Clearly, the theoretical modeling of nanoparticle–cell interactions is still in its infancy. Nonetheless, it is our hope and expectation that the next few years will see a rapid growth of interest in this topic, together with the development of new techniques and methods.

Acknowledgments

These studies were supported by The Dow Chemical Company (V.G. and S.B.) and National Science Foundation (A.B. and K.S.). We are thankful to D. Boverhof, B. Gollapudi, L. Hong, C. Christenson, D. West, E. Occhiello, T. Thompson, M. Debney (Dow), M. Banaszak Holl, B. Orr, P. Leroueil, C. Kelly (University of Michigan), D.M. Jasnow (University of Pittsburgh) and A. Alexeev (Georgia Tech) for helpful discussions, comments and suggestions.

References

1 Shenhar, R., Norsten, T.B. and Rotello, V.M. (2005) Polymer-mediated nanoparticle assembly: structural control and applications. *Advanced Materials*, **17**, 657–69 and references therein.

2 Bockstaller, M.R., Mickiewicz, R.A. and Thomas, E.L. (2005) Block copolymer nanocomposites. Perspectives for tailored functional materials, *Advanced Materials*, **17**, 1331–49 and references therein.

3 Moniruzzaman, M. and Winey, K.I. (2006) Polymer nanocomposites containing carbon nanotubes. *Macromolecules*, **39**, 5194–205 and references therein.

4 Salata, O. (2004) Applications of nanoparticles in biology and medicine. *Journal of Nanobiology*, **2**, 3–11 and references therein.

5 Kabanov, A.V. (2006) Polymer genomics: an insight into pharmacology and toxicology of nanomedicines. *Advanced Drug Delivery Reviews*, **58**, 1597–621 and references therein.

6 Brannon-Peppas, L. and Blanchette, J.O. (2004) Nanoparticle and targeted systems for cancer therapy. *Advanced Drug Delivery Reviews*, **56**, 1649–59 and references therein.

7 Brigger, I., Dubernet, C. and Couvrer, P. (2002) Nanoparticles in cancer therapy and diagnosis. *Advanced Drug Delivery Reviews*, **54**, 631–51 and references therein.

8 Verma, A. and Rotello, V.M. (2005) Surface recognition of biomacromolecules using nanoparticle receptors. *Chemical Communications*, 303–12 and references therein.

9 El-Sayed, I.H., Huang, X. and El-Sayed, M.A. (2005) Surface plasmon resonance scattering and absorption of anti-EGFR antibody conjugated gold nanoparticles in cancer diagnostics: applications in oral cancer. *Nano Letters*, **5**, 829–34.

10 Ferrari, M. (2005) Cancer nanotechnology: opportunities and challenges. *Nature Reviews Cancer*, **5**, 161–71 and references therein.

11 Nowack, B. and Bucheli, T.D. (2007) Occurrence, behavior and effects of nanoparticles in the environment. *Environmental Pollution*, **150**, 5–22 and references therein.

12 Hoet, P.H.M., Brüske-Hohlfeld, I. and Salata, O. (2004) Nanoparticles – known and unknown health risks. *Journal of Nanobiology*, **2**, 12–20 and references therein.

13 Nel, A., Xia, T., Mädler, L. and Li, N. (2006) Toxic potential of materials at the nanolevel. *Science*, **311**, 622–7 and references therein.

14 Cho, S.J., Maysinger, D., Jain, M., Roder, B., Hackbarth, S. and Winnik, F.M. (2007) Long-term exposure to CdTe quantum dots causes functional impairments in live cells. *Langmuir*, **23**, 1974–80.

15 Rothen-Rutishauser, B.M., Schürch, S., Haenni, B., Kapp, N. and Gehr, P. (2006) Interaction of fine particles and nanoparticles with red blood cells visualized with advanced microscopic techniques. *Environmental Science & Technology*, **40**, 4353–9.

16 Brunner, T.J., Wick, P., Manser, P., Spohn, P., Grass, R.N., Limbach, L.K., Bruinink, A. and Stark, W.J. (2006) In vitro cytotoxicity of oxide nanoparticles: comparison to asbestos, silica, and the effect of particle solubility. *Environmental Science & Technology*, **40**, 4374–81.

17 Mecke, A., Majoros, I.J., Patri, A.K., Baker, J.R. Jr, Banaszak Holl, M.M. and Orr, B.G. (2005) Lipid bilayer disruption by polycationic polymers: the roles of size and chemical functional group. *Langmuir*, **21**, 10348–54.

18 Hong, S., Bielinska, A.U., Mecke, A., Kezsler, B., Beals, J.L., Shi, X., Balogh, L., Orr, B.G., Baker, J.R. Jr and Banaszak Holl, M.M. (2004) Interaction of poly(amidoamine) dendrimers with supported lipid bilayers and cells: hole formation and the relation to transport. *Bioconjugate Chemistry*, **15**, 774–82.

19 Leroueil, P.R., Hong, S., Mecke, A., Baker, J.R. Jr, Banaszak Holl, M.M. and Orr, B.G. (2007) Nanoparticle interaction

with biological membranes: does nanotechnology present a janus face? *Accounts of Chemical Research*, **40**, 335 and references therein.
20 Pan, Y., Neuss, S., Leifert, A., Fischler, M., Wen, F., Simon, U., Schmid, G., Brandau, W. and Jahnen-Dechent, W. (2007) Size-dependent cytotoxicity of gold nanoparticles. *Small*, **3**, 1941–9 and references therein.
21 Volkenstein, M.V. (2003) *General Biophysics*, Academic Press, New York.
22 Jain, M. and Wagner, R.C. (1980) *Introduction to Biological Membranes*, John Wiley & Sons, Inc., New York.
23 Tristram-Nagle, S. and Nagle, J.F. (2004) Lipid bilayers: thermodynamics, structure, fluctuations, and interactions. *Chemistry and Physics of Lipids*, **127**, 3–14 and references therein.
24 Gouliaev, N. and Nagle, J.F. (1998) Simulations of interacting membranes in the soft confinement regime. *Physical Review Letters*, **81**, 2610–14.
25 Nagle, J.F. (1980) Theory of the main lipid bilayer phase transition. *Annual Review of Physical Chemistry*, **31**, 157–95.
26 Nagle, J.F. and Tristram-Nagle, S. (2000) Structure of lipid bilayers. *Biochimica et Biophysica Acta. Reviews on Biomembranes*, **1469**, 159–95.
27 Granick, S., Kumar, S.K., Amis, E., Antonietti, M., Balazs, A.C., Chakraborty, A.K., Grest, G.S., Hawker, C., Janmey, P., Kramer, E.J., Nuzzo, R., Russell, T.P. and Safinya, C. (2003) Macromolecules at surfaces: research challenges and opportunities from tribology to biology. *Journal of Polymer Science: Part B: Polymer Physics*, **41**, 2755–93 and references therein.
28 Saiz, L., Bandyopadhyay, S. and Klein, M.L. (2002) Towards an understanding of complex biological membranes from atomistic molecular dynamics simulations. *Bioscience Reports*, **22**, 151–73.
29 Discher, D.E., Ortiz, V., Srinivas, G., Klein, M.L., Kim, Y., Christian, D., Cai, S., Photos, P. and Ahmed, F. (2007) Emerging applications of polymersomes in delivery: from molecular dynamics to shrinkage of tumors. *Progress in Polymer Science*, **32**, 838–57 and references therein.
30 Saiz, L. and Klein, M.L. (2002) Computer simulation studies of model biological membranes. *Accounts of Chemical Research*, **35**, 482–9.
31 Moore, P.B., Lopez, C.F. and Klein, M.L. (2001) Dynamical properties of a hydrated lipid bilayer from a multinanosecond molecular dynamics simulation. *Biophysical Journal*, **81**, 2484–94.
32 Lopez, C.F., Nielsen, S.O., Ensing, B., Moore, P.B. and Klein, M.L. (2005) Structure and dynamics of model pore insertion into a membrane. *Biophysical Journal*, **88**, 3083–94.
33 Shi, Q., Izvekov, S. and Voth, G.A. (2006) Atomistic, mixed and coarse-grained molecular dynamics: simulation of a membrane-bound ion channel. *Journal of Physical Chemistry B*, **110**, 15045–8.
34 Brewer, M., Schmitt, U.W. and Voth, G.A. (2001) The formation and dynamics of proton wires in channel environments. *Biophysical Journal*, **80**, 1691–702.
35 Ayton, G., Bardenhagen, S.G., McMurtry, P., Sulsky, D. and Voth, G.A. (2001) Interfacing continuum and molecular dynamics: an application to lipid bilayers. *Journal of Chemical Physics*, **114**, 6913–24.
36 Chang, R. and Violi, A. (2006) Insights into the effect of combustion-generated carbon nanoparticles on biological membranes: a computer simulation study. *Journal of Physical Chemistry B*, **110**, 5073–83.
37 Tian, P. (2008) Molecular dynamics simulations of nanoparticles. *Annual Reports on the Progress of Chemistry Section C Physical Chemistry*, **104**, 142–64 and references therein.
38 Nielsen, S.O., Lopez, C.F., Srinivas, G. and Klein, M.L. (2004) Coarse grain models and the computer simulation of soft materials. *Journal of Physics – Condensed Matter*, **16**, R481–512 and references therein.
39 Srinivas, G. and Klein, M.L. (2004) Computational approaches to nanobiotechnology: probing the interaction of synthetic molecules with phospholipid bilayers via a coarse grain model. *Nanotechnology*, **15**, 1289–95.

40 Srinivas, G., Discher, D.E. and Klein, M.L. (2004) Self-assembly and properties of diblock copolymers by coarse-grain molecular dynamics. *Nature Materials*, **3**, 638–44 and references therein.

41 Lopez, C.F., Moore, P.B., Shelley, J.C., Shelley, M.Y. and Klein, M.L. (2002) Computer simulation studies of biomembranes using a coarse grain model. *Computer Physics Communications*, **147**, 1–6.

42 Shelley, J.C., Shelley, M.Y., Reeder, R.C., Bandyopadhyay, S. and Klein, M.L. (2001) A coarse grain model for phospholipid simulations. *Journal of Physical Chemistry B*, **105**, 4464–70.

43 Pickholz, M., Saiz, L. and Klein, M.L. (2005) Concentration effects of volatile anesthetics on the properties of model membranes: a coarse-grain approach. *Biophysical Journal*, **88**, 1524–34.

44 Lopez, C.F., Nielsen, S.O., Srinivas, G., DeGrado, W.F. and Klein, M.L. (2006) Probing membrane insertion activity of antimicrobial polymers via coarse-grain molecular dynamics. *Journal of Chemical Theory and Computation*, **2**, 649–55.

45 Nielsen, S.O., Ensing, B., Ortiz, V., Moore, P.B., Klein, M.L. and Bilayer, L. (2005) Perturbations around a transmembrane nanotube: a coarse grain molecular dynamics study. *Biophysical Journal*, **88**, 3822–8.

46 Katsov, K., Müller, M. and Schick, M. (2004) Field theoretic study of bilayer membrane fusion. I. Hemifusion mechanism. *Biophysical Journal*, **87**, 3277–90.

47 Katsov, K., Müller, M. and Schick, M. (2006) Field theoretic study of bilayer membrane fusion. II. Mechanism of a stalk-hole complex. *Biophysical Journal*, **90**, 915–26.

48 Lee, J.Y. and Schick, M. (2007) Field theoretic study of bilayer membrane fusion. III. Membranes with leaves of different composition. *Biophysical Journal*, **92**, 3938–48.

49 Müller, M., Katsov, K. and Schick, M. (2006) Biological and synthetic membranes: what can be learned from a coarse-grained description? *Physics Reports*, **434**, 113–76 and references therein.

50 Wu, J. (2006) Density functional theory for chemical engineering: from capillarity to soft materials. *AIChE Journal*, **52**, 1–25 and references therein.

51 Frink, L.J.D. and Frischknecht, A.L. (2006) Computational investigations of pore forming peptide assemblies in lipid bilayers. *Physical Review Letters*, **97**, 208701.

52 Yamamoto, S., Maruyama, Y., Hyodo, S. (2002) Dissipative particle dynamics study of spontaneous vesicle formation of amphiphilic molecules. *Journal of Chemical Physics*, **116**, 5842–9.

53 Yamamoto, S. and Hyodo, S. (2003) Budding and fission dynamics of two-component vesicles. *Journal of Chemical Physics*, **118**, 7937–44.

54 Groot, R.D. and Rabone, K.L. (2001) Mesoscopic simulation of cell membrane damage, morphology change and rupture by nonionic surfactants. *Biophysical Journal*, **81**, 725–36.

55 Groot, R.D. and Warren, P.B. (1997) Dissipative particle dynamics: bridging the gap between atomistic and mesoscopic simulation. *Journal of Chemical Physics*, **107**, 4423–35.

56 Gao, L., Shillcock, J. and Lipowsky, R. (2007) Improved dissipative particle dynamics simulations of lipid bilayers. *Journal of Chemical Physics*, **126**, 015101.

57 Illya, G., Lipowsky, R. and Shillcock, J.C. (2006) Two-component membrane material properties and domain formation from dissipative particle dynamics. *Journal of Chemical Physics*, **125**, 114710.

58 Ortiz, V., Nielsen, S.O., Discher, D.E., Klein, M.L., Lipowsky, R., Shillcock, J. (2005) Dissipative particle dynamics simulations of polymersomes. *Journal of Physical Chemistry B*, **109**, 17708–14.

59 Shillcock, J.C. and Lipowsky, R. (2002) Equilibrium structure and lateral stress distribution of amphiphilic bilayers from dissipative particle dynamics simulations. *Journal of Chemical Physics*, **117**, 5048–61.

60 Shillcock, J.C. and Lipowsky, R. (2002) Composition and amphiphile architecture dependence of bilayer membrane

properties from dissipative particle dynamics. *Biophysical Journal*, **82**, 159.
61 Shillcock, J.C. and Lipowsky, R. (2006) The computational route from bilayer membranes to vesicle fusion. *Journal of Physics–Condensed Matter*, **18**, S1191–219.
62 Revalee, J.D., Laradji, M. and Kumar, P.B.S. (2008) Implicit-solvent mesoscale model based on soft-core potentials for self-assembled lipid membranes. *Journal of Chemical Physics*, **128**, 035102.
63 Laradji, M. and Kumar, P.B.S. (2005) Domain growth, budding, and fission in phase-separating self-assembled fluid bilayers. *Journal of Chemical Physics*, **123**, 224902.
64 Laradji, M. and Kumar, P.B.S. (2006) Anomalously slow domain growth in fluid membranes with asymmetric transbilayer lipid distribution, *Physical Review E*, **73**, 40901.
65 Laradji, M. and Kumar, P.B.S. (2004) Dynamics of domain growth in self-assembled fluid vesicles. *Physical Review Letters*, **93**, 198105.
66 Dias, R.S. and Linse, P. (2008) Colloid adsorption onto responsive membranes. *Biophysical Journal*, **94**, 3760–8.
67 Noguchi, H. and Takasu, M. (2002) Adhesion of nanoparticles to vesicles: a Brownian dynamics simulation. *Biophysical Journal*, **83**, 299–308.
68 Helfrich, W. (1973) Elastic properties of lipid bilayers: theory and possible experiments. *Zeitschrift für Naturforschung*, **28**, 693–703.
69 Deserno, M. and Gelbart, W.M. (2002) Adhesion and wrapping in colloid-vesicle complexes. *Journal of Physical Chemistry B*, **106**, 5543.
70 Deserno, M. (2004) When do fluid membranes engulf sticky colloids? *Journal of Physics–Condensed Matter*, **16**, S2061–S2070.
71 Deserno, M. (2004) Elastic deformation of a fluid membrane upon colloid binding. *Physical Review E*, **69**, 031903.
72 Deserno, M. and Bickel, T. (2003) Wrapping of a spherical colloid by a fluid membrane. *Europhysics Letters*, **62**, 767–73.
73 Ginzburg, V.V. and Balijepalli, S. (2007) Modeling the thermodynamics of the interaction of nanoparticles with cell membranes. *Nano Letters*, **7**, 3716–22.
74 Smith, K.A., Jasnow, D. and Balazs, A.C. (2007) Designing synthetic vesicles that engulf nanoscopic particles. *Journal of Chemical Physics*, **127**, 084703.
75 Alexeev, A., Uspal, W., Balazs, A.C. and Janus, H. (2008) Nanoparticles to create controllable pores in membranes, *ACS Nano*, **2**, 1117–22.
76 Zhang, L. and Granick, S. (2006) How to stabilize phospholipid liposomes (using nanoparticles). *Nano Letters*, **6**, 694–8.
77 Zeng, Q.H., Yu, A.B. and Lu, G.Q. (2008) Multiscale modeling and simulation of polymer nanocomposites. *Progress in Polymer Science*, **33**, 191–269 and references therein.
78 Allegra, G., Raos, G. and Vacatello, M. (2008) Theories and simulations of polymer-based nanocomposites: From chain statistics to reinforcement. *Progress in Polymer Science*, **33**, 683–731 and references therein.
79 Glotzer, S.C. and Solomon, M.J. (2007) Anisotropy of building blocks and their assembly into complex structures. *Nature Materials*, **6**, 557–62.
80 Vacatello, M. (2003) Predicting the molecular arrangements in polymer-based nanocomposites. *Macromolecular Theory and Simulations*, **12**, 86–91.
81 Huh, J., Ginzburg, V.V. and Balazs, A.C. (2000) Thermodynamic behavior of particle/diblock copolymer mixtures: simulation and theory. *Macromolecules*, **33**, 8085–96.
82 Balazs, A.C., Ginzburg, V.V., Qiu, F., Peng, G. and Jasnow, D. (2000) Multi-scale model for binary mixtures containing nanoscopic particles. *Journal of Physical Chemistry B*, **104**, 3411–22.
83 Thompson, R.B., Ginzburg, V.V., Matsen, M.W. and Balazs, A.C. (2001) Predicting the mesophases of copolymer-nanoparticle composites. *Science*, **292**, 2469–72.
84 Thompson, R.B., Ginzburg, V.V., Matsen, M.W. and Balazs, A.C. (2002) Block copolymer-directed assembly of nanoparticles: forming mesoscopically

ordered hybrid materials. *Macromolecules*, **35**, 1060–71.
85 Zhang, L., Lin, J. and Lin, S. (2007) Self-assembly behavior of amphiphilic block copolymer/nanoparticle mixture in dilute solution studied by self-consistent-field theory/density functional theory. *Macromolecules*, **40**, 5582–91.
86 Ren, C.-L. and Ma, Y.Q. (2007) Structure and organization in inclusion-containing bilayer membranes, Condensed Matter Archive http://arXiv.org/abs/0711.1220v1 (accessed 1 February 2008).
87 Reister, E. and Fredrickson, G.H. (2005) Phase behavior of a blend of polymer-tethered nanoparticles with diblock copolymers. *Journal of Chemical Physics*, **123**, 214903.
88 Sides, S.W., Kim, B.J., Kramer, E.J. and Fredrickson, G.H. (2006) Hybrid particle-field simulations of polymer nanocomposites. *Physical Review Letters*, **96**, 250601.
89 Cao, D. and Wu, J. (2007) Density functional theory for a primitive model of nanoparticle-block copolymer mixtures. *Journal of Chemical Physics*, **126**, 144912.
90 McGarrity, E.S., Frischknecht, A.L., Frink, L.J.D. and Mackay, M.E. (2007) Surface-induced first-order transition in athermal polymer-nanoparticle blends. *Physical Review Letters*, **99**, 238302.
91 Matsen, M.W. and Thompson, R.B. (2008) Particle distributions in a block copolymer nanocomposite. *Macromolecules*, **41**, 1853–60.
92 Pryamitsyn, V. and Ganesan, V. (2006) Strong segregation theory of block copolymer-nanoparticle composites. *Macromolecules*, **39**, 8499–510.
93 Huggins, M.L. (1941) Solutions of long chain compounds. *Journal of Chemical Physics*, **9**, 440.
94 Flory, P.J. (1941) Thermodynamics of high polymer solutions. *Journal of Chemical Physics*, **9**, 660–1.
95 Tarazona, P. (1984) A density functional theory of melting. *Molecular Physics*, **52**, 81–96.
96 Carnahan, N.F. and Starling, K.E. (1969) Equation of state for noninteracting rigid spheres. *Journal of Chemical Physics*, **51**, 635–6.
97 Drolet, F. and Fredrickson, G.H. (1999) Combinatorial screening of complex block copolymer assembly with self-consistent field theory. *Physical Review Letters*, **83**, 4317–20.
98 Rasmussen, K.O. and Kalosakas, G. (2002) Improved numerical algorithm for exploring block copolymer mesophases. *Journal of Polymer Science: Part B: Polymer Physics*, **40**, 1777–83.
99 Herant, M., Heinrich, V. and Dembo, M. (2005) Mechanics of neutrophil phagocytosis: behavior of the cortical tension. *Journal of Cell Science*, **118**, 1789–97.
100 Herant, M., Heinrich, V. and Dembo, M. (2006) Mechanics of neutrophil phagocytosis: experiments and quantitative models. *Journal of Cell Science*, **119**, 1903–13.
101 Tan, Y.C., Hettiarachchi, K., Siu, M. and Pan, Y.P. (2006) Controlled microfluidic encapsulation of cells, proteins, and microbeads in lipid vesicles. *Journal of the American Chemical Society*, **128**, 5656–8.
102 Jahn, A., Vreeland, W.N., Gaitan, M. and Locascio, L.E. (2004) Controlled Vesicle Self-Assembly in Microfluidic Channels with Hydrodynamic Focusing. *Journal of the American Chemical Society*, **126**, 2674–5.
103 Hong, J.W. and Quake, S.R. (2003) Integrated nanoliter systems. *Nature Biotechnology*, **21**, 1179–83.
104 Thorsen, T., Roberts, R.W., Arnold, F.H. and Quake, S.R. (2001) Dynamic pattern formation in a vesicle-generating microfluidic device. *Physical Review Letters*, **86**, 4163–6.
105 Gao, C., Leporatti, S., Moya, S., Donath, E. and Mohwald, H. (2001) Stability and mechanical properties of polyelectrolyte capsules obtained by stepwise assembly of poly (styrenesulfonate sodium salt) and poly (diallyldimethyl ammonium) chloride onto melamine resin particles. *Langmuir*, **17**, 3491–5.
106 Lulevich, V.V., Radtchenko, I.L., Sukhorukov, G.B. and Vinogradova, O.I.

(2003) Mechanical properties of polyelectrolyte microcapsules filled with a neutral polymer. *Macromolecules*, **36**, 2832–7.

107 Plimpton, S. (1995) Fast parallel algorithms for short-range molecular dynamics. *Journal of Comparative Physiology*, **117**, 1–19.

108 Shillcock, J.C. and Lipowsky, R. (2005) Tension-induced fusion of bilayer membranes and vesicles. *Nature Materials*, **4**, 225–8.

109 Veatch, S.L. and Keller, S.L. (2003) Separation of liquid phases in giant vesicles of ternary mixtures of phospholipids and cholesterol. *Biophysical Journal*, **85**, 3074–83.

110 de Carmo, M.P. (1976) *Differential Geometry of Curves and Surfaces*, Prentice-Hall, Englewood Cliffs, N.J.

111 Goetz, R. and Lipowsky, R. (1998) Computer simulations of bilayer membranes: Self-assembly and interfacial tension. *Journal of Chemical Physics*, **108**, 7397–409.

112 Schofield, P. and Henderson, J.R. (1982) Statistical mechanics of inhomogeneous fluids. *Proceedings of the Royal Society of London Series A-Mathematical, Physical and Engineering Sciences*, **379**(1776), 231–46.

113 Goetz, R., Gompper, G. and Lipowsky, R. (1999) Mobility and elasticity of self-assembled membranes. *Physical Review Letters*, **82**, 221–4.

114 Strey, H., Peterson, M. and Sackmann, E. (1995) Measurement of erythrocyte membrane elasticity by flicker eigenmode decomposition. *Biophysical Journal*, **69**, 478–88.

115 Revenga, M., Zuniga, I. and Espanol, P. (1999) Boundary conditions in dissipative particle dynamics. *Computer Physics Communications*, **122**, 309–11.

116 Willemsen, S.M., Hoefsloot, H.C.J. and Iedema, H.C. (2000) No-slip boundary condition in dissipative particle dynamics. *International Journal of Modern Physics C*, **11**, 881–90.

117 Pivkin, I.V. and Karniadakis, G.E. (2005) A new method to impose no-slip boundary conditions in dissipative particle dynamics. *Journal of Computational Physics*, **207**, 114–28.

118 Siegel, D.P. (1993) Energetics of intermediates in membrane fusion: comparison of stalk and inverted micellar intermediate structures. *Biophysical Journal*, **65**, 2124–40.

119 Siegel, D.P. (1999) The modified stalk mechanism of lamellar/inverted hexagonal phase transitions and its implications for membrane fusion. *Biophysical Journal*, **76**, 291–313.

120 Malinin, V.S. and Lentz, B.R. (2004) Energetics of vesicle fusion intermediates comparison of calculations with observed effects of osmotic and curvature stresses. *Biophysical Journal*, **86**, 2951–64.

121 Siegel, D.P. (2006) Determining the ratio of the Gaussian curvature and bending elastic moduli of phospholipids from QII phase unit cell dimensions. *Biophysical Journal*, **91**, 608–18.

122 Julicher, F. and Lipowsky, R. (1996) Shape transformations of vesicles with intramembrane domains. *Physical Review E*, **53**, 2670–83.

123 Julicher, F., Seifert, U. and Lipowsky, R. (1993) Phase diagrams and shape transformations of toroidal vesicles. *Journal De Physique II*, **3**, 1681–705.

124 Kim, B.J., Bang, J., Hawker, C.J. and Kramer, E.J. (2006) Effect of areal chain density on the location of polymer-modified gold nanoparticles in a block copolymer template. *Macromolecules*, **39**, 4108–14.

125 Chiu, J.J., Kim, B.J., Kramer, E.J. and Pine, D.J. (2005) Control of nanoparticle location in block copolymers. *Journal of the American Chemical Society*, **127**, 5036–7.

Abstract

In this chapter we review recent developments in the area of theory and modeling of nanoparticle–cell membrane interactions. Attention is focused mainly on hybrid self-consistent mean-field theory (SCMFT) and dissipative-particle dynamic (DPD) studies of spherical nanoparticles near model lipid bilayers. The study results showed that spherical nanoparticles with characteristic size on the order of membrane thickness ($R_p \sim 1$–10 nm) can induce dramatic changes in the membrane. These changes may range from simple attachment to the membrane surface to incorporation into the membrane, and/or the creation or stabilization of pores or channels in the membrane. In all cases, the changes in membrane morphology in the presence of a particle are driven by the desire of the system to reduce its overall free energy and transition into the lowest-free-energy state. Thus, some particles can 'peel off' enough lipids to create a hole in the membrane, while others can simply attach to the membrane surface, depending on their radius and type of surface chemistry. The simulations suggest a qualitative understanding of these phenomena, thus providing important tools to understand the mechanisms of nanoparticle cytotoxicity and/or nanoparticle activity as tumor imaging or drug delivery vehicles.

Keywords

nanoparticle; cell membrane; theory; simulation; dissipative particle dynamics; self-consistent mean-field theory

11
Porous Silicon Particles for Imaging and Therapy of Cancer

Rita E. Serda, Ciro Chiappini, Daniel Fine, Ennio Tasciotti and Mauro Ferrari

11.1
Introduction

The aim of the National Cancer Institute is to eliminate death and suffering from cancer by 2015, by harnessing the power of nanotechnology to provide new tools for diagnosing, imaging and treating cancer. Funded research projects include the design and fabrication of multifunctional nanodevices which promise to change the way we pinpoint cancer and deliver anticancer drugs. Major advances in our comprehension of how cancer develops come from the huge array of knowledge achieved by cancer genomics and proteomics. Unfortunately, to date only a very small fraction of the potential carried by these discoveries has been translated into clinical practice. Most of this gap can be accounted for by technological challenges inherent in designing systems able to function in the complex biological milieu [1, 2]. The ability to translate extremely developed and established technologies, such as silicon technology, into the biosciences offers an enormous advantage due to immediate access to a wide array of sophisticated tools.

Silicon technology is already established in terms of production, characterization and translation into nanotechnologies. An expansive set of miniaturized sensor and actuators have been developed that, in the biological context, could be used as building blocks for complex interacting systems [3–5]. Scalability, precision and reproducibility are characteristics of these processes that will be extremely valuable when translated into clinical applications. For these reasons, an enormous interest in the design and fabrication of silicon devices for biomedical application exists, and many research projects are now under way to characterize these systems within biological environments.

Since the 1980s, silicon-based sensors and microelectromechanical devices (MEMS) have been used *ex vivo* for tasks such as pressure sensing, blood chemistry analysis, flow cytometry and electrophoresis [6]. The term 'BioMEMS' was subsequently coined to describe the wide array of tools developed using silicon as a platform. Extremely sophisticated systems are now available, such as functionalized microcantilevers for molecule adsorption, recognition and quantification, as

Nanomaterials for the Life Sciences Vol. 2: Nanostructured Oxides. Edited by Challa S. S. R. Kumar

ISBN: 978-3-527-32152-0

well as 'Lab-on-a-Chip' devices which scale single or multiple laboratory processes into a compact chip-format [6].

Silicon-based implantable and transdermal devices have been proposed and realized. Arrays of implantable single-dose microreservoirs [7], or drug-releasing chips equipped with microneedles [8], have been prototyped and are currently undergoing animal testing, or are already in clinical trials. One of the major obstacles encountered in the successful implementation of implantable silicon devices has been their poor biocompatibility [9] and nonbiodegradability.

In 1995, the first study hinting at the biocompatibility and bioactivity of silicon-based devices was presented [10]. Scientists reported that silicon could be made biocompatible by making it porous, with the pore size directly affecting biodegradability. Porous silicon (pSi) and porous silica are obtained through sol–gel techniques [11] or from bulk silicon by means of electrochemical etch [12]. pSi was first observed some 50 years ago by Ulhir and Turner [13, 14] while experimenting with different techniques to electropolish silicon surfaces. The anodic electrochemical etching of silicon in an aqueous or organic solution of hydrofluoric acid (HF) creates pores the sizes of which vary depending on the experimental conditions.

In 1990, Canham discovered the photoluminescence properties of pSi, and shortly thereafter electroluminescence and chemoluminescence were observed [15], spurring an enormous interest in pSi as an optoelectronic material. However, almost 20 years of continual research in the field, the optical efficiency and long-term stability of pSi remain too low for any functional optoelectronic application [15].

In this chapter we present a complete overview of pSi bioapplications, from their discovery and synthesis to current biological testing and visionary ideas for bypassing multiple biological barriers for the effective delivery of drugs and imaging agents to the tumor site. First, we focus on the production of pSi, and then define the mechanisms used to characterize porosity. In the next section, we address biocompatibility and biodegradation, both of which are directly related to the degree of porosity. The loading and quantification of drugs (therapeutics and imaging agents), together with a description of nanovector design for optimal delivery, are then presented. Finally, the effect of particle size, shape and surface modification (including serum opsonization) on the phagocytosis of particles by cells is discussed, and an example of *in vivo* imaging with fused pSi and iron oxide nanoparticles is presented.

This chapter is unique in that it describes the fabrication, characterization and current biological applications of pSi, whereas previous reviews have focused either solely on the formation and modification of pSi, or on pSi microparticles for the detection of chemical and biological compounds. In 1997, Canham produced a book entitled, *Properties of Porous Silicon*, which contained a collection of the physical and chemical properties of pSi. In this chapter, we include details of tested and visionary ideas on nanosized and microsized delivery systems, both of which are today emerging as powerful tools for the systemic delivery of therapeutic molecules and imaging agents for different biomedical applications, from

cancer [16, 17] to cardiovascular diseases [18]. These delivery systems can be loaded with a multitude of drug molecules and contrast agents to provide simultaneous therapeutic and imaging capabilities.

11.2 Porous Silicon

Two top-down strategies have been developed for the production of pSi. The most widely used strategy is electrochemical etch, while the other approach, stain etch, is rarely used in practice due to its severe lack of flexibility [19]. The most widely employed top-down approach produces pSi through electrochemical etch of a bulk silicon wafer. The pSi can then be oxidized to take advantage of silane chemistry. Alternatively, its surface can be carbon-terminated to obtain a hydrophilic chemically stable interface [20].

Bottom-up strategies, which employ silicate precursors, such as tetraethoxysilane (TEOS), produce porous silicon dioxide. Silicon dioxide is a much more chemically stable interface than silicon, and precludes some forms of surface functionalization, such as carbonization, which is used to tune particle properties. Additionally, bottom-up approaches are limited to the production of either spherical or ellipsoid particles, unless used in conjunction with top-down lithography. Shape has been shown fundamentally to determine several properties of the particle that are relevant for drug delivery, such as flow dynamics, margination, degradation rate and cell uptake [21, 22]. For these reasons, top-down approaches to the production of pSi for biomedical applications have been historically favored.

Porous silicon dioxide is formed by the anodic dissolution of single-crystal silicon in an HF solution. A bulk silicon wafer is placed in an aqueous or organic solution containing less than 50% volume of HF. The cathode is immersed in the solution while the silicon wafer itself constitutes the anode. The porosification process is sustained as long as a current is applied. Figure 11.1 is a scanning electron microscopy (SEM) image of a cleaved pSi layer etched in a silicon wafer. The main characteristics of the porous layer – that is, porosity, pore size, length, orientation and morphology – are determined by the current intensity, the doping characteristics of the silicon wafer, the etch duration and the composition of the etchant solution. The most common solution used for the production of pSi is $HF : H_2O :$ ethanol. This solution is considered to be aqueous as ethanol does not take an active part in the porosification reaction, but is employed merely as a surfactant [12, 19].

The underlying porosification mechanism is still widely debated. All currently accepted theories require the presence of excess positive carriers (holes) at the silicon surface for etching to occur. In aqueous solution, two competing dissolution pathways are observed (Figure 11.2), both of which initially require the replacement of an H atom at the silicon surface with an F^- ion from solution. This step constitutes the electrical part of the etch, as the hole necessary to neutralize the SiF bond must be supplied by the silicon wafer. In the second dissolution step

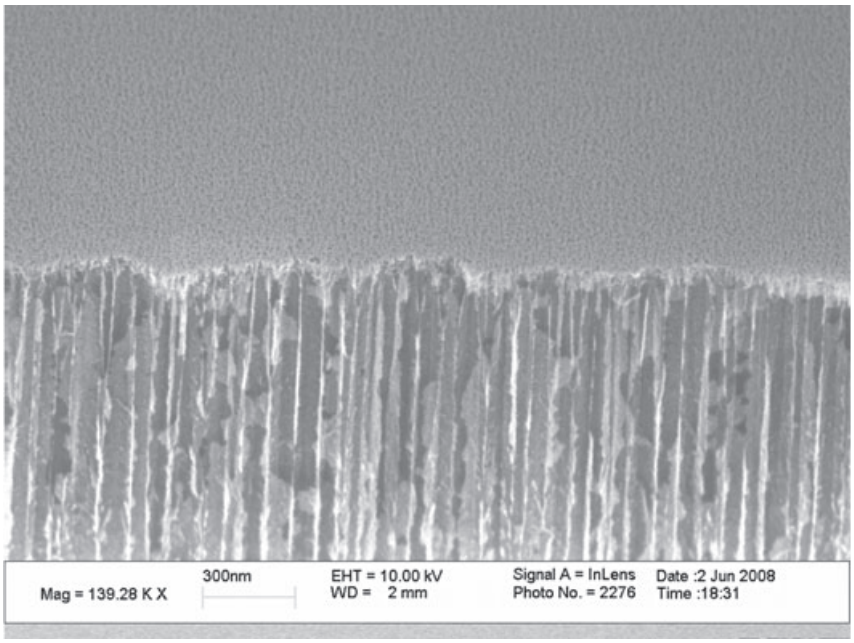

Figure 11.1 A 45° cross-sectional scanning electron micrograph of a cleaved porous silicon layer etched in a highly doped p-type silicon wafer.

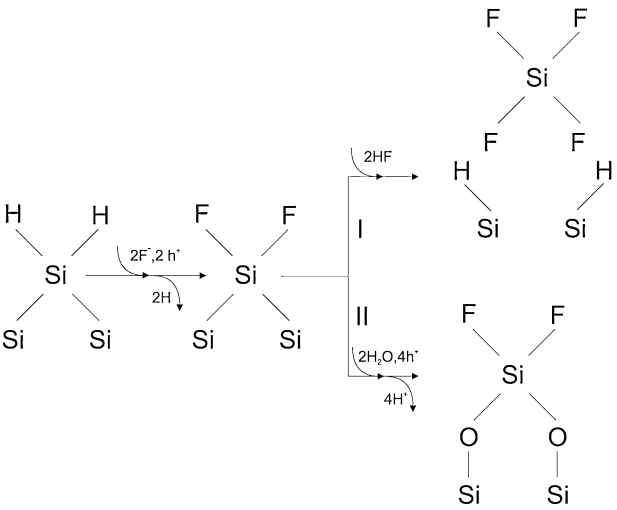

Figure 11.2 Competing silicon dissolution pathways during electrochemical etch leading to the formation of porous silicon. h^+ indicates positive charge carriers (holes) from bulk silicon.

of pathway I, the Si—SiF bond is broken by reacting with HF, which results in the removal of a silicon atom from the bulk. No carriers from the solid Si are required in this second step, which constitutes the chemical part of the etch process. In the competing pathway II, the backbone of Si—SiF is broken by reacting with H_2O; this results in Si—O—Si bonds that are unstable in HF. Thus, pathway I leads to the direct dissolution of silicon, while pathway II results in an indirect dissolution. Pathway II leads to a passivated surface in which dissolution depends heavily on the HF concentration. It is proposed that the ratio of the two pathways influences the final pore structure. Phenomenological analysis has shown that porosification occurs almost exclusively at the bottom of the currently formed pore, while the formation of lateral pores or an enlargement of the existing pore is a minor effect [12, 19].

Currently proposed porosification models disagree in delineating the factors that determine pore morphology, separation and orientation. Surface space charges, quantum confinement, surface curvature, local surface crystalline anisotropies, combinations of the former and many other effects have been proposed as mechanisms determining pore characteristics, but none is sufficiently convincing so as to achieve a consensus [12, 19].

As a result of the lack of a valid porosification model, general predictive guidelines to determine the final porous structure for a given set of etch parameters do not exist. Thus, several phenomenological rules, approximate guidelines and trial and error are employed to obtain structures with predefined morphological characteristics. Once defined, however, etching parameters used to obtain the desired configuration and pore characteristics are highly reproducible.

The silicon doping type and concentration influences pore size, porosity and pore structure. For highly doped [dopant concentration $D_c > 10^{15}$] p-type wafers, an increase in doping increases the pore size from 10 to 100 nm. In lightly doped p-type silicon ($D_c < 10^{15}$), the pore size increases with decreasing doping from 1 nm to the micrometer scale [19]. n-type wafers electrochemically etched in the dark instead tend to form larger pores. Heavily doped wafers ($D_c > 10^{19}$) produce pores in the 10 to 100 nm range, while lightly doped ones ($D_c < 10^{19}$) result in pore sizes ranging from 1 to 10 μm. The illumination of n-type silicon affects pore formation, both in structure and size, due to the significant increases in the amount of holes made available to the etch process. In general, n-type wafers tend to be less porous than p-type [12, 19]. The pore size distribution breadth is observed to increase with increasing pore size, and is independent of the details of pore formation [12].

The nature of the exposed surface is an extremely important factor contributing to the final pore structure. Pores tend to grow not only along the (100) crystalline direction but also towards the source of the holes, which is orthogonal to the surface. When the exposed surface is the (100) orientation there is no conflict, and in general straight pores orthogonal to the interface are observed, possibly with 90° branches depending on the wafer doping characteristics. However, if the interface is along another crystalline plane then, depending on the etch conditions, pores may orient either along the (100) direction, along the holes source, or somewhere in between, giving rise to a chaotic, branched porous structures [12, 19].

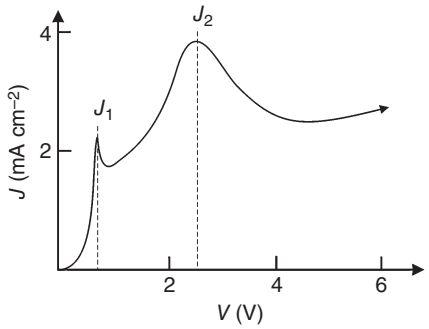

Figure 11.3 Typical current–voltage (I–V) curve for a moderately doped pSi diluted HF solution.

In the standard aqueous solution HF : H_2O : ethanol, the HF concentration determines a sub-range of pore sizes and porosity within the range set by the wafer doping. As a general rule, more diluted solutions tend to form larger-diameter pores [12, 19]. The etch current intensity also contributes to the pore size distribution; with all the other parameters kept equal, larger currents tend to form bigger pores. In order to obtain a porous layer with uniform pore size and porosity across the entire wafer, the current density must be kept constant across the surface. In contrast, it is possible to exploit anisotropic currents in order to form a continuous layer with a pore size gradient at the surface [19, 20]. Modulation of the current during the etch process allows the formation of pores with variable diameter along their growth axis. For every set of parameters there exists a limiting current (J_1), above which electrochemical etch does not occur. For currents larger than J_1, but smaller than the threshold current J_2, a transitional regime is observed, while for currents larger than J_2, electropolishing dominates and entire layers of silicon are removed instead of pores being formed (Figure 11.3) [12, 19]. This property is often exploited in order to release porous layers from the wafer by removing entire layers at the interface between the porous silicon and the wafer.

Great versatility is thus achieved through the electrochemical etch porosification approach. Fine-tuning the porosification parameters makes it possible to obtain pSi structures of extremely different characteristics, ranging from very low porosity (15–20%) to very high porosity (>90%), with pore sizes ranging from a few nanometers to tens of microns, and completely different pore structures and morphologies. As these materials have significantly different behaviors when employed as drug delivery systems, the remainder of this chapter will be devoted to microfabrication for clinical applications and biological validation.

The lack of reliable predictive rules for the effect of etch parameters on the final result may be seen as a drawback of the technique. However, phenomenological guidelines are usually sufficient to direct the exploration of the parameter space and significantly limit the number of trials required to obtain the desired results in terms of film porosity, pore size distribution and thickness.

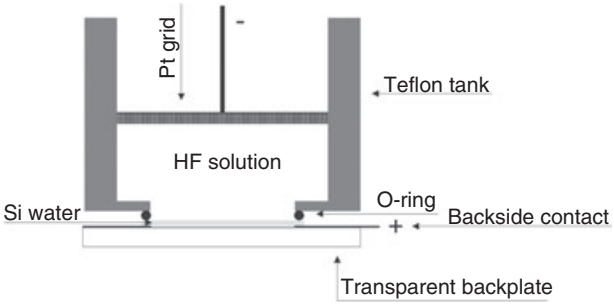

Figure 11.4 Schematic representation of a single tank electrochemical etch chamber. The backplate is transparent in order to allow backside illumination of the wafer. Frontside illumination is provided by shining light through the platinum grid.

11.3 Microfabrication

The production of pSi microparticles generally starts with the porosification of a silicon wafer in an apposite etch tank (Figure 11.4). The tank is composed of HF-resistant materials such as polytetrafluoroethylene or aluminum oxide. The wafer is placed in the tank with the frontside facing the etch solution and the rearmost side in contact with the anode of a power supply. If no backside illumination of the wafer is required, a metallic layer is deposited over the entire wafer backside to provide a better current uniformity; otherwise, an annular contact along the wafer edge is employed. As an alternative, a backside electrolytic solution can be used to obtain a better contact, but at the expense of flexibility [12, 19].

The cathode is composed of an HF-resistant material (e.g. platinum) which is immersed in the etch solution. If a uniform current density is required, a mesh cathode with surface area larger than the silicon wafer must be used and placed in the solution parallel to the wafer, and at a suitable distance so that the current flow at the interface between the wafer and the solution is spatially uniform. Alternatively, when a pore size gradient is pursued, a rod-like Pt cathode is immersed at a specific position within the solution [12, 19].

The current flow through this system induces porosification of the silicon wafer by the anodic electrochemical etch process previously described. Throughout the process, hydrogen is evolved at the anode while fluoride ions are bonded to silicon while HF is consumed; this in time causes a change in the solution concentration at the wafer interface. In order to prevent this phenomenon from interfering with the etch process, a pumping system that continuously provides fresh solution is usually present [19]. Once the porous layer has formed, a final electropolishing step at high current is performed which causes the layer to detach from the silicon wafer [12, 19]. The detached layer is then rinsed, transferred to a 2-propanol solution, and sonicated until it is broken down into microparticles within the desired

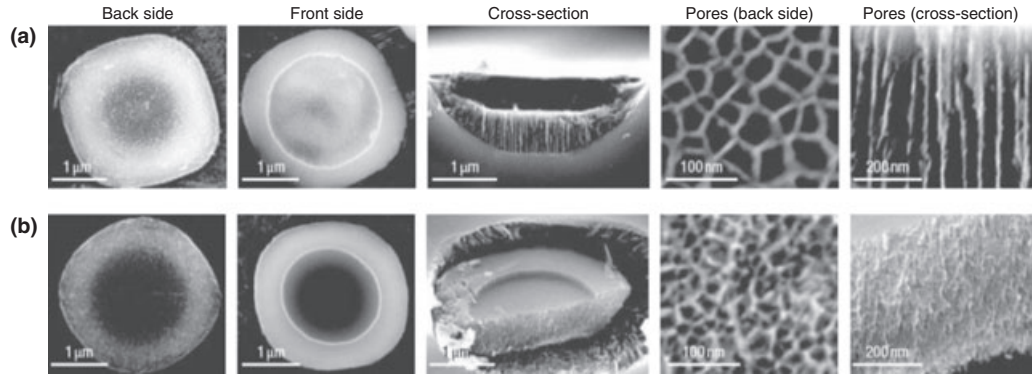

Figure 11.5 Scanning electron microscopy (SEM) images of hemispherical mesoporous silicon microparticles containing either large pores (a) or small pores (b). Reproduced from Ref. [16], courtesy of Nature Publishing Group.

size range. The particles obtained when using this approach are characterized by their irregular shape and size polydispersion. Although a selection for size is usually obtained through filtering, selection for shape cannot be achieved [19, 23].

The size polydispersion, and the very small yield in the micron size range suitable for drug delivery applications, constitutes a significant drawback of this technique. Size uniformity is important for shared biodegradation rates, which depend on both size and porosity. Another drawback of this technique is the shape polydispersion, which affects both the cellular uptake of pSi particles and blood flow characteristics [24]. Microparticle uptake by the reticuloendothelial system (RES), as well as margination and adhesion dynamics in the bloodstream, are strongly correlated to both the shape and size of the particles [21, 25, 26].

Ferrari *et al*. developed a porosification process involving photolithography that allows extreme control over particle size and geometry [16]. In this process, an initial two-dimensional (2-D) shape is transferred through photolithography of a silicon nitride-coated wafer. Reactive ion etch (RIE) is then employed to transfer the pattern through the silicon nitride layer and confer an initial three-dimensional (3-D) structure to the particle, etching a trench within the silicon. The exact 3-D shape of the trench is determined by the 2-D shape of the pattern and the RIE conditions (Figure 11.5).

The patterned wafer then undergoes selective electrochemical etch. Here, the silicon nitride acts as an etch stop layer, and the wafer is differentially porosified only where the silicon is directly exposed to the etchant solution. A second etch step with current intensity in the transition region leads to the formation of a high-porosity layer at the interface between the porosified particle and the silicon wafer. The Si_3N_4 layer is removed by means of prolonged soaking in HF. Finally, the particles are detached from the silicon substrate by disrupting the high-porosity layer through sonication in 2-propanol. The final particle shape is determined

by the initial trench shape and the effects of the electrochemical etch (Figure 11.5). The electrochemical etch profile is determined by the local current intensity gradients at the silicon interface. This technique is both extremely controllable and reproducible, and allows the manufacture of particles with characteristic sizes in the micron range and monodisperse in terms of both particle and pore size. The particle shapes attainable are limited by the 3-D patterns achievable through the combination of photolithographic techniques and the characteristic profile of the electrochemical etch.

11.4 Characterization

Once the porous silicon microparticles have been fabricated, they must be carefully characterized to insure that the desired particle specifications have been achieved and that there is minimal batch-to-batch variation. Good Manufacturing Practice (GMP) must be maintained to ensure replicability of microparticle fabrication between lots and to exclude particle structural variability as a source of experimental observation in biological experiments. Given the complexity and size scales involved with the internal structure of these microparticles, a battery of techniques must be employed to quantify the important metrics, such as porosity, pore size, density, interior volume, surface area, surface charge and surface modification.

11.4.1 Gravimetry

One of the most straightforward and accurate ways to measure the porosity and density of pSi is through the gravimetric technique [27]. First, the silicon substrate is weighed before any electrochemical etching is performed (m_1). The silicon substrate is then electrochemically etched and then re-weighed again (m_2). Finally, the pSi layer is removed using an etch solution of NaOH and the silicon substrate weighed a third time (m_3). The porosity of the pSi is then determined according to the following relationship:

$$p = \frac{m_1 - m_2}{m_1 - m_3} \tag{11.1}$$

The thickness (W) of the pSi layer can also be determined from m_1 and m_3 according to the following relationship:

$$W = \frac{m_1 - m_3}{A \cdot d_o} \tag{11.2}$$

where A is the area of the silicon substrate exposed to the HF solution and d_o is the density of silicon [27].

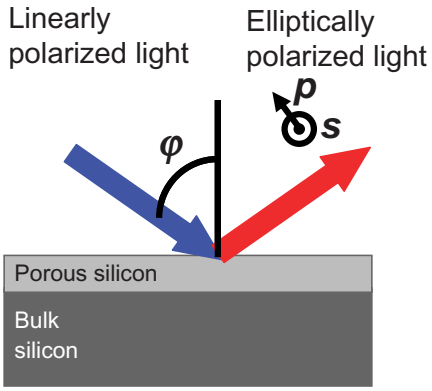

Figure 11.6 A representation of the ellipsometric measurement. The blue arrow represents the incident light with a known linear polarization, while the red arrow represents the reflected light with an unknown elliptical polarization to be measured. φ is the angle of incidence, which equals the angle of reflectance, *p* represents the electric-field components of the light waves oriented parallel to the plane of incidence, and *s* represents the electric-field components of the light waves oriented perpendicular to the plane of incidence. Adapted from Ref. [29].

11.4.2 Spectroscopic Ellipsometry

Although gravimetry is a straightforward and accurate technique [28], it is a destructive methodology for determining porosity. Spectroscopic ellipsometry is an optical technique (Figure 11.6), whereby the porosity of the pSi layer is determined by illumination of its surface with linearly polarized light, which then interacts with the porous material to emerge elliptically polarized upon reflection [29].

The reflected light is decomposed into its perpendicular (s-direction) and parallel (p-direction) components (with respect to the plane of incidence) and their amplitudes and phase shift are measured, as determined by the following relationship [29]:

$$\rho = \frac{R_p}{R_s} = \tan(\psi)\cdot e^{i\Delta} \tag{11.3}$$

where R_p and R_s are the complex reflection coefficients, $\tan(\psi)$ is the ratio of the reflected amplitudes, and Δ is the phase shift [29]. Once the change in polarization has been determined, a complex dielectric constant (ε) can be calculated [30]:

$$\varepsilon = \varepsilon_1 + i\varepsilon_2 = \sin^2\varphi + \left[\frac{(1-\rho)}{(1+\rho)}\right]^2 \sin^2\varphi \tan^2\varphi \tag{11.4}$$

where ε_1 and ε_2 are the real and imaginary components of the complex dielectric constant and φ is the angle of incidence. Once the dielectric constant for the overall

porous silicon layer is obtained, an analytical model is used to determine the contribution of the dielectric constants of the crystalline silicon and the air-filled voids to the overall measured dielectric constant, which is dependent on the porosity of the film. One heavily used model for this purpose is the Effective-Medium Theory corrected for dipole–dipole interactions, which models the voids as ellipsoids inside the crystalline silicon matrix [31]. From this theory the porosity can be calculated as follows [31]:

$$\frac{1}{3}C\alpha + \frac{(1-C)(\varepsilon_m - \varepsilon)}{(\varepsilon_m + 2\varepsilon)} = 0 \tag{11.5}$$

for a 3-D system where ε_m is the dielectric constant of the surrounding crystalline silicon and C is the porosity. α can be calculated through the following equation [31]:

$$\alpha = \frac{1}{3}\sum_{i=1}^{3}\frac{(\varepsilon_v - \varepsilon)}{\varepsilon + L_i(\varepsilon_v - \varepsilon)} \tag{11.6}$$

where the L_i indicates the depolarization triplets governed by the ratio of the axes of the ellipsoid shaped voids and ε_v is their dielectric constant [31]. Although this is a good approximation of the porosity, it is not perfect due to the fact that voids in the pSi layer cannot be completely approximated as ellipsoids leading to a discrepancy between the modeled and actual porosities [27].

11.4.3 X-Ray Diffraction

Another nondestructive technique for measuring the interaction of electromagnetic radiation with the pSi layer to determine its important characteristics is X-ray diffraction (XRD) [32]. This technique relies on pSi retaining the single crystal nature of the original silicon wafer even though it contains voids. Measurements are performed using monochromatic X-rays with a wavelength of 1.54 Å emitted from copper subjected to a high-energy electron beam. The X-rays are reflected off the surface of the pSi layer at varying angles of incidence, and collected by a detector at an equal angle of reflection [33]. The diffraction pattern thus reconstructed is related to the arrangements of interatomic planes in the crystal. The intensity peaks in the diffraction pattern are related to the wavelength of the X-rays (λ), the spacing between atomic planes (d), and angle of incidence according to the Bragg equation:

$$n\lambda = 2d\sin\theta \tag{11.7}$$

where θ is the Bragg angle and n is an integer multiple of the wavelength [34]. A representative XRD measurement is shown in Figure 11.7 for pSi layers of three different porosities [32]. The rocking curves shown in Figure 11.7 are collected, keeping the angle of incidence fixed and scanning the angle of reflection in a small

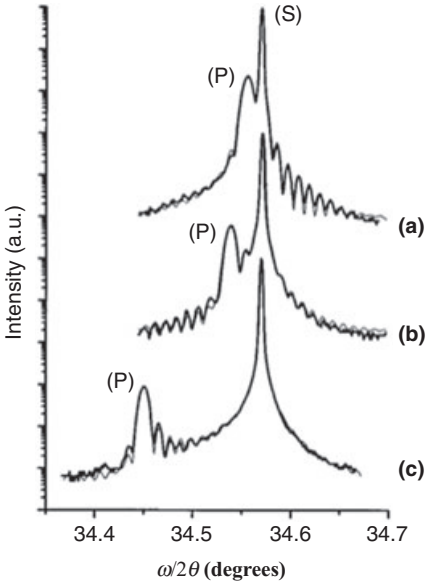

Figure 11.7 Experimental and simulated rocking curves, in the vicinity of the (004) reflection, of various thin PS [(pSi)] samples of: (a) p+ type [substrate doping], 36% porosity, thickness of 500 nm; (b) p+ type [substrate doping], 60% porosity, thickness of 500 nm; (c) p-type [substrate doping], 65% porosity, thickness of 500 nm. The values of each parameter used for the simulations are reported in Table I of Ref. [6]. Reproduced from Ref. [32], courtesy of American Institute of Physics.

range around the equal angle of reflectance. The S Bragg peak corresponds to the sharp peak produced by the highly ordered single crystal silicon substrate. The P peak, which is lower in intensity and broader, is produced by the pSi layer. The lattice mismatch parameter between the lattice constant of the silicon and that of the pSi layer can be calculated by evaluating the angular separation of the two peaks and used in conjunction with the dynamical theory of XRD [35] to determine the porosity [32]. Furthermore, the pSi layer thickness can be ascertained from the frequency of the small intensity fringes at the edges of the rocking curves away from the main Bragg peaks S and P. X-ray diffraction, like spectroscopic ellipsometry, can be used to determine porosity nondestructively, and in the case of XRD the thickness of the pSi layers is usually in good agreement with measurements made using the gravimetric method [30, 32].

11.4.4 Nitrogen Adsorption

Spectroscopic ellipsometry and XRD measurements require large areas of continuous films. In order to directly measure the properties of pSi particles, it is possible to exploit the principle of gas adsorption [28], with the most commonly employed

gas for this analysis being nitrogen. This technique allows the total surface area of the porous material to be calculated, simply by knowing the adsorbate's molar volume and adsorption cross-sectional area [36]. Furthermore, by knowing the surface tension of the gas species when it is in liquid form, and how the surface curvature adjusts the condensing properties of the gas from a flat surface, it is also possible to obtain a pore size distribution [37].

To perform these measurements, a known amount of gas is introduced into a chamber containing the porous sample. The system is then allowed to reach equilibrium, after which the deviation of the equilibrium pressure from the ideal pressure that would result if no adsorption was taking place, is measured [38, 39]. Under isothermal conditions, which can be achieved by immersing the sample in liquid nitrogen for example, the pressure difference can be related to a volume which, when divided by the mass of the sample, represents the specific volume of gas adsorbed (in $cm^3 g^{-1}$). The results of these measurements are known as *isotherm curves* (see Figure 11.8). Depending on the experimental apparatus used, the pressure can either be adjusted incrementally or, in some of the latest adaptations, adjusted continuously at a rate that guarantees the attainment of quasi-equilibrium conditions [40]. The pressure (as represented on the x-axis) is the relative pressure p/p_0 where p is the supplied pressure and p_0 is the saturation pressure

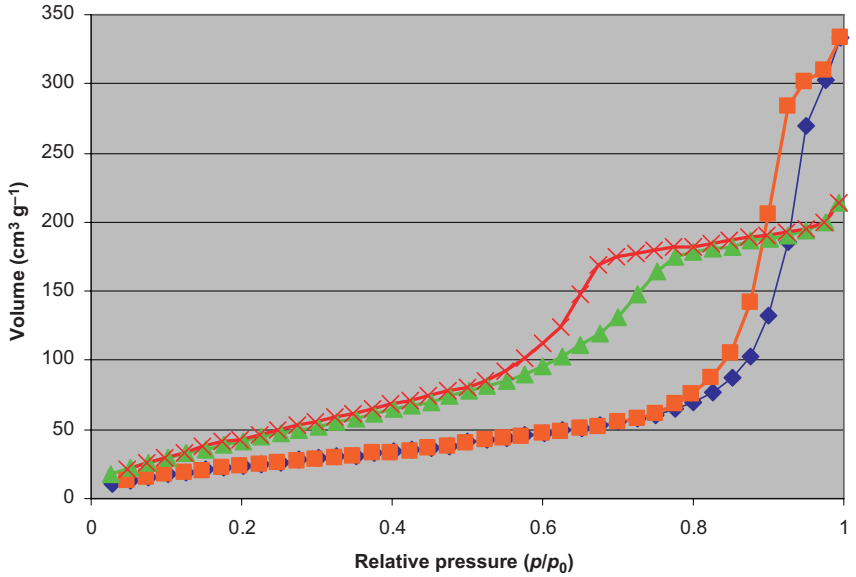

Figure 11.8 Isotherms generated for microparticle samples with two different mean pore sizes. The green and dark red curves are the adsorption and desorption isotherms, respectively, for microparticles with a diameter of 3.2 µm and a mean pore size of 7.4 nm. The blue and orange curves are the adsorption and desorption isotherms, respectively, for microparticles with a diameter of 3.5 µm and a mean pore size of 24.2 nm.

of liquid nitrogen (the pressure at which liquid nitrogen boils at a given temperature). When the pressure in the chamber exceeds the saturation pressure, the gas condenses. The experiment is usually performed by sweeping the relative pressure in both directions to measure adsorption as well as desorption. As can be seen from Figure 11.8, hysteresis is usually observed; this is due to the particular structure of the pores (e.g. pores resembling straight cylinders versus pores with constrictions anywhere along their length) and/or the interaction between the adsorbate and the sample surface [40]. Although these interactions can be quite complex, the hysteresis for pSi tends to be quite consistent for samples fabricated under the same conditions, and so can serve as a qualitative check on the most likely pore configuration for a given sample [28]. A quick estimate of the total pore volume for pSi can be gleaned directly from the saturated area of the isotherm present at high values of relative pressure (this is not the case for all materials, as isotherms of different materials do not always saturate) [28]. Given that a calculation of the total volume of the pSi material can be made, the porosity can quickly be calculated (porosity = pore volume/total volume) and is usually in good agreement with data provided by the gravimetric method [28].

From the isotherms in Figure 11.8 a range of information can be obtained. The first important piece of information is the total surface area of the porous material, which can be calculated using the Brunauer–Emmett–Teller (BET) method. This derives a relationship between the volume and relative pressure, based on how the molecular layers of adsorbate build up on the surface of the porous material [36]. The BET equation is as follows:

$$\frac{p}{v(p_o - p)} = \frac{1}{v_m c} + \frac{c-1}{v_m c}\frac{p}{p_o} \tag{11.8}$$

where p is the measured pressure, p_0 is the saturation pressure, v is the adsorbed volume, v_m is the adsorbed volume when the entire surface of the sample is covered with a unimolecular layer of adsorbate, and c is a parameter obtained from to the following relationship;

$$c \approx e^{\frac{E_1 - E_L}{RT}} \tag{11.9}$$

where E_1 is the heat of adsorption of the first layer of adsorbate, E_L is the heat of liquefaction used for all subsequent layers of adsorbate, R is the gas constant, and T is the temperature [36]. In order to calculate the total surface area it is necessary to plot $p/(v(p_0 - p))$ versus p/p_0, using values of volume obtained from the isotherm over the range where the isotherm is approximately linear, which for silicon usually corresponds to values of p/p_0 from 0.05 to 0.35 (this range is material-dependent) [36]. Both v_m and c can be calculated from the line where $1/v_m c$ is the y-intercept and $(c-1)/m_e$ is the slope. When v_m has been determined, by multiplying the ratio of v_m and the molar volume by Avogadro's number and the adsorbate cross-sectional area, it is possible to determine the total surface area of the sample

[36]. Outside the range of relative pressures listed above, either the entire surface area is not covered with adsorbate, leading to sublinear behavior, or condensation has begun inside the pores due to their extreme curvature at a pressure level lower than the onset of condensation on a flat surface, leading to super-linear behavior [37]. These two effects therefore exclude those regions of the isotherm from being used to determine total surface area through the BET model.

The super-linear region of the isotherm at higher values of relative pressure is used to determine the pore size distribution. As the super-linear behavior is due to the early onset of condensation in the pores, a mathematical relationship was developed by Barrett, Joyner and Helena (BJH) which equated the change in desorbed volume from one measurement point to the next to a release of condensate from pores of a particular radius, plus the thinning of the adsorbed layer in pores which were already empty [37]. The pore volume is then calculated according to the following equation [37]:

$$V_{pn} = R_n\left(\Delta V_n - \Delta t_n \sum_{j=1}^{n-1} c_j A_{pj}\right) \tag{11.10}$$

where V_{pn} is the average volume of the pores which are currently releasing their condensate (the range of pore sizes which must be averaged depends on the resolution of the measurement apparatus as it is related to the minimum relative pressure step), ΔV_n is the measured decremental desorbed volume change, Δt_n is the decremental adsorbate layer thickness change, R_n is the radial adjustment to convert the capillary volume (the volume of the actual pore minus the volume of the adsorbed sheath) to the actual pore volume, A_{pj} is the actual area of each of the pores already emptied, and c_j is the radial adjustment to convert the actual pore area to the capillary area. $R_n = r_{pn}{}^2/(r_k + \Delta t_n)^2$, and takes into account not only the capillary volume, with radius r_k, but also the decremental change in the adsorbate volume, with thickness Δt_n. Finally, $A_{pj} = 2V_{pj}/r_{pj}$, and is calculated for each pore which has already been emptied, multiplied by $c_j = (r_{pj} - t_n)/r_{pj}$, where t_n is the total adsorbed layer thickness for the current relative pressure, and then summed together for all previous emptied pores [37]. This term constitutes the adsorbate volume released from all of the previously emptied pores, and must be removed from the measured decremental volume in order to accurately calculate V_{pn}. The value of the capillary radius, r_k, relates to the relative pressure by way of the Kelvin equation [41]:

$$r_k = \frac{-2\gamma V_m}{RT \ln(p/p_0)} \tag{11.11}$$

where V_m and γ are the molar mass and surface tension of the adsorbate, R is the gas constant, and T is the temperature in Kelvin. The relationship between the total sheath thickness t to the relative pressure – 'the t-curve' – has been determined previously through a variety of techniques. One way is to determine the t-curve

experimentally by measuring an isotherm for an unporosified sample of the same material, and dividing the isotherm by the BET-calculated unimolecular volume V_m to extract the number of molecular layers present for a given relative pressure, and then multiply by the radius of molecular nitrogen [42, 43]. This can then be directly ported to the porous sample. If no exact reference material exists (i.e. the material does not exist in bulk form), then a similar material can be used. This reference substitute is selected based on its possessing a comparable *c*-value, as calculated by the BET model [43]. The other commonly used methodology for calculating the *t*-curve is to use a semi-empirical version of the Frenkel–Hill–Halsey equation:

$$t = \frac{1}{\left(\frac{-RT}{\alpha}\ln\left(\frac{p}{p_0}\right)\right)^{1/s}} \tag{11.12}$$

where s and α are constants, α being the Hamaker constant of the system (which is a measure of the van der Waals interactions between the adsorbate and the sample) [41, 44, 45]. In the literature, values of $s = 2$ and $s = 3$ have been used to generate *t*-curves, but for the case of porous silicon $s = 3$ has been shown to produce quite consistent results [29]. The various radii and thicknesses used in the model and listed above are depicted in Figure 11.9. When all of these components have been taken into account and the pore volume has been computed

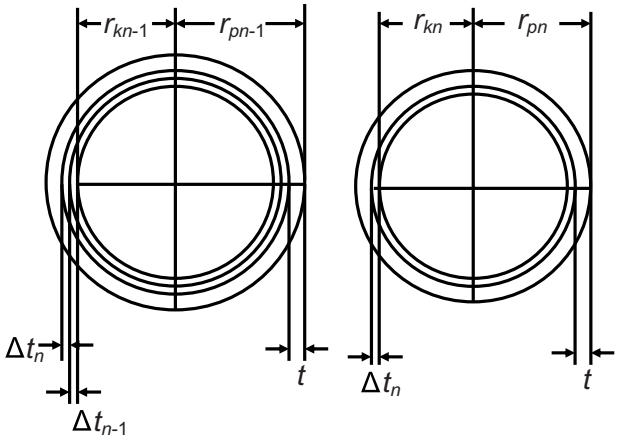

Figure 11.9 A schematic representation of the desorption mechanism described in the BJH pore size distribution model, indicating the origin of the physical parameters of the cylindrically modeled pores. r_{kn}, r_{pn} and r_{kn-1}, r_{pn-1} are the radii of the capillaries and pores which have released their condensate in the current relative pressure step n and the previous relative pressure $(n-1)$ step. t is the current thickness of the adsorbate, with Δt_n and Δt_{n-1} representing the current and previous change in adsorbate thickness. Adapted from Ref. [37].

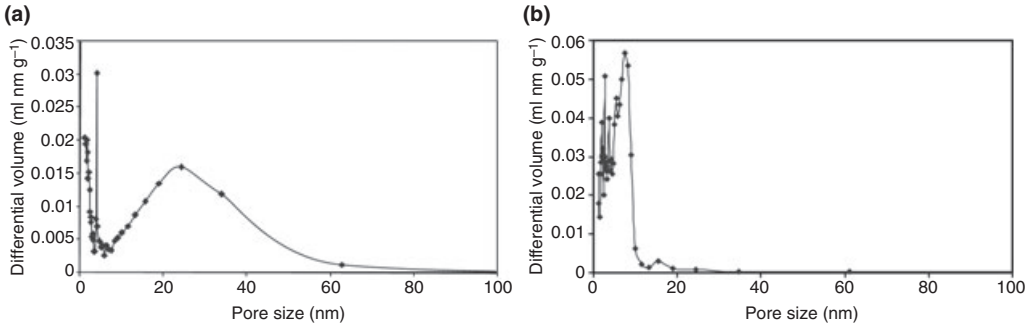

Figure 11.10 The pore size distributions, calculated using the adsorption isotherms from Figure 11.8, for pSi microparticles with mean pore sizes of (a) 24.2 nm and (b) 7.4 nm. Reprinted from Ref. [16], courtesy of Nature Publishing Group.

for all pores with radii r_p, the values of V_p are divided by Δr_p (the change in the computed pore radius from one point to the adjacent point) to determine the differential volume for each pore size, given in units of $cm^3 g^{-1} Å^{-1}$ [37]. The plot of the differential pore volume versus r_p yields the pore size distribution representing the total area of the surface that each size of pore occupies. As an internal check for consistency, the summation of the surface area over all the radii from the pore size distribution should be within a few percent of the total surface area calculated from the BET model [37]. Figure 11.10 shows calculated pore size distributions for hemispherical microparticles similar to the microparticles depicted in Figure 11.5, but fabricated under two different electrochemical etch conditions [16]. One distribution constitutes microparticles with a diameter of 3.5 µm and a mean pore size of 24.2 nm, while the other is comprised of microparticles with a diameter of 3.2 µm and a mean pore size of 7.4 nm. These two distributions were calculated from the isotherms in Figure 11.8, and seem to agree quite well with the visual inspection of the microparticles as viewed using scanning electron microscopy.

11.4.5
Sample Preparation for Electron Microscopy: Sectioning

Although the above-described techniques are quite effective for large areas and/or large ensembles of pSi microparticles, they require large sample sizes to be generated from either entire wafer surfaces or microparticles to be gathered from multiple wafers. It is therefore necessary to check a sampling of microparticles produced from each wafer by using electron microscopy in the form of scanning electron microscopy (SEM), transmission electron microscopy (TEM) and scanning transmission electron microscopy (STEM) [16, 46–48].

SEM requires almost no sample preparation beyond fabrication of the microparticles because pSi is a semiconductor formed in solutions of HF and therefore

lacks any appreciable surface oxide layer that may prevent effective imaging. If an insulating oxide layer were to be formed on the surface, the SEM image would become distorted due to charging of the surface dielectric causing an electrostatic interaction with the incident electron beam [49]. Storing the particles in 2-propanol maintains this surface state, with at worst the formation of a thin native oxide layer which has a minimal effect on imaging. SEM is thus a quick but accurate technique to observe the overall microparticle shape and structural integrity, as well as allowing for the inspection of surface pore sizes, for a representative sampling from a single wafer. It is also possible to observe cross-sections of the microparticles using the SEM (Figure 11.5) by cleaving the wafers upon which the particles are fabricated before they are released [16].

Given the resolution achievable by SEM, several reasons lead to the use of high-resolution TEM (HRTEM) or STEM. One reason is to investigate the crystalline structure of the pSi layer [47], and indeed HRTEM achieves sub-Angstrom resolution by exploiting the change in phase that the electrons experience as they pass through and interact with the sample, essentially measuring the beam's interference with itself [50]. STEM achieves the same result measuring electrons which are scattered from the sample at high angles, away from the optical axis of the beam [51].

A second reason to investigate pSi layers with high-resolution imaging is to assess the loading efficiency of primary-stage pharmaceuticals [52], secondary-stage delivery agents (such as liposomes [53]), or imaging agents such as iron oxide [54, 55]. In addition to HRTEM and STEM being able to observe loaded material at a higher resolution than SEM, STEM – by using high-angle scattering to create the image and employing a rastering beam with a 2 Å or less spot size containing electrons the kinetic energy of which is closely matched – can use electrons that are transmitted through the sample close to the optical axis for electron energy loss spectroscopy (EELS) [56]. EELS measures the change in the energy of transmitted electrons as they are inelastically scattered by the sample. Such scattering can arise from a number of sources, including phonon and plasmon excitations, but they can also occur through interband transitions in atoms which produce characteristic spectrographic signatures in the transmitted electron energies [57, 58]. These characteristic spectra can be used to identify and determine the relative abundances of different elements in the sample [57]. The effect range of EELS is capable of observing the interband transitions of lighter elements such as carbon [57], while the analysis of heavier atoms requires the use of electron dispersive X-ray spectroscopy (EDX) [59]. EDX relies on the radioactive emission from atoms excited from their ground state by the interaction with an electron from the STEM beam. When another electron from a higher energy level falls into the lower energy level that was just vacated, an X-ray is released [59]. The emission energies are characteristic of the specific energetic levels involved, and as they differ for different elements, they allow an estimation to be made of the chemical composition of the sample [59]. This technique has been employed to probe metal deposition on pSi [60]. Although SEM also has EDX capability, the penetration depth of the

SEM beam is in the low micron range [61], and so does not allow for sufficient z-resolution to differentiate thin samples from their substrates, thus precluding an accurate analysis of the sample composition. Therefore, the use of TEM and STEM, where the electron beam travels solely across the specimen, provides a more accurate characterization of the chemical composition of the sample. The 2 Å spot size rastering beam of STEM also allows for minimum background noise and high-resolution x,y mapping of the sample surface.

11.4.5.1 **Sample Preparation**

Sample preparation for both HRTEM and STEM is significantly more complex than for SEM. The TEM sample must allow a certain degree of electron transmission in order for the electrons to be collected at the detector and form an image [62]. Conventional TEM sample preparation for hard materials such as semiconductors requires a combination of mechanical grinding, mechanical, ionic or focused ion-beam milling, or dry or wet etching [62, 63]. For pSi, the energy involved in these processes is known to lead to structural damage of the sample. However, by borrowing from a biological methodology for sample preparation, the authors' group has developed an ultramicrotomy protocol to prepare samples for imaging [64, 65]. In the basic protocol, the sample – after being rendered into the desired state – is embedded in an epoxy resin which is cured and then shaved into nanometer-thick slices using a diamond-blade microtome [66]. In the initial protocol a formulation of Spurr resin was used [66]; this is a mixture of vinylcyclohexane dioxide (VCD), a flexibilizer made from the diglycidyl ether of polypropyleneglycol (DER 786), a hardener consisting of nonenyl succinic anhydride (NSA), and an accelerator of dimethylaminoethanol (DMAE) [66]. The uncured resin is characterized by a very low viscosity that allows it to efficiently penetrate the nanosized features of the sample. The main drawback is the hydrophobic nature of the resin, which prevents the embedding of hydrated samples [66], and it is therefore necessary to dehydrate the sample first by using ethanol and then acetone. Although this method is effective for pristine porosified silicon, problems can occur when the microparticle has been loaded, as the acetone may dissolve out any loaded material that is not firmly bound in the sample. One means of alleviating this problem is to use a water-soluble embedding material such as agarose [67]. Agarose contains a crosslinkable polysaccharide that can be used in aqueous solution, but unfortunately it is quite soft, which makes it a poor choice for sectioning relatively hard silicon microparticles. It can, however, maintain the relative positions of the components within the aqueous media once it has been polymerized. The agarose can then be crushed and embedded in a firmer epoxy, such as Spurr.

When the sample has been embedded it is necessary to shape the block face down to a small area (<0.7 mm on each side). The sample is then sectioned using an ultramicrotome (e.g. the Leica-UCT) [64, 65]. The ultramicrotome uses a mechanical or thermal advance to move the epoxy block towards a stationary glass or diamond knife (in this case, a diamond knife with a 35° blade) while

simultaneously sweeping the sample vertically (perpendicular to the blade edge) [64–66]. A glass knife is used initially to smooth the block face and to supply thick sections for imaging by optical microscopy (this indicates the best location from where to take the ultrathin sections with the diamond knife) [66]. As the sample approaches the blade edge, the sweep rate of the arm slows dramatically so that a thin slice is removed. Due to the porous nature of the silicon microparticles, the block can be sectioned without damaging the blade (this would not be possible with bulk silicon). The tool is capable of stepping the arm anywhere, from many microns down to 20–30 nm [66]. The diamond blade is mounted in a chassis which can accommodate a liquid reservoir directly behind the blade [64]. When the block face has been sliced, the hydrophobic sections float on top of the reservoir in a ribbon, and may be collected by pressing a copper grid, treated by immersion in hydrochloric acid, onto the liquid's meniscus where the sections are located [66]. The grids can then be loaded into the TEM for observation. The process of embedding and microtoming provides an effective means of preparing porous silicon TEM samples and, in a more general sense, of creating thin cross-sections of microparticles in order to examine their structure and/or the effectiveness of loading protocols. SEM can also be used to examine sections to check for loading efficiency; whether the material being loaded is sufficiently large and has good contrast, such as gold nanoparticles. Images of sectioned microparticles taken using SEM, TEM, STEM and HRTEM are shown in Figure 11.11. The loading of quantum dots in porous silica beads using fluorescent images has also been demonstrated [69].

As mentioned above, the hydrophobic nature of the epoxy and the embedding procedure may cause any loaded material to dissolve out of the pSi during the process. As an alternative to using a water-soluble embedding material, it is possible to use flash-freezing, cryosectioning and cryo-TEM to prepare and subsequently image the material [70]. If an aqueous solution can be frozen quickly enough, the water surrounding it can be vitrified, as opposed to frozen into a crystalline form that causes sample damage [70]. The usual protocol consists of plunging a small droplet of the sample containing an aqueous solution into a liquid, such as ethane, at liquid nitrogen temperature [70]. Immersion directly into liquid nitrogen is ineffective due to the Leidenfrost effect, whereby a liquid in contact with another material at a temperature much higher than its boiling point will be insulated for a certain period of time by a thin vapor film that is present due to the flash boiling of the cooler liquid at the interface [71]. This vapor film will insulate the bulk of the liquid, thus slowing down the transfer of heat along the temperature gradient [71]. The water in the aqueous solution containing the sample then has sufficient time to crystallize and damage the sample [70]. When the sample has been frozen, both ultramicrotoming and TEM can be performed under cryostatic conditions [70]. In this way, a 'snapshot' of the material interaction between the silicon microparticle and the material to be loaded can be achieved. This is an especially useful technique for visualizing the loading of soft material, such as liposomes, as the more standard embedding techniques are too destructive for these organic structures [72].

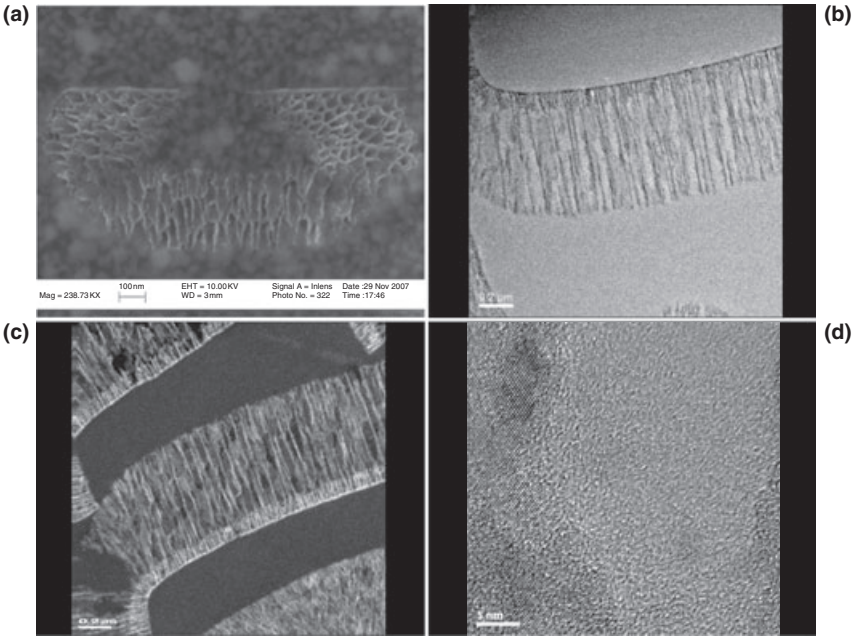

Figure 11.11 (a) SEM; (b) TEM; (c) STEM; and (d) HRTEM images of sectioned pSi microparticles. In (d) the crystal lattice of the pSi can be observed.

Having described some of the standard techniques used to characterize microparticles from a materials standpoint, it is also important to understand their behavior from a biological standpoint. This requires another set of tools and techniques, some of will now be discussed in the context of using pSi particles as vectors for the targeted delivery of drug molecules and contrast agents.

11.5
Nanovectors for the Delivery of Therapeutics

11.5.1
Biocompatibility and Biodegradation

Silicon is the most abundant element on Earth after oxygen [73]. When in solution, silicon is not ionized but rather is present as orthosilicic acid, $Si(OH)_4$, the dissolution product of silica in water. Silicon is used for skeletal strengthening by sea sponges, and by organisms for bone development [74]. Experimentally, silicon implanted into humans has been shown to contribute to bone growth by stimulating the formation of hydroxyapatite [74]. In addition to bone, silicon is required for cartilage and connective tissue formation [75, 76].

Crystallized silicon is very nonreactive and requires extremely high temperatures to become reactive. It is also known to be a nonbiocompatible material with very poor hemocompatibility [9]. However, in 1995, Canham [10] demonstrated the bioactivity of pSi layers in simulated body fluids (SBFs). Here, the term 'bioactive' refers to silicon as a biomaterial, which is defined as a nonviable material intended to interact with biological systems when used in a medical device. As noted by Canham, the transition of silicon to a bioactive state via the introduction of pores is consistent with the fact that all other natural biological materials are porous [77]. In Canham's study, 1 µm-thick pSi layers were incubated in various SBFs for periods ranging from 6 h to 6 weeks. While the highly porous Si (porosity >70%) dissolved in all SBFs tested, the silicon with medium porosity (<70%) was slowly biodegradable. Similar to solid silicon, very low-porosity silicon was shown to be bioinert. Thus, porosity is directly related to bioactivity.

Other studies have also analyzed the degradation of pSi layers in SBFs [68, 78]. Both, inductively coupled plasma (ICP) and mass spectroscopy (MS) measurements of solutions containing porosified wafers were used to determine the amount of dissolved pSi from 64%, 83% and 88% porosity layers over 24 h at different pH levels. Triplicate experiments were performed on five different buffered solutions with pH values of 2, 4, 6, 7 and 8, after which ICP-MS was used to determine the amount of silicon in solution at different time points [68]. At pH 7, medium-porosity (62%) pSi showed almost no dissolution at 6 h, and very little at 24 h. Both, high (83%) and very high (88%) -porosity films showed an exponential increase in silicon dissolution over time, with a maximum of 61.3 ± 7.6% for high-porosity films and 45.5 ± 3.3% for very high-porosity films [68] (Figure 11.12). Dissolution at 6 and 24 h under different pH conditions showed a positive correla-

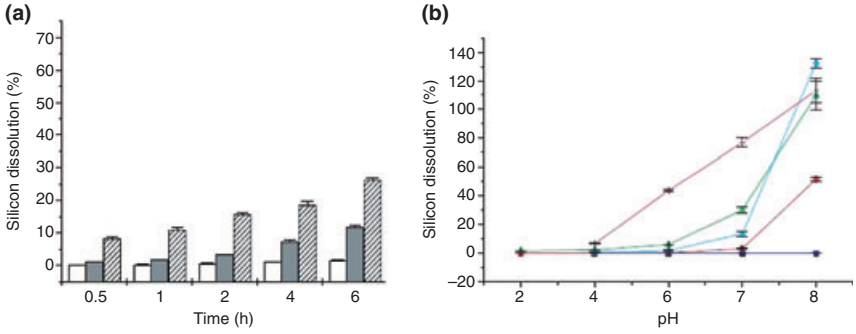

Figure 11.12 Effect of porosity and pH on dissolution kinetics of pSi. (a) Medium-porosity (62%) film (white); high-porosity (83%) film (gray); and very high-porosity (88%) film (hatched); (b) Bulk (nonporous) films: dark blue line is 6 h (square points), superimposed horizontal line is 24 h (triangular points); medium-porosity films (62%): red line is 6 h (circles), light blue line is 24 h (diamonds); high-porosity films (83%): green line is 6 h (triangles), purple line is 24 h (crosses). Reprinted from Ref. [68] courtesy of Wiley-VCH.

tion between dissolution and increasing pH (Figure 11.12). The low- and high-porosity layers dissolved completely at pH 8 at 24 h, whereas at pH ≤4, little or no dissolution was observed [68].

Ferrari's research team has confirmed the impact of pore size on degradation kinetics [79]. 3-Aminopropyltriethoxysilane (APTES) -modified silicon microparticles, which are hemispherical in shape and have a diameter of 3.0–3.2 μm, contained either small (5–10 nm) or large (30–50 nm) pores. The microparticles were incubated in phosphate-buffered saline (PBS) with shaking at 37 °C. Degradation was measured by inductively coupled plasma atomic emission spectrometry (ICP-AES) analysis of the released silicon. While small pores particles remained intact at 4 and 6 h, large-pore particles released 15% and 35% of their silicon content, respectively. After 32 h, small-pore particles were 25% degraded, and large-pore particles 85% degraded. In agreement with previous reports, the degradation kinetics was heavily dependent on the pore size, with small-pore particles degrading much more slowly than their large-pore counterparts.

The hydrosilylation of pSi layers with 1-dodecyne yields a dodecenyl-terminated surface which is completely stable for weeks in both simulated blood plasma and alkaline solutions [78]. Another surface modification which has been shown to slow degradation is to coat the pSi with a hydrophilic 'stealth' polymer, such as poly(ethylene glycol) (PEG). In a study conducted by Godin *et al.* [79], the pSi was surface modified with one of seven PEGs of which the molecular weight (MW) ranged from 245 to 5000, in either PBS or 100% serum at 37 °C with constant shaking. The pSi was seen to degrade faster in serum than in PBS, while the MW of the PEG correlated negatively with the degradation rate. Conjugation of the shortest PEG (PEG-245) to the particle surface did not affect the degradation kinetics in serum compared to the parent APTES pSi, but did delay pSi degradation in PBS. pSi particles with longer PEG chains degraded within 18–24 h in serum, and within 48 h in PBS. The most dramatic effect on degradation rate was observed for particles coated with PEG-3400 or PEG-5000, both of which extended the life of the particles to more than three days under these harsh conditions.

The 'stealthing' of delivery vehicles with PEG is also used to prolong the blood circulation time by reducing the surface charge and creating steric hindrance, both of which interfere with the binding and uptake of particles by cells of the mononuclear phagocyte system, such as macrophages. One mechanism by which PEG reduces the uptake of pSi by phagocytic cells is through reduced serum opsonization, which mediates recognition by phagocytic cells. The main drawbacks of this approach include a reduced ability to attach targeting ligands to the particle surface, the involvement of distally located ligands which may accelerate removal, and the possible elicitation of an immune response [80]. Additional drawbacks of using PEG to limit phagocytosis include the shielding of pores during the loading process and hindered drug release *in vivo* at the pathological site. In order to enhance the therapeutic efficacy of 'stealthed' particles, techniques aimed at causing the polymer coat to be 'shed' at the lesion site are being developed [81].

For the extracellular release of drugs, a delayed degradation of the silicon particle with polymers, followed by shedding after arrival at the target site, would lead to a directed drug release [81]. The extracellular shedding of the polymer coat at the pathological site also restores interactions with target cell membranes and facilitates uptake if desired. Shedding approaches include using linkers with predetermined cleavage points between the polymer chain and anchoring moieties. Stimuli eliciting such release include proteases, pH changes and reducing agents. For example, the extracellular pH of solid tumors is significantly more acidic than that of normal tissues, leading to a selective release at the tumor site [82]. Alternatively, internalized particles encounter consecutive drops in pH as they transition from early to late endosomes, and then to lysosomes. Intracellular delivery could also benefit from linkers sensitive to protonation for the release of therapeutics. One example of a linker which is sensitive to hydrolysis of the linker bond is diorthoester [83]; at low pH, this bond forms a stable dialkoxy carbonium intermediate and leads to dissociation of the polymer. Other acid-labile linkers include vinyl ether, hydrazone, beta-thiopropionate and phosphoramidate [81]. With regards to reducing agents, a switch from an oxidizing to a reducing environment occurs as particles transition from the extracellular to the cytosolic environment. The reduction of disulfide bonds, such as a dithio-3-hexanol linker, for example, could release polymers, carrier caps or covalently attached drug molecules. The third cleavage approach – proteolysis-induced shedding – relies on enzymes present at high concentrations at the pathological site. For example, lysozymes and cathepsins are present at inflammatory sites, including cancer lesions [81].

One important issue concerning biocompatibility is the toxicity of the dissolved silicon. Fortunately, pSi degrades predominantly into monomeric silicic acid ($Si(OH)_4$) which, as stated previously, is the natural form of silicon in water. The average daily dietary intake of silicon, an essential nutrient, in the Western world is approximately 20–50 mg per day [84]. The mean daily silicon intake in men is 30–33 mg, significantly higher than for women (24–25 mg); for both men and women, the mean daily intake is decreased with age. As an example of dietary silicon content, an average beer contains 19.2 $mg\,l^{-1}$ silicon [85]; due to a 55% absorption rate, serum and urinary silicon levels are considerably increased following the consumption of 600 ml of beer. Fortunately, the dietary intake of silicic acid was balanced by its urinary excretion, which is highly efficient. The dietary importance of silicon was demonstrated definitively by excluding silicon from the diet of rats; this led to a growth reduction of 30–35% and to the development of bone deformations [86].

Consistent with variations in dietary silicon intake, serum silicon levels in adults vary with both gender and age. In a study of 1325 healthy volunteers [87], median serum concentrations were higher in women aged 30–44 years (11.1 $\mu mol\,l^{-1}$), as compared to women aged less than 30 years, and decreased in both men and women with increasing age (7.7 and 8.0 $\mu mol\,l^{-1}$, respectively). The decease in silicon levels in relation to age was faster in women. For men, steady-state silicon levels (9.5 $\mu mol\,l^{-1}$) were maintained between 18 and 59 years.

Sapelkin *et al.* [88] cultured rat hippocampal neurons (B50 cell line) with stain-etched pSi and showed that cells were capable of adhering to the silicon surface. Portions of the crystalline silicon surface were treated, creating either square regions with pore sizes varying from 50–100 nm, or 30 μm- and 100 μm-wide stripes, separated by untreated surfaces. The cells showed a clear preference for adherence to porous regions, with growth ending abruptly at boundaries between the crystalline and porous regions. In the case of porous lines etched onto the silicon, the cells aligned along the channels. Thus, the surface topology clearly influenced cell proliferation. Khung *et al.* [89] further showed that SK-N-SH neuroblastoma density and morphology were dramatically influenced by pSi surface topography. The cells were sensitive to nanoscale surface topography, responding to features of less than 20 nm. Neuroblastoma cells were grown on pSi gradients, with pore sizes ranging from 5 to 3000 nm. Unlike B50 cells, the SK-N-SH cells appeared healthy and had well-spread processes when grown on either unetched flat silicon or pSi with 5 to 20 nm pore sizes. For large pore sizes, the cell morphology mirrored the structure of the pores, but for pore sizes <1000 nm (but >20 nm) the increased cell clustering and shortening of neuritic processes continued with decreasing pore size. In addition to increased clustering, the cell density was decreased with decreasing pore size (from 1000 to 20 nm), but increased on pore sizes below 20 nm; this suggested that the nanoscale surface topography had been 'sensed' by the growing cells.

Bayliss cultured Chinese hamster ovary (CHO) cells and rat hippocampal neurons (B50) on pSi layers in tissue culture media for four days [90]. The cell viability in terms of respiration and membrane integrity was measured using MTT [3-(4,5-dimethylthiazolyl-2)-2,5-diphenyltetrazolium bromide] and neutral red (NR) assays. Cell viability was significantly higher for B50 neurons cultured on pSi than on poly-silicon or bulk silicon, as well as control glass coverslips, supporting the nontoxicity of pSi under these conditions [90]. However, CHO cells were less viable on pSi than on crystalline silicon and glass, which suggested that coating with matrix proteins such as collagen might be important for specific populations.

In another study, primary mammalian hepatocytes isolated from a three-month-old female Lewis rat were cultured on either untreated pSi, fetal bovine serum-treated pSi or collagen-coated pSi [91]. After a 24 h incubation period, measurements of cell adhesion showed the collagen-coated pSi to be by far the optimal substrate, but after five days the cell viability in the presence of pSi was similar to that in the presence of polystyrene. The production of albumin and urea, which were respectively considered as markers of hepatocyte synthetic function and of intact nitrogen metabolic pathways, was monitored in the cell culture for 14 days and shown to be comparable to values observed in the presence of polystyrene. Taken together, these data suggest that pSi does not exhibit any significant cytotoxic effects towards primary mammalian cell lines.

Although studies to determine *in-vivo* biocompatibility, biodegradation and biodistribution studies are currently under way, no results have yet been presented. As mentioned above, *in vitro* dissolution studies have shown that silicic acid

concentrations can be controlled by adjusting the porosity of pSi [92]. The major obstacle to successful *in-vivo* studies is the dietary dose of silicon in animals. Therapeutic doses of drug-carrying pSi are two to three orders of magnitude lower than the dietary intake, and therefore administered silicon is difficult to detect accurately in biodistribution assays. Whilst radioactive silicon may help to overcome this detection issue, the half-life of ^{31}Si (the only isotope that can be obtained through the irradiation of Si) is 157.3 min, and clearly inadequate for long-term studies. The production of single-crystal silicon wafers enriched with more stable Si radioactive isotopes is, as yet, unheard of. Studies of the biodistribution path of other elements (i.e. fluorescent molecules), either loaded into or covalently attached to the pSi particle, represent an indirect alternative that is currently being used to measure the biodistribution of silicon.

Reports on the use of ^{32}P-doped pSi (Brachysil®) for brachytherapy in nonresectable hepatocellular carcinoma have so far accounted for the first – and only – published study of an in-human use of pSi particles [93]. A collection of phosphate-doped 20 μm pSi particles were neutron-irradiated to obtain a significant increase in the level of radioactive ^{32}P. Previous animal model studies have established that nonirradiated particles were biologically inert; irradiated ^{32}P pSi implantation into pig livers also failed to show any systemic toxicity, with minimal leakage. For human studies, all eight subjects considered for a clinical trial were characterized by the Eastern Cooperative Oncology Group performance status 0–2, Okuda Stage I and II, life expectancy greater than 12 weeks, as well as adequate hematologic, renal and hepatic functions. Any patients with encephalopathy, prior radiotherapy, significant history of cardiac disease or a serious, active infection were excluded. A maximum of three tumors per patient was identified and monitored, after which patients were scheduled to receive intratumoral implantation of Brachysil under radiologic imaging guidance and local anesthesia. None of the patients had any detectable radioactivity levels in their blood immediately after implantation, which showed that the device had remained *in situ*, without systemic dissemination. The 24-week follow-up showed no adverse events related to the therapeutic formulation, and the authors concluded that, 'The lack of any serious adverse events, and the absence of systemic leakage, indicate that this device is relatively safe for use in clinical settings'. All target tumors showed a size reduction at 12 weeks after implantation, with 100% regression in two patients. Further tumor size reductions were observed in four patients at 24 weeks. The final assessment, at 24 weeks, showed two complete responses, two partial responses, three stable diseases, and one progressive disease.

As with all therapeutic applications, aseptic techniques are necessary for production. It has been shown, using *in vitro* cell cultures, that both bacteria and fungi will readily colonize pSi, thus establishing a need for sterilization prior to their use in clinical applications [77]. Although some preliminary studies on pSi sterilization, including autoclaving, have been presented, few reported data are available. Current clinical applications, which are limited to BioSilicon carriers, use irradiated products and a sterile formulant [93].

11.5.2
Drug Loading and Quantification of Drug Load

A variety of techniques have been used to load drugs into pSi mesopores, including the immersion of particles into a loading solution containing an appropriate solvent for the target drug [94–96]. Another method is to load dry pSi particles or chips with a drug solution by capillary action; this is also known as the incipient wetness method [97–99]. Drying pSi particles has been achieved by freeze or vacuum drying [96, 100] as well as thermal drying [52]. While these loading techniques may appear simple, factors such as pH dependency, time and temperature, as well as interactions between the drug and the particles, the drug and the solvent, and the solvent and the particles, must all be taken into account. Retention of the drug occurs by a nontrivial combination of electrostatic attraction, van der Waals forces, H-bonding and hydrophobic interactions, depending on the pSi surface chemistry and the drug choice. pSi can be made hydrophobic for the loading of hydrophobic drugs, such as dexamethasone; conversely, the loading of hydrophilic drugs may be aided by an appropriate surfactant [99]. Once loaded, a balance between sufficient washing and drug retention must be achieved whilst at the same time releasing the surface fraction.

A more irreversible loading technique involves entrapment by volume expansion [55]. For example, an iron oxide nanoparticle payload was loaded into pSi and then locked into place by oxidation of the pSi. When silicon is oxidized to SiO_2, a volume expansion occurs which shrinks the pores and traps the payload. This procedure involves loading nanoparticles immeresed in a basic aqueous solution and then drying the sample in an oven (both of these steps may contribute to oxidation). Another loading technique is covalent attachment of the payload, in which the hydrosilylation layer on oxidized silicon provides a means for using bioconjugation chemistry. As an example, in order to attach a payload to pSi, it might be possible to react the oxidized pSi with a carboxyalkene to create functional carboxyl units on the pSi surface. The final result of loading is pSi particles containing a payload, the release of which is dependent upon degradation of the matrix. An advantage of the more stable loading techniques is that the loaded pSi can be more vigorously washed, thus facilitating release of the surface fraction.

A unique attribute of pSi is the ability to optically report on the loading of a molecule within the porous nanostructure. The optical interference spectrum from multilayers has been used in sensor applications, where changes in the optical reflectivity spectrum indicate the capture of a chemical or biological species [101–106]. However, these properties can also be used to monitor the release of a drug loaded into pSi. The Fourier transform of the optical reflectivity spectrum provides a simple means of monitoring the drug loading and release [107] since, when the loading has been completed, both the quantity and chemical purity of the drug can be determined using high-performance liquid chromatography (HPLC) analysis. For this, two different methods can be used. In the first method,

any depletion in the drug concentration of the loading solution can be determined during the loading procedure. In the second method, the drug concentration is determined after complete extraction of the drug residing in the PSi particles [97]. In addition, as noted in Section 11.4.3, high-resolution imaging (e.g. STEM and EELS) can be used to visualize and quantitate the sample loading.

In a detailed *in vitro* study, Salonen and coworkers studied the loading of five model drugs into pSi particles, and their subsequent release [52]. Here, antipyrine, ibuprofen, griseofulvin, ranitidine and furosemide were chosen to represent a wide range of solubilities, as well as different acid–base characteristics and lipophilicity. The pSi surface was treated with a two-step thermal carbonization process in order to obtain a chemically stable hydrophilic Si—C interface. The drugs were then loaded in different solutions and conditions due to their different solubility characteristics. The loaded particles were filtered and dried at high temperature (65–105 °C) for 1 h. The characterization of the drug loading was performed using techniques which included thermogravimetry, differential scanning calorimetry, helium pycnometry, N_2 desorption, X-ray diffraction and HPLC. Such use of multiple techniques allowed the investigators not only to obtain more reliable results but also to localize the drug in the pores, or on the surface of the microparticle. Drug release was studied at different pH values (5.5, 6.8, 7.4) and quantified through HPLC. The five drugs each showed different loading capabilities and release profiles:

- Antipyrine: The average load of antipyrine, a highly soluble drug, was 53.4% (w/w) after 1.5 h in aqueous solution, but 14.5% of the loaded drug was in crystalline form on the surface. A rapid early release, which slowed after 5 min, was due to the dissociation of surface antipyrine. A pH-independent dissolution of 80% of the loaded drug occurred at 75 min, while unloaded drug required 45 min for 80% dissolution.

- Ibuprofen: The average ibuprofen load, in ethanol after 1 h, was 30.4%, with a minimal amount of crystallized drug on the surface. The lower loading efficiency and negligible presence on the surface were expected due to the lower solubility of ibuprofen. Although ibuprofen solubility is pH-dependent, dissolution of the loaded drug was less pH-dependent than unloaded ibuprofen, and the release profile of loaded ibuprofen was similar to that of loaded antipyrine.

- Griseofulvin: The griseofulvin loading efficiency was 12.4–16.5%, with minimal traces on the surface; this was an extremely good result considering the poor solubility of the molecule. Griseofulvin solubility is not pH-dependent while loaded, however, griseofulvin release was pH-dependent, which suggested that the enhanced release at high pH might be due to effects of the pH on surface interaction between the pSi and the drug, or to an enlargement of the pores at high pH due to surface degradation.

- Furosemide: Furosemide, which also is poorly soluble in aqueous media, had an average load of 41.3%, with no drug crystallized on the surface. Its release at pH 5.5 was significantly improved by loading into porous silicon. At pH 6.8 and 7.4,

furosemide release was still slightly increased by loading, as was the case for the other poorly soluble molecules.

- Ranitidine: Surprisingly, despite the high aqueous solubility of ranitidine, the average load was only 13.2%, with no drug crystallized on the surface. As in the case of antipyrine, loading of the drug into porous silicon particle slowed the release rate of this highly soluble molecule.

The results of this study indicated that the chemical nature of the drug and the loading solution were critical for efficient loading. Clearly, the surface properties constitute an essential aspect in the design of porous silicon particles for drug delivery, and there is great potential for tailoring the surface properties of silicon to suit the compound being loaded. The release rate of the pSi-loaded drug was dependent on the solubility of the drug molecule. For highly soluble molecules, the pSi loading caused a slightly delayed release with respect to the unloaded drugs, whereas for poorly soluble drugs their dissolution was significantly improved by loading. In addition, loading in general reduced any pH-dependence of dissolution. Another important result of this study was the direct observation and quantification of actual loading of the drug inside the silicon matrix pores. The advantages of having the drug on the surface of the silicon particle are extremely limited, both in terms of sustained release enhancement and of protection from physiological biobarriers. It is necessary, therefore, to achieve a significant pore loading in order to fully exploit any advantages of pSi as a drug carrier.

PSi loading and release of a model protein have also been studied [108]. Here, aqueous solutions containing papain at different concentrations (1–10%, w/w) were incubated with pSi particles that had been presoaked in methanol to enhance loading. The particles were then washed, and a portion of the loaded particles examined using Fourier transform infrared (FTIR) analysis to assess the loading level. The FTIR analysis was used to characterize the chemical state of the pSi loaded with papain by monitoring any absorbance that was correlated to specific functional groups. The remaining particles were transferred to PBS, at 37 °C, and at multiple time points the PBS was collected for the quantitation of released papain. FTIR analysis showed a decrease in the Si—H_x signal which indicated a strong physical binding or chemisorption between the Si—H groups and specific functional groups in the papain. Asdorbance at 2100 cm^{-1} due to Si—H_x stretching decreased with increasing papain solution concentration, which suggested an increased loading level. A significant initial burst release was observed that indicated the presence of surface-bound papain. Increasing the loading level of papain decreased the initial release percentage, suggesting that with increasing protein concentration a greater proportion of papain was being loaded into the pores. After the initial burst, a linear relationship between papain release and time was observed, suggesting a zero-order release. The results of this study support pore internalization of the protein through FTIR analysis, as well as the presence of a possible loading interaction mechanism and how this reflects on the release profile. Also, the selected surface termination of the silicon, and its interaction

with the loaded moiety, was also indicated as an extremely important factor affecting loading.

In the future, additional knowledge regarding the loading process itself will undoubtedly be needed. Typically, some drugs seem to be easily loaded into pSi, while the loading of other drugs is quite complicated, especially when the behavior is not dictated solely by the surface chemistry of the pore walls. In summary, the use of alternative solvents, an optimized pH value and an appropriate temperature may enhance loading efficiency, especially when considering hydrophobic drugs and the loading of nanoparticles such as liposomes.

11.5.3
Nanovectors for the Delivery of Therapeutics

Nanovectors are drug delivery vehicles engineered with details and features in the nanosize range. These nanovectors are designed to optimize delivery to pathological sites and to provide a sustained, controlled release of drug therapies. Alternatively (or simultaneously), nanovectors can deliver concentrated payloads of contrast agents that can be used to image the pathological site and/or monitor drug delivery [109]. The localization, controlled release and monitoring of drug delivery within the body represent key challenges in the design of effective, targeted drug therapies [110–116].

In its simplest embodiment, a nanovector comprises the particle and the biologically active principle it carries (Figure 11.13a). Experience with particulates, such as liposomes, has shown that nanovectors of dimensions between 10 and 1000 nm are cleared very rapidly from the bloodstream by means of uptake by phagocytic cells of the RES [117]. In order to decrease the clearance time, and thereby allow

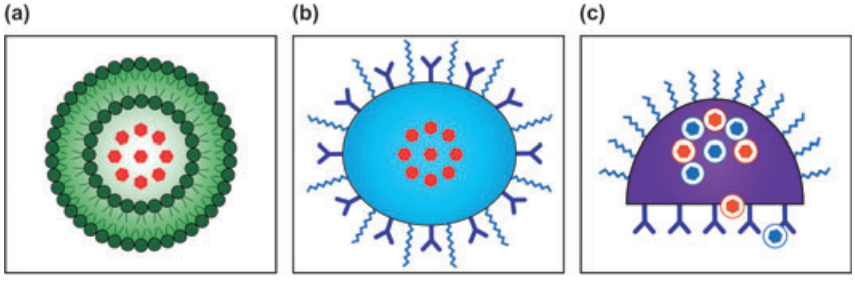

Figure 11.13 (a) First-generation nanovectors are characterized by the vector itself (e.g. liposome) and the drug payload; (b) Second-generation nanovectors have a more complex modification of their surface. The addition of targeting molecules (e.g. antibodies) and shielding molecules (e.g. PEG) convey new functions to the vector; (c) Third-generation nanovectors consist of multiple components optimized to fulfill all the tasks required by a drug delivery vector. These tasks include bypassing sequential biological barriers, protecting the drug payload, and releasing the drug payload at the pathological site in a time-dependent manner.

longer circulation time and improve localization at the desired target location, vectors can be surface-decorated with PEG or other shielding moieties, as described previously [118]. A nanoparticle comprising a drug and a stealthing layer is defined as a second-generation nanovector (Figure 11.13b). The liposomal drug formulations that are currently available in the clinic belong to this class of nanovectors. First- and second-generation nanovectors accumulate at the tumor site by escaping the vascular compartment through fenestrations' these are openings that characterize the tumor-associated, neovascular endothelium and render the blood vessels hyperpermeable compared to the normal vasculature. This passive localization mechanism is known as enhanced permeation and retention (EPR).

During the past two decades, several different strategies have been proposed to add biological targeting capabilities to nanovectors [119]. The dominant strategy involves the conjugation of targeting moieties to the surface of the nanovector, including antibodies [120], ligands [121], aptamers [122] and small peptides [123]. Targeting has been directed towards cancer cell-surface markers and to molecules expressed in the tumor microenvironment, most notably on the tumor-associated vascular endothelium.

After loading with drugs, the pores in the nanoparticles can be closed by constructing appropriate cap structures (Figure 11.14). The ability to control the release of anticancer drugs provides mesoporous silicon nanoparticles with advantages over other drug delivery systems, such as liposomal particles or albumin-based nanoparticles [124]. For example, environmentally responsive nanovectors are designed to release their therapeutic payload upon encountering external conditions that are associated with cancers. For instance, pH-sensitive polymers exist that become destabilized in the acidic environments of tumor lesions [125, 126], leading to a localized release of the drug cargo (Figure 11.15a). Tumor-associated enzymes, such as matrix metalloproteinases, may also be employed for preferential release at lesions that present a markedly invasive phenotype [128] (Figure 11.15b).

11.5.4
Towards a Multi-Stage Drug Delivery System

In order to develop the optimal drug delivery system it is important to consider the localization and negotiation of biological barriers. Following injection, therapeutic agents encounter a multiplicity of biological barriers that adversely impact their ability to reach the intended target at the desired concentrations [129]. Barriers of epithelial and endothelial nature, such as blood vessel walls and the blood–brain barrier, are among the most common examples of biobarriers to therapeutic action (Figure 11.16). These barriers are based on tight-junctions, which either prevent or limit the paracellular transport of agents. Endothelial/epithelial barriers are themselves multiplex and sequential in nature.

An entirely different biobarrier against the penetration of therapeutic agents, especially if they are formulated as large particulates, is the increased, adverse osmotic oncotic pressure developed by cancer lesions during their growth (Figure

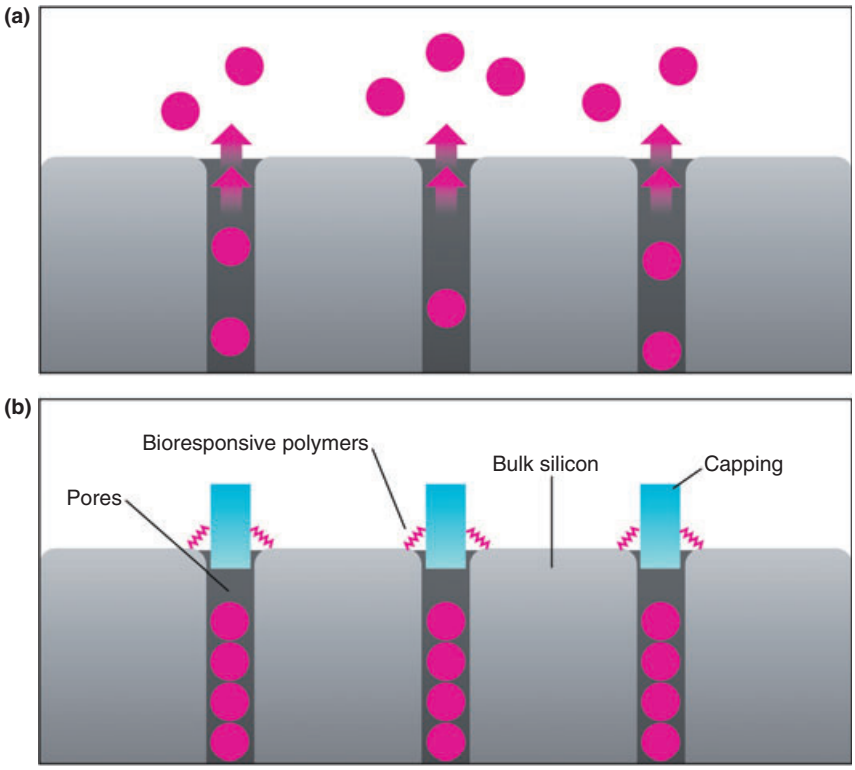

Figure 11.14 (a) With time, the payload naturally diffuses out of the pores into the surrounding solvent; (b) Several techniques exist to temporarily seal the pores. For example, pH-sensitive polymers can be used to cap the openings of the pores, creating a directly selective release at the tumor site.

11.16). Recent studies have shown that the hemodynamics within cancer lesions constitutes another type of barrier to particle localization [21]. Delivery vehicles of different shapes and sizes can offer a dramatic increase in therapeutic index, by optimizing their properties of margination, extravasation, firm adhesion to the vascular endothelium and control of phagocytic uptake.

In response to the need to bypass multiple biological barriers, third-generation nanovectors are being introduced which perform multiple functions in a sequential fashion. These nanovectors contain all the characteristics of the previous two generations – that is, they contain a therapeutic payload and have targeting and shielding moieties on their surfaces – but they are also able to perform a time sequence of functions which involves multiparticle coordination (see Figure 11.13c). An example of a third-generation nanovector is the 'nanoshuttle', which is a cluster of bacteriophage-entrapped metal nanoparticles [123]. The multistage systems which recently were demonstrated represent another example of

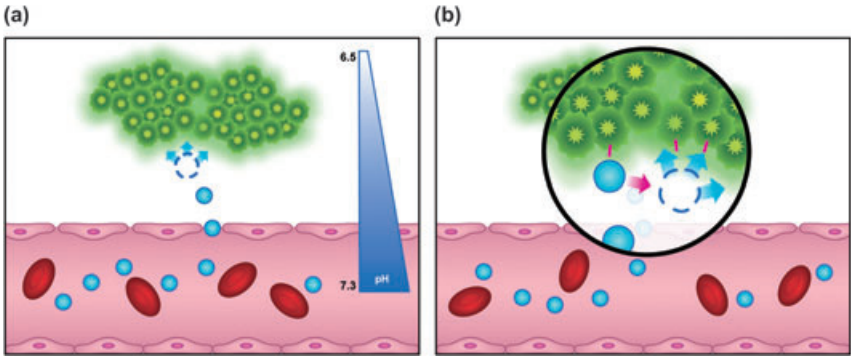

Figure 11.15 (a) pH-responsive particles (blue) retain their payload while in the normal circulation. At the site of the tumor lesion, the characteristic enlarged fenestrations (leaky vessels) favor extravasation of the particles into the tumor tissues. After diffusion and penetration into the tumor mass, the conditions of the tumor microenvironment (acidic pH) trigger the release of the therapeutic payload; (b) Another release mechanism is enzymatic cleavage or dissociation of the particle, for example, via overexpression of matrix metalloproteinases in highly invasive tumors.

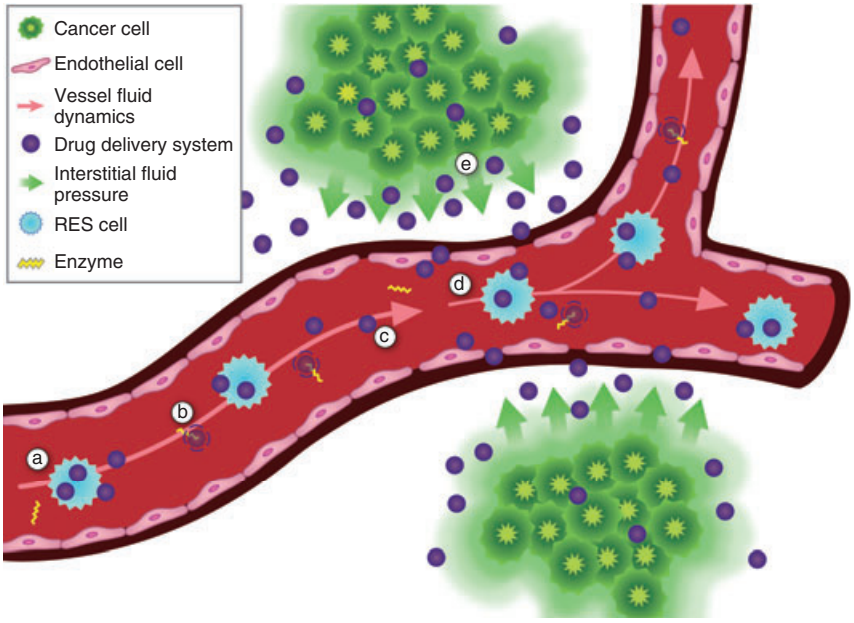

Figure 11.16 Major obstacles exist that prevent the majority of the injected drug from reaching the intended target. An efficient drug delivery system must be able to negotiate each of these obstacles in order to localize the therapeutic action at the target site. The nature of these biological barriers is sequential, and a delivery vector requires multiple layers of function in order to overcome each of these barriers. Examples of biological barriers are: reticuloendothelial system (RES) uptake, enzymatic degradation, hemorheology, endothelial barriers and the tumor-associated osmotic and interstitial pressures. Adapted from Ref. [154].

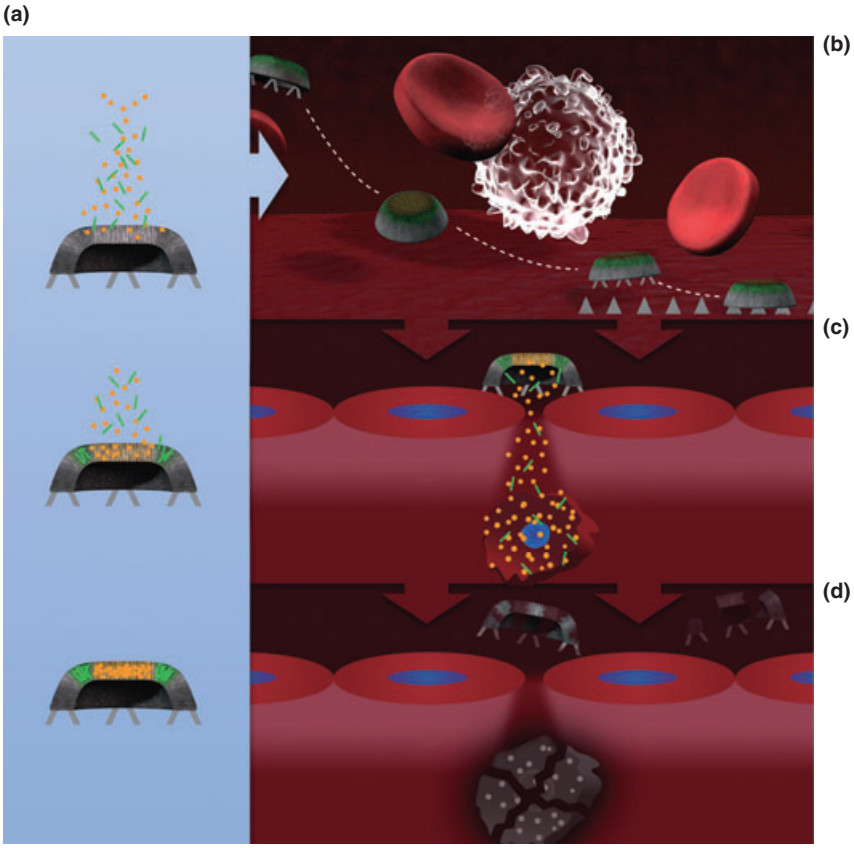

Figure 11.17 An example of a third-generation nanovector: the multistage delivery system. (a) The system is composed of a first-stage component which can be loaded with multiple second-stage nanoparticles; (b) After intravenous injection, the particles travel through the bloodstream and, based on their rational design and unique size, shape and chemical modifications, avoid RES uptake, and finally migrate to the vessel wall where they dock to the target endothelium; (c) The first-stage carrier releases the nanoparticle payload, which extravasates through the fenestrations of target vasculature and eventually penetrates into the cancer tissue surrounding the vessel; (d) Finally, the nanoparticles are taken up by the cells where they accomplish their final tasks (cell killing), while the first-stage carriers degrade into nontoxic, benign materials. Adapted from Ref. [16].

third-generation nanovectors [16]. As illustrated in Figure 11.17, these comprise a first-stage module that houses groups of different nanoparticles (Figure 11.17a); the particles then dock on the target vessel walls (Figure 11.17b) where they release the second-stage nanoparticles (Figure 11.17c). The second-stage nanoparticles can be released with different kinetics and rates in accordance with their structure, size, shape and chemical composition [16]. Complete drug release is accomplished

by the degradation of first-stage particles into biologically benign components (Figure 11.17d). The multistage strategy, summarized in Figure 11.17 combines the ability to perform sequential functions, offers opportunities to negotiate multiple, serially presented biological barriers, and therefore opens new frontiers in drug delivery [16].

11.6 Cellular Uptake of pSi Particles

As stated previously, pSi particles are targets for internalization by cells of the mononuclear phagocyte system, and 'stealthing' with PEG delays their uptake. For third-generation delivery systems, the first level of targeting for intravascularly administered particulates is the vascular endothelium. *In vitro*, vascular endothelial cells are able to internalize micron-sized pSi particles by phagocytosis and macropinocytosis (R.E. Serda *et al.*, unpublished results). This is more complicated *in vivo*, where serum opsonization coats the microparticles and alters their ability to adhere to the vascular wall. In this section we describe cellular uptake of pSi nanoparticles and microparticles, and examine the characteristics of pSi microparticles which alter this phenomenon.

11.6.1 Tumor Microenvironment

In order to target cancer lesions, an understanding of the microenvironment is essential for the design of the delivery vector. For instance, a clear association exists between chronic inflammation and malignant transformation. As an example, inflammatory bowel disease and *Helicobacter pylori* are associated with high rates of colon and gastric cancer, respectively [130]. Also, the relative risk of prostate cancer is increased in men with a history of sexually transmitted disease and prostatitis [131]. In fact, 15% of all cancers are associated with microbially induced inflammation [132]. In breast carcinogenesis, affinity mature B cells are found in tumor-associated stroma and secondary lymphoid tissues, and they are enriched in sentinel lymph nodes [133]. The proportions of B cells in sentinel and axillary lymph nodes of breast cancer patients correlate with increases in disease stage and total tumor burden [134, 135]. The high incidence of chronic inflammation in cancer explains why the long-term use of non-steroidal anti-inflammatory drugs is correlated with a decreased risk of various types of cancer, including colorectal and esophageal adenocarcinoma [136, 137].

Inflammatory mediators released by resident neutrophils and mast cells in solid tumors attract migrating monocytes, which differentiate into macrophages. Local chemokines and cytokines activate macrophages, which become phagocytic and release additional inflammatory mediators. When mice deficient in macrophages were crossed with mice predisposed to mammary cancer, the rate of tumor pro-

gression decreased and metastasis was inhibited [138]. This was most likely due to the positive role of tumor associated macrophages in stimulation of tumor growth and progression [139]. An example of inflammatory cytokine secretion by macrophages is the release of tumor necrosis factor-α (TNF-α), which increases the surface expression of adhesion molecules on endothelial cells, including intercellular adhesion molecule-1 (ICAM-1), vascular cell adhesion molecule-1 (VCAM-1) and endothelium leukocyte adhesion molecule-1 (ELAM-1) [140]. Enhanced numbers of adhesion molecules enhance the capture of leukocytes [141, 142], and may also increase the adhesion and capture of pSi particles (i.e. drug delivery vehicles).

The luminal surfaces of blood vessels contain a monolayer of endothelial cells that govern vascular tone and create a blood–tissue interface/barrier. As most drugs lack an affinity for endothelial cells, the endothelium is an important therapeutic target for delivery vectors. Endothelial cells are diverse in nature, and an understanding of their surface determinants guides the selection of targeting ligands that decorate the nanovector. The optimized treatment for cardiovascular and cancer pathologies benefits from a knowledge of endothelial receptor expression induced under inflammatory conditions. As stated previously, targeting ligands include antibodies, peptides and thioaptamers; these ligands target receptors for growth factors, cell adhesion molecules and transport proteins. Currently, 'Zip codes' are being identified which describe the molecular topography of surface determinants for defined vascular areas [143]. That is, addresses are being defined based on endothelial surface determinants expressed at pathological lesion sites. Ligands which recognize these addresses bind to the respective surface receptors, and can either internalize adherent delivery vehicles into cells through endocytic pathways, or provide prolonged residence on the surface, allowing time-dependent drug release.

11.6.2
Effect of Microparticle Shape on Margination

Theoretical models [21, 25], recently corroborated by experimental results [26], have shown that nonspherical objects have superior margination and endothelial adhesion properties compared to spherical objects of the same characteristic size. These findings give nonspherical particles significant advantages over their spherical counterparts. Hemispherical pSi particles have been fabricated as drug delivery vehicles (Figure 11.18) [16]. Enhanced margination improves the ability of particles to sense the endothelium and detect biological and biophysical aberrations, such as the overexpression of specific antigens or the presence of openings and fenestrations in the endothelium. Better margination abilities also enhance the particle's ability to leave the larger for the smaller vessels at branching points, resulting in a more complete exploration of the vascular system. As stated above, an enhanced adhesion of microparticles to the endothelium at the pathological site either permits the extracellular release of a payload or facilitates cellular uptake.

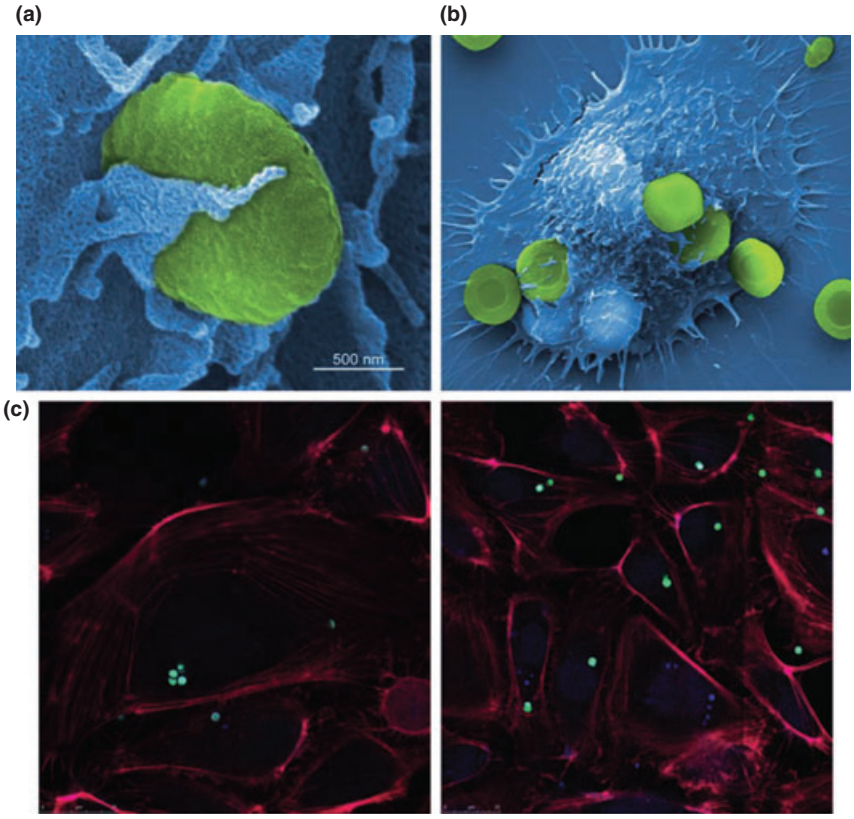

Figure 11.18 (a, b) Scanning electron micrographs showing phagocytosis of pSi hemispherical microparticles by endothelial cells (HUVECs). HUVECs were incubated with pSi microparticles for either 15 min (a) or 60 min (b) at 37 °C in serum-free media; (c) Confocal micrographs showing HUVECs with internalized pSi microparticles (green) after incubation for 60 min at 37 °C.

11.6.3
Effect of Microparticle Size on Cellular Uptake

As demonstrated by Chung *et al.* [144], human mesenchymal stem cell internalization of pSi nanoparticles (108–115 nm) can be regulated by altering the degree of positive surface charge on the nanoparticles. For example, increasing the positive charge on pSi nanoparticles, from a zeta potential of 15.6 to 19.5, caused a significant increase in nanoparticle uptake in serum-free conditions. However, a change in zeta potential from –4.90 to 15.6 did not significantly alter the number of nanoparticles internalized.

When using human umbilical endothelial cells (HUVECs) as a model of the vascular endothelium, hemispherical pSi microparticles were shown to be inter-

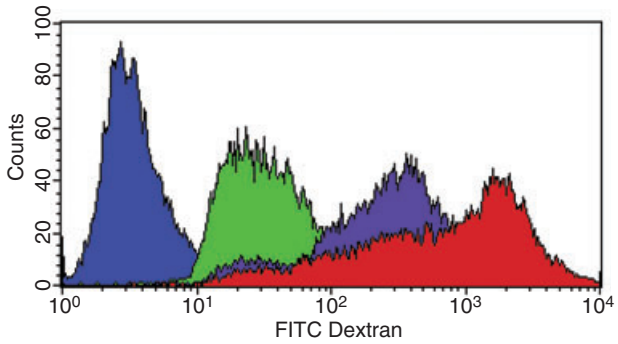

Figure 11.19 Macropinocytosis of pSi microparticles by HUVECs. HUVECs were incubated with either 1.6 µm (red) or 3.2 µm (purple) pSi hemispherical microparticles for 1 h at 37 °C in media containing FITC-dextran. Also included are cells cultured without particles in the presence (green) and absence (blue) of FITC-dextran. Uptake of FITC-dextran is indicative of fluid uptake, and is therefore a metric for macropinocytosis.

nalized in a process characterized by the formation of pseudopodia – that is, the extension of rope-like protrusions from the cell surface (Figure 11.18a). Within 1 h, the HUVECs had completely internalized multiple pSi particles (Figure 11.18 b and c). Two sizes of microparticles, with diameters of 1.6 and 3.2 µm, were both shown to be internalized via an actin-dependent process. While the uptake of larger particles was consistent with classical phagocytosis, with the hallmark image of an actin cup holding a microparticle, the smaller particles were internalized by both phagocytosis and macropinocytosis. Macropinocytosis, similar to phagocytosis, is actin-dependent, but results in the bulk uptake of both fluid and solid cargo [145]. Support for macropinocytosis as a mechanism utilized by endothelial cells is derived from a study conducted by Hartig *et al.* [146], in which nonspecifically bound nanoparticulate complexes were taken up by microvascular endothelial cells via macropinocytosis. The role of macropinocytosis in pSi microparticle uptake of 1.6 µm particles is supported by an enhanced uptake of fluorescein isothiocyanate (FITC)-dextran from the cell media (Figure 11.19).

Based on TEM analysis, HUVECs incubated with 1.6 µm oxidized pSi microparticles for 2 h at 37 °C show microparticles located in the perinuclear region of the cell (Figure 11.20a) indicative of microtubule-based transport [147]. A clear membrane can be seen surrounding an internalized 1.6 µm pSi particle. The larger 3.2 µm pSi particles, on the other hand, are more disperse and the majority of the microparticles show no evidence of membrane enclosure (Figure 11.20b). When pSi microparticles were labeled with DyLight 488 NHS ester (Pierce) to give them green fluorescent properties, a large number of the 1.6 µm particles colocalized with acidic vesicles (labeled with Lysotracker Red; Invitrogen) at 2 h. However, only a few of the 3.2 µm particles colocalized with acidic vesicles, supporting a cytoplasmic localization for the majority of the larger particles (R.E. Serda *et al.* unpublished results).

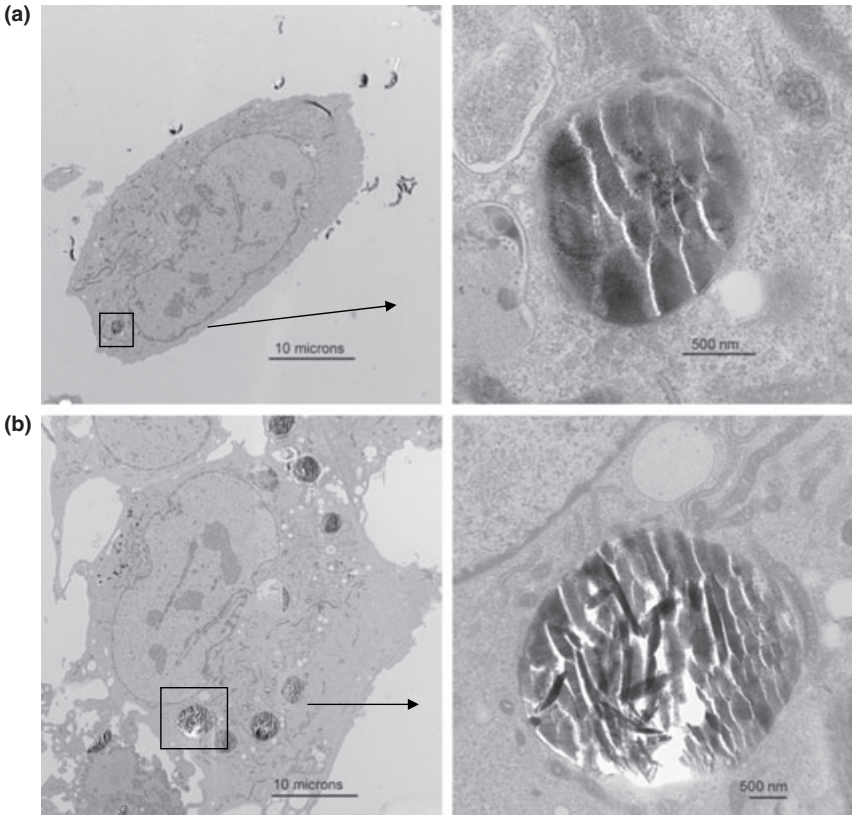

Figure 11.20 Location of internalized pSi microparticles in endothelial cells (HUVECs). HUVECs were incubated with either 1.6 µm (a) or 3.2 µm (b) pSi hemispherical microparticles for 2 h at 37 °C in serum-free media. The TEM images were taken by Kenneth Dunner, Jr., provided courtesy of the authors.

Slowing *et al.* [148] reported that mesoporous silica nanoparticles are internalized by human cervical cancer cells (HeLa) within 1 h in D-10 growth media. For pSi particles ranging from 150 to 300 nm, smaller particles were taken up more efficiently. To examine the endosomal escape of pSi nanoparticles, cells were stained with a red fluorescent endosomal marker (FM 4-64). The more negatively charged silica nanoparticles were able to escape from endosomes within 6 h, while the more positively charged particles remained trapped within endosomes. This effect was attributed to the 'proton sponge effect', in which the negative charge on the particles could buffer the acidic environment and disrupt endosomal function.

A comparison of cellular uptake of mesoporous silica nanoparticles and microparticles was performed using dendritic cells [149]. Two sizes of particles, namely 270 nm (AMS-6) and 2.5 µm (AMS-8), were incubated with dendritic cells in

culture medium for 24–48 h. For both sizes, the majority of cells had internalized the particles within 60 min. Based on TEM analysis, AMS-6 nanoparticles were encapsulated into vesicular compartments, while the larger microparticles appeared to lack membrane enclosure. Clearly, for drug therapy the intracellular release of delivery vehicles and their therapeutic payload is highly desirable; hence, a more detailed study relating particle size, charge and temporal endosomal release of particles is required.

The degree of apoptosis and necrosis in dendritic cells with internalized pSi particles was measured using the Annexin V-fluorescein and inclusion/exclusion of propidium iodide. Only at the highest concentration (50 $\mu g\,ml^{-1}$) was any decrease in cell viability seen at 24 h (viabilities: control 89%, AMS-6 81%, AMS-8 69%). However, the larger AMS-8 particles induced the expression of activation (costimulatory) markers at 24 h, suggesting that pSi microparticles might induce specific immune regulatory signals in dendritic cells. The nature of the immune signals is currently unknown, and whether they elicit proinflammatory or anti-inflammatory responses is yet to be determined.

11.6.4
Effect of Surface Modification on pSi Particle Uptake

Since attractive and resistive forces govern the binding and uptake of microparticles, the effect of surface chemistry on the uptake of pSi microparticles by HUVECs was investigated. Three classes of microparticle were examined: (i) negatively charged oxidized microparticles; (ii) positively charged APTES-modified microparticles; and (iii) methoxy poly(ethylene glycol) (mPEG)-5000-modified microparticles. Both, oxidized and APTES-modified pSi microparticles, were internalized under serum-free conditions by actin-dependent phagocytosis/macropinocytosis. Therefore, the binding of pSi microparticles to the cell membrane is not mediated solely by electrostatic interactions. As seen by others, PEGylated pSi microparticles are less able to be internalized.

In a separate study, the effect of surface charge, as well as labeling pSi nanoparticles with a cancer-specific targeting ligand, was examined by attaching various functional groups to the surface of pSi nanoparticles [23]. Nonfunctionalized, negatively charged silica nanoparticles were taken up by HeLa cells via nonspecific adsorptive endocytosis in serum-free media. On the other hand, the uptake of *N*-folate-3-aminopropyl pSi particles was sensitive to the addition of folic acid to the culture media, thus supporting a role for folic acid receptor-mediated endocytosis. Similar to studies with HUVECs in serum-free media, all particles were internalized, although the mechanism varied. Fluorescein (−34 mV) and folate (+13 mV) grafted particles were internalized by a clathrin-dependent mechanism, 3-aminopropyl (−5 mV) and guanidinopropyl (−3 mV) particle uptake was caveolae-dependent, and 3-[*N*-(2-guanidinoethyl)guanidine]propyl (+0.5 mV) uptake was via an unidentified mechanism.

With regards to other types of nanoparticles, a recent *in vivo* study showed that cationic liposomes have a propensity for localizing in tumor vessels [150]. Increas-

ing the cationic charge on PEGylated liposomes lowered uptake by the spleen and increased uptake by the liver. While the overall localization of liposomes in tumor cells in a severe combined immunodeficiency (SCID) mouse model did not increase, there was an increase in the accumulation of liposomes in tumor-associated blood vessels. Using a dorsal window chamber to view tumors, liposomes containing 10 and 50 mol% of cationic lipids were associated with 14 and 27% of the vascular area, respectively. These findings suggest that the physicochemical properties of drug carriers (e.g. liposomes and pSi particles) should be optimized to exploit the physiological features of the tumor and thereby enhance vascular targeting.

11.6.5
Serum Opsonization Inhibits Uptake of Oxidized pSi Microparticles

The results of several *in vivo* studies have suggested that the pattern of opsonins adsorbed to the surface of particulates determines the population of phagocytic cells responsible for their clearance [151]. For example, plasma protein adsorption by poly(D,L-lactic acid) nanoparticles enhances uptake by monocytes, while decreasing binding to lymphocytes [152]. In a recent study, regardless of the initial surface functionalization (oxidized, APTES or mPEG), all serum-opsonized pSi microparticles had a negative surface charge based on zeta potential measurements. The internalization of opsonized oxidized microparticles by HUVECs was inhibited (ca. 70%) compared to uptake under serum-free conditions. However, serum opsonization failed to have any impact on the internalization of APTES-modified microparticles. Serum opsonization also inhibited the uptake of negatively charged 1 μm polystyrene microparticles by HUVECs. Similar to the *in vivo* data described above, these data also support preferred vascular uptake of cationic particles in the presence of serum.

11.7
Cancer Imaging

Si-han Wu (2008) [153] demonstrated imaging capabilities for mesoporous silicon particles by fusing FITC-conjugated mesoporous silicon nanoparticles with $Fe_3O_4 \cdot SiO_2$ nanoparticles (1 MSN : 1 $Fe_3O_4 \cdot SiO_2$). Their product, known as 'Mag-Dye · MSNs', possessed magnetic resonance imaging (MRI)-enhancing, luminescent and porous properties. The iron content of the Mag-Dye · MSNs was 1 wt%, with a T_2 relaxivity (r_2) of 153 $mM^{-1}s^{-1}$. Within 1 h of incubation with 40 $\mu g\,ml^{-1}$ Mag-Dye · MSNs in serum-free media, more than 90% of NIH 3T3 fibroblasts and rat bone marrow stromal cells were labeled. Confocal images showed that the fused nanoparticles were internalized and localized around the nucleus.

In the same study, Wu *et al.* [153] showed contrast agent in the liver of mice by MRI as soon as 5 min after the administration of Mag-Dye · MSNs. Immunochemical staining and Perl's Prussian blue staining of liver sections demonstrated

a limited uptake by macrophages. In addition, the perfusion of mice at 30 min after injection of Mag-Dye·MSNs showed reduced fluorescent foci, indicating that the Mag-Dye·MSNs may still be located in the blood vessels at this early time point. One unsettling finding was that MR contrast in the liver lasted for up to 90 days, although whether the Mag-Dye·MSNs were still intact or only the contrast agent remained was not addressed. This study emphasizes the need for further *in vivo* studies of biocompatibility and biodegradation, which are currently under way.

11.8 Conclusions

A thorough knowledge of silicon's fundamental physico-chemical properties, its relative ease of production, limited costs, high scalability and solid – as well as extensively developed – manufacturing technology, makes pSi drug delivery vehicles good candidates for the mass production required for clinically available applications. The high flexibility in system design can accommodate a multitude of delivery mechanisms and payloads, which represents a significant advantage compared to many currently explored alternatives.

Ferrari's vision of multistage carriers, where each stage performs part of the journey from the site of administration to the cancer cell, negotiating one or more biological barriers, and adding a degree of targeting selectivity in each step, is a promising approach. The biological selectivity comprising cell target recognition by surface molecules, as well as mathematics-based rational design of the size, shape and physical properties of the vector particles, enhance the probability of recognition of the target cell – a synergy between molecular biology, physics, engineering and mathematics.

References

1 Langer, R. (1998) Drug delivery and targeting. *Nature*, **392**, 5–10.

2 Duncan, R. (2003) The dawning era of polymer therapeutics. *Nature Reviews. Drug Discovery*, **2**, 347–60.

3 Ho, C. and Tai, Y. (1996) Review MEMS and its applications for flow control. *Journal of Fluids*, **118**, 437–47.

4 Haque, M.A. and Saif, M.T.A. (2003) A review of MEMS-based microscale and nanoscale tensile and bending testing. *Experimental Mechanics*, **43**, 248–55.

5 Baltes, H., Brand, O., Hierlemann, A., Lange, D. and Hagleitner, C. (2002) CMOS MEMS – present and future. *Proceedings of the Fifteenth IEEE International Conference on Micro-Electro-Mechanical Systems*, pp. 459–66.

6 Bhattacharya, S., Jang, J., Yang, L., Akin, D. and Bashir, R. (2007) BIOMEMS and nanotechnology-based approaches for rapid detection of biological entities. *Journal of Rapid Methods and Automation in Microbiology*, **15**, 1–32.

7 Shawgo, S., Richards Grayson, A.C., Li, Y. and Cima, M.J. (2002) BioMEMS for drug delivery, Rebecca. *Current Opinion in Solid State and Materials Science*, **6**, 329–34.

8 Prausnitz, M.R. (2004) Microneedles for transdermal drug delivery. *Advanced Drug Delivery Reviews*, **56**, 581–7.

9 Kanda, Y., Aoshima, R. and Takada, A. (1981) Blood compatibility of components and materials in silicon integrated circuits. *Electronics Letters*, **17**, 558–9.

10 Canham, L.T. (1995) Bioactive silicon structure fabrication through nanoetching techniques. *Advanced Materials*, **7**, 1033–7.

11 Gallardo, J., Galliano, P.G. and Porto Lopez, J.M. (2002) Preparation and in vitro evaluation of porous silica gels. *Biomaterials*, **23**, 4277–84.

12 Zhang, G.X. (2004) Morphology and formation mechanisms of porous silicon. *Journal of the Electrochemical Society*, **151**, C69–80.

13 Turner, D.R. (1958) Electropolishing silicon in hydrofluoric acid solution. *Journal of The Electrochemical Society*, **105**, 402–8.

14 Uhlir, A., Jr (1956) Electrolytic shaping of germanium and silicon. *The Bell System Technical Journal*, **35**, 333–47.

15 Cullisa, A.G., Canham, L.T. and Calcott, P.D.J. (1987) The structural and luminescence properties of porous silicon. *Journal of Applied Physics*, **82**, 909–65.

16 Tasciotti, E., Liu, X., Bhavane, R., Plant, K., Leonard, A.D. *et al.* (2008) Mesoporous silicon particles as a multistage delivery system for imaging and therapeutic applications. *Nature Nanotech*, **3**, 151–7.

17 Sakamoto, J., Annapragada, A., Decuzzi, P. and Ferrari, M. (2007) Antibiological barrier nanovector technology for cancer applications. *Expert Opinion on Drug Delivery*, **4**, 359–69.

18 Cyrus, T., Lanza, G.M. and Wickline, S.A. (2007) Molecular imaging by cardiovascular MR. *Journal of Cardiovascular Magnetic Resonance*, **9**, 827–43.

19 Canham, L.T. (1997) *Properties of Porous Silicon* (ed. L.T. Canham), Inspec/IEE, London, UK.

20 Salonen, J., Laine, E. and Niinisto, E. (2002) Thermal carbonization of porous silicon surface by acetylene. *Journal of Applied Physics*, **91**, 456–61.

21 Decuzzi, P., Lee, S., Bhushan, B. and Ferrari, M. (2005) A theoretical model for the margination of particles within blood vessels. *Annals of Biomedical Engineering*, **33**, 179–90.

22 Decuzzi, P. and Ferrari, M. (2008) The receptor-mediated endocytosis of nonspherical particles. *Biophysical Journal*, **94**, 3790–7.

23 Slowing, I., Trewyn, B.G. and Lin, V.S. (2006) Effect of surface functionalization of MCM-41-type mesoporous silica nanoparticles on the endocytosis by human cancer cells. *Journal of the American Chemical Society*, **128**(46), 14792–3.

24 Euliss, L.E., DuPont, J.A., Gratton, S. and DeSimone, J. (2006) Imparting size, shape, and composition control of materials for nanomedicine. *Chemical Society Reviews*, **35**, 1095–104.

25 Decuzzi, P. and Ferrari, M. (2006) The adhesive strength of non-spherical particles mediated by specific interactions. *Biomaterials*, **27**, 5307–14.

26 Decuzzi, P., Gentile, F., Granaldi, A., Curcio, A., Causa, F., Indolfi, C. *et al.* (2007) Flow chamber analysis of size effects in the adhesion of spherical particles. *International Journal of Nanomedicine*, **2**, 689–96.

27 Qin, L.H. and Zhang, Y.D. (1994) Ellipsometric studies of porous silicon. *Applied Physics A: Solids and Surfaces*, **58**, 163–5.

28 Herino, R., Bomchil, G., Barla, K. and Bertand, C. (1987) Porosity and pore size distributions of porous silicon layers. *Journal of the Electrochemical Society*, **134**, 1994–2000.

29 Arwin, H. (2001) Is ellipsometry suitable for sensor applications. *Sensors and Actuators A. Physical*, **92**, 43–51.

30 Pickering, C., Beale, M.I.J., Robbins, D.J., Pearson, P.J. and Greef, R. (1984) Optical studies of the structure of porous silicon films formed in p-type degenerate and non-degenerate silicon. *Journal of Physics C: Solid State Physics*, **17**, 6535–52.

31 Granqvist, C.G. and Hunderi, O. (1978) Conductivity of inhomogeneous materials: effective-medium theory with dipole-dipole interaction. *Physical Review B*, **18**, 1554–61.

32 Buttard, D., Bellet, D., Dolino, G. and Baumbach, T. (1998) Thin layers and multilayers of porous silicon: X-ray diffraction investigation. *Journal of Applied Physiology*, **83**, 5814–22.

33 Cavalleri, A., Siders, C.W., Brown, F. L.H., Leitner, D.M., Toth, C. *et al.* (2000) Anharmonic lattice in geranium measured with ultrafast X-Ray diffraction. *Physical Review Letters*, **85**, 586–9.

34 You, S.Z., Long, Y.F., Xu, S., Zhu, Z.Q., Shi, Y.L. *et al.* (2003) Fabrication and characterization of thick porous silicon layers for rf circuits. *Sensors and Actuators A. Physical*, **108**, 117–20.

35 Authier, A. (2004) *Dynamical Theory of X-Ray Diffraction*, Oxford University Press, USA.

36 Brunauer, S., Emmett, P.H. and Teller, E. (1938) Adsorption of gases in multimolecular layers. *Journal of the Electrochemical Society*, **60**, 309–19.

37 Barrett, E.P., Joyner, L.G. and Halenda, P.P. (1951) The determination of pore volume and area distributions in porous substances. I. Computations from nitrogen isotherms. *Journal of the American Chemical Society*, **73**, 373–80.

38 Wang, D., Wei, F. and Wang, J. (2006) Method and apparatus to measure gas amounts adsorbed on a powder sample, United States Patent no. 6981426.

39 Keller, J.U. and Robens, E. (2003) A note on sorption measuring instruments. *Journal of Thermal Analysis and Calorimetry*, **71**, 37–45.

40 Sing, K. (2001) The use of nitrogen absorption for the characterisation of porous materials. *Colloids and Surfaces*, **187**, 3–9.

41 Miyata, T., Endo, A., Ohmori, T., Akiya, T. and Nkaiwa, M. (2003) Evaluation of pore size distribution in boundary region of micropore and mesopore using gas adsorption method. *Journal of Colloid and Interface Science*, **262**, 116–25.

42 Shull, C.G. (1948) The determination of pore size distribution from gas adsorption data. *Journal of the American Chemical Society*, **70**, 1405–10.

43 Raoof, A., Guilbaud, J.P., Damme, H.V., Porion, P. and Levitz, P. (1998) Analysis of the multilayer thickness relationship for the water vapor and nitrogen adsorption. *Journal of Colloid and Interface Science*, **206**, 1–9.

44 Vorberg, J. and Herminghaus, S. (2001) Adsorption isotherms of hydrogen: the role of thermal fluctuations. *Physical Review Letters*, **87**, 1–4.

45 Shokuie, K., Paulus, M., Sternemann, C., Fendt, R. and Tolan, M. (2007) Adsorption of thin isobutene films on silicon investigated by X-ray reflectivity measurements. *Thin Solid Films*, **505**, 5660–3.

46 Dian, L., Macek, A., Niznansky, D., Nemec, I., Vrkoslav, T. *et al.* (2004) SEM and HRTEM study of porous silicon-relationship between fabrication, morphology, and optical properties. *Applied Surface Science*, **238**, 169–74.

47 Dimov, V.I. and Vitanov, P.K. (2005) Formation of porous silicon: electron microscope investigation. *Journal of Applied Physiology*, **98**, 1–9.

48 Starkov, V.V., Red'kin, A.N. and Dubonos, S.V. (2006) Carbon nanofibers in a gradient-porous silicon structure. *Technical Physics Letters*, **32**, 82–3.

49 Ichinokawa, T., Iiyama, M., Onoguchi, A. and Kobayashi, T. (1974) Charging effect of specimen in scanning electron microscopy. *Japanese Journal of Applied Physiology*, **13**, 1272–7.

50 O'Keefe, M.A., Allard, L.F. and Blom, A. (2005) HRTEM imaging of atoms as sub-Ångström resolution. *Journal of Electron Microscopy*, **54**, 169–80.

51 Watanabe, K., Yamazaki, T., Kikuchi, Y., Kotaka, Y., Kawasaki, M. *et al.* (2001) Atomic-resolution incoherent high-angle annular dark field STEM images of Si(011). *Physical Review B*, **63**, 1–5.

52 Salonen, J., Laitinen, L., Kaukonen, A.M., Tuura, J., Björkqvist, M. *et al.* (2005) Mesoporous silicon microparticles for oral drug delivery: loading and release of five model drugs. *Journal of Controlled Release*, **108**, 362–74.

53 Lasic, D.D., Martin, F.J., Gabizon, A., Huang, S.K. and Paphadjopoulos, D. (1991) Sterically stabilized liposomes: a hypothesis on the molecular origin of the extended circulation times. *Biochimica et Biophysica Acta*, **1070**, 187–92.

54 Corot, C., Robert, P., Idée, J.M. and Port, M. (2006) Recent advances in iron oxide nanocrystal technology for medical imaging. *Advanced Drug Delivery Reviews*, **58**, 1471–504.

55 Dorvee, J.R., Sailor, M.J. and Miskelly, G.M. (2008) Digital microfluidics and delivery of molecular payloads with magnetic porous silicon chaperones. *Dalton Transactions*, **6**, 721–30.

56 Klie, R.F. and Zhu, Y. (2005) Atomic resolution STEM analysis of defects and interfaces in ceramic materials. *Micron*, **36**, 219–31.

57 Williams, P., Levy-Clement, C., Albu-Yaron, A., Brun, N. and Colliex, C. (2000) Near-field electron energy loss spectroscopy in porous silicon. *Journal of Porous Materials*, **7**, 159–63.

58 Egerton, R.F. (1996) *Electron Energy-Loss Spectroscopy, in The Electron Microscope*, 2nd edn, Plenum Press, New York., pp. 1–9 and 131–244.

59 Reed, S.J.B. (1997) *Electron Microprobe Analysis*, 2nd edn, Cambridge University Press, Cambridge, UK.

60 Pap, A.E., Kordás, K., Peura, R. and Leppävuori, S. (2002) Simultaneous chemical silver and palladium deposition on porous silicon; FESEM, TEM, EDX, and XRD investigation. *Applied Surface Science*, **201**, 56–60.

61 Goldstein, J., Newbury, D., Joy, D., Lyman, C. and Echlin, P. (2003) *Scanning Electron Microscopy and X-Ray Microanalysis*, 3rd edn, Springer Science + Business Media, Inc., New York, NY.

62 Lee, M.R., Bland, P.A. and Graham, G. (2003) Preparation of TEM samples by focused ion beam (FIB) techniques: applications to the study of clays and phyllosilicates in meteorites. *Mineralogical Magazine*, **63**, 581–92.

63 Perdu, P., Desplats, R. and Beaudoin, F. (2000) A review of sample backside preparation techniques for VLSI. *Microelectronics Reliability*, **40**, 1431–6.

64 Pease, D.C. and Porter, K.R. (1981) Electron microscopy and ultramicrotomy. *Journal of Cell Biology*, **91**, 287s–92s.

65 Gelber, D. (1957) Thin sectioning: details of techniques. *Journal of Biophysical and Biochemical Cytology*, **3**, 311–16.

66 Bozzola, J.J. and Russell, L.D. (1999) *Electron Microscopy: Principles and Techniques for Biologists*, 2nd edn, Jones and Bartlett Publishers, Inc., Sudbury, MA.

67 Kao, Y.J. and Lichtenberger, L.M. (1990) A method to preserve extracellular surfactant-like phospholipids on the luminal surface of rodent gastric mucosa. *Journal of Histochemistry and Cytochemistry*, **38**, 427–31.

68 Anderson, H.C., Elliott, H., Wallis, D.J., Canham, L.T. and Powell, J.J. (2003) Dissolution of different forms of partially porous silicon wafers under simulated physiological conditions. *Physica Status Solidi (A)*, **203**(197), 331–5.

69 Gao, X. and Nie, S. (2003) Doping mesoporous materials with multicolor quantum dots. *Journal of Physical Chemistry*, **107**, 11575–8.

70 Al-Amoudi, A., Chang, J.-J., Leforestier, A., McKowall, A., Salamin, L.M. *et al.* (2003) New EMBO member's review: cryo-electron microscopy of vitreous sections. *EMBO Journal*, **23**, 3583–8.

71 Bernardin, J.D. and Mudawar, I. (2002) A cavity activation and bubble growth model of the leidenfrost point. *Journal of Heat Transfer: Transaction of the ASME*, **124**, 864–74.

72 Almgren, M. (2003) Alexander Lecture 2003: cubosomes, vesicles, and perforated bilayers in aqueous systems of lipids, polymers, and surfactants. *Australian Journal of Chemistry*, **56**, 959–70.

73 Masterson, W.L. and Slowinski, E.J. (1977) *Chemical Principles*, Saunders, Philadelphia, PA.

74 Canham, L.T. (1996) Bioactive polycrystalline silicon. *Advanced Materials*, **8**, 850–2.

75 Schwarz, K. (1973) A bound form of silicon in glycosaminoglycans and polyuronides. *Proceedings of the National*

Academy of Sciences of the United States of America, **70**, 1608–12.
76 Fregert, S. (1959) Studies on silicon in tissues with special reference to skin. *Acta Dermato-Venereologica. Supplementum*, **39**, 1–92.
77 Canham, L. (2000) Porous silicon as a therapeutic biomaterial. *1st Annual International IEEE-EMBS Special Topic Conference on Microtechnologies in Medicine and Biology*, pp. 109–12.
78 Canham, L.T., Reeves, C.L., Newey, J.P., Houlton, M.R., Cox, T.I. *et al.* (1999) Derivatized mesoporous silicon with dramatically improved stability in simulated human blood plasma. *Advanced Materials*, **11**, 1505–7.
79 Godin, B., Gu, J., Serda, R.E., Ferrati, S. and Liu, X. (2008) Multistage mesoporous silicon-based nanocarriers: biocompatibility and controlled degradation in physiological fluids. *35th Annual Meeting & Exposition of the Controlled Release Society 575, 2008, New York City, NY*.
80 Allen, T.M., Brandeis, E., Hansen, C.B., Kao, G.Y. and Zalipsky, S. (1995) A new strategy for attachment of antibodies to sterically stabilized liposomes resulting in efficient targeting to cancer cells. *Biochimica et Biophysica Acta*, **1237**, 99–108.
81 Romberg, B., Hennink, W.E. and Storm, G. (2008) Sheddable coatings for long-circulating nanoparticles. *Pharmaceutical Research*, **25**, 55–71.
82 De, M.A. and Fais, S. (2005) Tumor acidity, chemoresistance and proton pump inhibitors. *Future Oncology (London, England)*, **1**, 779–86.
83 Ahmad, M., Bergstrom, R.G., Cashen, M.J., Chiang, Y., Kresge, A.J. *et al.* (1979) Ortho ester hydrolysis: direct evidence for a three-stage reaction mechanism. *Journal of the American Chemical Society*, **101**, 2669–77.
84 Jugdaohsingh, R., Anderson, S.H., Tucker, K.L., Elliott, H., Kiel, D.P. *et al.* (2002) Dietary silicon intake and absorption. *The American Journal of Clinical Nutrition*, **75**, 887–93.
85 Sripanyakorn, S., Jugdaohsingh, R., Elliott, H., Walker, C., Mehta, P. *et al.* (2004) The silicon content of beer and its bioavailability in healthy volunteers. *British Journal of Nutrition*, **91**, 403–9.
86 Smith, J.C. and Schwarz, K. (1967) A controlled environment system for new trace element deficiencies. *Journal of Nutrition*, **93**, 182–8.
87 Bisse, E., Epting, T., Beil, A., Lindinger, G., Lang, H. and Wieland, H. (2005) Reference values for serum silicon in adults. *Analytical Biochemistry*, **337**, 130–5.
88 Sapelkin, A.V., Bayliss, S.C., Unal, B. and Charalambou, A. (2006) Interaction of B50 rat hippocampal cells with stain-etched porous silicon. *Biomaterials*, **27**, 842–6.
89 Khung, Y.L., Barritt, G. and Voelcker, N.H. (2008) Using continuous porous silicon gradients to study the influence of surface topography on the behaviour of neuroblastoma cells. *Experimental Cell Research*, **314**, 789–800.
90 Bayliss, S.C., Heald, R., Fletcher, K.I. and Buckberry, L.D. (1999) The culture of mammalian cells on nanostructured silicon. *Advanced Materials*, **11**, 318–21.
91 Chin, V., Collins, B.E., Sailor, M.J. and Bhatia, S.N. (2001) Compatibility of primary hepatocytes with oxidized nanoporous silicon. *Advanced Materials*, **13**, 1877–80.
92 Anderson, S.H.C., Elliott, H., Reeves, C.R., Powell, J.J. and Canham, L.T. (2003) Dissolution of different forms of partially porous silicon wafers under simulated physiological conditions. *Physica Status Solidi (A)*, **197**, 331–5.
93 Soon-Whatt Goh, A., Yaw-Fui, C.A., Houa-Gong, L.R., Te-Neng, L. and Wing-Kwong, Y.S. (2007) A novel approach to brachytherapy in hepatocellular carcinoma using a phosphorus^{32} (^{32}P) brachytherapy delivery device : a first-in-man study. *International Journal of Radiation Oncology*Biology*Physics*, **67**, 786–92.
94 Munoz, B., Ramila, A., Perez-Pariente, J.P., Diaz, I. and Vallet-Regi, M. (2003) MCM-41 organic modification as drug delivery rate regulator. *Chemistry of Materials*, **15**, 500–3.
95 Doadrio, A.L., Sousa, E.M., Doadrio, J.C., Perez, P.J., Izquierdo-Barba, I. and Vallet-Regi, M. (2004) Mesoporous SBA-15

HPLC evaluation for controlled gentamicin drug delivery. *Journal of Controlled Release*, **97**, 125–32.

96 Song, S.W., Hidajat, K. and Kawi, S. (2005) Functionalized SBA-15 materials as carriers for controlled drug delivery: influence of surface properties on matrix-drug interactions. *Langmuir*, **21**, 9568–75.

97 Charnay, C., Begu, S., Tourne-Peteilh, C., Nicole, L., Lerner, D.A. *et al.* (2004) Inclusion of ibuprofen in mesoporous templated silica: drug loading and release property. *European Journal of Pharmaceutics and Biopharmaceutics*, **57**, 533–40.

98 Batra, I., Coffer, J.L. and Canham, L.T. (2006) Electronically-responsive delivery from a calcified mesoporous silicon structure. *Biomedical Microdevices*, **8**, 93–7.

99 Foraker, A.B., Walczak, R.J., Cohen, M.H., Boiarski, T.A., Grove *et al.* (2003) Microfabricated porous silicon particles enhance paracellular delivery of insulin across intestinal Caco-2 cell monolayers. *Pharmaceutical Research*, **20**, 110–16.

100 Prestidge, C.A., Barnes, T.J., Mierczynska-Vasilev, A., Skinner, W., Peddie, F. *et al.* (2007) Loading and release of a model protein from porous silicon powders. *Physica Status Solidi (A)*, **204**, 3361–6.

101 Lin, V.S., Motesharei, K., Dancil, K.P., Sailor, M.J. and Ghadiri, M.R. (1997) A porous silicon-based optical interferometric biosensor. *Science*, **278**, 840–3.

102 Dancil, K.-P.S., Greiner, D.P. and Sailor, M.J. (1999) A porous silicon optical biosensor: detection of reversible binding of IgG to a protein A-modified surface. *Journal of the American Chemical Society*, **121**, 7925–30.

103 Chan, S., Horner, S.R., Fauchet, P.M. and Miller, B.L. (2001) Identification of Gram negative bacteria using nanoscale silicon microcavities. *Journal of the American Chemical Society*, **123**, 11797–8.

104 Gao, J., Gao, T. and Sailor, M.J. (2000) A porous silicon vapor sensor based on laser interferometry. *Applied Physics Letters*, **77**, 901–3.

105 Gao, T., Gao, J. and Sailor, M.J. (2002) Tuning the response and stability of thin film mesoporous silicon vapor sensors by surface modification. *Langmuir*, **18**, 9953–7.

106 Allcock, P. and Snow, P.A. (2001) Time-resolved sensing of organic vapors in low modulating porous silicon dielectric mirrors. *Journal of Applied Physics*, **90**, 5052–7.

107 Anglin, E.J., Schwartz, M.P., Ng, V.P., Perelman, L.A. and Sailor, M.J. (2004) Engineering the chemistry and nanostructure of porous silicon Fabry-Perot films for loading and release of a steroid. *Langmuir*, **20**, 11264–9.

108 Prestidge, C.A., Barnes, T.J., Mierczynska-Vasilev, A., Skinner, W. and Peddie, F. (2007) Loading and release of a model protein from porous silicon powders. *Physica Status Solidi*, **204**, 3361–6.

109 Choi, Y. and Baker, J.R., Jr (2005) Targeting cancer cells with DNA-assembled dendrimers: a mix and match strategy for cancer. *Cell Cycle*, **4**, 669–71.

110 Brigger, I., Dubernet, C. and Couvreur, P. (2002) Nanoparticles in cancer therapy and diagnosis. *Advanced Drug Delivery Reviews*, **54**, 631–51.

111 Braeckmans, K., De Smedt, S.C., Leblans, M., Pauwels, R. and Demeester, J. (2002) Encoding microcarriers: present and future technologies. *Nature Reviews. Drug Discovery*, **1**, 447–56.

112 St'astny, M., Plocova, D., Etrych, T., Kovar, M., Ulbrich, K. and Rihova, B. (2002) HPMA-hydrogels containing cytostatic drugs. Kinetics of the drug release and in vivo efficacy. *Journal of Controlled Release*, **81**, 101–11.

113 Begu, S., Durand, R., Lerner, D.A., Charnay, C., Tourne-Peteilh, C. *et al.* (2003) Preparation and characterization of siliceous material using liposomes as template. *Chemical Communications*, **5**, 640–1.

114 Begu, S., Girod, S., Lerner, D.A., Jardiller, N., Tourne-Peteilh, C. *et al.* (2004) Characterization of a phospholipid bilayer entrapped into non-porous silica nanospheres. *Journal of Materials Chemistry*, **14**, 1316–20.

115 Tourne-Peteilh, C., Lerner, D.A., Charnay, C., Nicole, L., Begu, S. and Devoisselle, J.M. (2003) The potential of ordered mesoporous silica for the storage of drugs: the example of a pentapeptide encapsulated in a MSU-tween 80. *Chemphyschem*, **4**, 281–6.

116 Li, Y.Y., Cunin, F., Link, J.R., Gao, T., Betts, R.E., Reiver, S.H. *et al.* (2003) Polymer replicas of photonic porous silicon for sensing and drug delivery applications. *Science*, **299**, 2045–7.

117 Gabizon, A., Chisin, R., Amselem, S., Druckmann, S., Cohen, R., Goren, D. *et al.* (1991) Pharmacokinetic and imaging studies in patients receiving a formulation of liposome-associated adriamycin. *British Journal of Cancer*, **64**, 1125–32.

118 Harris, J.M. and Chess, R.B. (2003) Effect of pegylation on pharmaceuticals. *Nature Reviews. Drug Discovery*, **2**, 214–21.

119 Brannon-Peppas, L. and Blanchette, J.O. (2004) Nanoparticle and targeted systems for cancer therapy. *Advanced Drug Delivery Reviews*, **56**, 1649–59.

120 Torchilin, V.P. (2007) Targeted pharmaceutical nanocarriers for cancer therapy and imaging. *The AAPS Journal*, **9**, E128–47.

121 Saul, J.M., Annapragada, A.V. and Bellamkonda, R.V. (2006) A dual-ligand approach for enhancing targeting selectivity of therapeutic nanocarriers. *Journal of Controlled Release*, **114**, 277–87.

122 Yang, X., Wang, H., Beasley, D.W., Volk, D.E., Zhao, X., Luxon, B.A. *et al.* (2006) Selection of thioaptamers for diagnostics and therapeutics. *Annals of the New York Academy of Sciences*, **1082**, 116–9.

123 Souza, G.R., Christianson, D.R., Staquicini, F.I., Ozawa, M.G., Snyder, E.Y. *et al.* (2006) Networks of gold nanoparticles and bacteriophage as biological sensors and cell-targeting agents. *Proceedings of the National Academy of Sciences of the United States of America*, **103**, 1215–20.

124 Salonen, J., Kaukonen, A.M., Hirvonen, J. and Lehto, V.P. (2008) Mesoporous silicon in drug delivery applications. *Journal of Pharmaceutical Sciences*, **97**, 632–53.

125 Rijcken, C.J., Soga, O., Hennink, W.E. and van Nostrum, C.F. (2007) Triggered destabilization of polymeric micelles and vesicles by changing polymers polarity: an attractive tool for drug delivery. *Journal of Controlled Release*, **120**, 131–48.

126 Tannock, I.F. and Rotin, D. (1989) Acid pH in tumors and its potential for therapeutic exploitation. *Cancer Research*, **49**, 4373–84.

127 Riehemann, K., Fuchs, H., Schneider, S.W., Luger, T., Godin, B. and Ferrari, M. (2008) Nanotechnology–challenge and opportunity in clinical applications. *Angewandte Chemie–International Edition* (in press).

128 Sarkar, N., Banerjee, J., Hanson, A.J., Elegbede, A.I., Rosendahl, T. *et al.* (2008) Matrix metalloproteinase-assisted triggered release of liposomal contents. *Bioconjugate Chemistry*, **19**, 57–64.

129 Ferrari, M. (2005) Cancer nanotechnology: opportunities and challenges. *Nature Reviews Cancer*, **5**, 161–71.

130 Macarthur, M., Hold, G.L. and El-Omar, E.M. (2004) Inflammation and cancer II. Role of chronic inflammation and cytokine gene polymorphisms in the pathogenesis of gastrointestinal malignancy. *American Journal of Physiology. Gastrointestinal and Liver Physiology*, **286**, G515–G520.

131 Palapattu, G.S., Sutcliffe, S., Bastian, P.J., Platz, E.A., De Marzo, A.M. *et al.* (2005) Prostate carcinogenesis and inflammation: emerging insights. *Carcinogenesis*, **26**, 1170–81.

132 Kuper, H., Adami, H.O. and Trichopoulos, D. (2000) Infections as a major preventable cause of human cancer. *Journal of Internal Medicine*, **248**, 171–83.

133 DeNardo, D.G. and Coussens, L.M. (2007) Inflammation and breast cancer. Balancing immune response: crosstalk between adaptive and innate immune cells during breast cancer progression. *Breast Cancer Research*, **9**, 212.

134 Wernicke, M. (1975) Quantitative morphologic assessment of immunoreactivity in regional lymph

nodes of patients with carcinoma of the breast. *Surgery, Gynecology & Obstetrics*, **140**, 919–24.

135 Morton, B.A., Ramey, W.G., Paderon, H. and Miller, R.E. (1986) Monoclonal antibody-defined phenotypes of regional lymph node and peripheral blood lymphocyte subpopulations in early breast cancer. *Cancer Research*, **46**, 2121–6.

136 Gupta, R.A. and DuBois, R.N. (2001) Colorectal cancer prevention and treatment by inhibition of cyclooxygenase-2. *Nature Reviews Cancer*, **1**, 11–21.

137 Gupta, R.A. and DuBois, R.N. (2002) Cyclooxygenase-2 inhibitor therapy for the prevention of esophageal adenocarcinoma in Barrett's esophagus. *Journal of the National Cancer Institute*, **94**, 406–7.

138 Lin, E.Y. and Pollard, J.W. (2004) Macrophages: modulators of breast cancer progression. *Novartis Foundation Symposium*, **256**, 158–68.

139 Yuan, A., Chen, J.J. and Yang, P.C. (2008) Pathophysiology of tumor-associated macrophages. *Advances in Clinical Chemistry*, **45**, 199–223.

140 Cotran, R.S. and Pober, J.S. (1999) Cytokine-endothelial interactions in inflammation, immunity, and vascular injury. *Journal of the American Society of Nephrology*, **1**, 225–35.

141 Hammer, D.A. and Apte, S.M. (1992) Simulation of cell rolling and adhesion on surfaces in shear flow: general results and analysis of selectin-mediated neutrophil adhesion. *Biophysical Journal*, **63**, 35–57.

142 von Andrian, U.H., Hasslen, S.R., Nelson, R.D., Erlandsen, S.L. and Butcher, E.C. (1995) A central role for microvillous receptor presentation in leukocyte adhesion under flow. *Cell*, **82**, 989–99.

143 Oh, P., Li, Y., Yu, J., Durr, E., Krasinska, K.M. *et al.* (2004) Subtractive proteomic mapping of the endothelial surface in lung and solid tumours for tissue-specific therapy. *Nature*, **429**, 629–35.

144 Chung, T.H., Wu, S.H., Yao, M., Lu, C.W., Lin, Y.S. *et al.* (2007) The effect of surface charge on the uptake and biological function of mesoporous silica nanoparticles in 3T3-L1 cells and human mesenchymal stem cells. *Biomaterials*, **28**, 2959–66.

145 Falcone, S., Cocucci, E., Podini, P., Kirchhausen, T., Clementi, E. *et al.* (2006) Macropinocytosis: regulated coordination of endocytic and exocytic membrane traffic events. *Journal of Cell Science*, **119**, 4758–69.

146 Hartig, S.M., Greene, R.R., Carlesso, G., Higginbotham, J.N., Khan, W.N. *et al.* (2007) Kinetic analysis of nanoparticulate polyelectrolyte complex interactions with endothelial cells. *Biomaterials*, **28**, 3843–55.

147 Loubery, S., Wilhelm, C., Hurbain, I., Neveu, S., Louvard, D. *et al.* (2008) Different microtubule motors move early and late endocytic compartments. *Traffic*, **9**, 492–509.

148 Slowing, I.I., Trewyn, B.G. and Lin, V.S. (2007) Mesoporous silica nanoparticles for intracellular delivery of membrane-impermeable proteins. *Journal of the American Chemical Society*, **129**, 8845–9.

149 Vallhov, H., Gabrielsson, S., Stromme, M., Scheynius, A. and Garcia-Bennett, A.E. (2007) Mesoporous silica particles induce size dependent effects on human dendritic cells. *Nano Letters*, **7**, 3576–82.

150 Campbell, R.B., Fukumura, D., Brown, E.B., Mazzola, L.M., Izumi, Y. *et al.* (2002) Cationic charge determines the distribution of liposomes between the vascular and extravascular compartments of tumors. *Cancer Research*, **62**, 6831–6.

151 Borchard, G. and Kreuter, J. (1996) The role of serum complement on the organ distribution of intravenously administered poly(methyl methacrylate) nanoparticles: effects of pre-coating with plasma and with serum complement. *Pharmaceutical Research*, **13**, 1055–8.

152 Leroux, J.C., Gravel, P., Balant, L., Volet, B., Anner, B.M. *et al.* (1994) Internalization of poly(D,L-lactic acid) nanoparticles by isolated human leukocytes and analysis of plasma

proteins adsorbed onto the particles. *Journal of Biomedical Materials Research*, **28**, 471–81.

153 Wu, S.H., Lin, Y.S., Hung, Y., Chou, Y.H., Hsu, Y.H. *et al.* (2008) Multifunctional mesoporous silica nanoparticles for intracellular labeling and animal magnetic resonance imaging studies. *Chembiochem*, **9**, 53–7.

154 Sanhai, W., Sakamoto, J., Canady, R. and Ferrari, M. (2008) Seven challenges for nanomedicine. *Nature Nanotech*, **3**, 242–4.

Keywords

silicon; porous; microparticles; nanoparticles; drug; delivery

12
Spherical and Anisotropic Hydroxyapatite Nanocrystals

Susmita Bose, Weichang Xue, Ashis Banerjee and Amit Bandyopadhyay

12.1
Introduction

Musculoskeletal disorders and bone deficiencies have been established as among the most important human health conditions that exist today, costing more than $16 billion for biomedical implants in 2006 in the US, and afflicting one out of seven Americans. According to US Census Bureau projections, the proportion of people aged over 55 years will rise by more than 37% during the next 10 years. Hence, as musculoskeletal disorders are prevalent in the older population, it is expected that the number of individuals with a bone deficiency will increase even more over the coming years, as the average age of the population continues to rise. Yet, in spite of the enormous magnitude of this problem, there remains a need for materials that can be implanted into individuals to restore their lost structure and function. The human skeletal system not only supports and protects the body but also provides sites for muscle attachments and the production of blood cells. On average, the skeleton of an adult human is composed of an average of 206 bones, although this number decreases with age as some bones become fused together. Unlike adults, the skeleton of an embryo comprises about 350 completely cartilaginous bones – over 140 more than an adult. As children grow, many of the bones fuse together during the development of the circulatory and nervous systems, and reach full maturity at the age of about 25 years.

12.1.1
Bone Structure

Bone has a complex hierarchical structure, which is still not very well understood. The basic building blocks are the extremely small plate-shaped crystals of carbonate apatite, just tens of nanometers in length and width, with some being only 2–3 nm thick. The crystals are arranged in parallel layers within the collagenous

Nanomaterials for the Life Sciences Vol. 2: Nanostructured Oxides. Edited by Challa S. S. R. Kumar

ISBN: 978-3-527-32152-0

framework. At the next hierarchical level, these mineral-filled collagen fibrils are ordered into arrays in which the fibril axes and crystal layers are all organized into a three-dimensional (3-D) structure that makes up a single layer or lamella of bone, which is a few microns thick [1]. The organic matter in bone is collagen, which is bonded to form linear chains that are arranged in fibers giving rise to various macroscopic structures. In between the collagen molecules there are small interstitial empty compartments, regularly spaced, where the apatite nanocrystals are deposited. The biomineralization process involves more than 200 different acid proteins, which act as inhibitors, nucleators or templates for the epitaxial growth of nanocrystals, anchored to the collagen [2].

The inorganic phase, hydroxyapatite (HA), which accounts for 69% of the weight of the bone, is comprised primarily of very small mineralites. The size and shape of these mineralites play fundamental roles in maintaining ionic homeostasis and in the biomechanical function of bone. The results of previous studies have shown that mature bovine cortical bone mineralites are predominantly plate-like in shape, having a high length-to-thickness ratio [3, 4]. The reported sizes of bone crystals vary, with values ranging from lengths of 30 to 50 nm, widths of 15 to 30 nm, and thicknesses of 2 to 10 nm. Recent atomic force microscopy (AFM) studies have shown that bone crystals are longer than those observed by transmission electron microscopy (TEM), with a mean length-to-thickness ratio of 20 : 3 [5]. These mineralites appear to be one unit cell thick, to grow preferentially along one axis, and have mean dimensions of $12 \times 10 \times 0.61$ nm. Approximately 2% of the mineralites have orders of magnitude larger thickness values and the thick plates have a mean length-to-thickness ratio around 2.7 : 1.

Not only are bone crystallites extremely small, they are often described as poorly crystalline because of the broad X-ray diffraction (XRD) peaks (relative to synthetic HA). Bone mineral is a calcium-deficient apatite, with a Ca : P ratio less than 1.67, which is the theoretical value for pure HA, $Ca_{10}(PO_4)_6(OH)_2$ [6, 7]. Bone mineral is also incorporated with some impurities, such as carbonate, sodium and magnesium ions (4–6% carbonate; 0.9% Na; 0.5% Mg) [7, 8]. The carbonated form of apatite has the mineral name of Dahllite, which is sometimes used in the bone literature [9], although more commonly biological apatite is referred to as HA. A schematic cross-section of bone is shown in Figure 12.1.

Because bone is a living tissue that is continuously undergoing remodeling and repair, the small size, low crystallinity and nonstoichiometry of the crystals presumably bestows the mineral phase with the solubility needed for resorption by osteoclasts, that is, the bone-resorbing cells [10]. For example, bone substitutes made of synthetic HA, although bioactive (stimulatory for bone formation), are rather slow to resorb due to the low solubility of HA under physiological conditions [11]. The teeth exhibit similar characteristics to the bones, except for their external surface coating, the enamel. Dental enamel has a much larger inorganic content than the bone (up to 90%), and is formed by prismatic crystals of larger dimensions that are strongly oriented. CaP crystals in enamel exhibit a higher crystallin-

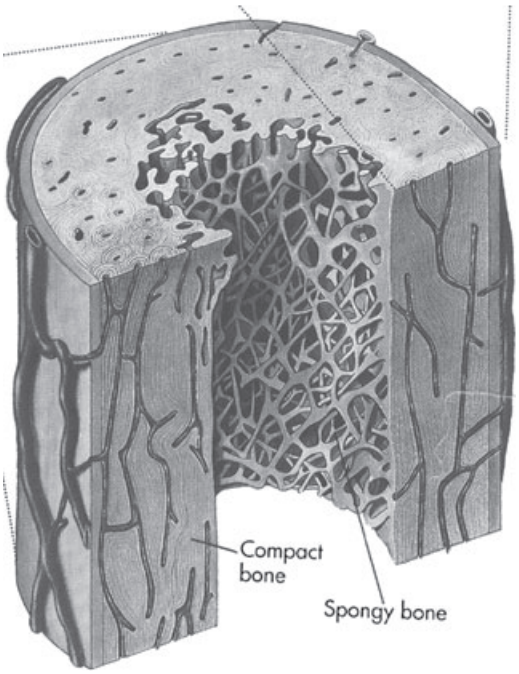

Figure 12.1 Schematic representation of human bone, in cross-section.

ity and have a higher carbonate content compared to bone. Enamel is considered as the toughest material in the biological world [2].

12.1.2
Hydroxyapatite and its Crystal Structure

Calcium phosphates have been investigated and used in clinical applications to repair and reconstruct bone defects for over four decades. The most common form of calcium phosphate in biomedical application is HA [$Ca_{10}(PO_4)_6(OH)_2$], as it has a similar composition to the mineral component of bone. The crystal structure of HA is hexagonal, and is part of the P63/m space group, characterized by a sixfold c-axis perpendicular to three equivalent a-axes at 120° angles to each other. Calcium cations (Ca^{2+}) and phosphate anions (PO_4^{3-}) are arranged around columns of monovalent hydroxyl anions (OH^-) [12, 13]. It is this network of phosphate groups that provides the skeletal framework and gives the HA structure its stability. Considering the HA lattice parameters (a~0:95 nm and c~0:68 nm), and its symmetry (hexagonal, S.G. P63/m), it is most likely that unit cells of HA will be arranged along the c-axis [2]. Such an arrangement causes a preferred orientation along the c-axis during the growth of HA crystals with a needle-like morphology.

12.1.3 Synthetic HA Nanocrystals: Application to Bone Replacement and Drug/Protein Delivery

Due to increases in the average life span and consequent increases in numbers of the aging population, the market for orthopedic implants is growing at a rapid rate. Each year, in the USA, more than 600 000 joint replacements are performed, while the estimated worldwide costs are in excess of US$ 3 billion. One of the key factors towards the design of orthopedic implants relates to tissue regeneration around the biomaterial immediately after implantation. It is known that the implantation of biomaterials into a living organism causes specific reactions in the biological environment. The biomolecules and cells, together with the intrinsic as well as surface properties of the biomaterials, determine the biocompatibility and longevity of the implants. As the biomolecule or cell–material interaction at the surface of the biomaterial is an important phenomenon in the evaluation of the biomaterial, biomaterial scientists continue to investigate the pertinent host–cell interactions in order to design materials that facilitate favorable interactions and enhance tissue regeneration. To date, research results have indicated that all living systems are governed by their molecular behavior at the nanometer scale. The properties of proteins, nucleic acids, lipids and carbohydrates – the molecular building blocks of life – are determined by their size, folding and patterns at the nanoscale. Specifically, cellular organization and corresponding tissue properties are found to depend heavily on the structure of the extracellular matrix (ECM). The ECM is characterized by a complex hierarchical structure with a spatial organization that spans several orders of magnitude, from the nanometer to the centimeter scale. It is for this reason that the cells in our body are predisposed to interact with nanostructured surfaces – and also the reason that structural components with nanoscale features are being considered as promising biomaterials.

Favorable responses in terms of cell adhesion and cell proliferation of different types of cell to HA have been widely reported. It seems that cells cannot distinguish between the bone surface and HA, which indicates the similarity in their surface chemistries. HA is neither osteogenic nor osteoinductive. In the case of osteoinduction, the conversion of soft tissue cells to osseous tissue-formers by an appropriate stimulus (e.g. demineralized bone matrix or bone morphogenic proteins) takes place. Osteogenesis is the formation of mineralized tissue by osteoblasts. Autogenous bone grafting is osteogenetic, but HA is osteoconductive. In the case of living bone replacement, the process is very slow, as the dead bone is first resorbed by osteoclastic activity and then replaced by creeping substitution. However, HA is not resorbed and acts as an osteoconductive agent that is integrated with new osseous tissue. Although it is not yet commercially available as a competitive material with respect to other forms of HA, nano-sized HA is currently being considered for several applications, among which synthetic HA in bone replacement and drug/protein delivery are the two most common.

12.1.3.1 Bone Replacement

Hydroxyapatite is a bioactive ceramic that is commonly used in particulate form in bone repairs, as well as coatings for metallic prostheses to improve their *in vivo* biological response. Due to the chemical similarity between HA and mineralized bone, synthetic HA exhibits a strong affinity to host hard tissues. The formation of chemical bonds with the host tissue offers HA a greater advantage in clinical applications over other bone substitutes such as allografts or xenografts.

Strietzel *et al.* [14] conducted a preliminary two-center clinical prospective study to evaluate the tissue composition of augmented sites with a nanocrystalline HA (ncHA) bone substitution material using clinical and histological examinations. The results obtained indicated that small amounts of ncHA could be found even after 6 months in bone biopsies. The former defect space was filled with newly formed bone, while the alveolar ridge width gain was found to be significant after lateral augmentation utilizing ncHA, providing a quantitatively and qualitatively sufficient site for primary stable implant placement. Du *et al.* [15] studied the tissue response of nano-HA–collagen implants in marrow cavities, and concluded that nanoparticles allowed for a quicker implant surface turnover. The process of implant resorption and bone substitution was similar to bone remodeling. When Muller-Mai *et al.* [16] tested nanoapatite and nanoapatite/organic implants *in vivo*, their results suggested that both materials were suitable for bone replacement, and also for the release of drugs such as antibiotics and growth factors. In addition, the organic component could be used to further control physical properties in the bone implantation bed.

The applications of HA in periodontal and alveolar ridge augmentation are limited due to its particle mobilization and slow resorbable nature. In order to overcome these limitations, HA is widely used in combination with some polymers and other compounds in the form of a composite. Hence, composite preparations with various matrix materials such as chitosan [17], collagen [18–20] and other polymers [21] have been reported that have helped in promoting osteoconduction, thus providing the scaffolding properties required for tissue engineering.

12.1.3.2 Drug Delivery

It is believed that nanoscale HA has the potential to significantly impact the field of drug delivery. When studying the possibility of using calcium-deficient HA (CDHA) nanocrystals for *in vitro* drug delivery, Liu *et al.* [22] incorporated the nanocrystals with bovine serum albumin (BSA) to form BSA-loaded nanocarriers via both *in situ* and *ex situ* processes. For the nanocarrier prepared *ex situ*, the subsequent release profile showed a bursting behavior. However, for the sample synthesized *in situ* a slower release profile, without bursting behavior, was observed. This difference, which was considered due to dissolution of the BSA-incorporated CDHA crystal, was confirmed by high-resolution TEM studies that indicated the different extents of interaction between BSA and CDHA. In another study, Olton *et al.* [23] reported a novel method for the consistent synthesis of efficient, nano-sized, mono-dispersed CaP-pDNA particles. This was accomplished by optimizing

both the stoichiometry (Ca/P ratio) of the CaP particles as well as the mode in which Ca and P precursor solutions were mixed. The results indicated that the precursors, when mixed in a controlled and regulated manner, resulted in nanosized particles that consistently yielded higher transfection efficiencies than particles synthesized by manual mixing. Maximum transfection efficiencies in both HeLa and MC3T3-El cells lines were also obtained when a Ca/P ratio of between 100 and 300 was used. In another study, Ong *et al*. reported the potential of using nanosized HA for the systemic delivery of radioisotopes or drugs. Here, drug-loaded or radiolabeled HA nanoparticles (HNP) could be processed by exploiting the high-affinity (poly)phosphonate–HA interaction. Potentially, numerous clinically available bisphosphonate drugs or phosphonate-labeled radionuclides can be exploited for HA loading, and these loaded HNPs may be useful for the targeted delivery of radiation or drugs to the liver [24]. Further findings for the use of HA in drug delivery are discussed later in the chapter, when we define future trends for the application of HA nanocrystals in bioengineering.

12.2 Synthesis of Hydroxyapatite Nanocrystals

To date, several methods for the preparation of HA crystals have been reported, the most common being:

- wet chemical precipitation
- sol–gel synthesis
- biomimetic synthesis
- hydrothermal synthesis
- mechanochemical powder synthesis
- solid-state reaction
- microwave-assisted synthesis
- emulsion-mediated synthesis.

While some of these methods have the capability to synthesize nanoscale powders, most do not demonstrate any control of the morphology or aspect ratio of nanoparticles during synthesis. In the following sections we describe some of the key research findings regarding the synthesis of HA nanocrystals using different methods, including some of their advantages and disadvantages.

12.2.1 Wet Chemical Precipitation

Wet chemical precipitation is a popular method, used widely for synthesizing nano-HA at low temperature. A precipitation reaction is a common type of chemical reaction in solution chemistry where two or more solutions are combined to produce an insoluble solid product, a precipitate. Typically, these types of reaction involve ionic compounds in aqueous solution. To initiate precipitation, the solu-

tion must be supersaturated, a condition which can be achieved by various methods such as mixing solutions containing reactants, by changing the solubility, or by increasing/decreasing the temperature. Precipitation takes place into two stages: first, nucleation, followed by growth of the nuclei to macroscopic scale. It is not easy to detect the formation of submicron nuclei, and generally both nucleation and growth occur simultaneously in solution. Other processes may also occur during the time when particles age in the mother liquor, notably agglomeration, disruption and Ostwald ripening.

The HA powders synthesized using this method are in homogeneous phase composition, but are poorly crystallized owing to the low temperature of the process. One common wet chemical method used to synthesize HA is based on the following equation, which uses calcium hydroxide and orthophosphoric acid as calcium and phosphorus precursors, respectively:

$$10\,Ca(OH)_2 + 6\,H_3PO_4 \rightarrow Ca_{10}(PO_4)_6(OH)_2 + 18\,H_2O$$

Calcium phosphate precipitation has been described as a fairly complicated process, and is known to depend on several parameters, such as the calcium and phosphate ion concentrations, pH and temperature [25]. Although the thermodynamics and kinetics of HA precipitation have been reported, there is no clear correlation between precipitation conditions, the driving force for precipitation, and the morphology of the HA powders synthesized from these reactions. When Kumar *et al*. analyzed the changes in HA morphology in relation to the reaction temperature, they found that needle-shaped particles with a high aspect ratio were formed at 40 °C, but that spheroidal particles formed when the precipitation temperature was increased to 100 °C [26].

Pang and Bao also synthesized HA using this method, and showed that the crystallinity and crystallite size of HA increased with an increase in synthesis temperature and ripening time [27]. When $CaCl_2$ and $(NH_4)_2HPO_4$ were used as starting materials, the morphology change of HA nanoparticles was seen to be related to their crystallinity. A raised in temperature led to an increased crystallinity of the synthesized HA powder, while the particle morphology changed from an irregular to a regular shape. Those nanoparticles with a lower crystallinity showed a needle-like shape with a rough surface and blurred contour, whereas those with a higher crystallinity had bar-like shape with a smooth surface and clear contour. Both. a lengthening of the ripening time and an increase in calcination temperature led to an increased in the crystallinity of the powder.

Bouyer *et al*. reported the details of a morphological study of an HA nanocrystals suspension prepared using a wet chemical precipitation method at different synthesis temperatures, and with various reactant addition rates [28]. These authors showed that the shape, size and specific surface area of the HA nanoparticles were highly sensitive to the reaction temperature and reactant addition rate. Moreover, the reactant addition rate also determined the purity of the synthesized HA, and had a major influence on the pH-value obtained on completion of the synthesis. The reaction temperature also determined whether the crystals were

monocrystalline or polycrystalline. HA nanoparticles synthesized at low temperature ($T < 60\,^{\circ}C$) were monocrystalline, with a needle shape oriented following the c-axis of the hexagonal HA structure. A transition temperature ($T = 60\,^{\circ}C$) was defined as a limit for obtaining monocrystalline HA nanocrystal, above which the nanocrystals became polycrystalline.

Hydroxyapatite can also be synthesized using calcium nitrate ($Ca(NO_3)_2 \cdot 4H_2O$) and ammonium hydroxide phosphate ($(NH_4)_2HPO_4$) as the calcium and phosphorus precursors, respectively [29]:

$$10\,Ca(NO_3)_2 + 6\,(NH_4)_2HPO_4 \rightarrow Ca_{10}(PO_4)_6(OH)_2 + 6\,H_2O + 20\,NH_4NO_3$$

Using this method, Yubao *et al.* prepared calcium phosphate needle-like crystals at a pH between 10 and 12, at room temperature [30]. The Ca/P ratio of the calcium phosphate precipitate was between 1.5 and 1.67, and demonstrated a poorly crystallized apatite structure at room temperature. However, after sintering at 1100 °C a biphasic HA–tricalcium phosphate (TCP) structure evolved. Morphologically, these crystals were rod-shaped.

Gomez-Morales *et al.* [31] have reported a continuous synthetic process using highly concentrated $CaCl_2$ and K_2HPO_4 in a mixed suspension, mixed product removal (MSMPR) reactor at 85 °C in N_2 atmosphere, with the ultimate particle size being in the nanometer size range. Torrent-Burgues and Rodriguez-Clemente [32] reported HA preparation by using same starting materials, thus producing synthesized particles in the size range of 60 to 200 nm at 85 °C and pH 8–9.

Ahn *et al.* [33] have investigated the effect of synthesis parameters on the crystallite size, morphology and chemical stability of HA, using $Ca(NO_3)_2$ and $(NH_4)_2HPO_4$ as starting materials. Here, an increase in pH caused a preferred growth along the <002> axis of HA (as observed using X-ray diffraction), such that the final product demonstrated an increasingly rod-like morphology and a larger particle size. A longer aging time led to the removal of occluded impurities, a recrystallization into a more ordered form, and a uniform morphology. Those samples synthesized with an insufficient aging time underwent severe decomposition during sintering, which suggested that the precipitate was thermally unstable due to its poor compositional uniformity. The temperature had a significant effect on the powder composition and particle shape, with an increase in temperature changing the particle shape from spherical to whisker. When Liu *et al.* [34] studied the kinetics of HA precipitation at pH 10–11 using $Ca(NO_3)_2$ and $(NH_4)_2HPO_4$ as starting materials, the reaction was reported to undergo the following phase-transition sequence:

> Octacalcium phosphate (OCP) → amorphous calcium phosphate (ACP) → calcium-deficient hydroxyapatite (DCP or CDHA) → hydroxyapatite.

The increase in temperature led to increases in both HA formation and particle size.

Lazic *et al.* [35] investigated the effect of temperature on the stoichiometry, morphology and crystallinity of HA prepared from calcium hydroxide and phosphoric acid. It was shown that the crystal ordering was increased as the synthesis temperature increased, while near-theoretical values for lattice parameters were obtained for samples precipitated at 95 °C. The size of the crystal increased with temperature, when the particle size was in the nanometer range.

12.2.2 Sol–Gel Process

The sol–gel approach has attracted much attention for HA synthesis because of its well-known inherent advantages for the generation of glass, glass-ceramic and ceramic powders with excellent chemical homogeneity. These advantages include a homogeneous molecular level mixing of calcium and phosphorous precursors, a low synthesis temperature, and a high product purity when compared to other conventional methods. The sol–gel technique is also capable of generating nano-sized particles and thin films. In fact, whereas temperatures >1000 °C are usually required to sinter the fine apatite crystals prepared from wet precipitation, temperatures several hundred degrees lower are required to densify sol–gel HA. Furthermore, the high reactivity of the sol–gel powders results in a reduction of the calcining and sintering temperatures. Sol–gel-derived HA, due to poor crystallinity and the presence of carbonate ions in the crystal lattice, has shown better bioactivity compared to others [36]. However, reports on sol–gel-derived HA have also indicated that the synthesis of HA is always accompanied by a secondary phase of calcium oxide (CaO) [37, 38]. As CaO reduces the biocompatibility of HA, attempts to overcome this problem represent a major theme of current research in this area.

In the past, many variations of the sol–gel process have been developed and used to produce powders with different Ca/P ratios, by altering not only the quantity and composition of precursors but also the processing variables. As the synthesis of HA requires a calcium to phosphorus molar ratio of 1.67 : 1 in the final product, a number of calcium/phosphorus precursor combinations have been used in the preparation of HA powders. For example, calcium nitrate or different calcium alkoxides and 2-ethyl-hexyl phosphate, triethyl phosphate or orthophosphoric acid, have been used as the calcium and phosphorus precursors, respectively. The major limitation for application of the sol–gel process was shown to be the very poor solubility of the calcium alkoxides in organic solvents, and the poor reactivity of the phosphorous compounds. The effective control of stoichiometry due to the volatility of the phosphorous compounds used also represented a challenge.

Both, Gross *et al.* and Masuda *et al.* used calcium diethoxide ($Ca(OEt)_2$) and triethyl phosphate ($PO(OEt)_3$) to form phase-pure HA at temperatures in excess of 600 °C [39, 40]. These groups showed that an aging time >24 h was critical for the solution system to stabilize, in order that a monophasic HA could be produced. Otherwise, major weight losses occurred during the pyrolysis, with the resultant

formation of undesirable phases such as CaO. Jillavenkatesa and Condrate synthesized HA using calcium acetate and triethyl phosphate as precursors at a relatively low temperature (ca. 500 °C), and noted that a higher temperature was essential to increase the HA yield [37]. This process also required further hydrochloric acid leaching to eliminate the CaO, leading to pure HA phase formation. Elsewhere, Brendel *et al.* produced HA at temperatures as low as 400 °C using calcium nitrate ($Ca(NO_3)_2 \cdot 4H_2O$) and phenyldichlorophosphite ($C_6H_5PCl_2$) as precursors [41]; however, the resultant HA was of low purity and poor crystallinity. A further increase in the synthesis temperature to 900 °C resulted in a pure, well-crystallized HA phase. Takahashi *et al.* [42] developed a gel route using calcium nitrate and phosphonoacetic acid ($HOOCCH_2PO(OH)_2$) in an aqueous solution, and obtained a pure HA powder at 700 °C; here, the HA crystallinity was seen to increase with temperature up to 1100 °C. When Haddow *et al.* [43] used calcium acetate, together with a number of phosphorus precursors (i.e. phosphoric acid (H_3PO_4), phosphorous pentoxide (P_2O_5) and triethyl phosphite) for HA coating applications, the films prepared from triethyl phosphite and calcium acetate were shown to have the best wetting characteristics, while the temperature required to form an apatitic phase was >600 °C.

Kuriakose *et al.* reported an alternative method to produce pure, stoichiometric, stable, crystalline HA phase at a lower temperature by using ethanol as solvent rather than phosphorous alkoxides and gels [44]. The presence of alcohol provided not only a thermally stable but also a nanocrystalline HA; moreover, with a particle radius in the range of 1.3 nm this material which would serve as an ideal bone replacement. The aqueous route of sol–gel preparation offers an effective and relatively simple means of producing HA. For example, Bogdanoviciene *et al.* developed an aqueous sol–gel chemistry route to prepare HA based on ammonium-hydrogen phosphate and calcium acetate monohydrate as precursors [45]. In this processes, aqueous solutions of ethylene diamine tetraacetic acid (EDTA) or tartaric acid (TA) as complexing agents were added to the reaction mixture. Subsequently, the monophasic HA powder was obtained by calcination of the precursor gels for 5 h at 1000 °C.

The sol–gel synthesis process of amorphous calcium phosphate (CaP) using calcium salts, ethanol and phosphoric acid, was reported by Layrolle *et al.* [46]. This group showed that when calcining at 600 °C, amorphous CaP was converted to crystalline HA, with the average particle size of amorphous CaP being 22 nm and that of HA 200 nm. A water-based sol–gel synthesis of HA was developed by Liu *et al.* [47, 48], using calcium nitrate and triethyl phosphite as Ca and P precursors, respectively. The initial particle size was in the nanometer range, but was increased as the temperature was raised. The structural evolution upon the transformation of sol to gel, and from gel to final ceramic powder during HA synthesis, was also reported. A two-step procedure was used to synthesize HA in which the phosphite was initially hydrolyzed with water for 24 h, followed by the addition of an aqueous nitrate solution. The apatitic phase was seen to be formed at a temperature as low as 350 °C, while the calcined gels showed a nanoscale microstructure, with grain diameters of 20 to 50 nm. With an appropriate heat treatment

between 300 and 400 °C, the apatite produced was nanostructured, low-crystalline and carbonated, closely resembling human bone apatite.

A citrate-nitrate combustion method for the synthesis of nanocrystalline HA was reported by Han *et al.* [49], using calcium nitrate and diammonium hydrogen phosphate as starting materials. The synthesis was carried out under acidic conditions by the addition of HNO_3. Citric acid was used as chelating agent to form stable complex with metal ions under acidic conditions, and also acted as a fuel in the reaction and as a powerful reducing agent, where nitrate was a strong oxidant. The exothermic reaction between citric acid and nitrate led to the production of HA, with a grain size between 80 and 150 nm being obtained by calcining at 750 °C. The reaction sequence was as follows:

$$C_6H_8O_7 + Ca^+ \rightarrow C_6H_6O_7 + 2\,H^+$$

$$9\,Ca(NO_3)_2 + 5\,C_6H_8O_7 \rightarrow 30\,CO_2 + 9\,N_2 + 20\,H_2O + 9\,CaO$$

$$10\,CaO + 6\,(NH_4)_2PO_4 \rightarrow Ca_{10}(PO_4)_6(OH)_2 + 12\,NH_3 + 8\,H_2O$$

A novel method for the preparation of HA using a sucrose-templated sol–gel method was developed by Bose *et al.* [50]. Here, the starting materials were calcium nitrate and ammonium hydrogen phosphate, and sucrose was used as both a chelating agent and a fuel for the reaction. An increase in the quantity of sucrose led to a decrease in HA formation due to dehydration, and resulted in the formation of β-TCP. The HA phase was stabilized using Al_2O_3, which acted as a Lewis acid. Subsequently, it was shown that 5 mol% Al_2O_3 dopant produced 100% phase-pure HA, with an average particle size of 30 nm at 650 °C (see Figure 12.2). Moreover, a further increase in temperature led to an increase in the particle size.

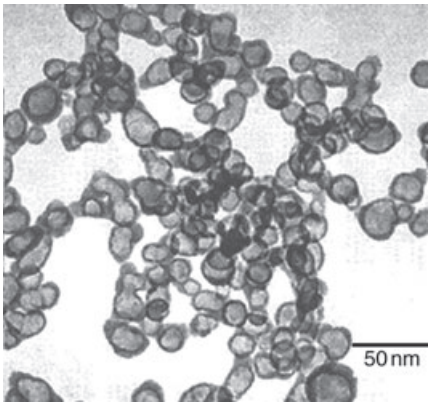

Figure 12.2 Transmission electron microscopy image of 5% alumina-doped hydroxyapatite powders calcined at 650 °C for 1 h with a Ca : sucrose ratio of 1 : 15.

Eshtiagh-Hosseini *et al*. studied the process parameters, such as sol temperature, aging time and heat treatment temperature, on apatite formation, and found that increasing both the aging time and the mixed sol solution temperature up to 80 °C led to a reduction in the impurity phases of CaO [51]. In addition, with an increase in calcination temperature to >600 °C, the calcium phosphate impurity phases disappeared. The mean crystallite size was also increased, while the microstrain decreased significantly due to the rise in firing temperature.

12.2.3 Biomimetic Synthesis

Biomimesis is the study of the structure, function and optimization of biological materials and systems as archetypes that inspire the design of analogous synthetic materials. The biomimetic design of man-made materials with properties similar to bone and dentin represents a major challenge because of their complex nature. Mineralized tissues such as bone and dentin are unique biocomposites of a structured organic matrix impregnated with oriented carbonated apatite crystals. Osteoblasts and odontoblasts, respectively, are the cells responsible for the formation of bone and dentin matrices, mixtures of type I collagen and specialized noncollagenous proteins. The mineral deposited on the organic framework locally adopts a preferred orientation relative to the matrix. Although, HA is thermodynamically the most stable form among all CaPs, it does not crystallize spontaneously from physiological calcium and phosphate buffer solutions. Rather, HA formation is accelerated by nucleators such as certain extracellular matrix (ECM) macromolecules. Nonetheless, details of the apatite crystallization process remain obscure, while the molecular recognition mechanisms that occur at the interface between proteins and biominerals are poorly understood.

In many cases, biomimetic strategies do not set out to copy directly the structures of biological materials, but aim to abstract the key concepts from biological systems, such that they can be adapted within a synthetic context. Thus, biomimetic materials are invariably less complex than their biological counterparts and, to date, hierarchical architectures (such as those observed in bone) remain outside the current technologies. Currently, the simplest biomimetic approach involves the design of single-component systems that mimic the chemistry of bone tissue.

Metastable synthetic (or modified) simulated body fluids (SBFs), with an inorganic salt composition similar to that of human blood plasma, incubate and facilitate the spontaneous nucleation and growth of nanosized, carbonated and 'bone-like' apatite at physiological pH and temperature. SBFs were first used by Kokubo and Takadama [52] in biomimetic synthesis to prove the similarity between the *in vitro* and *in vivo* behaviors of certain glass–ceramic compositions. Some typical SBF compositions are listed in Table 12.1. In these studies, the glass–ceramic samples were soaked in SBF solutions and their surfaces coated with a poorly crystallized calcium-deficient and carbonate-containing apatite, similar to bone apatite. A metastable SBF has been proven to incubate and facilitate the

Table 12.1 Ion concentrations of human blood plasma and stimulated body fluids (SBFs) [52].

	Ion concentration (m*M*)							
	$Na+$	K^+	Mg^{2+}	Ca^{2+}	Cl^-	HCO_3^-	HPO_4^{2-}	SO_4^{2-}
Human blood plasma	142.0	5.0	1.5	2.5	103.0	27.0	1.0	0.5
Original SBF	142.0	5.0	1.5	2.5	148.8	4.2	1.0	0
Corrected SBF (c-SBF)	142.0	5.0	1.5	2.5	147.8	4.2	1.0	0.5
Revised SBF (r-SBF)	142.0	5.0	1.5	2.5	103.0	27.0	1.0	0.5
Newly improved SBF (n-SBF)	142.0	5.0	1.5	2.5	103.0	4.2	1.0	0.5

spontaneous generation and growth of a carbonated and 'bone-like' calcium apatite on immersed silica or titania gels, bioglass and titanium samples at physiological pH and temperatures. The results of previous studies have indicated that Si—OH [53], Ti—OH [54], Zr—OH [55], Nb—OH [56] and Ta—OH [57] groups are effective for inducing apatite formation within the environment of the body. The presence of this carbonated apatite layer, formed by a biomimetic process on several materials, was proven to promote osteoblast responses (attachment, proliferation and differentiation), and subsequent bone matrix apposition, which allows a strong bond to bone.

It is possible to prepare even, thin films or coatings of bone-like apatite on bone implants by using a biomimetic process, which mimics the bone mineralization process by immersing implants in SBF [58, 59]. The microstructural nature of the CaP coating, its dissolution rate and its specific interactions with body fluids, can influence the osteogenicity of the coating, as well as the bone remodeling process. By using the biomimetic coating method, in contrast to other coating techniques, biologically active agents can be added to the supersaturated solutions and gradually be coprecipitated with the calcium phosphate crystals, thus forming a layer on the metal implants [60, 61]. This creates the possibility of uniformly incorporating an antibiotic within the biomimetic coating and releasing it at a controlled rate, thus preventing localized, postoperative infections.

In Nature, the nucleation and growth of mineralized materials are often controlled by organic macromolecules such as proteins and polysaccharides. Bone and teeth consist of a small amount of organic matrix which manipulates the formation of apatite into distinct microstructures suitable for the mechanical forces encountered *in vivo* [62]. The biomimetic synthesis of CaP within polymer matrices was reported to produce composites that could initiate osteogenesis when implanted in bony sites [63]. Polymers with distinct molecular organizations were used as a template to control the geometry of the apatite to mimic that found in bone.

Both, Wan *et al.* and Hutchens *et al.* prepared HA by using a biomimetic synthesis approach, with a bacterial cellulose hydrogel as template [64, 65]. Their results indicated that spherical HA particles comprised of nanosized crystallites

with a lamellar morphology had formed in the cellulose; moreover, the biomimetic HA comprised 10 to 50 nm anisotropic crystallites elongated along the c-axis, similar to natural bone apatite. Tao *et al.* [66] reported a potential mechanism for the formation of highly organized biomineralized structures, including oriented crystal growth on templates, the aggregation of nanocrystals by oriented attachment, and the assembly of inorganic nanoparticles mediated by organic molecules into aggregated structures. In these studies, the potential role of ACP in facilitating the assembly of HA nanoparticles into highly ordered structures was evaluated. An enamel-like HA architecture was produced in the presence of biological additives such as 10 m*M* glycine or 1.25 μ*M* amelogenin, while large plate-like crystals (as seen in bone) were induced when the additive was 10 m*M* glutamic acid. Hence, these biological molecules regulated the assembly process – specifically the assembly kinetics – and determined the structural characteristics of the final HA architecture.

Hoffmann *et al.* introduced a biomimetic method for the precipitation of nanosized CaPs using alkaline phosphatase (ALP), which is responsible for the hydrolysis of organic and inorganic phosphates *in vivo* [67]. Buffered solutions containing glycerol-2-phosphate and $CaCl_2$, in addition to $MgCl_2$ and a variety of enzymes, were prepared for calcium phosphate precipitation. The calcium phosphate powders obtained showed globular agglomerates with crystal sizes of 9 to 25 nm. By using this technique, it was possible to synthesize 100 g of bone-like Ca—P materials in one day. In a similar study, when Kim *et al.* [68] conducted a biomimetic synthesis of collagen-derived gelatin–HA nanocomposites, they noted that the osteoblast cells had a stronger attachment and greater proliferation on these nanocomposites, as well as a higher ALP activity and osteocalcin production. By comparison, when Kikuchi *et al.* fabricated an HA–collagen composite under biomimetic conditions through a self-organization mechanism [69], the composite showed a bone-like orientation, with the c-axis of the HA nanocrystals being aligned regularly along the collagen fibrils. Bone tissue reactions with this composite demonstrated an osteoclastic resorption of the composite, followed by new bone formation by osteoblasts, which was very similar to the reaction of transplanted, autogenous bone.

12.2.4
Hydrothermal Method

The synthesis of ceramic powder using hydrothermal methods has been recognized for many decades. For this method, the reaction takes place in an aqueous or an aquo-organic environment, but at a relatively high temperature and high pressure with respect to the ambient conditions. The process involves heating the reactants (often metal salts, oxides, hydroxides or metal powders) as a solution or suspension, usually at high temperature (80–400 °C) and high pressure (~100 MPa). The reactions are most often carried out in a hardened steel autoclave, inside which noble metal liners or capsules (open or closed) are often used to insulate

the reactants from impurities; the vessel may also be fitted with polymer linings to protect it against corrosion. Powders obtained by hydrothermal methods generally exhibit certain desirable characteristics, such as: (i) a fine particle size; (ii) a narrow particle size distribution; (iii) chemically pure and homogeneous; (iv) well crystallized; (v) low agglomeration; and (vi) relatively strain free. The hydrothermal syntheses of CaP-based powders have been reported by several groups [70–72].

The synthesis of HA nanopowder was reported by Riman *et al.* [73] using calcium nitrate, diammonium hydrogen phosphate, ammonium dihydrogen phosphate, ammonium hydroxide and nitric acid. Powders prepared at an alkaline pH were well crystallized and phase-pure, with surface areas in the range of 44 to 136 $m^2 g^{-1}$, corresponding to an estimated equivalent spherical diameter of 14 to 44 nm. As expected, an increase in the reaction temperature led to an increase in the crystallite size. Liu *et al.* reported an influence of pH and temperature on the morphology of HA synthesized by the hydrothermal method [74]. Here, HA whiskers and crystals were synthesized using $Ca(OH)_2$ and $CaHPO_4 \cdot 2H_2O$ as precursor chemicals.

It has been reported that, at alkaline pH, HA was well crystallized, whereas at a very high pH (~14) it showed poor crystallinity. Based on these reports, it is clear that during the hydrothermal synthesis of HA, the pH has significant effect on particle morphology (see Figure 12.3).

Yubao *et al.* [30] reported the synthesis of nanoscale, osteoapatite-like, rod-shaped crystals from $Ca(NO_3)_2$ and $(NH_4)_2HPO_4$, using a hydrothermal method; the crystal sizes were reported to be in the range of 40 to 150 nm. A surfactant-assisted hydrothermal synthesis of HA nanorods was reported by Yan *et al.*, using $Ca(NO_3)_2$ and H_3PO_4 as Ca and P precursor materials, and with cetyltrimethylammonium bromide (CTAB), sodium dodecyl sulfate (SDS) and poly(vinyl alcohol) (PVA) as surfactants [75]. While the presence of CTAB and SDS helped in the formation of HA nanorods after hydrothermal treatment, with average particle dimensions of 150×10 nm, the PVA-assisted synthesis produced mostly HA aggregates. Chen *et al.* [76] reported that HA nanorods could self-organize through a process of oriented attachment during hydrothermal treatment, using a template of ordered organic molecules. The HA crystals prepared using this approach were self-organized, with slip-shaped pores of approximately 3.5 nm diameter.

12.2.5
Mechanochemical Powder Synthesis

Mechanochemical processing (MCP) represents a compelling method for the production of nanostructured HA, during which the reaction is activated by mechanical milling. Mechanochemical powder synthesis is a solid-state synthesis method that takes advantage of the perturbation of surface-bonded species by pressure or mechanical forces to enhance the thermodynamic and kinetic reactions between solids [77]. Pressure can be applied via conventional milling

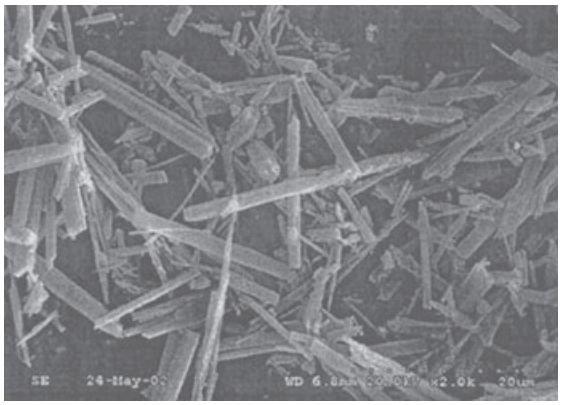

(a)

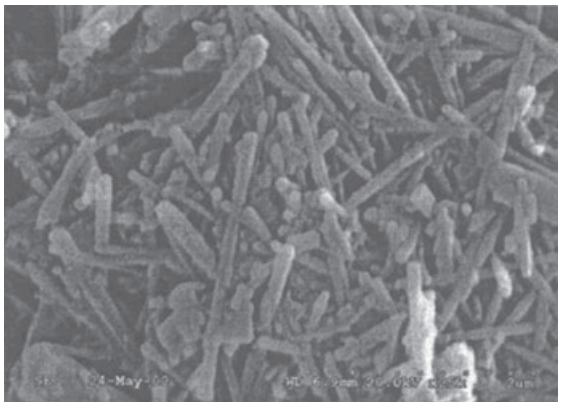

(b)

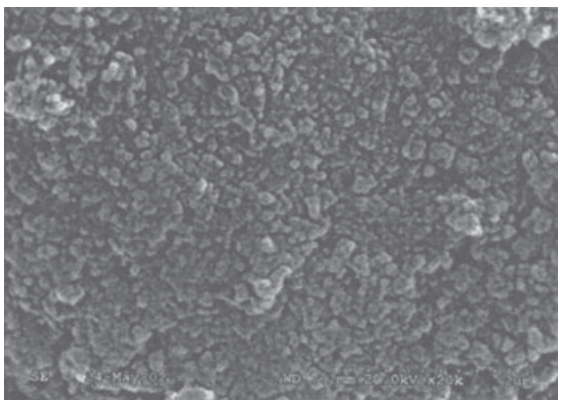

(c)

Figure 12.3 Scanning electron microscopy images of HA whiskers and crystals with different pH values at the same temperature 140 °C. (a) pH 6; (b) pH 9; (c) pH 14.

equipment, ranging from low-energy ball mills to high-energy stirred mills. In a mill, the reactants are crushed between the balls and wall (horizontal or planetary ball mill, attritor, vibratory ball mill), or between rings or ring and wall (multi-ring media mill). The reagents absorb part of the energy provided by the collisions or frictions that provide the energy necessary for the reaction [78].

Mechanochemical syntheses were originally designed for the production of oxide dispersion-strengthened (ODS) alloys. Over the past 20 years, however, the number of available mechanochemical syntheses has grown and the method diverged, such that today it is used for the fabrication of a wide range of advanced materials, both metallic and nonmetallic in composition. The mechanochemical syntheses of HA powders were accomplished at room temperature, under either dry conditions or in water, using either $CaHPO_4$ or $Ca(H_2PO_4)_2$ as sources of calcium and phosphorus, and CaO, $Ca(OH)_2$ and $CaCO_3$ as sources of extra calcium. Yeong *et al*. reported a single-phase HA of high crystallinity that had been synthesized by more than 20 h of mechanical activation [79]; the resultant HA powder had an average particle size of 25 nm and a specific surface area of $76\,m^2\,g^{-1}$. In the initial stage of activation, a significant refinement of the crystallite size occurred, and this was followed by the steady formation and subsequent growth of HA crystals with increasing mechanical activation. The use of $CaCO_3$ as a starting material resulted in the formation of strongly carbonated apatite powders [80]. It is possible also to incorporate certain dopants or substituents, such as magnesium [81], silicate [82], fluorine [83] and carbonates [84], into the HA during mechanochemical synthesis [85].

Whilst the main advantages of the mechanochemical synthesis of ceramic powders are simplicity and low cost, the main disadvantages are the low crystallinity and calcium-deficient nonstoichiometry (Ca/P molar ratio 1.50–1.64) of the HA powders, as this results in their partial or total transformation into β-TCP during calcination.

The mechanochemical synthesis of HA can be performed under wet or dry conditions, although in most studies involving this procedure a wet mechanochemical synthesis, or perhaps a mechanochemical–hydrothermal synthesis, was used in preference. Wet mechanochemical synthesis involve grinding an aqueous suspension of the starting materials with a liquid-to-powder ratio that generally ranges from 60 to 95 wt%. An aqueous phase can actively participate in the mechanochemical reaction by accelerating the kinetic processes that normally are rate-limiting, such as dissolution, diffusion, adsorption, reaction rate and crystallization (nucleation and growth) [86]. The mechanochemical activation of slurries can generate local zones of high temperatures (up to 450–700 °C), as well as high pressures due to friction effects and adiabatic heating of gas bubbles (if present in the slurry), while the overall temperature is close to ambient [87]. Thus, the mechanochemical–hydrothermal technique can be envisioned as being located at the intersection of hydrothermal and mechanochemical processing. Although the mechanochemical–hydrothermal route is capable of producing large quantities of HA powder, it also utilizes a lower temperature (i.e. room temperature) as compared to 90–200 °C for the hydrothermal process.

12.2.6
Solid-State Reactions

Very few studies have been conducted on the solid-state-reaction processing of HA. In general, solid-state reactions are performed at high temperature, and the HA powders synthesized in this way usually have irregular shapes with larger grain sizes. They also quite often exhibit heterogeneity in the phase composition, owing to chemical reactions resulting from the small diffusion coefficients of ions within the solid [88]. A typical formation of HA using a solid-state method is based on the following equation [89]:

$$4\,CaCO_3 + 6\,CaHPO_4 \cdot 2H_2O \rightarrow Ca_{10}(PO_4)_6(OH)_2 + 4\,CO_2 + 14\,H_2O$$

The key ingredients of this reaction are basically in solid phase in which $CaCO_3$, CaO or calcium hydroxide act as a calcium precursor and tricalcium phosphate or $CaHPO_4 \cdot 2H_2O$ act as a phosphorus precursor in the formation of HA. Usually, solid-state reactions take place at a very high temperature (~1000 °C). For example, Rao *et al.* reported the synthesis of HA using a solid-state reaction between commercially available tricalcium phosphate and calcium hydroxide powders, at temperatures between 700 and 1000 °C [90]. The reaction of TCP and calcium hydroxide in a 3 : 2 molar ratio at 1000 °C produced pure HA phase. A method for the preparation of HA fibers was introduced by heating compacts consisting of calcium metaphosphate fibers with calcium hydroxide particles at 1000 °C in air [91], such that the HA fibers obtained had nanostructural features. Pramanik *et al.* reported the preparation of high-strength HA ceramics using CaO and P_2O_5 as starting materials [92]. Overall, despite solid-state reactions representing a simple approach for large-quantity powder processing, the lack of control of the powder's particle properties and phases limits the use of this process for HA powder synthesis.

12.2.7
Microwave-Assisted Synthesis

The microwave-assisted synthesis of nanophase ceramic materials is relatively new, but is rapidly attracting interest for the synthesis of nano-HA materials. Compared to conventional high-temperature sintering, the microwave process has particular advantages, such as rapid volumetric heating and high reaction rates, leading to products with small particle sizes, a narrow size distribution and high purity [93, 94]. Thus, microwave heating, as an important processing method, was introduced to the synthesis of HA by solid-state reaction at room temperature [95].

Feng *et al.* prepared HA nanoparticles or nanorods by microwave heating in a very short reaction time, in which $Ca(NO_3)_2 \cdot 4H_2O$ and $Na_3PO_4 \cdot 12H_2O$ were used as the starting materials [96]. The same group also concluded that, in the microwave heating method, the Ca/P ratio and water of crystallization in the starting materials were important because of their influences on the morphology of

the HA product. By using a simple, one-step microwave-assisted solid-state reaction at room temperature, Cao *et al.* produced HA nanorods with diameters between 60 and 80 nm and lengths of about 400 nm [94, 96]. When microwave heating and conventional heating for the synthesis of HA nanorods were compared in terms of product morphology, microwave radiation was seen to play an important role, due mainly to the shorter reaction time.

In addition to solid-state reactions, microwave radiation can also be used in conjunction with wet precipitate processes. For example, Sarig and Kahana investigated the wet synthesis of HA using a microwave system [97] in which $CaCl_2$ and NaH_2PO_4 aqueous solutions were used as starting materials. When heating was conducted in a 2.45 GHz microwave oven at maximum power for 5 min, the powder obtained was composed of spherulites that were about 2–4 μm diameter and consisted of ultrafine platelets of about 300 nm length. Notably, the powder produced was nonaggregated and remained free-flowing after three years of storage. The precipitation of HA in a continuous process using microwave heating was also reported by Torrent-Burgues *et al.* [98], with needle-like calcium-deficient HA particles in the nanometer size range (<100 nm) being obtained.

12.2.8 Emulsion Process

The emulsion process can be used to synthesize inorganic and metallic nanoparticles with controlled particle size and morphology [99, 100]. An emulsion is defined as a colloidal suspension of a liquid within another liquid. Emulsions can be divided into two categories: (i) oil-in-water, where the oil droplets are suspended homogeneously in water (the droplets are referred to as micelles); and (ii) water-in-oil, where water droplets are suspended homogeneously in oil, known as reverse micelles.

12.2.8.1 Surfactants

Often, a surface-active agent or surfactant may be added to stabilize an emulsion; the role of a surface-active agent is to reduce the difference in surface tension between the water and oil such that they form a stable phase in one another. The emulsion process depends heavily on the type of surfactant used, their concentration, and the aqueous-to-organic phase ratio in the liquid medium.

Surfactants are molecules of a particular design which have one polar end or head-group, and another nonpolar end, and may be either nonionic or ionic. While nonionic surfactants do not ionize when dissolved in liquid, their ionic counterparts do. Ionic surfactants may be of two different types, namely anionic and cationic. Anionic surfactants have a relatively large nonpolar group and a negatively charged polar group, while cationic surfactants have a positively charged polar group. A third type of surfactant – an ampholytic surfactant – consists of both cationic and anionic head-groups and, depending on the pH of the solution and its structure, it can behave as an anionic, cationic or a neutral species. When the surfactant dissolves in organic solvents, it forms spheroidal aggregates, and this

may occur in either the presence or absence of water. When the medium is completely water-free, the aggregates are small and polydispersed; however, the presence of water increases the size of the surfactant aggregates as the water becomes trapped by the polar core of the surfactant. The water-trapped polar core is termed the 'water pool', and is defined by the water-to-surfactant molar ratio ($w = [H_2O]/[S]$). When the amount of water is less ($w < 15$), the situation is referred to as a 'reverse micelle', whereas the presence of large amounts of water molecules ($w > 15$) correspond to 'microemulsions'. The size of the water droplet inside the core can be calculated by assuming that water in oil is spherical, and is expressed as:

$$R = 3V/\Sigma$$

where R is the radius of sphere, V is the volume of sphere and Σ is the surface of the sphere, assuming that the volume and the surface of the droplets are governed by the volume of the water and by the surfactant molecules, respectively. The water pool radius is then the same as the radius of the sphere, and can be expressed as:

$$R_w = 3\,V_{aq}[H_2O]/\sigma[S],$$

where V_{aq} is the volume of water molecules and Σ is the area. Various experiments have been conducted to confirm the linear variation of water pool radius with water content [101].

12.2.8.2 **Reverse Micelles**

Figure 12.4 shows a schematic diagram of a water-in-oil microemulsion or reverse micelle. Reverse micelle-templated synthesis has the ability to control particle size and morphology. Reverse micelles are formed when the aqueous phase is dispersed as microdroplets, and those microdroplets of water that are stabilized in a nonaqueous phase by a surfactant act as a microreactor or nanoreactors in which reactions are conducted. These spatially and geometrically restricted,

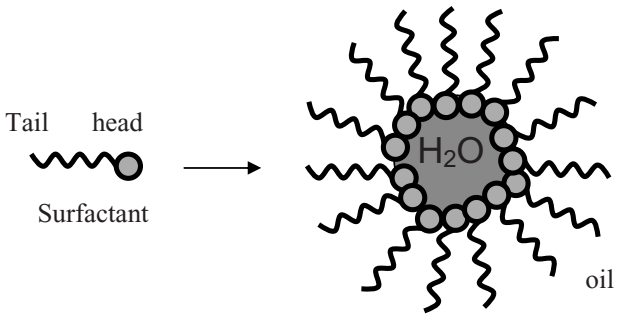

Figure 12.4 A schematic diagram of a reverse micelle.

self-assembling media of reverse micelles can be used in the synthesis of nanophase materials, with minimal agglomeration and a high surface area.

Most current methods produce HA powder where the agglomeration cannot be controlled during the synthesis or drying steps. In order to produce a sintered monolithic HA part with desired mechanical properties, it is necessary to use an agglomerate-free, low-aspect ratio fine HA powder with a high surface area. Agglomeration can cause not only a lower sintered density but also crack-like voids during densification. A high-aspect ratio morphology in the starting powder can also cause poor packing, which may result in an exaggerated grain growth during sintering. This microstructural heterogeneity can seriously affect the mechanical properties of sintered HA parts. The reverse micelle or microemulsion template system represents a useful process for synthesizing nanopowders [99] and, indeed, microemulsion has been shown to be one of the few techniques capable of producing nanometer-sized particles with minimal agglomeration.

Bose *et al*. have reported the synthesis of the HA nanopowders with a surface area as high as $130\,m^2\,g^{-1}$ by using a reverse micelle template system and particle sizes in the range of 30 to 50 nm, with different morphologies depending on the reaction parameters and the related powder characterization [102, 103]. Calcium nitrate and phosphoric acid were used as calcium and phosphorus precursors, respectively, cyclohexane as the organic phase, and poly(oxyethylene)$_5$ nonylphenol ether (NP-5) or poly(oxyethylene)$_{12}$ nonylphenol ether (NP-12) as the surfactant. The calcium-to-phosphorus atom ratio in the precursor was maintained at 1.67 to 1 in all cases, and a surfactant (10 vol%) was added to cyclohexane to create the organic phase. The aqueous solution and organic phase were mixed to obtain the reverse micelle systems, after which the emulsion was converted into a transparent gel during mixing and stirring. After ageing at room temperature, the emulsion was evaporated and dried on a hotplate to obtain the HA precursor powders. Finally, the crystalline HA powders were obtained by heat treatment at different temperatures, from 450 to 650 °C. Several experimental parameters were shown to have an effect on the surface area, including the crystalline phase purity, the particle size and morphology of the HA nanopowders. It was also shown that not only the surface area but also the morphology of the HA nanopowders could be tailored by varying different synthesis parameters, such as the aqueous : organic ratio, the metal ion concentration and the ageing time.

The pH of the reverse microemulsion was found to have a significant influence on the formation of HA. The emulsions obtained after mixing the aqueous and organic phases had a pH of 2, but the results indicated that HA was not formed at this pH. However, when the pH of the microemulsion was adjusted to 7, using ammonium hydroxide solution, the HA phase was formed.

The composition of the reverse microemulsion governs the shape and size of the reverse micellar domains, as well as the particle morphology and size. As the aqueous : organic ratio increases, the size of the polar core of the reverse micelle increases, leading to a bigger particle size and a decrease in the surface area. Figure 12.5 shows that the needle-shaped particles with a high aspect ratio were formed when the aqueous : organic phase volume ratio was 1 : 5 in the reverse emulsion.

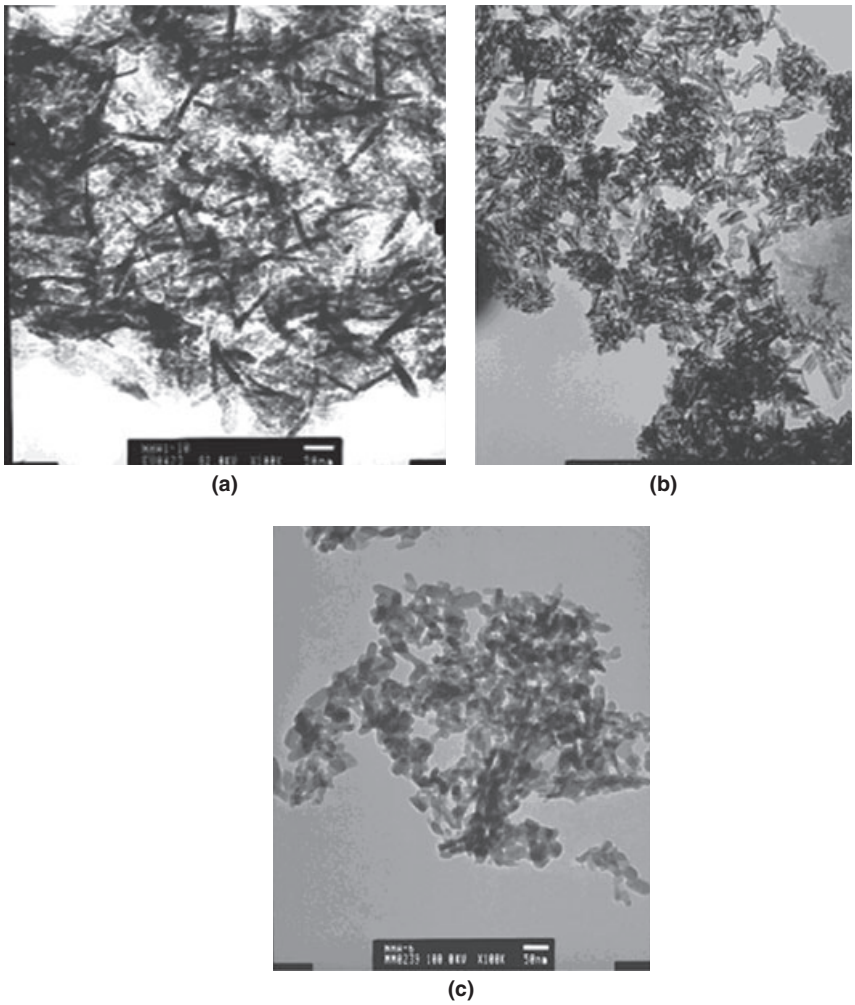

Figure 12.5 Changes in morphology of HA powders as the aqueous organic phase volume ratio changes, synthesized by using NP5 + NP12 as surfactant: $[Ca^{2+}] = 5.0\,M$; aging time = 12 h; aging temperature = 25 °C. (a) The aqueous organic phase volume ratio is 1 : 5 (BET surface area = 103 $m^2 g^{-1}$); (b) 1 : 10 (BET surface area = 130 $m^2 g^{-1}$); (c) 1 : 15 (BET surface area = 73 $m^2 g^{-1}$).

The average widths of the particles were in the range of 5–10 nm, and the length between 50 and 100 nm for powders calcined at 450 °C. The aspect ratio of the particles decreased as the aqueous : organic phase volume ratio was increased to 1 : 10, and platelet-shaped particles were formed under these conditions. The particles had an average width of less than 10 nm, and a length in the range of 30 to 50 nm. Yet, when the aqueous : organic phase volume ratio was further increased

to 1:15, the aspect ratio of the particles decreased even more, together with a decrease in surface area. It was also noted that powders obtained from emulsions having an aqueous:organic phase volume ratio of 1:15 were more agglomerated with respect to the powders made with 1:5 and 1:10 aqueous:organic ratios. The high surface area of the latter powders, with respect to the former, supports this observation. Surfactants dissolved in organic solvents form spherical aggregates known as reverse micelles, although if the medium is completely free of water the aggregates are very small and polydisperse. The presence of water is necessary to form relatively large surfactant aggregates, which can be used for both micro- and/or nanoreactors for chemical reactions. The shape of the polar core depends on the amount of water, the organic solvent and the surfactant, and on their ratio – which can make the core elongated or spherical. The formation of acicular or spherical particles at different organic:aqueous phase volume ratios can be explained by the formation of different shapes of the polar cores in the emulsion. The control of nanocrystal shape represents a major challenge, and additional investigations are required to confirm the exact mechanism that determines the nanocrystal morphology.

12.2.8.3 **Effect of Ageing**

The aging time was also shown to affect the particle morphology, with HA particles being shown to have a rectangular platelet morphology after a 1 h period of ageing. However, powders obtained after 12 h of aging were almost spherical, with a lower aspect ratio. By increasing the aging time of the emulsion to 72 h, the BET (Brunauer–Emmett–Teller) surface area of the powders was decreased significantly, though this may be due to crystal growth within the emulsion for an extended period of time.

12.2.8.4 **Effect of Metal Ion Concentration**

The metal nitrate concentration in the aqueous phase may also affect the surface area of synthesized nanopowders. For example, by increasing the metal ion concentration from 1.0 to 5.0 *M*, the BET surface area of the powders was increased from 86 to 130 $m^2 g^{-1}$. The morphology of the HA particles was also shown to depend on the initial Ca^{2+} ion concentration in solution, with near-spherical particles being produced from a solution containing 1.0 *M* Ca^{2+} ions, and with a narrow size distribution of 30 to 50 nm. In contrast, needle-shaped particles were formed with a 5.0 *M* Ca^{2+} ion solution.

Lim *et al.* [104–106] have reported on the synthesis and characterization of HA nanopowders by microemulsion using poly(oxyethylene)$_5$ nonylphenol ether (NP-5) and poly(oxyethylene)$_{12}$ nonyl phenol ether (NP-12) as the surfactant, and cyclohexane as the oil phase. The starting materials of $CaCl_2$ and $(NH_4)_2HPO_4$ were used as sources of Ca and P, respectively. The phase diagram of the cyclohexane–(NP-5 + NP-9)–aqueous solution of $CaCl_2$ is shown in Figure 12.6. The calcination temperatures were reported as 600 to 1200 °C, and the particle sizes between 190 nm and 1.95 μm. A simple route for the synthesis of HA nanofibers was reported by Liu *et al.* [107], who used $CaCl_2$ and Na_3PO_4 as starting materials and

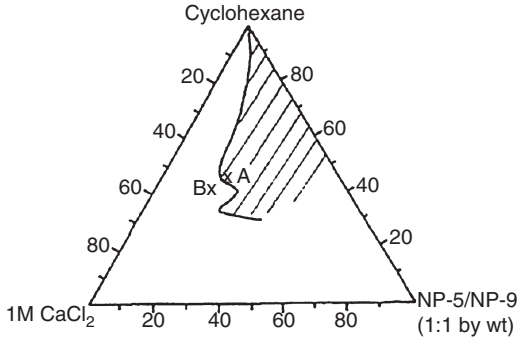

Figure 12.6 The partial phase diagram for the system of cyclohexane–(NP-5 + NP-9)–aqueous solution of 1 *M* $CaCl_2$ at room temperature. A is a microemulsion; B is an emulsion region.

CTAB as surfactant. The average size of the nanofibers was 120–160 nm length and 5 nm width. The same type of surfactant (CTAB) was used by Yao *et al.* [108] for the synthesis of nanostructured HA from $K_2HP_4 \cdot 3H_2O$ and $CaCl_2$, with the resultant particles being 500–1000 nm long and 50–100 nm thick. Likewise, Koumoulidis *et al.* [109] reported the synthesis of HA nanopowders in the range of 40–120 nm when using CTAB as surfactant and $Ca(H_2PO_4)_2 \cdot H_2O$, $CaCl_2$ and ammonia solution as the starting materials.

Micelle-templated synthesis was reported by Wu *et al.* when HA nanopowders were synthesized with a high surface area and a particle size of 60–80 nm, using SDS as surfactant [110]. The influence of emulsion process on crystal growth and particle shape was also studied by Sonoda *et al.* [111], who found the edge of HA particles derived from the emulsion method to be curved and rounded, while those from the nonemulsion method were straight and truncated. The increase in temperature also led to an increase in particle size.

12.2.9 Other Processes

Besides the above-mentioned synthesis procedures, various other methods have been reported for the synthesis of nanocrystalline HA. For example, when the synthesis of HA from $Ca(NO_3)_2$ and $(NH_4)_2HPO_4$ using polyacrylic acid (PAA) was reported by Bertoni *et al.* [112] and Zhang and Gonsalves [113], the presence of PAA was seen to reduce the final HA crystal dimensions, such that the crystal became more acicular. However, at high PAA concentrations the crystals aggregated into clusters. Sinha *et al.* [114] reported the synthesis of nanosized and microporous HA precipitates using synthetic polymers and biopolymers systems; here, $Ca(NO_3)_2$ and $(NH_4)_2HPO_4$ were used as the starting reagents, while polyvinyl alcohol (PVA) and bovine serum albumine (BSA) gels were used as polymers. This process was similar to biomineralization, and highly controlled with respect to the microstructural features such as size and shape. The synthesis of ultrafine HA

powders by radiofrequency (RF) plasma processing was investigated by Kumar *et al.* [115]. In these studies, the amount of nanosized clusters was increased with increasing thermal treatment, while the average particle size was inversely proportional to the severity of the thermal treatment. In another study, Wang *et al.* [116] reported a novel strategy to synthesize HA nanorods based on a liquid–solid–solution (LSS) method, such that HA nanorods with tunable sizes, aspect ratios and surface properties were obtained. In fact, this method may be useful for the controlled synthesis of biomedical inorganic materials with tailored shapes and surface properties.

12.3 Characterization of Hydroxyapatite Nanocrystals

Synthesized HA nanoparticles can be characterized using a variety of techniques, depending on the properties of interest and their applications. In general, these characterization techniques can be broadly grouped into three categories:

- Composition and phase analysis
- Characterization of nanoparticles for size and morphology
- Biological characterization.

In the following sections we provide detailed descriptions of the techniques required for such characterization.

12.3.1 Composition and Phase Analysis

Conventional chemical analysis techniques such as wet analysis or atomic absorption (AA) can provide a relatively accurate chemical composition for studying the Ca/P ratio and stoichiometric composition of HA. Energy dispersive spectroscopy (EDS), typically in conjunction with scanning electron microscopy (SEM) or transmission electron microscopy (TEM) has also been used extensively to analyze chemical composition, both quickly and directly. This technique allows the incident electron beam to be moved from one surface region to another for mapping the localized surface elemental composition and their distribution. However, low concentrations of elements are not measured accurately when using EDS.

X-ray diffraction analyses are normally used to identify the phase composition of HA samples. By comparing standard data and previously published information, the crystal structures and phases of different materials can be characterized using XRD. In the case of HA, a common challenge is to identify other phases of calcium phosphates, which are usually present in most synthesized powders. First, a qualitative evaluation of the presence or absence of different phases is possible using XRD. Second, XRD can also be used to calculate the quantitative amounts of different phases present in a mixed phase materials. Figure 12.7 shows a typical XRD pattern of synthesized HA nanopowders; here, the results show that the synthesized nanopowders have a phase-pure HA crystalline structure. A minimal

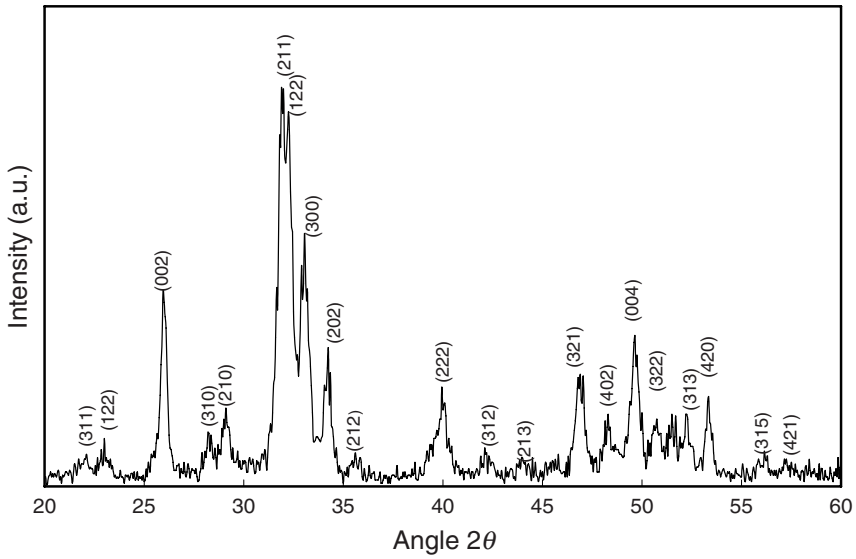

Figure 12.7 X-ray diffraction plots for synthesized HA nanopowders.

broadening of the peaks explains the smaller particle and crystallite size. The crystallinity of a synthesized HA powder can then be calculated by comparison with a standard HA calibration.

The reflection broadening in the XRD pattern is attributed to the contributions of the crystallite size, microstrain and the instrument itself. The crystal size D is inversely proportional to the peak breadth, according to the Scherrer's formula [117]:

$$\Delta(2\theta) = \frac{0.9\lambda}{D\cos(\theta)}$$

where Δ (2θ) represents the peak width at half-maximum intensity (in radian), λ the wavelength for Cu K_α ($\lambda = 0.154\,18$ nm), and D is the crystal size (in nm). In this case, from the line-broadening data using Scherrer's equation, the calculated crystallite sizes of the samples are ~20 nm in Figure 12.7.

Further, it is also possible to determine the crystallographic characteristics of HA crystals from the XRD data. HA has the hexagonal crystallographic structure, where the relationship between the distance (d) of two adjacent net planes and the (*hkl*) Miller indices of the reflection planes, is given by [51]:

$$d = \frac{1}{\sqrt{\frac{4}{3}\cdot\frac{h^2+hk+l^2}{a^2}+\frac{l^2}{c^2}}}$$

A slight shift of the diffraction peaks can be observed when some trace elements are incorporated into the HA crystal.

Fourier transform infrared (FTIR) spectroscopy is another technique normally used to study chemical structures, such as OH^- and CO_3^{2-} groups, in HA samples. In general, bands at 3572 and 631 cm^{-1} are assigned to stretching mode, librational mode and translational mode, respectively, of the hydroxyl group, OH. Bands at 1087, 1072–1032, 962, 601, 571 and 474 cm^{-1} are assigned to vibrations of the phosphate group, PO_4. The first peak at 1087 cm^{-1} emanates from a triply degenerated asymmetric stretching mode vibration. The other two components of this triply degenerated vibration, of the P—O bond of the phosphate group appear at 1046 and 1032 cm^{-1}. The peak at 962 cm^{-1} is assigned to a nondegenerated symmetric stretching mode of the P—O bond of the phosphate group, PO_4. The peaks at 601, 575 and 561 cm^{-1} are assigned to a triply degenerated bending mode of the O—P—O bond. The weak peaks at 472 and the shoulder at 462 cm^{-1} are components of the doubly degenerated bending mode of the phosphate group, PO_4.

12.3.2
Nanoparticle Characterization for Size and Morphology

The most widely used technique for nanoparticle characterization is that of TEM, by which nanoparticles can be viewed and their size, shape and morphology documented. Modern research TEM systems can be used to obtain information on features on the scale of 0.1 nm or smaller, and at magnifications of 50 million times.

The BET approach, another important analysis technique used to measure the specific surface area of a material, is based on the rules for the physical adsorption of gas molecules on a solid surface [118]. Here, the surface area is expressed in square meters per gram ($m^2 g^{-1}$) or square meters per cubic meter ($m^2 m^{-3}$), and is the result of measuring surface roughness as well as the quantity and size distribution of open pores. Although the theory is complex, BET measurements are relatively simple to obtain, widely applicable, and the results are highly reproducible. The most often used gas is nitrogen, as its molecular size is well established, it is inert, and is available in highly pure form at reasonable cost. The results from previous studies have indicated that HA nanoparticles by emulsion methods have very high BET specific average surface areas, which depends on the particle size and morphology. A BET surface area >100 $m^2 g^{-1}$ was measured for needle-shaped particles with a high aspect ratio, >130 $m^2 g^{-1}$ for platelet-shaped particles, and >70 $m^2 g^{-1}$ for agglomerated HA nanoparticles.

The technique of dynamic light scattering (DLS) can be used to measure the particle size of nanoscale HA, notably when only small amounts of powder are available. For this, approximately 1–5 mg of HA powder is added to 50 ml of water, typically at basic pH (e.g. pH 10), and ultrasonicated for 15–30 min to minimize the degree of agglomeration. An aqueous suspension of HA nanoparticles at a higher pH would be stable against flocculation for a long time, under the influence of a strong electric double layer repulsion around the negatively charged particle surface. The particle suspension is then filled into a borosilicate glass tube and inserted into the DLS instrument for particle size analysis. Particle sizes are

automatically determined from the autocorrelation function using the Stokes–Einstein equation: $r = kT/6Dph$, where r is the particle radius, k the Boltzmann constant, T the absolute temperature, D the diffusion coefficient, and h the viscosity of the liquid in which the particles were suspended. The values for the above parameters at room temperature are: $k = 1 : 38 \times 10^{-23}\,m^2\,kg\,s^{-2}\,K^{-1}$; $T = 293\,K$; and viscosity (η) = 0.891 cP.

12.3.3 Biological Characterization

Biological characterizations are performed using either a Petri dish (*in vitro*) or within the animal body (*in vivo*). The details of a range of frequently used investigational techniques are provided in the following sections.

12.3.3.1 *In Vitro* Evaluation Methods: Simulated Body Fluids and Cell Culture

Studies of the bone–biomaterials interface have revealed that one common characteristic of bioactive materials is the consistent presence of an interfacial apatite layer [119]. Kokubo and Takadama proposed that the essential requirement for an artificial material to bond to living bone is the formation of bone-like apatite on its surface when implanted in the living body, and that this *in vivo* apatite formation can be reproduced in a SBF with ion concentrations almost equal to those of human blood plasma [52]. This means that the *in vivo* bone bioactivity of a material can be predicted from the apatite formation on its surface in the SBF. The presence of a SBF has been proven to induce the formation of bone-like apatite on some biomaterials, such as silica or titania gels, bioglass and calcium phosphates ceramics, at physiological pH and temperatures. In recent studies, doped HA compositions showed significantly better apatite layer formation in SBF than pure compositions; one such example was that of strontium doping in HA [120].

Cell culture testing is used widely *in vitro* to evaluate the biocompatibility of HA samples. For this, several osteoblast cell lines have been developed to assess biomaterials performance *in vitro*, including a murine osteoblastic cell line (MC3T3-E1) [121], a human osteoblastic precursor cell line (OPC1) [122] and a human osteoblast cell line (hFOB 1.19) [123]. Osteoblast cells interact differently with material structures, depending on the combinations of chemical, structural and environmental variables. The biocompatibility of HA surfaces can be assessed using cell–material interaction studies such as attachment, proliferation and differentiation. Cell proliferation on HA samples is normally investigated with a mitochondrial (MTT) assay, which permits the quantitative estimation of the number of living cells on a material.

Both, optical and electron microscopy are used to observe cell morphology and to understand cell attachment and differentiation on materials.

Confocal scanning microscopy is used to assess the expression of specific osteoblast proteins, such as ALP and osteopontin (OPN).

12.3.3.2 *In Vivo* Animal Testing

Although *in vitro* tests provide a rapid means of evaluating the biocompatibility of HA, animal experiment remain the preferred method of testing the biological properties of materials. Whilst a complex biological environment cannot be simulated completely by *in vitro* experiments, it is possible to make reliable evaluations by implanting biomaterials directly into the bone tissue. Compared to *in vitro* tests, animal tests require a longer experimental term that usually lasts from several months to several years. Any changes in the HA materials within the body environment, such as dissolution and delamination as well as bone tissue formation, can then be studied histologically, often using SEM. If necessary, the physical bonding between bone and HA materials can be evaluated quantitatively using mechanical tests.

12.3.3.3 Toxicology of HA Nanoparticles

Bauer *et al.* [124] reported details of the internalization pathway of HA nanoparticles into cells. In a cell culture medium, the HA nanoparticles tended to agglomerate to form clusters that were 500–700 nm in size, and became unstable. An investigation using TEM showed that the internalized HA were captured by vacuoles in the cytoplasm of hepatocellular carcinoma cells. Moreover, the invaginations apparent in the cell membrane before nanoparticle uptake suggested that internalization of the agglomerates had resulted from an energy-dependent, clathrin-mediated endocytosis.

12.4 Bulk Structures Using Hydroxyapatite Nanocrystals

Nanomaterials can improve sinterability due to their high surface energy and, therefore, also improve mechanical properties. Sintering behavior, however, depends not only on particle size but also on size distribution and the morphology of the powder particles. A large particle size, combined with hard agglomerates, will lead to a lower densification in HA. As differences in shrinkage between the agglomerates is also responsible for the production of cracks in the sintered HA, the synthesis of agglomerate-free or soft agglomerated nanostructured HA may represent an important step in the achievement of good mechanical properties for dense nanostructures.

To date, few reports are available on the effect of the powders' properties such as particle size, distribution, density and morphology on the densification behavior and the mechanical and microstructural characteristics of those powder compacts [33, 125–128]. In order to study the aspect ratio effect on densification, high-aspect ratio nanopowder or rod-shaped particles (aspect ratio 7.2) and low-aspect ratio or spherical nanopowders (aspect ratio 1.3 ± 0.3) were synthesized using an emulsion technique with different parameters [103]. The specific average surface areas of the as-synthesized spherical and rod-shaped HA powders were 39 and 29 $m^2 g^{-1}$,

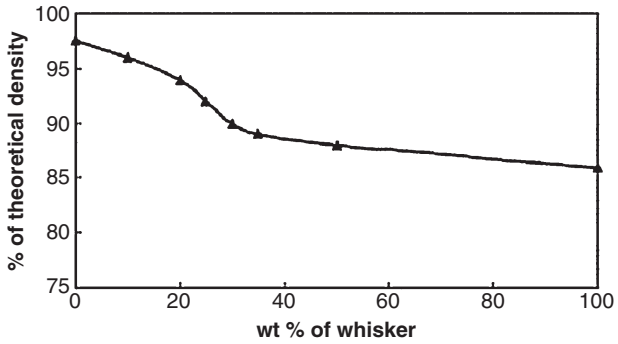

Figure 12.8 Densification behavior of HA compacts at 1250 °C for 3 h with different rod-shaped (whisker) particle contents.

respectively. The effect of rod-shaped particle addition on the densification of a spherical nanopowder is shown in Figure 12.8. It was observed that an increase in rod-shaped particles content decreased the density of the sintered sample. Spherical nanopowders have a higher surface energy per unit volume than rod-shaped particles. The addition of rod-shaped particles decreased the overall surface energy of the system, which is the driving force for solid-state sintering, and reduced the densification rate. A sintering plot shows three distinct regions with different slopes:

- In the first region (up to 20 wt% rod-shaped particles), the densification rate slowly decreased linearly with rod-shaped particle addition. Densification in this zone was primarily controlled by the spherical powders and their distribution.
- In the second, transitional, region (20–30 wt% rod-shaped particles), the densification rate control changed from spherical to rod-shaped particles.
- In the third region (>30 wt% rod-shaped particles), the densification kinetics was very slow and controlled by the rod-shaped particles.

In all cases, the sintered microstructure did not show any rod-shaped particles in the final structure of these nanopowders due to grain growth.

12.4.1 Microwave Sintering of Nanopowders

The heating of a solid material occurs via two main processes:

- By energy transfer from the surface to the center, via thermal conduction. This is the case of conventional heating, and it is a slow process due to the low thermal conductivity of ceramics. Although various energy losses are associated with this method, it is still the most often used for carrying out various types of heat treatments.

- By energy conversion, where the material as a whole absorbs electromagnetic radiation and converts it into heat via dielectric, magnetic permittivity/eddy currents loss mechanisms. This is the case in RF – induction heating, in lasers, and in microwave processing, all of which provide rapid, highly efficient heating and rapid sintering. (Occasionally, the two methods are combined.)

Microwave energy has been used for over 50 years in a variety of applications, including communications, food processing, rubber vulcanization, textile and wood products, and the drying of ceramic powders. Although the widespread use of microwave home ovens has revolutionized home-cooking, the use of microwaves in the processing of ceramics, especially the sintering of materials, is relatively new.

While the first reported use of microwave in ceramics dates back to 1968, activity in this field began to gather momentum in the late 1970s and continued – with great enthusiasm and excitement – during the 1980s. Due to the internal heating of microwave processing, it is possible to sinter many materials at a much lower temperature and for a shorter time than would be required with conventional methods. In fact, the use of microwave processing reduces typical sintering times by a factor of 10 or more in many cases, thereby minimizing grain growth. Thus, it is possible to retain the initial fine grain structure without using grain growth inhibitors. Recently, it has been shown that the microwave sintering of HA ceramics, both in pure and doped forms, can achieve comparable physical and mechanical properties within 1 h, compared to an 8 h heating cycle under conventional sintering. This significant reduction in processing time is possible due to the volumetric heating of microwaves. The retention of fine grain microstructure and shorter times in microwave sintering are very important. Recently, it was shown that HA nanopowders with <100 nm average size and compacted in a uniaxial press followed by cold isostatic pressing, could be sintered to >95% theoretical density at 1150 °C using a 3 kW microwave source. The final average grain size was <300 nm – which was significantly less than that of conventionally sintered HA. A SEM image of a bulk nanograin HA that has been microwave-sintered at 1150 °C is shown in Figure 12.9. The average grain size in the sample was <250 nm, while the surface hardness was >9 GPa and the compressive strength >400 MPa. Both of these values were significantly higher than reported elsewhere for pure HA ceramics [129].

The effect of HA nanocrystal morphology on bioactivity has also been demonstrated. For this, two types of HA with different nanocrystal morphologies were synthesized using a simple aqueous precipitation method with different reactant molar ratios. The spherical crystal was 40–60 nm in diameter, while the rod-like crystal was 40–55 nm in diameter and 79–100 nm in length. The results indicated that there was a significantly higher cell proliferation on the surface of HA with spherical crystal than with rods. Subsequent SEM observations showed that osteoblasts had spread out a host of filopodia onto the spherical crystal surface, thus exhibiting a much more active cell morphology. These results suggested that HA with spherical nanocrystals showed more favorable properties for osteoblasts than those with a rod-like morphology.

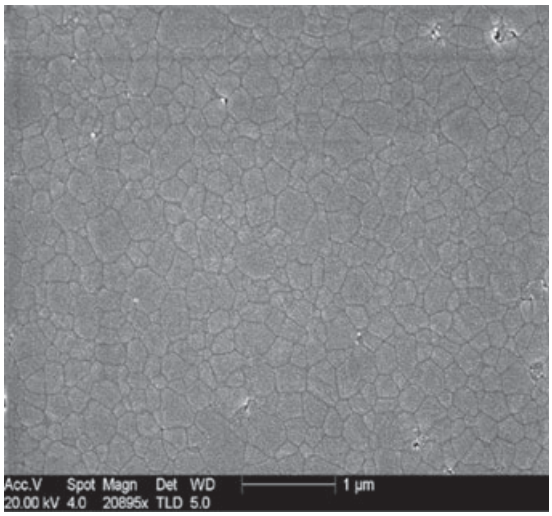

(a)

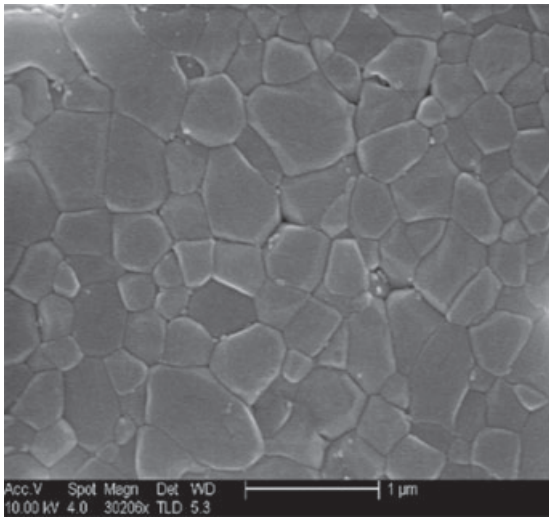

(b)

Figure 12.9 Scanning electron microscopy images of sintered nano-HA, sintered at (a) 1000 and (b) 1100 °C for 30 min in a 3 kW commercial 2.45 GHz microwave.

12.5 Future Trends

Currently, much of the research on HA nanocrystals is broadly classifiable into four categories: (i) high-strength HA using nano-HA and dopants; (ii) HA

scaffolds in tissue engineering; (iii) nanoscale HA coatings for load-bearing implants; and (iv) HA in drug/protein delivery. Among these areas, efforts have been focused on the synthesis of HA nanocrystals with tailored morphology and their processing for bulk nanostructured materials, and also on modifying their surface chemistry to improve drug/protein delivery and *in vitro* and *in vivo* responses.

12.5.1
High-Strength HA using Nano-HA and Dopants

Bone defects are frequently caused by trauma, disease, developmental deformity and tumor removal. Currently, the repair of such bone sites involves a variety of medical and surgical techniques, including the use of autogenous grafts, allogenous grafts, internal and external fixation devices, electrical stimulation and replacement implants. Although effective in many cases, these existing technologies are still plagued with numerous difficulties and disadvantages. Based on *in vivo* response of HA-based materials, it has long been envisioned that HA could be applied to a variety of applications for dental and orthopedic repair and restoration. However, due to the poor mechanical strength of HA-based materials, most of these applications remain focused on coatings or powdered materials only. It is believed that nano-HA, when densified with nanoscale grains, will provide improved strength. Moreover, recent results have suggested that small quantities of dopants may also improve the mechanical properties of HA. Thus, research into nano-HA with dopants is currently being pursued by many groups to produce HA-based parts such as screws, pins and small plates for the repair and reconstruction of bone defects.

12.5.2
HA Scaffolds in Tissue Engineering

One of the key factors identified in the failure of tissue-engineering scaffolds has been insufficient tissue regeneration around and inside the biomaterial, mainly because of a poor surface interaction of the biomaterial with the host tissues. The biomolecules and cells, together with the intrinsic and surface properties of the biomaterials, determine the biocompatibility of the scaffolds. As the biomolecule or cell–material interaction at the surface of a biomaterial is an important phenomenon in its evaluation, biomaterials scientists have begun to investigate the pertinent host–cell interactions in order to design materials that facilitate favorable interactions and enhance tissue regeneration. Because of their excellent cell–materials interactions, HA-based materials are favored as scaffolds for tissue engineering. Today, among the key challenges, the creation of porous scaffolds with mechanical properties comparable to those of cancellous bones, and biological properties that will allow viable tissue ingrowth, represent some of the actively pursued areas.

12.5.3
Nanoscale HA Coatings for Load-Bearing Implants

Today, the most important problem associated with load-bearing implants is their limited lifetime. A simple example is a total hip prosthesis (THP); this is a metallic implant that has a typical lifetime of 7–12 years. Surprisingly, this lifetime has remained constant over the past 50 years, despite several billion dollars having been spent on research and development to effect an increase. Consequently, if a 30-year-old patient receives a THP, by the time they are aged 50 the implant will no longer function. The problem with the THP lies in the bond between the tissue and the implant; a strong bond can potentially double or triple the lifetime of an implant, but too often a weak bond will cause a shortening. In order to develop strong bonds to improve the lifetime of metallic implants, bioactive coatings may be applied. The ideal coating should be gradient in composition from the surface to the inside for better mechanical strength. It is also advantageous to have a controlled porosity in the coatings in order to provide a better biological anchoring and thus improve the cell–material interaction. Likewise, as nanograin HA has demonstrated a better cell–material interaction than micron-grained materials, it is preferable that the final coatings retain a nanograin morphology. Today, several research groups are investigating different coating technologies to produce nanograin HA coatings on metallic surfaces that are not only very adherent but also last longer *in vivo*.

12.5.4
HA in Drug/Protein Delivery

Nanotechnologies have already brought about significant changes in the scale and methods of drug delivery, and show huge potential for future developments. New formulations and routes for drug delivery have shown promise for the delivery of new types of medicine to previously inaccessible sites in the body. In addition to developing completely new therapeutic values, the introduction of upgraded formulations can greatly reduce the risk, time and capital invested in new drug development. Nanoparticle-based drug delivery technology allows the reformulation of existing drugs to increase a product's lifecycle, increase profitability, and expand intellectual property estate. Calcium phosphate (CaP) nanoparticles, including HA nanoparticles, have been recognized as potentially good candidates for carrying biocompatible drugs and biomolecules to targeted sites, as they may be resorbed by cells and promote new bone formation by releasing Ca^{2+} and PO_4^{3-} ions. The CaP nanoparticles, which also possess versatile properties suitable for cellular delivery, are widely available with variable stoichiometry and functionality. Because of the high surface charge density, the surface functionalization of CaP nanoparticles is relatively easy, and this attributes to their potential capabilities for the targeted delivery of drugs and biomolecules to specific sites, and with controlled release properties. Among specific research areas, tailoring of nanoparticle size and morphology, in addition to the chemistry of controlled-release kinetics,

are perhaps the most active. In this way, it might become possible to use these inorganic nanomaterials to release site-specific drugs for several days, rather than simply the first few hours, after administration.

References

1 Weiner, S. and Traub, W. (1992) Bone structure: from angstroms to microns. *FASEB Journal*, **6**, 879–85.

2 Vallet-Regí, M. and González-Calbet, J.M. (2004) Calcium phosphates as substitution of bone tissues. *Progress in Solid State Chemistry*, **32**, 1–31.

3 Eppell, S.J., Tong, W., Katz, J.L., Kuhn, L. and Glimcher, M.J. (2001) Shape and size of isolated bone mineralites measured using atomic force microscopy. *Journal of Orthopaedic Research*, **19**, 1027–34.

4 Jackson, S.A., Cartwright, A.G. and Lewis, D. (1978) The morphology of bone-mineral crystals. *Calcified Tissue International*, **25**, 217–22.

5 Hassenkam, T., Fantner, G.E., Cutroni, J.A., Weaver, J.C., Morse, D.E. and Hansma, P.K. (2004) High resolution AFM imaging of intact and fractured trabecular bone. *Bone*, **35**, 4–10.

6 Dorozhkin, S.V. and Epple, M. (2002) Biological and medical significance of calcium phosphates. *Angewandte Chemie – International Edition in English*, **41**, 3130–46.

7 LeGeros, R.Z. (1991) Calcium phosphate in oral biology and medicine. *Monographs in Oral Science*, **15**, 1–201.

8 Glimcher, M.J. (1998) The nature of the mineral phase in bone: biological and clinical implications, in *Metabolic Bone Disease and Clinically Related Disorders* (eds L.V. Avioli and S.M. Krane), Academic Press, San Diego, CA, pp. 23–50.

9 Weiner, S. and Wagner, H.D. (1998) The material bone: structure mechanical function relations. *Annual Review of Materials Science*, **28**, 271–98.

10 Olszta, M.J., Cheng, X., Soo Jee, S., Kumar, R., Kim, Y.Y., Kaufman, M.J., Douglas, E.P. and Gower, L.B. (2007) Bone structure and formation: a new perspective. *Materials Science and Engineering R*, **58**, 77–116.

11 Zhang, Q., Chen, J., Feng, J., Cao, Y., Deng, C. and Zhang, X. (2003) Dissolution and mineralization behaviors of HA coatings. *Biomaterials*, **24**, 4741–8.

12 White, A.A., Best, S.M. and Kinloch, I.A. (2007) Hydroxyapatite-carbon nanotube composites for biomedical applications: a review. *International Journal of Applied Ceramic Technology*, **4**, 1–13.

13 Posner, A.S., Perloff, A. and Diorio, A.F. (1958) Refinement of the hydroxyapatite structure. *Acta Crystallographica*, **11**, 308–9.

14 Strietzel, F.P., Reichart, P.A., Graf, H.L. (2007) Lateral alveolar ridge augmentation using a synthetic nano-crystalline hydroxyapatite bone substitution material (Ostim®). Preliminary clinical and histological results. *Clinical Oral Implants Research*, **18**, 743–51.

15 Du, C., Cui, F.Z., Feng, Q.L., Zhu, X.D. and de Groot, K. (1998) Tissue response to nano-hydroxyapatite/collagen composite implants in marrow cavity. *Journal of Biomedical Materials Research*, **42**, 540–8.

16 Muller-Mai, C.M., Stupp, S.I., Voigt, C. and Gross, K.A. (1995) Nanoapatite and organoapatite implants in bone: histology and ultrastructure of the interface. *Journal of Biomedical Materials Research*, **29**, 9–18.

17 Yamaguchi, I., Tokuchi, K., Fukuzaki, H., Koyama, Y., Takakuda, K., Monma, H. and Tanaka, J. (2001) Preparation and microstructure analysis of chitosan/hydroxyapatite nanocomposites. *Journal of Biomedical Materials Research*, **55**, 20–7.

18 Itoh, S., Kikuchi, M., Koyama, Y., Takakuda, K., Shinomiya, K. and Tanaka, J. (2002) Development of an artificial vertebral body using a novel biomaterial,

hydroxyapatite/collagen composite. *Biomaterials*, **23**, 3919–26.
19 Kikuchi, M., Itoh, S., Ichinose, S., Shinomiya, K. and Tanaka, J. (2001) Self-organization mechanism in a bone like hydroxyapatite/collagen nanocomposite synthesized *in vivo* and its biological reaction *in vivo*. *Biomaterials*, **22**, 1705–11.
20 Du, C., Cui, F.Z., Zhu, X.D. and de Groot, K. (1999) Three-dimensional nano-HAp/collagen matrix loading with osteogenic cells in organ culture. *Journal of Biomedical Materials Research*, **44**, 407–15.
21 Cho, C., Kobayashi, A., Takei, R., Ishihara, T., Maruyama, A. and Akaike, T. (2001) Receptor-mediated cell modulator delivery to hepatocyte using nanoparticles coated with carbohydrate-carrying polymers. *Biomaterials*, **22**, 45–51.
22 Liu, T.Y., Chen, S.Y., Liu, D.M. and Liou, S. (2005) On the study of BSA-loaded calcium-deficient hydroxyapatite nano-carriers for controlled drug delivery. *Journal of Controlled Release*, **107**, 112–21.
23 Olton, D., Li, J., Wilson, M.E., Rogers, T., Close, J., Huang, L., Kumta, P.N. and Sfeir, C. (2007) Nanostructured calcium phosphates (NanoCaPs) for non-viral gene delivery: influence of the synthesis parameters on transfection efficiency. *Biomaterials*, **28**, 1267–79.
24 Ong, H.T., Loo, J.S.C., Boey, F.Y.C., Russell, S.J., Ma, J. and Peng, K.-W. (2008) Exploiting the high-affinity phosphonate-hydroxyapatite nanoparticle interaction for delivery of radiation and drugs. *Journal of Nanoparticle Research*, **10**, 141–50.
25 Montastruc, L., Azzaro-Pantel, C., Biscans, B., Cabassud, M., and Domenech, S. (2003) A thermochemical approach for calcium phosphate precipitation modeling in a pellet reactor. *Chemical Engineering Journal*, **94**, 41–50.
26 Kumar, R., Prakash, K., Cheang, P. and Khor, K. (2004) Temperature driven morphological changes of chemically precipitated hydroxyapatite nanoparticles. *Langmuir*, **20**, 5196–200.
27 Pang, Y. and Bao, X. (2003) Influence of temperature, ripening time and calcination on the morphology and crystallinity of hydroxyapatite nanoparticles. *Journal of the European Ceramic Society*, **23**, 1697–704.
28 Bouyer, E., Gitzhofer, F. and Boulos, M. (2000) Morphological study of hydroxyapatite nanocrystal suspension. *Journal of Materials Science: Materials in Medicine*, **11**, 523–31.
29 Jarcho, M., Kay, J., Gumaer, K., Doremus, R. and Drobeck, H. (1977) Tissue, cellular and subcellular events at bone ceramic hydroxyapatite interface. *Journal of Bioengineering*, **1**, 79–92.
30 Yubao, L., de Groot, K., De Wijn, J., Klein, C.P.A.T. and Meer, S.V.D. (1994) Morphology and composition of nanograde calcium phosphate needle-like crystals formed by simple hydrothermal treatment. *Journal of Materials Science: Materials in Medicine*, **5**, 326–31.
31 Gomez-Morales, J., Torrent-Burgues, J., Boix, T., Fraile, J. and Rodriguez-Clemente, R. (2001) Precipitation of stoichiometric hydroxyapatite by a continuous method. *Crystal Research and Technology*, **36**, 15–26.
32 Torrent-Burgues, J. and Rodriguez-Clemente, R. (2001) Hydroxyapatite precipitation in a semibatch process. *Crystal Research and Technology*, **36**, 1075–82.
33 Ahn, E., Gleason, N., Nakahira, A. and Ying, J. (2001) Nanostructure processing of hydroxyapatite-based bioceramics. *Nano Letters*, **1**, 149–53.
34 Liu, C., Huang, Y., Shen, W. and Cui, J. (2001) Kinetics of hydroxyapatite precipitation at pH 10 to 11. *Biomaterials*, **22**, 301–6.
35 Lazic, S., Zec, S., Miljevic, N. and Milonjic, S. (2001) The effect of temperature on the properties of hydroxyapatite precipitated from calcium hydroxide and phosphoric acid. *Thermochimica Acta*, **374**, 13–22.
36 Elliott, J., Holcomb, D. and Young, R. (1985) Infrared determination of the degree of substitution of hydroxyl by

carbonate ions in human dental enamel. *Calcified Tissue International*, **37**, 372–5.

37 Jillavenkatesa, A. and Condrate, R. (1998) Sol-gel processing of hydroxyapatite. *Journal of Materials Science: Materials in Medicine*, **33**, 4111–19.

38 Lopatin, C., Pizziconi, V., Alford, T. and Laursen, T. (1998) Hydroxyapatite powders and thin films prepared by a sol-gel technique. *Thin Solid Films*, **326**, 227–32.

39 Gross, K., Chai, C., Kannangara, G.S.K., Ben-Nissan, B. and Hanley, L. (1998) Thin hydroxyapatite coatings via sol-gel synthesis. *Journal of Materials Science: Materials in Medicine*, **9**, 839–43.

40 Masuda, Y., Matubara, K. and Sakka, S. (1990) Synthesis of hydroxyapatite from metal alkoxides through sol-gel technique. *Journal of the Ceramic Society of Japan*, **98**, 1266–77.

41 Brendel, T., Engel, A. and Russel, C. (1992) Hydroxyapatite coating by polymeric route. *Journal of Materials Science: Materials in Medicine*, **3**, 175–9.

42 Takahashi, H., Yashima, M., Kakihana, M. and Yoshimura, M. (1995) Synthesis of stoichiometric hydroxyapatite by a gel route from the aqueous solution of citric and phosphoneacetic acids. *European Journal of Solid State Inorganic Chemistry*, **32**, 829–35.

43 Haddow, D., James, P. and Van Noort, R. (1996) Characterization of sol-gel surfaces for biomedical applications. *Journal of Materials Science: Materials in Medicine*, **7**, 255–60.

44 Kuriakose, T., Kalkura, S., Palanichamy, M., Arivuoli, D., Dierks, K., Bocelli, G. and Betzel, C. (2004) Synthesis of stoichiometric nano crystalline hydroxyapatite by ethanol-based sol–gel technique at low temperature. *Journal of Crystal Growth*, **263**, 517–23.

45 Bogdanoviciene, I., Beganskiene, A., Tõnsuaadu, K., Glaser, J., Meyer, H. and Kareiva, A. (2006) Calcium hydroxyapatite, $Ca_{10}(PO_4)_6(OH)_2$ ceramics prepared by aqueous sol–gel processing. *Materials Research Bulletin*, **41**, 1754–62.

46 Layrolle, P., Ito, A. and Tateishi, T. (1998) Sol-gel synthesis of amorphous calcium phosphate and sintering into microporous hydroxyapatite bioceramics. *Journal of the American Ceramic Society*, **81**, 1421–8.

47 Liu, D., Troczynski, T. and Tseng, W. (2001) Water-based sol–gel synthesis of hydroxyapatite: process development. *Biomaterials*, **22**, 1721–30.

48 Liu, D., Yang, Q., Troczynski, T. and Tseng, W. (2002) Structural evolution of sol–gel-derived hydroxyapatite. *Biomaterials*, **23**, 1679–87.

49 Han, Y., Li, S., Wang, X. and Chen, X. (2007) Preparation of hydroxyapatite rod-like crystals by protein precursor method. *Materials Research Bulletin*, **42**, 1169–77.

50 Bose, S. and Saha, S. (2003) Synthesis of hydroxyapatite nanopowders via sucrose-templated sol-gel method. *Journal of the American Ceramic Society*, **96**, 1055–7.

51 Eshtiagh-Hosseini, H., Housaindokht, M. and Chahkandi, M. (2007) Effects of parameters of sol–gel process on the phase evolution of sol–gel-derived hydroxyapatite. *Materials Chemistry and Physics*, **106**, 310–16.

52 Kokubo, T. and Takadama, H. (2006) How useful is SBF in predicting in vivo bone bioactivity? *Biomaterials*, **27**, 2907–15.

53 Li, P., Ohtsuki, C., Kokubo, T., Nakanishi, K., Soga, N., Nakamura, T. and Yamamuro, T. (1992) Apatite formation induced by silica gel in a simulated body fluid. *Journal of the American Ceramic Society*, **75**, 2094–7.

54 Li, P., Ohtsuki, C., Kokubo, T., Nakanishi, K., Soga, N. and de Groot, K. (1994) A role of hydrated silica, titania and alumina in forming biologically active bone-like apatite on implant. *Journal of Biomedical Materials Research*, **28**, 7–15.

55 Uchida, M., Kim, H.M., Kokubo, T. and Nakamura, T. (2001) Bonelike apatite formation induced on zirconia gel in simulated body fluid and its modified solutions. *Journal of the American Ceramic Society*, **84**, 2041–4.

56 Miyazaki, T., Kim, H.M., Kokubo, T., Ohtsuki, C., Kato, H. and Nakamura, T.

(2001) Apatite-forming ability of niobium oxide gels in a simulated body fluid. *Journal of the Ceramic Society of Japan*, **109**, 929–33.

57 Miyazaki, T., Kim, H.M., Kokubo, T., Kato, H. and Nakamura, T. (2001) Induction and acceleration of bonelike apatite formation on tantalum oxide gel in simulated body fluid. *Journal of Sol-Gel Science and Technology*, **21**, 83–8.

58 Barrére, F., van der Valk, C., Dalmeijer, R., Van Blitterswijk, C., de Groot, K. and Layrolle, P. (2003) *In vivo* and *in vivo* studies of biomimetic octacalcium phosphate and carbonate apatite coatings on titanium implants. *Journal of Biomedical Materials Research*, **64A**, 378–87.

59 Habibovic, P., Barrére, F., van Blitterswijk, C., de Groot, K. and Layrolle, P. (2002) Biomimetic hydroxyapatite coating on metal implants. *Journal of the American Ceramic Society*, **85**, 517–22.

60 Liu, Y., Layrolle, P., van Blitterswijk, C. and de Groot, K. (2001) Biomimetic coprecipitation of calcium phosphate and bovine serum albumin on titanium alloy. *Journal of Biomedical Materials Research*, **57**, 327–35.

61 Wen, H., de Wijn, J., van Blitterswijk, C. and De Groot, K. (1999) Incorporation of bovine serum albumin in calcium phosphate coating on titanium. *Journal of Biomedical Materials Research*, **46**, 245–52.

62 Stupp, S. and Braun, P. (1997) Molecular manipulation of microstructures: biomaterials, ceramics, and semiconductors. *Science*, **277**, 1242–8.

63 Kokubo, T., Kim, H. and Kawashita, M. (2003) Novel bioactive materials with different mechanical properties. *Biomaterials*, **24**, 2161–75.

64 Wan, Y., Hong, L., Jia, S., Huang, Y., Zhu, Y., Wang, Y. and Jiang, H. (2006) Synthesis and characterization of hydroxyapatite-bacterial cellulose nanocomposites. *Composites Science and Technology*, **66**, 1825–32.

65 Hutchens, S., Benson, R., Evans, B., O'Neill, H. and Rawn, C. (2006) Biomimetic synthesis of calcium-deficient hydroxyapatite in a natural hydrogel. *Biomaterials*, **27**, 4661–70.

66 Jinhui, T., Pan, H., Zeng, Y., Xu, X. and Tang, R. (2007) Roles of amorphous calcium phosphate and biological additives in the assembly of hydroxyapatite nanoparticles. *Journal of Physical Chemistry B*, **111**, 13410–18.

67 Hoffmann, C., Zollfrank, C. and Ziegler, G. (2008) Enzyme-catalysed synthesis of calcium phosphates. *Journal of Materials Science: Materials in Medicine*, **19**, 907–15.

68 Kim, H., Kim, H. and Salih, V. (2005) Stimulation of osteoblast responses to biomimetic nanocomposites of gelatin–hydroxyapatite for tissue engineering scaffolds. *Biomaterials*, **26**, 5221–30.

69 Kikuchi, M., Ikoma, T., Itoh, S., Matsumoto, H., Koyama, Y., Takakuda, K., Shinomiya, K. and Tanaka, J. (2004) Biomimetic synthesis of bone-like nanocomposites using the self-organization mechanism of hydroxyapatite and collagen. *Composites Science and Technology*, **64**, 819–25.

70 Suchanek, W., Byrappa, K., Shuk, P., Riman, R., Janas, V. and TenHuisen, K. (2004) Preparation of magnesium-substituted hydroxyapatite powders by the mechanochemical–hydrothermal method. *Biomaterials*, **25**, 4647–57.

71 Li, Y., de Wijn, J., Klein, C., Van De Meer, S. and De Groot, K. (1994) Preparation and characterization of nanograde osteoapatite-like rod crystals. *Journal of Materials Science: Materials in Medicine*, **5**, 252–5.

72 Li, Y., de Groot, K., De Wijn, J., Klein, C.P.A.T. and Meer, S.V.D. (1994) Morphology and composition of nanograde calcium phosphate needle-like crystals formed by simple hydrothermal treatment. *Journal of Materials Science: Materials in Medicine*, **5**, 326–31.

73 Riman, R., Suchanek, W., Byrappa, K., Chen, C., Shuk, P. and Oakes, C. (2002) Solution synthesis of hydroxyapatite designer particulates. *Solid State Ionics*, **151**, 393–402.

74 Liu, J., Ye, X., Wang, H., Zhu, M., Wang, B. and Yan, H. (2003) The influence of pH and temperature on the morphology

of hydroxyapatite synthesized by hydrothermal method. *Ceramic International*, **29**, 629–33.
75 Yan, L., Li, Y., Deng, Z., Zhuang, J. and Sun, X. (2001) Surfactant-assisted hydrothermal synthesis of hydroxyapatite nanorods. *International Journal of Inorganic Materials*, **3**, 633–7.
76 Chen, J.D., Wang, Y.J., Wei, K., Zhang, S.H. and Shi, X.T. (2007) Self-organization of hydroxyapatite nanorods through oriented attachment. *Biomaterials*, **28**, 2275–80.
77 Gutman, E. (1997) *Mechanochemistry of Materials*, Cambridge International Science Publishing, Cambridge, UK.
78 El Briak-BenAbdeslam, H., Ginebra, M., Vert, M. and Boudeville, P. (2008) Wet or dry mechanochemical synthesis of calcium phosphates? Influence of the water content on DCPD–CaO reaction kinetics. *Acta Biomaterialia*, **4**, 378–86.
79 Yeong, K., Wang, J. and Ng, S. (2001) Mechanochemical synthesis of nanocrystalline hydroxyapatite from CaO and $CaHPO_4$. *Biomaterials*, **22**, 2705–12.
80 Toriyama, M., Ravaglioli, A., Krajewski, A., Celotti, G. and Piancastelli, A. (1996) Synthesis of hydroxyapatite-based powders by mechano-chemical method and their sintering. *Journal of the European Ceramic Society*, **16**, 429–36.
81 Suchanek, W.L., Byrappa, K., Shuk, P., Riman, R.E., Janas, V.F. and TenHuisen, K.S. (2004) Preparation of magnesium-substituted hydroxyapatite powders by the mechanochemical–hydrothermal method. *Biomaterials*, **25**, 4647–57.
82 Tian, T., Jiang, D., Zhang, J. and Lin, Q. (2008) Synthesis of Si-substituted hydroxyapatite by a wet mechanochemical method. *Materials Science and Engineering C*, **28**, 57–63.
83 Nikcevic, I., Jokanovic, V., Mitric, M., Nedic, Z., Makovec, D. and Uskokovic, D. (2004) Mechanochemical synthesis of nanostructured fluorapatite/fluorhydroxyapatite and carbonated fluorapatite/fluorhydroxyapatite. *Journal of Solid State Chemistry*, **177**, 2565–74.
84 Cai, S., Wang, Y., Lu, H., Peng, Z. and Yao, K. (2005) Synthesis of carbonated hydroxyapatite nanofibers by mechanochemical methods. *Ceramics International*, **31**, 135–8.
85 Coreno, A., Coreno, A., Cruz, R. and Rodriguez, C. (2005) Mechanochemical synthesis of nanocrystalline carbonate-substituted hydroxyapatite. *Optical Materials*, **27**, 1281–5.
86 Yoshimura, M. and Suchanek, W. (1997) In situ fabrication of morphology-controlled advanced ceramic materials by soft, solution processing. *Solid State Ionics*, **98**, 197–208.
87 Kosova, N., Khabibullin, A. and Boldyrev, V. (1997) Hydrothermal reactions under mechanochemical treating. *Solid State Ionics*, **101–103**, 53–8.
88 Murugan, R. and Ramakrishna, S. (2007) Development of cell-responsive nanophase hydroxyapatite for tissue engineering. *American Journal of Biochemistry and Biotechnology*, **3**, 118–24.
89 Arita, I., Castano, V. and Wilkinson, D. (1995) Synthesis and processing of hydroxyapatite ceramic tapes with controlled porosity. *Journal of Materials Science: Materials in Medicine*, **6**, 19–23.
90 Rao, R., Roopa, H., and Kannan, T. (1997) Solid state synthesis and thermal stability of HAP and HAP-beta-TCP composite ceramic powders. *Journal of Materials Science: Materials in Medicine*, **8**, 511–18.
91 Ota, Y., Iwashita, T., Kasuga, T. and Abe, Y. (1998) Novel preparation method of hydroxyapatite fibers. *Journal of the American Ceramic Society*, **81**, 1665–8.
92 Pramanik, S., Agarwal, A., Rai, K. and Garg, A. (2007) Development of high strength hydroxyapatite by solid-state-sintering process. *Ceramics International*, **33**, 419–26.
93 Fowler, B. (1974) Infrared studies of apatites II. Preparation of normal and isotopically substituted calcium, strontium, and barium hydroxyapatites and spectra-structure-composition correlations. *Inorganic Chemistry*, **13**, 207–14.
94 Cao, J., Feng, J., Deng, S., Chang, X., Wang, J., Liu, J., Lu, P., Lu, H., Zheng,

M., Zhang, F. and Tao, J. (2005) Microwave-assisted solid-state synthesis of hydroxyapatite nanorods at room temperature. *Journal of Materials Science: Materials in Medicine*, **40**, 6311–13.

95 Parhi, P., Ramanan, A. and Ray, A. (2004) A convenient route for the synthesis of hydroxyapatite through a novel microwave-mediated metathesis reaction. *Materials Letters*, **58**, 3610–12.

96 Feng, J., Cao, J. and Deng, S. (2005) A novel microwave solid-state method of nano-hydroxyapatite. *Chinese Journal of Inorganic Chemistry*, **21**, 801–4.

97 Sarig, S. and Kahana, F. (2002) Rapid formation of nanocrystalline apatite. *Journal of Crystal Growth*, **237–239**, 55–9.

98 Torrent-Burgues, J., Gomez-Morales, J., Lopez-Macipe, A. and Rodriguez-Clemente, R. (1999) Continuous precipitation of hydroxyapatite from Ca/citrate/phosphate solutions using microwave heating. *Crystal Research and Technology*, **34**, 757–62.

99 Pileni, M. (1993) Reverse micelles as microreactors. *Journal of Physical Chemistry*, **97**, 6961–73.

100 Pileni, M., Zemb, T. and Petit, C. (1985) Solubilization by reverse micelles: solute localization and structure perturbation. *Chemical Physics Letters*, **118**, 414–20.

101 Zulauf, M. and Eicke, H. (1979) Inverted micelles and microemulsions in the ternary system H_2O/aerosol-OT/isooctane as studied by photon correlation spectroscopy. *Journal of Physical Chemistry*, **83**, 480–6.

102 Bose, S. and Saha, S. (2003) Synthesis and characterization of hydroxyapatite nanopowders by emulsion technique. *Chemistry of Materials*, **15**, 4464–9.

103 Banerjee, A., Bandyopadhyay, A. and Bose, S. (2007) Hydroxyapatite nanopowders: synthesis, densification and cell–materials interaction. *Materials Science and Engineering C*, **27**, 729–35.

104 Lim, G., Wang, J., Ng, S., Chew, C. and Gan, L. (1997) Processing of hydroxyapatite via microemulsion and emulsion routes. *Biomaterials*, **18**, 1433–9.

105 Lim, G., Wang, J., Ng, S. and Gan, L. (1999) Formation of nanocrystalline hydroxyapatite in nonionic surfactant emulsions. *Langmuir*, **15**, 7472–7.

106 Lim, G., Wang, J., Ng, S. and Gan, L. (1999) Nanosized hydroxyapatite powders from microemulsions and emulsions stabilized by a biodegradable surfactant. *Journal of Materials Chemistry*, **9**, 1635–9.

107 Liu, Y., Wang, W., Zhan, Y., Zheng, C. and Wang, G. (2002) A simple route to hydroxyapatite nanofibers. *Materials Letters*, **56**, 496–501.

108 Yao, J., Tjandra, W., Chen, Y., Tam, K., Ma, J. and Soh, B. (2003) Hydroxyapatite nanostructure material derived using cationic surfactant as a template. *Journal of Materials Chemistry*, **13**, 3053–7.

109 Koumoulidis, G., Katsoulidis, A., Ladavos, A., Pomonis, P., Trapalis, C., Sdoukos, A. and Vaimakis, T. (2003) Preparation of hydroxyapatite via microemulsion route. *Journal of Colloid and Interface Science*, **259**, 254–60.

110 Wu, Y., Bose, S. and Hydroxyapatite, N. (2005) Micelle templated synthesis and characterization. *Langmuir*, **21**, 3232–4.

111 Sonoda, K., Furuzono, T., Walsh, D., Sato, K. and Tanaka, J. (2002) Influence of emulsion on crystal growth of hydroxyapatite. *Solid State Ionics*, **151**, 321–7.

112 Bertoni, E., Bigi, A., Falini, G., Panzavolta, S. and Roveri, N. (1999) Hydroxyapatite polyacrylic acid nanocrystals. *Journal of Materials Chemistry*, **9**, 778–82.

113 Zhang, S. and Gonsalves, K. (1997) Preparation and characterization of thermally stable nanohydroxyapatite. *Journal of Materials Science: Materials in Medicine*, **8**, 25–8.

114 Sinha, A., Nayar, S., Agrawal, A. and Bhattacharyya, D. (2003) Synthesis of nanosized and microporous precipitated hydroxyapatite in synthetic polymers and biopolymers. *Journal of the American Ceramic Society*, **86**, 357–9.

115 Kumar, R., Cheang, P. and Khor, K. (2001) RF plasma processing of ultra-fine hydroxyapatite powders. *Journal of*

Materials Processing Technology, **113**, 456–62.

116 Wang, X., Zhuang, J., Peng, Q. and Li, Y. (2006) Liquid-solid-solution synthesis of biomedical hydroxyapatite nanorods. *Advanced Materials*, **18**, 2031–4.

117 Scherrer, P. (1918) *Gottinger Nachrichten*, **2**, 98.

118 Brunauer, S., Emmett, P. and Teller, E. (1938) Adsorption of gases in multimolecular layers. *Journal of the American Chemical Society*, **60**, 309–19.

119 Ducheyne, P. and Qiu, Q. (1999) Bioactive ceramics: the effect of surface reactivity on bone formation and bone cell function. *Biomaterials*, **20**, 2287–303.

120 Xue, W., Moore, J., Hosick, H., Bose, S., Bandyopadhyay, A., Lu, W., Cheung, K. and Luk, K. (2006) Osteoprecursor cell response to strontium-containing hydroxyapatite. *Journal of Biomedical Materials Research*, **79A**, 804–14.

121 Lee, K., Wang, S., Yaszemski, M. and Lu, L. (2008) Physical properties and cellular responses to crosslinkable poly(propylene fumarate)/hydroxyapatite nanocomposites. *Biomaterials*, **29**, 2839–48.

122 Rokusek, D., Davitt, C., Bandyopadhyay, A., Bose, S. and Hosick, H.L. (2005) Interaction of human osteoblasts with bioinert and bioactive ceramic substrates. *Journal of Biomedical Materials Research*, **75**, 588–94.

123 Balani, K., anderson, R., Laha, T., Andara, M., Tercero, J., Crumpler, E. and Agarwal, A. (2007) Plasma-sprayed carbon nanotube reinforced hydroxyapatite coatings and their interaction with human osteoblasts in vitro. *Biomaterials*, **28**, 618–24.

124 Bauer, I.W., Li, S.P., Han, Y.C., Yuan, L. and Yin, M.Z. (2008) Internalization of hydroxyapatite nanoparticles in liver cancer cells. *Journal of Materials Science: Materials in Medicine*, **19**, 1091–5.

125 Murray, M.G.S., Wang, J., Ponton, C.B. and Marquis, P.M. (1995) An improvement in processing of hydroxyapatite ceramics. *Journal of Materials Science: Materials in Medicine*, **30**, 3061–74.

126 Luo, P. and Neigh, T.G. (1996) Preparing hydroxyapatite powders with controlled morphology. *Biomaterials*, **17**, 1959–64.

127 Ruys, A.J., Wei, M., Sorell, C.C., Dickson, M.R., Brandwood, A. and Milthrope, B.K. (1995) Sintering effects on the strength of hydroxyapatite. *Biomaterials*, **16**, 409–15.

128 Aizawa, M., Hanazawa, T., Itatani, K., Howell, F.S. and Kishioka, A. (1999) Characterization of hydroxyapatite powders prepared by ultrasonic spray-pyrolysis technique. *Journal of Materials Science: Materials in Medicine*, **34**, 2865–73.

129 Dasgupta, S. (2008) Nanostructured hydroxyapatite and tricalcium phosphate based ceramics for bovine serum albumin protein delivery and bone implants using microwave sintering. PhD Thesis, Washington State University.

Keywords

hydroxyapatite; nanoparticles; synthesis; processing; surfactant; nanograin; microwave sintering; bioceramic

13
Calcium Phosphate Nanoparticles in Biomineralization and Biomaterials

Ruikang Tang and Yurong Cai

13.1
Introduction

Living organisms are capable of creating amazing ways to produce high-performance materials, with in excess of 60 such different biological minerals already having been identified [1]. Among these, calcium phosphates have a special place as they are the most important inorganic constituents of biological hard tissues in vertebrates [2, 3]. In the form of carbonate-containing hydroxyapatite (HA), calcium phosphates are present in bone, teeth and tendons to provide these organs with stability, hardness and function [4, 5]. Although it is unclear why high-intelligence animals select calcium phosphates as their crucial biomineral for survival, the current biomedical questions of persistent pathological and physiological mineralization in the body have forced investigators to focus on the occurrence, formation and degradation of calcium phosphate minerals in living organisms [6–8].

Calcium phosphates are sparingly soluble electrolytes, and can be conveniently synthesized in the laboratory simply by mixing calcium and phosphate in aqueous solution. The calcium phosphate crystals produced in the supersaturated aqueous solution always have a considerable size [9, 10], whereas biologically formed calcium phosphate [3] often occurs as nanocrystals that are precipitated under mild conditions. Based on many reports, the size of biological apatite in biological hard tissues always ranges from a few nanometers to many hundreds of nanometers [11]. In differing from synthesized bulk materials, biominerals exhibit many levels of hierarchical structure, from the macroscale to the nanoscale [12, 13]. Despite their complicated hierarchical structures, the smallest building blocks among these biomaterials are generally on the nanometer scale [14]; for example, within the collagen matrix, tens to hundreds of nanometer-sized calcium phosphate crystals combine into self-assembled apatite during the formation of bone and enamel. Recent advances have suggested that this process is a natural selection, as nanostructured materials provide the capability for specific interactions with proteins [15].

Biological mineralization ('biomineralization') is the process of the *in vivo* formation of inorganic minerals. The new theory of 'aggregation-based crystal growth'

Nanomaterials for the Life Sciences Vol. 2: Nanostructured Oxides. Edited by Challa S. S. R. Kumar

ISBN: 978-3-527-32152-0

[16] and the new concept of 'mesocrystals' [17, 18] highlight the roles of nanoparticles in biological crystal engineering, and the mimicking of the formation of natural calcium phosphate hard tissues has contributed significantly towards identifying the biological function of these engineered materials. Recently, with the rapid growth of nanotechnology, many advances have been made in biomaterials [19] such that today, the study of calcium phosphates represents a specific area of nanotechnology that may be applied readily to the repair of hard and soft skeletal tissues [20, 21].

Other related areas include the creation of new biocompatible delivery systems for cellular therapy and agricultural fertilizers [22, 23]. It has been suggested that nanophase calcium phosphates can mimic the dimensions of constituent components of natural tissues, and consequently nanocalcium phosphates can be utilized for tissue-engineered implants with improved biocompatibility [24]. In this respect, it is the development of calcium phosphate biomedical materials that stands to benefit most from such nanotechnology.

Calcium phosphates have for a long time attracted intensive attention due to their biological and medical significances. While Dorozhkin and Epple [25] originally introduced the different phase of calcium phosphates and their applications in biomedical materials, it was shown recently that nano-calcium phosphate can provide a protective environment that shields biomolecules from degradation, while providing a pathway for controlled release. Adamopoulos and Papadopoulos [26] summarized the applications of nano-calcium phosphate ceramics and suggested that the combination of bioceramics and nanotechnology would result in enhanced skeletal interactions in maxillofacial applications. Calcium phosphate materials serve as attractive cement materials because of their established biocompatibility and ease of handling. Recently, Ginebra *et al.* [27] reviewed the development of calcium phosphate as biological cements, highlighting the performances of calcium phosphate cements as carriers of different types of drug, including antibiotics, analgesics and anticancer and anti-inflammatory agents, as well as growth factors. Bohner [28] referred to an understanding of the processes involved during the various stages of the calcium phosphate cement setting reaction, by reviewing the current methods used to monitor and modify calcium phosphate cement setting rates. Bohner concluded that a better control of calcium phosphate cement setting rate might be achieved by optimizing the fabrication parameters of cement. Cui *et al.* [29] discussed the current understanding of the structure, self-assembly mechanisms and properties of mineralized collagen fibril composites in connective tissues, as well as involving the biomimetic synthesis of new materials with the structure of mineralized collagen and applications of mineralized collagen composites in bone regeneration.

In the present authors' laboratory, the studies focus on the preparation, assembly and application of nano-calcium phosphate in biomineralization and biomaterials, including the discovery of nano-calcium phosphate in bone and dental enamel, its stability within a biological milieu, biomimetic construction by using nano-calcium phosphates, and their application in biomaterials.

13.2
Nano-Calcium Phosphates in Hard Tissues

13.2.1
Bone

Bone – which is the most typical calcified tissue among organisms – is produced in all sorts of shapes and sizes, the goal being to achieve various functions of protection and mechanical support for the body. The major inorganic component of bone mineral is HA [30, 31]; in fact, the structural chemistry of biological apatite is highly complex because the mineral is not compositionally pure, often being calcium-deficient and enriched in carbonate [32]. Although we generally refer to the bone mineral as HA, several other calcium phosphate phases are known to exist in the biological mineral, including octacalcium phosphate (OCP) and amorphous calcium phosphate (ACP). The structural distinctions of these phases derive from the different ratios of Ca : P and different degrees of protonation of PO_4^{3-} and hydroxylation of Ca^{2+} that have been identified as intermediates in the biomineralization of HA [33].

Many levels of the hierarchical structure of bone, from macroscopic to microscopic length scales, represent yet another marvel that has been developed by these organisms. According to Weiner and Wagner [34], isolated nanosized calcium phosphate crystals from human bone, together with part of an unmineralized and unstained collagen fibril, comprise the first level of the hierarchical structure, while at the second level the crystals are embedded in the fibrous protein collagen. These mineralized fibers lie bundled together and attached to each other, and this comprises the third level of bone structure. At the next level (level 4), several fibers come together to form sheets that are then assembled with bone cells residing between adjacent layers. Together, these are either stacked in parallel arrays or arranged concentrically into a cylindrical structure, referred to as the osteon (level 5). Each layer of the osteon has its constituent fibrils oriented in alternate directions, in the same way as plywood. On a larger scale, the osteons are grouped together into long bundles that form the basic building blocks of various bone microstructures. These include highly porous frameworks and more dense architectures, such as those found in cortical bone (level 6). Each of these structures has a similar underlying building block, but different spatial organizations according to certain structure–function relationships within the whole bone. Finally, at the macroscopic level, each bone has a specific shape and structure so that the skeleton can function as an integrated whole (level 7). Several levels of the hierarchical structure of bone, from macroscopic to microscopic scales, have been extensively discussed [35]. At the nanometer level, the structure consists of type I collagen molecules interspersed with nanocrystals of carbonated HA. A composite of these two constituents forms the mineralized nanocollagen fibril. It is of interest to note that the smallest building blocks in biological minerals are generally designed at the nanoscale, and this is why bone is usually referred to as a

fiber-reinforced composite in which nanometer-sized hard inclusions are embedded in the soft protein matrix [36]. Although the reported sizes of bone crystals vary according to the different treatment methods and analytical techniques, in general they retain a nanometer level with lengths ranging from 30 to 50 nm, width from 15 to 30 nm, and thicknesses from 2 to 10 nm [37]. The question remains, however, as to why the nanometer scale is so important to bone? It was shown recently that, in Nature, nanocomposites exhibit a generic mechanical structure in which the nanometer size of mineral particles is selected to ensure the optimum strength and maximum tolerance of flaws [38, 39]. In addition, nanosized HA has another crucial function for organisms, serving as a vast reservoir of the calcium and phosphate ions that re necessary for a wide range of metabolic functions [40]. In this way, both calcium and phosphate can be made available or consumed via a so-called 'remodeling of the biomineral' process as a result of the resorption and formation of nano-HA by osteoclasts and osteoblasts, in a delicate equilibrium.

13.2.2 Tooth

Tooth is another calcified phase in human and other vertebrates. Unlike bone, teeth consist of at least two different biominerals, the enamel (crown, the part above the gum line) and dentin (roots, the part below the gum line) [41].

Enamel typically contains 96% mineral, 1% organic material and 3% water, with the apatite rods being composed of rod-like HAP crystals measuring 25 to 100 nm in diameter, and with an undetermined length ranging from 100 nm to 100 μm, or longer, along the c-axis [42–45]. When examined with atomic force microscopy (AFM), the apatite crystals in enamel can be seen to exhibit regular subdomains or subunits with distinct chemical properties [46]. Enamel also has a seven-level hierarchical structure, from macrostructure to microstructure, to ensure a specific mechanical stress (Figure 13.1) [47]. At level 1, the major component is hexagonal HA crystals, whilst at the nanoscale the crystals initially form mineral nanofibrils (level 2). These nanofibrils are the most unique structural units of enamel, and align lengthways and aggregate into fibrils (level 3) and further into thicker fibers (level 4). The fibrils and fibers then cluster parallel to each other in two different preferential orientations, assembling into prism/interprism continua (level 5) at the mesoscale. At the microscale, prisms assemble into prism bands (level 6), which present differing arrangements across the thickness of the enamel layer (level 7). These compositional and structural characters endow enamel with special properties such as an anisotropic elastic modulus, effective viscoelastic properties, much higher fracture toughness and a stress–strain relationship which is more similar to that for metals than for ceramics.

The nanosized HA building block in dentin is smaller than that of enamel, being about 25 nm wide, 4 nm thick and 35 nm long. Dentin is similar to bone in many respects, including a similar composition and hierarchical structure up to the level of the lamellae bone; hence, most of the statements made above relating to bone are equally applicable to dentin. Although the chemical composition of mineral in

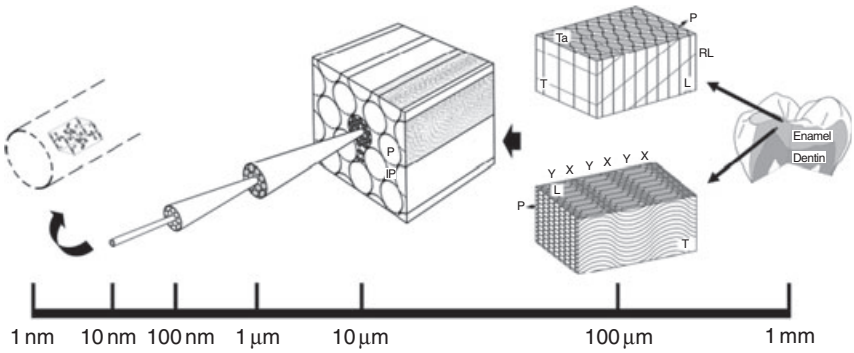

Figure 13.1 Schematic illustration (not drawn to scale) of the hierarchical assembly of enamel structure, from the millimeter to the nanometer scale. The ruler below the diagram demonstrates the typical scale distribution of each assembly level. IP, interprism; L, longitudinal plane; P, prism; RL, Retzius line; T, transverse plane; Ta, tangential plane; X, prisms appear as bands of approximately cross-sectioned; Y, prisms are relatively longitudinally arrayed. Reprinted from Ref. [47].

enamel and dentin is HA, some OCP has also been found at the centers of enamel crystals and dentin; this has been considered as an intermediate phase from younger enamel/dentin to mature enamel/dentin. The enamel mineral differs from ideal HA, as it incorporates HPO_4^{2-}, CO_3^{2-}, Na^+ and other ions within its apatite lattice.

13.2.3
Other Biological Organisms

Except for bone and tooth, normal calcium phosphate minerals also exist in mineralized cartilage, which appears during bone formation in the endochondral plate or as a final mineralized product (only in sharks and certain other fishes) [48]. Mineralized cartilage consists of the unmineralized cartilage and crystals of nano-HA, in addition to considerable amounts of amino acids, phosphoserine and other biological compounds. Mineralized cartilage and bone, which have similar macromolecular constituents and both contain HA, coexist in close proximity in the endochondral plate during bone formation. However, the shape of the HA crystals in mineralized cartilage tends to resemble that in enamel, being needle-like but much shorter (25~160 nm) than those of enamel (up to 100 μm). The average thickness of the HA crystals in mineralized cartilage has been reported as 1.5~7.5 nm [49].

In recent years an increasing of reports have been made regarding ectopic calcifications (pathological biomineralization) that involve calcium phosphate [50] and lead to conditions such as urinary stones, atherosclerosis, dental calculus and calcified menisci. One reverse pathological biomineralization related to calcium phosphate is that of osteoporosis, which results from an excessive degradation of the calcium phosphate crystals of bone.

13.3 Biological Formation of Calcium Phosphates

Today, although complete details of the biological mechanism of bone formation remain unclear, research investigations continue to be made worldwide in this direction. It is strongly believed that the key to bone strength is the complex structural hierarchy in a self-assembling mode [51, 52]. Yet, despite these complicated hierarchical structures it is interesting to note that the smallest building blocks in such materials are generally on the nanometer length scale. Indeed, the questions of why the elementary structures of biocomposites are always on the nanoscale, and how these nanosized crystals are formed, remain two major issues among the 'biomineralization fraternity'.

The mechanism of formation of biological calcium phosphate minerals in vertebrates remains the subject of much controversy, despite several theories having been proposed to elucidate the process. One proposal is the theory of nucleation and growth process [53, 54], where ions are adsorbed onto the surface of the substrate (collagen), leading to the nucleation and formation of HA crystals of nanometer size. This process involves the building up of a tissue in a proteinaceous framework, after which the framework is broken down in order for the further crystal growth to achieve the required hardness. Many proposals have been made providing supportive proof for the theory of phase transformation [55], in which nano-HA crystals originate from the deposition of an amorphous calcium phosphate precursor. Examples include Lowenstam and Weiner [56], who have found that the carbonated apatite formed via the ACP phase in the chiton tooth, while Brown [57] suggested that the poorly crystalline and highly substituted apatite of vertebrate bone mineral might have a precursor such as OCP. The ACP suggestion persists because it may explain, to some extent, the differences between the nonage bone and mature bone mineral (crystallinity, shape, composition, solubility, size). Likewise, Arnold *et al.* [58] explained why the organism would select ACP as the precursor phase, by suggesting that gaps existed between the collagen molecular ends that could be used as sites of nucleation and growth of calcium phosphate mineral. These gaps were very small, such that larger crystals could not be embedded directly into them. However, a disordered phase such as ACP could be molded 'at will', and thus be readily introduced into the very small spaces within the collagen fibril. Another advantage would be that the amorphous mineral phase is, in essence, a highly concentrated solution and, upon crystallization, water must be removed from the mineralization site [59]. In some cases, OCP and brushite ($CaHPO_4 \cdot 2H_2O$) have been considered as alternative intermediate phases during bone formation. For example, a line – the central dark line (CDL) – of 1–1.5 nm width along the enamel centers is seen when the enamel crystallites are observed under transmission electron microscopy (TEM). This implies the coexistence of OCP, and consequently CDL is suggested as an intermediate status between OCP and HA [60, 61]. It is well known that HA is the most thermodynamically phase among calcium phosphates.

Studies of various mineralization processes have shown that biology is able to utilize both the transient precursor strategy as well as the nucleation strategy in

order to control mineral formation. These two processes are clearly integrated in an invertebrate organism. For example, during formation of the sea urchin larval spicule, the oriented nucleation of a single crystal of calcite is found at a specific location within a large vesicle delimited by a membrane [62]. The vesicle is loaded with amorphous phase, and a single crystal continues to grow at the expense of the amorphous phase until the entire spicule becomes a single crystal. It is conceivable that the fusion of membrane-coated amorphous particles with the large vesicle cavity initiates their transformation into crystals. A similar phenomenon is believed to exist in vertebrates.

At present, approaches to the size-control mechanism of biological HA remain a major challenge, the function of protein in controlling the formation of HA having been highlighted on numerous occasions [63, 64]. As noted above, bone is a fiber-reinforced composite in which HA serves as a reinforcing phase embedded in the collagen matrix. In the case of bone collagen, which is rod-like and has a typical fibrous structure, the molecules cannot be joined end-to-end in the fibrils, but rather are staggered and overlapped along their long axes, leaving gaps between the molecular ends. This arrangement of collagen results in the formation of a regular array of small gaps between filaments aligned within the same row. The spaces formed are 40 nm long and 5 nm wide, and are normally referred to as 'hole zones'; these are considered to serve as loci for the specific nucleation and growth of crystals of HA that are organized in bands across the collagen fibrils. It is possible that an inhibition of the size and shape of the hole zones results in HA crystals being formed with a plate-like shape and nanometer size. However, the collagen does not nucleate the crystals. The mineral-related noncollagenous proteins are present only near the region where mineral deposition begins, and localize on the collagen fibril surfaces at the gap zones, thus nucleating the crystal formation and guiding crystal growth. Thus, in the matrix-mediated scheme, the collagen fibril matrix provides the scaffold and space for the mineral, while the noncollagenous matrix proteins nucleate the crystals and determine their growth and orientation in the gaps.

13.4
Characteristic Mechanical Properties

Biomineralized tissues such as bone and tooth, possess various functions of protection and mechanical support, without compromising the requirement for mobility. It is known that the soft matrix in bone is collagen, which has a quite high volume fraction, while the stiffness phase in bone is HA. Based on a materials chemistry perspective, the bone collagen is stiff under tension yet compliant under compression, whereas the bone mineral is stiff under compression yet fragile under tension. Although both minerals have a poor mechanical strength (20 and 30 MPa, respectively), a combination of the inorganic and organic components provides an improved mechanical property for bone. For example, human cortical bone strength can reach 150 MPa, which is far higher than that of HA and collagen alone. One must marvel at Nature's ability to produce such hard and

tough materials using such soft and brittle raw materials! The origins of the strength of bone are both interesting and important. It has been proved that the hierarchical structure of bone, from macrostructure to nanostructure, and the molecular-level alliance between bone collagen and bone mineral, play key roles in providing bone with its distinct mechanical properties. The dispersion of HA nanocrystals, and their highly ordered arrangement, represent additional causative factors for the extreme strength of bone.

Conventional mechanical testing procedures require crystals of the order of centimeters, which are not only very difficult to grow but also deviate from the size of natural crystals. Recently, several advanced techniques have been developed to investigate the mechanical properties and deformation mechanisms of bone. For example, Habelitz *et al*. [65] investigated the plastic–elastic response of enamel under certain etching conditions using AFM combined with a nanoindentation technique, and showed that the elasticity and hardness of enamel was dependent on the content and orientation of the HA nanocrystals. When the test sites possess an orderly alignment of HA nanocrystals, with a perpendicular direction to the enamel rods and a high content of nanocrystals, a higher Young's moduli and hardness can be detected. Similar results have been reported by He and Swain [66]. Gupta *et al*. [67] have probed the deformation of bone tissue under tensile loading using time-resolved X-ray diffraction (XRD) and scattering, and noted that the tensile strain occurred in a ratio of 12 : 5 : 2 at the tissue, fibril and mineral particle levels. It was presumed that the HA nanocrystals had suppressed any cracks that might have led to catastrophic failure in larger bone fragments. Tai *et al*. [68] also studied the functions of HA nanoparticles in relation to the strength of bone, using a combination of dual nanoindentation, three-dimensional elastic–plastic finite element analysis (using a Mohr–Coulomb cohesive–frictional strength criterion) and angle of repose measurements. Tai's group considered nanogranular friction between the mineral particles to be responsible for the increased yield resistance in compression relative to tension, and proposed that cohesion originated from within the organic matrix itself, rather than from organic–mineral bonding. In these studies, Raman spectroscopy was used to probe the ultrastructural (molecular) changes in the mineral and matrix (protein and glycoprotein, predominantly type I collagen) components in real time, and of murine cortical bone as it responded to elastic deformation by Morris *et al*. [69]. The results of the latter study showed that bone mineral is not a passive contributor to tissue strength, which may serve as a local energy storage and dissipation mechanism to protect the tissues against catastrophic damage. Taken together, the results of all these studies have confirmed that the unique properties of bone are indeed due to the presence of nanocrystallite.

Due to the limitations of the test techniques, and the absence of any direct experimental data, the function of HA nanocrystals has rather been presumed on the basis of several deformation models of bone. These include shear transfer between mineral particles via intermediate ductile organic layers, slippage at the collagen–mineral interface, phase transformation of the mineral phase, sacrificial bond disruption between fibrils, microcracking, and uncracked ligament bridging.

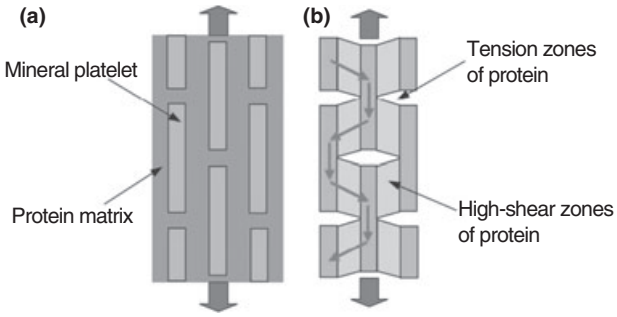

Figure 13.2 A model of biocomposites. (a) Schematic diagram of staggered mineral crystals embedded in a protein matrix; (b) Simplified model showing the load-carrying structure of the mineral–protein composites. Most of the load is carried by the mineral platelets, whereas the protein transfers load via the high-shear zones between mineral platelets. Reprinted from Ref. [38].

These types of study were strongly promoted by Gao and coworkers [38] who, on the basis of the Jaeger–Fratzl model and using the fracture mechanics concept, explained why mother Nature selected nanocrystals as her building block. Here, the nanometer size, which makes normally brittle mineral crystals insensitive to crack-like flaws, is a key factor. However, below a critical size on the nanometer length scale, the mineral crystals no longer fail due to the propagation of preexisting cracks, but rather by a uniform rupture near their limiting strength (Figure 13.2). While many riddles persist regarding the role of HA nanocrystals in hard tissues, such as its nucleation and growth, its highly ordered alignment and its origin of degradation, its function on mechanical is slowly beginning to be understood. It must be said, nonetheless, that studies of the mechanical properties of nano-calcium phosphate are today still at a very primitive and premature stage (Table 13.1).

13.5
Stability of Nano-Calcium Phosphates

The Ostwald–Freundlich equation (Equation 13.1) is frequently used to discuss the relationship between the particle size and the solubility in liquids [70],

$$dz\frac{RT}{M}\ln\frac{S_r}{S_\infty}=\frac{2\gamma_{SL}}{r} \tag{13.1}$$

where d is the solid density, S_r is the solubility of particles of size radius r, S_∞ is the normal solubility value of a plane surface, z represents the number of moles of ions formed from one mole of electrolyte, R is the gas content, T is temperature,

Table 13.1 The biomechanical properties of bone [51].

Property	Measurements	
	Cortical bone	**Cancellous bone**
Young's modulus (Gpa)	14–20	0.05–0.5
Tensile strength (MPa)	50–150	10–20
Compressive strength (MPa)	170–193	7–10
Fracture toughness ($MPa \cdot m^{1/2}$)	2–12	0.1
Strain to failure (%)	1–3	5–7
Density ($g\,cm^{-3}$)	18–22	0.1–1.0
Apparent density ($g\,cm^{-3}$)	1.8–2.0	0.1–1.0
Surface/bone volume ($mm^2\,mm^{-3}$)	2.5	20
Total bone volume (mm^3)	1.4×10^6	0.35×10^6
Total internal surface (mm^2)	3.5×10^6	7.0×10^6

and γ_{SL} is the interfacial energy between the solid and liquid. Many experimental investigations have been made to test this relationship between supersaturation, particle size and solid–liquid interfacial tension [71, 72]. It should be noted that this equation implies that nanoparticles are not thermodynamically stable in solution as they can be dissolved readily (the solubility of nanoparticles is significantly higher than that of bulk materials). A question is thereby raised as to whether nano-calcium phosphates can be stabilized in biological fluids, or not.

13.5.1 Demineralization of Biominerals

An abnormal phenomenon – yet fact – is that the mass loss of enamel surfaces occurs extremely slowly under physiological conditions. *In vitro* investigations have shown that the demineralization of enamel will take place only at relatively high undersaturation and at a lower pH (<5.5); otherwise, no spontaneous dissolution can be detected experimentally [73–75]. At pH 4.5, the demineralization of enamel has been studied quantitatively over an extended period using a nanomolar-sensitive constant composition (CC) technique combined with *in situ* AFM. The study results showed that nanosized apatite particles were produced during the reaction rather than calcium and phosphate ions. Interestingly, the further dissolution of these nanosized particles was suppressed, even though the solution was undersaturated. These nanoparticles could be observed on the dissolving enamel surfaces and in acidic solutions (Figure 13.3) [76, 77]. Most of the mineral crystals in bone are platelets of carbonated apatite, of a few nanometers thickness, embedded in a collagen matrix [78]. It has also been reported that spherically to cylindrically shaped nanosized particles form an integral part of the bone structure, as observed with high-resolution scanning electron microscopy (SEM). High-resolution back-scattered electron (BSE) imaging revealed that the 20–40 nm

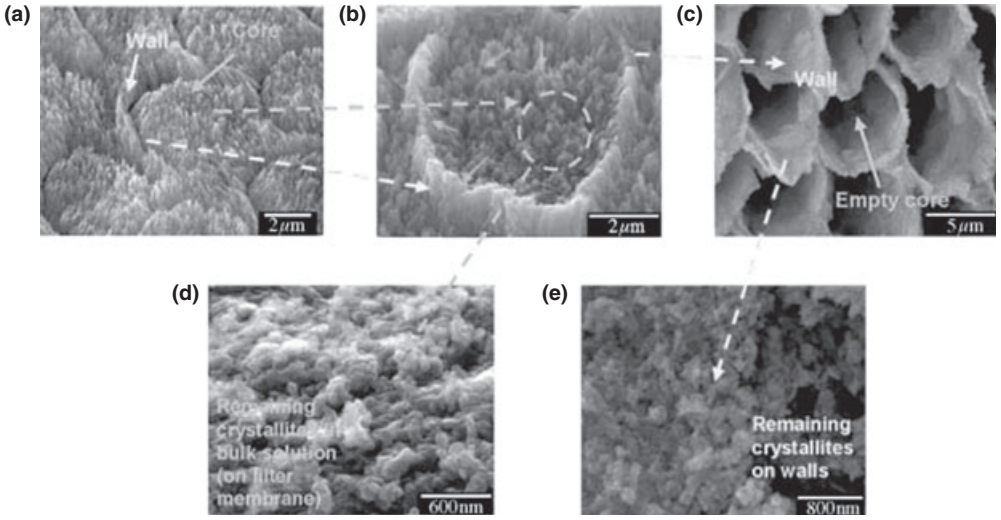

Figure 13.3 Demineralization of dental enamel. Yellow and orange labels mark the dissolution of the walls and cores, respectively, thus showing that they undergo similar dissolution processes. (a) Well-organized rod structures on mature human enamel surfaces; (b) During dissolution, crystallites becomes smaller and nanosized apatite particles (shown by green arrows; see also Figure 13.2) are formed on both walls and cores; (c) The cores are emptied but the walls remain; (d) Nanosized apatite particles collected from the bulk solution; (e) The wall at higher magnification; nanosized apatite residues are retained on the wall surfaces. Reprinted from Ref. [77].

spherical particles had a contrast similar to that of the crystal platelets, which suggested that they would likely have similar mineral properties. By means of CC dissolution, similar-sized nanoparticles were shown to be insensitive to demineralization and so were thought to be dynamically stabilized.

The presence of apatite nanoparticles in mature bone and enamel may also be due to the stabilization of some nanosized particles during the formation process in the fluctuating biological milieu (note: the biological milieu is extremely conservative = homeostasis!) [37]. Demineralization studies of bone and enamel have shown that the nanostructured apatite particles can be extremely stable in the solutions. These phenomena agree with the proposal that nanoparticles may act as the building blocks of the biomaterials, and thus can be considered as basic units [38, 79]. The results also showed that the biomaterials become insensitive to dissolution at the nanoscale level.

Another excellent example was also seen in studies of caries lesion formation. Enamel surfaces remain undissolved in water (pH = 5.5–5.8), in spite of any undersaturation; consequently, caries (dissolution) will only be induced at localized sites where the bacteria have produced strong acidic conditions. The mineral crystallites can be stabilized in the fluctuating physiological fluids. Such nanodissolution behavior of nanoparticles may also be significant with regards to solvent stability and reactivity in working nanoparticle-based structures and sensors.

13.5.2 Dissolution of Pure HAP

In order to exclude the influence of complicating biological factors, such as the possible presence of organic matrix components, CC dissolution studies have been conducted using synthetic HA samples of high purity (>99.4%) with a needle-like morphology (400–600 nm long, 60–100 nm wide). A similarly reproducible self-inhibited dissolution is observed with these nanosized crystallites, with the rates decreasing during the reaction. CC dissolution also indicates the creation of metastable states in which the reaction is effectively terminated, even though the apatite crystallites remain in contact with the undersaturated solutions. This result is similar to observations made during enamel/bone demineralization. The residual crystallites are confirmed to have the same chemical composition as the initial seed crystals.

Clearly, this dissolution termination is a kinetic phenomenon and cannot be attributed to reaction retardation as a result of surface modification by additives. However, it can be explained in terms of a dissolution model incorporating particle size considerations. It has been suggested, and confirmed by experiment, that the demineralization of sparingly soluble salts such as apatite is generally initiated and accompanied by the formation and development of pits on the crystal surfaces, and that the dissolution rates are also determined by the pit densities and spreading velocities [75, 80, 81].

Analogous to the formation of two-dimensional nuclei/hillocks for crystal growth, in dissolution the rate of step movement from a pit of radius r can be obtained from treatments similar to the model of Burton, Cabrera and Frank [82],

$$R(r) = R_\infty\left[1 - \frac{e^{(1-S)r^*/r-1}}{e^{1-S}-1}\right] \approx R_\infty\left(1 - \frac{r^*}{r}\right) \tag{13.2}$$

where S is the saturation ratio and r^* is the critical radius for the formation of a 2-D pit/dissolution step, as given by Equation 13.3:

$$r^* = \frac{\gamma_{SL}\Omega}{|\Delta g|} \quad \text{and} \quad \Delta g = kT\ln S \tag{13.3}$$

where γ_{SL} is the interfacial tension, k is the Boltzmann constant, Ω is the area occupied by each dissolution unit, and Δg is the change in Gibbs' free energy for dissolution. It has been shown that only pits larger than r^*, providing the active dissolution sites, contribute to the reaction. In Equation 13.2, R_∞ is the velocity of dissolution steps at $r \to \infty$. It follows that when r is closer to r^*, its dissolution rate decreases and approaches zero when $r \to r^*$. When the dimensions of the crystallites are of the same order as r^*, it can be assumed that the formation of active pits becomes difficult on such a small crystal faces, and their enlargement is strongly inhibited by the limitation of pit/crystal size. It has also been suggested that if the undersaturation (driving force for demineralization) is low, the pits will

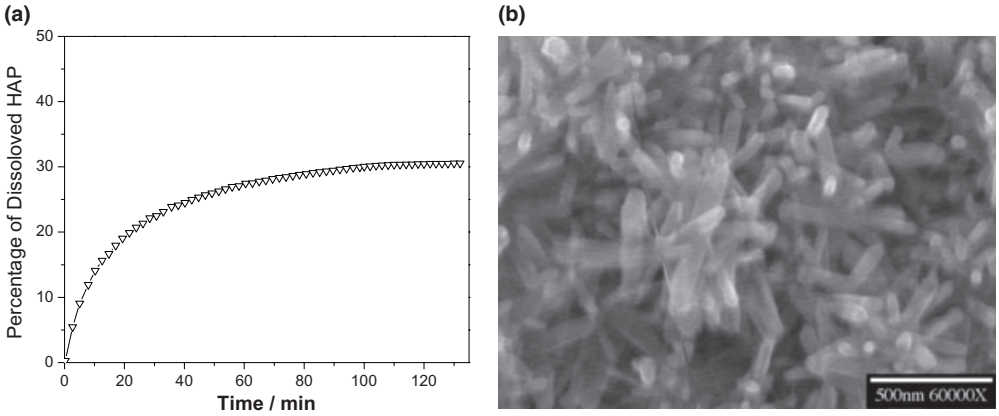

Figure 13.4 (a) Dissolution of pure HA in a constant undersaturated solution (saturation ratio of 0.325), such that the dissolution cannot be completed; (b) Residues of nano-HA at the end of the demineralization experiment. At the higher undersaturation, the residual crystallites may be smaller. Reprinted from Ref. [81].

not open up and the defect sites will not lead to stepwaves forming far from the localized etch pits due to the low driving force (Figure 13.4).

13.5.3 Nanosize Effects in Biomaterials

In many biological systems the mineral phases are composed of tiny, sparingly soluble crystallites that are tens to thousands of nanometers in size; it appears that this is the most natural selection. It is well known that there is a close relationship between solubility and γ_{SL} [83].

During dissolution, some neighboring ions on the surface are replaced by water molecules to form units that escape into the bulk solution. Higher values of γ_{SL} indicate a greater difficulty in forming such an interface between the solid and aqueous phases. Thus, sparingly soluble salts in aqueous solution always have much higher interfacial free energy values than soluble salts [84], and this results in greater values of r^* (10–100 nm). As biological minerals have sizes within this critical range, they may be protected from dissolution as the reaction in the metastable region will be significantly inhibited. This accounts for the observation that the dissolution of biomineral powders is always slower than that of synthesized relatively large crystallites after normalization for specific surface area. In addition to these interesting conclusions from dissolution studies, it is also widely accepted that the growth of tiny apatite seeds is rarely observed at low supersaturation ($S < 4$) [85] due to extremely slow growth rates which, again, can be attributed to a kinetic size effect. It is important that the mineral crystallites can be stabilized

in the fluctuating physiological fluids, thus exercising a degree of self-preservation as the result of this kinetic size-effect at the nanoscale level.

13.6
Synthesis of Nano-Calcium Phosphates

13.6.1
Synthesis of Nano-Calcium Phosphate Particles

Many methods have been proposed for the preparation of nanocrystalline HA, including sol–gel synthesis, coprecipitation, hydrothermal reaction, mechanochemical synthesis and vibro-milling methods from natural bone [86–89]. Although each of these methods can provide a plentiful supply of HA nanoparticles of various shapes and sizes, and has both scientific and practical relevance, very little attention has been paid to the physico-chemical details involved for the careful control of particle size distribution, as well particle shape. In fact, most of these HA synthetic routes actually produce a particle mixture with a wide size distribution, ranging from tens to hundreds of nanometers. The control of HA nanoparticle shape represents an additional problem for these methods, which commonly produce pin-like or irregularly shaped particles. It is well known that natural minerals in bone are homogeneous plate-like HA crystals (15–30 nm wide, 30–50 nm long), whilst in enamel they are ribbon-like (60–70 nm wide, 1 μm long, and 25–30 nm thick). Studies of biomineralization and biomimical assembly at a higher level require the use of advanced methods in order to provide an accurate control of HA nanocrystal synthesis, and several such techniques have recently been developed [90, 91]. A pathway in which the reaction spaces are limited can result in a size-controlled synthesis. Here, the nanosized reaction vessels are selected as reverse micelles, microemulsions, vesicles, ferritin and viroid cages, lipid bilayer films and bacterial threads, and so on [92–101]. Among these methods, reverse micelles and microemulsions have been applied to the synthesis of nano-HA [102, 103]. In some cases, specialized polymers can be used as spatial reaction vessels for the fabrication of HA. For example, Shchukin *et al.* [104] used the poly(allylamine hydrochloride)/ PO_4^{3-} complex as a source of phosphate anions to capture calcium cations and make them react in the capsule volume. The use of a biomimetic synthesis led to the most typical HA forms being located on the inner side of the capsule shell. Mann and coworkers used self-assembled shell crosslinked poly(acrylic acid-*b*-isoprene) (PAA78-*b*-PI97) micelles or crosslinked PAA nanocages in aqueous solution as templates for the preparation of novel polymer–calcium phosphate nanocapsules, and obtained hybrid nanostructures of 50–70 nm diameter that consisted of spherical polymer nanoparticles or nanocages enclosed within a continuous 10–20 nm-thick surface layer of amorphous calcium phosphate [105]. One important aspect in the biomineralization process is the role played by functional groups on the surface of organic crystallization sites; consequently, interest among the biomineralization research fraternity has centered on

the use of such films as templates for inorganic crystal precipitation [106]. Insoluble amphiphilic molecules can accumulate at the gas–solution interface and form highly organized monomolecular films, a characteristic which has been exploited to induce the precipitation of orderly biominerals with monolayer or multilayers. Molecules assembled in these forms have been often used as model organic matrices, such as Langmuir monolayer films, Langmuir–Blodgett (LB) films and self-assembled monolayers (SAMs) [107, 108]. Common examples include dipalmitoylphosphatidylcholine (DPPC), arachidic acid (AA), octadecylamine (ODA), stearyl amine and alkane thiol molecules and organosilane molecules [109]. Apart from film templates, polymers are used as templates in solution systems to control the shape and size of HA crystals. Bose and Saha [103] synthesized nanocrystalline HA powder using the reverse micelle-processing route; here, the particle size was between 30 and 50 nm with a needle shape and spherical morphology. Cyclohexane was used as the oil phase, and a mixture of poly(oxyethylene) nonylphenol ether and poly(oxyethylene) nonylphenol ether (NP-12) as the surfactant phase.

In our laboratory, we use hexadecyl(cetyl) trimethyl ammonium bromide (CTAB) as an efficient agent to modulate the formation of HA nanoparticles; the particle size can be easily regulated by changing the concentration of CTAB in the calcium phosphate supersaturated solutions [110]. As an example, three different spherical-like HA nanoparticles with average diameters of 20 ± 5, 40 ± 10 and 80 ± 12 nm were fabricated using a series of concentrations of CTAB to control the particle size (Figure 13.5). The results showed that the size distributions of as-prepared HA nanoparticles were relatively uniform [87], whereas those grown in the absence of any organic additives were typically rod-like with length of hundreds of nanometers and width of tens of nanometers.

13.6.2
Biomimetic Construction using HA Nanoparticles

The morphological control of bioinorganic materials using biomimetic methods represents another important issue in biomineralization, by which inorganic materials with complex morphologies can be produced. Chen *et al.* [111] reported a method to create special enamel structures by modifying synthetic HA nanorods with a surfactant of bis(2-ethylhexyl)sulfosuccinate salt (AOT) that allowed the nanorods to self-assemble into an enamel prism-like structure at a water–air interface (Figure 13.6). When Fowler *et al.* [112] synthesized an HA bundle structure directly from a solution containing AOT, water and oil, the bundles were only 750 nm to 1 μm long, 250–350 nm wide, and had an enamel-like shape. In biological bone, the composite structure of nanosized HA-reinforced collagen offers a route to the production of materials with properties such as high strength and toughness. Recent attempts to create artificial bone materials with a bone-like nanostructure and chemical composition have been made, with some significant achievements [113, 114]. For example, a biomimetic synthesis was selected by Cui *et al.* to fabricate a bone scaffold material (nano-HA/collagen/PLA composite) that showed some features of natural bone, not only in its main composition but also

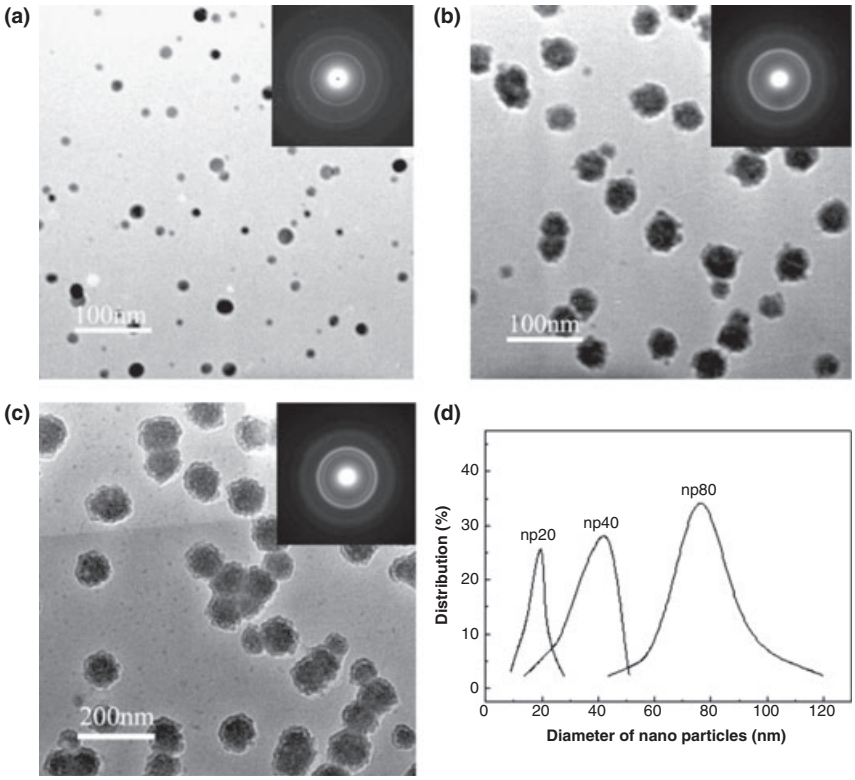

Figure 13.5 Controlled size synthesis of spherical nano-HA. (a) 20 nm (np20); (b) 40 nm (np40); (c) 80 nm (np80); (d) Particle size distribution of the nanoparticles. Reprinted from Ref. [110].

in the hierarchical microstructure of cancellous bone [113]. The porous scaffold showed the bioactivity and bone-remodeling ability of the composite according to experimental results obtained *in vitro* and *in vivo*. The effect of noncollagenous proteins (polyaspartate) on the mineralization process of collagenous proteins has also been interpreted, this being responsible for improving the connection between calcium phosphate and collagen [114]. These results are of great help in our understanding of the biomineralization mechanism.

The classical model of biomineralization considers mineral formation as an amplification process in which individual atoms or molecules add to existing nuclei or templates [115]. In contrast, living organisms utilize proteins and peptides to deterministically modify nucleation, growth and facet stability [116, 117]. This conventional concept for crystal growth has been recently challenged, however, by a model involving aggregation-based growth. Banfield *et al.* [16, 118, 119] have shown that inorganic nanocrystals can aggregate into ordered solid phases via oriented attachment in order to control the reactivity of nanophase materials in

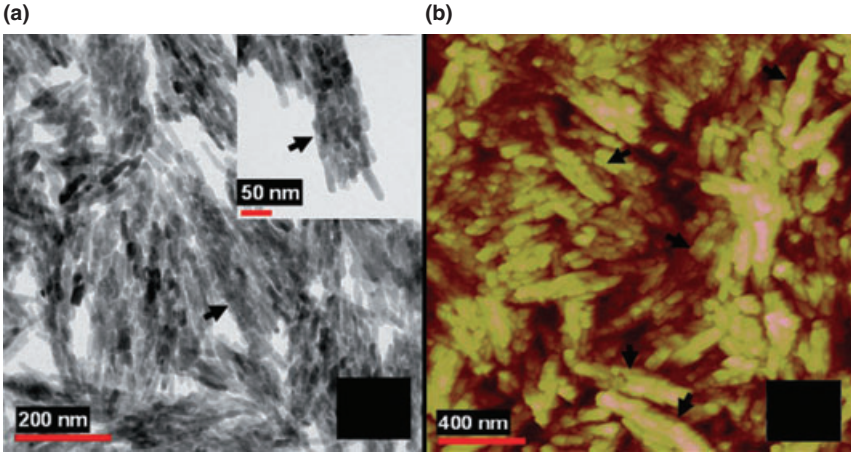

Figure 13.6 (a) Transmission electron microscopy images of HA assemblies, 10–20 nm in cross-section and 50–70 nm in length. The arrows indicate the ordered, prism-like structures. The size of these ordered prism-like structures is approximately 400 nm in length and 100 nm in section; (b) Tapping mode atomic force microscopy (AFM) image of the LB films consisting of HA nanorods. The arrows indicate the ordered, prism-like structures. (AFM image size $2 \times 2\,\mu m$; left: height image, z-range, 100 nm.) Reprinted from Ref. [111].

nature. The arrangement of nanocrystallites can be realized with the 'fusion' of blocks as they share a common crystallographic orientation at the interface, which has been used successfully to synthesize many nanomaterials [120–122]. Yet, another concept of mesocrystal, which consists of crystallographically oriented crystallites connected by polymers or surfactants [123], has been suggested for studies of biomineralization [124]. The formation of mesocrystals has been observed previously in the growth process of $CaCO_3$, CdS, $BaSO_4$ and CuO, under the regulation of various organic molecules [125–128]. In these mesocrystals, the building blocks are the fully crystallized inorganic phase, while the organic molecules connect the adjacent crystallites, resulting in the formation of superstructures. The interaction between the crystallites and organic molecules represents a crucial condition in the architecture of mesocrystals.

Recently, Tao *et al.* [129] proposed a new model which involved the biological aggregation of apatite nanoparticles. The process employs an inorganic phase, ACP, that cements the crystallized, nano-HAP, while the biological molecules serve as the modifier during the nanoarchitecture. By using HA nanospheres as the building blocks, the highly ordered enamel-like and bone-like apatites could be constructed in hierarchical fashion in the presence of glycine (Gly) and glutamate (Glu), respectively (Figure 13.7).

The formation of enamel-liked apatites has been repeated by using bovine amelogenin. At a concentration of $1.25\,\mu M$ amelogenin, the large enamel-like HA mesocrystals appeared within only three days (Figure 13.8), which was about

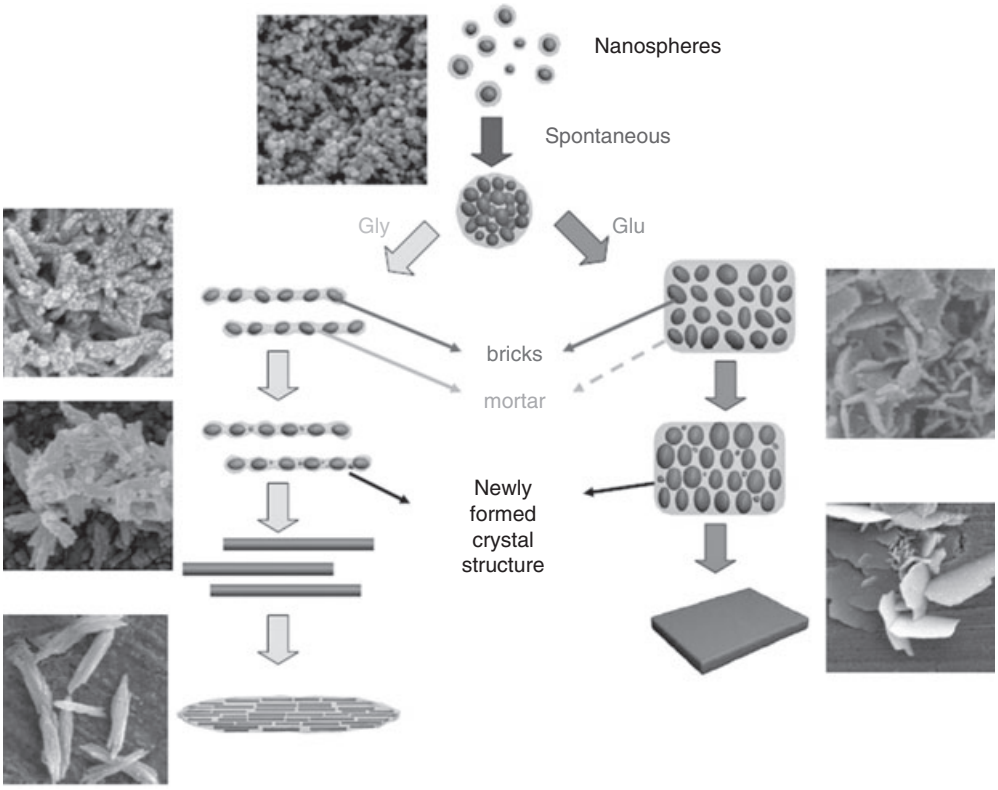

Figure 13.7 Schematic model of apatite evolution via the conglutination of HA nanocrystallites. Under the control of biological components such as Gly and Glu, the HA subunits could be reorganized. The modifiers could determine the different evolutionary forms, for example, one-dimensional linear assemblies or two-dimensional plates. The crystallized HA were cemented by the amorphous phase with the flexible structure. The ACP could transform into the thermodynamically stable HA phases with time, and the individual HA domains could fuse to form the single HA crystals (red). These single crystals might be used as the building blocks in the next level of architectures, such that the hierarchical structure of apatite was achieved. The SEM images show the corresponding experimental states of the nanoassembly of HA. Reprinted from Ref. [129].

20-fold faster than with 10 m*M* Gly. These findings show that amelogenin, which is a well-known effective modifier during *in vivo* tooth enamel formation, can dramatically accelerate the kinetics of nanoassembly. This result was also in agreement with a previous report that amelogenin promoted the formation of elongated apatite microstructures [130].

Taken together, the results of these studies have provided evidence of a new mechanism for the assembly of biominerals and biological molecules present

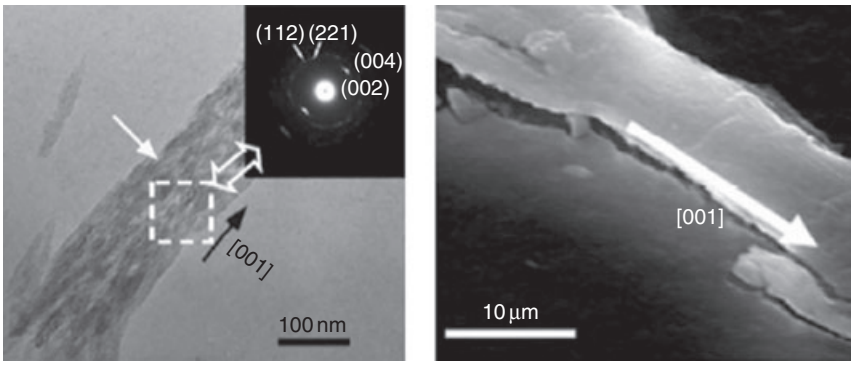

Figure 13.8 Hierarchical constructed enamel-like apatite in the presence of amelogenin by using nano-HA as the building blocks. Reprinted from Ref. [129].

during the process of biomineral assembly, and which specifically regulates the assembly kinetics and determines the structural characteristics of the final HA architecture.

13.6.3
Nano-HA–Collagen Composites

The ideal bone scaffold should promote early mineralization and support new bone formation, whilst at the same time allowing for replacement by new bone. Based on this principle, nano-HA–collagen based composites, inspired from research on natural bone, have attracted much attention. Previously, a method was proposed for the fabrication of nano-HA–collagen composites, in which composites can be created by blending or mixing a heterogeneous combination of two or more materials, each differing in their morphology or composition. It is well known that the blending of multiple materials with different characteristics leads to composites with tailor-made properties, although it may be difficult to control the homogeneity and uniformity of the secondary or reinforcing phases. Currently available commercial HA–collagen composites are all direct mixtures of these two components [131]. In blended HA–collagen composites, the crystallite sizes of HA are not uniform, and the HA is often aggregated and randomly distributed into the fibrous matrix. Thus, there is a compositional similarity but no structural similarity to natural bone. Recently, a novel method of fabricating nanocomposite bone grafts using strategies found in Nature has attracted much attention and has been perceived to be beneficial over conventional methods; this is the coprecipitation self-assembly method. Using this method, a direct nucleation of HA nanocrystals onto collagen fibers was performed, starting from an aqueous suspension of calcium solution and phosphate solution, together with a collagen solution at pH 9–10, and at room temperature. Solution conditions of a high ionic concentration and high pH were employed, while the possible mineral content of the

composites was up to 60%. As this process mimics the mineralization of natural bone to a certain extent, it has been suggested that the HA–collagen nanocomposite could be used for bone repair in orthopedic and maxillofacial surgery. Subsequently, some modifications of the method were carried out which included the addition of glutaraldehyde or poly(lactic acid) (PLA) polymer in order to enhance the mechanical properties or biocompatibility of the composite.

13.6.4 Nano-HA Coating

In spit of their excellent biocompatibility, calcium phosphate materials cannot be used at high-load-bearing sites, such as the femoral and tibial bones, because their fracture toughness values are less than that of human cortical bone. In practice, the latter is normally replaced by a biomedical metal such as a cobalt–chromium alloy, titanium (and its alloys) or stainless steel 316L. Unfortunately, the failure of conventional orthopedic and dental metal implants is often due to an insufficient bonding of the metal with the juxtaposed bone or tissue. Timely and desirable responses from surrounding cells and tissues are required to enhance deposition of the mineralized matrix at the tissue–implant interface, which in turn provides crucial mechanical stability to the implant. This requirement, in addition to the hardness and strength of the metallic implant, can be greatly increased by nanostructuring. Current, commercially available HA coatings include pulsed laser deposition and thermal plasma spraying, both of which can create a strong joint between the metal matrix and the HA coating [132, 133].

Other approaches include dip coating, electrophoretic deposition and sol–gel methods [134–137], all of which can be used to coat complicated and porous devices, along with the incorporation of biologically active substances (e.g. proteins or antibiotics) into the coating, albeit with a weak bonding force. In biomimetic coating, which may have some advantages over conventional coating, the coating is composed of uniform nanocrystalline HA, and has been shown capable of conducting bone formation and promoting direct osseointegration with the juxtaposed bone.

The importance of the nanostructure of HA coatings for biomedical devices has only been realized during the past 10 years or so, with thin-film deposition processes having been adapted from the electronics industry and used in an attempt to produce superior HA implant coatings. The nanostructure processing of HA-based composites has led to the design of structural and surface features inspired by the architecture of bone, and also allowed chemical homogeneity and microstructural uniformity to be achieved for HA. Consequently, fully dense bioceramics can now be generated at low sintering temperatures, with a significant reduction in flaw size. In addition, the density of HA powders can be increased to more than 98% theoretical density, resulting in an ultrafine-grained (125 nm) compact that exhibits superior compressive and bending strengths and fracture toughness [138].

In some cases, nano-HA–collagen composites have been selected as coating materials for other bioinert materials in order to improve their biocompatibility.

In a study conducted by Fan *et al.* [139], a uniform collagen fibril–OCP composite coating on a silicon substrate was prepared by using electrolytic deposition. The coating process involved the self-assembly of collagen fibrils and subsequent deposition of calcium phosphate minerals as a result of the cathode (Si) reaction and a local pH increase. The porous composite layer consisted of a collagen fibril network on which clusters of OCP crystals could nucleate and grow. The preliminary results of nanoindentation testing showed that the correctly prepared composite coatings might have a higher elastic modulus and improved scratch resistance compared to monolithic porous calcium phosphate coatings. Poorly crystallized HA–collagen composite coatings formed on the surface of NiTi shape memory alloys were studied by introducing collagen to a simulated body fluid [140]. The morphology of the composite coatings produced was uniform, and the micromorphology lamellar; such a coating may be very useful for enhancing the bioactivity of NiTi shape memory alloys.

13.7
Nano-Calcium Phosphate in Biomedical Engineering

13.7.1
Bone Repair

Calcium phosphate ceramics have been used in orthopedics for over 30 years, largely on the basis of their excellent biocompatibility [141]. However, with the development of nanotechnology, the application of nanophase calcium phosphates has attracted much attention due to the similar dimensions of the constituent components of natural tissues, and their special effects on cells. In contrast, nanophase calcium phosphates have unique surface properties, such as an increased number of atoms, boundaries of the grains of the material and defects at the surface, surface area and altered electronic structure, compared with conventional micron-sized HA. For example, the contact angles (a quantitative measure of the wetting of a solid by a liquid) are significantly lower for nano-HA (6.1) compared to conventional HA (11.51), while the pore diameter in a nanophase HA is fivefold smaller (6.6 Å) than in its conventional, grain-sized HA counterpart (1.98–3.10 nm); these variations are reflected in the different mechanical properties and biocompatibility of these materials [142–144]. Some recent developments in nanophase ceramic matrices used for bone tissue engineering are discussed in the following sections.

Nanoparticles of HA can be used as fillers, a conventional example being the sponge-like structure (made by a freeze-drying process) which consists of collagen fibers embedded with HA nanocrystals. For this material, the main challenge is to achieve a uniform dispersion of the nanoparticles, which tend to aggregate into micron-sized agglomerates. It is also possible that both the matrix and filler are nanoscale-sized. In other aspects, some nanofiber composites have been produced by blending nano-HA with various polymers, such as polycaprolactone (PCL), silk

fibroin, polyhydroxybutyrate-*co*-valerate and PLA. Moreover, nanoparticles can either be delivered as free particles or immobilized on a surface or in a matrix. They also have a high specific surface area; for example, reducing the particle size from micrometer to nanometer scale for a given quantity of material, the total surface increases 1000-fold. Free nanoparticles may also be used as carriers of drug, as they are small enough to move easily within cells. For example, in 2001, when Paul and Sharma entrapped insulin using orally administered nano-HA particles [145], the insulin release profile showed promising results for orally administered insulin rather than for repeated injections.

The introduction of a gene of interest into a cell in order to promote a specific cell function may represent an effective therapeutic strategy for bone regeneration, and both viral and nonviral vectors have been used for this purpose. Viral vectors, including retroviruses, adenoviruses, adenoassociated virus (AAV), lentivirus and herpes simplex virus (HSV), possess relatively high transduction efficiencies but have potential safety problems. In the past, nonviral vectors have received much attention in order to eliminate any possible risk from viral vectors, such as a plasmid vector (pDNA). Liposomal, polycationic, dendrimer and silica nanoparticles are normally used as both protector and enhancer for pDNA in order to increase the efficacy of pDNA transfection. Among these materials, HA has been considered to have great potential as a gene-carrier candidate due to its established biocompatibility, ease of handling and notorious affinity for adsorption. In fact, the nonviral transfer of DNA into cells ('transfection') is a routine procedure in modern biochemistry and is carried out by the *in situ* precipitation of calcium phosphate. Such transfection by calcium phosphates has been described elsewhere as 'simple but insufficiently reproducible', there being a low transfection efficiency due to unstable experimental conditions. According to the current state of knowledge, calcium phosphate nanoparticles may be incorporated into the cells by endocytosis (penetration of the cell membrane and uptake into an intracellular vesicle). It is possible to promote the transfection efficiency of calcium phosphate by using its nanoparticle, and this concept has been proved through a series of experiments. Most recently, Sfeir *et al.* [146] compared the transfection efficiency of nano-calcium phosphates with commercially available calcium phosphate kits (CalPhos; Clontech and FuGENE; Roche Diagnostics). The results showed that the nanomaterials exhibited a 25-fold increase in transfection efficiency compared to CalPhos at 12 h.

The green fluorescent protein (GFP) gene has also been used to determine the proportion of cells transfected with the nano-calcium phosphates/GFP, and similar results were obtained. This high transfection efficiency indicates the potential of nano-calcium phosphates in gene delivery. Recently, Welzel *et al.* [147] evaluated the possibility of calcium phosphate nanoparticle as a gene carrier by preparing spherical particles of calcium phosphate with diameters of 10–20 nm and covered by a hull of DNA (Figure 13.9). Subsequently, a successful transfection of transformed human endothelial cells was achieved by adding the dispersion of nanoparticles to the cell culture. The functionalized nanoparticles formed a stable colloid and did not lose their ability for cell transfection during a two- to three-week period

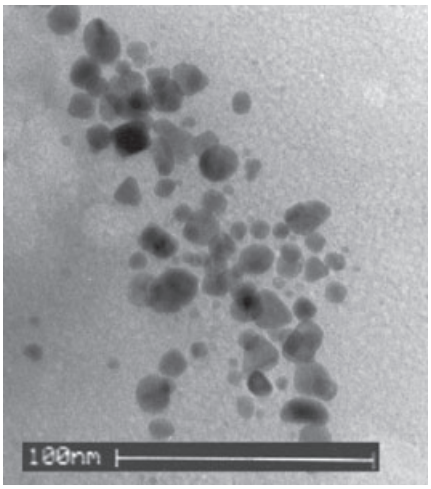

Figure 13.9 Transmission electron microscopy image of calcium phosphate nanoparticles that are functionalized by DNA. The particles have a typical size of 10 to 20 nm. Reprinted from Ref. [147].

of storage. The authors assumed that the small particle size was responsible for the good transfection efficiency compared to that seen with standard methods.

In bulk form, many different calcium phosphates ceramics are available commercially for the treatment of bone defects following orthopedic removal, bone tumor extraction, complicated fracture, and so on [148]. In these cases, the site of the bone defect must be filled with a dense or porous bulk biomaterial that can provide support for new bone growth (either on or in the filler), while avoiding the growth of fibrous tissue. For this, the material should – if possible – be biocompatible, bioactive and biodegradable. From a chemical aspect, the synthetic bulk biomaterials are normally based on calcium phosphates and, with the rapid development of nanotechnology, nano-HA may eventually find a use in this field. The NanOss bone void filler, produced by Angstrom Medica [149], was considered to be the first nanotechnology medical device to receive clearance by the US Food and Drug Administration (FDA), in 2005. NanOss is prepared by precipitating nanoparticles of calcium phosphate in aqueous phase, and compressing and heating the resultant white powder to form a dense, transparent and nanocrystalline material. According to the manufacturer, NanOss duplicates the microstructure, composition and performance of human bone, and also possesses highly osteoconductive and bone remodeling properties. In order to improve the mechanical properties of pure HA bulk, zirconia nanocrystals have been added to further toughen the nano-HA matrix. Following pressure- and temperature-assisted sintering, the resultant nanocomposite could achieve more than 98% theoretical density with a grain size <125 nm. The incorporation of a highly dispersed zirconia

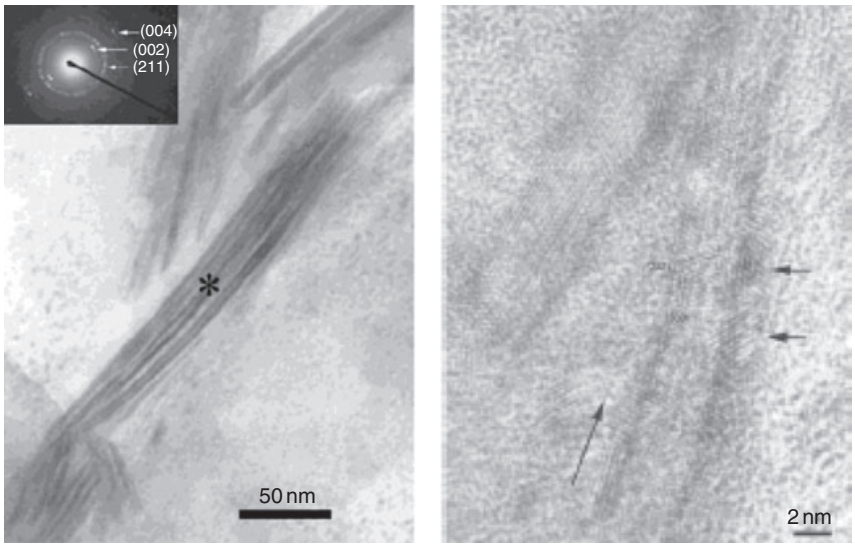

Figure 13.10 (a) High-magnification image of the mineralized collagen fibrils. The inset shows a selected area electron diffraction (SAED) pattern of the mineralized collagen fibrils. The asterisk marks the center of the area, the diameter of which is ca. 200 nm; (b) High-resolution TEM image of mineralized collagen fibrils. The long arrow indicates the longitudinal direction of the collagen fibril; the two short arrows indicate two HA nanocrystals. Reprinted with permission from Ref. [150].

has been shown to significantly enhance the fracture toughness and bending strength of HA-based bioceramics for load-bearing implant applications.

A central principle of biomineralization is that the nucleation, growth, morphology and assembly of the inorganic crystals are regulated by organized assemblies of the organic macromolecules. The nanostructure processing of HA-based composites has allowed for the design of structural and surface features inspired by the architecture of bone. The elective organic phase in the composites are collagen, alginate, chitosan, silk fibroin and several bioresorbable polymers, including PLA and PCL. The various fabrication methods have been described. For example, Cui *et al.* [29, 150] developed a nano-HA–collagen (NHAC) composite by the coprecipitation of apatite with collagen. The composites mimic the HA nanocrystal-type I collagen nanostructure of natural bone, which can be incorporated into bone metabolism instead of being a permanent implant (Figure 13.10). In addition, nanocomposites containing HA and chitosan [151], HA–silver composites [152], fluorapatite–collagen composites [153] and nanocrystalline yttria-stabilized zirconia-reinforced HA [154] have been developed for specialized functions, including antimicrobial benefits, an improvement of the structural stability and cellular responses, and enhancement of strength and toughness. However, due to processing difficulties and the poor mechanical properties of bulk HA, its applications are currently confined to nonload-bearing implants and porous bodies/scaffolds.

Porous 3-D nanocomposites of HA and collagen/polymer mimic natural bone in both composition and microstructure, and so can be employed as a matrix for the tissue engineering of bone.

A new concept in the treatment of bone defects has been introduced with bone cements based on calcium phosphates; these have many advantages, including their self-setting form and excellent biocompatibility and bone-repair properties [155, 156]. The cement properties, such as setting time, degradable speed, porosity or mechanical behavior, can be controlled by changing the cement components, including the type or amount of calcium phosphate and additives [24]. In the past, nano-calcium phosphate has generally been selected as the major component because of its accepted improved sinterability, enhanced densification and better bioactivity than coarser crystals [157]. By improving those cements which are based on nano-HA in terms of their rheological, exothermal and mechanical behaviors, some are starting to be used in the clinical situation. An example is Ostim, an injectable bone matrix which is prepared in paste form and which received the CE (Conformité Européenne) marking in 2002. Ostim is composed of synthetic nanoparticulate HA, and can be used in metaphyseal fractures and cysts, acetabulum reconstruction and periprosthetic fractures during hip prosthesis exchange operations, osteotomies, filling cages in spinal column surgery, and so on [149]. Moreover, cements based on calcium phosphate can also be used as convenient carriers of drugs, ranging from antibiotics and anti-inflammatory agents to bone morphogenetic proteins (BMPs) or transforming growth factor-β (TGF-β) [28]. Unlike other carriers, where the drugs are normally adsorbed to the surface, in the case of cements the drugs can be incorporated throughout the whole material volume, simply by adding them into one of the two cement phases. This ability to release the drug over more prolonged periods provides a great potential for this type of material in the controlled delivery of drug to target sites within the skeletal system.

13.7.2
Bone-Related Cells

It is well accepted that bone-related cells (notably osteoblasts and osteoclasts) play a key role in the physiological formation of bone. Bone-related cells are considered not only to take part in the formation of the biomineral and macrostructure construction of bone, but also to modulate, on a continuous basis, the density, regeneration and degradation of bone, where the most common phenomena include bone regeneration under mechanical pressure, the appearance of calculi and osteoporosis. Consequently, the relationship between bone-related cells and calcium phosphates has attracted much attention in the quest to elucidate the formative mechanism of bone, the prevention and cure of bone-related disease, and the design of novel biomaterials.

The *in vitro* functions of osteoblasts and osteoclasts have been studied in much greater detail on nanophase HA than on conventional, grain-sized HA. In fact, nano-HA has demonstrated an enhanced osteoblast proliferation, as indicated by

the synthesis of 37% more ALP and twofold higher concentration of calcium in the extracellular matrix (ECM) at 28 days of culture compared to conventional HA [158]. There is also further evidence to suggest that reducing the particle size to nanoscale may promote osteoblast adhesion. Nanophase HA has also shown evidence of an enhanced synthesis of tatrate-resistant acid phosphatase (TRAP; this is secreted to aid osteoclast resorption of the bone ECM) and an enhanced formation of resorption pits (an index of bone resorption activity) by osteoclast-like cells compared to devitalized bone as a reference [159]. Due to its notorious adsorption, the surface of the nano-HA enriches many specific proteins derived from blood, bone marrow and other tissues, including fibronectin, vironectin, vitronectin and denatured collagen. Each of these could improve the biological behavior of cells on the matrix, including adhesion, differentiation and growth. The nanophase materials may possess optimal surface properties (higher surface area, lower contact angle) and surface features (more nanoscale pores) that influence the type and degree of adsorption of selective proteins that can in turn enhance specific osteoblast adhesion. In fetal bovine serum, nanophase HA was shown to adsorb 11% more protein per cm^2 than conventional HAP [160]. Fetal bovine serum contains unknown amounts of various proteins, such as albumin, fibronectin, vitronectin, and denatured collagen proteins, which enhance osteoblast adhesion when present in greater concentrations. Overall, the surface features of nano HA appear to favor the adsorption of specific proteins (e.g. vitronectin) that mediate the enhanced functions of osseous cells. It has been noted that vitronectin and other proteins that are crucial for osteoblast adhesion are well-spread, are unfolded to a great extent, and expose larger numbers of osteoblast-adhesive epitopes, such as arginine-glycine-aspartic acid (RGD), on interacting with nano-HA compared to conventional HA.

A better supermicrostructural biomimicry and osteoconductivity can be achieved when using nano-sized HA as a mechanical reinforced phase and collagen/polymer in the scaffold matrix. The biocompatibility of these materials is key to their possible application within the clinical setting. When the adhesion, proliferation and differentiation of mesenchymal stem cells (MSCs) was investigated on nano-HA/polyamide (n-HA/PA) composite scaffolds, the latter were shown to exhibit good biocompatibility and extensive osteoconductivity with host bone both *in vitro* and *in vivo*. Consequently, the n-HA/PA scaffolds have the potential to be applied in orthopedic, reconstructive and maxillofacial surgery. Nanostructured coatings with nanometer-sized grains and a high volume fraction of grain boundaries have also shown increased osteoblast adhesion, proliferation and mineralization.

Recently, the present authors' group has studied the size-effects and the influence of crystallinity of nano-HA on bone-related cells [110, 161]. Different HA nanoparticles, typically 20 ± 5, 40 ± 10 and 80 ± 12 nm in diameter, were prepared and their effects on the proliferation of two bone-related cells – bone MSCs and osteosarcoma cells (U2OS and MG63) – were studied. The cell-culture experiments show an improved cytophilicity of the nanophase mineral when compared to conventional HA (Figure 13.11), while a greater cell viability and proliferation of MSCs was identified on the nano HA, most remarkably for the 20 nm particles

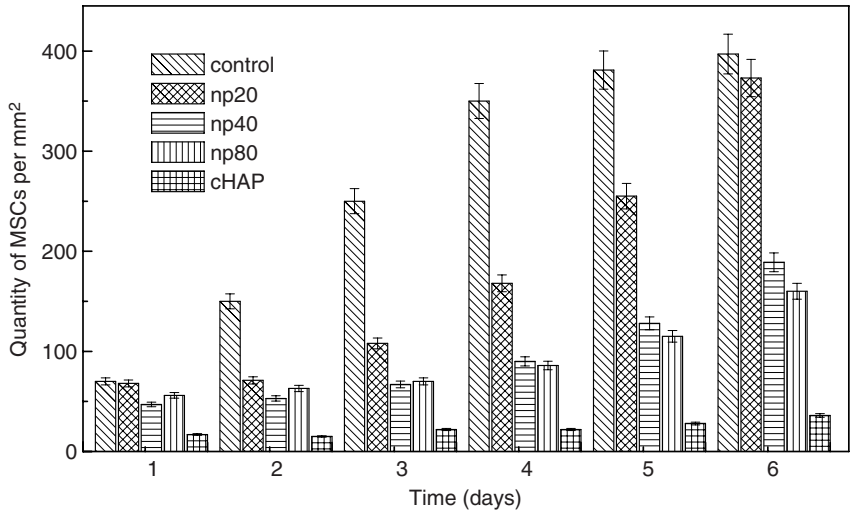

Figure 13.11 Proliferation of mesenchymal stem cells (MSCs) on different HA substrates; the control experiment was performed on glass.

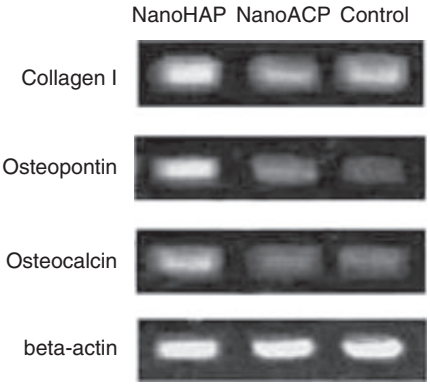

Figure 13.12 Agarose electrophoresis gels showing the relative collagen I, osteopontin, osteocalcin and beta-actin expression levels studied by RT-PCR. The cells were cultured for two weeks under the same conditions as those in the ALP assay. The data show that nano-HA can act as an inorganic inducer in the differentiation. Reprinted from Ref. [161].

(Figure 13.12). A contrasting phenomenon was observed, however, when bone tumor cells were cocultured with HA nanoparticles, which inhibited the proliferation of both U2OS and MG63 cells. Moreover, the degree of inhibition was inversely proportional to the particle size – that is, the smaller nanoparticle possessed a greater ability to prevent cell proliferation. It is suggested that the HA

nanoparticles can exhibit favorable cell proliferation to optimize biological functionality, in which particle size is believed to play a key role. These *in vitro* findings are of major significance in our understanding of cytophilicity and the biological activity of nanoparticles during biomineralization.

It is accepted among research groups investigating biomedical materials that ACP can be adsorbed and assimilated more readily by living organisms to produce new bone tissue than can crystallized calcium phosphates such as HA. The results of previous studies have also confirmed that ACP has an improved bioactivity compared to HA, since a greater degree of adhesion and proliferation of osteogenic cells was observed on ACP substrates. It has also been noted that the different size-effects of calcium phosphates were not taken into account in these studies, and that the ACP used were always smaller than the HA [162]. In order to understand and compare the influence of the crystallinity of calcium phosphate on osteogenic cells correctly, it is critical to use ACP and HA nanoparticles with the same size distribution. Hence, ACP and HAP particles of ~20 nm were synthesized and their effects on the crystallinity of calcium phosphates studied. The adhesion, proliferation and differentiation of bone marrow stromal cells (BMSCs) were measured on the ACP and HA films, which were compared at the same size scale. Surprisingly, more cells were adsorbed and proliferated on the well crystallized HA film than on the ACP film. Both, the activity of ALP and reverse transcriptase-polymer chain reaction (RT-PCR) assay showed that the differentiation of MSCs to osteoblasts was promoted significantly by nano-HA, despite it being well known that such differentiation cannot be initiated without a biological inducer. These current experimental phenomena show clearly that the crystallized phase of calcium phosphate (HA) provides a better substrate for MSCs than does its amorphous counterpart (ACP), when the factor of size-effect is removed. These new concepts on the relationship between the crystallinity of calcium phosphate and the responses of BMSCs support the importance of size- and phase-controls in the application of biomedical materials.

Given that the cell is sensitive to its ambience, very small alterations in particle size and topography – even down to nanoscale – could lead to a diversity of cell behavior [163, 164]. An understanding of HA nanoparticle–cell interaction is very important for subsequent use in *in vivo* situations, as very little is currently known about how cells recognize these alterations of materials. Hence, the mechanisms which cause such effects of HA nanoparticles on bone-related cells will require further systematic study.

13.7.3 Enamel Repair

Dental caries is a ubiquitous and worldwide oral disease. In the initial stages of caries lesions, oral bacteria cause damage to the enamel that serves as the exterior coating of teeth and which demonstrates remarkable hardness and resistance. As the most highly mineralized structure in the vertebrate body, enamel is composed of numerous needle-like apatite crystals, bundled in parallel ordered prisms to

ensure unique mechanical strength and biological protection [165]. While the principal proteins (amelogenins, ameloblastins, proteinases) involved in the hierarchical construction of enamel apatite are unaffected [166], the proteins that induce/control the crystallization of apatite are almost completely degraded or removed during enamel maturation. As a non-living tissue, the main component (97 wt%) of mature enamel is inorganic apatite, such that enamel will not undergo self-repair following substantial mineral loss [167]. Conventionally, filling with artificial materials is used to repair damaged enamel, with any defects being refilled with unstructured substitutes such as amalgam, metal alloys, ceramics or composite resins [168–170]. Unfortunately, however, secondary caries frequently arises at the interfaces between the tooth and foreign materials [171].

In the past, HA has always been considered a model compound for enamel, due to their chemical similarities [172]; consequently, the remineralization of enamel minerals using synthetic apatite or metastable calcium phosphate has always been suggested in dental research [173]. These chemically analogous compounds of enamel are not widely applied in clinic practice, however, as the native structure of enamel is too complex to be remodeled and the synthesized apatite crystallites often have different dimensions, morphologies and orientations from their natural counterparts. The result is poor adhesion and mechanical strength during restoration [174]. Despite their complicated hierarchical structures, the basic building blocks of enamel are the 20–40 nm particles of HA. Recent advances in biomineralization have also highlighted the fact that the features of smaller HA nanoparticles may more closely approximate those of biological apatite than of the larger HA particles that are used conventionally. It has been shown previously that HA nanoparticles can self-assemble to form enamel-like structures in the laboratory. Hence, a biomimetic technique has been proposed whereby localized repairs of the enamel surface can be improved by using nano-HA (dimension of 20 nm), the analogue of the basic building blocks of enamel rods. In differing from other frequently used calcium phosphates in biomineralization, such as the conventional HA (cHA; rod-like with lengths of hundreds of nanometers) and ACP, the biocompatibility between nano-HA and enamel can be greatly improved. It has been found that nano-HA can adsorb very strongly to an enamel surface, and may even be integrated into the natural enamel structure (Figure 13.13).

Surprisingly, the 20 nm HA nanoparticles can significantly inhibit future mineral loss from enamel surfaces. Without treatment, the demineralization of a natural enamel surface is remarkable in an acidic solution (pH = 4.5 ± 0.1; experimental period 2 days); the corrupted sites can be clearly observed, and the rate of mass loss is approximately $0.12 \pm 0.04\,\mathrm{mg\,mm^{-2}\,day^{-1}}$. In contrast, the layer of nano-HA on the treated enamel surface remained almost unchanged in acidic solution, with the rate of mass loss approaching zero ($<0.02\,\mathrm{mg\ mm^{-2}\,day^{-1}}$), which was beyond the sensitivity of the method used. As the new nano-HA is insensitive to dissolution, the underlying enamel surface is well protected in acidic conditions. With the restored enamel surface being the hardest biological component, its mechanical strength is the key parameter, and can be monitored by using the technique of nanoindentation. The 20 nm HA-coated enamel surface was shown to have a

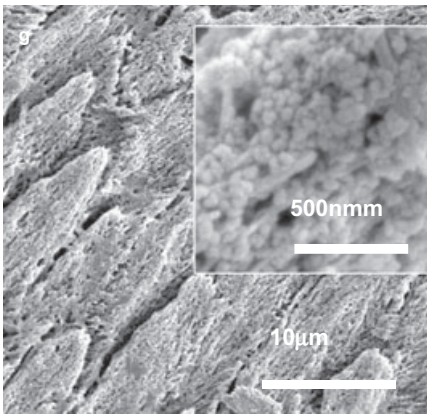

Figure 13.13 The strong adsorption effect of 20 nm-sized HA particles on a natural enamel surface.

hardness of 4.6 ± 0.4 GPa and an elastic modulus of 95.6 ± 8.4 GPa, values which were very similar to those of the natural materials (4.2 ± 0.2 and 94.1 ± 5.4 GPa, respectively) [66]. The nanometer scale of crystals in many biological hard tissues (such as enamel or vertebral bone) is selected by Nature to ensure optimal strength and a maximum tolerance of flaws (robustness). These features confer the 20 nm HA, or the basic building blocks of enamel, with an improved mechanical strength at an earlier stage. A similar mechanism has been suggested for restorative purposes by using 20 nm HA, although it is important that the featured hardness of enamel remains following the artificial repair.

The similarities between 20 nm HA and the building blocks of enamel apatite result in a biocompatible adsorption and fusion of the artificial material to the natural tissue. In fact, the enamel structure would even be reinforced by the nano HA, as secondary caries formation would be suppressed while the hardness remained. Such a strategy might have prospective application in dentistry as it offers a straightforward, but very effective, method for reconstructing tooth enamel that is suffering from mineral loss. Overall, the results of these studies suggest that analogues of nano building blocks will play a future role in biomineralization, despite the complicated morphology and structures of the natural materials.

13.7.4 Other Applications

Currently, a number of alternative applications of nanostructured calcium phosphate are under investigation, some of which will be introduced at this point. For example, Shirkhanzadeh1 [175] has synthesized a nano-HA coating via an electrochemical method and doping with silver ions (using silver nitrate solution at room

temperature), which demonstrated antimicrobial properties against a variety of bacteria. In addition, the surface modification of calcium phosphate nanoparticles can be performed to modulate its colloid stability, prevent its dissolution in the case of low pH, inflammation, and serve as an intermediate layer to allow strong bond formation between HA–polymer matrices and potentially enhance its bioactivity. Such treatment might also improves the conjugational ability of these materials with special functional groups (e.g. monoclonal antibodies) [15, 176].

A design strategy to create a nanocomposite using HA, collagen and chondroitin sulfate (proteoglycans) has been developed, with the intention to use this as a biomimetic bone graft for cartilage repair as a pre-mature bone [177]. Chondroitin sulfate is best known for its ability to promote the binding of chondronectin (the chondrocyte attachment factor) to collagen, and thus its use will gradually stimulate chondrocyte adhesion. Accordingly, this nanocomposite system is likely to provide specific binding sites for chondrocytes. In addition, the HA–collagen composite system has been used as a drug delivery device for neurotropin-nerve growth factor-beta. It is exciting to see that HA–collagen composites enriched with neurogenic-osteogenic factor can stimulate the formation of both periosteal and endocortical woven bone, and also of lamellar bone. In fact, Asaumi *et al.* [178] concluded that neurotropins and their receptors are expressed in bone-forming cells, and suggested that they might also be involved in the regulation of bone formation as an autocrine and paracrine factor *in vivo*. Future research in this area can be expected to highlight the potential utility of multifaceted approaches in engineering the simultaneous regeneration of multiple tissue types.

As particles, hollow spheres are extremely attractive, mainly because they can greatly enhance load quantities. The suggested candidates are lipids, polymer materials and porous inorganic materials such as silica-based materials [179]. Although these novel materials can improve the total intake of drugs, they also bring about new problems, for example, uncontrolled release kinetics and an unreasonable metabolism of the carriers [180]. In order to solve these problems, a biocompatible mineral phase – calcium phosphate – was selected as the carrier material. As calcium phosphate is native to the body, the metabolic problems should be greatly reduced, and the compound should demonstrate a unique potential for the delivery of bone and dentin therapeutics. The most important feature here is that, the hollow-structured calcium phosphate nanospheres can be collapsed and transferred into pin-shaped crystallites under ultrasonic treatment, during which the encapsulated compounds can be released. The main advantages of ultrasound are that it is noninvasive in biological applications and can penetrate deep into the interior of the body. It can also be carefully controlled via parameters such as power density, duty cycles and time of application [181, 182]. Thus, ultrasonic treatment can be used to precisely regulate morphological transformation, achieving 'smart' on/off and kinetic control of drug release.

Hollow calcium phosphate nanospheres can synthesized using an ultrasonic-assisted wet chemical reaction, with CTAB as modifier [183]. The uniform calcium phosphate hollow spheres formed are monodispersed in solution (Figure 13.14a),

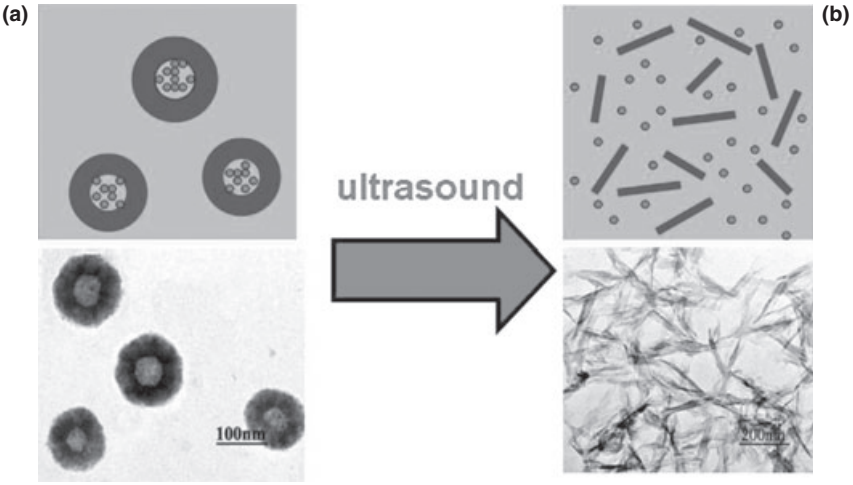

Figure 13.14 Hollow-structured calcium phosphate nanospheres can be transferred into pin-shaped crystallites under ultrasonic treatment. In this way the release of encapsulated compounds can be triggered on/off and its kinetics precisely regulated by the power density, duty cycle and application time of the ultrasound. Calcium phosphate nanospheres and ultrasonic treatment can be developed to create an ideal system for drug delivery and release. It was suggested that the release kinetics in this model system was related to ultrasonic power as well as to the treatment time. This feature could be developed into a useful strategy for the 'smart' control of drug release *in vivo*. Reprinted from Ref. [183].

and generally stable in air or in aqueous solutions, without ultrasonic application. While a slight aggregation may be observed in solution, the hollowed structures are unaffected. However, when an ultrasonic treatment is applied the hollow structures are deconstructed such that pin-like nanocrystallites of calcium phosphate are produced (Figure 13.14b). Unlike the free and slow diffusion of encapsulated drugs from the cavity through the shells [184], the release kinetics in this system is triggered by ultrasound, and the release process can be further controlled by ultrasonic application. Thus, an on/off control of the release can be achieved which is especially important in the clinical situation. It should be noted that, when the same ultrasonic treatment time periods are applied, the amounts of amylose released are virtually unchanged. Furthermore, the dynamics of release can also be conveniently regulated via the power density of ultrasound. As the pin-like calcium phosphate crystallites formed have similar behaviors to the biological HAs, it has been suggested that a combination of these hollow calcium phosphate nanospheres and ultrasonic treatment might be developed as an ideal system for drug delivery and release. It has also been suggested that the release kinetics in this model system is related to ultrasonic power, as well as to the treatment time – a feature that may be developed as a useful strategy for the smart control of drug release *in vivo*.

13.8 Summary

As the basic building blocks of biological tissues such as bone, dentin and enamel, HA nanoparticles play an important role in the construction of biominerals. It has been shown that nano-HA can confer on biomaterials an excellent biocompatibility, mechanical strength and self-preservation, and it is suggested therefore that nano-HAs can serve as ideal biomaterials, based on their excellent biocompatibility and bone/enamel integration. The production of nanostructured calcium phosphates represents an attractive field of research where many promising results have already been achieved. Much of the research conducted in this area will lead to enhanced applications in drug delivery systems and resorbable scaffolds that, with the passage of time, will be replaced by endogenous hard tissues. The future ability to functionalize surfaces with different molecules of varying nature and dimensions, by using their attachment to cells, as well as the ability to nanostructure the surface via the selection of biological species such as proteins and peptides. The ability to synthesize and process nano calcium phosphates with controlled structures and topographies – the aim being to simulate the basic nano units of natural materials – will allow the design of novel proactive bioceramics. However, the initial positive results of biocompatibility and biomimicity of novel nanostructured bioceramics to natural bone merit further consideration.

Many questions remain unanswered, however, regarding calcium phosphate chemistry, and further investigations must be undertaken to analyze cell behavior in terms of their interaction with nano calcium phosphates. One important, though as yet unresolved, question is how cells recognize the particle size and crystallinity of nano calcium phosphates. By what signal do nano calcium phosphates promote cell proliferation and differentiation, and how can these pathways be identified? It has been shown previously that smaller nano particles enter cells more readily, and that the bioactivity of calcium phosphate does not depend on its concentration in bulk solution. Initially, we should show how nanoparticles enter cells through membranes, and then examine the intracellular metabolic processes of nano calcium phosphate particles so that we can understand their role during biological processes. A second, critical, step will be to investigate changes in gene or protein expression in the absence and/or presence of calcium phosphate nanoparticles, as this may relate directly to cell proliferation and differentiation. It is in this type of study that the involvement of biologists will be vital.

An understanding of the interactions of nanoparticles with cells is crucial in order to improve their behavior *in vivo* and *in vitro*. Here, the main challenge is to develop novel methods for the *in situ* and real-time examination of nanoparticles in cells. These would include: (i) a detailed interfacial structure of nano calcium phosphates and the specific adsorption of proteins or other matrixes; (ii) the uptake process of nanoparticles by cells; and (iii) the intracellular metabolism of calcium phosphates, and its interaction with physiological reactions. Before attempting these investigations, however, it is important to determine how nanoparticles can be marked, without significantly altering their surface properties, and for this we

must first develop particles the sizes of which extend to only tens of nanometers. The final point to consider is that of 'biological security'. Although calcium phosphate nanomaterials will promote bone repair, the effect is nonspecific and they are equally capable of penetrating other areas, such as the circulatory system. Consequently, an understanding of how nano calcium phosphates exert their influences from a higher level will be essential if we are to develop the biological nanotechnology of the future. Of course, such an approach will be extremely complicated and necessitate an effective collaboration with scientists from many different disciplines.

Acknowledgments

These research studies were supported financially by the National Basic Research Program of China (2007CB516806), the National Natural Science Foundation of China (20571064 and 10672145), and the Zhejiang Provincial Natural Science Foundation of China (R407087). Dr Cai wishes especially to thank the Program for Innovative Research Team (IRT0654) and the Program for New Century Excellent Talents (NCET070763) in Zhejiang Sci-Tech University.

References

1 Mann, S. (2001) *Biomineralization Principles and Concepts in Bioinorganic Materials Chemistry*, Oxford University Press, New York.

2 Driessens, F.C.M., van Dijk, J.W.E. and Borggreven, J.M.P.M. (1978) Biological calcium phosphates and their role in the physiology of bone and dental tissues I. Composition and solubility of calcium phosphates. *Calcified Tissue International*, **26**, 127–37.

3 Vallet-Regí, M. and María González-Calbet, J. (2004) Calcium phosphates in the substitution of bone tissue. *Progress in Solid State Chemistry*, **32**, 1–31.

4 Weiner, S. and Addadi, L. (1997) Design strategies in mineralized biological materials. *Journal of Materials Chemistry*, **7**, 689–702.

5 Tang, R., Darragh, M.R., Orme, C.A., Hoyer, J.R. and Nancollas, G.H. (2005) Biological Modification in Brushite Crystallization. MRS Bulletin.

6 Giachelli, C.M. (1999) Ectopic calcification: gathering hard facts about soft tissue mineralization. *American Journal of Pathology*, **154**, 671–5.

7 Kirsch, T. (2006) Determinants of pathological mineralization. *Current Opinion in Rheumatology*, **18**, 174–80.

8 Christian, R.C. and Fitzpatrick, L.A. (1999) Vascular calcification. *Current Opinion in Nephrology and Hypertension*, **8**, 443–8.

9 Feng, Q.L., Cui, F.Z., Wang, H., Kim, T.N. and Kim, J.O. (2000) Influence of solution conditions on deposition of calcium phosphate on titanium by NaOH-treatment. *Journal of Crystal Growth*, **210**, 735–40.

10 Wang, L.J., Tang, R., Bonstein, T., Bush, P. and Nancollas, G.H. (2006) Enamel demineralization in primary and permanent teeth. *Journal of Dental Research*, **85**, 359–63.

11 Boskey, A. (2003) Bone mineral crystal size. *Osteoporosis International*, **14**(Suppl. 5), 16–21.

12 Lieber, R.L. (1992) *Skeletal Muscle Structure and Function*, Williams and Wilkins, Baltimore, MD.

13 Baer, E., Cassidy, J.J. and Hiltner, A. (1991) Hierarchical structure of collagen composite systems. *Pure and Applied Chemistry*, **63**, 961–73.

14 Alivisatos, A.P. (2000) Biomineralization: enhanced: naturally aligned nanocrystals. *Science*, **289**, 736–7.

15 Narayan, R.J., Kumta, P.N., Sfeir, C., Lee, D.H., Choi, D. and Olton, D. (2004) Nanostructured ceramics in medical devices: applications and prospects. *Journal of the Minerals, Metals and Materials Society of the United States*, **56**, 38–43.

16 Banfield, J.F., Welch, S.A., Zhang, H., Ebert, T.T. and Penn, R.L. (2000) Aggregation-based crystal growth and microstructure development in natural iron oxyhydroxide biomineralization products. *Science*, **289**, 751–4.

17 Cölfen, H. (2007) Bio-inspired mineralization using hydrophilic polymers. *Topics in Current Chemistry*, **271**, 1–77.

18 Oaki, Y. and Imai, H. (2005) Nanoengineering in echinoderms: the emergence of morphology from nanobricks. *Small*, **2**, 66–70.

19 Yamamoto, S., Yoshioka, H., Uraoka, Y., Fuyuki, T., Okuda, M. and Yamashita, I. (2007) Surface potential difference of biomineralized inorganic nanodot by Kelvin probe force microscopy. *Japanese Journal of Applied Physics*, **46**, 5647–51.

20 Lee, S.-H. and Shin, H. (2007) Matrices and scaffolds for delivery of bioactive molecules in bone and cartilage tissue engineering. *Advanced Drug Delivery Reviews*, **59**, 339–59.

21 Xu, H.H.K., Weir, M.D., Burguera, E.F. and Fraser, A.M. (2006) Injectable and macroporous calcium phosphate cement scaffold. *Biomaterials*, **27**, 4279–87.

22 Chowdhury, E.H., Kunou, M., Nagaoka, M., Kundu, A.K., Hoshiba, T. and Akaike, T. (2004) High-efficiency gene delivery for expression in mammalian cells by nanoprecipitates of Ca–Mg phosphate. *Gene*, **341**, 77–82.

23 Bouldin, D.R. and Sample, E.C. (1959) Calcium phosphate fertilizers: III. The effect of surface area on the availability coefficients of the dicalcium phosphates. *Soil Science Society of America Journal*, **23**, 276–81.

24 Ginebra, M.P., Driessens, F.C.M. and Planell, J.A. (2004) Effect of the particle size on the micro and nanostructural features of a calcium phosphate cement: a kinetic analysis. *Biomaterials*, **25**, 3453–62.

25 Dorozhkin, S.V. and Epple, M. (2002) Biological and medical significance of calcium phosphates. *Angewandte Chemie–International Edition in English*, **41**, 3130–46.

26 Adamopoulos, O. and Papadopoulos, T. (2007) Nanostructured bioceramics for maxillofacial applications. *Journal of Materials Science: Materials in Medicine*, **18**, 1587–97.

27 Ginebra, M.P., Traykova, T. and Planell, J.A. (2006) Calcium phosphate cements as bone drug delivery systems: a review. *Journal of Controlled Release*, **113**, 102–10.

28 Bohner, M. (2007) Reactivity of calcium phosphate cements. *Journal of Materials Chemistry*, **17**, 3980–6.

29 Cui, F.Z., Li, Y. and Ge, J. (2007) Self-assembly of mineralized collagen composites. *Materials Science and Engineering R*, **57**, 1–27.

30 Weiner, S., Traub, W. and Daniel Wagner, H. (1999) Lamellar bone: structure–function relations. *Journal of Structural Biology*, **126**, 241–55.

31 Olszta, M.J., Cheng, X., Jee, S.S., Kumar, R., Kim, Y.-Y., Kaufmane, M.J., Douglas, E.P. and Gower, L.B. (2007) Bone structure and formation: a new perspective. *Materials Science and Engineering R*, **58**, 77–116.

32 Wong, S.Y., Kariks, J., Evans, R.A., Dunstan, C.R. and Hills, E. (1985) The effect of age on bone composition and viability in the femoral head. *Journal of Bone and Joint Surgery*, **67**, 274–83.

33 Mann, S. (2006) *Biominerals and Biomineralization in Biological Inorganic Chemistry: Structure and Reactivity*, University Science Books, Sausalito, CA, p. 79.

34 Weiner, S. and Wagner, H.D. (1998) The material bone: structure mechanical function relations. *Annual Review of Materials Science*, **28**, 271–98.

35 Currey, J.D. (2005) Materials science: hierarchies in biomineral structures. *Science*, **309**, 253–4.

36 Ji, B. and Gao, H. (2006) Elastic properties of nanocomposite structure of bone. *Composites Science and Technology*, **66**, 1212–18.

37 Wang, L., Nancollas, G.H., Henneman, Z.J., Klein, E. and Weiner, S. (2006) Nanosized particles in bone and dissolution insensitivity of bone mineral. *Biointerphases*, **1**, 106–11.

38 Gao, H., Ji, B., Jager, I.L., Arz, E. and Fratzl, P. (2003) Materials become insensitive to flaws at nanoscale: lessons from nature. *Proceedings of the National Academy of Sciences of the United States of America*, **100**, 5597–600.

39 Gupta, H.S., Seto, J., Wagermaier, W., Zaslansky, P., Boesecke, P. and Fratzl, P. (2006) Cooperative deformation of mineral and collagen in bone at the nanoscale. *Proceedings of the National Academy of Science of the United States of America*, **103**, 17741–1746.

40 Raisz, L.G. and Kream, B.E. (1981) Hormonal control of skeletal growth. *Annual Review of Physiology*, **43**, 225–38.

41 Porter, A.E., Nalla, R.K., Minor, A., Jinschek, J.R., Kisielowski, C., Radmilovic, V., Kinney, J.H., Tomsia, A.P. and Ritchie, R.O. (2005) A transmission electron microscopy study of mineralization in age-induced transparent dentin. *Biomaterials*, **26**, 7650–60.

42 Kirkham, J., Brookes, S.J., Shore, R.C., Wood, S.R., Smith, D.A., Zhang, J., Chen, H. and Robinson, C. (2002) Physico-chemical properties of crystal surfaces in matrix–mineral interactions during mammalian biomineralisation. *Current Opinion in Colloid and Interface Science*, **7**, 124–32.

43 Daculsi, G., Mentanteau, J., Kerebel, L.M. and Mitre, D. (1984) Length and shape of enamel crystals. *Calcified Tissue International*, **36**, 550–5.

44 Yamagishi, K., Onuma, K., Suzuki, T., Okada, F., Tagami, J., Otsuki, M. and Senawangse, P. (2005) A synthetic enamel for rapid tooth repair. *Nature*, **433**, 819.

45 Chen, H., Holl, M.B., Orr, B., Majoros, I. and Clarkson, B.H. (2003) Interaction of dendrimers (artificial proteins) with biological hydroxyapatite crystals. *Journal of Dental Research*, **82**, 443–8.

46 Chen, H., Tang, Z., Liu, J., Sun, K., Chang, S.R., Peters, M.C., Mansfield, J.F., Czajka-Jakubowska, A. and Clarkson, B.H. (2006) Acellular synthesis of a human enamel-like microstructure. *Advanced Materials*, **18**, 1846–51.

47 Cui, F.Z. and Ge, J. (2007) New observations of the hierarchical structure of human enamel, from nanoscale to microscale. *Journal of Tissue Engineering and Regenerative Medicine*, **1**, 185–91.

48 Moss, M.L., Moss-Salentijn, L. and Cartilage, I. (1983) *Structure, Function and Biochemistry* (ed. B.K. Hall) Academic Press, New York, p. 1.

49 Robinson, R.A. and Cameron, D.A. (1956) Electron microscopy of cartilage and bone matrix at the distal epiphyseal line of the femur in the newborn infant. *Journal of Biophysical and Biochemical Cytology*, **2**, 253–60.

50 Giachelli, C.M. (2001) Ectopic calcification: new concepts in cellular regulation. *Zeitschrift für Kardiologie*, **90**(Suppl. 3), 31–7.

51 Murugan, R. and Ramakrishna, S. (2005) Development of nanocomposites for bone grafting. *Composites Science and Technology*, **65**, 2385–406.

52 Moreau, J.W., Weber, P.K., Martin, M.C., Gilbert, B., Hutcheon, I.D. and Banfield, J.F. (2007) Extracellular proteins limit the dispersal of biogenic nanoparticles. *Science*, **316**, 1600–3.

53 Inoue, S. and Okazaki, I. (1977) Biocrystals. *Scientific American*, **236**, 82–4.

54 Ahmad, Z. and Mark, J.E. (1998) Biomimetic materials: recent development in organic-inorganic hybrids. *Materials Science and Engineering C*, **6**, 183–96.

55 Brecevic, L.J. and Furedi-Milhofer, H. (1972) Precipitation of calcium

phosphates from electrolyte solutions II. The formation and transformation of the precipitates. *Calcified Tissue International*, **10**, 82–90.

56 Lowenstam, H.A. and Weiner, S. (1985) Transformation of amorphous calcium phosphate to crystalline dahillite in the radular teeth of chitons. *Science*, **227**, 51–3.

57 Brown, W.E. (1966) Crystal growth of bone mineral. *Clinical Orthopaedics and Related Research*, **44**, 205–20.

58 Arnold, S., Plate, U., Wiesmann, H.P., Stratmann, U., Kohl, H. and Hohling, H.J. (2001) Quantitative analyses of the biomineralization of different hard tissues. *Journal of Microscopy*, **202**, 488–94.

59 Weiner, S., Sagi, I. and Addadi, L. (2005) Structure biology: choosing the crystallization path less traveled. *Science*, **309**, 1027–8.

60 Tohda, H., Yamada, M., Yamaguchi, Y. and Yanagisawa, T. (1997) High-resolution electron microscopical observations of initial enamel crystals. *Journal of Electron Microscopy*, **46**, 97–101.

61 Meneghini, C., Dalconi, M.C., Nuzzo, S., Mobilio, S. and Wenk, R.H. (2003) Rietveld refinement on X-ray diffraction patterns of bioapatite in human fetal bones. *Biophysical Journal*, **84**, 2021–19.

62 Beniash, E., Aizenberg, J., Addadi, L. and Weiner, S. (1997) Amorphous calcium carbonate transforms into calcite during sea urchin larval spicule growth. *Proceedings of the Royal Society of London B*, **264**, 461–5.

63 TenHuisen, K.S., Martin, R.I., Klimkiewicz, M. and Brown, P.W. (1995) Formation and properties of a synthetic bone composite: hydroxyapatite–collagen. *Journal of Biomedical Materials Research*, **29**, 803–10.

64 Miyamoto, Y., Ishikawa, K., Takechi, M., Toh, T., Yuasa, T., Nagayama, M. and Suzuki, K. (1998) Basic properties of calcium phosphate cement containing atelocollagen in its liquid or powder phases. *Biomaterials*, **9**, 707–15.

65 Habelitz, S., Marshall, S.J., Marshall, G.W. Jr, and Balooch, M. (2001) Mechanical properties of human dental enamel on the nanometre scale. *Archives of Oral Biology*, **46**, 173–83.

66 He, L. and Swain, M.V. (2007) Enamel–a 'metallic-like' deformable biocomposite. *Journal of Dentistry*, **35**, 431–7.

67 Gupta, H.S., Wagermaier, W., Zickler, G.A., Hartmann, J., Funari, S.S., Roschger, P., Wagner, H.D. and Fratzl, P. (2006) Fibrillar level fracture in bone beyond the yield point. *International Journal of Fracture*, **139**, 425–36.

68 Tai, K., Ulm, F. and Ortiz, C. (2006) Nanogranular origins of the strength of bone *Nano Letters*, **6**, 2520–5.

69 Morris, M.D., Finney, W.F., Rajachar, R.M. and Kohn, D.H. (2004) Bone tissue ultrastructural response to elastic deformation probed by Raman spectroscopy. *Faraday Discussions*, **126**, 159–68.

70 Freundlich, H. (1923) *Colloid and Capillary Chemistry*, Dutton, New York, p. 153.

71 Tang, R. and Nancollas, G.H. (2002) New mechanism for the dissolution of sparingly soluble minerals. *Pure and Applied Chemistry*, **74**, 1851–7.

72 Tang, R., Orme, C.A. and Nancollas, G.H. (2003) A new understanding of demineralization: the dynamics of brushite dissolution. *Journal of Physical Chemistry B*, **107**, 10653–7.

73 Barralet, J., Akao, M. and Aoki, H. (2000) Dissolution of dense carbonate apatite subcutaneously implanted in Wistar rats. *Journal of Biomedical Materials Research*, **49**, 176–82.

74 Tang, R. and Nancollas, G.H. (2000) Abnormal dissolution of octacalcium phosphate crystals at constant undersaturation. *Journal of Crystal Growth*, **212**, 261–9.

75 Tang, R., Wu, W., Hass, M. and Nancollas, G.H. (2001) Kinetics of dissolution of β-tricalcium phosphate. *Langmuir*, **17**, 3480–5.

76 Tomson, M.B., Nancollas, G.H. and Kinetics, M. (1978) A constant composition approach. *Science*, **200**, 1059–60.

77 Tang, R., Wang, L., Orme, C.A., Bonstein, T., Bush, P.J. and Nancollas, G.H. (2004) Dissolution at the nanoscale: self-preservation of biominerals. *Angewandte Chemie–International Edition in English*, **43**, 2697–701.

78 Roschger, P., Grabner, B.M., Rinnerthaler, S., Tesch, W., Kneissel, M., Berzlanovich, A., Klaushofer, K. and Fratzl, P. (2001) Structural development of the mineralized tissue in the human L4 vertebral body. *Journal of Structural Biology*, **136**, 126–36.

79 Roschger, P., Goldenberg, F., Klaushofer, K. and Fratzl, P. (2001) Graded microstructure and mechanical properties of human crown dentin. *Calcified Tissue International*, **69**, 147–57.

80 Lasaga, A.C. and Luttge, A. (2001) Variation of crystal dissolution rate based on a dissolution stepwave model. *Science*, **291**, 2400–4.

81 Tang, R., Wang, L. and Nancollas, G.H. (2004) Size-effects in the dissolution of hydroxyapatite: an understanding of biological demineralization. *Journal of Materials Chemistry*, **14**, 2341–6.

82 Burton, W.K., Cabrera, N. and Frank, F.C. (1949) Role of dislocations in crystal growth. *Nature*, **163**, 398–9.

83 Traube, I., Schoning, I. and Weber, L.J. (1927) *Solubility and Surface Tension*, **Ber 60B**, 1808–14.

84 Wu, W. and Nancollas, G.H. (1999) Determination of interfacial tension from crystallization and dissolution data: a comparison with other methods. *Advances in Colloid and Interface Science*, **79**, 229–79.

85 Christoffersen, J. and Christoffersen, M.R. (1992) A revised theory for the growth of crystals by surface nucleation. *Journal of Crystal Growth*, **121**, 608–16.

86 Kuriakose, T.A., Kalkura, S.N., Palanichamy, M., Arivuoli, D., Dierks, K., Bocellif, G. and Betzel, C. (2004) Synthesis of stoichiometric nano crystalline hydroxyapatite by ethanol-based sol–gel technique at low temperature. *Journal of Crystal Growth*, **263**, 517–23.

87 Tas, A.C. (2000) Synthesis of biomimetic Ca-hydroxyapatite powders at 37 degrees C in synthetic body fluids. *Biomaterials*, **21**, 1429–38.

88 Suchanek, L.W., Shuk, P., Byrappa, K., Riman, R.E., TenHuisen, K.S. and Janas, V.F. (2002) Mechanochemical–hydrothermal synthesis of carbonated apatite powders at room temperature. *Biomaterials*, **23**, 699–710.

89 Ruksudjarit, A., Pengpat, K., Rujijanagul, G. and Tunkasiri, T. (2008) Synthesis and characterization of nanocrystalline hydroxyapatite from natural bovine bone. *Current Applied Physics*, **8**, 270–2.

90 Martin, C.R. (1996) Membrane-based synthesis of nanomaterials. *Chemistry of Materials*, **8**, 1739–46.

91 Wang, X., Zhuang, J., Peng, Q. and Li, Y. (2005) A general strategy for nanocrystal synthesis. *Nature*, **437**, 121–4.

92 Hiroko, F., Hideyuki, Y. and Mamoru, A. (2008) In vitro synthesis of calcium nanoparticles using the protein cage of apoferritin. *Key Engineering Materials*, **361–363**, 183–6.

93 Faivre, D. (2007) Biomimetic formation of magnetite nanoparticles, in *Handbook of Biomineralization: Biomimetic and Bioinspired Chemistry*, Wiley-VCH Verlag GmbH, Weinheim, pp. 159–71.

94 Ciftcioglu, N., McKay, D.S., Mathew, G. and Kajander, E.O. (2006) Nanobacteria: fact or friction? Characteristics, detection, and medical importance of novel self-replicating, calcifying nanoparticles. *Journal of Investigative Medicine*, **54**, 385–94.

95 Ingert, D. and Pileni, M.P. (2001) Limitations in producing nanocrystals using reverse micelles as nanoreactors. *Advanced Functional Materials*, **11**, 136–9.

96 Zhang, B., Li, G., Zhang, J., Zhang, Y. and Zhang, L. (2003) Synthesis and characterization of PbS nanocrystals in water/C12E9/cyclohexane microemulsions. *Nanotechnology*, **14**, 443–6.

97 Zhang, B., Davis, S.A., Mann, S. and Mendelson, N.H. (2000) Bacterial templating of zeolite fibres with hierarchical structure. *Chemical Communications*, 781–2.

98 Shenton, W., Douglas, T., Young, M., Stubbs, G. and Mann, S. (1999) Inorganic-organic nanotube composites from template mineralization of tobacco mosaic virus. *Advanced Materials*, **11**, 253–6.

99 Wong, K.K.W. and Mann, S. (1996) Biomimetic synthesis of cadmium sulfide-ferritin nanocomposites. *Advanced Materials*, **8**, 928–32.

100 Douglas, T. and Young, M. (1998) Host-guest encapsulation of materials by assembled virus protein cages. *Nature*, **393**, 152–5.

101 Baral, S. and Schoen, P. (1993) Silica-deposited phospholipid tubules as a precursor to hollow submicron-diameter silica cylinders. *Chemistry of Materials*, **5**, 145–7.

102 Sun, Y., Guo, G., Tao, D. and Wang, Z. (2007) Reverse microemulsion-directed synthesis of hydroxyapatite nanoparticles under hydrothermal conditions. *Journal of Physics and Chemistry of Solids*, **68**, 373–7.

103 Bose, S. and Saha, S.K. (2003) Synthesis and characterization of hydroxyapatite nanopowders by emulsion technique. *Chemistry of Materials*, **15**, 4464–9.

104 Shchukin, D.G., Sukhorukov, G.B. and Mohwald, H. (2003) Biomimetic fabrication of nanoengineered hydroxyapatite/polyelectrolyte composite shell. *Chemistry of Materials*, **15**, 3947–50.

105 Perkin, K.K., Turner, J.L., Wooley, K.L. and Mann, S. (2005) Fabrication of hybrid nanocapsules by calcium phosphate mineralization of shell cross-linked polymer micelles and nanocages. *Nano Letters*, **5**, 1457–61.

106 Shenton, W., Pum, D., Sleytr, U. and Mann, S. (1997) Biocrystal templating of CdS superlattices using self-assembled bacterial S-layers. *Nature*, **389**, 585.

107 Koinkar, V.N. and Bhushan, B. (1996) Microtribological studies of unlubricated and lubricated surfaces using atomic force/friction force microscopy. *Journal of Vacuum Science and Technology*, A**14**, 2378–91.

108 Carpick, R.W. and Salmeron, M. (1997) Scratching the surface: fundamental investigations of tribology with atomic force microscopy. *Chemical Reviews*, **97**, 1163–94.

109 Zhang, L.J., Liu, H.G., Feng, X.S., Zhang, R.J., Zhang, L., Mu, Y.D., Hao, J.C., Qian, D.J. and Lou, Y.F. (2004) Mineralization mechanism of calcium phosphates under three kinds of langmuir monolayers. *Langmuir*, **20**, 2243–9.

110 Cai, Y., Liu, Y., Yan, W., Hu, Q., Tao, J., Zhang, M., Shi, Z. and Tang, R. (2007) Role of hydroxyapatite nanoparticle size in bone cell proliferation. *Journal of Materials Chemistry*, **17**, 3780–7.

111 Chen, H., Clarkson, B.H., Sun, K. and Mansfield, J.F. (2005) Self-assembly of synthetic hydroxyapatite nanorods into an enamel prism-like structure. *Journal of Colloid and Interface Science*, **288**, 97–103.

112 Fowler, E., Li, M., Mann, S. and Margolis, H.C. (2005) Influence of surfactant assembly on the formation of calcium phosphate materials – a model for dental enamel formation. *Journal of Materials Chemistry*, **15**, 3317.

113 Liao, S.S., Cui, F.Z., Zhang, W. and Feng, Q.L. (2004) Hierarchically biomimetic bone scaffold materials: nano-HA/collagen/PLA composite. *Journal of Biomedical Materials Research B*, **69**B, 158–65.

114 Bradt, J.H., Mertig, M., Teresiak, A. and Pompe, W. (1999) Biomimetic mineralization of collagen by combined fibril assembly and calcium phosphate formation. *Chemistry of Materials*, **11**, 2694–701.

115 Yoreo, D., Vekilov, J.J. and Rev, P.G. (2003) Principles of crystal nucleation and growth. *Reviews in Mineralogy and Geochemistry*, **54**, 57–93.

116 Colfen, H. and Mann, S. (2003) Higher-order organization by mesoscale self-assembly and transformation of hybrid nanostructures. *Angewandte Chemie–International Edition in English*, **42**, 2350–65.

117 Gilbert, B. and Banfield, J.F. (2005) Molecular-scale processes involving nanoparticulate minerals in

biogeochemical systems. *Reviews in Mineralogy and Geochemistry*, **59**, 109–55.

118 Penn, R.L. and Banfield, J.F. (1998) Imperfect oriented attachment: dislocation generation in defect-free nanocrystals. *Science*, **281**, 969–71.

119 Penn, R.L. (2004) Kinetics of oriented aggregation. *Journal of Physical Chemistry B*, **108**, 12707–12.

120 Huang, F., Zhang, H.Z. and Banfield, J.F. (2003) Two-stage crystal-growth kinetics observed during hydrothermal coarsening of nanocrystalline ZnS. *Nano Letters*, **3**, 373–8.

121 Yang, H.G. and Zeng, H.C. (2004) Self-construction of hollow SnO(2) octahedra based on two-dimensional aggregation of nanocrystallites. *Angewandte Chemie–International Edition in English*, **43**, 5930–3.

122 Cho, K.S., Talapin, D.V., Gaschler, W. and Murray, C.B. (2005) Designing PbSe nanowires and nanorings through oriented attachment of nanoparticles. *Journal of the American Chemical Society*, **127**, 7140–7.

123 Colfen, H. and Antonietti, M. (2005) Mesocrystals: inorganic superstructures made by highly parallel crystallization and controlled alignment. *Angewandte Chemie - International Edition in English*, **44**, 5576–91.

124 Addadi, L., Raz, S. and Weiner, S. (2003) Taking advantage of disorder: amorphous calcium carbonate and its roles in biomineralization. *Advanced Materials*, **15**, 959–70.

125 Sethmann, I., Putnis, A., Grassmann, O. and Lobmann, P. (2005) Observation of nano-clustered calcite growth via a transient phase mediated by organic polyanions: a close match for biomineralization. *American Mineralogist*, **90**, 1213–17.

126 Wang, T., Colfen, H. and Antonietti, M. (2005) Nonclassical crystallization: mesocrystals and morphology change of $CaCO_3$ crystals in the presence of a polyelectrolyte additive. *Journal of the American Chemical Society*, **127**, 3246–7.

127 Xu, A., Antonietti, M., Colfen, H. and Fang, Y. (2006) Uniform hexagonal plates of vaterite $CaCO_3$ mesocrystals formed by biomimetic mineralization. *Advanced Functional Materials*, **16**, 903–8.

128 Zhang, Z.P., Sun, H.P., Shao, X.Q., Li, D.F., Yu, H.D. and Han, M.Y. (2005) Three-dimensionally oriented aggregation of a few hundred nanoparticles into monocrystalline architectures. *Advanced Materials*, **17**, 42–7.

129 Tao, J., Pan, H., Zeng, Y., Xu, X. and Tang, R. (2007) Roles of amorphous calcium phosphate and biological additives in the assembly of hydroxyapatite nanoparticles. *Journal of Physical Chemistry B*, **111**, 13410–18.

130 Wang, L., Guan, X., Du, C., Moradian-Oldak, J. and Nancollas, G.H. (2007) Amelogenin promotes the formation of elongated apatite microstructures in a controlled crystallization system. *Journal of Physical Chemistry C*, **111**, 6398–404.

131 Laurencin, C., Khan, Y. and El-Amin, S.F. (2006) Bone graft substitute materials. *Expert Review of Medical Devices*, **3**, 49–57.

132 Kurella, A. and Dahoter, N.B. (2005) Surface modification for bioimplants: the role of laser surface engineering. *Journal of Biomaterials Applications*, **20**, 5–50.

133 Ong, J.L., Lucas, L.C., Lacefield, W.R. and Rigney, E.D. (1992) Structure, solubility and bond strength of thin calcium phosphate coatings produced by ion beam sputter deposition. *Biomaterials*, **13**, 249–54.

134 Yan, W.Q., Nakamura, T., Kawanabe, K., Nishigochi, S., Oka, M. and Kokubo, T. (1997) Apatite layer-coated titanium for use as bone bonding implants. *Biomaterials*, **18**, 1185–90.

135 Barrere, F., Layrolle, P., van Blitterswijk, C.A. and de Groot, K. (2004) Biomimetic coatings on titanium: a crystal growth study of octacalcium phosphate. *Journal of Materials Science: Materials in Medicine*, **12**, 529–34.

136 Loty, C., Sautier, J.M., Boulekbache, H., Kokubo, T., Kim, H.M. and Forest, N. (2000) In vitro bone formation on a bone-like apatite layer prepared by a biomimetic process on a bioactive glass-ceramic. *Journal of Biomedical Materials Research*, **49**, 423–34.

137 Kim, H.M., Miyazaki, T. and Kokubo, T. (2001) *Bioceramics*, Vol. 13, Trans Tech Publ., Switzerland, pp. 192–5.

138 Catledge, S.A., Fries, M.D., Vohra, Y.K., Lacefield, W.R., Lemons, J., Woodard, S. and Venugopalan, R. (2002) Nanostructured ceramics for biomedical implants. *Journal of Nanoscience and Nanotechnology*, **2**, 1–20.

139 Fan, Y., Duan, K. and Wang, R. (2005) A composite coating by electrolysis-induced collagen self-assembly and calcium phosphate mineralization. *Biomaterials*, **26**, 1623–32.

140 Doi, Y., Horiguchi, T., Moriwaki, Y., Kitago, H., Kajimoto, T. and Iwayama, Y. (1996) Formation of apatite–collagen complexes. *Journal of Biomedical Materials Research*, **31**, 43–9.

141 Stupp, S.I. and Braun, P.V. (1997) Molecular manipulation of microstructures: biomaterials, ceramics, and semiconductors. *Science*, **277**, 1242–8.

142 Webster, T.J., Ergun, C., Doremus, R.H. and Siegel, R.W. (2000) Specific proteins mediate enhanced osteoblast adhesion on nanophase ceramics. *Journal of Biomedical Materials Research*, **51**, 475–83.

143 Xu, H.H.K., Weir, M.D., Sun, L., Takagi, S. and Chow, L.C. (2007) Effects of calcium phosphate nanoparticles on Ca-PO_4 composite. *Journal of Dental Research*, **86**, 378–83.

144 Müller, W.E.G., Boreiko, A., Wang, X., Krasko, A., Geurtsen, W., Custódio, M.R., Winkler, T., Lukić-Bilela, L., Link, T. and Schröder, H.C. (2007) Morphogenetic activity of silica and bio-silica on the expression of genes controlling biomineralization using SaOS-2 cells. *Calcified Tissue International*, **81**, 382–93.

145 Paul, W. and Sharma, C. (2001) Porous hydroxyapatite nanoparticles for intestinal delivery insulin. *Trends in Biomaterials and Artificial Organs*, **14**, 37–8.

146 Sfeir, C., Bennett, J. and Kumta, P. (2003) Nanosized calcium phosphate particles for plasmid gene delivery. *Molecular Therapy*, **7**, s225.

147 Welzel, T., Radtke, I., Meyer-Zaika, W., Heumann, R. and Epple, M. (2004) Transfection of cells with custom-made calcium phosphate nanoparticles coated with DNA. *Journal of Materials Chemistry*, **14**, 2213–17.

148 Rueger, J.M. (1998) Bone substitution materials. Current status and prospects. *Orthopade*, **27**, 72–9.

149 Paul, W. and Sharma, C.P. (2006) Nanoceramic matrices: biomedical applications. *American Journal of Biochemistry and Biotechnology*, **2**, 41–8.

150 Cui, F.Z., Li, Y., and Ge, J. (2007) Self-assembly of mineralized collagen composites. *Materials Science and Engineering Reports*, **57**, 1–27.

151 Zhang, Y. and Zhang, M.Q. (2002) Calcium phosphate/chitosan composite scaffolds for controlled in vitro antibiotic drug release. *Journal of Biomedical Materials Research*, **62**, 378–86.

152 Shirkhanzadeh, M. and Azadegan, M. (1998) Formation of carbonate apatite on calcium phosphate coatings containing silver ions. *Journal of Materials Science: Materials in Medicine*, **9**, 385–91.

153 Yoon, B.H., Kim, H.W., Lee, S.H., Bae, C.J., Koh, Y.H., Kong, Y.M. and Kim, H.E. (2005) Stability and cellular responses to fluorapatite–collagen composites. *Biomaterials*, **26**, 2957–63.

154 Guo, H., Khor, K.A., Boey, Y.C. and Miao, X. (2003) Laminated and functionally graded hydroxyapatite/yttria stabilized tetragonal zirconia composites fabricated by spark plasma sintering. *Biomaterials*, **24**, 667–75.

155 Brown, W.E. and Chow, L.C. (1983) A new calcium phosphate setting cement. *Journal of Dental Research*, **62**, 672–9.

156 Constantz, B.R., Ison, I.C., Fulmer, M.T., Poser, R.D., Smith, S.T., VanWagoner, M., Ross, J., Goldstein, S.A., Jupiter, J.B. and Rosenthal, D.I. (1995) Skeletal repair by in situ formation of the mineral phase of bone. *Science*, **267**, 1796–9.

157 Han, Y., Li, S., Wang, X. and Chen, X. (2004) Synthesis and sintering of nanocrystalline hydroxyapatite powders by citric acid sol–gel combustion method. *Materials Research Bulletin*, **39**, 25–32.

158 Webster, T.J., Ergun, C., Doremus, R.H., Siegel, R.W. and Bizio, R. (2000) Enhanced functions of osteoblasts on nanophase ceramics. *Biomaterials*, **21**, 1803–10.

159 Webster, T.J., Ergun, C., Doremus, R.H., Siegel, R.W. and Bizio, R. (2001) Enhanced osteoclast-like cell functions on nanophase ceramics. *Biomaterials*, **22**, 1327–33.

160 Chan, C.K., Kumar, T.S.S., Liao, S., Murugan, R. and Ramakrishnan, M.N.S. (2006) Biomimetic nanocomposites for bone graft applications. *Nanomedicine*, **1**, 177–88.

161 Hu, Q., Tan, Z., Liu, Y., Tao, J., Cai, Y., Zhang, M., Pan, H., Xu, X. and Tang, R. (2007) Effect of crystallinity of calcium phosphate nanoparticles on adhesion, proliferation, and differentiation of bone marrow mesenchymal stem cells. *Journal of Materials Chemistry*, **17**, 4690–8.

162 Balasundaram, G., Sato, M. and Webster, T.J. (2006) Using hydroxyapatite nanoparticles and decreased crystallinity to promote osteoblast adhesion similar to functionalizing with RGD. *Biomaterials*, **27**, 2798–805.

163 Stevens, M.M. and George, J.H. (2005) Exploring and engineering the cell surface interface. *Science*, **310**, 1135–8.

164 Gupta, A.K., Gupta, M., Yarwood, S.J. and Curtis, A.S.G. (2004) Effect of cellular uptake of gelatin nanoparticles on adhesion, morphology and cytoskeleton organisation of human fibroblasts. *Journal of Controlled Release*, **95**, 197–207.

165 Dorozhkin, S.V. and Epple, M. (2002) Biological and medical significance of calcium phosphates. *Angewandte Chemie–International Edition in English*, **41**, 3130–46.

166 Fincham, A.G., Moradian-Oldak, J. and Simmer, J.P. (1999) The structural biology of the developing dental enamel matrix. *Journal of Structural Biology*, **126**, 270–99.

167 Busch, S. (2004) Regeneration of human tooth enamel. *Angewandte Chemie–International Edition in English*, **43**, 1428–31.

168 Raskin, A., Michotte-Theall, B., Vreven, J. and Wilson, N.H.F. (1999) Clinical evaluation of a posterior composite 10-year report. *Journal of Dentistry*, **27**, 13–19.

169 Wilson, N.H.F. and Major, I.A. (2000) The teaching of class I and class II direct composite restorations in European dental schools. *Journal of Dentistry*, **28**, 15–21.

170 Hilton, T. (2002) Can modern restorative procedures and materials reliably seal cavities? In vitro investigations. Part 1. *American Journal of Dentistry*, **15**, 198–210.

171 Onuma, K., Yamagishi, K. and Oyane, A. (2005) Nucleation and growth of hydroxyapatite nanocrystals for nondestructive repair of early caries lesions. *Journal of Crystal Growth*, **282**, 199–207.

172 Narasaraju, T.S.B. and Phebe, D.E. (1996) Some physico-chemical aspects of hydroxylapatite. *Journal of Materials Science: Materials in Medicine*, **31**, 1–21.

173 de Leeuw, N.H. (2004) Resisting the onset of hydroxyapatite dissolution through the incorporation of fluoride. *Journal of Physical Chemistry B*, **108**, 1809–11.

174 Whitters, C.J., Strang, R., Brown, D., Clarke, R.L., Curtis, R.V., Hatton, P.V. *et al.* (1999) Dental materials: 1997 literature review. *Journal of Dentistry*, **27**, 401–35.

175 Shirkhanzadeh1, M. (1998) Direct formation of nanophase hydroxyapatite on cathodically polarized electrodes. *Journal of Materials Science: Materials in Medicine*, **9**, 67–72.

176 Borum, L. and Wilson, O.C. (2003) Surface modification of hydroxyapatite. Part II. Silica. *Biomaterials*, **24**, 3681–8.

177 Rhee, S.H. and Tanaka, J. (2001) Synthesis of a hydroxyapatite/collagen/chondroitin sulfate nanocomposite by a novel precipitation method. *Journal of the American Ceramic Society*, **84**, 459–61.

178 Asaumi, K., Nakanishi, T., Asahara, H., Inoue, H. and Takigawa, M. (2000) Expression of neurotrophins and their

receptors (TRK) during fracture healing. *Bone*, **26**, 625–33.

179 Chen, J.F., Ding, H.M., Wang, J.X. and Shao, L. (2004) Preparation and characterization of porous hollow silica nanoparticles for drug delivery application. *Biomaterials*, **25**, 723–7.

180 Allen, T.M. and Cullis, P.R. (2004) Drug delivery systems: entering the mainstream. *Science*, **303**, 1818–22.

181 Gao, Z.G., Fain, H.D. and Rapoport, N. (2005) Controlled and targeted tumor chemotherapy by micellar-encapsulated drug and ultrasound. *Journal of Controlled Release*, **102**, 203–22.

182 Kim, H., Matsuda, H., Zhou, H. and Honma, I. (2006) Ultrasound-triggered smart drug release from a poly(dimethylsiloxane)-mesoporous silica composite. *Advanced Materials*, **18**, 3083–8.

183 Cai, Y., Pan, H., Xu, X., Hu, Q., Li, L. and Tang, R. (2007) Ultrasonic controlled morphology transformation of hollow calcium phosphate nanospheres: a smart and biocompatible drug release system. *Chemistry of Materials*, **19**, 3081–3.

184 Kreilgaard, M. (2002) Influence of microemulsions on cutaneous drug delivery. *Advanced Drug Delivery Reviews*, **54**, 77–98.

Keywords

calcium phosphate; nanoparticles; biomineralization; biomaterials; stability; synthesis; application

Index

Nanomaterials for the Life Sciences Vol. 2: Nanostructured Oxides. Edited by Challa S. S. R. Kumar

ISBN: 978-3-527-32152-0